

STRUCTURAL HEALTH MONITORING FOR CIVIL STRUCTURES: FROM THE LAB TO THE FIELD

GUEST EDITORS: PIERVINCENZO RIZZO, YI QING NI, AND JINYING ZHU





Structural Health Monitoring for Civil Structures: From the Lab to the Field

Advances in Civil Engineering

Structural Health Monitoring for Civil Structures: From the Lab to the Field

Guest Editors: Piervincenzo Rizzo, Yi Qing Ni,
and Jinying Zhu



Copyright © 2010 Hindawi Publishing Corporation. All rights reserved.

This is a special issue published in volume 2010 of "Advances in Civil Engineering." All articles are open access articles distributed under the Creative Commons Attribution License, which permits unrestricted use, distribution, and reproduction in any medium, provided the original work is properly cited.

Editorial Board

Abir Al-Tabbaa, UK
Serji N. Amirkhanian, USA
Tom Baldock, Australia
William Burgos, USA
Siu-Lai Chan, Hong Kong
Ghassan Chehab, Lebanon
M. C. Deo, India
Ahmed Elghazouli, UK
Amr Elnashai, USA
Polat Gülkan, Turkey
Muhammad Hadi, Australia
Kent A. Harries, USA
Kirk Hatfield, USA

Bassam A. Izzuddin, UK
Tarun Kant, India
Andreas Kappos, Greece
Bryan W. Karney, Canada
Chungxiang Li, China
Samer Madanat, USA
John Mander,, USA
Amir Mirmiran, USA
Abolfazl Mohammadian, USA
Ayman Mosallam, USA
Abhijit Mukherjee, India
Kenneth W. Neale, Canada
Manolis Papadrakakis, Greece

Ram M. Pendyala, USA
Jean-Herve Prevost, USA
Ser Tong Quek, Singapore
Graham Sander, UK
E. J. Sapountzakis, Greece
Rajan Sen, USA
Khaled A. Soudki, Canada
Farid Taheri, Canada
Cumaraswamy Vipulanandan, USA
Wei-Chau Xie, Canada
Jianqiao Ye, UK
Solomon C. Yim, USA
Ben Young, Hong Kong

Contents

Structural Health Monitoring for Civil Structures: From the Lab to the Field, Piervincenzo Rizzo, Yi Qing Ni, and Jinying Zhu
Volume 2010, Article ID 165132, 1 page

Image-Based Framework for Concrete Surface Crack Monitoring and Quantification, ZhiQiang Chen and Tara C. Hutchinson
Volume 2010, Article ID 215295, 18 pages

An FBG-Based Impact Event Detection System for Structural Health Monitoring, C. S. Shin, B. L. Chen, and S. K. Liaw
Volume 2010, Article ID 253274, 8 pages

Structural Health Monitoring of Precast Concrete Box Girders Using Selected Vibration-Based Damage Detection Methods, Zhengjie Zhou, Leon D. Wegner, and Bruce F. Sparling
Volume 2010, Article ID 280685, 12 pages

Ultrasonic Guided Waves-Based Monitoring of Rail Head: Laboratory and Field Tests, Piervincenzo Rizzo, Marcello Cammarata, Ivan Bartoli, Francesco Lanza di Scalea, Salvatore Salamone, Stefano Coccia, and Robert Phillips
Volume 2010, Article ID 291293, 13 pages

Intelligent Wireless Sensors with Application to the Identification of Structural Modal Parameters and Steel Cable Forces: From the Lab to the Field, Y. Lei, W. A. Shen, Y. Song, and Y. Wang
Volume 2010, Article ID 316023, 9 pages

Structural Health Monitoring Using High-Frequency Electromechanical Impedance Signatures, Wei Yan and W. Q. Chen
Volume 2010, Article ID 429148, 11 pages

Laboratory Evaluation of Time-Domain Reflectometry for Bridge Scour Measurement: Comparison with the Ultrasonic Method, Xinbao Yu and Xiong Yu
Volume 2010, Article ID 508172, 12 pages

Integration of Networks of Sensors and Electronics for Structural Health Monitoring of Composite Materials, Fabrizia Ghezzi, Anthony F. Starr, and David R. Smith
Volume 2010, Article ID 598458, 13 pages

IEEE 802.11-Based Wireless Sensor System for Vibration Measurement, Yutaka Uchimura, Tadashi Nasu, and Motoichi Takahashi
Volume 2010, Article ID 631939, 9 pages

Casing Pipe Damage Detection with Optical Fiber Sensors: A Case Study in Oil Well Constructions, Zhi Zhou, Jianping He, Minghua Huang, Jun He, and Genda Chen
Volume 2010, Article ID 638967, 9 pages

A Neural-Wavelet Technique for Damage Identification in the ASCE Benchmark Structure Using Phase II Experimental Data, Mahmoud M. Reda Taha
Volume 2010, Article ID 675927, 13 pages



Smart Sensing Technologies for Structural Health Monitoring of Civil Engineering Structures, M. Sun,
W. J. Staszewski, and R. N. Swamy
Volume 2010, Article ID 724962, 13 pages

Water and Wastewater Pipe Nondestructive Evaluation and Health Monitoring: A Review,
Piervincenzo Rizzo
Volume 2010, Article ID 818597, 13 pages

Decision Fusion for Structural Damage Detection: Numerical and Experimental Studies, Yong Chen,
Senyuan Tian, and Bingnan Sun
Volume 2010, Article ID 820762, 12 pages

**Truly Distributed Optical Fiber Sensors for Structural Health Monitoring: From the Telecommunication
Optical Fiber Drawing Tower to Water Leakage Detection in Dikes and Concrete Structure Strain
Monitoring**, Jean-Marie Henault, Gautier Moreau, Sylvain Blairon, Jean Salin, Jean-Robert Courivaud,
Frédéric Taillade, Erick Merliot, Jean-Philippe Dubois, Johan Bertrand, Stéphane Buschaert, Stefan Mayer,
and Sylvie Delepine-Lesoille
Volume 2010, Article ID 930796, 13 pages

Editorial

Structural Health Monitoring for Civil Structures: From the Lab to the Field

Piervincenzo Rizzo,¹ Yi Qing Ni,² and Jinying Zhu³

¹ *Department of Civil & Environmental Engineering, Swanson School of Engineering, University of Pittsburgh, Pittsburgh, PA 15260, USA*

² *The Hong Kong Polytechnic University, Kowloon, Hong Kong*

³ *Civil, Architectural and Environmental Engineering Department, University of Texas at Austin, Austin, TX 78712-0273, USA*

Correspondence should be addressed to Piervincenzo Rizzo, pir3@pitt.edu

Received 11 August 2010; Accepted 11 August 2010

Copyright © 2010 Piervincenzo Rizzo et al. This is an open access article distributed under the Creative Commons Attribution License, which permits unrestricted use, distribution, and reproduction in any medium, provided the original work is properly cited.

The field of structural health monitoring (SHM) is rapidly growing to provide robust diagnosis and prognosis of many engineering systems spanning from civil and transportation infrastructures to aerospace and military applications. The development and deployment of a robust SHM scheme is pivotal to ensure the safe and cost-effective operation of any engineering system. SHM is mainly a process of (i) observing or tracing the performance of an engineering structure/system under environmental and operational loads by sensors and instrumentation devices, (ii) evaluating the performance of the structure/system for any development of defect or damage by use of the measured data and analytical tools, and (iii) issuing an alarm when the designated performance criteria are exceeded.

Compared to other engineering fields, the research on SHM is relatively young and therefore most of the work has been conducted at universities or companies that have an interest in research and development.

This special issue of the journal is mainly dedicated to those SHM strategies that after being successfully proven in the laboratory were or are currently deployed in the field for field testing and validation.

This special issue contains twelve research papers and three review articles. The topics dealt with in these papers cover a wide variety of SHM methodologies (in alphabetical order): acoustic emission, electromechanical impedance, fiber optics, guided ultrasonic waves, imaging, time-domain reflectometry, and vibration measurements. These methods are applied to one of the following: (1) detection of damage

in an ASCE benchmark structure, composite materials, concrete structures, dikes, precast concrete box girders railroads, and water and wastewater pipelines; (2) evaluation bridge scour; (3) measurement of stress or strain in oil and gas pipes, concrete structures, or cables; (4) detection of low to medium energy impact in wind turbine blades; (5) detection of water leaks; (6) identification of modal parameters; (7) measurement of vibration of high-rise reinforced concrete building.

Thanks are given to the issue's guest editors Dr. Yi Qing Ni from The Hong Kong Polytechnic University and Dr. Jinying Zhu from The University of Texas for help in soliciting papers, keeping track of submissions, reviews, rebuttals, and followups. Also, special thanks go to Dina Attia for help in the organization of the accepted papers and the final production of the special issue.

*Piervincenzo Rizzo
Yi Qing Ni
Jinying Zhu*

Research Article

Image-Based Framework for Concrete Surface Crack Monitoring and Quantification

ZhiQiang Chen and Tara C. Hutchinson

Department of Structural Engineering, University of California, San Diego, CA 92093, USA

Correspondence should be addressed to Tara C. Hutchinson, tara@ucsd.edu

Received 5 September 2009; Revised 25 December 2009; Accepted 10 March 2010

Academic Editor: Jinying Zhu

Copyright © 2010 Z. Chen and T. C. Hutchinson. This is an open access article distributed under the Creative Commons Attribution License, which permits unrestricted use, distribution, and reproduction in any medium, provided the original work is properly cited.

In the engineering community, nondestructive imaging has been widely used for damage identification by capturing anomalies on the surface or inside of structural elements. In this paper, we focus on one of the most common damage types observed in civil engineering, namely, concrete surface cracks. To identify this type of damage, we propose an image-based framework, whereby optical cameras provide the source images. The framework involves several advanced image processing methods, including: (i) the determination of damage occurrence using time-series images, (ii) the localization of damage at each image frame, and (iii) the geometric quantification of damage. Challenges that may arise when images are obtained in the laboratory or field environment are addressed. Two application examples are provided to demonstrate the use and effectiveness of the proposed approach.

1. Introduction

In the communities of structural health monitoring (SHM) and nondestructive evaluation (NDE), development of an automated structural damage identification solution has been a key objective. Most SHM methodologies rely on sensing of one-dimensional vibration signals, which are used to extract global modal features as signatures of structural integrity by using system identification-based or statistical pattern recognition-based methods [1, 2]; therefore, the awareness of structural damage is usually based on classifying these indirect signatures. Different from these SHM methodologies, NDE methods, especially when 2- or higher-dimensional imaging methods are employed, are able to provide a direct characterization of local structural damage. Depending on the nature of images, spatial extent and spectral variation of damage usually manifest themselves in the captured images. Subsequently, one can employ photogrammetric or image analysis methods to extract these damage characteristics quantitatively.

A variety of imaging technologies have been developed in the NDE community in an effort to detect local structural damage to civil/mechanical systems or components.

Widely used imaging devices include infrared thermography, microwave imaging, acoustic imaging, X-ray imaging, and other radiography-based methods [3]. Common types of structural damage encountered in practice include external or internal cracks, voids, delamination, and ablation, to name a few. To detect these different types of damage, the imaging device must often be customized to capture the characteristics associated with the physical damage; hence the resulting equipment may be expensive. In civil engineering, however, optical imaging by means of commercially inexpensive cameras has become an important, economically feasible utility for recording structural damage. Its use has been extensive in the laboratory setting; however, use in the field has also recently become commonplace due to the low cost of high-resolution optical cameras and associated support equipment. To expedite and automate damage recognition using the captured digital image, computational image processing tools have been attempted to detect or track structural damage in static images or dynamic image frames [4–8].

In this paper, we consider one of the most commonly observed types of damage in civil engineering, namely, concrete surface cracks. Concrete is the most widely used

man-made material for constructed systems, and surface cracks are a reality due to its low tensile strength and environmental sensitivity. As a result, it is well known that a primary damage modality of concrete structures is that of surface cracks. In engineering practice, the identification of concrete surface cracks is an indispensable task in the process of conducting damage- or failure- prevention structural upgrading. Very narrow to hairline cracks, however, as may occur due to the natural process of shrinkage for example, are usually not significant enough to change the global structural integrity of the element hence they are not identifiable using SHM technologies. However, the appearance of these cracks and their propagation in concrete structures may indicate potential inception of degradation of structural integrity or associated softening of the system. In practice, visual inspection of the concrete surface is a common approach. For example, a considerable amount of human effort is devoted to periodic visual inspection of concrete bridges in the United States [9].

In Figure 1, two groups of manually prepared image mosaics are shown. In Figure 1(a), the example surfaces display normal concrete finish whereas in Figure 1(b) concrete surfaces with evident cracks are shown. Generally, the surface objects in optical images display distinct features in terms of their spectral intensities and their topographical patterns. More specifically, the normal concrete surface generally can be viewed as a type of texture with lighter intensities and visually identifiable spotted air pockets. Cracks, on the other hand, are usually darker with approximately uniform spectral intensities. In addition cracks in images can be geometrically described as elongated “narrow” 2D objects with closed boundaries. From an image analysis point of view, the concrete surface in images provides rich and diverse patterns for exploring different analysis methods.

1.1. Problem Definition and Previous Work. Detection of cracks with images of concrete surfaces has been explored by many researchers using a variety of methods. However, a comprehensive image-based damage identification framework is still lacking in the literature. Such a framework needs to provide a complete solution to the final goal, which is damage quantification. Herein, we define damage identification as a three-level probing process, which includes

- (1) temporal monitoring of the inception or propagation of damage using time-series images (the occurrence determination problem);
- (2) detection of the boundary of damage at each image frame (the localization problem);
- (3) quantitative, geometric characterization of individual damage objects (the quantification problem).

If only static images instead of multiple images in a temporal sequence are available, identification reduces to the problems of damage boundary localization and damage quantification (Levels 2 and 3). In previous work, efforts have stressed more on boundary detection [4, 5, 10–12]. Among these efforts, the simplest solution is to determine the intensity gradients across the image, and boundaries between

different image objects are extracted based on local variations of gradient magnitudes and orientations. This detection process in image processing is termed *gradient-based* edge detection. Common gradient-based edge detectors include the Roberts, Sobel, Prewitt, and Canny edge detector [13]. In these detectors, the approximation of intensity gradients is based on the concept of convolution with a set of directional derivative masks at a specified scale. To deal with the multiresolution nature of edges, researchers have proposed an automatic scale-selection approach [14]; however, this approach has not been investigated in the crack detection literature. Another approach to overcome the multiresolution problem is to use wavelet-based image transform. Wavelets are special basis functions, localized in both spatial and frequency domains. Short-duration wavelets can isolate fine variations of image intensity while long-duration wavelets can isolate coarse variations. Image structures, such as edges, at different scales are obtained by computing wavelet coefficients at different resolutions [15]. Subsequently, the obtained wavelet coefficients are thresholded to determine edges at different scales.

1.2. Scope of This Work. Regardless of the previous methods adopted, a major difficulty lies in the postprocessing steps. When geometric quantities of detected cracks are to be extracted, the processing usually becomes a tedious step with many manual interventions. This is due to the lack of a geometric model for the cracks. On the other hand, there is no previous work that has addressed an image-based monitoring problem in the context of concrete surface crack identification. In what follows, first, we discuss the implementation challenges when raw laboratory or field images are used. Subsequently, a unified framework is proposed, which involves (i) a manifold-distance computing algorithm for image-based damage monitoring and (ii) a level-set active contour model-based method for damage boundary detection and geometric quantification. To demonstrate the use of the proposed framework, two application examples are presented. One example uses a field image, and the other uses time-series images taken in a controlled laboratory environment. The later provides direct comparison with analog measurements for validation of the analysis results.

2. Practical Challenges

Although image samples shown in Figure 1 are valuable in the context of building library of damage patterns and testing new crack detection methods, significant practical difficulties exist when raw images captured in the laboratory or field are considered. Considering Figure 2, an image taken in the field of a shear crack at a bridge abutment, although it is visually easy to identify the crack in the image, many noisy artifacts are found, which prevent from realizing an automated, algorithm-based identification. These noisy artifacts include, for example, decoloration, occlusion, and solar illumination-related photometric variabilities (e.g., shadows). In addition, the relative large size of image compared to the cracked sub-region impedes a computationally efficient implementation.

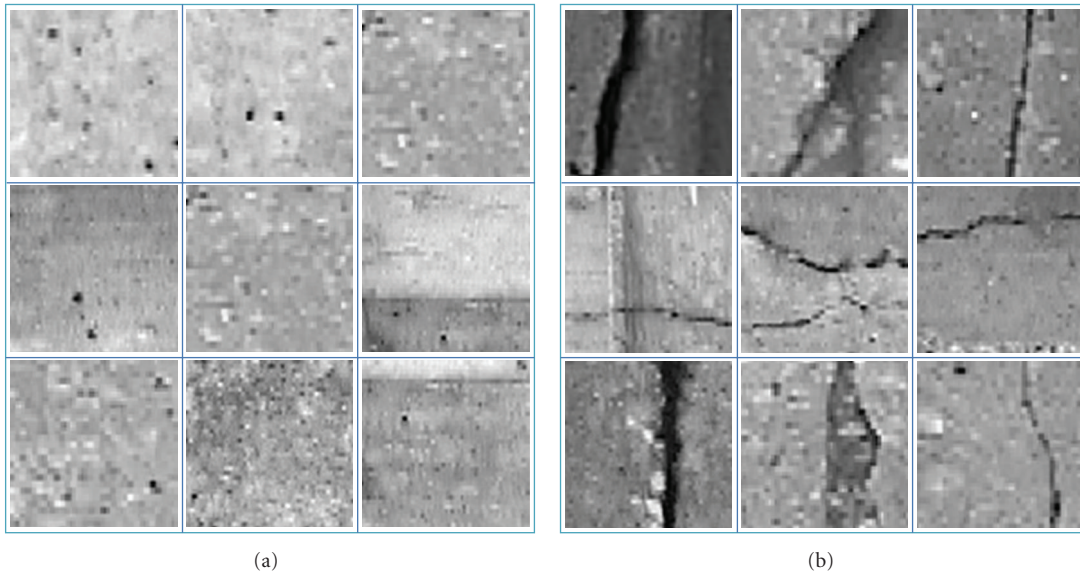


FIGURE 1: Example concrete surface images: (a) concrete surfaces with normal finish; (b) concrete surfaces with evident cracks.



FIGURE 2: A field image taken under the over-crossing bridge of Wailua river, Kapaa, Hawaii, which shows a long crack on the bridge abutment.

Even in a controlled environment, for example, laboratory testing, although test configuration is adjustable, the optimal one is often not for imaging. Hence, use of images for a quantitative damage identification faces significant challenges as well. Figures 3(a) and 3(b) show two images, which display the same concrete wall specimen that has been subject to biaxial loading at two different cyclic displacement peaks [16]. From Figure 3(a) to Figure 3(b), it can be seen that additional cracks were developed due to the increased displacement demand. One may attempt to use a boundary detection method to locate the cracks in either of the two images. However, it is not difficult to reason that the obtained boundaries would include many falsealarms (e.g., those associated with the diagonal displacement transducers), thereby preventing from an automated damage quantification.

3. Proposed Framework

A straightforward approach to addressing the aforementioned adverse factors may be achieved by performing nonsupervised image segmentation. However, in most image segmentation methods, the number of image modalities must be known a priori [17]. Therefore, for a field image as shown in Figure 2 where the number of different texture regions is arbitrary, segmentation approach is not practical.

This difficulty may be solved if continuous imaging through routine inspection is conducted, or more ideally, permanent camera sensors are installed to monitor the surface change of a critical structural component. Therefore, multitemporal images for the same structural surface can be obtained. This situation admits a digital change detection-based solution [18]. The applicability of a change detection method is based on a reasonable assumption that two temporally adjacent images may only differ in illumination-induced photometric distortion (e.g., solar or laboratory illumination variations), structural motion or camera motion-induced geometric distortion, and most importantly, structural damage. Meanwhile, most of the image artifacts in the scene, including decoloration and other texture objects, remain in the image sequence; hence, simple differencing operations can theoretically remove their influence if the image distortions are handled appropriately. To deal with geometric or photometric distortions, relatively simple models can be used; if these models or model parameters are estimated, a measure that is sensitive to the occurrence of structural damage by distortion can be subsequently extracted (i.e., distortion-invariant measure). As shown in the later formulation, this is the basic idea underlying the proposed manifold distance-based structural damage monitoring.

From the reasoning above, one can see that an appropriate modeling for geometric or photometric distortions

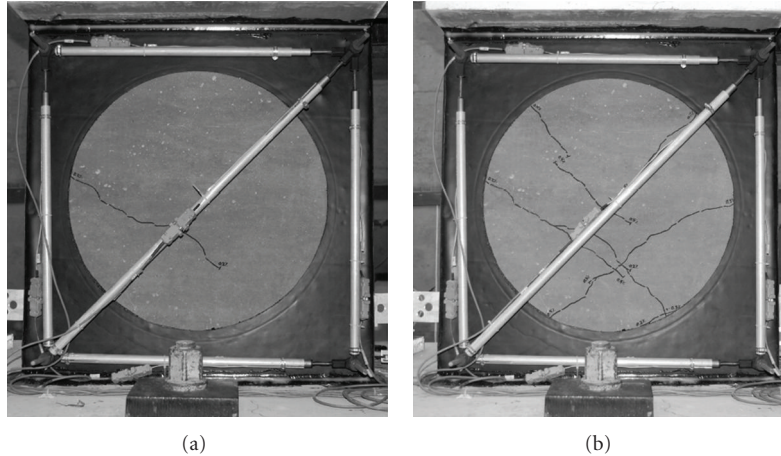


FIGURE 3: A laboratory biaxial test specimen under cyclic loading (a) at drift ratio of $\gamma = 0.21\%$ and (b) $\gamma = 0.41\%$ (images courtesy of Soppe and Hutchinson, [16]).

becomes the critical path in realizing a distortion-invariant damage detection. For mitigating illumination-induced photometric distortion, a common technique is normalization of spectral intensities in small image regions through subdividing the image domain to many small subdomains. For geometric distortion, the prevailing adverse factor that complicates this concept is the motion of structural objects. For a structure under loading, any point within the structure potentially undergoes some spatial motion across time. To extract a robust feature representing crack damage from a time series of images, modeling the motion of structural objects in the images is a critical issue.

With the background information introduced in the above, we propose an image-based structural damage monitoring and quantification framework. As illustrated in Figure 4, the proposed framework has three operational components. First, image acquisition is conducted. The success of this element relies upon reliable assembly of hardware and careful design of acquisition software, which is not in the scope of this paper. It should be noted that computing is necessary in this step, which usually includes camera calibration and image correction. When a 3D scene is projected into an image plane, geometric distortion is associated with the projection determined by the intrinsic and extrinsic parameters of the digital camera [17]. In practice, a process known as *camera calibration* has to be conducted. Once calibration parameters are estimated, acquired images can be easily corrected to remove this distortion. In the following, we describe the subsequent two key elements to the framework, which are *temporal image-based damage monitoring* and *geometric image-based quantification of damage*.

4. Manifold-Distance Concrete Crack Monitoring Using Time-Series Images

We approach our image-based damage monitoring problem as a temporal change detection problem, wherein structural damage is treated as a type of local anomaly with

its amount measurable between temporal image frames. Due to the aforementioned adverse effects of structural motion in images, a seemingly straightforward approach—image differencing—is not appropriate since it requires strict spatial alignment between the temporal image pair. A simple remedy is to first extract the underlying motion parameters, then with the estimated motion parameters, the temporal image frames can be coregistered, such that image differencing can be performed, and motion-invariant features useful for representing concrete cracks can be defined. This approach was proposed in our previous work in [19]. In this section, we will briefly present this combined motion estimation and feature extraction procedure.

4.1. Assumptions about Structural Motion in Images. Theoretically, the displacement field of the structural member is governed by the material's stress-strain relation and the geometric boundary condition of the structural member, which may be in a form or a combination of bending, axial, shear deformation, and rigid-body motion. However, the motion of the structural members cannot be fully captured without loss of accuracy due to the limit of image resolution. Suppose that a resolution of 1 mm/pixel may suffice for the purpose of monitoring crack damage for concrete structures. With this resolution and a common image size of 480×640 , the field of view (FoV) on the surface of the target member is approximately a $480 \times 640 \text{ mm}^2$ rectangular zone. For normal-weight concrete under compression, the ultimate compressive strain is about 0.003 [20]. At this limit state, the maximum relative deformation due to compression within this FoV is about 1.92 mm. Since the original image domain is usually divided into multiple subdomains (e.g., 10×10 subdomains) in order to minimize photometric distortions, the maximum within a subdomain is much less than 1 mm. A direct consequence is that the relative deformation captured in an image subdomain can be reasonably assumed to be negligible. It is noted that the above reasoning is based on

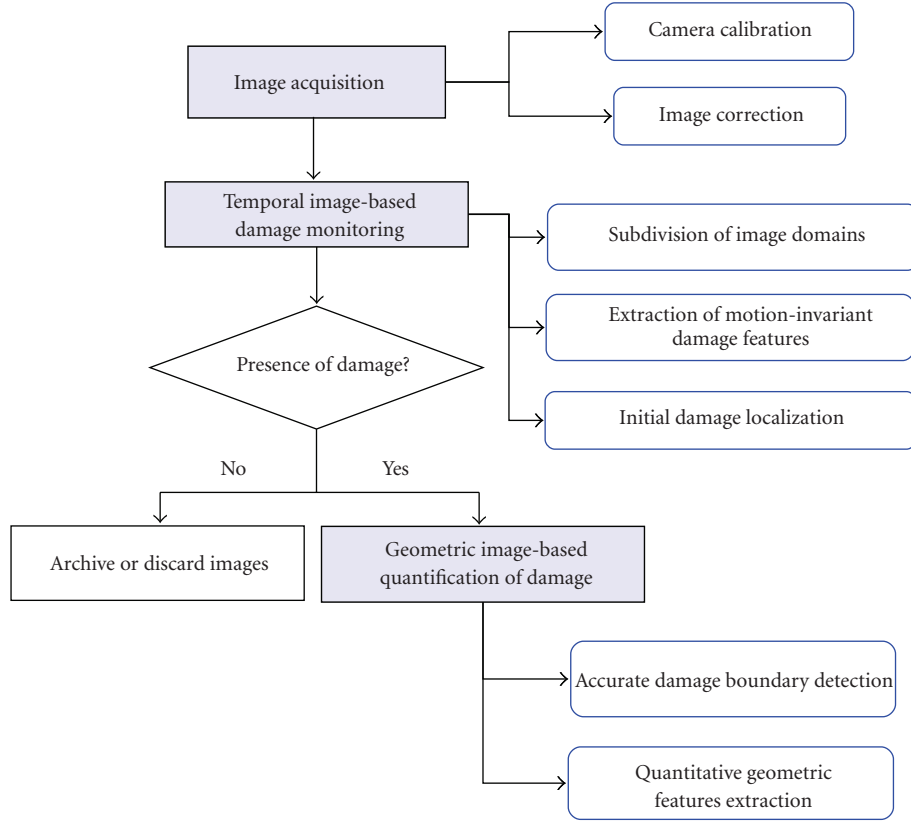


FIGURE 4: Proposed image-based structural damage monitoring and quantification framework.

the maximum compressive strain; however, cracks are due to local extensive tensile strain, which is much smaller. This strengthens that local deformation is generally not captured by optical cameras.

We also limit the study in this paper to consider the structural motion plane only approximately parallel with the image plane, resulting in a linearly scaled planar motion in the image domain. Therefore, we assume that the structural motion considered is rigid-body motion only, which includes the two orthogonal translations and one in-plane rotation.

4.2. Formulation of Manifold Distance Measure. To present the formulation of both motion estimation and damage feature extraction using a time series of images, we use two notations to describe an image acquired at time t . First, $u(\mathbf{x}, t)$ is used to denote a continuous image function or an intensity value at the location \mathbf{x} and the time t . Second, if a digital image is treated as a vector, it is denoted as $\mathbf{u}(t)$ with dimension of N indicating the number of pixels. For a sequence of image vectors across time, they can be denoted by $\{\mathbf{u}(t_0), \mathbf{u}(t_1), \dots, \mathbf{u}(t_i), \dots\}$.

Given a current intensity value at time t_i by $u(\mathbf{x}, t_i)$ and its temporally previous value by $u(\mathbf{x}, t_{i-j})$ ($j \geq 1$), the current intensity value $u(\mathbf{x}, t_i)$ can be obtained by evolving $u(\mathbf{x}, t_{i-j})$ through a spatial transformation of the coordinates $\mathbf{x} = (x, y)$ if there is no photometric transformation. Without

loss of generality, we use $u^t(\mathbf{x})$ to replace $u(\mathbf{x}, t_i)$ and $u(\mathbf{x})$ to replace $u(\mathbf{x}, t_{i-j})$ for notational simplicity. Therefore, the above transformation is written as

$$u^t(\mathbf{x}) = u[\phi(\mathbf{x}, \boldsymbol{\theta})], \quad (1)$$

where the function $\phi : \mathbb{R}^2 \times \mathbb{R}^M \rightarrow \mathbb{R}^2$ defines a generic transformation model $\phi(\mathbf{x}, \boldsymbol{\theta}) = [\phi(\mathbf{x}, \boldsymbol{\theta}), \psi(\mathbf{x}, \boldsymbol{\theta})]^T$ parameterized by $\boldsymbol{\theta}$ (an $M \times 1$ vector quantity with $M \ll N$). This expression in the visual tracking literature is traditionally called the *image constancy assumption* [21]. The parameterized transformation model $\phi(\mathbf{x}, \boldsymbol{\theta})$ is differentiable with respect to both \mathbf{x} and $\boldsymbol{\theta}$. Additionally, an initialization is usually adopted for $\boldsymbol{\theta} = \mathbf{0}$, which is $u[\phi(\mathbf{x}, \mathbf{0})] = u(\mathbf{x})$. If the assumed transformation holds globally in the spatial domain \mathcal{X} , then any image can be fully determined by another image and the spatial transformation model $\phi(\mathbf{x}, \boldsymbol{\theta})$ between them. Formally, images like these can be treated as a lower-dimensional manifold, denoted by $\mathbf{u}(\boldsymbol{\theta})$, embedded in the original high-dimensional observation space \mathbb{R}^N . In this case, the intrinsic dimension of such a manifold space is the number of motion parameters M , which has six parameters for an affine transformation model or three parameters for a rigid-body motion model. Note that the intrinsic dimension M is generally far less than the dimension of the image observation space N .

The geometric structure of an image manifold is usually augmented and complicated by some lighting-induced photometric perturbations and the development of cracks across the image sequence. Technically, the photometric perturbation can be modeled by some parametric intensity transformation [22]. As a result, more intrinsic dimensions are added into the previous M dimensions. In this paper, we accept the fact that lighting is time varying across the image sequence however, we assume that it is statistically stationary within a small image domain at one acquisition time. Therefore, this type of perturbation can be removed through a simple intensity standardization (i.e., subtracting the sample mean intensity from the raw image) to remove constant variation. Cracks may also be viewed as a sort of geometric deformation occurring at some intrinsic dimensions. However, the irregular topological shape of cracks in the image domain indicates that they have highly nonlinear curvature locally in both observation and manifold spaces. Therefore, it is hard to find an explicit parametric model defined globally in the image domain to represent the cracks.

Leaving the potential crack development not modeled at a pixel \mathbf{x} , we treat it as a residue expressed by $|u[\phi(\mathbf{x}, \theta^*)] - u^t(\mathbf{x})|^2$ and denote the total residue over the spatial domain by $r(\theta^*, t) = (\int_{\mathcal{X}} d\mathbf{x} |u[\phi(\mathbf{x}, \theta^*)] - u^t(\mathbf{x})|^2)^{1/2}$, where θ^* contains the ground truth values of motion parameters that fully accounts for the spatial transformation occurring in the image frames from \mathbf{u} to \mathbf{u}^t . Ideally, if there are no cracks developing at time t (more exactly, within a duration from t_{i-j} to t_i), but only spatial transformation, the total residue will yield a value of zero. If crack damage does occur, the total residue should be larger than zero, and the same amount of cracks corresponds to the same value of the total residue yet with possibly different motion parameters θ^* s. Therefore, $r(\theta^*, t)$ is theoretically an ideal feature of crack occurrence that is invariant to the underlying motion of the structural component.

If one replaces θ^* with an unknown motion parameter vector θ in the previous definition of the total residue, a parameterized total residue is yielded, $r(\theta, t)$, which is essentially a varying Euclidean distance (ED) between a parameterized image vector with a base at \mathbf{u} and the reference image vector \mathbf{u}^t . On the other hand, if the image vectors are viewed in the manifold space, then this distance metric quantifies the distance between the manifold $\mathbf{u}(\theta)$ and the reference point \mathbf{u}^t . It is reasoned that given some potential crack occurrence left unmodeled and a certain amount of motion determined by θ^* , the quantity $r(\theta^*, t)$ is therefore the minimum distance between $\mathbf{u}(\theta)$ and \mathbf{u}^t , which is called *manifold distance* (MD) in the literature [23, 24]. In this paper, we define an MD measure at time t given \mathbf{u} and \mathbf{u}^t :

$$\text{MD}(t) = r(\theta^*, t) \equiv \inf \{ r(\theta, t) \mid \theta \in \mathbb{R}^M \}. \quad (2)$$

In particular, if θ^* is equal to $\mathbf{0}$, that is, there is no spatial motion, MD(t) degrades to the constant Euclidean distance between \mathbf{u} and \mathbf{u}^t , which is $\text{ED}(t) = (\int_{\mathcal{X}} d\mathbf{x} |u(\mathbf{x}) - u^t(\mathbf{x})|^2)^{1/2}$. Therefore, the seeking of a motion-invariant crack damage feature entails a proper estimate of θ^* , which

leads to the following optimization problem:

$$\text{minimize} \quad r^2(\theta, t) = \int_{\mathcal{X}} d\mathbf{x} |u[\phi(\mathbf{x}, \theta)] - u^t(\mathbf{x})|^2, \quad (3)$$

$$\text{subject to} \quad u[\phi(\mathbf{x}, \mathbf{0})] = u(\mathbf{x}). \quad (4)$$

4.3. Estimation of Motion Parameters. The objective function $r^2(\theta, t)$ in (3) unlikely owns a convex surface due to the highly nonlinear nature of an image function in terms of both \mathbf{x} and θ . To address this, one may approximate the functional $u[\phi(\mathbf{x}, \theta)]$ in the manifold space at $\theta = \mathbf{0}$ by carrying out a Taylor series expansion by considering the parameterized model $\phi(\mathbf{x}, \theta)$. Suppose that the translation vector is denoted by $(\theta_1, \theta_2)^T$, and the rotation angle is θ_3 , which constitutes the motion parameter vector $\theta = (\theta_1, \theta_2, \theta_3)^T$. The motion function is therefore

$$\begin{aligned} \phi(\mathbf{x}, \theta) &= \begin{pmatrix} \cos \theta_3 & \sin \theta_3 \\ -\sin \theta_3 & \cos \theta_3 \end{pmatrix} \begin{Bmatrix} x \\ y \end{Bmatrix} + \begin{Bmatrix} \theta_1 \\ \theta_2 \end{Bmatrix} \\ &= \begin{Bmatrix} \theta_1 + x \cos \theta_3 + y \sin \theta_3 \\ \theta_2 - x \sin \theta_3 + y \cos \theta_3 \end{Bmatrix} = \begin{Bmatrix} \phi(\mathbf{x}, \theta) \\ \psi(\mathbf{x}, \theta) \end{Bmatrix}. \end{aligned} \quad (5)$$

With some steps of vector calculus computation, one arrives at an approximate form of (3):

$$\begin{aligned} \overline{r^2}(\theta, t) &= C_0 + C_1\theta_1 + C_2\theta_2 + C_3\theta_3 + C_4\theta_1^2 + C_5\theta_2^2 + C_6\theta_3^2 \\ &\quad + C_7\theta_1\theta_2 + C_8\theta_1\theta_3 + \cdots + C_9\theta_2\theta_3 + C_{10}\theta_1\theta_3^2 \\ &\quad + C_{11}\theta_2\theta_3^2 + C_{12}\theta_3^3 + C_{13}\theta_3^4, \end{aligned} \quad (6)$$

where the constant coefficients $C_0 \sim C_{13}$ are integrations over the image domain \mathcal{X} . Detailed derivation of these constant coefficients may be found in [19]. The approximate squared residue in (6) is a fourth-order polynomial; hence it provides a tractable basis for studying the solution of this optimization problem defined in (3) and (4). Although analytical forms of the solution are available, they are extremely lengthy. A more common approach in practice is to use the standard Newton method for the numerical solutions, which is expressed an iterative procedure:

$$\theta^{(k+1)} = \theta^{(k)} - \mathbf{H}^{-1}(\theta^{(k)}, t) \mathbf{g}(\theta^{(k)}, t), \quad (7)$$

where $\mathbf{H}(\cdot)$ and $\mathbf{g}(\cdot)$ are the Hessian matrix and the gradient vector of (6) with respect to θ , respectively, and their analytical forms are found in [19]. Upon convergence of the iteration, the MD measurement is computed by

$$\text{MD}(t) \simeq [\overline{r^2}(\hat{\theta}, t)]^{1/2}, \quad (8)$$

where $\hat{\theta}$ is the estimated motion parameter vector from (7).

If one is given a time series of images $\{\mathbf{u}(t_0), \mathbf{u}(t_1), \mathbf{u}(t_2), \dots, \dots\}$, there are two ways to compute a sequence of time-varying MD measurements. First, one can compute an MD measurement for any temporally adjacent image frames, that is, $\text{MD}(t_i)$ between $\mathbf{u}(t_{i-1})$ and $\mathbf{u}(t_i)$. In this paper, MD measurements resulting from this method can be used to monitor the inception of concrete cracks. Another method is that upon cracks having appeared at time t_i , the subsequent MD measurements at time t_j are all computed relative to the time t_i , that is, $\text{MD}(t_j)$ is obtained based on $\mathbf{u}(t_i)$ and $\mathbf{u}(t_j)$ where t_i is fixed. This approach can be used to monitor the continuous growth of cracks.

4.4. Damage Localization. The MD measurement computed at an arbitrary time in essence offers a *lump sum* indication of occurrence for the concrete cracks in an image domain. However, if the image domain is relatively large, it does not provide an indication regarding the location of cracks. In this paper, we localize concrete cracks in images by dividing the 2D image domain into multiple subdomains before computing the MD measurements. Another advantage of this treatment is that it can minimize the disturbance of photometric distortions. The criterion for the subdivision is that the size of the subdomain should be much larger than the potential motion change between two temporal image patches upon which an MD measurement is computed. In practice, one needs a priori knowledge about the magnitude of the potential motion change in order to make such subdivision.

Suppose that the image domain is divided into $K \times L$ subdomains, therefore, a matrix ($K \times L$) of MD measurements can be obtained at an arbitrary acquisition time. With the MD measurements at different times, one can perform a nonsupervised outlier analysis to determine which MD measurement statistically guarantees an instance of crack occurrence. The outlier analysis, in its simplest form, is implemented by assuming that the underlying features follow a normal distribution (for more rigorous treatment about modeling the distribution of outliers, one may refer to [25]). The subdomains that are determined statistically to have crack occurrence hence provide a description of the initial location of damage.

5. Level-Set Representation of Concrete Cracks and Quantification

The image-processing procedure presented in the previous section offers a means of monitoring the inception or propagation of structural damage; meanwhile, a simple method for approximately locating the potential cracks is given. In the following, a method for geometric boundary detection and detailed damage quantification of concrete surface cracks is presented, in which we proposed a level-set active contour model-based approach for this purpose.

5.1. Active Contour Models for Boundary Detection. The basic idea in active contour models is to evolve a curve subject to constraints in a given image, and eventually the curve

converges to the closed boundary of objects in the image. Since the invention of the classical active contour model [26], many geometric versions have been proposed, such as the Geodesic active contour model [27]. In the expressions of the resulting partial differential equations in these contour models, a stopping function is used to stop the curve evolution, which is usually defined based on image gradients.

In cases of image-based detection of concrete cracks, another cue is that concrete surface images can be approximated by piecewise, multiphase cartoon images. For a cracked concrete surface image, the simplest form contains two phases, the normal background or the cracked areas. This implication inspires us to use the Mumford-Shah segmentation model [28], which is further extended by Chan and Vese in a level-set framework [29]. A level-set method is a general technique for evolving curves (surfaces) that undergo complex topographical changes such as merging and pinching [30, 31]. It has been proven efficient in recent years in problems ranging from tracking, modeling, and simulating motion of dynamic surfaces in the fields of graphics, image analysis, fluid dynamics, fracture mechanics, and optimal topology control.

The Chan-Vese level-set active contour model can detect object boundaries without relying on image gradients, eliminating the need to define a gradient-based stopping function. In addition, the most appealing aspect of the Chan-Vese model is that it has a level-set representation, which offers the following benefits: (i) automatic handling of topographical merging and pinching of evolving contours, (ii) detection of interior contours, (iii) initial contours can be anywhere in images, and (iv) its level-set representation offers the capability to extract geometric quantities of concrete damage within a formal mathematical framework.

5.2. Level-Set Representation. Suppose that an original concrete surface image is denoted by $u_0(x, y)$ defined in a 2D domain Ω ; an evolving curve attempting to locate objects of interest in the image is denoted by Γ ; one further denotes the open sub-domains inside and outside of Γ by Ω^+ and Ω^- , respectively. In the spirit of level-set methods, the curve Γ is embedded as the zero level set of a Lipschitz continuous function $\phi : \Omega \rightarrow \mathbb{R}$, denoted by $\{\phi(x, y) = 0\}$. Correspondingly, Ω^+ is written as $\{\phi(x, y) > 0\}$ and Ω^- as $\{\phi(x, y) < 0\}$. Let $H(\cdot)$ be the Heaviside function. The energy Chan-Vese functional is

$$\begin{aligned} E[c_1, c_2, \phi(x, y, t) \mid u_0(x, y)] &= \int_{\Omega} |u_0(x, y) - c_1|^2 H(\phi) dx dy \\ &+ \int_{\Omega} |u_0(x, y) - c_2|^2 [1 - H(\phi)] dx dy \\ &+ \mu \int_{\Omega} |\nabla H(\phi)| dx dy, \end{aligned} \quad (9)$$

where c_1 and c_2 are the average intensities across the inside (Ω^+) and the outside (Ω^-) regions, μ is the associated length scale, and t is a pseudo time variable. Generally, the parameter μ controls the smoothness of the curve; therefore

$\mu|\Gamma|$ is a regularizer in the above functional. The time-dependent (a pseudocomputational time will be introduced in evolving Γ) constants c_1 and c_2 vary as the curve evolves in $u_0(x, y)$.

By minimizing (9) with respect to c_1 , c_2 , and ϕ , one arrives at the following Euler-Lagrange equations:

$$\frac{\partial \phi}{\partial t} = \delta(\phi) \left[\mu \nabla \cdot \left(\frac{\nabla \phi}{|\nabla \phi|} \right) - |u_0(x, y) - c_1|^2 + |u_0(x, y) - c_2|^2 \right], \quad (10)$$

$$c_1(t) = \frac{\int_{\Omega} u_0(x, y) H(\phi) dx dy}{\int_{\Omega} H(\phi) dx dy}, \quad (11)$$

$$c_2(t) = \frac{\int_{\Omega} u_0(x, y) [1 - H(\phi)] dx dy}{\int_{\Omega} [1 - H(\phi)] dx dy}, \quad (12)$$

where δ is the Dirac delta function defined by $\delta(\phi) = (d/d\phi)H(\phi)$. With the initial contour denoted by $\phi(x, y, 0) = \phi_0(x, y)$, one can see that (10)–(12) construct a recursive procedure when solving for the implicit level-set function ϕ .

5.3. Extraction of Geometric Properties. In this paper, the numerical schemes for solving (10) are not included; one may refer to [32] for more details. To summarize, by iteratively integrating (10) numerically, the level-set function $\phi(x, y, t)$ will eventually converge at a time, denoted by t_e ; hence, we obtain the final level-set function $\phi_e = \phi(x, y, t_e)$. Many geometric quantities of detected cracks, such as perimeter (total length of closed boundary), area, curvature, and normal direction of crack boundaries, can be computed directly with ϕ_e . However, we believe that the area, perimeter, and width are of primary engineering interest.

5.3.1. Area and Perimeter of Cracks. In the Chan-Vese model, the computation of areas and perimeters of detected objects has been embedded in (10)–(12): the area $A = \int_{\Omega} H(\phi_e) dx dy$, and the perimeter $P = \int_{\Omega} |\nabla H(\phi_e)| dx dy$. However, for the purpose of computing areas and perimeters, a more “smeared-out” approximation will offer more numerical accuracy, which is

$$H_{\theta}(\phi) = \begin{cases} 1 & \text{if } \phi > \theta, \\ 0 & \text{if } \phi < -\theta, \\ \frac{1}{2} \left[1 + \frac{\phi}{\theta} + \frac{1}{\pi} \sin\left(\frac{\pi\phi}{\theta}\right) \right] & \text{if } |\phi| \leq \theta, \end{cases} \quad (13)$$

where the parameter θ is selected comparable to the used space step. In the work of Osher and Sethian [31], $\theta = 1.5h$ is recommended.

5.3.2. Extraction of Crack Width. Another important geometric quantity of engineering interest is crack width. However, unlike the computation of areas or perimeters for concrete cracks, the extraction of crack width is a nontrivial problem. First, the concept of *width* is empirical. Recall that

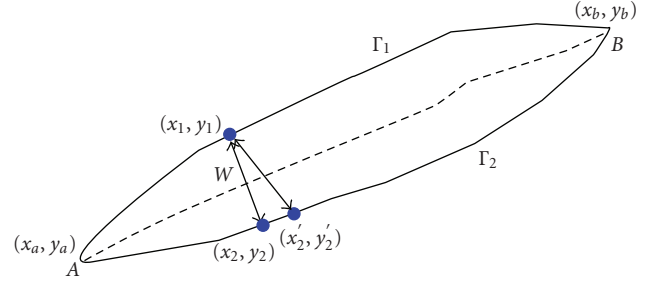


FIGURE 5: Definition of crack width: the distance from (x_1, y_1) to (x_2, y_2) is the shortest compared with others, for example, from (x_1, y_1) to (x'_2, y'_2) ; the former defines the crack width w at (x_1, y_1) .

we adopt a nonrigorous way to describe cracks, namely, cracks in images are spatially narrow, elongated objects with strong contrast with the background, where the qualitative terms “narrow” or “elongated” are related to “width” without explicit definitions. In engineering practice, first, one needs to manually identify two end points for a single crack or multiple end points for a crack with a complex pattern; then by starting any of these end points, widths can be measured along the cracks continuously. To compute the crack widths analytically, a rigorous definition for crack width is necessary.

Considering a simple case (Figure 5), where a crack, with its closed boundary denoted by Γ , has two end points $A : (x_a, y_a)$ and $B : (x_b, y_b)$, therefore, the boundary of this crack can be split into two open boundaries, Γ_1 and Γ_2 , which both start at A and end at B . The width w at a pixel (x_1, y_1) along one side of the crack boundaries, say, Γ_1 , is the shortest Euclidean distance (L_2 distance) from (x_1, y_1) to a point (x_2, y_2) in the other side of boundaries Γ_2 . For cracks with complex patterns, for example, a continuous crack with “T”, “+” shapes, or other multiple angle splits, more than two end points have to be specified. One can break these cracks into several segments, wherein each segment has two end points, hence two sides of boundaries. The Euclidean distance-based definition for widths associated with these crack segments can be defined similarly.

5.3.3. Automated Extraction Method. The preceding definition of crack width may give rise to an exact solution to compute widths with known end points for a given crack. However, as the topographical patterns of cracks become more complex, the manual intervention for specifying the possible end points will be more tedious. Herein, we propose an approximate method for width extraction. This approximate method relies on the extraction of centerlines of detected cracks as well as the construction of a so-called signed distance function (SDF). An SDF, denoted by $\varphi(x, y)$, defines the distance values from (x, y) to the evolving zero level-set $\Gamma(t) = \{\phi(x, y, t) = 0\}$, which are positive inside of $\Gamma(t)$ and negative outside of $\Gamma(t)$, and satisfies $|\nabla \varphi| = 1$ everywhere. The steady state of $\varphi(x, y)$ is obtained through solving

$$\frac{\partial \varphi}{\partial \tau} + \text{sgn}(\phi) (|\nabla \varphi| - 1) = 0, \quad (14)$$

where $\text{sgn}(\phi) = 2H(\phi) - 1$ is a signum function, and τ is another pseudotime variable added in the dependents of ϕ . With the initial condition $\phi(x, y, 0) = \phi(x, y, t)$, the zero level set $\Gamma(t)$ will be preserved during evolving $\phi(x, y, \tau)$. For centerline extraction, although a level set-based extraction of centerlines is possible [33], we employ a simple morphological skeleton operator that can preserve the connectivity of the original topographical patterns [32]. Theoretically, for objects with general topographical shapes, morphological skeletonization does not usually produce the ideal centerlines; nonetheless, for narrow, elongated 2D objects, such as cracks, morphological skeletonization is sufficiently accurate.

The proposed width extraction method is summarized in the following:

- (1) from $H_\theta(\phi_e) > 0.5$, a binary image $b(x, y)$ is obtained, wherein the detected cracks are marked by unity;
- (2) perform skeletonization on $b(x, y)$, and a new binary image $c(x, y)$ is produced wherein the centerlines are unity;
- (3) solve for an SDF $\psi(x, y)$ using (14) with $\psi(x, y, 0) = \text{sgn}(\phi) = 2H_\theta(\phi_e) - 1$;
- (4) the shortest distances from the centerlines to the zero level set are obtained by a simple Boolean operation, which is denoted by $d(x, y) = \psi(x, y)$, for all $(x, y) \in \{(x, y) \mid c(x, y) = 1\}$, the widths along cracks are approximated by $w(x, y) \simeq 2d(x, y)$.

In this approximate method, there is no restriction to the complexity of topographical patterns of cracks as well as no need to manually specify the end points of cracks. Regarding the accuracy of this method, the approximate widths will be slightly greater than the exact values for a simple crack similar to Figure 5.

6. Application I: Field Image

In routine field inspection of concrete structures, a large amount of digital images are usually collected. Well-organized image archives as well as text-based documents provide an informative means of reporting the structural integrity of civil infrastructure objects. However, these field images are mostly used as a visual media only—readers or analysts read the images visually and may subjectively correlate visual identification with other engineering knowledge. To obtain more quantitative information, an effective image analysis method is needed. In what follows, we present a comparative study to demonstrate that the proposed framework provides a quantitative image-mining solution to this problem, which is unparalleled compared to other non-contour-based image analysis methods.

Figure 6 displays a field image of the surface of a concrete region that has clearly observed cracks. One first notices that the surface textures vary spatially showing different modalities (e.g., lighter versus darker texture). Second, there are a large number of small air pockets on the surface.

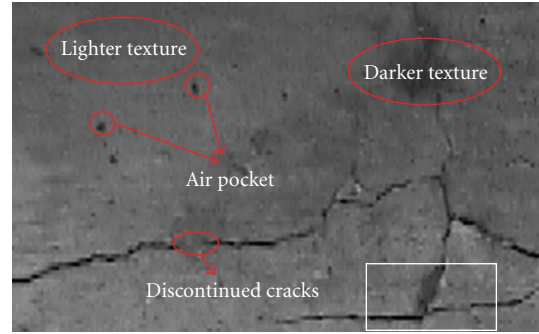


FIGURE 6: Example image taken from a concrete component in the field. Note the non-crack image artifacts annotated. The subregion in the bottom-right bounding box is used to illustrate the proposed level-set detection approach.

Finally, cracks are not fully connected; rather discontinuities are observed between crack segments. The presence of these artifacts results in significant adverse effects and prevents from realizing an automatic identification of concrete cracks.

We first attempt to use a traditional approach. In Figure 7, two crack detection results are shown using the classical Canny edge detector [34]. The two results are presented using different analysis parameters. It is seen that the two results are dramatically different, and it is very difficult to differentiate the boundaries of the concrete cracks from the noisy edges in the background. Although some statistical methods can mitigate this parameter selection problem (e.g., [35]), the critical difficulty that prohibits subsequent geometric quantification is that the detected edges are merely nonclosed segments rather than closed contours. This difficulty exists similarly if other non-model-based edge detectors (e.g., a Sobel detector or wavelet transform-based detectors) are used.

The proposed level-set active contour approach can avoid this difficulty. Before applying this approach, we note that the purpose of crack identification in this situation is to obtain subsequent quantitative characteristics of the cracks rather than to solely determine the presence of the cracks (i.e., the analyst knows that there are cracks in the image). Therefore, we assume that the analyst interactively selects a region of interest (ROI) in the image domain then seeks a quantitative characterization. In Figure 8(a), such an ROI is shown, which contains multiple intersecting cracks. Starting with the initialization in Figure 8(b), we apply the level-set based detection, which iteratively converges to the final detected image contours as shown in Figures 8(c), 8(d), and 8(e). In the final result of Figure 8(e), one observes that small contours that come from air pockets are detected as well. These small non-crack boundaries can be easily removed by a labeling and area thresholding process, and the final crack contours are shown in Figure 8(f).

Different from the detection results shown in Figure 7, each detected crack segment in Figure 8(f) is featured with a closed contour (and an underlying mathematical level-set function). This property determines that the quantitative extraction of crack width and other geometric properties can

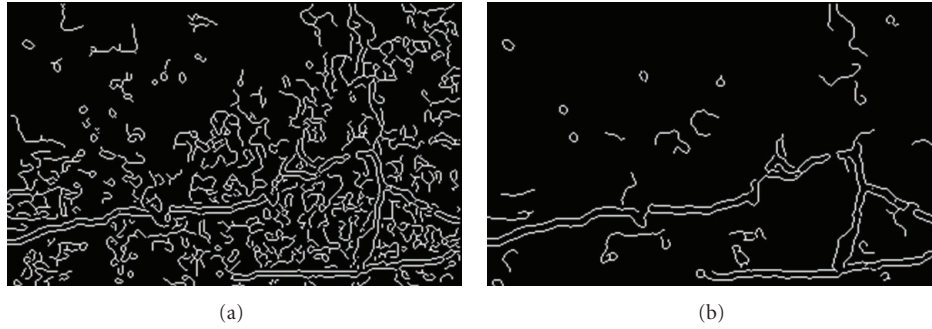


FIGURE 7: Crack detection using the Canny edge detector (as implemented in the Matlab Image Processing Toolbox, [8]), with different parameters: (a) threshold parameter = 0.1, Gaussian smoothing parameter = 1.0; (2) threshold parameter = 0.2, Gaussian smoothing parameter = 1.5.

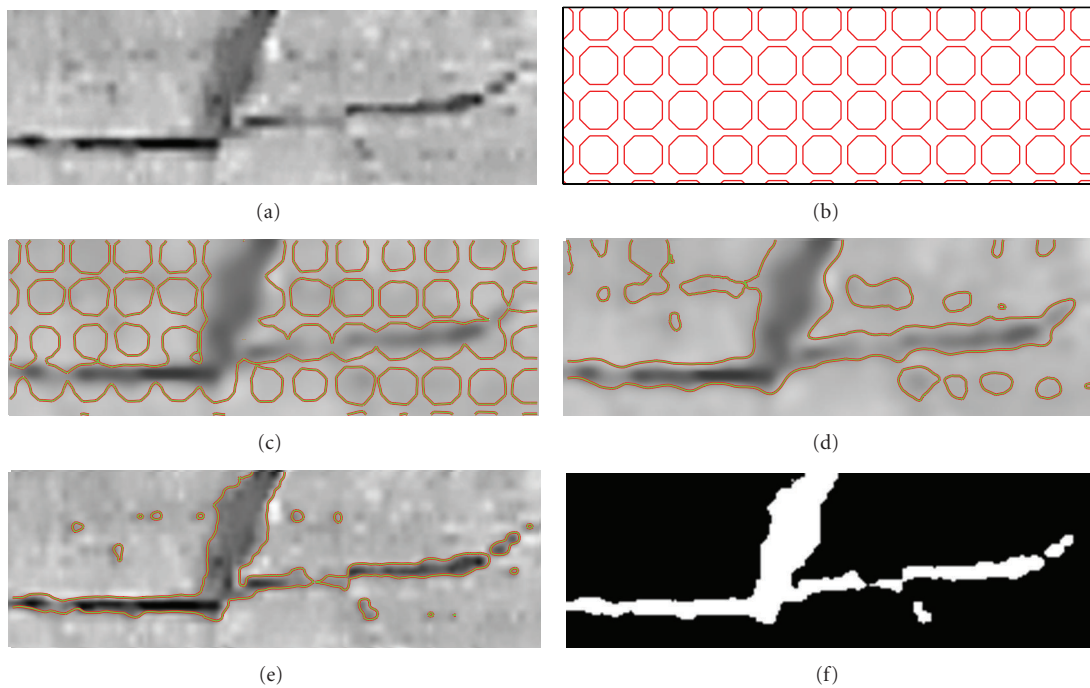


FIGURE 8: Crack detection using the level set-based active contour method: (a) the selected ROI, also shown in Figure 6; (b) the initialized contours; (c) and (d) intermediate detection results; (e) the converged result; (f) the cleaned detection result with contours for the air pockets removed.

be readily produced using the proposed methods in the previous section. We demonstrate this application thoroughly in the next section.

7. Application II: Laboratory Images

To demonstrate a complete process of concrete surface crack monitoring and damage quantification using the proposed framework, a laboratory beam is loaded and monitored using an array of cameras. As shown in Figure 9(a), the experiment involves a simply supported concrete beam loaded at mid-span controlled with linearly increasing displacements. A 2-point arrangement of loading is provided resulting in a region of constant moment. The beam span is 60 inches (1524 mm), and its section size is 5 inches \times 7 inches

(127 mm \times 177.8 mm). It was designed to fail in a shear mode using 4000 psi (27.6 MPa) concrete with no shear-resisting stirrups. The front view of the beam was monitored during loading by four digital cameras. The resolution of the image frames in the recorded video streams is 0.89 mm/pixel, and the frequency of camera capture was set at 40 frames/sec.

To illustrate the use of image-based crack damage monitoring and quantification, we select a short sequence of image frames generated from Camera C1, which were continuously captured within a 1.725-second duration, resulting in 70 image frames. In Figure 10, we illustrate six frames that are representative of the temporal development of crack occurrence. Note that the images shown here are cropped from the raw image frames, resulting in a smaller image domain, which is 240 \times 268.

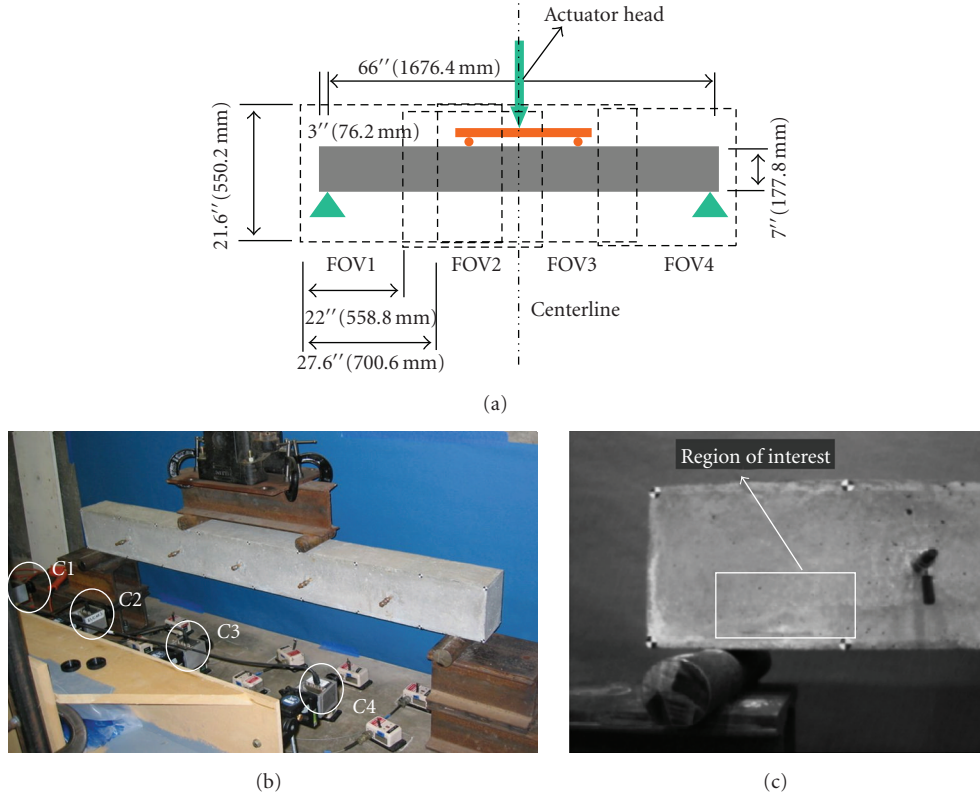


FIGURE 9: (a) Schematic of test set-up for a simple supported beam captured by four cameras (C1–C4 as seen in (b)); the fields of views (FOV1–FOV4) of the four cameras are overlapped and symmetric with the centerline; (b) the four cameras (C1–C4) in the real set-up; (c) the captured scene before loading by the camera C1 and the region of interest.

7.1. Crack Damage Monitoring

7.1.1. Computation of Time-Series Damage Measures. In Figure 10(a), we show that the image domain is divided into 10×10 subdomains; each of the subdomains has 24×26 pixels except the subdomains in the far right column which are of size 24×34 . For each subdomain, we compute the time-varying MD measurements (as well as the motion estimates). Two methods of computing MD measurements are conducted in parallel. First, we compute the MD measurements using temporally adjacent image patches. In Figure 11(a), MD measurements resulting from this method are plotted against time. For completeness, we illustrate the extracted progressive motion quantities across time in Figure 11(b), which are the average motion quantities based on the center 2×2 image patches. The second method of computing MD measurements, which uses a fixed image frame at a certain time as the base, will not be started until crack damage is detected.

From Figure 11(a), it can be seen that all MD measurements computed before $t = 0.650$ seconds from the 100 image patches are in a narrow band (about $0.1 \sim 0.2$). At $t = 0.650$ seconds, peak values of the MD measurements from some subdomains emerge, which are a strong indication of crack damage occurrence. The evolution of extracted motion quantities in the center of the beam agrees with the time of this crack event (Figure 10(c)). However, we see that these

motion quantities, if used as features of crack occurrence, are not as discriminative as the MD measures across time.

7.2. Outlier Analysis and Initial Damage Localization. The above conclusion regarding when the crack event occurs is based on subjective observation. In a practical structural damage monitoring context, an outlier analysis may be employed to automate this process. An outlier analysis, in its simplest form, is implemented by assuming that the underlying features follow a normal distribution (for more rigorous treatment about modeling the distribution of outliers and other approaches, one may refer to [25]). Herein, we take advantage of the fact that there is no crack in the second image frame (at 0.025 seconds), therefore the first group of MD measures at this moment are used to extract the sample mean and the sample standard deviation of MD measures, denoted by μ_m and σ_m . At the next image frame (at 0.050 seconds), the MD measures $MD[i, j]$ ($1 \leq i, j \leq 10$) are used to test the hypothesis that if $H_o : |MD[i, j] - \mu_m| < \lambda \sigma_m$ holds for a fixed threshold λ . Any $MD[i, j]$ s that fail the test H_o are treated as outliers indicating crack damage; otherwise, they are normal MD measures, and are used to update the sample mean μ_m and the sample standard deviation σ_m . In addition, as the hypothesis test goes, at each time, a binary damage map for the divided image domain is generated progressively, where the subdomain is set unity if

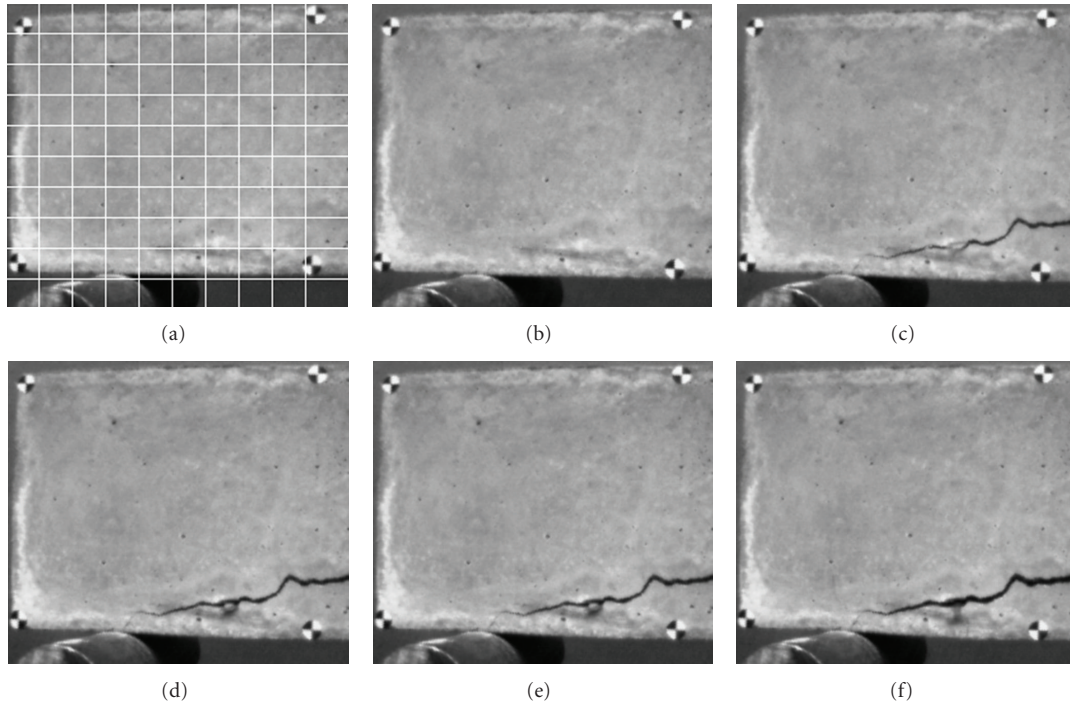


FIGURE 10: Concrete surface at different acquisition times: (a) at 0 second (the first frame with dividing grids of the image domain); (b) at 0.625 second (the 26th frame); (c) at 0.65 second (the 27th frame at which the first crack appeared); (d) at 0.80 second (the 33rd frame); (e) at 1.20 seconds (the 45th frame); (f) at 1.85 second (the 70th frame). In (a), the 10×10 subdivisions for the image domain are overlaid with the image.

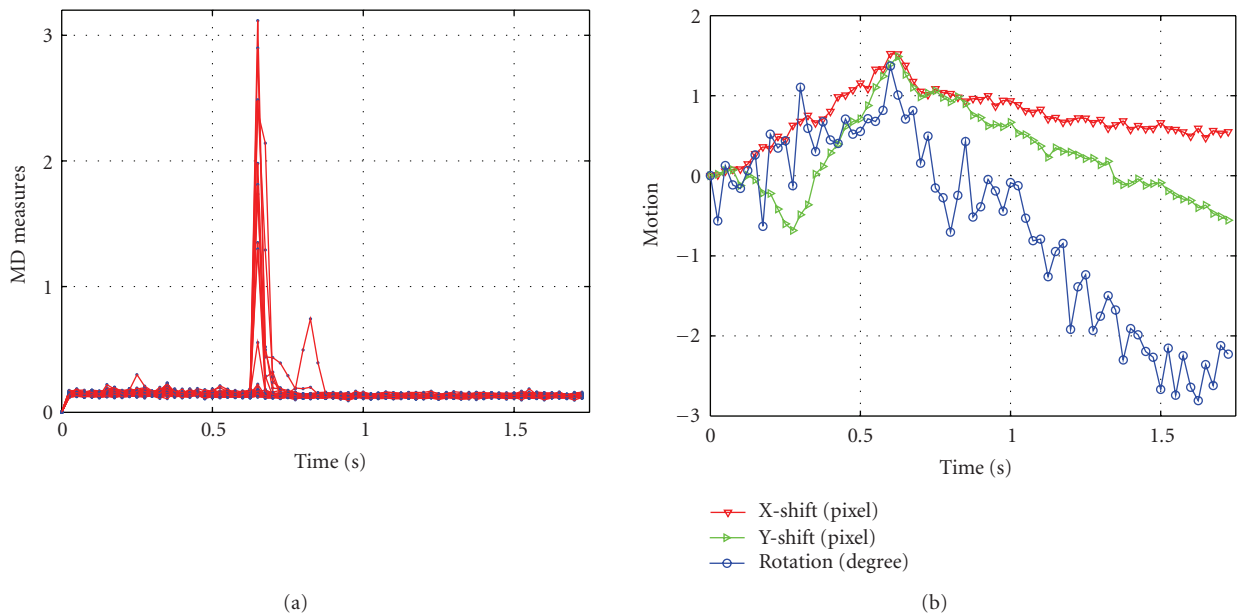


FIGURE 11: (a) Manifold-distance measurements across time; (b) the corresponding motion of the centerline of the beam.

it is determined as a damaged region. In Figure 12, this initial damage localization is illustrated.

7.3. Crack Damage Boundary Detection and Quantification. In Figure 13, images showing the cracked regions at later

times are shown. These are automatically cropped based on the initial localization information presented in Figure 12(b). In the following numerical studies, we generally choose the parameters as follows: space step $h = 1$, time step $\Delta t = 0.1$ for (10) and $\Delta t = 0.25$ for (14), and $\epsilon = h = 1$ and $\theta = 1.5h = 1.5$ for the approximate Heaviside functions. The length scale

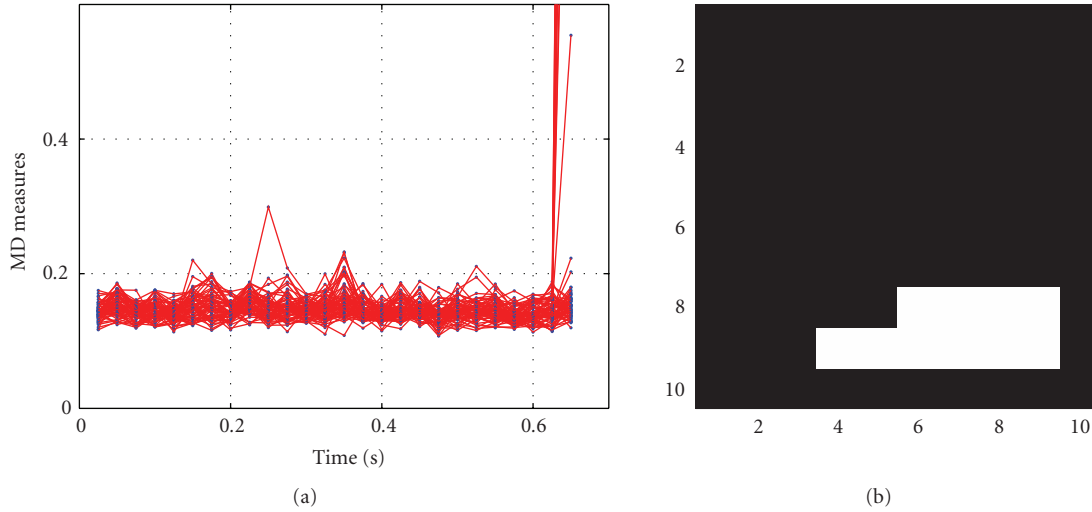


FIGURE 12: Distance measurements before 0.650 seconds: (a) manifold distance; (b) crude damage localization at $t = 0.650$ seconds, where the axis numbers mark the location of different subdomains shown in Figure 10(a).

μ in principle should vary relative to the scale of the target objects, and empirical investigation needs to be conducted to determine the suitable range of this parameter. In this paper, we use the average of these bounds, approximately $\mu = 0.008 \cdot 255^2$, throughout this work.

7.3.1. Damage Detection for Regions of Interest. Recall that the Chan-Vese active model in this paper is derived for two-phase images, namely, assuming that the images contain only two objects, the normal background and the potential structural damage. This limitation in practice should be considered when selecting the regions of interest in structural components. Thus, we only consider a small area in the left shear zone of the beam as shown in Figure 9(c). Also, since a large number of image frames were recorded, we subsampled and selected three representative image frames in this work. Figures 13(a)–13(c) show the three images captured at different times for the same target region as shown in Figure 9(c). In Figures 14(a)–14(c), the boundaries of the cracks are successfully detected by applying the Chan-Vese active contour model. It is notable that in Figure 14(a), an interior noncracked area appears, which visually can be seen in Figure 13(a).

7.3.2. Extraction of Geometric Quantities: Areas and Perimeters. By visually inspecting the detected cracks in Figures 14(a)–14(c), one can observe that their topographical patterns change significantly with time ($T1 \rightarrow T3$) due to increasing mid-span displacements. We first compute the areas and perimeters of these cracks using the methods discussed previously. In Table 1, these results are reported as well as their corresponding true values considering the image resolution. The true values are determined by manually summing the pixels. It is interesting to note that the areas of the cracks increase; however, the perimeters of the cracks with increasing mid-span displacements do not necessarily

TABLE 1: Extracted areas and perimeters of cracks (numbers in parentheses are true values of extracted quantities: for areas, the multiplier is 0.89^2 mm^2 ; for perimeter, the multiplier is 0.89 mm).

| Geometric quantities | Crack images at | | |
|----------------------|-------------------------------|--------------------------------|---------------------------------|
| | $T1$ | $T2$ | $T3$ |
| Areas | 793 (628 mm ²) | 1240 (982 mm ²) | 1698 (1345 mm ²) |
| Perimeters | 308 (274 mm) | 279 (248 mm) | 289 (257 mm) |

increase. This is due to the higher topographical variations of concrete cracks at lower displacement levels.

7.3.3. Extraction of Crack Widths. In accordance with the approximate procedure for extraction of crack width, we first perform skeletonization over the binary detection results at time $T1$, $T2$, and $T3$. Figures 14(d)–14(f) illustrate the centerlines of these multitemporal cracks. By solving (14) for the SDFs and conducting Boolean operations to extract distance values at the centerlines, one obtains the approximate widths along cracks, denoted by $w_{T1}(x, y)$, $w_{T2}(x, y)$, and $w_{T3}(x, y)$. Table 2 summarizes the statistics of these crack widths. Since it is difficult to plot extracted crack widths along the crack in a 2D domain, for width values in $w(x, y)$, we plot the pairs $(x, \max_y[w(x, y)])$, that is, the x -coordinate versus the maximum width in y direction given x . These plots are shown in Figures 15(a)–15(c).

To evaluate the accuracy of the above approximate crack widths, we use an explicit searching method to extract the exact crack widths: first, we explicitly start traveling along one side of the two boundaries (e.g., the Γ_1 in Figure 5) from one end point, which can be realized by searching the 8 connected neighborhoods repeatedly; then at each pixel (x, y) , the shortest distance to the other side of the two boundaries (Γ_2) is computed by minimizing the distance

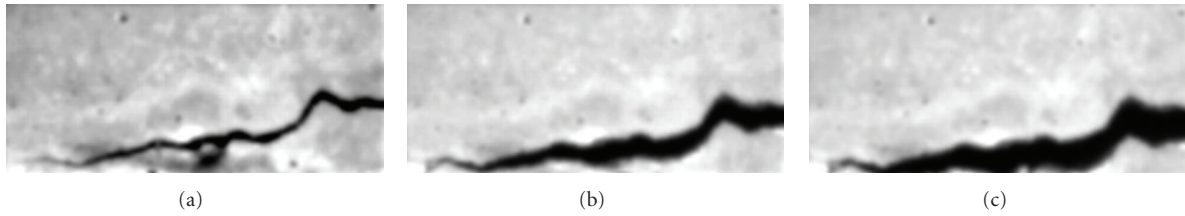


FIGURE 13: Cropped images (72×160 pixels) of concrete cracks at different times, from (a) to (c), denoted by T_1, T_2 , and T_3 . By synchronizing with the loading time, $T_1 = 30.5$ seconds, $T_2 = 34.75$ seconds, and $T_3 = 39.75$ seconds (these time stamps are different from the relative ones used in Figure 10).

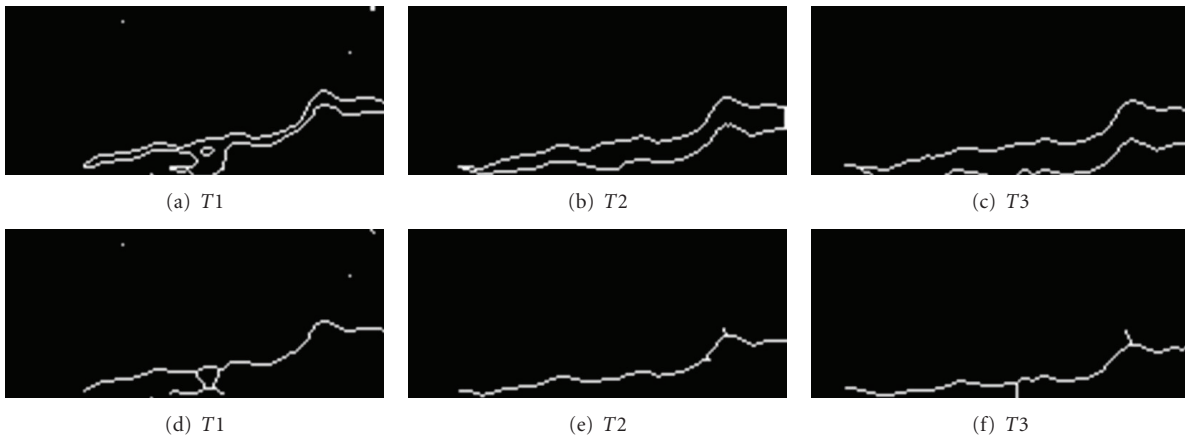


FIGURE 14: (a)–(c) Boundaries of detected cracks at different times; (d)–(f) extracted centerlines of detected cracks by morphological skeletonization.

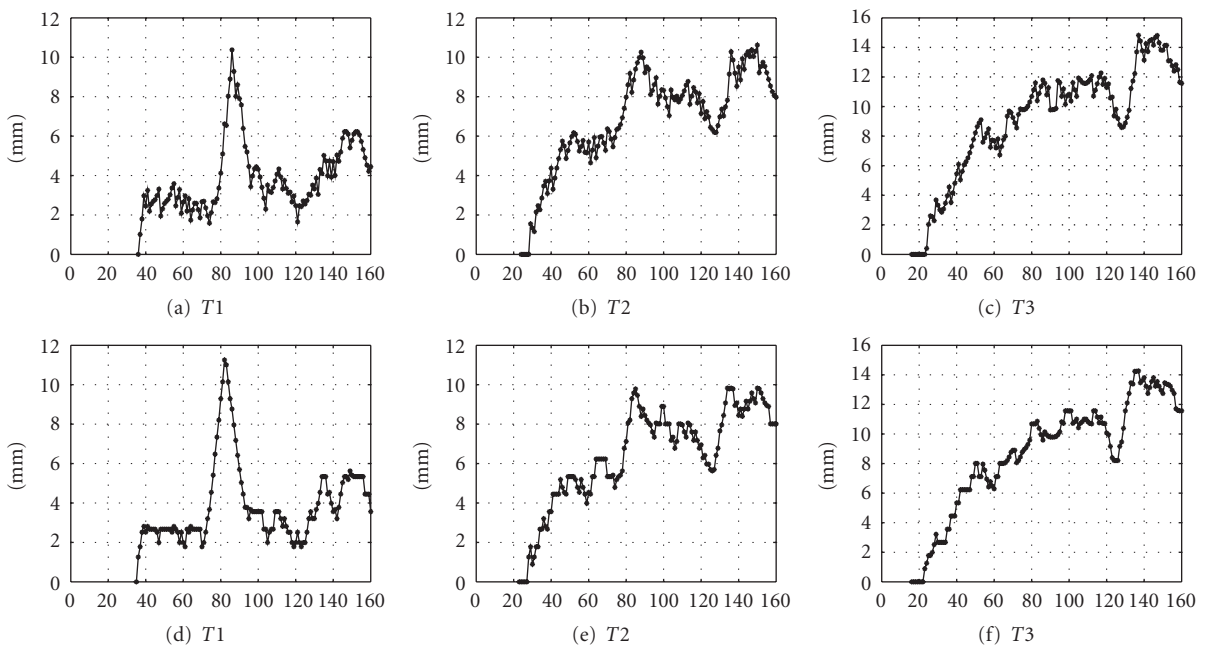


FIGURE 15: Plots of the extracted crack widths at times T_1, T_2 , and T_3 (a)–(c) using the proposed level set-based approximate method and (d)–(f) using the explicit exact method.

TABLE 2: Crack width statistics for detected cracks at different times: the top two rows are from the level set-based approximate method, and the bottom two rows are from the explicit searching method (numbers in parentheses are true values of crack width considering the image resolution).

| Crack width statistics | | Crack images at | | |
|------------------------|---------|-----------------|----------------|----------------|
| | | $T1$ | $T2$ | $T3$ |
| Approximate | Maximum | 11.8 (10.4 mm) | 11.9 (10.6 mm) | 16.7 (14.8 mm) |
| | Average | 4.3 (3.8 mm) | 7.5 (6.7 mm) | 9.9 (8.8 mm) |
| Exact | Maximum | 12.6 (11.2 mm) | 11.1 (9.9 mm) | 16.0 (14.2 mm) |
| | Average | 4.3 (3.8 mm) | 7.3 (6.5 mm) | 9.8 (8.7 mm) |

values from (x, y) to all the pixels in Γ_2 . This explicit searching method yields the exact values of crack width along a simple crack. Certainly this method suffers from the limitations that manual intervention is needed to provide the end points, and further generalization to complex crack patterns is difficult. Nonetheless, it provides the baseline for comparison with the approximate method. The bottom two rows of Table 2 summarize the width statistics of the obtained exact crack widths, and in Figures 15(d)–15(f) the crack widths are again plotted along the x -axis.

By comparing the statistics results from the two extraction methods in Table 2, one can see that the basic statistics of extracted crack widths at the three different times are considerably close. One can further compare the plots of extracted width along x -axis in Figure 15; visually, at each time of $T1, T2$, or $T3$, the obtained widths from the two methods agree very well. Quantitatively, we compute the root-mean-square-error (RMSE) over the results from the exact method and from the approximate method: at $T1$, $RMSE = 2.2$ mm at $T2$, $RMSE = 0.7$ mm and at $T3$, $RMSE = 1.1$ mm. At time $T1$, slightly higher error is produced because in the exact method, the small interior noncracked region within the detected crack is ignored, therefore, higher widths are yielded around this region while in using the level set-based approximate method, the interior noncracked region is automatically excluded in computing the width.

7.3.4. Correlation with Displacement and Load Amplitudes. In this laboratory experiment, the linearly increasing displacements at the mid-span and associated load amplitudes from the actuator were recorded at 40 Hz. Based on the synchronized computer times of the image-acquisition workstation and the actuator-controller workstation, each captured image frame can be mapped to a simultaneous mid-span displacement and load amplitude. In Figure 16(a), the linearly-increased mid-span displacement versus time is plotted, with the times when the crack images used previously were captured articulated. In Figure 16(b), the load-displacement curve is provided, wherein there simultaneous values of average crack width at times $T1 - T3$ are annotated.

These correlation plots illustrate that cracks in a critical region of a structural component can be captured continuously with a proper camera array setup, and if available, this data can be synchronized with other measurements. It is noted that this continuous sampling of realistic 3D objects, as made possible with the 2D images, is not possible

with any other current measurement methods that are discontinuous in space. With an offline analysis proposed in this paper, the positions of cracks and the associated geometric quantities can be tracked continuously in time. Hence, one can correlate the crack characteristics to other quantities of interest, such as load amplitude, displacement, or other measured response data.

8. Concerns Prior to Practical Application

8.1. Desired Resolution. In the previous two sections, the proposed framework and the component algorithms are applied in two different practical situations. In either of these example applications, if engineering properties are to be extracted, the resolution of the images must be carefully considered. In the field, with a large amount of (potentially manually captured) images, it may not be feasible to reliably configure the camera capture hardware to accomplish consistent and reasonable resolution. One of the easiest solutions is to place a small pattern, for example, drawn onto paper, within the field of view. Using this reference pattern, a simple calculation based on the known size of the pattern and its size in the image domain may give an approximate estimate of the image resolution (e.g., in terms of length unit per pixel).

The laboratory application example demonstrates a complete application of the proposed framework. In this experiment, the image resolution is determined to be 0.89 mm/pixel. It is noted that narrower, hairline cracks, which may have widths as small as 0.1 mm cannot be captured with this set-up. This is primarily a limitation of the hardware set-up. Alternative camera type and placement relative to the field of view of interest can resolve this issue. If the width of the cracks is still less than the image resolution, a detection method with subpixel accuracy may be necessary. The level-set active contour method as presented in this paper has not been calibrated to solve this problem, as it internally relies on the calculation of the mean intensity values within contoured image areas. Multiple overlapping fields of view have been used with success in other applications to achieve subpixel accuracy; however, this would be a subject of future study using the currently presented methods.

8.2. Image Noise and Size. A practical problem in any image-based analysis situation is that noisy image artifacts

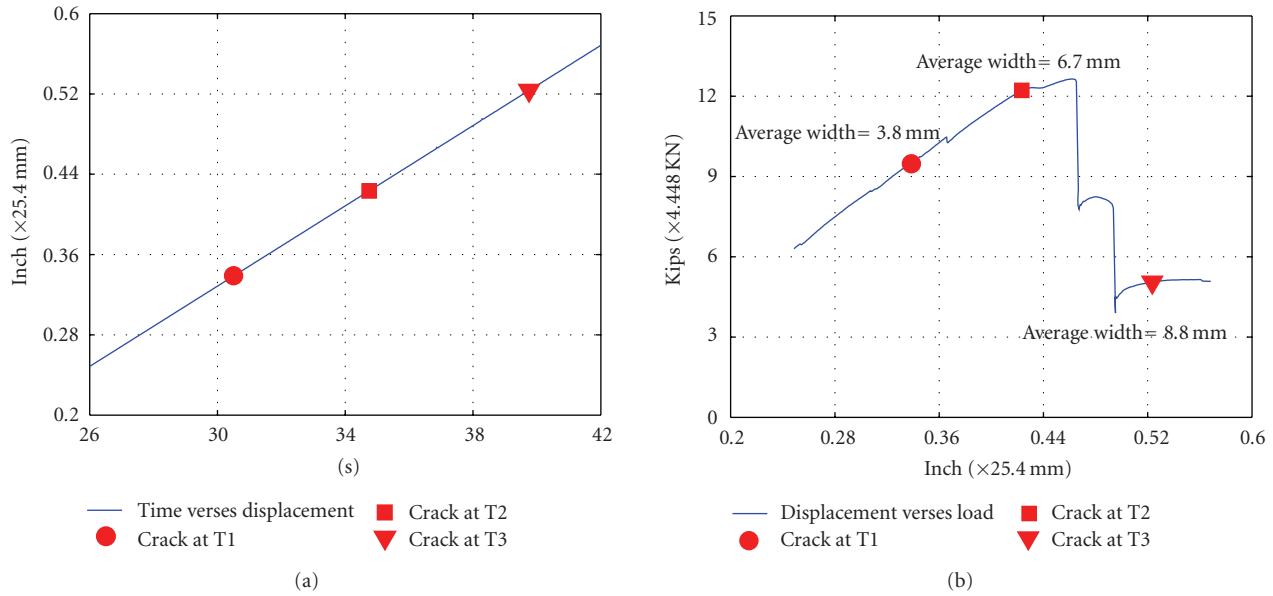


FIGURE 16: (a) Displacements versus time at mid-span; (b) measured load amplitude versus displacement at the mid-span, and the extracted average crack widths at $T1$, $T2$, and $T3$.

may exist in the domain. In the case of concrete surface images, these artifacts include large decolored, roughed, or spalled concrete surface areas. In this situation, prior to turning to other image segmentation or object recognition methods, we propose that a subdomain approach may be used first. Such an approach may be in the form of dividing the image domain into multiple subdomains or in the form of identifying user-selected ROIs. It is noted that the influence of noisy artifacts will appear in the first application example if a different ROI is selected (Figure 6). Another practical issue, with a related solution, is that of image size. If images with very large sizes are encountered, computational cost may increase significantly; meanwhile robustness to noisy artifacts likely decreases. In this situation, the subdomain approach is an effective solution as well.

8.3. Computational Cost. The algorithms in the proposed framework, including the manifold-based monitoring algorithm and the level set-based crack detection and quantification algorithms, comprise a large number of basic vector or matrix operations with the complexity order at $O(N)$ or $O(N^2)$. As a result, the associated computational cost is considerably larger than the traditional simple filtering-based methods. Computational cost is a concern if the framework is needed for online monitoring and quantification of rapidly captured image sequences. For offline processing of single images, however, the computation time is acceptable based on our implementation of the proposed algorithms in a Matlab environment [36]. If the framework is used as an online monitoring solution, fine tuning of the image capture rate and the image processing time is subject to further investigation. A plausible solution may be to subsample

the captured images (i.e., only process a fraction of the images). It is noted that most of the time consumed from an operational point of view is spent tuning the internal parameters. This issue is expected to be mitigated when more empirical knowledge is obtained.

9. Conclusions

In this paper, a novel image-based framework is proposed to monitor and quantify one of the most common types of structural damage in civil engineering, namely, concrete surface cracks. In this case, optical camera images are used. Using illustrative examples, we first discuss the technological challenges in implementing any image-based damage identification approach using field or laboratory images. These include various instances of photometric and geometric distortions. For the latter, structural motion in the images forms one of the major challenges.

By means of integrating two advanced image modeling algorithms, the proposed framework provides a full solution to the common damage identification objectives encountered in practice. First, through the novel use of manifold-distance computation based on multi-temporal images, motion-invariant features of crack occurrence are extracted. Second, a level set-based active contour algorithm is applied to realize a model-based boundary detection for concrete surface cracks. Based on the obtained level-set crack boundaries, an approximate method for determining continuous crack widths is developed. Two example applications are provided to demonstrate use of the proposed framework. Results show the success in monitoring temporally and quantifying geometrically the concrete cracks.

Acknowledgments

Support for this work was provided by a National Science Foundation (NSF) Grant (CMS-0510802) and a research assistantship from the University of California, San Diego. The authors would like to thank Dr. Kai-Uwe Doerr and Professor Falko Kuester for assistance with the image capture during the laboratory experiment and Mr. Robert Kazanjy and laboratory staff at University of California, Irvine for assistance during testing. Opinions, findings, and conclusions expressed in this paper are those of the authors and do not necessarily reflect those of the sponsoring organizations.

References

- [1] S. W. Doebbling, C. R. Farrar, and M. B. Prime, "A summary review of vibration-based damage identification methods," *Shock and Vibration Digest*, vol. 30, no. 2, pp. 91–105, 1998.
- [2] C. R. Farrar and K. Worden, "An introduction to structural health monitoring," *Philosophical Transactions of the Royal Society A*, vol. 365, no. 1851, pp. 303–315, 2007.
- [3] P. Shull, *Nondestructive Evaluation: Theory, Techniques, and Applications*, CRC Press, Boca Raton, Fla, USA, 2002.
- [4] I. Abdel-Qader, O. Abudayyeh, and M. E. Kelly, "Analysis of edge-detection techniques for crack identification in bridges," *Journal of Computing in Civil Engineering*, vol. 17, no. 4, pp. 255–263, 2003.
- [5] T. C. Hutchinson and Z. Chen, "Improved image analysis for evaluating concrete damage," *Journal of Computing in Civil Engineering*, vol. 20, no. 3, pp. 210–216, 2006.
- [6] T. C. Hutchinson, F. Kuester, K.-U. Doerr, and D. Lim, "Optimal hardware and software design of an image-based system for capturing dynamic movements," *IEEE Transactions on Instrumentation and Measurement*, vol. 55, no. 1, pp. 164–175, 2006.
- [7] T. Zhang and G. Nagy, "Surface tortuosity and its application to analyzing cracks in concrete," in *Proceedings of the 17th International Conference on Pattern Recognition (ICPR '04)*, vol. 2, pp. 851–854, Cambridge, Mass, USA, August 2004.
- [8] Z. Zhu and I. Brilakis, "Detecting air pockets for architectural concrete quality assessment using visual sensing," *Electronic Journal of Information Technology in Construction*, vol. 13, pp. 86–102, 2008.
- [9] M. Moore, D. Rolander, B. Graybeal, B. Phares, and G. Washer, "Highway bridge inspection: state-of-the-practice survey," Tech. Rep. FHWA-RD-01-033, Federal Highway Administration, McLean, Va, USA, 2001, <http://www.tfhrc.gov/hnr20/nde/pdfs/01033.pdf>.
- [10] Y. Fujita, Y. Mitani, and Y. Hamamoto, "A method for crack detection on a concrete structure," in *Proceedings of the 18th International Conference on Pattern Recognition (ICPR '06)*, vol. 3, pp. 901–904, Hong Kong, August 2006.
- [11] A. Ito, Y. Aoki, and S. Hashimoto, "Accurate extraction and measurement of fine cracks from concrete block surface image," in *Proceedings of the 28th Annual Conference of the IEEE Industrial Electronics Society*, vol. 3, pp. 2202–2207, Seville, Spain, November 2002.
- [12] G. De Schutter, "Advanced monitoring of cracked structures using video microscope and automated image analysis," *NDT & E International*, vol. 35, no. 4, pp. 209–212, 2002.
- [13] R. Gonzalez and R. Woods, *Digital Image Processing*, Prentice-Hall, Upper Saddle River, NJ, USA, 2002.
- [14] T. Lindeberg, "Edge detection and ridge detection with automatic scale selection," in *Proceedings of the IEEE Computer Society Conference on Computer Vision and Pattern Recognition (CVPR '96)*, pp. 465–470, San Francisco, Calif, USA, June 1996.
- [15] S. Mallat and S. Zhong, "Characterization of signals from multiscale edges," *IEEE Transactions on Pattern Analysis and Machine Intelligence*, vol. 14, no. 7, pp. 710–732, 1992.
- [16] T. Soppe and T. Hutchinson, "Experimental damage-gas flow correlations for cyclically loaded reinforced concrete walls," Tech. Rep. SSRP 09/07, Department of Structural Engineering, University of California, San Diego, Calif, USA, 2009.
- [17] D. A. Forsyth and J. Ponce, *Computer Vision: A Modern Approach*, Prentice-Hall, Upper Saddle River, NJ, USA, 2002.
- [18] R. J. Radke, S. Andra, O. Al-Kofahi, and B. Roysam, "Image change detection algorithms: a systematic survey," *IEEE Transactions on Image Processing*, vol. 14, no. 3, pp. 294–307, 2005.
- [19] Z. Chen, B. Chang, and T. C. Hutchinson, "Image-based monitoring of structural damage: concrete surface cracks," in *Smart Sensor Phenomena, Technology, Networks, and Systems*, vol. 6933 of *Proceedings of SPIE*, San Diego, Calif, USA, March 2008.
- [20] ACI Committee 318, *Building Code Requirements for Structural Concrete*, American Concrete Institute, Farmington Hills, Mich, USA, 2008.
- [21] B. Horn, *Robot Vision*, MIT Press, Cambridge, Mass, USA, 1996.
- [22] P. W. Hallinan, "A low-dimensional representation of human faces for arbitrary lighting conditions," in *Proceedings of the IEEE Computer Society Conference on Computer Vision and Pattern Recognition (CVPR '94)*, pp. 995–999, Seattle, Wash, USA, June 1994.
- [23] P. Y. Simard, Y. A. Le Cun, J. S. Denker, and B. Victorri, "Transformation invariance in pattern recognition: tangent distance and propagation," *International Journal of Imaging Systems and Technology*, vol. 11, no. 3, pp. 181–197, 2000.
- [24] N. Vasconcelos and A. Lippman, "A multiresolution manifold distance for invariant image similarity," *IEEE Transactions on Multimedia*, vol. 7, no. 1, pp. 127–142, 2005.
- [25] V. J. Hodge and J. Austin, "A survey of outlier detection methodologies," *Artificial Intelligence Review*, vol. 22, no. 2, pp. 85–126, 2004.
- [26] M. Kass, A. Witkin, and D. Terzopoulos, "Snakes: active contour models," *International Journal of Computer Vision*, vol. 1, no. 4, pp. 321–331, 1988.
- [27] V. Caselles, R. Kimmel, and G. Sapiro, "Geodesic active contours," *International Journal of Computer Vision*, vol. 22, no. 1, pp. 61–79, 1997.
- [28] D. Mumford and J. Shah, "Optimal approximation by piecewise smooth functions and associated variational problems," *Communications in Pure and Applied Mathematics*, vol. 42, no. 1, pp. 577–685, 1989.
- [29] T. F. Chan and L. A. Vese, "Active contours without edges," *IEEE Transactions on Image Processing*, vol. 10, no. 2, pp. 266–277, 2001.
- [30] S. Osher and R. Fedkiw, *Level Set Methods and Dynamic Implicit Surfaces*, Springer, New York, NY, USA, 2002.
- [31] S. Osher and J. A. Sethian, "Fronts propagating with curvature-dependent speed: algorithms based on Hamilton-Jacobi formulations," *Journal of Computational Physics*, vol. 79, no. 1, pp. 12–49, 1988.

- [32] P. Soille, *Morphological Image Analysis: Principles and Applications*, Springer, New York, NY, USA, 1999.
- [33] M. S. Hassouna and A. A. Farag, "Robust centerline extraction framework using level sets," in *Proceedings of IEEE Computer Society Conference on Computer Vision and Pattern Recognition (CVPR '05)*, vol. 1, pp. 458–467, San Diego, Calif, USA, June 2005.
- [34] J. Canny, "A computational approach to edge detection," *IEEE Transactions on Pattern Analysis and Machine Intelligence*, vol. 8, no. 6, pp. 679–698, 1986.
- [35] Y. Yitzhaky and E. Peli, "A method for objective edge detection evaluation and detector parameter selection," *IEEE Transactions on Pattern Analysis and Machine Intelligence*, vol. 25, no. 8, pp. 1027–1033, 2003.
- [36] MathWorks, Inc, 2010, <http://www.mathworks.com/>.

Research Article

An FBG-Based Impact Event Detection System for Structural Health Monitoring

C. S. Shin,¹ B. L. Chen,¹ and S. K. Liaw^{1,2}

¹Department of Mechanical Engineering, National Taiwan University, Taipei 10617, Taiwan

²Department of Electronic Engineering, National Taiwan University of Science and Technology, Taipei 106, Taiwan

Correspondence should be addressed to C. S. Shin, csshin@ntu.edu.tw

Received 1 September 2009; Revised 5 December 2009; Accepted 26 January 2010

Academic Editor: Yi Qing Ni

Copyright © 2010 C. S. Shin et al. This is an open access article distributed under the Creative Commons Attribution License, which permits unrestricted use, distribution, and reproduction in any medium, provided the original work is properly cited.

Some structures are vulnerable to localized internal damages incurred by impact of small objects. An impact monitoring system using fiber Bragg grating (FBG) sensors has been established. Its ability to detect very low to medium energy impacts has been demonstrated on an aluminum plate and a 22 m long wind turbine blade. Previous analysis of this technique showed that the accuracy by which an impact position can be located is limited by equipment noises and angular insensitivity of the FBG. By employing two intensity demodulation schemes with different demodulation sensitivities and ranges, we try to differentiate the relative importance of the above limiting effects. Based on the results, directions for further improvement on impact source locating accuracy will be discussed and the implication of applying such systems on large-scale structures will be examined.

1. Introduction

Impacts due to bird-strike and hailstorm may do much harm to structures such as aircraft and wind turbine blades. The structure will be especially vulnerable if it is made of polymeric composite as impacts may induce localized small internal damages. On acting upon by fluctuating service loading, these insidious defects may grow and eventually lead to catastrophic failures. Although nondestructive examination techniques for the detection of internal damages are available, they are limited in resolution. Moreover, to stage a thorough examination over the entire structure can be highly time and resource consuming for a large-scale structure. The problem can be much alleviated if one knows where to look at and what to look for.

The current work investigates the possibility of establishing an impact event monitoring system using fiber Bragg grating (FBG). FBG has found increasing applications as sensors in aerospace, structural, medical, and chemical applications for vibration, temperature, strain, impact, and general structural health monitoring [1–5]. It is chosen in the current task because of its good long-term durability and stability. In case of composite structures, optical fiber

sensors possess the additional advantage of being compatible with common polymeric materials, making them easily embeddable inside a structure without inducing significant weakening of the material.

Previous works on impact location identification mostly used piezoelectric sensors (e.g., [6, 7]). A three-sensor-based scheme was used to locate the impact position of a projectile on a target screen by measuring acoustic waves with microphones [8, 9]. However, this scheme requires *a priori* knowledge of the wave speed. For practical applications, calibration of the wave speed in advance may not be feasible. Our own work showed that the whereabouts of an impact event can be located by analyzing the differential time-of-flight among signals picked up by four different FBG sensors [10]. Changes in the measurand are reflected as shift in the characteristic Bragg wavelength of an FBG. Light intensity demodulation techniques [11–13] have been shown to possess the required dynamic response for logging impact events [10, 14, 15]. In this work, two different light intensity demodulation schemes have been compared. The possibility of logging and locating impact will be tested on a flat aluminum plate and a wind turbine blade.

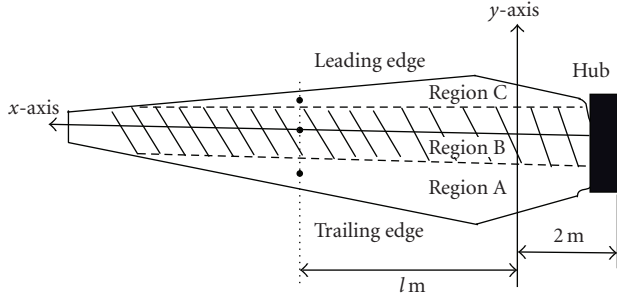


FIGURE 1: 2D Schematics of the blade (hatched area indicates region with interior box beam).

2. Experimental and Analysis Procedures

2.1. Impact Testing. Impact testing was made on a $0.8\text{ m} \times 0.8\text{ m}$ square aluminum plate with a thickness of 6 mm and a retired 22 m long composite blade from a 660 kW wind turbine. The cross section of the blade essentially consists of an upper and lower aerodynamic surfaces with a reinforcing box beam sandwiched in between. Figure 1 shows a 2D schematics of the top surface of the blade. For convenience in the following description, the blade is divided into 3 regions. The hatched area, designated Region B, indicates the position of the box beam. Regions A and C are, respectively, the trailing and leading edges of the blade. The longitudinal mid-axis of the beam is taken as the x -axis. The corresponding y -axis is situated 2 m from the hub base. Sensing FBGs oriented along the x direction were stuck on the y -axis at the center of each of the three regions. Impact events were generated using a Bruel & Kjaer Type 8202 hammer at various distances l m from the y -axis. At any section, impact was made at the center of a region (the dots in Figure 1). For the aluminum plate, impacts were made by dropping a 70 g aluminum projectile from various heights H . For impact source locating, impacts from $H = 15$ cm were made on a grid at 10 cm increment along the horizontal and vertical directions. Because of symmetry, impacts were made only on half of the plate. Location of the sensing FBGs on the plate will be described in a latter section. All FBGs used in the current work were fabricated by side writing on single mode photosensitive fibers. The reflectivity of the FBG was about 99%, with the peak wavelengths between 1551 nm and 1552 nm. The shift of the peak wavelength caused by transient stress waves was interrogated with two different intensity demodulation schemes.

2.2. FBG Interrogating Schemes. Figure 2 shows the two light intensity demodulation schemes employed. For the one involving an ASE light source (Figure 2(a)), a commercial edge filter (Santec OTF300-03-S3) was used to modify the broadband light. Its peak wavelength is tunable between 1530 nm and 1570 nm. Figure 3(a) shows the spectrum of one of the sensing FBGs relative to the filtered output from the edge filter. In Figure 2(b), the filtered spectrum basically corresponds to the reflected Bragg spectrum of the filter FBG.

The laser ring serves to amplify the light intensity of this spectrum. The resulting output spectrum together with the spectrum of the sensing FBG is shown in Figure 3(b). The overlapped regions (hatched areas in Figure 3) loosely illustrate the light energy that will be reflected and transformed into voltage signals by the photodetectors. On receiving a strain wave signal from an impact, the wavelengths of the FBG spectra will shift to and fro horizontally, giving rise to variations of the hatched areas. The voltage outputs from the photodetectors will therefore change corresponding to the strain signal. This forms the basis of light intensity demodulation. The voltage signals were recorded with a 4-channel digital storage scope. Note that the FBG spectra in Figure 3 are obtained by using an unfiltered broadband light and so they appear similar in Figures 3(a) and 3(b). In the actual measuring schemes, the amount of energy reflected (or the hatched areas) will depend on the intensity of the sources. Considering the mechanism of demodulation, the usable demodulation range of the ASE scheme is ~ 0.5 nm and that of the laser ring is ~ 0.2 nm. It can be seen that the peak intensity from the laser ring output is much higher than that from the ASE source. With a higher peak intensity and narrower wavelength range, the slope of the edge filter will be steeper, resulting in a more sensitive demodulation with better wavelength resolution. Thus we expect the output from the laser ring scheme to be larger for the same strain disturbance. The sensitivity and accuracy of the measuring system as a whole depends not only on the sensitivity of the demodulation scheme but also on the intrinsic sensitivity of an FBG to the impact stress wave. It is hoped that by employing the above schemes with different output signal strengths and demodulation ranges, the relative importance of the two effects on the overall sensitivity and accuracy can be differentiated.

2.3. Impact Source Locating. To do away with the need for *a priori* knowledge on the wave speed when using the three-sensor-based impact source locating scheme [8, 9], a four-sensor-based algorithm with layout and nomenclature shown in Figure 4 was employed for the aluminum plate. The location of an impact (X, Y) is related to the coordinates (x_i, y_i) of a sensing FBG through the following set of equations:

$$\begin{aligned}
 & \sqrt{(X - x_2)^2 + (Y - y_2)^2} \\
 &= \sqrt{\left(\sqrt{(X - x_1)^2 + (Y - y_1)^2} + C \times t_{21}\right)^2}, \\
 & \sqrt{(X - x_3)^2 + (Y - y_3)^2} \\
 &= \sqrt{\left(\sqrt{(X - x_1)^2 + (Y - y_1)^2} + C \times t_{31}\right)^2}, \\
 & \sqrt{(X - x_4)^2 + (Y - y_4)^2} \\
 &= \sqrt{\left(\sqrt{(X - x_1)^2 + (Y - y_1)^2} + C \times t_{41}\right)^2},
 \end{aligned} \tag{1}$$

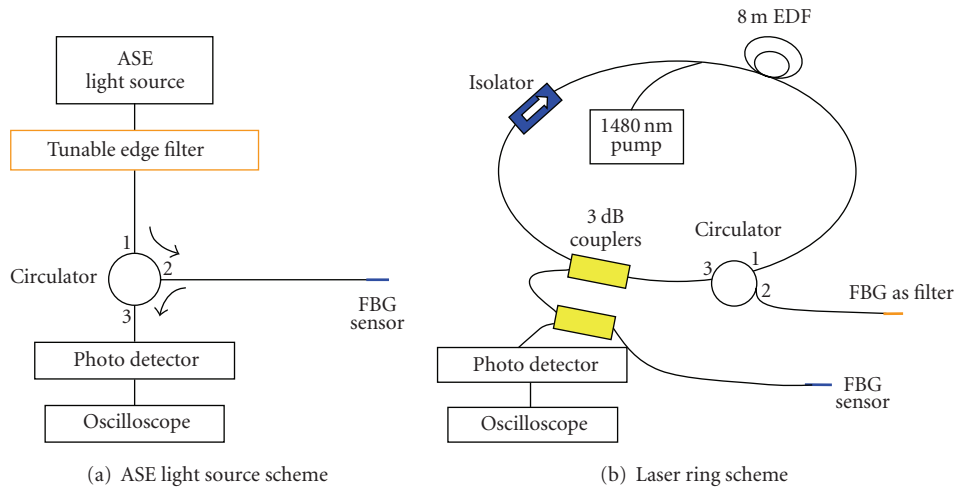


FIGURE 2: Two interrogation schemes used to demodulate the wavelength variations in the sensing FBG.

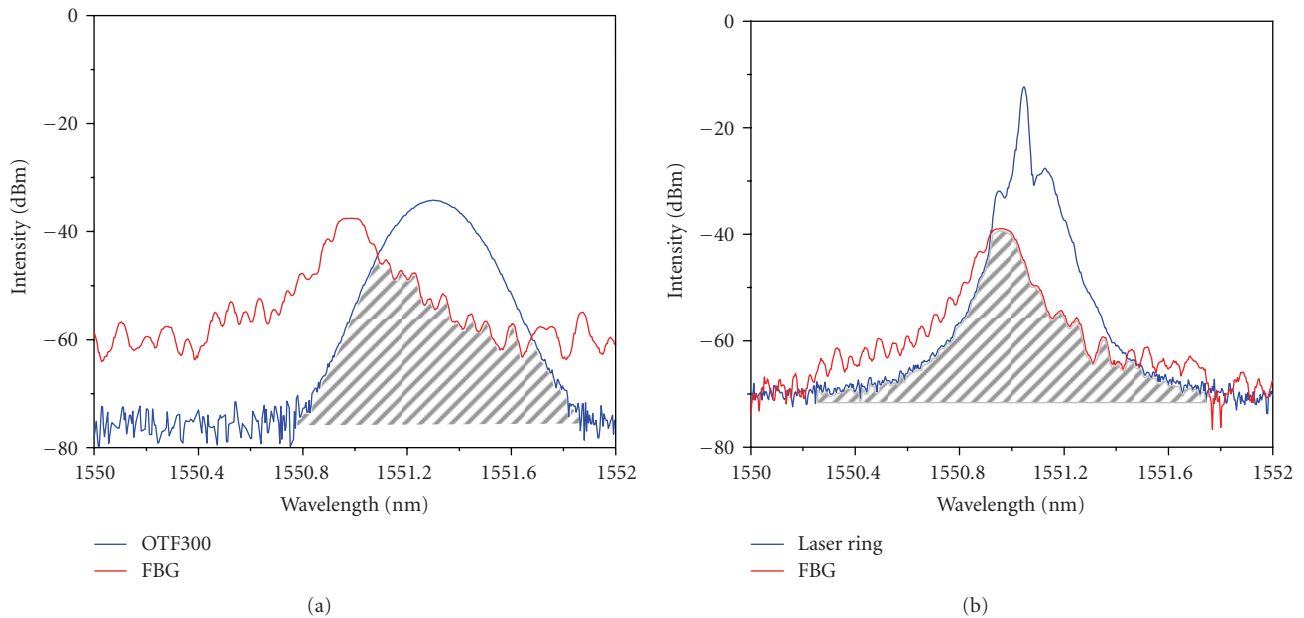


FIGURE 3: Relative spectra between the light source and the sensing FBG for schemes involving (a) an ASE source modified with an edge filter, (b) a laser ring configuration.

where C is the wave speed and t_{ij} is the difference in the time of receiving the wave signal between the sensor i and the sensor j . t_{ij} 's are derived from the oscilloscope recorded signals. Either side of (1) can only take the positive value as the physical meaning of distance.

In the above algorithm, the wave speed C is assumed to be homogeneous at all places and in all directions. Such is the case for the aluminum plate. The material and structural make-up of a wind turbine blade are highly complex and this homogeneous wave speed requirement will certainly be violated. Moreover, with the FBGs deployed near the hub base and the slender aspect ratio of the blade, the

distances between impact points with the same x -coordinate but different y -coordinates and a far away FBGs will be similar. It will be difficult to differentiate the y -coordinates from the difference in time-of-flight of the signals. So in the case of the blade we aim at locating the x -coordinate of an impact in this preliminary work. The wave speed was empirically calibrated by knocking on a series of known locations first. Then knocking on a different set of target locations was made. The time-of-flight data, with reference to the signals from the instrumented hammer, were noted and the corresponding x -coordinates were computed from these time data and the average wave speed.

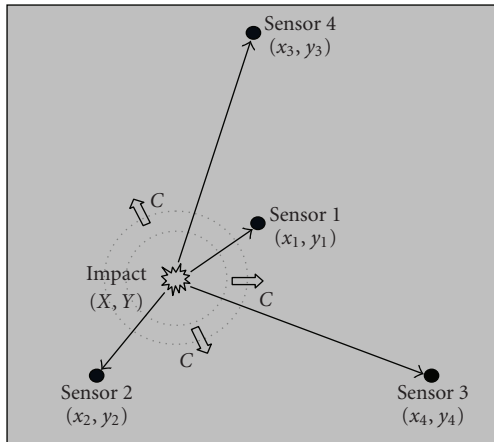


FIGURE 4: Nomenclature for the 4-sensor algorithm to evaluate the impact location.

3. Results and Discussion

3.1. Detection of an Impact Event. Figure 5 compares the signal received when impacts on the aluminum plate were made at a distance of 60 cm from the sensor with an extremely low energy ($H = 0.1$ mm) and a relatively high energy ($H = 50$ mm) using the two different demodulation schemes. Dotted lines in the figure indicate the first arrival of the impact signal. This time was obtained by first filtering the waveform with a digital band-pass filter with cutoff frequencies of 1 kHz and 100 kHz. A proper length of the leading part of the filtered waveform excluding the impact signal was then chosen to compute the average noise level. The first point where the waveform deviates 20% beyond this average noise level is taken as the first arrival point. With this criterion, the standard deviation of arrival time difference from three identical impact events at a particular impact position was found to be within $2 \mu\text{sec}$. in the angular sensitive range of the FBG.

With the same impact energy, the waveforms of the signals obtained from both schemes are similar. For the ASE light source scheme, the signal is heavily masked by background noises. Although a disturbance can be discerned, clear definition of the first arrival of the stress wave is difficult when the impact is from the extremely small height of 0.1 mm (Figure 5(a)). When the impact energy is relatively high, the signal-to-noise ratio is high enough to allow an unambiguous detection of the impact. With the laser ring scheme, the low energy impact can be comfortably detected (Figure 5(b)). With a 1-microstrain disturbance, the signal outputs are 6.6 mV and 623 mV for the ASE and laser ring schemes, respectively. The noise levels of both schemes are roughly the same at 5 mV as the main source of noise is from the photodiode circuitry. Thus the signal-to-noise ratio of the laser ring scheme is approximately 100 times that of the ASE scheme. This high signal strength is a direct consequence of the high intensity light source from the laser ring configuration.

Figure 6 compares the signal received when the impacts on the wind turbine blade were made at $x = 10$ m and 20 m with a momentum roughly equivalent to the impact of a 10 g bird flying at 10 m/s towards the blade. As before, for the same impact condition, the waveforms of the signals from both schemes are basically alike. With the current strength of impact, the signal levels from either schemes allow an unambiguously detection of the occurrence of stress wave disturbance. The signal-to-noise ratio from the ASE scheme (Figure 6(a)) is significantly lower than that from the laser ring scheme (Figure 6(b)) but the initial disturbance signals are clear enough to be defined.

3.2. Impact Source Location. As is evident from (1), accurate determination of the difference in the times of receiving the wave signals between any pair of FBGs is crucial to the accurate evaluation of an impact location. It has been shown that error in the signal receiving time arises due to (i) angular insensitivity of the FBG; (ii) attenuation of signal over distance, and (iii) intrinsic background noises of the optical and electronic circuits [10]. Angular insensitivity results when the impact stress wave fails to cause significant strain variations on the FBG because its incidence is at an oblique angle with the FBG axis. As can be seen in Figure 5, the initially arrived disturbance is very small. Previous work [10] showed that when the point of impact is 20 cm from the FBG and within $\pm 30^\circ$ about the FBG axis, the first arrival of the impact signal was marked with a clearly defined deviation from the background noises. This initial deviation became smaller as the off-axis angle is increased. At an off-axis angle of 60° , the deviation was very small and difficult to discern so that the arrival time was subject to an error upward of $1 \mu\text{sec}$. This uncertainty increased rapidly with the off-axis angle and at 75° , the error was likely to be around $10 \mu\text{sec}$. This sort of error would be aggravated if the impact occurred at a larger distance from the FBG as signal strength is further degraded by attenuation.

Figures 7(a) and 7(b) compare the experimental impact positions (open circles) on the plate with the locations estimated using the 4-FBGs algorithm (crosses) with the ASE light source and the laser ring scheme, respectively. The corresponding predicted and actual positions are connected with a straight line. For points where discrepancy between the actual and predicted locations is large, only some typical data are shown for clarity of presentation. The layout of the FBGs is also indicated in the figures. The dotted lines in Figures 7(a) and 7(b) define the $\pm 60^\circ$ off-axis boundary of the FBGs and may be treated as the tentative envelop of angular sensitivity limits. The areas bounded by these dotted lines represent regions which are within the $\pm 60^\circ$ off-axis boundary of all four FBGs. It can be seen that all the favorably correlated predicted-actual position pairs do lie within or close to the dotted boundary, suggesting that angular sensitivity of the FBG is a necessary requirement for accurate prediction. Within the dotted line bound regions, significant discrepancies can still occur. Examples for the latter can be found within the triangle near the top and the quadrilateral near the bottom. Incidentally, these two

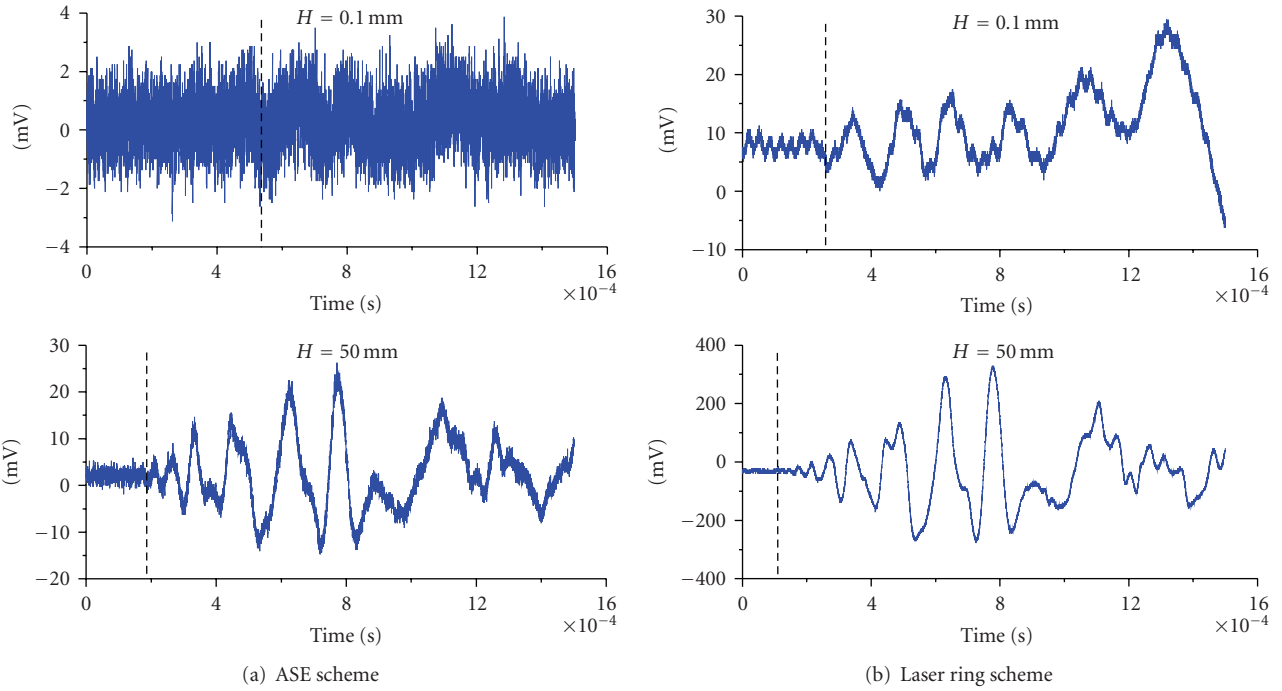


FIGURE 5: Impact signals obtained on the aluminum plate using (a) the ASE light source and (b) the laser ring scheme. (Dotted lines indicate the signal first arrival time).

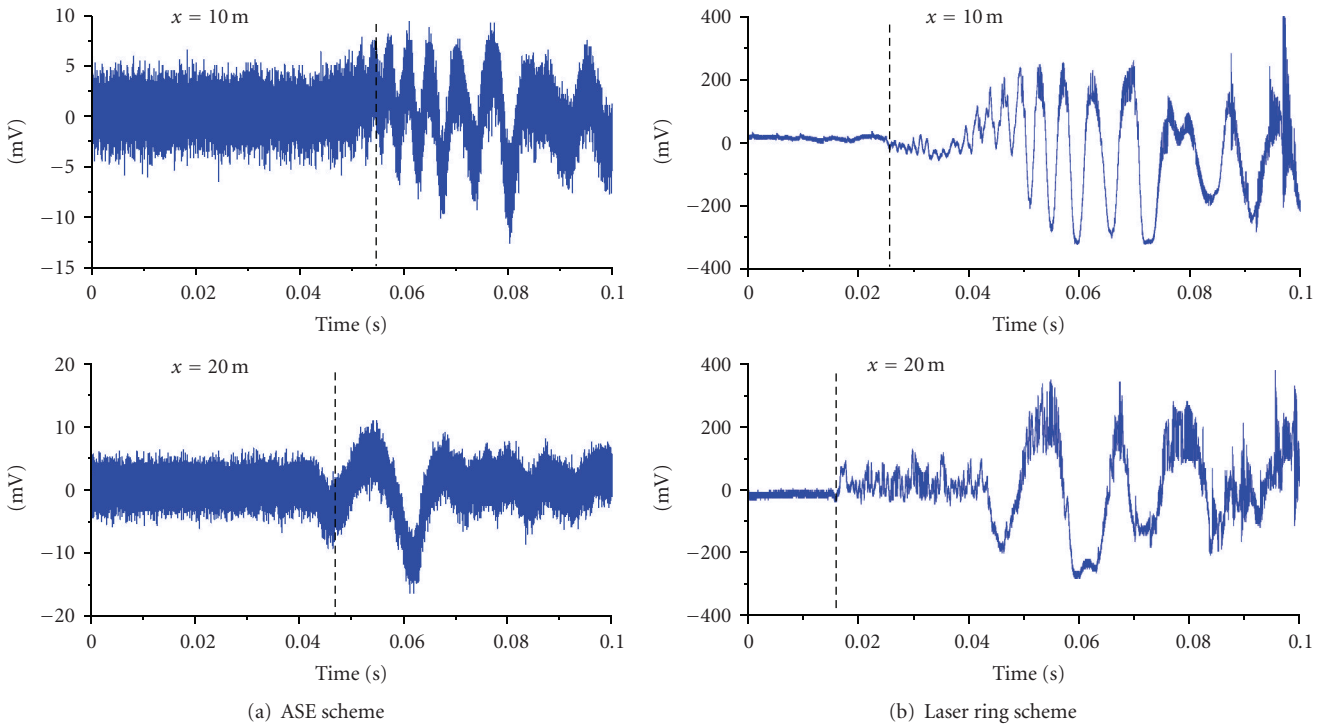


FIGURE 6: Impact Signals obtained from the wind turbine blade using (a) the ASE light source and (b) the laser ring scheme. (Dotted lines indicate the signal first arrival time).

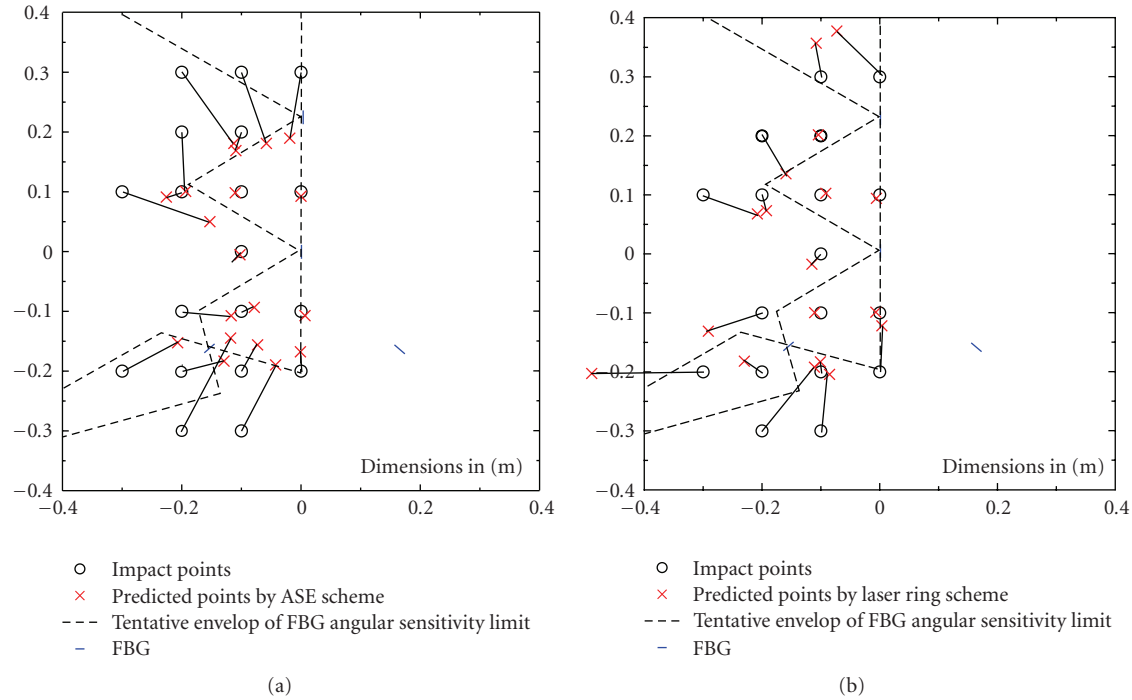


FIGURE 7: Comparison of the actual and calculated impact locations on the aluminum plate using (a) the ASE light source scheme and (b) the laser ring scheme.

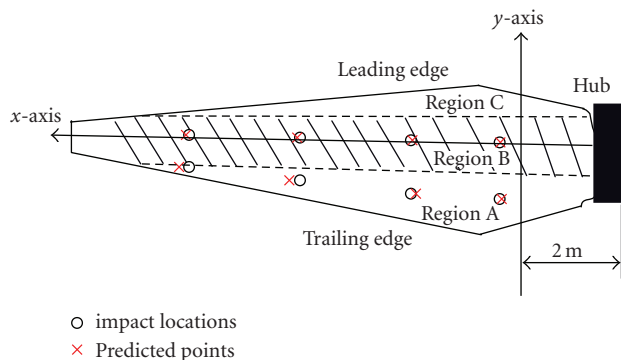


FIGURE 8: Comparison of the x -coordinates of the experimental impact and predicted locations for Regions A and B on the wind turbine blade.

regions lie far away from one or more of the FBGs. As a result the angular insensitivity of the FBGs concerned is aggravated by signal attenuation and one or more of the t_{ij} 's in (1) will be highly erroneous, leading to an inaccurate prediction of the impact position. If we compare the corresponding points in Figures 7(a) and 7(b), it can be seen that the prediction error based on the laser ring scheme is in general smaller than that on the ASE scheme. This is reasonable as the former has a higher intensity source and the problems of signal attenuation and background noise will be alleviated. However, the fact that the laser ring scheme is only marginally better suggests that the bottleneck of location accuracy is on the angular insensitivity of an FBG.

The underlying cause of angular insensitivity is rooted from the way an impact stress wave interacts with an FBG. This fact cannot be modified with a more intense light source and/or steeper filter slope. Hence, to improve the prediction accuracy, other ways have to be sought. A possible method is to use an FBG rosette involving two or three FBGs connected in series at an angle to one another. Preliminary results using FBG rosettes are compared with the above results at two impact positions where the angular insensitivity effect contributed heavily to the location errors (Table 1). The FBG rosettes were made from two FBGs at right angle to each other. For impact at $(-0.2, 0)$, both the ASE and laser ring systems with standalone FBGs failed to give convergent solution while the ASE system with FBG rosettes predicted to within 5 cm of the impact position. For impact at $(-0.2, 0.2)$, the distance between the predicted and the actual impact positions is 3.3 cm for the rosette system. This is significantly better than the 7.6 cm and 10 cm, respectively, for the laser ring and ASE systems with standalone FBGs.

For practical large-scale structures, the intense light source from the laser ring scheme will still be advantageous as signal attenuation will be serious in these cases. Also, with a large structure, the number of deployed sensors may have to be increased. With its high intensity, it is possible to use one laser ring to feed a larger number of FBG sensors, thus reducing the overall equipment cost.

For the ASE scheme (Figure 7(a)), most of the predicted locations tend to locate at the right-hand-side of the actual impact point. The reason of this may be attributed to the nonlinearity of the edge filter and the fact that it is not possible to get exactly the same Bragg spectra for the four

TABLE 1: Comparison of prediction accuracy among systems using single FBG and FBG rosette.

| Impact Locations (units in m.) | Predicted locations | | |
|-----------------------------------|------------------------|------------------------|-----------------------------|
| | ASE System | Ring Laser System | ASE System with FBG Rosette |
| (-0.2, 0) | no convergent solution | no convergent solution | (-0.164, -0.036) |
| (-0.2, 0.2) | (-0.193, 0.101) | (-0.159, 0.136) | (-0.225, 0.222) |

sensor FBGs. Thus sensitivities of the FBGs to strain wave will be slightly different. A particular FBG may be slightly less sensitive (or more sensitive) and shift the predicted positions towards one side. With the much increased sensitivity of the laser ring scheme, such slight discrepancies may be overridden. In fact, for the laser ring scheme (Figure 7(b)), the deviation to the right or left is more balanced.

In the case of the wind turbine blade, calibration showed that the wave velocities in Regions A and B are fairly constant and equal to 370 ± 21 m/s and 1278 ± 31 m/s, respectively. Calibration in Region C gave random wave speeds, presumably due to the interaction of the stress wave with the complex material composition as well as the irregular boundary geometry. With the wave speed data for Regions A and B, the x -coordinates of the impact locations can be evaluated when hammer knockings are made at different positions along the blade in these two regions. Figure 8 shows the predicted locations agreed reasonably well with the impact locations. It should be pointed out that an underlying assumption in the current prediction is that the region of knocking is known in advance. Previous work suggested that the region of impact may be identified by the characteristic waveform shapes [15]. Another notable point is that the current prediction does not provide information about the y -coordinates of the impact. In practice, knowing the region and the x -coordinates of a severe impact should be helpful enough to pinpoint the location for more detailed nondestructive examination to ensure structural integrity.

4. Conclusions

An impact monitoring system using fiber Bragg grating sensors has been established. With a laser ring scheme for FBG interrogation, an excellent signal-to-noise ratio is obtained that enables both extremely low energy and higher energy impacts to be detected with ease. The scheme with an ASE light source offered a lower signal strength and is good only for higher energy impacts. With FBGs deployed near the base hub, both schemes are able to detect the occurrence of an impact equivalent to a small bird striking even at the far end tip on a wind turbine blade. In an aluminum plate with homogeneous wave speed which is not known beforehand, location of impact positions is possible with a 4-FBG array. In this case, the laser ring scheme only performed marginally better than the ASE scheme, suggesting that the bottleneck

of impact source location accuracy is on the limitation of the angular insensitivity of an FBG. For the wind turbine blade, with precalibrated wave speeds, the longitudinal coordinate of an impact can be located reasonably well in the box beam reinforced region and the trailing edge region. Impact source location in the leading edge region was not successful as the wave speed varied with positions in this region.

Acknowledgments

This work was carried out with support of the National Science Council projects (NSC96-2628-E-002-223-MY3). The authors indebted to Taiwan Power Research Institute for some of the equipment support.

References

- [1] Y. J. Rao, "Recent progress in applications of in-fibre Bragg grating sensors," *Optics and Lasers in Engineering*, vol. 31, no. 4, pp. 297–324, 1999.
- [2] F. G. Tomasel and P. A. A. Laura, "Assessing the healing of mechanical structures through changes in their vibrational characteristics as detected by fiber optic Bragg gratings," *Journal of Sound and Vibration*, vol. 253, no. 2, pp. 523–527, 2002.
- [3] J. S. Leng and A. Asundi, "Non-destructive evaluation of smart materials by using extrinsic Fabry-Perot interferometric and fiber Bragg grating sensors," *NDT and E International*, vol. 35, no. 4, pp. 273–276, 2002.
- [4] J. Leng and A. Asundi, "Structural health monitoring of smart composite materials by using EFPI and FBG sensors," *Sensors and Actuators A*, vol. 103, no. 3, pp. 330–340, 2003.
- [5] H.-Y. Ling, K.-T. Lau, L. Cheng, and W. Jin, "Fibre optic sensors for delamination identification in composite beams using a genetic algorithm," *Smart Materials and Structures*, vol. 14, no. 1, pp. 287–295, 2005.
- [6] P. T. Coverley and W. J. Staszewski, "Impact damage location in composite structures using optimized sensor triangulation procedure," *Smart Materials and Structures*, vol. 12, no. 5, pp. 795–803, 2003.
- [7] M. Meo, G. Zumpano, M. Piggott, and G. Marengo, "Impact identification on a sandwich plate from wave propagation responses," *Composite Structures*, vol. 71, no. 3-4, pp. 302–306, 2005.
- [8] A. Tobias, "Acoustic-emission source location in two dimensions by an array of three sensors," *Non-Destructive Testing*, vol. 9, no. 1, pp. 9–12, 1976.
- [9] H. A. Canistraro and E. H. Jordan, "Projectile-impact-location determination: an acoustic triangulation method," *Measurement Science and Technology*, vol. 7, no. 12, pp. 1755–1760, 1996.
- [10] B. L. Chen and C. S. Shin, "Fiber Bragg gratings array for structural health monitoring," *Materials and Manufacturing Processes*, vol. 25, no. 1-4, 2010.
- [11] L. Zhang, R. Fallon, L. A. Everall, J. A. R. Williams, and I. Bennion, "Large-dynamic-range and high-resolution from a strain sensing system using long-period grating interrogating FBG strain sensor," in *Proceedings of the 24th European Conference on Optical Communication (ECOC '98)*, vol. 1, pp. 609–610, Madrid, Spain, September 1998.
- [12] R. W. Fallon, L. Zhang, A. Gloag, and I. Bennion, "Multiplexed identical broad-band-chirped grating interrogation system for

- large-strain sensing applications,” *IEEE Photonics Technology Letters*, vol. 9, no. 12, pp. 1616–1618, 1997.
- [13] R. W. Fallon, L. Zhang, A. Gloag, and I. Bennion, “Identical broadband chirped grating interrogation technique for temperature and strain sensing,” *Electronics Letters*, vol. 33, no. 8, pp. 705–707, 1997.
- [14] C. S. Shin, B. L. Chen, and C. C. Chiang, “A dynamic strain measurement system using fiber grating sensors and its application in structural health monitoring,” in *Proceedings of the World Forum on Smart Materials and Smart Structures Technology (SMSST '07)*, p. 335, Nanjing, China, May 2007.
- [15] C. S. Shin, B. L. Chen, J. R. Cheng, and S. K. Liaw, “Impact response of a wind turbine blade measured by distributed FBG sensors,” *Materials and Manufacturing Processes*, vol. 25, no. 1-4, 2010.

Research Article

Structural Health Monitoring of Precast Concrete Box Girders Using Selected Vibration-Based Damage Detection Methods

Zhengjie Zhou,¹ Leon D. Wegner,² and Bruce F. Sparling²

¹ Bridge and Structural Design Unit, Road Service Division, King County Department of Transportation, KSC-TR-0242, 201 South Jackson Street, Seattle, WA 98104-3856, USA

² Department of Civil and Geological Engineering, University of Saskatchewan, 57 Campus Drive, Saskatoon, SK, Canada S7N 5A9

Correspondence should be addressed to Leon D. Wegner, leon.wegner@usask.ca

Received 15 October 2009; Revised 30 January 2010; Accepted 23 March 2010

Academic Editor: Yi Qing Ni

Copyright © 2010 Zhengjie Zhou et al. This is an open access article distributed under the Creative Commons Attribution License, which permits unrestricted use, distribution, and reproduction in any medium, provided the original work is properly cited.

Precast, prestressed concrete box girders are commonly used as superstructure components for short and medium span bridges. Their configuration and typical side-by-side placement make large portions of these elements inaccessible for visual inspection or the application of nondestructive testing techniques. This paper demonstrates that vibration-based damage detection (VBDD) is an effective alternative for monitoring their structural health. A box girder removed from a dismantled bridge was used to evaluate the ability of five different VBDD algorithms to detect and localize low levels of spalling damage, with a focus on using a small number of sensors and only the fundamental mode of vibration. All methods were capable of detecting and localizing damage to a region within approximately 1.6 times the longitudinal spacing between as few as six uniformly distributed accelerometers. Strain gauges configured to measure curvature were also effective, but tended to be susceptible to large errors in near support damage cases. Finite element analyses demonstrated that increasing the number of sensor locations leads to a proportional increase in localization accuracy, while the use of additional modes provides little advantage and can sometimes lead to a deterioration in the performance of the VBDD techniques.

1. Introduction

Although there has been a growing awareness of the declining state of the civil infrastructure in North America for several decades, recent catastrophic bridge failures have highlighted both the severity of the problem as it relates to bridges, and the inadequacy of current inspection and monitoring practices to assess their condition [1]. More objective means for monitoring the structural health of bridges have been pursued for some time by the research community. While a number of local nondestructive evaluation (NDE) methods [2, 3] or global response-based methods [4–6] are either in current use or are at various stages of development, the application of a specific structural health monitoring (SHM) technique will be most successful when its capabilities are closely matched to the features and requirements of a particular bridge component.

Vibration-based damage detection (VBDD) may be particularly well-suited to assessing the condition of precast,

prestressed concrete box girders. This type of girder is commonly employed as a superstructure component for short and medium span bridges. Available in standard cross sectional dimensions and lengths, they are typically used in simple span construction, with multiple units arranged side-by-side and connected by shear keys or in some other manner to facilitate load sharing. Large portions of these elements remain inaccessible to inspection either visually or by common NDE methods. VBDD techniques, on the other hand, are capable of assessing the condition of an entire structural component simultaneously and are not limited to the interrogation of accessible regions. They have also been shown to be capable of identifying the presence and location of low levels of damage on other types of simple-span structures [7]. The capabilities of VBDD methods therefore appear to closely match the monitoring requirements of precast concrete box girders, although the application of VBDD methods to these components has apparently not been reported in the literature.



FIGURE 1: Photograph of the bridge prior to girder replacement.

To clarify the principle underlying VBDD techniques, the vibration characteristics of a structure (e.g., its natural frequencies and mode shapes) can be considered to be a global response signature that can be used as the basis for assessing its condition because they contain embedded information about the structure's inherent properties. Changes in the structural condition will be reflected in the vibration signature, making it theoretically possible to identify the presence of damage by tracking changes to that signature. On this basis, numerous VBDD indices have been proposed [6, 8, 9], including those that rely on shifts in natural frequencies [10–12], direct changes to mode shapes [13, 14], changes to mode shape curvatures [15, 16], changes to measurement-derived flexibility or stiffness matrices [17, 18], changes to modal strain energy [19, 20], and numerical model updating [21, 22].

Having been applied to numerous different types of structures [17, 23, 24], including real bridge structures [12, 20, 25–30], VBDD has yet to find widespread acceptance as an SHM tool for bridges. In fact, the authors are not aware of a single case in which these techniques are being routinely applied as a component of a systematic monitoring strategy for bridge management; successful application remains limited to investigations by experts in a research context. However, as a relatively simple component in form as well as application, precast concrete box girders may be particularly amenable to the application of VBDD.

The objective of the current study was to assess the ability of VBDD techniques to identify damage on precast, prestressed concrete box girders. It should be noted, though, that the results can be applied to any simple-span beam-like structural component. In order to consider an approach that could be practically applied in the field, the focus was on detecting low (incipient) levels of damage using a small number of sensors and only the fundamental mode of vibration. The study was carried out in the laboratory using a box girder that had been reclaimed from a dismantled bridge. Given that arrangement of these components in the field is very similar to the laboratory setup, it is believed that the findings of the laboratory investigation can be transferred directly to the field, provided that similar experimental techniques can be applied in the field application and that care is taken to mitigate the effects of environmental influences. Experimental data were supplemented by finite element analyses to explore additional considerations, including a larger number of damage scenarios, the influence of the

number of measurement points used to define mode shapes, and the influence of accounting for additional vibration modes.

2. Experimental Study

The study was performed using a precast, prestressed concrete box girder that was removed from a bridge on Provincial Highway No. 56 over the Qu'Appelle River in southern Saskatchewan. Figure 1 shows the bridge prior to girder replacement. Originally constructed in 1972, the bridge featured two 12.2 m end spans and a central 15.2 m span with nine box girders arranged side-by-side on each span, supported by timber bents and piles. The girders were replaced in 2001 due to extensive corrosion after less than 30 years in use. At that time, one of the dismantled 12.2 m long girders was transported to the structural laboratory at the University of Saskatchewan for testing (Figure 2(a)). The standard double box girder had a 1216×508 mm cross section, as seen in Figure 2(b). It was simply supported in the laboratory at each of its four corners, resulting in a longitudinal span of 11.9 m.

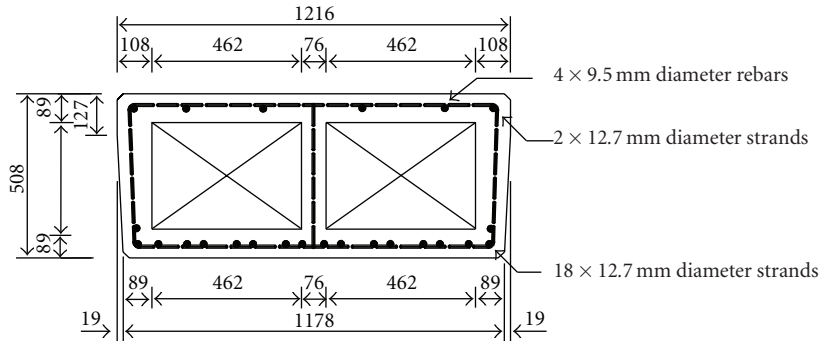
The procedures used for the experimental study were intended to simulate methods that could be practically applied in a field application. This included the use of a relatively small number of sensors and of “output-only” modal analysis methods, which do not require the measurement of the excitation force and, therefore, do not make use of the frequency response function (FRF). Field applications would typically involve the measurement of the dynamic properties of the girder on a periodic basis, likely at a similar time of year to avoid large temperature differences between successive tests which could introduce additional variability in the vibration characteristics [31].

The experimental test procedure consisted of measuring the initial dynamic properties of the girder, and then incrementally inducing a succession of new damage states and measuring the dynamic properties associated with each new state. The baseline dynamic signature for a particular damage state was taken to be that measured for the previous state of damage. Well-defined “spalling” damage was induced into the girder by physically removing small square blocks of concrete, 150×150 mm in plan and 30 mm deep, from the top surface of the deck, as shown in Figure 3. This was done incrementally at the twelve locations shown in Figure 4, in which damage states are numbered according to the sequence in which they were introduced. The twelve cases represented a wide variety of longitudinal and transverse locations to test the damage localization capability of the VBDD techniques over a large range of possible damage locations. Each incremental damage state corresponded to a local reduction in flexural rigidity of approximately 2.5%.

Common forms of damage experienced by this type of structural element include localized corrosion, surface spalling, and abrasion of the wearing surface. The type of damage induced experimentally was considered to be representative of any form of damage that causes a localized reduction in the flexural rigidity. Therefore, the findings



(a)



(b)

FIGURE 2: The prestressed concrete box girder used for the experimental study: (a) photograph of the girder set up for testing in the laboratory, and (b) transverse cross section (dimensions in mm).

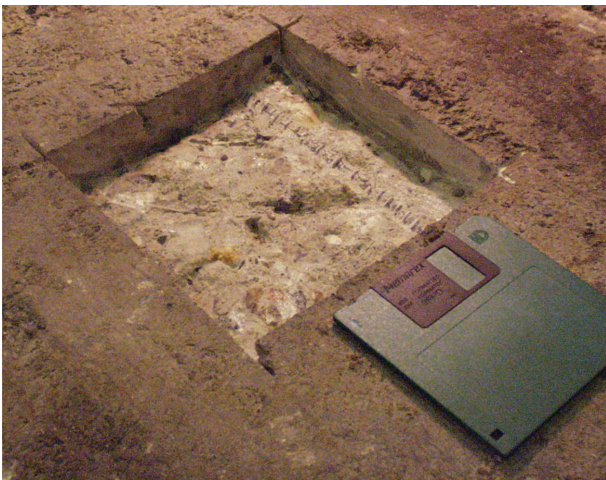


FIGURE 3: Photograph of damage induced on the girder.

should not be considered to be limited to the specific type of damage imposed here.

A hydraulic shaker, seen in Figure 2(a), was anchored directly to the top surface of the girder and used to induce dynamic excitation. The signal for the shaker was generated using LabView software [32] implemented on a personal computer. As mentioned above, the excitation force was not measured.

The dynamic response was measured using two different types of sensors: accelerometers and strain gauges. Data were acquired using a 12-bit data acquisition system (National Instruments SCXI 1001, LabView 6i). The single axis accelerometers (EpiSensor ES-U, Kinemetrics Inc., Pasadena, CA) were configured for a maximum range of $\pm 0.5g$ and a precision of 0.00025 g and were oriented to measure

vertical acceleration. Six accelerometers were bonded to the top surface of the girder, first along one side and then the other, at evenly spaced longitudinal intervals of 1.7 m, as indicated in Figure 4. Vertical displacements at each accelerometer location were obtained by integrating the acceleration signal twice to obtain first velocity and then displacement, incorporating appropriate digital filters at each stage to remove baseline drift. Strictly speaking, the acceleration signals could have been used directly, without conversion to displacements, since the amplitudes of the two signals are exactly proportional at any given frequency. In practice, however, the numerical integration over time and the additional filtering that was employed served to attenuate noise in the signals, thus resulting in more repeatable natural frequencies and mode shapes. Each displacement-time series was then scaled using a Parzen window function [33] to reduce leakage before applying a Fast Fourier Transform (FFT) to obtain a Fourier spectrum of the response amplitude.

The use of strain gauges permitted a comparison of the performance of the VBDD techniques using data from both sets of sensors. Electrical resistance foil strain gauges (model PL-90-11, Tokyo Sokki Kenkjujo Co. Ltd., Japan) with a 90 mm gauge length and 120 ohm resistance were bonded to the vertical side surfaces of the girder in vertically aligned groups of three, oriented to measure longitudinal strain, at the same six longitudinal locations as used for the accelerometers along each side (see Figure 4). In a field application, the side faces would not be accessible for post-construction application of the gauges, since the girders are placed immediately adjacent to each other. However, the gauges could be installed in well-controlled conditions in the precast plant prior to placement of the girders. The strain profile through a vertical cross section at each location was obtained by fitting a least-squares regression line through the three

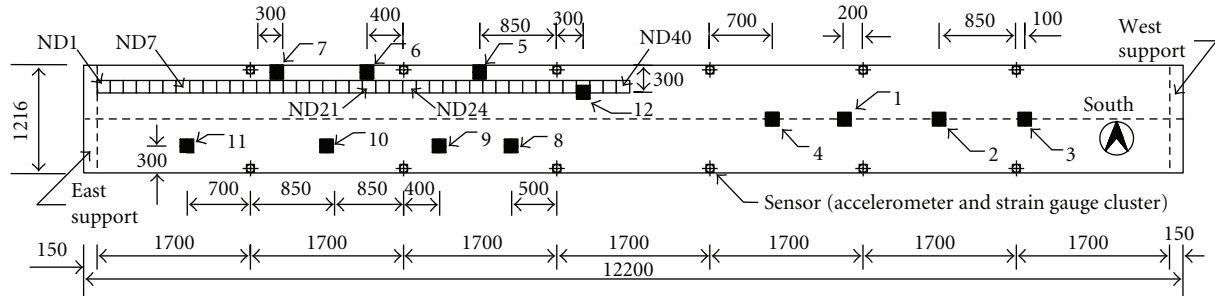


FIGURE 4: Schematic plan of girder showing locations of experimental damage cases (numbered and dimensioned black squares), numerical damage cases (open squares, selected cases labelled ND1, etc.), and sensors (dimensions in mm).

TABLE 1: Comparison of FE and experimental natural frequencies and mode shapes for the undamaged system.

| Parameter | Mode | | | |
|---------------------------|--------------|--------------|---------------|--------------|
| | 1 (flexural) | 2 (flexural) | 3 (torsional) | 4 (flexural) |
| Natural Frequencies (Hz) | | | | |
| Experimental model | 7.61 | 26.3 | 31.7 | 57.9 |
| Finite element model | 7.58 | 27.23 | 36.46 | 58.95 |
| Relative error (%) | -0.4 | 3.5 | 15.0 | 1.8 |
| Modal Assurance Criteria: | 0.9999 | 0.9967 | 0.9882 | 0.9865 |

individual strain measurements at each instant in time. This linear profile was used to calculate the bending curvature at each location. Once again, a Parzen window function was applied to the curvature-time series to reduce leakage, and an FFT was used to obtain spectrum data for the curvatures. The fundamental mode curvatures at measurement points were used to calculate the change of curvature vector, $\Delta\phi''$, as described in Section 4, for use with the mode shape curvature method. Intermediate values of $\Delta\phi''$ between measurement points were generated using a Bézier interpolation technique [34].

Natural frequencies were identified from the average of ten root-mean-square (rms) normalized frequency response spectra. These were obtained from tests during which data were acquired at a rate of 150 samples per second for a period of 220 seconds while the shaker subjected the girder to a white noise excitation. After natural frequencies had been identified, a resonant harmonic excitation was applied at each of the identified natural frequencies in sequence to accurately measure the corresponding mode shapes. During this procedure, each set of data was acquired at 300 samples per second for 21 seconds. The average of ten mode shape measurements was used in subsequent damage detection algorithms. While only the fundamental mode was used for damage detection experimentally, the first four modes were used for calibration of the finite element (FE) model described below.

3. Numerical Simulations

A finite element (FE) model of the girder was prepared and calibrated to match the experimentally measured dynamic

properties, with the purpose of investigating the influence of several factors that could not easily be studied experimentally on the performance of the VBDD techniques. These factors included the number of measurement points and modes used, as well as a wider range of damage locations. The commercial FE analysis package ANSYS [35] was used to perform eigenvalue analyses of the girder when subjected to several states of damage in order to generate the natural frequencies and mode shapes of the system at these various states. The girder was divided into 8-node 3-dimensional isoparametric brick elements. A total of 84 elements were used longitudinally (including two elements beyond the supports at each end to model the end plates), with the top and bottom flanges divided into twenty-four elements transversely, and two (for the bottom plate) or three (for the top plate) elements through the thickness. The vertical webs were divided into five elements vertically and two elements through the thickness, and the prestressing tendons were modelled using linear truss elements.

Boundary conditions were imposed at the four support nodes, each located 150 mm from the ends and 50 mm from the sides, restraining them against movement in the vertical direction. In addition, one of these nodes was restrained in both the longitudinal and transverse directions, a second in the longitudinal direction, and a third in the transverse direction, preventing rigid body movement of the system. Elastic and section properties of the physical components were applied as model parameters.

The model was calibrated to the four lowest natural frequencies and mode shapes of the undamaged physical system by adjusting the value used for Young's modulus

of the concrete. Table 1 shows that, with the exception of the third (torsional) mode, good agreement between predicted and measured natural frequencies was achieved; in addition, that the modal assurance criterion (MAC) values [36] comparing the first four measured and calculated mode shapes were excellent. A separate study found that the torsional mode was very sensitive to slight differences in support conditions. These differences could not be eliminated because it was not possible to adjust the supports perfectly so that the weight of the girder was equally distributed to the four supports. The good agreement otherwise is an indication that the model could be relied upon to provide a reasonably good estimate of the performance of the VBDD methods.

Once the model had been calibrated, damage to the girder was simulated by eliminating three transversely adjacent elements from the top surface of the girder, resulting in the removal of a region 149 mm long, 150 mm wide and 30 mm thick—a size similar to that investigated experimentally. A total of 40 damage cases were simulated. For these, the transverse location of damage remained centred 0.225 m from one side of the girder, while the central longitudinal location of the removed elements was varied from 0.074 to 5.876 m relative to the support at 0.149 m intervals (see Figure 4).

In order to simulate the acquisition of measured data from a limited number of sensors attached to a physical system, vertical modal displacements were extracted from the FE-generated eigenvectors at a small number of uniformly spaced “measurement” points along the longitudinal edges of the girder. It is noted that the location of simulated measurement points along the girder edges matched what was done experimentally, an arrangement that enabled the identification of torsional modes. Evaluation of the influence of the number of measurement points was facilitated by investigating three cases: one in which seven measurement points were used, one in which 15 measurement points were used, and a well-defined reference case in which 79 measurement points were used. In each case, the measurement points were uniformly distributed along the length of the girder. It should be noted that the smallest number of measurement points did not match the six used experimentally; as described above, the girder was divided into 80 elements along the span length (11.9 m) to accommodate the desired damage size, and this was compatible with seven uniformly spaced measurement points, but not six.

Regardless of the number of simulated measurement points, the modal displacement vectors ϕ used for calculations all contained 81 components, which included components of zero at each support. When seven or 15 simulated measurement points were used, the additional components between measurement points were interpolated as described in the following section. To clarify, when seven simulated measurement points were used, the modal displacements at nine intermediate points between each pair of adjacent measurement points were interpolated, while when 15 simulated measurement points were used, modal displacements at four intermediate points were interpolated.

While the focus of the study was on the performance of the damage detection techniques using only the fundamental mode, the use of the first three flexural modes was also investigated to ascertain the influence of the number of modes considered on the performance of the VBDD methods.

In order to establish the validity of the numerical calculations and justify the extension of the study to a larger number of damage cases using FE simulations, comparison of the numerical and experimental results for a representative damage case is presented in Appendix A.

4. Damage Detection Methods

Five of the most common VBDD techniques available in the literature were applied. These included the change in mode shape (CMS) method [37], the mode shape curvature (MSC) method [15], the change in flexibility (CF) method [17], the damage index (DI) method [38], and the change in uniform flexibility curvature (CUFC) method [28]. Among these, the MSC, DI, and CUFC methods—all calculated using mode shape curvatures—produced virtually identical results. For this reason, and for the sake of brevity, the DI method was selected as being representative of these three methods, with results for the other two curvature-based methods not provided. The exception to this is the results of the MSC method obtained using curvatures that were measured directly using a system of strain gauges presented in Section 5.2. It should be noted that all of the methods investigated are based only on measured data and do not require the use of a numerical model. This is considered to be an important feature of methods that could be practically applied to a large inventory of short and medium span bridges, for which the preparation of an FE model is generally unwarranted.

Each of the techniques applied in this study makes use of the measured mode shapes for the structure in baseline and damaged conditions, designated by modal amplitude vectors ϕ and ϕ^* , respectively. For the present study, these vectors corresponded to vertical modal amplitudes defined at a relatively small number of uniformly distributed measurement points along the girder, supplemented by additional interpolated modal amplitudes between measurement points. Since the scale of a mode shape is arbitrary by definition, mode shape vectors must be normalized to a common basis, thereby minimizing the difference between damaged and undamaged mode shapes in an averaged sense and accentuating localized changes caused by damage. Vectors were therefore scaled to possess a unit norm (i.e., $\phi^T \phi = 1$). In effect, this approach may be considered equivalent to mass orthonormalization assuming a uniform distribution of mass. Such an assumption is particularly justifiable when the structure is a prismatic flexural member for which modal amplitudes are defined at uniformly distributed points along the length of the span, as was the case for the current investigation.

Formulations for the VBDD techniques are provided in detailed form in the literature cited, but are briefly summarized here.

4.1. *Change in Mode Shape Method (CMS)*. The change in mode shape vector, $\Delta\phi$, was calculated by taking the simple difference between damaged and undamaged mode shapes

$$\Delta\phi = |\phi^*| - |\phi|, \quad (1)$$

where the absolute value symbols indicate evaluation of the absolute value of each component of the vector.

4.2. *Mode Shape Curvature Method (MSC)*. The MSC method considers the increase in modal curvature caused by damage:

$$\Delta\phi_i'' = |\phi_i^{*''}| - |\phi_i''|, \quad (2)$$

where the double prime notation indicates the second spatial derivative and the subscript i refers to the i th mode. Again, evaluation of absolute values is carried out on each component of the vector. If multiple modes are used, the sum of differences in curvature may be employed as a damage indicator, as expressed by

$$\Delta\phi'' = \sum_{i=1}^n \Delta\phi_i'', \quad (3)$$

where n is the number of modes used.

4.3. *Change in Flexibility Method (CF)*. As originally formulated [17], the CF method involves estimating the flexibility matrices for the undamaged and damaged structure, \mathbf{F} and \mathbf{F}^* , respectively, from one or more of the lower vibration modes as follows

$$\begin{aligned} \mathbf{F} &\approx \sum_{i=1}^n \frac{1}{\omega_i^2} \phi_i \phi_i^T, \\ \mathbf{F}^* &\approx \sum_{i=1}^n \frac{1}{\omega_i^{*2}} \phi_i^* \phi_i^{*T}, \end{aligned} \quad (4)$$

in which ω_i is the angular frequency of the i th mode and n is the number of measured modes. The change in flexibility matrix, $\Delta\mathbf{F}$, is then calculated as

$$\Delta\mathbf{F} = \mathbf{F}^* - \mathbf{F}. \quad (5)$$

The parameter $\bar{\delta}_j$, the maximum of the absolute values of the elements in column j of $\Delta\mathbf{F}$, is taken as a measure of the change of flexibility at point j of the structure. The maximum change of flexibility then provides an indication of the location of damage.

4.4. *Modified Change in Flexibility Method (MCF)*. For the present study, a slight modification to the CF method is proposed on the basis of physical arguments. Since column j of the flexibility matrix represents the deflected shape of the structure when a unit load is applied at location j , the change in flexibility at a location of damage should always be positive since the deflection under a unit load at that location should always increase when damage is inflicted at that point.

Therefore, it is proposed that the maximum positive value of elements in column j be used as the damage indicator, rather than the maximum of the absolute values. The modified approach was observed to improve the performance of the method, particularly when experimental data were used. Appendix B compares the distributions produced by the change in flexibility method in original and modified forms for a representative damage case.

4.5. *Damage Index Method (DI)*. The DI method is based on local changes in modal strain energy. In discrete form, the index takes the following form

$$\beta_{ji} = \frac{(\phi_{ji}''^*)^2 + \sum_{k=1}^m (\phi_{ki}''^*)^2}{(\phi_{ji}'')^2 + \sum_{k=1}^m (\phi_{ki}'')^2} \times \frac{\sum_{k=1}^m (\phi_{ki}'')^2}{\sum_{k=1}^m (\phi_{ki}''^*)^2} = \frac{\text{NUM}_{ji}}{\text{DEN}_{ji}}, \quad (6)$$

in which ϕ_{ji}'' corresponds to the j th element of the modal curvature vector ϕ'' for the i th mode. If more than one mode is used, a single index for each location, j , is formed by

$$\beta_j = \frac{\sum_{i=1}^n \text{NUM}_{ji}}{\sum_{i=1}^n \text{DEN}_{ji}}. \quad (7)$$

The index is normalized by considering it to be a normally distributed random variable

$$Z_j = \frac{\beta_j - \mu_\beta}{\sigma_\beta}, \quad (8)$$

where μ_β and σ_β are the mean and standard deviation of damage indices, respectively. Damage indices falling two or more standard deviations from the mean (i.e., $Z_j \geq 2$) are defined as being indicative of a possible damage location.

To further clarify the implementation of the methods used, it should be observed that the curvature-based methods (DI, MSC, CUFC) require estimates of modal curvature at measurement points. Elements of the modal amplitude vectors initially corresponded to values defined at a relatively small number of measurement points. In order to generate a sufficiently well-defined displacement profile required to facilitate a more accurate estimation of curvature, the displacement profile at up to nine points between each pair of adjacent sensor locations was estimated using a natural cubic spline interpolation scheme, which enforced continuity of the second derivative at measurement points and a zero second derivative at the simple supports. A similar approach has been reported in the literature [20, 39, 40]. Modal curvatures were then explicitly obtained from the resulting spline equations for use with the MSC and DI methods. Although interpolation was strictly not required to apply the MCF and CMS methods, its use was not found to impair the performance of the methods, and could actually improve their localization capabilities by permitting predicted damage locations to lie between measurement points. Therefore, the same interpolated mode shapes were used for all VBDD methods.

5. Results and Discussion

5.1. Performance Using Only a Small Number of Measurement Points

5.1.1. *Typical VBDD Parameter Distributions.* The distributions of the VBDD parameters calculated for experimental damage case 4 are provided in Figure 5, in which the locations of the accelerometers are indicated by the vertical gridlines. To facilitate the plotting of all distributions on a common scale, all parameters have been normalized in a manner similar to that used by the DI method; that is,

$$\hat{P}_i = \frac{P_i - \mu_P}{\sigma_P}, \quad (9)$$

where \hat{P}_i represents the normalized parameter at location i , P_i is the unnormalized VBDD parameter (i.e., CMS and MCF) at that location, μ_P is the mean of parameter values at all locations along the girder length, and σ_P is the standard deviation of parameter values.

The distributions shown in Figure 5 are typical of those produced for damage cases that were located approximately within the middle two-thirds of the span. In these cases, a clear maximum peak was produced at or near the same location by all methods, which corresponded to one of the two measurement points adjacent to the damage location, although not necessarily the nearest one. In addition, it is noted that the DI method produced a piecewise linear distribution between interior measurement points, which is a consequence of the cubic spline interpolation procedure used to estimate curvature values between measurement points. As such, the curvature-based methods are only capable of producing peaks at measurement points.

5.1.2. *Effect of Proximity of Damage to a Support.* The distributions associated with a sequence of damage locations moving from left to right (east to west) along the girder are illustrated in Figure 6. It is apparent that the distributions associated with near support damage cases (cases 11, 10, and 3) featured characteristics that clearly distinguished them from the other damage cases. These characteristics differed according to the method applied. For the CMS method, distributions for near support damage cases featured multiple undulations, the highest peak of which was located near the damage. For the MCF method, two significant peaks of similar magnitude were produced. The higher of the two peaks was not always the one closest to the damage (e.g., case 3), but one of the peaks was located near the damage while no peaks were located in the vicinity of the opposite support. For the DI method, near support damage cases featured multiple peaks, the most prominent of which was not located near the damage. As a result, the DI method was unable to locate near support damage cases, and the predicted damage location was erroneous when damage was located near a support.

As damage moved slightly farther from the support—generally beyond the first measurement point—a clear,

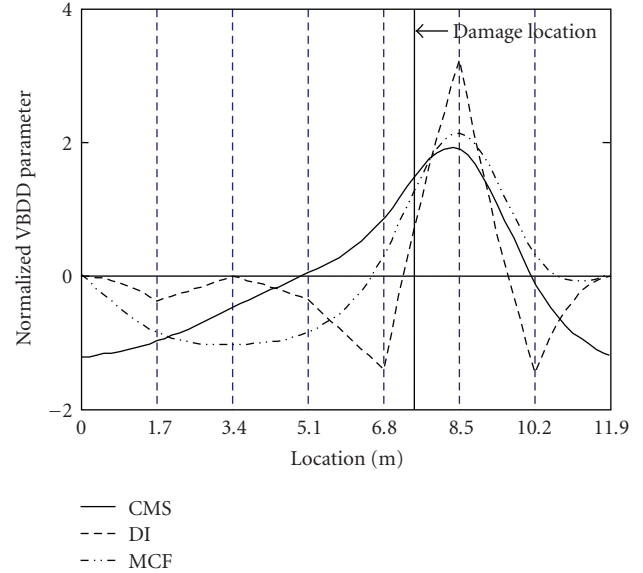


FIGURE 5: Distributions of normalized VBDD parameters for experimental damage case 4.

dominant peak was produced by all VBDD indices, as seen, for example, with damage case 2, located 2.55 m from the west (right) support. This feature characterized the distributions produced by all non-near support damage cases. On the other hand, damage case 10 was located the same distance (2.55 m) from the east (left) support, and still featured the near support characteristics just described. Damage case 6, however, located only slightly farther (3.0 m) from the east (left) support, produced a single dominant peak by all methods. This indicates that slight differences in support conditions affected the near support length within which distributions featured multiple peaks. For this particular study, it was not possible to distribute the girder's weight evenly to the simple supports at the four corners, making support conditions slightly different at each of the four support locations.

The above discussion indicates that damage located near supports is more challenging to identify by virtue of the appearance of multiple peaks in the VBDD distributions. However, the following results were consistently observed: when multiple peaks were produced by the CMS and MCF methods, and when the three VBDD parameters differed in the location of the maximum peak, the damage was located close to a support. In these cases, the MCF method consistently indicated which of the supports damage lay close to, and the CMS method always produced a maximum peak near the damage location, even when other peaks were present. The CMS method was, therefore, the most reliable among the methods investigated when localizing near support damage cases. The simultaneous application of the other methods, however, can provide an added level of confidence in the predicted damage location, particularly in terms of distinguishing near support damage cases from others.

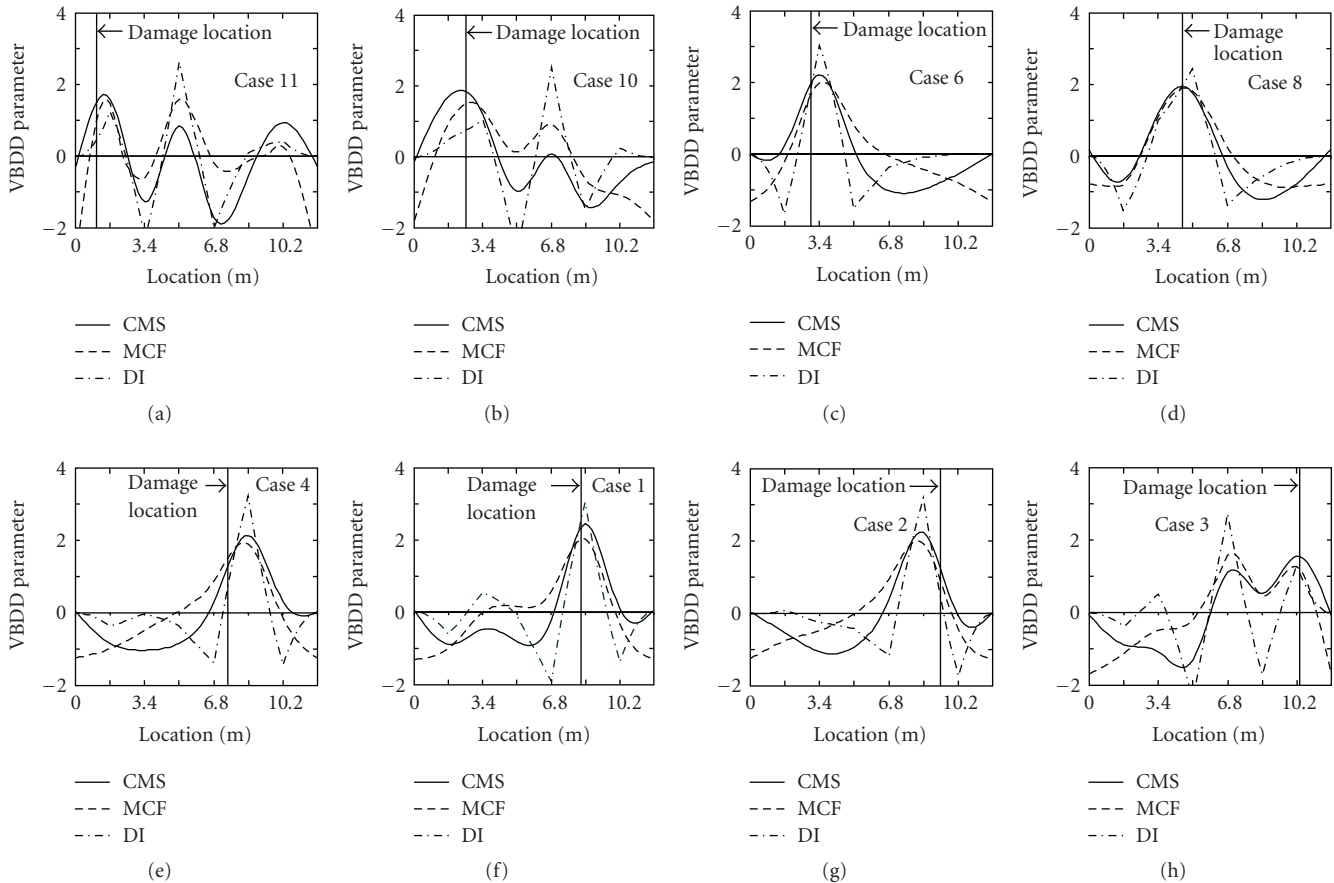


FIGURE 6: Normalized VBDD distributions for a sequence of experimental damage cases, with damage moving from east to west (left to right) along the girder.

5.1.3. Localization Accuracy. The performance of each of the methods in terms of its ability to identify the damage location is summarized in Figure 7, which plots the predicted versus actual locations of damage for all 12 experimental damage cases and all 40 numerical damage cases. In these figures, labelled gridlines correspond to the experimental measurement point locations, whereas the additional dotted gridlines correspond to the numerical measurement points. In addition, different symbols have been used to distinguish predictions that corresponded to a single clear peak in the distribution from those in which a second peak with at least 75% of the magnitude of the first also occurred. When the second largest peak appeared nearer to the damage location, that peak is plotted as the predicted location. In some cases, the peak that occurred nearer to the damage location did not meet the 75% threshold. In these cases, the height of the second peak relative to the first is provided as a percentage value next to the corresponding data point.

Comparing the performance of the three methods shown in Figure 7, it is apparent that the CMS method was most consistent in locating the damage without ambiguity. The numerical localization predictions for this method (Figure 7(a)) were also more accurate than the experimental predictions. This latter result is expected, since numerical

data were free from the uncertainties inherent in all experimental data. The MCF method (Figure 7(b)) tended to produce ambiguous results for near support damage cases. These ambiguities resulted from a second peak of roughly the same magnitude appearing farther from the support. Figure 7(c) clearly shows that the DI method was only capable of predicting damage to be located at measurement points, both experimentally and numerically.

Figures 7(a) and 7(b) also show that the use of interpolation to estimate modal displacements between measurement points allowed the CMS and MCF methods to predict damage locations between measurement points. In the case of the CMS method, interpolation permitted the localization of damage with greater accuracy over a wider range of damage locations when numerically simulated data were used. The use of interpolation is therefore advisable even in cases where it is not specifically required to estimate curvature. It also suggests that further benefit could be derived from the identification of interpolation techniques that are best able to reproduce the mode shapes from a small number of known values.

Comparisons between the predictive capabilities of the various methods may be made in quantifiable terms by referring to Table 2, which lists the maximum and average errors produced by each method, normalized by the spacing

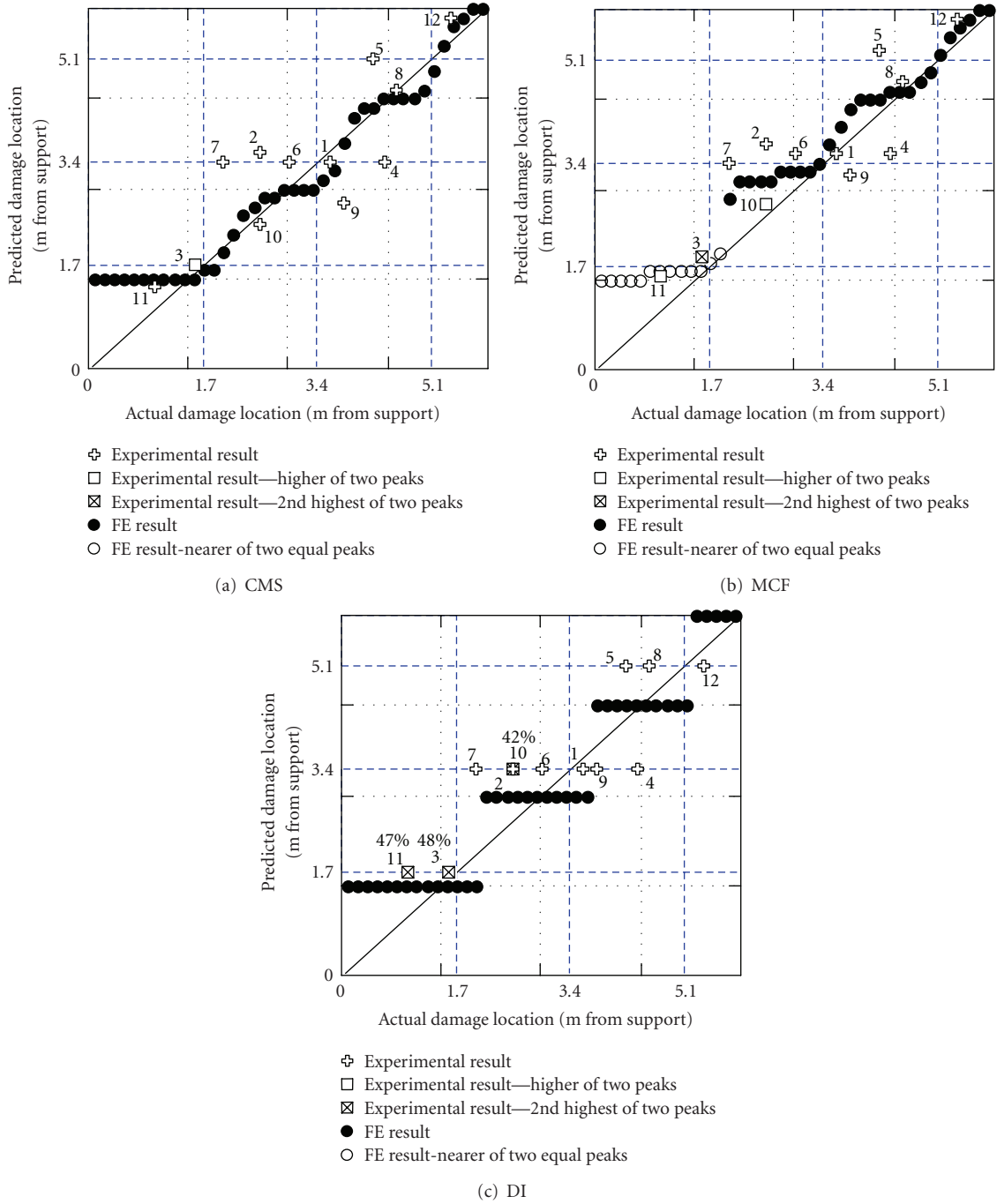


FIGURE 7: Correlation between predicted and actual longitudinal location of damage using six experimental measurement points and seven numerical measurement points, calculated by (a) CMS, (b) MCF, and (c) DI methods. Experimental data points are numbered according to the damage cases given in Figure 4.

TABLE 2: Error in predicted damage location by each method, listed as a fraction of measurement point spacing.

| Method | Experimental Results | | | | Numerical Results | | | |
|--------|----------------------|------------|-------------|----------|-------------------|------------|-------------|----------|
| | Max. error | Avg. error | Stand. dev. | % ambig* | Max. error | Avg. error | Stand. dev. | % ambig* |
| CMS | 0.82 | 0.34 | 0.27 | 8 | 0.25 | 0.12 | 0.07 | 0 |
| DI | 0.82 | 0.37 | 0.22 | 25 | 0.55 | 0.25 | 0.15 | 0 |
| MCF | 0.82 | 0.35 | 0.26 | 25 | 0.65 | 0.20 | 0.17 | 33 |

* indicates the percentage of damage cases that produced a second peak that was either at least 75% of the magnitude of the highest peak, or nearer to the damage location.

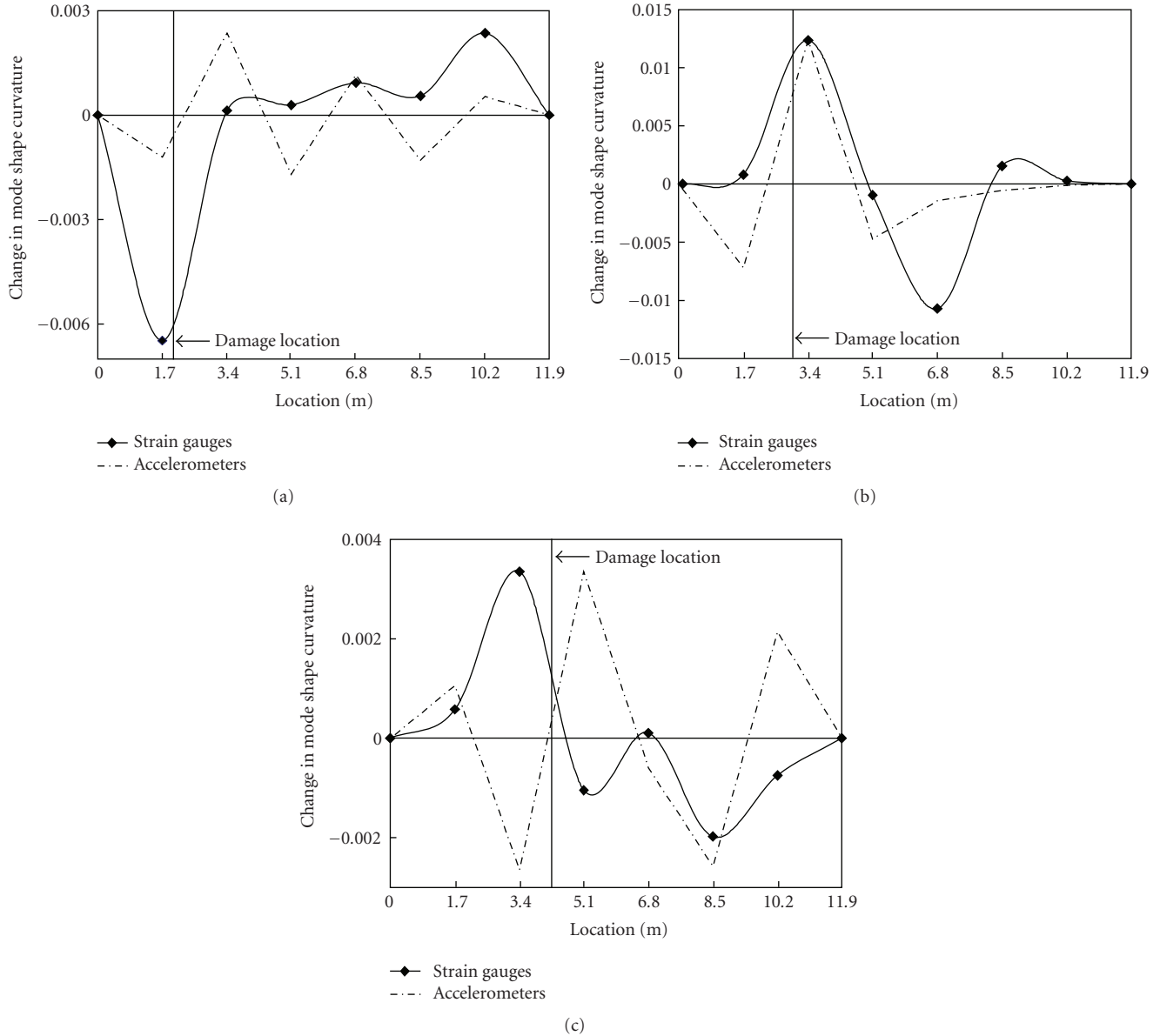


FIGURE 8: Comparison of MSC distributions produced using strain gauge measured curvatures and those derived from accelerometer data for experimental damage cases (a) 7, (b) 6, and (c) 5.

between measurement points, h , along with the standard deviation of the errors, provided here as an indication of the variability of the predictions. Also listed is the percentage of cases resulting in some ambiguity in the results, as defined earlier. Values corresponding to the numerical results in the table were calculated considering only damage cases located beyond the first measurement point from the support, since the results shown in Figure 7 suggest that damage cases closer to the support require special consideration.

The superior performance of the CMS method relative to other procedures is clearly evident in Table 2. Based on numerical results, the maximum error in the location of damage predicted by the CMS method was $0.25h$, with an average error of $0.12h$. This result was significantly

better than the other methods. The advantage diminishes, however, when experimental data are considered, for which all methods produced maximum errors on the order of $0.82h$ and average errors close to $0.35h$. However, with one exception, the CMS method always produced a clear maximum peak near the location of damage, thus precluding the possibility of uncertainty with regard to the predicted damage location.

The results presented in Figure 7 and Table 2 suggest that an analyst without any prior knowledge of the damage location would be successful at localizing the damage by interrogating a region within $0.82h$ on either side of the predicted location when an unambiguous peak appears in the VBDD parameter distributions. As discussed earlier,

if multiple peaks of similar magnitude appear, in which case the VBDD parameters may differ in the location of the maximum peak, the damage will be located near a support, and the CMS method can be used to localize it. In this case, interrogating a region within approximately $1.5h$ of the support would be successful at localizing the damage.

Based on these results, it is safe to conclude that the use of a relatively small number of measurement points to characterize the fundamental mode shape is sufficient to detect and localize low-intensity damage with a reasonable level of accuracy for simply supported beam-like structures.

5.2. Direct Measurement of Curvature Using Strain Gauge Clusters. The direct measurement of curvature using vertically aligned strain gauge clusters offers a number of potential advantages over using accelerometers when applying the mode shape curvature method. These include reducing instrumentation costs and increasing the conduciveness to permanent installation of the instrumentation. To facilitate the comparison of the two approaches, the MSC distributions for three representative damage cases are shown in Figure 8, presented in order of increasing distance from the support. Distributions derived from accelerometer data have been scaled such that the maximum values of the two distributions in each graph are identical.

As typical of near support damage cases, Figure 8(a) shows the distributions for experimental damage case 7, located 2.0 m from the east (left) support. The large negative peak observed near the damage location in this figure should not be construed as a possible indicator of damage, since this would imply that a local reduction in stiffness has resulted in a decrease in curvature at that location, which would contradict beam theory. For this damage case, then, the strain gauge approach performed very poorly compared to the accelerometer based approach, resulting in a misleading distribution that would lead one to believe that damage was actually located close to the opposite support. A similar result was realized for damage case 11 (not shown), located 1.0 m from the same support, although the negative peak was absent in this case.

Figure 8(b) shows the distributions for damage case 6, located 3.0 m from the east (left) support, and may be considered to be representative of damage cases located outside of the near support region. In this case, the two approaches yielded very similar distributions, predicting damage to lie at identical locations. Seven of the 12 damage cases fell into this category. Damage case 3 is included in this group, although it was located only 1.6 m from the west (right) support (closer to a support than damage case 7, shown in Figure 8(a)). This lends further support to the contention that support conditions have some influence over the near support distance within which distributions become more difficult to interpret. Uneven support conditions also appear to influence the two approaches somewhat differently. Whereas the accelerometer approach produced multiple peaks in near support damage cases, one of which was typically located near to the damage, the strain gauge approach

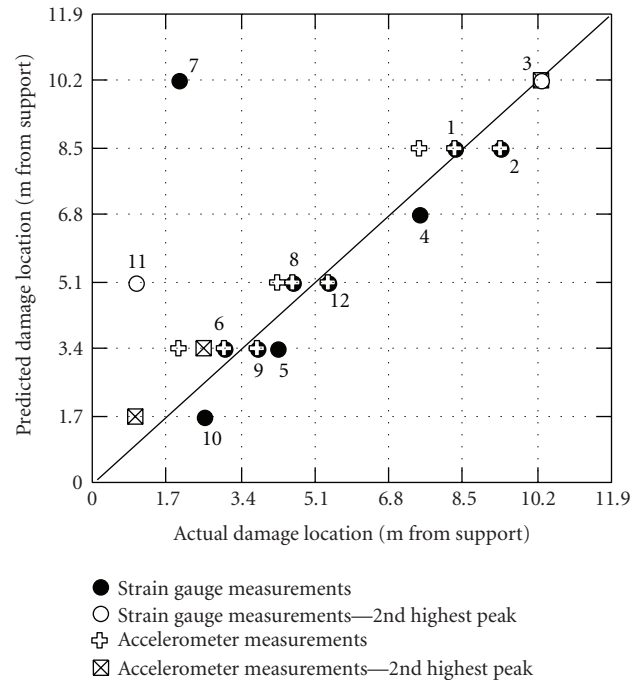


FIGURE 9: Correlation between predicted and actual damage locations, as calculated by the MSC method using strain gauge measured curvatures and those derived from accelerometer data. Numbers refer to experimental damage cases (see Figure 4).

produced distributions in which the most significant peaks were located some distance from the damage.

In two cases (damage cases 4 and 5, for which damage was located midway between two measurement points, the maximum peaks produced by the two approaches appeared on opposite sides of the damage, as seen in Figure 8(c). Such a result could be advantageous if the two instrumentation schemes are used simultaneously, because it would narrow the predicted damage location to lie between the two peaks.

The correlation between predicted and actual damage locations produced by the two approaches for all experimental damage cases is shown in Figure 9. The performance of the two approaches is seen to be generally comparable, with the obvious exception of the two near support damage cases 7 and 11, for which the strain gauge approach produced erroneous results. If these two cases are omitted, the strain gauge approach resulted in maximum and average localization errors of $0.50h$ and $0.30h$, respectively, which is an improvement over the MSC method using the accelerometer approach ($0.82h$ and $0.37h$, resp., identical to the DI method listed in Table 2). However, the strain gauge approach appears to be more susceptible to producing erroneous or ambiguous results for near support damage cases, perhaps because of lower signal-to-noise ratios near simple supports and the possibility of poor seating at the supports. Therefore, while the MSC method applied using strain gauge data could be used to supplement the other approaches, it should not be relied upon as a stand-alone method.

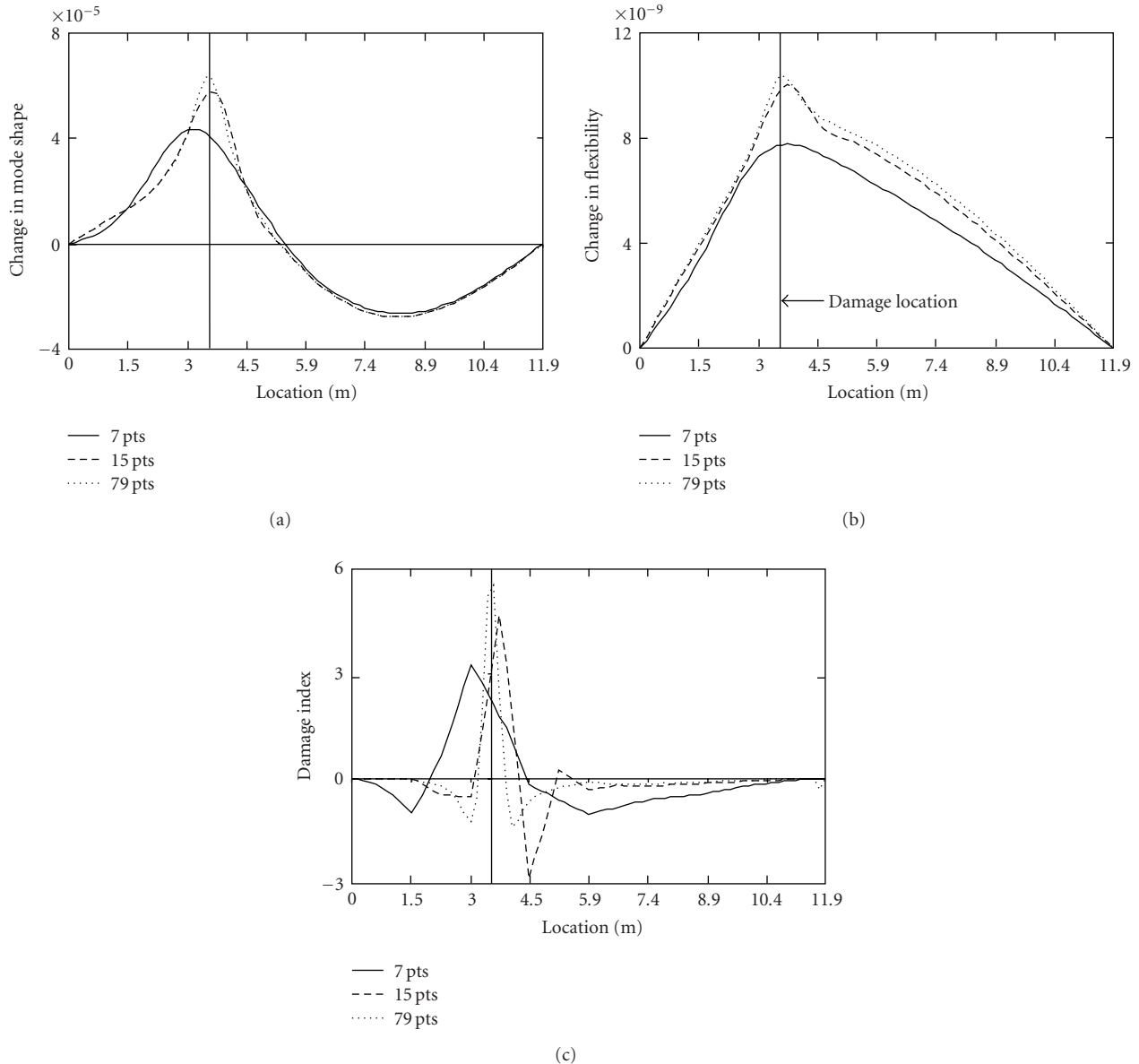


FIGURE 10: Comparison of VBDD parameter distributions for numerical damage case 24, obtained using 7, 15, and 79 measurement points for (a) the CMS, (b) MCF, and (c) DI methods. Labels along the location axis correspond to the seven measurement points.

5.3. Influence of the Number of Measurement Points. Figure 10 compares the VBDD parameter distributions obtained using an increasing number of FE simulated measurement points to define the fundamental mode shape for numerical damage case 24 (damage located 3.50 m from the support, as shown in Figure 4). As the number of measurement points increased, more distinct and narrower peaks were produced, particularly by the DI method; in addition, the peaks were located closer to the damage location. Improved predictive capability was therefore achieved by using a larger number of measurement points.

A similar trend was observed when damage was located nearer to a support, as shown in Figure 11 (corresponding

to numerical damage case 7, located 0.97 m from a support). In this case, increasing the number of measurement points effectively removed additional peaks produced by the DI method when a small number of points were used. However, the second broad hump produced by the MCF method was not affected by increasing the number of measurement points. This second hump is therefore not a direct result of the use of an inadequate number of measurement points. In fact, it can be demonstrated that this feature is characteristic of the MCF method for low level damage located near the support. It indicates that the maximum increase in deflection along the beam caused by inducing damage near the support is roughly the same whether a unit load is applied at the damage location or near midspan.

TABLE 3: Error in predicted damage location by each method, listed as a fraction of measurement point spacing, when 15 and 79 measurement points were used.

| Method | 15 points | | | | 79 points | | | |
|--------|------------|------------|-------------|----------|------------|------------|-------------|----------|
| | Max. error | Avg. error | Stand. dev. | % ambig* | Max. error | Avg. error | Stand. dev. | % ambig* |
| CMS | 0.30 | 0.12 | 0.06 | 0 | 0.50 | 0.50 | 0.003 | 0 |
| DI | 0.50 | 0.26 | 0.15 | 0 | 0.50 | 0.50 | 0.001 | 2.5 |
| MCF | 0.50 | 0.20 | 0.14 | 40 | 0.50 | 0.50 | 0.001 | 40 |

* indicates the percentage of the 40 cases that produced a second peak that was either at least 75% of the magnitude of the highest peak, or nearer to the damage location, including near support damage cases.

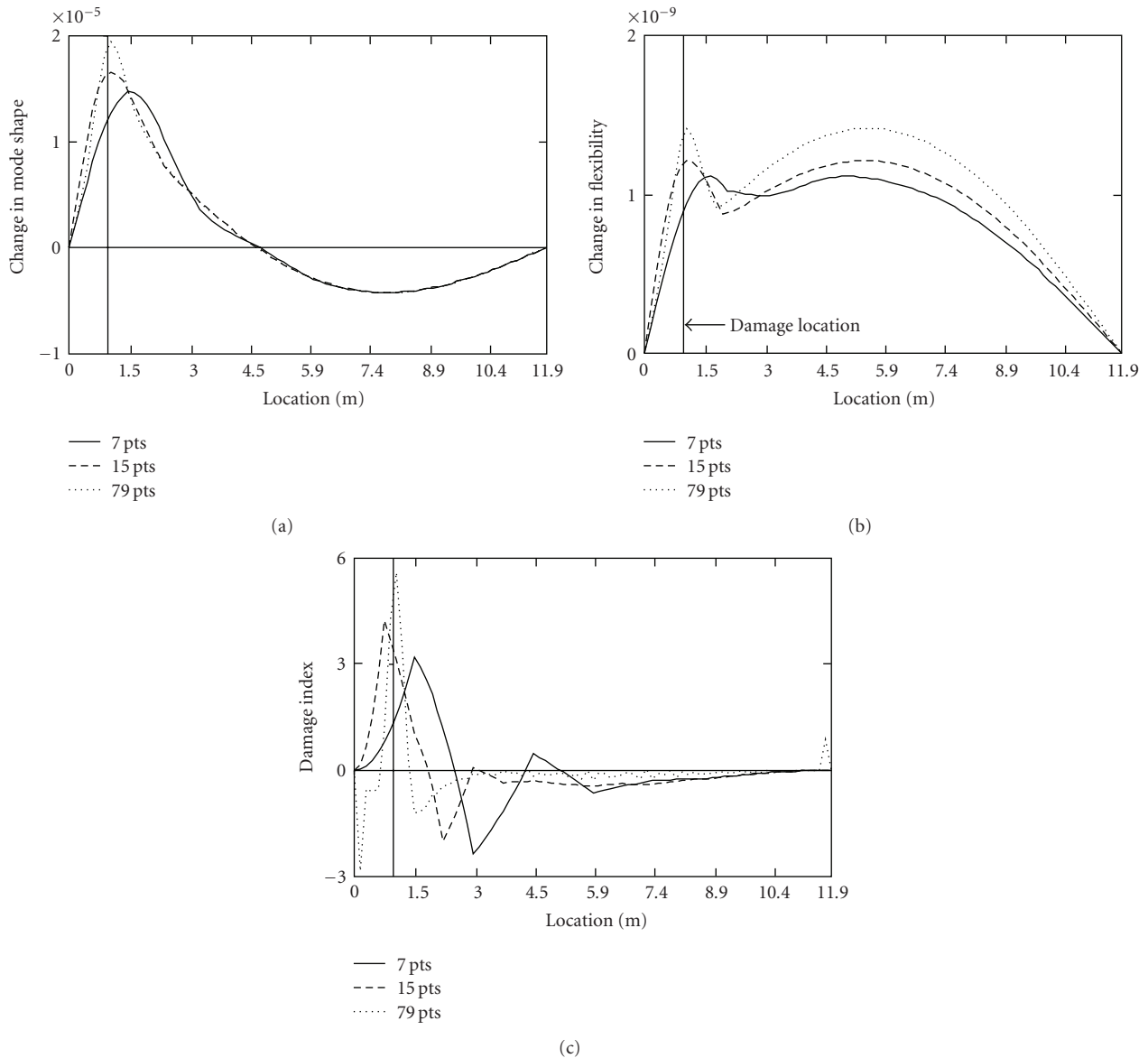


FIGURE 11: Comparison of VBDD parameter distributions for numerical damage case 7, obtained using 7, 15, and 79 measurement points for (a) the CMS, (b) MCF, and (c) DI methods. Labels along the location axis correspond to the seven measurement points.

The performance using 15 and 79 measurement points more generally is illustrated in Figure 12, in which correlations between predicted and actual locations of damage are plotted for the CMS and DI methods. The MCF method produced results similar to the CMS method, although with

greater ambiguity near the support. The improvement in localization accuracy with an increasing number of measurement points is clearly evident, with very well-defined mode shapes allowing damage to be localized with great accuracy, regardless of the method used. Although implementing

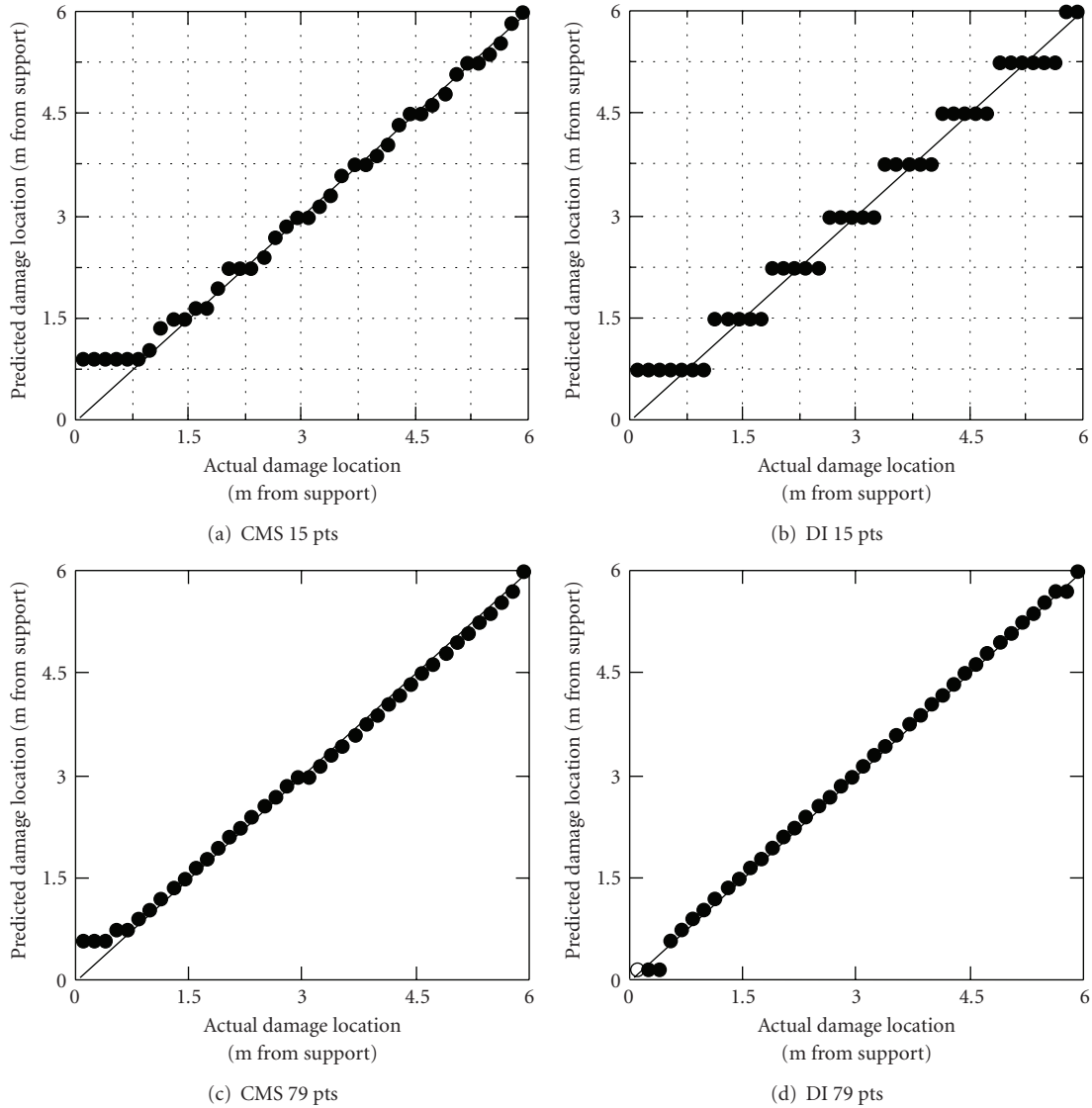


FIGURE 12: Correlation between predicted and actual damage locations, calculated using 15 measurement points by (a) the CMS and (b) the DI methods; and calculated using 79 measurement points by (c) the CMS and (d) the DI methods.

an experimental system to achieve this level of definition may be impractical, the excellent performance observed in Figures 12(c) and 12(d) confirms the soundness of the theory underlying VBDD and its applicability to a simply supported beam-like component.

The maximum and average errors produced by all methods, normalized by measurement point spacing, are summarized in Table 3. In relative terms, these results are seen to be very similar to those achieved using seven measurement points, as listed in Table 2. Localization accuracy is therefore directly proportional to measurement point spacing, h , with maximum errors in the order of $0.5h$ and average errors typically between $0.20h$ and $0.26h$ when seven or 15 measurement points were used. The CMS method performed somewhat better, but, as was previously mentioned, this improvement was not observed when experimental data were used.

5.4. Use of Additional Modes. Notwithstanding the excellent performance of the techniques using only the fundamental mode, perhaps leaving little room for expected improvement, the influence of including additional modes was also investigated. Conceptually, the use of additional modes might be expected to improve the performance of the VBDD methods by virtue of the fact that additional information is provided and that higher flexural modes should be more sensitive to local changes in stiffness. To investigate this hypothesis, the first three FE generated flexural modes (modes 1, 2, and 4 in Table 1) were incorporated into the methods.

The CMS was first calculated using each mode individually. Figure 13(a) shows the resulting distributions for numerical damage case 24, located 3.50 m from the support, when seven measurement points were used. When examined together, the set of three distributions provides a clear

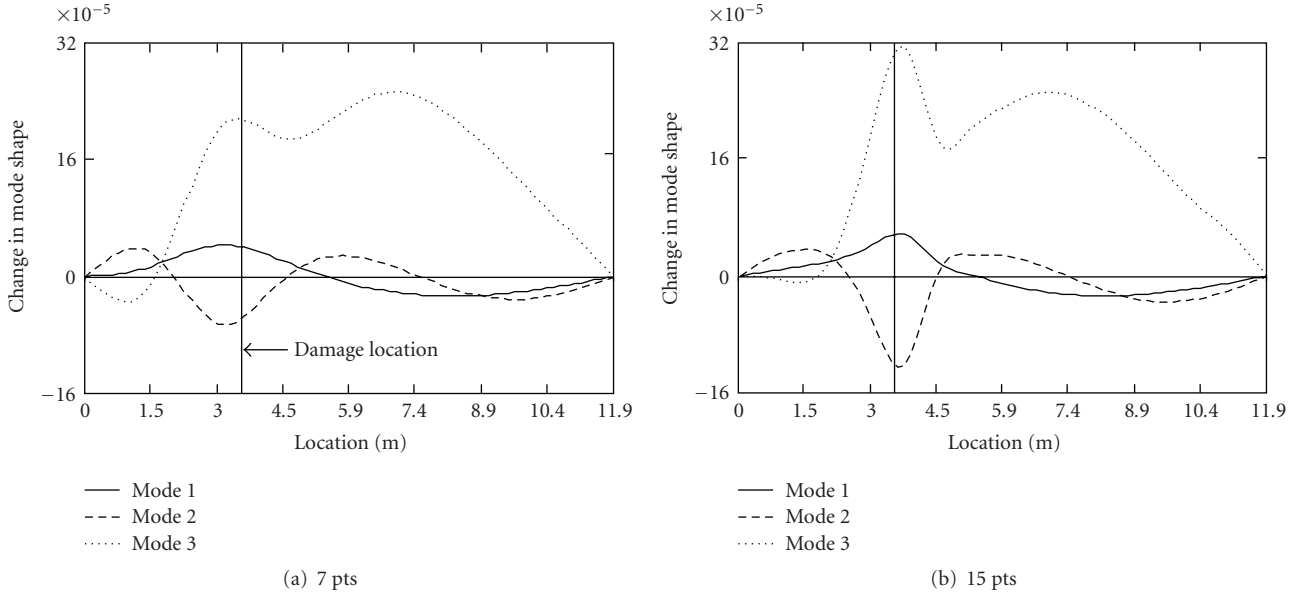


FIGURE 13: Changes in the first three flexural mode shapes caused by numerical damage case 24, located 3.50 m from the support, calculated using (a) 7 and (b) 15 simulated measurement points.

TABLE 4: Error in predicted damage location by each method, listed as a fraction of measurement point spacing, when two and three modes were used in combination with 7 measurement points.

| Method | 2 modes | | | | 3 modes | | | |
|--------|------------|------------|-------------|----------|------------|------------|-------------|----------|
| | Max. error | Avg. error | Stand. dev. | % ambig* | Max. error | Avg. error | Stand. dev. | % ambig* |
| CMS | 0.35 | 0.15 | 0.08 | 2.5 | 0.25 | 0.14 | 0.07 | 5 |
| DI | 0.95 | 0.33 | 0.24 | 2.5 | 0.65 | 0.26 | 0.18 | 22.5 |
| MCF | 0.45 | 0.18 | 0.13 | 0 | 0.45 | 0.16 | 0.11 | 7.5 |

* indicates the percentage of the 40 cases that produced a second peak that was either at least 75% of the magnitude of the highest peak, or nearer to the damage location, including near support damage cases.

indication of the location of the damage. Each distribution features a peak near the damage location, although it is not necessarily positive (mode 2) or the highest peak (mode 3). The latter difficulty was removed when mode shapes were defined by a larger number of measurement points (Figure 13(b)), but a significant second peak still remained in the change of the third mode shape. In addition, the magnitude of the peaks produced by different modes differed significantly.

In order to combine the three individual mode shape changes into a single distribution representative of the changes in all three mode shapes, the absolute value of each individual distribution was first calculated, the result was normalized by its root-mean-square (rms) value to remove the influence of magnitude differences, and then the three distributions were added together. Results of this approach are presented together with those of the other VBDD methods in the following paragraphs, with a focus on results achieved using seven measurement points.

Figure 14 shows how the distributions for the three methods changed as an increasing number of modes were used. This figure corresponds again to numerical damage case 24 and the use of seven measurement points. Very

little change in either the clarity or accuracy of the damage localization is observed as the number of modes increases, although one could argue that some improvement in clarity is apparent with the CMS method (Figure 14(a)). Similar results were observed for near support damage cases. The only improvement of significance occurred when the MCF method was used for near support damage cases (see Figure 15(a)). In these cases, the ambiguity caused by the occurrence of a second broader peak was removed when higher modes were considered. Interestingly, this improvement was not as significant when mode shapes were more well-defined using 15 measurement points, as seen in Figure 15(b), implying that the improvement for seven measurement points was artificial.

The performance of the methods more generally as the number of modes increased is shown in Table 4, in which the maximum and average localization errors for all 40 numerical damage cases are listed, along with the percentage of cases resulting in some ambiguity, when seven measurement points were used. Considering localization accuracy and the number of ambiguities produced, comparisons both within Table 4 and to Table 2 show that either no improvement was achieved with an increase in the number of

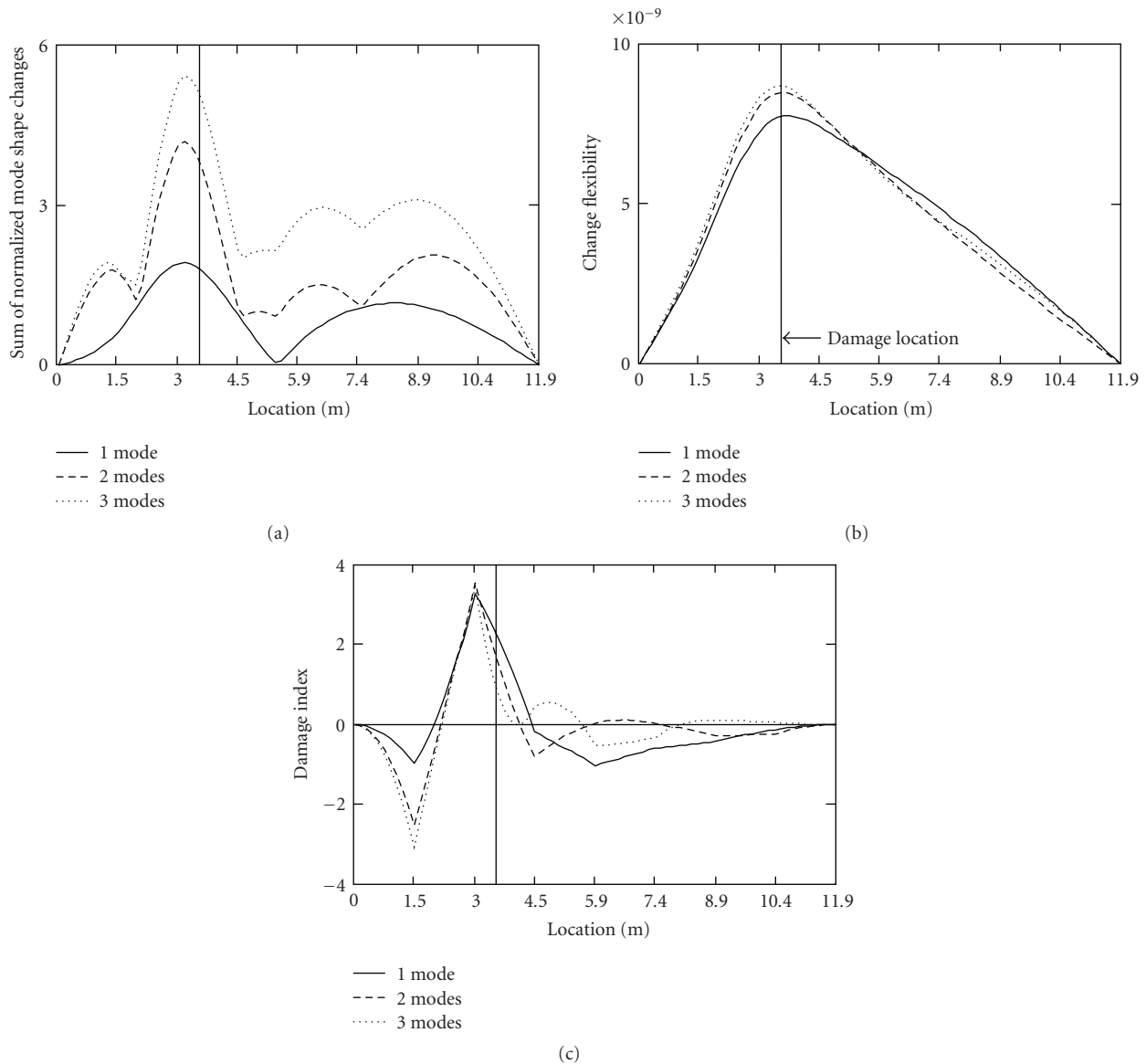


FIGURE 14: VBDD distributions calculated using the first three flexural modes and 7 measurement points for numerical damage case 24, located 3.50 m from the support, by the (a) CMS, (b) MCF, and (c) DI methods.

modes considered, or that a decline in performance resulted. The only exception to this trend was observed with the MCF method, which showed improvements in both criteria. In particular, increasing the number of modes effected a reduction in the ambiguities observed by the MCF method in near support damage cases. The decline in performance of the DI method was seen to be associated primarily with damage cases located near a node point for a particular mode shape. A similar decline was not observed for the other two curvature-based methods (MSC and CUFC methods).

Table 5 provides an indication of the performance as the number of modes increased when 15 measurement points were used to define the mode shapes. Comparison with Table 3 shows that the use of two or three modes produced either no improvement or a decline in performance relative

to the use of only the fundamental mode. Comparison with Table 4 shows that, in relative terms, the use of 15 points in combination with two or three modes produced marginal localization improvement only for the DI method, compared to seven measurement points. A decline was observed for other two methods, although localization was still observed to be more or less proportional to the spacing between measurement points.

Thus, any improvements associated with the use of higher modes were minimal and restricted to only one of the methods. Declines in performance were also observed. These results are not surprising. The excellent performance of the VBDD methods when using only the fundamental mode leaves very little room for improvement, given the theoretical limitations of the methods. Although not considered here,

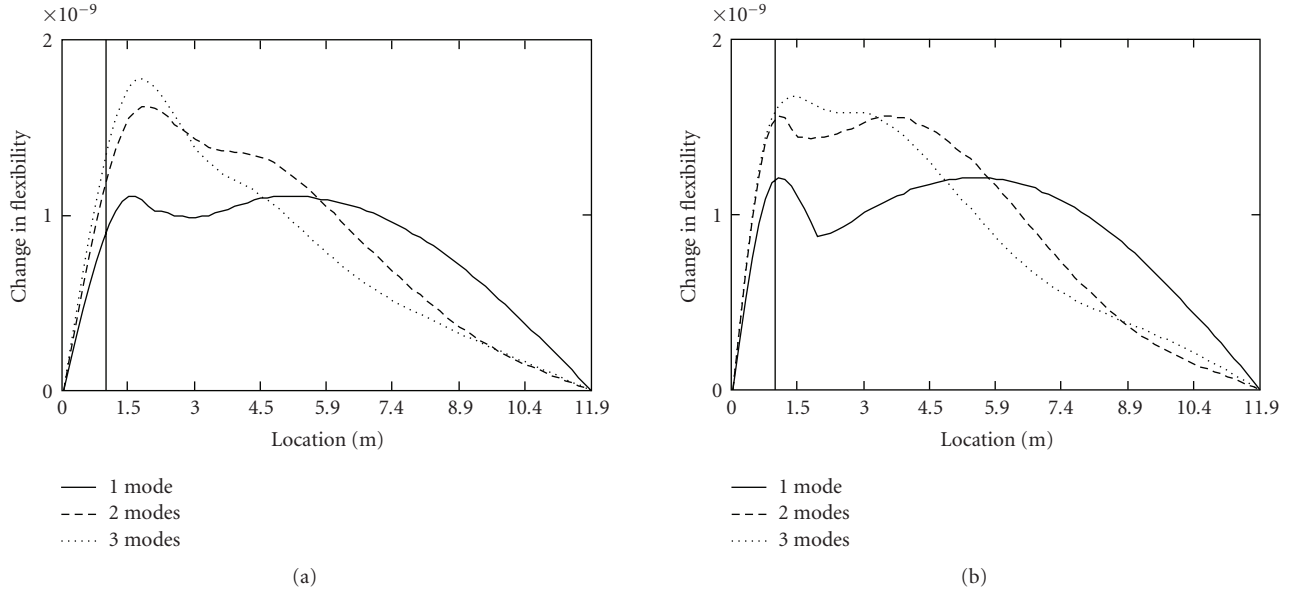


FIGURE 15: Change in flexibility calculated using the first three flexural modes for numerical damage case 7, located 0.97 m from the support, using (a) 7 and (b) 15 simulated measurement points.

TABLE 5: Error in predicted damage location by each method, listed as a fraction of measurement point spacing, when two and three modes were used in combination with 15 measurement points.

| Method | 2 modes | | | | 3 modes | | | |
|--------|------------|------------|-------------|----------|------------|------------|-------------|----------|
| | Max. error | Avg. error | Stand. dev. | % ambig* | Max. error | Avg. error | Stand. dev. | % ambig* |
| CMS | 0.50 | 0.14 | 0.09 | 2.5 | 0.50 | 0.14 | 0.09 | 0 |
| DI | 0.70 | 0.28 | 0.17 | 2.5 | 0.50 | 0.25 | 0.15 | 2.5 |
| MCF | 0.70 | 0.20 | 0.15 | 27.5 | 0.50 | 0.19 | 0.13 | 15 |

* indicates the percentage of the 40 cases that produced a second peak that was either at least 75% of the magnitude of the highest peak, or nearer to the damage location, including near support damage cases.

it should also be noted that, in practice, measurements of higher modes are generally subject to lower signal-to-noise ratios, since modal amplitudes tend to diminish with higher modes, leading to additional disincentive for using higher modes. To summarize, the minimal benefit and increased uncertainty associated with the use of higher modes provides a compelling argument in favour of using only the fundamental mode when applying the VBDD methods considered in this study.

5.5. *Summary.* Table 6 summarizes the results of this study, highlighting the influence of the factors investigated. The CMS method, applied using only the fundamental mode and a relatively small number of measurement points, appears to be the most attractive alternative.

6. Conclusions

This study has shown that damage on the surface of a full-scale precast, prestressed concrete box girder, corresponding to a local reduction in stiffness of only 2.5%, can be detected

using VBDD techniques and localized to a region within approximately 1.6 times the longitudinal spacing between uniformly distributed sensors, h . This was achieved using data for only the fundamental mode shape before and after damage, defined by as few as six evenly spaced measurement points. In contrast to the clear and unambiguous peaks generally observed in the VBDD distributions near the location of damage, damage cases located closer to supports resulted in VBDD distributions featuring multiple peaks and undulations. In these cases, damage could be localized to a region within approximately $1.5h$ from the support, although this “near support” region depended to some extent on support conditions.

While any of the VBDD methods considered was shown to be capable of detecting and localizing the majority of damage cases investigated, the CMS method provided the clearest indication of damage over the widest range of damage locations, particularly for near support damage cases. The CF method, modified slightly from its original formulation for improved performance, was less clear in its indication of near support damage cases. The DI method (as well as the other two curvature-based methods) tended to produce

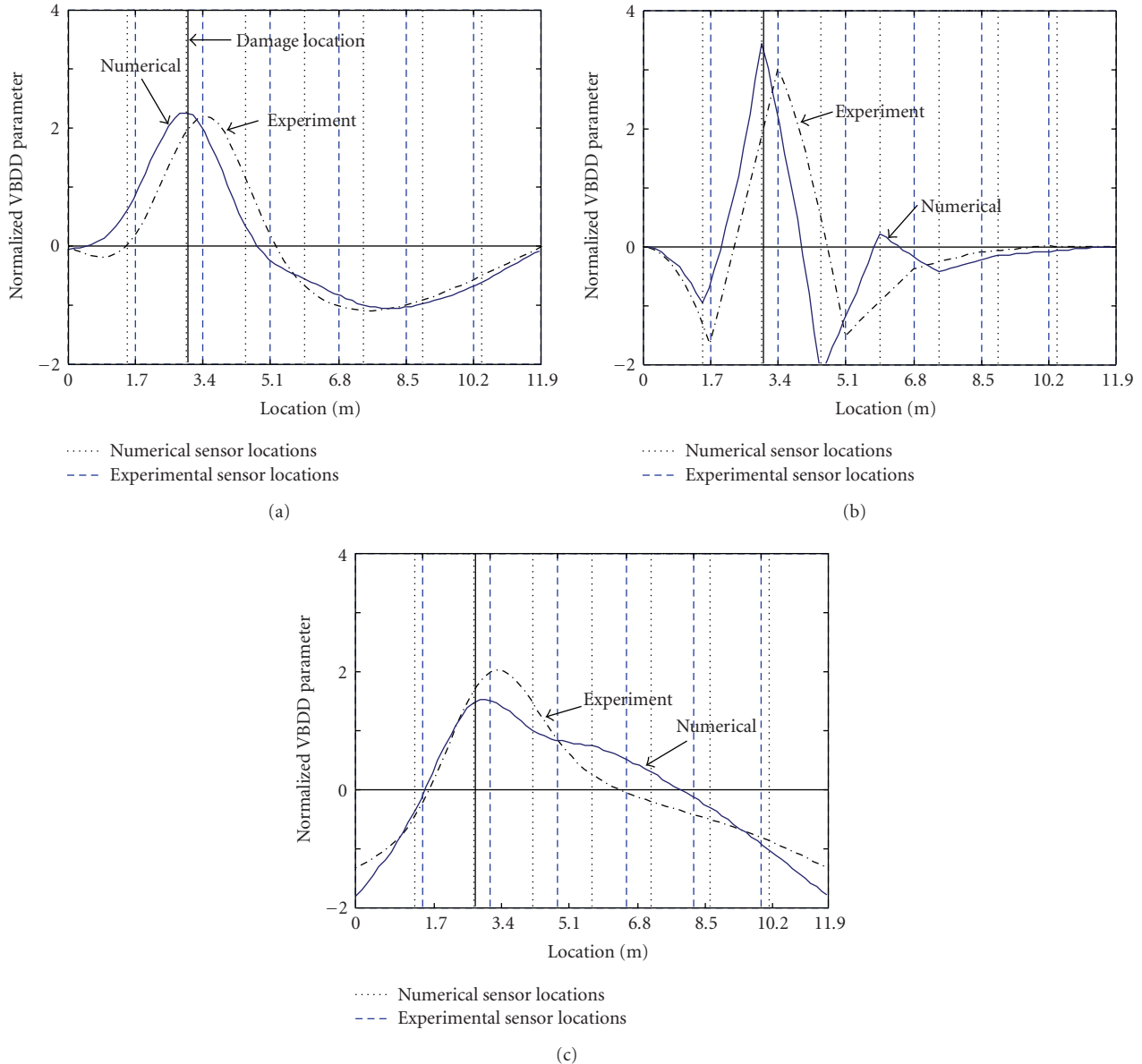


FIGURE 16: Comparison of VBDD parameter distributions produced for experimental damage case 6 (3.0 m from support, 6 measurement points) and numerical damage case 21 (3.05 m from support, 7 simulated measurement points) by (a) CMS, (b) DI, and (d) MCF methods.

several ambiguous indications of damage. Results indicated that the simultaneous use of several VBDD methods could provide an added level of confidence when localizing the damage, but that the CMS method was the most reliable.

In comparison to the use of accelerometers mounted on the top surface of the girder, application of the MSC method using data from strain gauge clusters configured to measure curvature directly was found to perform slightly better, as long as damage was not located too near a support (e.g., within approximately $1.5h$ of the support). In those cases, very misleading predictions sometimes resulted. Consequently, the use of strain gauge data alone is a less attractive alternative.

The accuracy of damage localization was directly proportional to the spacing between measurement points. Increasing the number of measurement points will therefore lead to a proportional increase in localization accuracy. All of the VBDD methods investigated were found to be extremely effective at pinpointing the location of damage when mode shapes were very well-defined with a large number of measurement points. Notwithstanding the challenges associated with achieving this level of mode shape definition in practice, this result confirms the soundness of VBDD theory and its usefulness for damage localization.

The use of two additional flexural modes, in addition to the fundamental vibration mode, did not generally improve

TABLE 6: Summary of performance of the three VBDD methods and the influence of the factors studied.

| Factors | CMS | MCF | DI |
|--|---|---|--|
| Reference conditions: (i) 7 meas. points (ii) Fundamental mode | Unambiguous indication of damage location within $\pm 0.8h$ | Unambiguous indication of damage location within $\pm 0.8h$ | Unambiguous indication of damage location within $\pm 0.8h$ |
| Near support damage cases | Able to locate damage with little ambiguity | Multiple peaks indicating that damage is located near a certain support | Misleading predictions of damage location |
| Use of additional measurement points | Proportional increase in localization accuracy | Proportional increase in localization accuracy | Proportional increase in localization accuracy |
| Use of additional modes | No improvement | Reduction in ambiguity for some near support damage cases | Decline in localization accuracy |
| Combined use of additional modes and additional measurement points | No improvement | No improvement | Some improvement relative to the use of additional modes alone |

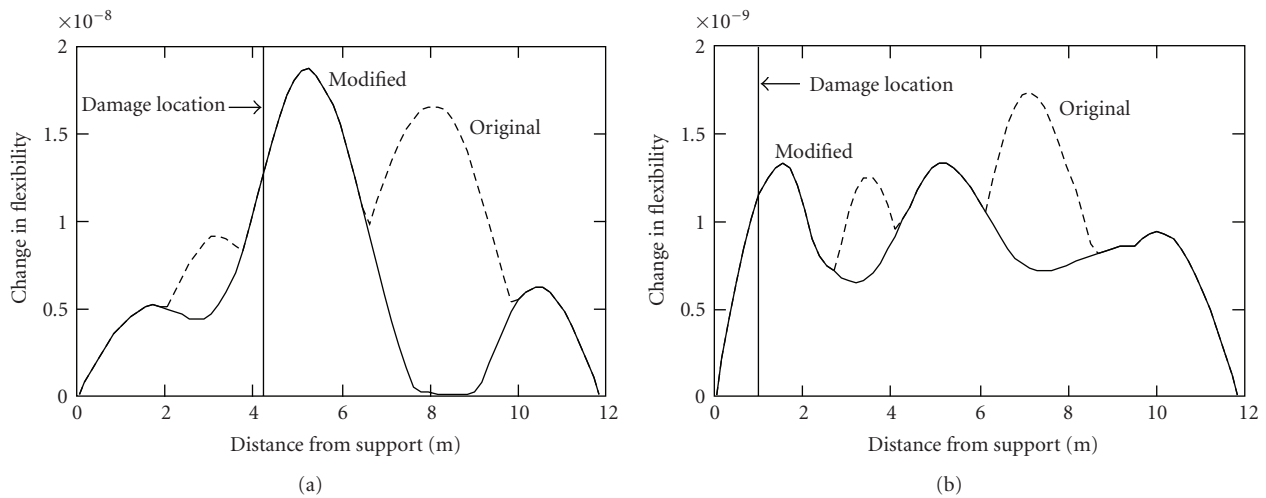


FIGURE 17: Distribution of change in flexibility by original and modified methods for experimental damage cases (a) 5 and (b) 11.

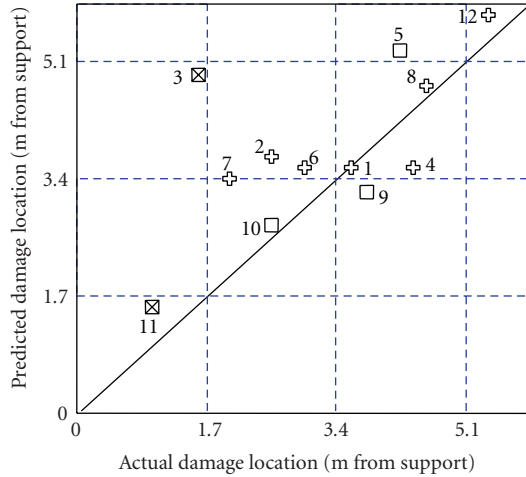
the performance of the VBDD techniques investigated. The only advantage appeared to be the removal of ambiguity when the MCF method was used for near support damage cases. For other VBDD methods, the use of two additional modes resulted in either no improvement, or a decline in performance. The use of only the fundamental mode is therefore considered to be sufficient for damage localization.

This study has shown that VBDD methods are effective at detecting and localizing damage on full-scale beam-like bridge elements, such as precast, prestressed concrete box girders, using data that can be obtained relatively easily using a small number of sensors and only the fundamental mode of vibration. Given that large portions of these elements are generally inaccessible to inspection by other SHM techniques, VBDD methods appear to be particularly attractive for the early detection of damage.

Appendices

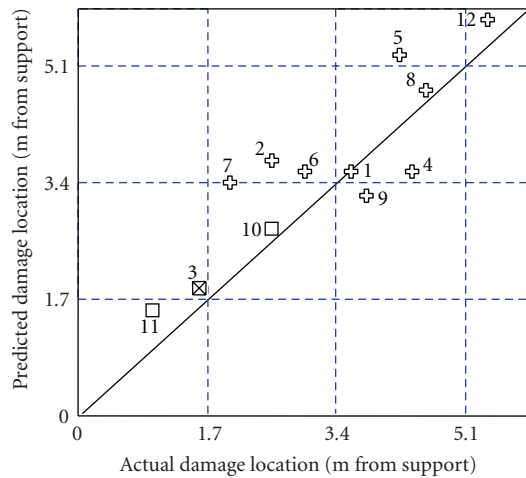
A. Validation of Numerical Simulations

In order to establish the validity of the numerical calculations and justify the extension of the study to a larger number of damage cases using FE simulations, comparison of the numerical and experimental results for a representative damage case is presented here. Figure 16 displays the VBDD distributions for experimental damage case 6 (3.0 m from support) and numerical damage case 21 (3.05 m from support). It should be recalled that six uniformly distributed measurement points were used experimentally, while seven were used numerically, so identical results should not be expected. Experimental measurement locations are indicated by the dashed and labelled gridlines, while numerical measurement points are indicated by additional dotted



⊕ Single clear peak
 □ Higher of two peaks
 ⊗ 2nd highest of two peaks

(a) CF



⊕ Single clear peak
 □ Higher of two peaks
 ⊗ 2nd highest of two peaks

(b) MCF

FIGURE 18: Correlation between predicted and actual location of experimental damage cases using six measurement points, calculated by the CF method in (a) original and (b) modified forms. Data points are numbered according to the experimental damage cases shown in Figure 4.

gridlines. The similarities between the resulting distributions are clearly evident for all VBDD methods, with each pair of distributions featuring similar characteristics and peaks occurring at the measurement point nearest to the damage location. The use of FE simulations to study a wider distribution of damage cases can therefore be shown to be well-founded.

B. Comparison of Change in Flexibility Method in Original and Modified Forms

To compare the distributions produced by the change in flexibility method in original and modified forms, Figure 17 presents the two distributions produced for experimental damage cases 5 (within the middle third of the span) and 11 (within 1 m of the support). As seen, the original and modified distributions are identical except at the dashed lines, where the original method picks up the absolute values of negative changes in flexibility to produce additional peaks. These additional peaks are invariably located farther from the damage than the most significant peak common to both distributions; in addition, some of the additional peaks are also higher in magnitude. As such, an added level of uncertainty is introduced by considering the absolute values, making the distributions more difficult to interpret.

Figure 18 illustrates the resulting localization performance of the two methods for all 12 experimental damage cases. It is evident that the modified method removes several ambiguities (cases 5, 9, and 11) and improves the accuracy of the predicted location (case 3). The modified method was therefore used for the current study. It should be noted, though, that differences between the two methods were only apparent when the experimental data were used. Numerically generated data always resulted in change in flexibility matrices that contained only positive values, as would be expected theoretically.

Acknowledgments

The financial support of the ISIS Canada Network of Centres of Excellence and the Natural Sciences and Engineering Research Council of Canada is gratefully acknowledged. The authors are also grateful to the Saskatchewan Ministry of Highways and Infrastructure for providing the girder.

References

- [1] Federal Highway Administration, "Reliability of visual inspection," Tech. Rep. FHWA-RD-01-020 and FHWA-RD-01-021, Federal Highway Administration, Washington, DC, USA, 2001.
- [2] L. Cartz, *Non-Destructive Testing*, ASM International, Materials Park, Ohio, USA, 1995.
- [3] B. Raj, T. Jayakumar, and M. Thavasimuthu, *Practical Non-Destructive Testing*, Narosa Publishing House, New Delhi, India, 2nd edition, 2002.
- [4] C. H. Jenkins, L. Kjerengtroen, and H. Oestensen, "Sensitivity of parameter changes in structural damage detection," *Shock and Vibration*, vol. 4, no. 1, pp. 27–37, 1997.
- [5] J. L. Schulz, B. Commander, G. G. Goble, and D. M. Frangopol, "Efficient field testing and load rating of short- and medium-span bridges," *Structural Engineering Review*, vol. 7, no. 3, pp. 181–194, 1995.
- [6] S. W. Doebling, C. R. Farrar, M. B. Prime, and D. W. Shevitz, "Damage identification and health monitoring of structural and mechanical systems from changes in their vibration characteristics: a literature review," Tech. Rep. LA 13070-MS, Los Alamos National Laboratory, Los Alamos, NM, USA, 1996.

- [7] Z. Zhou, L. D. Wegner, and B. F. Sparling, "Vibration-based detection of small-scale damage on a bridge deck," *Journal of Structural Engineering*, vol. 133, no. 9, pp. 1257–1267, 2007.
- [8] S. W. Doebbling, C. R. Farrar, and M. B. Prime, "A summary review of vibration-based damage identification methods," *Shock and Vibration Digest*, vol. 30, no. 2, pp. 91–105, 1998.
- [9] H. Sohn, C. R. Farrar, F. M. Hemez, D. D. Shunk, D. W. Stinemat, and B. R. Nadler, "A review of structural health monitoring literature: 1996–2001," Tech. Rep. LA-13976-MS, Los Alamos National Laboratory, Los Alamos, NM, USA, 2003.
- [10] P. Cawley and R. D. Adams, "The location of defects in structures from measurements of natural frequencies," *The Journal of Strain Analysis for Engineering Design*, vol. 14, no. 2, pp. 49–57, 1979.
- [11] O. S. Salawu, "Detection of structural damage through changes in frequency: a review," *Engineering Structures*, vol. 19, no. 9, pp. 718–723, 1997.
- [12] B. Peeters, *System identification and damage detection in civil engineering*, Ph.D. thesis, Department of Civil Engineering, Katholieke Universiteit Leuven, Leuven, Belgium, 2000.
- [13] C. H. J. Fox, "The location of defects in structures: a comparison of the use of natural frequency and mode shape data," in *Proceedings of the 10th International Modal Analysis Conference*, pp. 522–528, Society of Experimental Mechanics, Bethel, Conn, USA, 1992.
- [14] O. S. Salawu and C. Williams, "Damage location using vibration mode shapes," in *Proceedings of the 12th International Modal Analysis Conference*, pp. 933–939, Society of Experimental Mechanics, Bethel, Conn, USA, 1994.
- [15] A. K. Pandey, M. Biswas, and M. M. Samman, "Damage detection from changes in curvature mode shapes," *Journal of Sound and Vibration*, vol. 145, no. 2, pp. 321–332, 1991.
- [16] Z. Zhang and A. E. Aktan, "The damage indices for constructed facilities," in *Proceedings of the 13th International Modal Analysis Conference*, pp. 1520–1529, Society of Experimental Mechanics, Bethel, Conn, USA, 1995.
- [17] A. K. Pandey and M. Biswas, "Damage detection in structures using changes in flexibility," *Journal of Sound and Vibration*, vol. 169, no. 1, pp. 3–17, 1994.
- [18] D. C. Zimmerman and M. Kaouk, "Structural damage detection using a minimum rank update theory," *Journal of Vibration and Acoustics*, vol. 116, no. 2, pp. 222–231, 1994.
- [19] J.-T. Kim and N. Stubbs, "Model-uncertainty impact and damage-detection accuracy in plate girder," *Journal of Structural Engineering*, vol. 121, no. 10, pp. 1409–1417, 1995.
- [20] J.-T. Kim and N. Stubbs, "Nondestructive crack detection algorithm for full-scale bridges," *Journal of Structural Engineering*, vol. 129, no. 10, pp. 1358–1366, 2003.
- [21] P. Hajela and F. J. Soeiro, "Recent developments in damage detection based on system identification methods," *Structural Optimization*, vol. 2, no. 1, pp. 1–10, 1990.
- [22] J. R. Casas and A. C. Aparicio, "Structural damage identification from dynamic-test data," *Journal of Structural Engineering*, vol. 120, no. 8, pp. 2437–2449, 1994.
- [23] C. R. Farrar and T. A. Duffey, "Vibration-based damage detection in rotating machinery," *Key Engineering Materials*, vol. 167, pp. 224–235, 1999.
- [24] D. L. Hunt, S. P. Weiss, W. M. West, T. A. Dunlap, and S. R. Freesmeyer, "Development and implementation of a shuttle modal inspection system," *Sound and Vibration*, vol. 24, no. 8, pp. 34–42, 1990.
- [25] T. Toksoy and A. E. Aktan, "Bridge-condition assessment by modal flexibility," *Experimental Mechanics*, vol. 34, no. 3, pp. 271–278, 1994.
- [26] C. R. Farrar, W. E. Baker, T. M. Bell, et al., "Dynamic characterization and damage detection in the I-40 bridge over the Rio Grande," Tech. Rep. LA 12767-MS, Los Alamos National Laboratory, Los Alamos, NM, USA, 1994.
- [27] D. V. Jauregui and C. R. Farrar, "Comparison of damage identification algorithms on experimental modal data from a bridge," in *Proceedings of the 14th International Modal Analysis Conference*, pp. 1423–1429, Society of Experimental Mechanics, Bethel, Conn, USA, 1996.
- [28] Z. Zhang and A. E. Aktan, "Application of modal flexibility and its derivatives in structural identification," *Research in Nondestructive Evaluation*, vol. 10, no. 1, pp. 43–61, 1998.
- [29] F. N. Catbas and A. E. Aktan, "Condition and damage assessment: issues and some promising indices," *Journal of Structural Engineering*, vol. 128, no. 8, pp. 1026–1036, 2002.
- [30] A. B. Siddique, B. F. Sparling, and L. D. Wegner, "Assessment of vibration-based damage detection for an integral abutment bridge," *Canadian Journal of Civil Engineering*, vol. 34, no. 3, pp. 438–452, 2007.
- [31] B. Peeters, J. Maeck, and G. De Roeck, "Vibration-based damage detection in civil engineering: excitation sources and temperature effects," *Smart Materials and Structures*, vol. 10, no. 3, pp. 518–527, 2001.
- [32] LabView, *LabView™—version 6i*, National Instruments Corporation, Austin, Tex, USA, 2000.
- [33] R. Ramirez, *The FFT: Fundamentals and Concepts*, Prentice-Hall, Englewood Cliffs, NJ, USA, 1985.
- [34] M. E. Mortenson, *Mathematics for Computer Graphics Applications*, Industrial Press, New York, NY, USA, 1999.
- [35] ANSYS, *ANSYS User's Manual—version 7.1*, ANSYS Inc., Canonsburg, Pa, USA, 2003.
- [36] D. J. Ewins, *Modal Testing: Theory, Practice and Applications*, Research Studies Press, Hertfordshire, UK, 2nd edition, 2000.
- [37] Y. K. Ho and D. J. Ewins, "On the structural damage identification with mode shapes," in *Proceedings of the European COST F3 Conference on System Identification and Structural Health Monitoring*, pp. 677–686, Madrid, Spain, 2000.
- [38] N. Stubbs, Y. I. Kim, and C. R. Farrar, "Field verification of a nondestructive damage localization and severity estimation algorithm," in *Proceedings of the 13th International Modal Analysis Conference*, pp. 210–218, Society of Experimental Mechanics, Bethel, Conn, USA, 1995.
- [39] C. R. Farrar and D. A. Jauregui, "Comparative study of damage identification algorithms applied to a bridge: I. Experiment," *Smart Materials and Structures*, vol. 7, no. 5, pp. 704–719, 1998.
- [40] S. Choi, S. Park, and N. Stubbs, "Nondestructive damage detection in structures using changes in compliance," *International Journal of Solids and Structures*, vol. 42, no. 15, pp. 4494–4513, 2005.

Research Article

Ultrasonic Guided Waves-Based Monitoring of Rail Head: Laboratory and Field Tests

Piervincenzo Rizzo,¹ Marcello Cammarata,^{1,2} Ivan Bartoli,³ Francesco Lanza di Scalea,³ Salvatore Salamone,³ Stefano Coccia,³ and Robert Phillips³

¹Department of Civil and Environmental Engineering, University of Pittsburgh, 949 Benedum Hall, 3700 O'Hara Street, Pittsburgh, PA 15261, USA

²Department of Structural and Geotechnical Engineering, University of Palermo, Viale delle Scienze, 90128 Palermo, Italy

³NDE and Structural Health Monitoring Laboratory, Department of Structural Engineering, University of California, San Diego 9500 Gilman Drive, M.C. 0085, La Jolla, CA 92093-0085, USA

Correspondence should be addressed to Piervincenzo Rizzo, pir3@pitt.edu

Received 23 December 2009; Accepted 19 April 2010

Academic Editor: Jinying Zhu

Copyright © 2010 Piervincenzo Rizzo et al. This is an open access article distributed under the Creative Commons Attribution License, which permits unrestricted use, distribution, and reproduction in any medium, provided the original work is properly cited.

Recent train accidents have reaffirmed the need for developing a rail defect detection system more effective than that currently used. One of the most promising techniques in rail inspection is the use of ultrasonic guided waves and noncontact probes. A rail inspection prototype based on these concepts and devoted to the automatic damage detection of defects in rail head is the focus of this paper. The prototype includes an algorithm based on wavelet transform and outlier analysis. The discrete wavelet transform is utilized to denoise ultrasonic signals and to generate a set of relevant damage sensitive data. These data are combined into a damage index vector fed to an unsupervised learning algorithm based on outlier analysis that determines the anomalous conditions of the rail. The first part of the paper shows the prototype in action on a railroad track mock-up built at the University of California, San Diego. The mock-up contained surface and internal defects. The results from three experiments are presented. The importance of feature selection to maximize the sensitivity of the inspection system is demonstrated here. The second part of the paper shows the results of field testing conducted in south east Pennsylvania under the auspices of the U.S. Federal Railroad Administration.

1. Introduction

Safety statistics data from the US Federal Railroad Administration [1, 2] indicate that train accidents caused by track failures including rail, joint bars and anchoring resulted in 2700 derailments and \$441 M in direct costs, during the 1992–2002 decade. The primary cause of these accidents is the 'transverse defect' type that was found responsible for 541 derailments and \$91 M in cost during the same period. Transverse defects are cracks developing in a direction perpendicular to the rail running direction, and include transverse fissures, initiated inside the rail head, and detail fractures, initiated at the head surface as rolling contact fatigue defects.

The most common methods of rail inspection are magnetic induction and contact ultrasonic testing [3–5]. The

first method is affected by environmental magnetic noise and it requires a small lift-off distance for the sensors in order to produce adequate sensitivity [6, 7]. Ultrasonic testing is conventionally performed from the top of the rail head in a pulse-echo configuration. In this system, ultrasonic transducers are located inside a water-filled wheel and are oriented at 0° from the surface of the rail head to detect horizontal cracks and at 70° to detect transverse cracks. Such an approach suffers from a limited inspection speed and from drawbacks associated with the requirement of contact between the rail and the inspection wheel. More importantly, horizontal surface damage such as shelling and head checks can prevent the ultrasonic beams from reaching the internal defects resulting in false negative readings. The problem of surface shelling was highlighted in accidents like the ones in Superior, WI (U.S.) in 1991 and Hatfield (UK) in 2000.

Recently, a testing method based on infrared thermography has been proposed. This method however is challenging due to the optical obscuration caused by the various fittings and fixtures used to hold the rail in place, and to the attenuation produced by contaminants often present on the rail surface [8].

Ultrasonic guided waves (UGWs) are being considered in recent years for rail inspections as an improvement over wheel-type ultrasonic methods [9–18]. In general, UGWs are ideal in those monitoring applications that can benefit from built-in transduction, moderately large inspection ranges, and high sensitivity to small flaws. In rail applications, because these waves propagate along, rather than across the rail, they are ideal for detecting the critical transverse defects. They are also potentially not sensitive to surface shelling because they can run underneath this type of discontinuities. Sometimes when the wavelength of UGWs is in the same order of magnitude of the rail curvature radius, there are referred to as surface guided waves [11]. The frequency range at which the waves are generated typically varies according to the type of ultrasonic source used. The frequency range is important to achieve a penetration depth sufficient to probe the entire rail head cross-section, to allow screening of several meters of rail from a single inspection point, and to reduce the sensitivity to noncritical features.

In the last ten years, techniques that do not require contact between the interrogating (probe) and the interrogated (rail) systems, have been investigated to generate and detect UGWs. Noncontact rail testing has been demonstrated by the use of pulsed lasers and air-coupled transducers [16, 19], electro-mechanical acoustic transducers (EMATs) [12, 18, 20], and laser vibrometers [11]. However, the drawback of any noncontact testing when compared to conventional contact testing is a reduced signal-to-noise ratio. The use of signal processing based on the Discrete Wavelet Transform (DWT) helps in overcoming this problem, as recently demonstrated [3, 16, 21–24].

This paper presents a hybrid laser/air-coupled transducer system aimed at detecting defects in the rail head by means of UGWs. The laser is used to generate UGWs in the rail head. Pairs of air-coupled transducers are used to sense the waves propagating along the rail head. The system is coupled to a robust signal processing algorithm devoted to automatic damage detection. The algorithm consists of DWT, feature extraction, and outlier analysis. The DWT is applied to process the raw signals. Relevant statistical data extracted from the recorded signals and after DWT-processing are employed to construct a uni-dimensional or multidimensional damage index vector. The vector is then fed to an unsupervised algorithm based on outlier analysis.

The novelty of this paper is multifold. First, the outlier analysis is applied to problems associated with the detection of defects in rails. Second, the systematic investigation of feature selection, as an essential tool to maximize the sensitivity of the probing system, is conducted. Then, the attempt to discriminate between surface and internal defects in rail head is carried out by proposing a filtering separation process. The hardware/software/algorithm prototype deployed onto a cart moving on a laboratory rail mock up, represents another

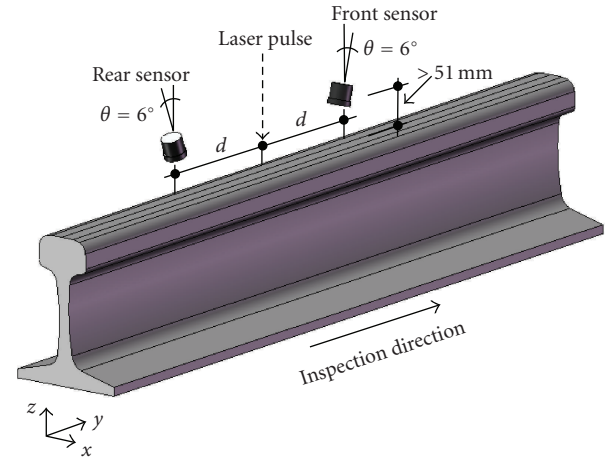


FIGURE 1: Schematic of the sensor pair position with respect to the laser pulse and rail head.

novelty of the present paper. Finally, the results from field testing where part of the inspection algorithm has been implemented are presented.

2. Laboratory Tests

2.1. Inspection Prototype. The rail inspection system consisted of a hybrid laser/air-coupled transducers system. A Nd:YAG, Q-switched type, pulsed laser was used to deliver through conventional optics 40 mm-long line beam on the rail head. The line source is known to effectively generate directional and broadband UGWs propagating perpendicular to the line.

Three pairs of air-coupled transducers were used to acquire the ultrasonic signals traveling along the rail head. The three pairs were deployed to provide coverage of the centerline, the gage side, and the field side of the rail head. The sensors were broadband transducers with ultrasonic bandwidth in air 40 kHz–2.25 MHz. As traditionally done with conventional wedge transducers, the alignment angle of the air-coupled detectors was adjusted to maximize the sensitivity to the guided waves, following Snell's law.

The sensors were located at distances larger than 50.8 mm (2") from the top of the rail head. Figure 1 shows that the laser was placed in between the sensor pairs. The longitudinal distance $2d$ between the transducers of the central pair was equal to 343 mm, whereas the distance between the elements of the gage side pair and between the elements of the field side pair was equal to 254 mm. These distances represented a good compromise between high signal-to-noise ratio and high inspection speed. The hybrid system was coupled to a portable PXI unit running under LabVIEW designed to perform laser control and data acquisition. A cart was used to host the hybrid system and the PXI unit.

The ultrasonic signals were acquired at a 5 MHz sampling rate, and successively analyzed using Matlab Wavelet Toolbox.

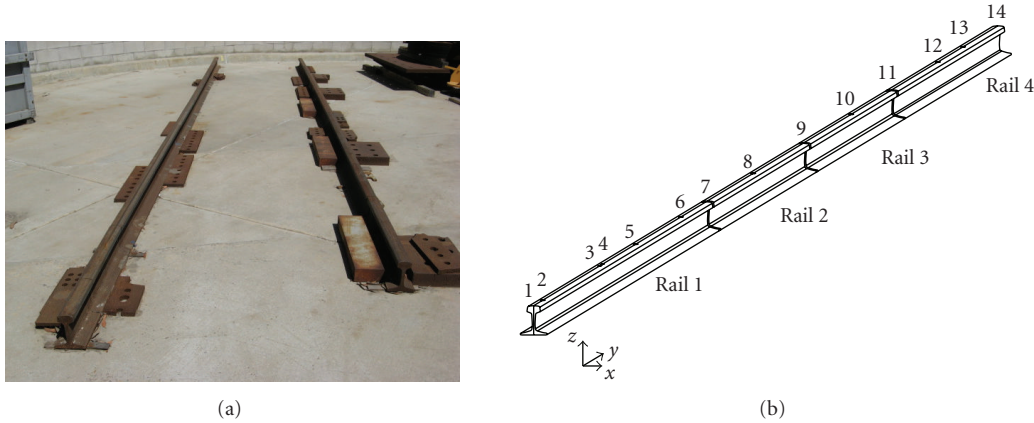


FIGURE 2: (a) Photo of the rail track mockup at UCSD; (b) layout of the tested mockup. The numbers on top of the rail layout represent the location number listed on the second column of Table 1.

2.2. Experimental Setup and Protocol. The rail-mock up featured approximately a 6 meter long rail track. A photo of such facility is presented in Figure 2(a). The tested segment consisted of four rail sections with surface and internal defects. Rails 1 and 4 were AREMA 110 sections, whereas rails 2 and 3 were AREMA 136 sections. The position of the rail joints and defects are enumerated and shown in Figure 2(b).

Details of the site layout are presented in Table 1. The starting point is identified as location #1 and it is the joint between a rail that is not drawn in Figure 2(b) and rail 1. The first rail section contained four surface defects: three transverse defects at locations #2, #5, and #6 and a longitudinal notch over 40 mm long. The second and third sections contained each an internal defect. These defects were at locations #8 and #10.

A hand mapping conducted with a commercial contact ultrasonic instrumentation located the internal defects closer to the gage side of the head. The mapping estimated that they extended over 8% and 23% of the cross-sectional head area, respectively. Finally, the fourth section contained an oblique defect oriented at 45 degrees on the x - z plane at location #12 and a surface transverse defect at position #13. All surface defects were machined by using an electrical saw.

Three tests were conducted. The cart was manually pushed on the mock-up and an ultrasonic acquisition was made every inch approximately. Each acquisition was enumerated progressively. For instance, during test 1, 78 acquisitions were made and column 5 of Table 2 shows which portion of the rail was probed during each acquisition by the central sensor pair.

Typical waveforms recorded during an acquisition are illustrated in Figure 3. Figures 3(a) and 3(b) present the waveforms recorded from the rear and front central transducers, respectively, when the laser illuminated the rail head at 1150 mm from the starting point. Ideally, shape and amplitude of the waveforms should be identical; however, slight variations of the sensor's inner sensitivity and alignment, and relative distance between transducers and the beam, produced small differences in the waveforms' amplitudes.

Figures 3(c) and 3(d) show the ultrasonic signals recorded when the laser light impinged on the rail head at 1965 mm. According to Table 1, this acquisition should detect the surface defect machined at location #6. The fact, that the amplitude of the signal detected by the front sensor is smaller than the signal amplitude from the rear sensor, proves that the laser illuminated a zone between the notch and the rear probe. This is also confirmed by the later pulse of Figure 3(c), which is the result of the reflection from the surface defect. Finally, Figures 3(e) and 3(f) show the ultrasonic signals affected by the presence of the second joint placed between the laser light and the front sensor. No ultrasonic trace is visible in Figure 3(f). The signal detected by the rear sensor, presented in Figure 3(e), shows the stress wave traveling from the laser light, and the echo from the joint.

3. Signal Processing

3.1. The Discrete Wavelet Transform. Ultrasonic signals were processed through the DWT, which decomposes the original time-domain signal by computing its correlation with a short-duration wave called the mother wavelet that is flexible in time and in frequency. DWT processing consists of two main parts: decomposition and reconstruction. The decomposition phase transforms the function into wavelet coefficients following hierarchical steps, or levels of different frequency bands. The denoising of the original signal can be achieved if only a few wavelet coefficients, representative of the signal, of one or more levels are retained and the remaining coefficients, related to noise, are discarded. In the reconstruction process, the coefficients pass through reconstruction filters that are closely related but not equal to those of the decomposition [24–27].

3.2. Outlier Analysis. An outlier is a datum that appears inconsistent with a set of data, the baseline that describes the normal condition of the structure under investigation. A set of p -dimensional (multivariate) data consists of n observations in p variables. In this study, the detection of

TABLE 1: Laboratory test site layout.

| Location # | Distance (mm) | Description | Head area reduction | Test 1 center head pair | Test 1 gage side pair | Test 2 center head pair | Test 2 gage side pair | Test 3 center head pair | Test 3 gage side pair | |
|------------|---------------|-------------|--|-------------------------|-----------------------|-------------------------|-----------------------|-------------------------|-----------------------|----------------|
| | 1 | 0 | | | 1-4 | 1-3 | 1-3 | 1-2 | 1-3 | 1 |
| | 2 | 127 | Surface transverse notch <i>No defect</i> | 1% | 5-6 7-11 | 4-5 6-11 | 4 5-10 | 3-4 5-10 | 4-5 6-11 | 2-4 5-1 |
| | 3 | 920 | Start longitudinal notch | | 12 | 12 | 11 | 11 | 12 | 12 |
| Rail 1 | 4 | 968 | End longitudinal notch <i>No defect</i> | | 15 16-17 | 15 16-18 | 15 16 | 14 15-17 | 15 16-17 | 15 16-18 |
| | 5 | 1428 | Surface transverse notch <i>No defect</i> | 16% | 18-21 22-24 | 19-21 22-25 | 17-20 21-24 | 18-20 21-24 | 18-21 22-25 | 19-21 22-25 |
| | 6 | 2060 | Surface transverse notch <i>No defect</i> | 5% | 25-29 — | 26-29 30 | 25-28 — | 25-28 29 | 26-29 — | 26-29 30 |
| | 7 | 2432 | Joint <i>No defect</i> | | 30-34 | 31-33 | 29-33 | 30-32 | 31-34 | 31-33 |
| Rail 2 | 8 | 3073 | Internal defect <i>No defect</i> | 8% | 35-38 39-41 | 34-38 39-41 | 34-36 37-41 | 33-37 38-40 | 35-37 38-41 | 34-38 39-41 |
| | 9 | 3789 | Joint <i>No defect</i> | | 42-46 47-50 | 42-46 47-50 | 42-46 47-49 | 41-46 47-49 | 42-46 47-50 | 42-47 48-50 |
| Rail 3 | 10 | 4445 | Internal defect <i>No defect</i> | 23% | 51-54 55-58 | 51-54 55-57 | 50-52 53-56 | 50-53 54-56 | 51-54 55-59 | 51-55 56-58 |
| | 11 | 5013 | Joint <i>No defect</i> | | 59-61 62-65 | 58-61 62-65 | 57-59 60-63 | 57-59 60-62 | 60-61 62-66 | 59-62 63-65 |
| Rail 4 | 12 | 5657 | Surface oblique notch <i>No defect</i> | 7% | 66-69 70-73 | 66-70 71-73 | 64-66 67-70 | 63-67 68-69 | 67-68 69-72 | 66-68 69-71 |
| | 13 | 6010 | Surface transverse notch | 20% | 74 75-78 | 74 75-78 | — 71-74 | 70-71 72-74 | — 73-77 | 72-73 75-77 |

TABLE 2: Mother wavelet, number of largest wavelet coefficients, and statistical features considered in the rail head algorithm monitoring system.

| Mother wavelet # | Mother wavelet | # | # of largest coefficients retained ⁽¹⁾ | Feature # | Statistical Feature |
|------------------|----------------|-----|---|-----------|---------------------|
| a | “db4” | I | 6-6 | 1 | RMS_o |
| b | db7’ | II | 6-10 | 2 | ppk_o |
| c | db10’ | III | 10-6 | 3 | CF_o |
| d | “coif4” | IV | 10-10 | 4 | RMS_w |
| e | “sym5” | | | 5 | ppk_w |
| f | sym7’ | | | 6 | CF_w |
| | | | | 7 | RMS_r |
| | | | | 8 | ppk_r |
| | | | | 9 | CF_r |
| | | | | 10 | Area_FFT |
| | | | | 11 | RMS_FFT |

⁽¹⁾The first number refers to the decomposition level 2 or 4 when the high-frequency bandwidth or the low-frequency bandwidth is considered, respectively. The second number refers to the decomposition level 3 or 5 when the high-frequency bandwidth or the low-frequency bandwidth is considered, respectively.

outliers is expressed by the Mahalanobis squared distance D_{ζ} , which is a nonnegative scalar defined as

$$D_{\zeta} = (\{x_{\zeta}\} - \{\bar{x}\})^T \cdot [K]^{-1} \cdot (\{x_{\zeta}\} - \{\bar{x}\}), \quad (1)$$

where $\{x_{\zeta}\}$ is the potential outlier vector, $\{\bar{x}\}$ is the mean vector of the baseline, $[K]$ is the covariance matrix of the

baseline and T symbolizes the transpose operation. Both vectors $\{x_{\zeta}\}$ and $\{\bar{x}\}$ are p -dimensional whereas $[K]$ is a square matrix of order p .

The mean and the standard deviation can be calculated with or without the potential outlier depending upon whether inclusive or exclusive measures are preferred. In the present study, since the potential outliers are always known a

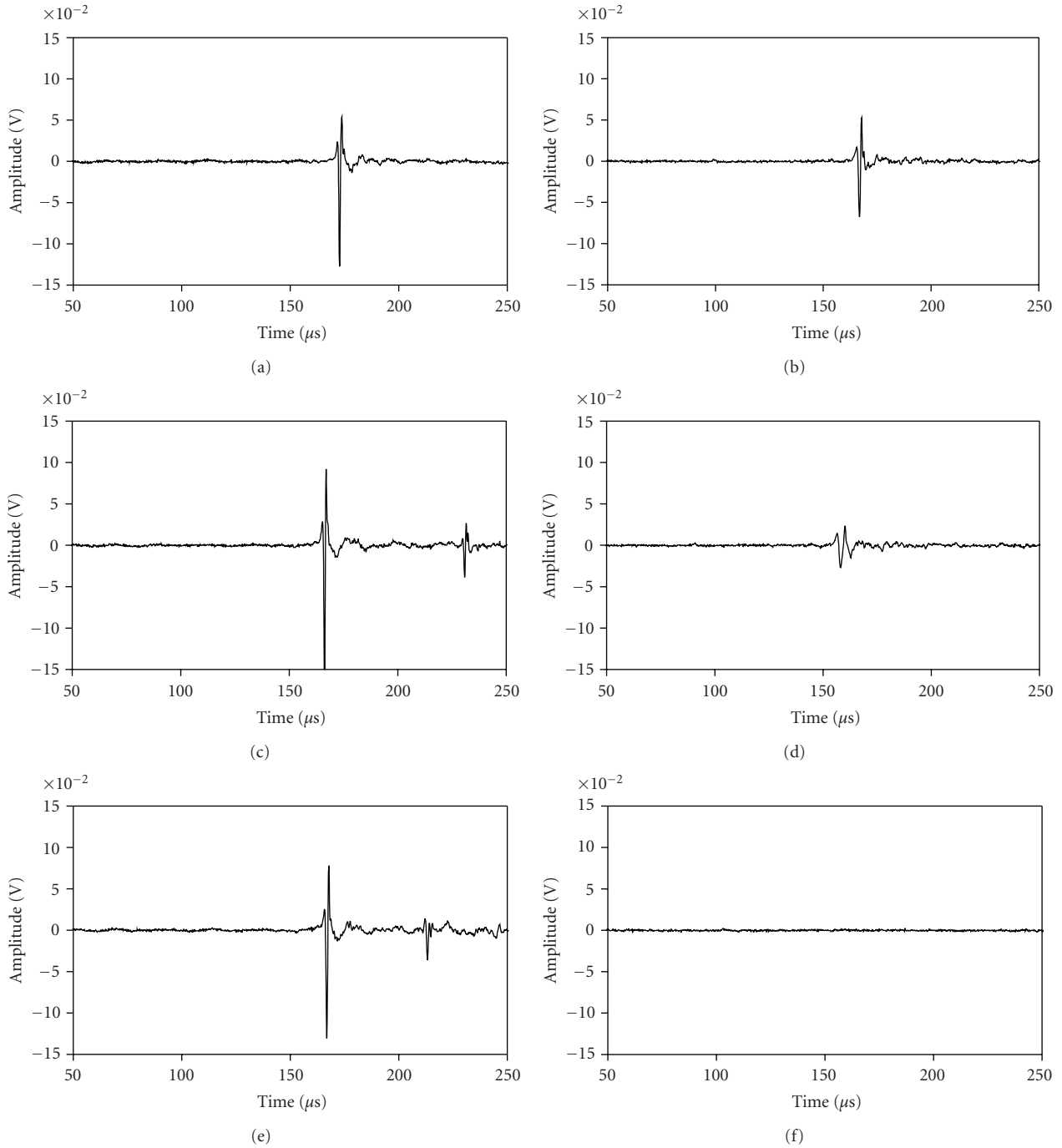


FIGURE 3: Typical waveforms detected by the hybrid laser/air-coupled transducer system. Time waveforms detected by the (a) rear and (b) front sensors when the inspection system is probing a pristine rail section. Time waveforms detected by the (c) rear and (d) front sensors when the inspection system is probing a transverse surface notch. Time waveforms detected by the (e) rear and (f) front sensors when the inspection system is probing a joint.

priori, D_{ζ} is calculated exclusively without contaminating the statistics of the baseline. In order to determine whether a new multidimensional datum is an outlier, the corresponding value of D_{ζ} has to be compared to a threshold. As the data set consisted of samples generated by adding artificial noise to the ultrasonic signals, once the values of D_{ζ} of the baseline distribution were determined, the threshold value was taken

as the upper value of 3σ , equal to 99.73% of the Gaussian confidence limit.

Anytime baseline samples exceed the threshold, they classify as outliers. In the context of the present framework, these values represent false indications of damage, that is, false positives. Conversely, anytime a datum associated with a defect is below the threshold, it is classified as a false negative.

3.3. Structural Health Monitoring Algorithm. The overall algorithm adopted to the laboratory tests is illustrated in the flowchart of Figure 4. From each ultrasonic measurement other 19 signals were obtained by adding white Gaussian noise. Thus, a total number of 20 samples per acquisition were available. As done in previous works [24, 27, 28] the noise was created by using MATLAB *randn* function. The statistical features of root mean square (RMS), crest factor (CF), and peak-to-peak (ppk) were computed from these signals. The DWT was applied to every signal. Two wavelet coefficient vectors were created by separating the second and third decomposition levels from the fourth and fifth decomposition levels. The second and the third levels comprise approximately the 300 kHz–1.2 MHz range. Such a range is hereafter indicated as high-frequency bandwidth. The fourth and fifth levels instead include approximately the 75 kHz–300 kHz range. This range is hereafter indicated as the low-frequency bandwidth. Owing to their small wavelength, high frequency acoustic signals are expected to be more sensitive to surface defects than internal defects. Each of the two coefficient vectors was threshold by retaining the largest wavelet coefficient moduli.

Denosed signals were obtained by using DWT reconstruction process. The same statistical features introduced above were applied both to the wavelet coefficient vectors and to the denosed signals.

In order to increase the set of features, the Fourier transform of the denosed signals was evaluated, and the area (Area_FFT) and the RMS (RMS_FFT) of the frequency spectrum were calculated.

3.4. Damage Index Vector. Each selected feature was employed to compute a damage index. As the laser light was delivered in the middle between the transducers, the damage index was calculated as the ratio between a certain feature of the signal detected by the front sensor, F_{front} , over the same feature from the rear sensor, F_{rear} . The inverse was computed as well

$$D.I._{f/r} = \frac{F_{\text{front}}}{F_{\text{rear}}}, \quad D.I._{r/f} = \frac{F_{\text{rear}}}{F_{\text{front}}}. \quad (2)$$

Only the largest value between $D.I._{f/r}$ and $D.I._{r/f}$ was considered. As such every time a defect was between the laser light and either one of the transducers, the damage index was expected to increase from its ideal value of 1 with increasing defect size. Two or more features were used as the elements of a multidimensional damage index vector, which represented the input of the multivariate analysis. Table 2 summarized the mother wavelets, the number of retained coefficients, and the features considered in the present study.

4. Experimental Results

4.1. Features and Frequency Bandwidth Sensitivity. The importance of selecting the appropriate statistical features and frequency bandwidths was investigated. Figure 5 compares the damage indexes associated with the vector of the wavelet coefficients obtained by decomposing the original

signals with the db10 mother wavelet. Six coefficients at both levels of each bandwidth were retained. Thus, following the notation introduced in Table 2, the filter combination c_I was used. The indexes are plotted as a function of the acquisition position. The statistical features of RMS, ppk, and CF, were used. For this particular study also the value of the largest coefficient modulus was considered. The results of test 1 are presented. The high frequency bandwidth contained in the signals acquired with the central transducers and the gage side transducers are illustrated in Figures 5(a) and 5(c), respectively. The results from the analysis of the low frequency components are instead presented in Figures 5(b) and 5(d), respectively. To improve the readability of the plots the vertical axes are scaled down. As expected, the transducer pair deployed on the gage side of the rail is less suitable to identify the presence of anomalies located on the central portion of the rail, but it is effective to unfold the presence of the gage oblique defect. This is demonstrated by the sharp increase of the damage index around acquisition #71.

In Figure 5(d) a peak at acquisition #39 is visible when considering the statistical feature of the CF. Such a peak is related to the presence of the first internal defect. This result confirms the diagnostics made by conventional ultrasonic contact probes, that is, that the internal defects were close to the gage side.

4.2. Multivariate Analysis. The purpose of combining features was to increase the sensitivity to the presence of damage. However, the use of all eleven features listed in Table 2 may not be necessary and the selection of all features may degrade the detection performance. To investigate this aspect, a parametric analysis was carried out. All of the features were considered ranging from all combinations of two-dimensional damage index vectors to the single combination of an 11-dimensional vector. Figure 6 shows the Mahalanobis squared distance of the best and worst combination as a function of the sample number. The values are related to the analysis of the high-frequency bandwidth of the ultrasonic signals acquired by the central sensor pair. The horizontal lines in this figure represent the 99.73% confidence thresholds. The algorithm performance ranged from 93% to 57%. The criterion used to sort the success rate was the same discussed in Section 4.3 Some false negatives are located in correspondence with the longitudinal and the gage oblique defects. The combination c_I-(1-3, 6, 9) yielded to the best performance. Such a combination used db10 mother wavelet, the six largest coefficients at both level 2 and 3 and five features. The values of the Mahalanobis squared distance associated with the presence of a defect are several orders of magnitude higher with respect to the threshold. The poor performance of the “worst combination” b_II-(9, 11) is noticed by the many false negatives located within the samples associated with the transverse defect.

The same routine was applied to process the waveforms detected by the gage transducer pair. Figures 7(a) and 7(b) show the Mahalanobis squared distance as a function of the sample numbers for the high-frequency and low-frequency bandwidths, respectively. For the low frequency component,

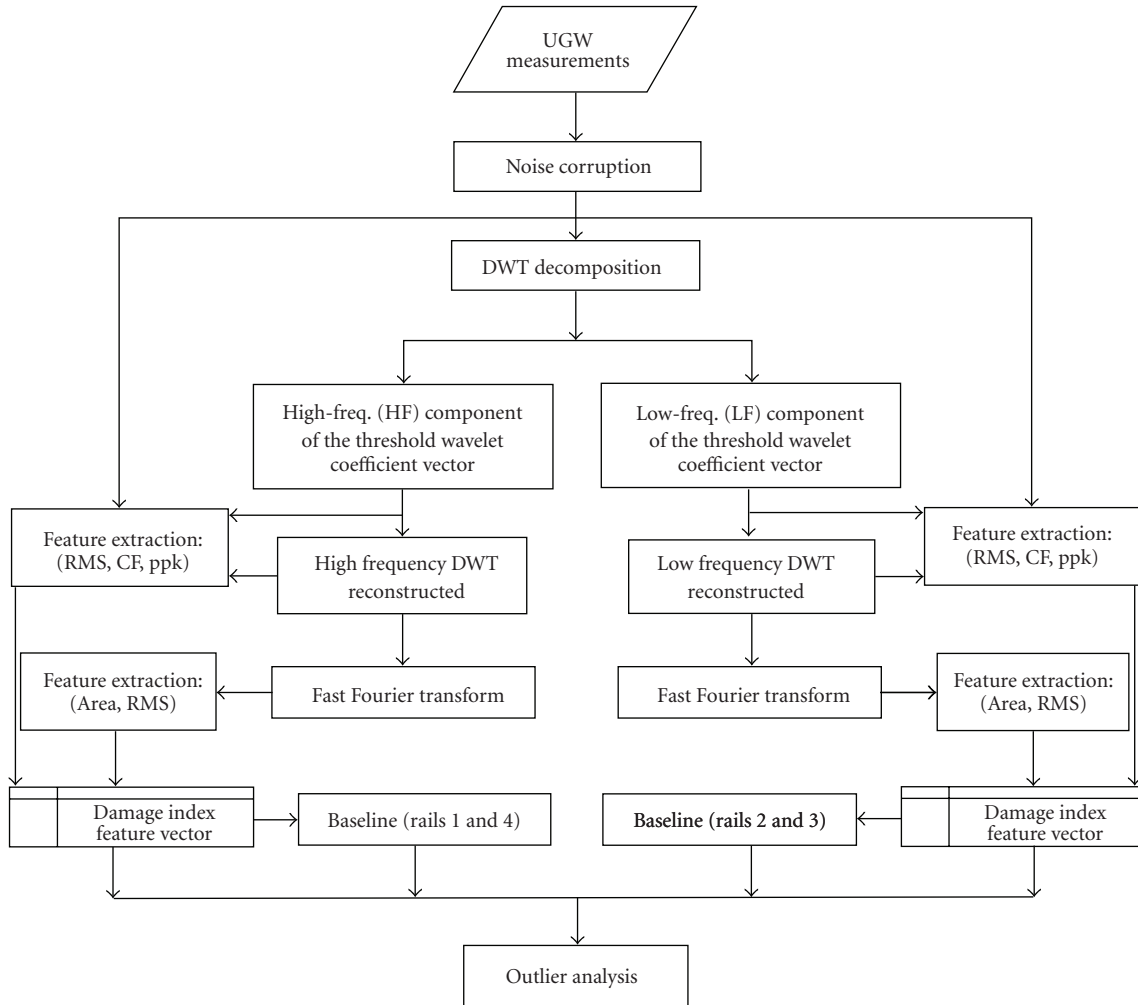


FIGURE 4: Flowchart of the automatic damage detection algorithm based on discrete wavelet transform, feature extraction, and outlier analysis.

the ranking criteria to assess the combination which provides the best algorithm performance were given by the highest percentage of outliers related to the internal defects and the lowest number of false positives.

The best performance was obtained filtering the signals with the *coif4* mother wavelet, retaining 10 and 6 of the largest coefficients at levels 4 and 5, respectively and using ten features. This means the combination *d_III_(2-11)*.

The first internal defect, comprised in the sample range 781–840, was detected by using both bandwidths. The second internal defect, comprised in the sample range 1101–1160, was detected only using the low frequency bandwidth.

The hand mapping revealed that the second internal defect was located more than 10 mm below the rail head surface, whereas the first internal defect lied underneath the rail surface. Therefore, the latter defect was also detectable exploiting the high-frequency bandwidth of the propagating guided waves. This outcome demonstrates that the proposed algorithm yields to the depth location of internal defects.

Table 3 summarizes the best and worst performances of the two transducer pairs at both frequency bandwidths.

4.3. Repeatability Tests. In order to verify the repeatability of the setup, two more tests were conducted on separate days. Between each test session, the cart hosting the prototype was removed from the rail. Minimal variations of the transducers orientation and alignment of the optical system, if any occurred, were unintended. The outlier analysis conducted on these two tests used the same baseline data of Test 1. The same level of noise was added to the raw waveforms recorded during Test 2 and Test 3. Figures 8(a) and 8(b) show the Mahalanobis squared distance as a function of the sample number for Test 2 and Test 3, respectively. The results are associated with the high frequency component of the waveforms acquired with the central pair. In Figure 8(a), the results from the features’ selection that maximize the detection of the transverse and longitudinal defects in Test 2 and Test 1 are superimposed. Similarly, Figure 8(b) shows

TABLE 3: Test 1. Multivariate analysis: percentage of outliers for various transducer pairs, frequency bandwidths, and damage types. The best and the worst combination of wavelet processing and damage index features are presented.

| DATA | Best/Worst | Combination | Defect type | | | |
|------------------------------|------------|-----------------------|-------------|--------------|---------|----------|
| | | | Transverse | Longitudinal | Oblique | Internal |
| Central sensors high-freq | B | c.I_(1-3,6,9) | 92.8% | 48.8% | 22.5% | |
| | W | b.II_(9,11) | 57.1% | 0% | 2.5% | |
| Central sensors low-freq | B | a.IV_(1-3,5-11) | 93.2% | 65% | 78.8% | |
| | W | a.II_(5,9) | 41.8% | 0% | 0% | |
| Gage sensors high-freq | B | a.II_(1-4,8-9) | 58.1% | 0% | 41.7% | |
| | W | a.IV_(3,5) | 23.5% | 0% | 5% | |
| Gage sensors low-freq | B | a.III_(1-3,5-11) | 70.4% | 8.8% | 68.3% | |
| | W | a.IV_(3,5) | 33.8% | 0% | 13.3% | |
| Central sensors high-freq | B | c.I_(1-2,4-9,11) | | | | 57.1% |
| | W | b.II_(4,5) | | | | 0% |
| Central sensors low-freq | B | f.IV_(1-3,5-6,8-9,11) | | | | 77.9% |
| | W | b.I_(1,2,10) | | | | 0% |
| Gage sensors high-freq | B | f.I_(1,4-9) | | | | 41.7% |
| | W | a.IV_(3,5) | | | | 0% |
| Gage sensors low-freq | B | d.III_(2-11) | | | | 60% |
| | W | a.IV_(3,5) | | | | 0% |

the results from the selections that maximize the detection of the transverse and longitudinal defects in Test 3 and Test 1. The values of the corresponding thresholds are superimposed. It is evident that the results are very similar. As the number of acquisitions changes, the total number of samples varies. This causes the slight shift between the two plots in Figure 8(a).

4.4. Discussion. Overall it was observed that the percentage of defects properly identified as outliers increases with the increase of the damage index vector dimension, whereas the number of false positives is relatively constant. This outcome is visualized in Figure 9 where the success rate is plotted as a function of the dimension of the damage index vector, that is, the number of features utilized. Each value in the plot is the average of all the rates resulted from the combinations that used the same number of features. The corresponding averages of false positives are superimposed. It can be seen that the selection of only five features provides a success rate nearly identical to the one obtained by considering all eleven features. The analysis presented in Figure 9 is associated with the detection of transverse defects by means of high frequency ultrasonic bandwidth. The time waveforms were recorded by the central transducer pair.

For the detection of the internal defects, it was found that the highest success rate was achieved with a high

number of features. However, the number of false positives was also found to be high. This is probably related to the inclination of the transducers with respect to the rail surface. In preparation of the set up, the sensors position was optimized with respect to rail Section 1. However, as two AREMA sections were simultaneously tested, the sensitivity over rails 2 and 3 was not optimal. As such, the higher number of false positives may have been arisen.

It must be highlighted that the detection rate discussed in Figure 9 is not conceptually identical to the probability of detection (POD). For instance, let us assume that a given defect was probed at least five times during each test, and three out of five acquisitions were correctly identified as outliers. The success rate of the outlier analysis is 60%. However, because the defect was identified at least once the probability of detection is 100%.

5. Field Test

This section presents the results of field testing activities conducted over the past two years near Gettysburg, Pennsylvania. The site consisted of a segment of railway siding, 160 ft (49 m) in length, containing known defects. Several joints were present along the test section. Three, 1.8 m (6 ft) long, 136-lb A.R.E.M.A. sections with known internal defects in the head were inserted, and secured with joint bars, in the

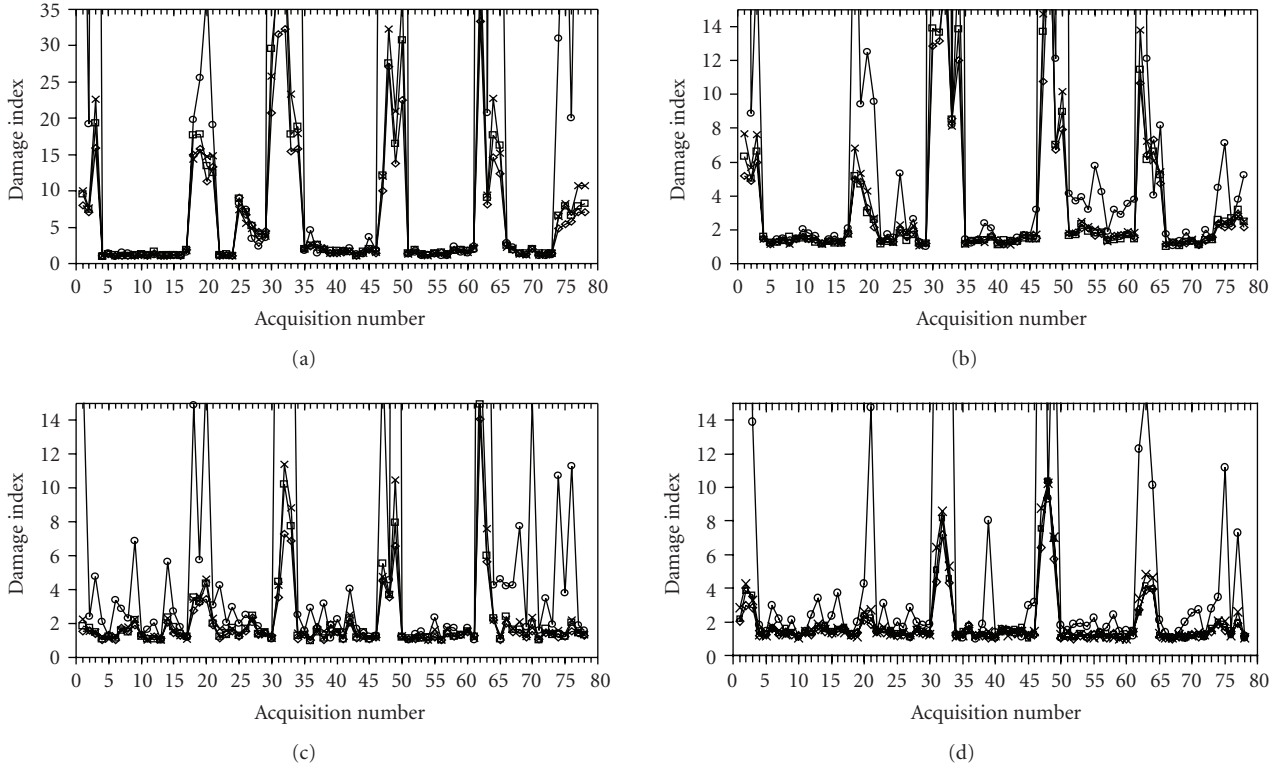


FIGURE 5: Test 1. Feature-based unidimensional damage index as a function of the acquisition number. The max amplitude (x), crest factor (o), peak-to-peak (\square), and the RMS (\diamond) of the wavelet coefficient vector are plotted for the (a) high frequency components and (b) low frequency components of the time waveforms acquired with the central pair transducers, and for the (c) high frequency components and (d) low frequency components of the time waveforms acquired with the gage side transducers.

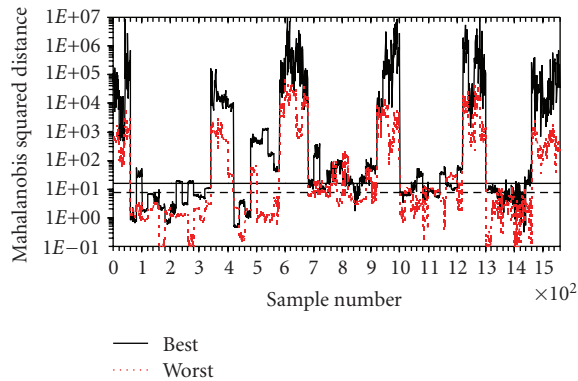


FIGURE 6: Test 1. Mahalanobis squared distance as a function of the sample number associated with the filtering combination that maximizes (best) and minimizes (worst) the detection of transverse surface defects probed using the central sensors pair and high-frequency bandwidth.

test section. From ultrasonic hand mapping, three internal defects were located and sized, with 3.5% head area (HA), 35% HA, and 12% HA, respectively. The hand mapping also indicated that all internal defects were primarily transverse, with two located in the gage side and one located in the head-center. In addition, two surface cuts were machined perpendicularly to the rail running direction, with sizes of

5% and 2% HA, respectively. Two oblique surface cuts (45 degree inclination from the running direction) were also added at the top of the head, both about 3.5% HA. A photo of the test site is shown in Figure 10(a). More details of the test site are in refs. [29, 30].

The prototype shown in Figure 10(b) was used for the test.

The signal processing algorithm implemented in the field test prototype was adapted to provide real-time indication of defects in a statistically robust manner and to provide two levels of classification. The first level identifies “discontinuities” in the track (including defects and joints); the second classification level flags each discontinuity as “joint,” “surface defect,” “internal defect,” or “unclassified defect.” The two-level classification was implemented to minimize the chances of missing a defect (i.e., minimizing false negatives) and, at the same time, to provide the defect classification (“surface defect” versus “internal defect”) whenever possible. Defects are flagged in real-time along with their position. The classification analyzes damage indexes. It must be pointed out that in the context of the field testing, the damage index is the Mahalanobis squared distance calculated by combining five statistical features associated with the time domain of the raw signals detected from air-coupled transducers pairs [31, 32].

Figure 11 shows a typical damage index plot as a function of the inspection distance. The largest peaks are rail joints

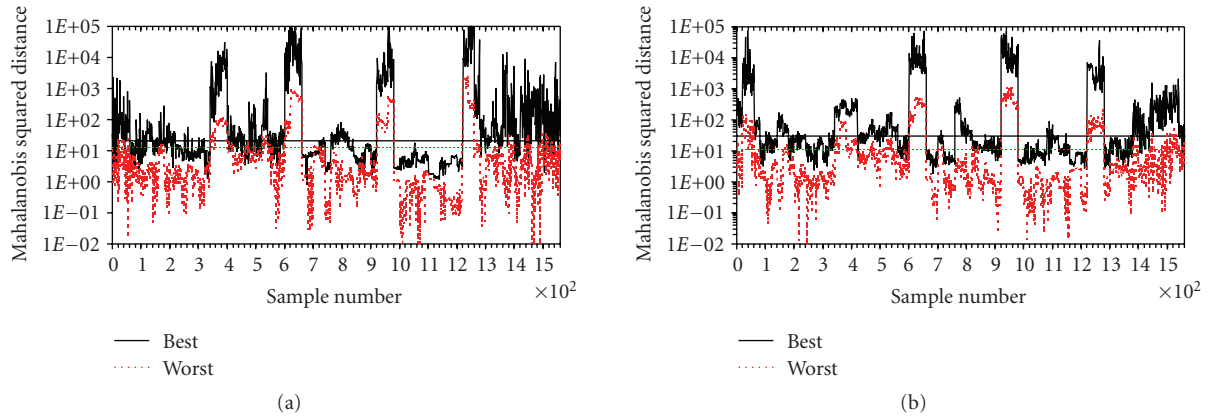


FIGURE 7: Test 1. Mahalanobis squared distance as a function of the sample number associated with the filtering combination that maximizes (best) and minimizes (worst) the detection of internal defects probed using (a) the gage sensors pair and high-frequency bandwidth and (b) the gage sensors pair and low-frequency bandwidth.

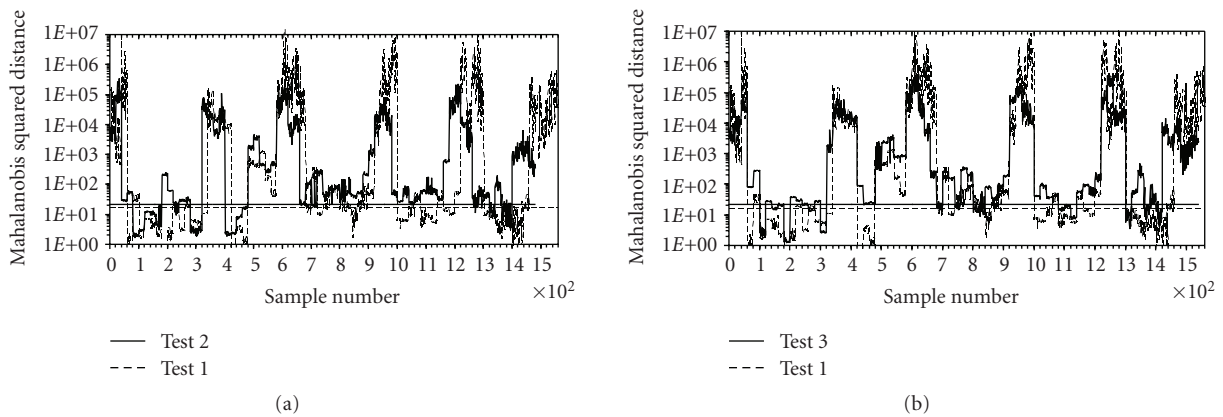


FIGURE 8: Mahalanobis squared distance as a function of the sample number associated with the filtering combination that maximizes (best) the detection of transverse surface defects probed using (a) the central sensors pair and high-frequency bandwidth during Test 1 and Test 2, and (b) the central sensors pair and high-frequency bandwidth during Test 1 and Test 3.

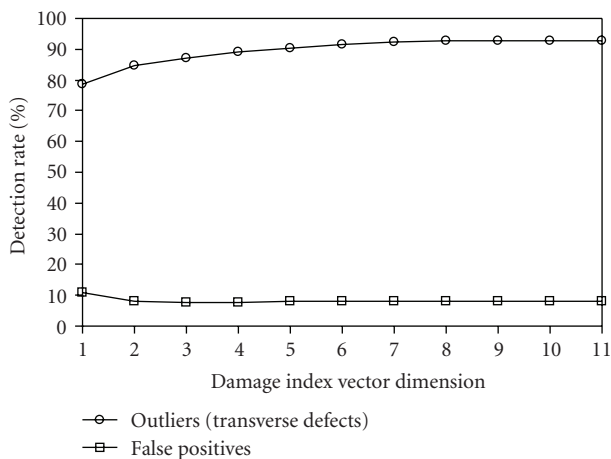


FIGURE 9: Average detection rate as a function of the dimension of the damage index vector as a result of probing transverse defects with central sensor pairs and high-frequency bandwidth in Test 1.

which the system interprets as “very large discontinuity”, and the smaller peaks are real defects. The discontinuity-free portions of the rail show an almost identically zero damage index.

Figure 12 shows the graphical user interface relative to the defect classification results. Notice that the plots are zoomed between locations 70 ft and 120 ft. The software shows two plots, namely the “Discontinuities” plot which includes both joints and defects, and the “Classification” plot which color codes the discontinuities according to the classes “Joint,” “Internal Defect,” “Surface Defect,” and “Unclassified Defect.”

Various runs were made during four days of testing. Twenty-four of these runs were used to collect Damage Index data for estimating the POD for the present defects. The other runs were performed to collect raw data for further analysis. To assess the robustness of the system, the tests were performed under various conditions including calm versus



FIGURE 10: (a) Test site near Gettysburg, Pennsylvania. (b) Photo of the latest inspection prototype tested in the field.

TABLE 4: Defect detection reliability during March 2008 field test at Gettysburg, PA.

| Defect | Surface cut (5% H.A.) | Surface cut (2% H.A.) | Internal defect (gage side, 3.6% H.A.) | Internal defect (gage side, 35% H.A.) | Oblique cut (3.5% H.A.) | Internal defect (center head, 12% H.A.) | Oblique cut (3.5% H.A.) | False positive % |
|---------------------|--------------------------|--------------------------|--|---|----------------------------|---|----------------------------|---------------------|
| Position from start | 81' _7" | 82' _7.5" | 86' _4" | 91' _3.5" | 95' _1" | 96' _4" | 97' _8" | |
| POD (5 MPH) | 100 | 97.7 | 100 | 81.8 | 95.5 | 84.1 | 100 | 0.8 |
| POD (10 MPH) | 100 | 100 | 100 | 100 | 75 | 87.5 | 100 | 2.9 |
| POD (Cumulative) | 100 | 98.1 | 100 | 84.6 | 92.3 | 84.6 | 100 | 1.1 |

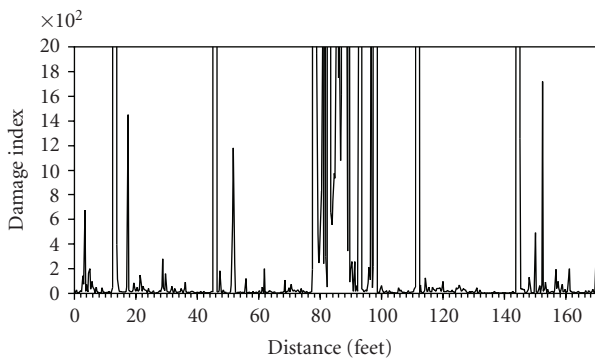


FIGURE 11: Field testing damage index as a function of the inspection distance. Large peaks denotes the presence of joints, smaller peaks denote the presence of defects.

windy, dry versus wet rail, 5 mph versus 10 mph, and using two different powers of laser excitation.

The performance of the prototype, evaluated in terms of POD, is summarized in Table 4. The results are shown separately for the 5 mph and the 10 mph testing speeds. The “cumulative” POD, obtained by considering all tests regardless of testing speed, is also shown. The POD was calculated as the ratio between the number of runs where a given defect was detected, over the total number of usable runs. A defect was considered detected when at least one of the statistical damage indices associated with the transducers’ pair was activated. An index was called “activated” when

the corresponding value was above a fixed threshold level. Table 4 shows an excellent performance in detecting all present defects. Particularly noteworthy is the high POD obtained for the three internal defects. The reliability of detection for the surface and the oblique cuts was also high. It is not clear why the POD of the 35% H.A. internal defect was smaller than that of the other two internal defects at 5 mph. It is possible that the 35% H.A. defect has a curvature that makes the ultrasonic detection more challenging. The fact that this effect was not seen at 10 mph could be due to the favorable position of the air-coupled sensors relative to the defect in the faster runs. Hence, for some of the defects, there seems to be a dependence of reliability of detection on the position of the sensors. This is not surprising, because the defect “ultrasonic shadow” footprint will change with position along the rail.

6. Conclusions

This paper describes a rail inspection prototype based on noncontact probing and ultrasonic guided waves coupled with a robust signal processing algorithm. The algorithm consists of discrete wavelet transform, feature extraction, and outlier analysis aimed at providing automatic damage detection and classification. The system uses laser generated guided waves to detect surface-breaking cracks and internal defects located in the rail head. Ultrasonic signals were detected by using three pairs of air-coupled transducers. Time waveforms were processed with the Discrete Wavelet

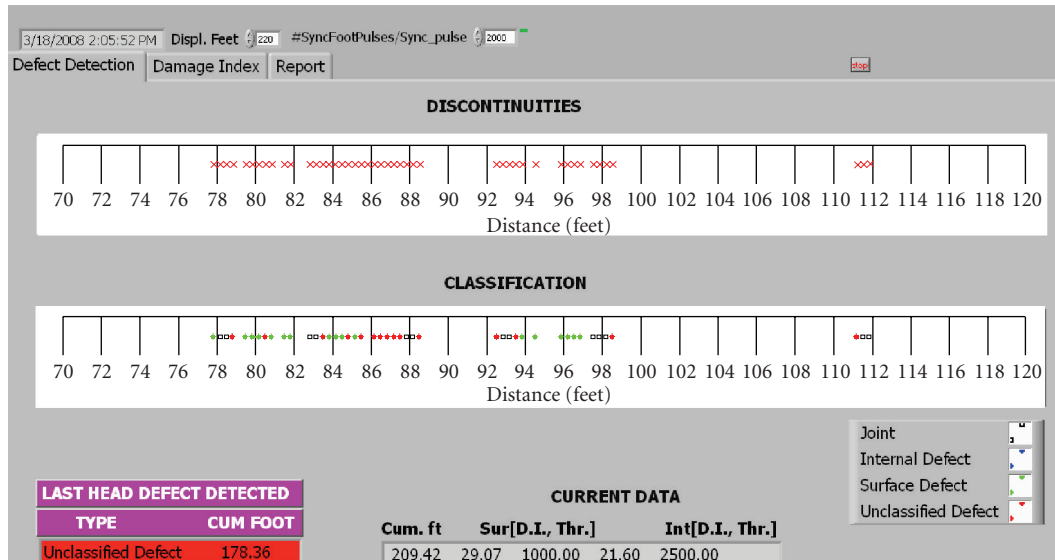


FIGURE 12: The “Defect Detection” window of the user’s interface showing the real-time classification of joints and defects as color-coded points.

Transform to denoise the signals and to generate a set of relevant damage sensitive features used to construct a uni or multidimensional damage index. The damage index was fed to an unsupervised learning algorithm based on outlier analysis aimed at detecting anomalous conditions of the rail head. The population of data for the outlier analysis was created by adding digital random noise to the ultrasonic measurements. A total of 20 samples per acquisition were thus obtained for the baseline constituting the undamaged condition and for each of the damage conditions.

The importance of feature selection related to damage detection performance was examined. It was shown that combining multiple features in a multivariate analysis substantially improves the performance of the system in terms of sensitivity to defect sizes’ detections and discrimination. By combining as few as five features, the improvement in defect detections was demonstrated. By separating the low-frequency from the high-frequency signal bandwidth, discrimination between internal and surface defects can be achieved. Moreover, by deploying sensors across the rail head width, the position of the defect within the head cross section can be identified.

The results presented here showed the effectiveness of deploying pairs of sensors over the entire rail width and the efficiency of performing robust signal processing to enhance the defect sensitivity of the inspection prototype. For instance, the oblique defect located was clearly identified through the analysis of the gage side data but barely visible through the analysis of the central transducers’ data. The proposed setup, not only adds complete coverage of the rail head, but also offers a tool to conduct defect location and classification across the rail head section.

The last part of the paper presented the status of the rail defect detection prototype being developed at UCSD under FRA sponsorship. The prototype was field tested at speeds of

up to 10 mph. The test track included three different sizes of Internal Head Defects (3.5%, 35% and 12% H.A.), two sizes of transverse Surface Head Cuts (2% and 5% H.A.), and one size of oblique Surface Head Cut (3.5% H.A.). The results of the tests indicated a high Probability of Detection for all defects present, ranging from 75% to 100% success rate over twenty-four runs conducted with varying environmental conditions including wind and rain. Unfortunately it was not possible to compare the proposed technology with existing rail inspection technologies. It is hoped that this comparison can be done in the near future.

Acknowledgments

This work, initially supported by the U.S. National Science Foundation through Grant no. CMS-84249, is being currently funded by the U.S. Federal Railroad Administration under Grant no. DTFR53-02-G-00011. The support of ENSCO, Inc. during the field tests is acknowledged and much appreciated. The authors are grateful to Mahmood Fateh, the FRA’s Technical Representative, for his technical guidance, and to Gary Carr, former Senior Mechanical Engineer of ENSCO, and now FRA’s Chief of Track Research Division, for providing technical and logistic support during the prototype assembling. M. Cammarata performed this research while visiting the University of Pittsburgh under a Study Abroad Fellowship (Decreto no 3684-2006) of the University of Palermo, Italy. Further support of the University of Pittsburgh to Mr. Cammarata through start up funding available to the first author is also acknowledged.

References

- [1] Federal Railroad Administration, “Safety statistics data: 1992–2002,” U.S. Department of Transportation, 2002.

- [2] <http://safetydata.fra.dot.gov/OfficeofSafety/>.
- [3] H. A. Toliyat, K. Abbaszadeh, M. M. Rahimian, and L. E. Olson, "Rail defect diagnosis using wavelet packet decomposition," *IEEE Transactions on Industry Applications*, vol. 39, no. 5, pp. 1454–1461, 2003.
- [4] R. Clark, "Rail flaw detection: overview and needs for future developments," *NDT and E International*, vol. 37, no. 2, pp. 111–118, 2004.
- [5] F. Lanza di Scalea, "Ultrasonic testing in the railroad industry," in *Non-Destructive Testing Handbook*, pp. 9–16, American Society for Nondestructive Testing, Columbus, Ohio, USA, 3rd edition, 2007.
- [6] L. Oukhellou, P. Aknin, and J.-P. Perrin, "Dedicated sensor and classifier of rail head defects," *Control Engineering Practice*, vol. 7, no. 1, pp. 57–61, 1999.
- [7] R. Pohl, A. Erhard, H.-J. Montag, H.-M. Thomas, and H. Wüstenberg, "NDT techniques for railroad wheel and gauge corner inspection," *NDT and E International*, vol. 37, no. 2, pp. 89–94, 2004.
- [8] R. J. Greene, J. R. Yates, and E. A. Patterson, "Crack detection in rail using infrared methods," *Optical Engineering*, vol. 46, no. 5, Article ID 051013, 2007.
- [9] P. Wilcox, M. Evans, B. Pavlakovic et al., "Guided wave testing of rail," *Insight*, vol. 45, no. 6, pp. 413–420, 2003.
- [10] P. Cawley, M. J. S. Lowe, D. N. Alleyne, B. Pavlakovic, and P. Wilcox, "Practical long range guided wave testing: applications to pipes and rail," *Materials Evaluation*, vol. 61, no. 1, pp. 66–74, 2003.
- [11] D. Hesse and P. Cawley, "Surface wave modes in rails," *Journal of the Acoustical Society of America*, vol. 120, no. 2, pp. 733–740, 2006.
- [12] J. L. Rose, M. J. Avioli, P. Mudge, and R. Sanderson, "Guided wave inspection potential of defects in rail," *NDT and E International*, vol. 37, no. 2, pp. 153–161, 2004.
- [13] J. L. Rose, M. J. Avioli, and W.-J. Song, "Application and potential of guided wave rail inspection," *Insight*, vol. 44, no. 6, pp. 353–358, 2002.
- [14] J. D. McNamara, F. Lanza di Scalea, and M. Fateh, "Automatic defect classification in long-range ultrasonic rail inspection using a support vector machine-based 'smart system,'" *Insight*, vol. 46, no. 6, pp. 331–337, 2004.
- [15] I. Bartoli, F. Lanza di Scalea, M. Fateh, and E. Viola, "Modeling guided wave propagation with application to the long-range defect detection in railroad tracks," *NDT and E International*, vol. 38, no. 5, pp. 325–334, 2005.
- [16] F. Lanza di Scalea, I. Bartoli, P. Rizzo, and M. Fateh, "High-speed defect detection in rails by non-contact guided ultrasonic testing," *Journal of the Transportation Research Board*, vol. 1961, pp. 66–77, 2006.
- [17] G. Alers, "Railroad rail flaw detection system based on electromagnetic acoustic transducers," Tech. Rep. DOT/FRA/ORD-88/09, U.S. Department of Transportation, 1988.
- [18] R. S. Edwards, S. Dixon, and X. Jian, "Characterisation of defects in the railhead using ultrasonic surface waves," *NDT and E International*, vol. 39, no. 6, pp. 468–475, 2006.
- [19] S. Kenderian, D. Cerniglia, B. B. Djordjevic, G. Garcia, J. Sun, and M. Snell, "Rail track field testing using laser/air hybrid ultrasonic technique," *Materials Evaluation*, vol. 61, no. 10, pp. 1129–1133, 2003.
- [20] T. Hayashi, W.-J. Song, and J. L. Rose, "Guided wave dispersion curves for a bar with an arbitrary cross-section, a rod and rail example," *Ultrasonics*, vol. 41, no. 3, pp. 175–183, 2003.
- [21] J. McNamara and F. L. di Scalea, "Improvements in non-contact ultrasonic testing of rails by the discrete wavelet transform," *Materials Evaluation*, vol. 62, no. 3, pp. 365–372, 2004.
- [22] F. L. di Scalea, P. Rizzo, S. Coccia et al., "Non-contact ultrasonic inspection of rails and signal processing for automatic defect detection and classification," *Insight*, vol. 47, no. 6, pp. 346–353, 2005.
- [23] W. Staszewski, C. Boller, and G. Tomlinson, *Health Monitoring of Aerospace Structures*, John Wiley & Sons, Munich, Germany, 2006.
- [24] P. Rizzo and F. Lanza di Scalea, "Wavelet-based unsupervised and supervised learning algorithms for ultrasonic structural monitoring of waveguides," in *Progress in Smart Materials and Structures Research*, chapter 8, pp. 227–290, Nova Science, Hauppauge, NY, USA, 2007.
- [25] P. Rizzo and F. L. di Scalea, "Wavelet-based feature extraction for automatic defect classification in strands by ultrasonic structural monitoring," *Smart Structures and Systems*, vol. 2, no. 3, pp. 253–274, 2007.
- [26] P. Rizzo and F. L. di Scalea, "Ultrasonic inspection of multi-wire steel strands with the aid of the wavelet transform," *Smart Materials and Structures*, vol. 14, no. 4, pp. 685–695, 2005.
- [27] P. Rizzo, I. Bartoli, M. Cammarata, and S. Coccia, "Digital signal processing for rail monitoring by means of ultrasonic guided waves," *Insight*, vol. 49, no. 6, pp. 327–332, 2007.
- [28] P. Rizzo, M. Cammarata, D. Dutta, H. Sohn, and K. A. Harries, "Unsupervised learning algorithm for fatigue crack detection in waveguides," *Smart Materials and Structures*, vol. 18, Article ID 025016, 11 pages, 2009.
- [29] P. Rizzo, S. Coccia, I. Bartoli, and F. Lanza di Scalea, "On line high-speed rail defect detection—prototype assembling and field testing," Tech. Rep. SSRP-06/17, University of California, San Diego, Calif, USA, 2006.
- [30] S. Coccia, I. Bartoli, F. Lanza di Scalea, and P. Rizzo, "Non-contact rail defect detection: first and second field tests," Tech. Rep. SSRP-07/15, University of California, San Diego, Calif, USA, 2007.
- [31] S. Coccia, R. Phillips, I. Bartoli, S. Salamone, and F. Lanza di Scalea, "Non-contact rail defect detection," Tech. Rep. SSRP-08/02, Federal Railroad Administration, University of California, San Diego, Calif, USA, 2008.
- [32] S. Coccia, I. Bartoli, R. Phillips, S. Salamone, and F. Lanza di Scalea, "Non-contact rail defect detection: fourth field test," Tech. Rep. SSRP-09/04, Federal Railroad Administration, University of California, San Diego, Calif, USA, 2009.

Research Article

Intelligent Wireless Sensors with Application to the Identification of Structural Modal Parameters and Steel Cable Forces: From the Lab to the Field

Y. Lei,¹ W. A. Shen,¹ Y. Song,¹ and Y. Wang²

¹Department of Civil Engineering, Xiamen University, Xiamen, Fujian 361005, China

²School of Civil and Environmental Engineering, Georgia Institute of Technology, Atlanta, GA 30332, USA

Correspondence should be addressed to Y. Lei, ylei@xmu.edu.cn

Received 3 October 2009; Revised 1 February 2010; Accepted 6 May 2010

Academic Editor: Piervincenzo Rizzo

Copyright © 2010 Y. Lei et al. This is an open access article distributed under the Creative Commons Attribution License, which permits unrestricted use, distribution, and reproduction in any medium, provided the original work is properly cited.

Wireless sensing systems have been proposed for structural health monitoring in recent years. While wireless sensors are cost-competitive compared to tethered monitoring systems, their significant merit also lies in their embedded computational capabilities. In this paper, performance of the two embedded engineering algorithms, namely the fast Fourier transform and peak-picking algorithm implemented in the wireless sensing nodes codeveloped at Stanford University and the University of Michigan is investigated through laboratory and field experimental studies. Furthermore, the wireless sensor network embedded with the engineering algorithms is adopted for the identification of structural modal parameters and forces in steel bridge cables. Identification results by the embedded algorithms in the intelligent wireless sensors are compared with those obtained by conventional offline analysis of the measured time-history data. Such a comparison serves to validate the effectiveness of the intelligent wireless sensor network. In addition, it is shown that self-interrogation of measurement data based upon the two embedded algorithms in wireless sensor nodes greatly reduces the amount of data to be transmitted by the wireless sensing network. Thus, the intelligent wireless sensors offer scalable network solutions that are power-efficient for the health monitoring of civil infrastructures.

1. Introduction

Conventional structural monitoring systems are wire-based systems, which require extensive lengths of cables to transmit recorded data from multiple sensors to a centralized data repository. Installation and maintenance of such wired systems for the structural health monitoring (SHM) of civil infrastructures, including high-rise buildings and long-span bridges, is time consuming and expensive. With the advances in wireless communication and microelectronics, wireless monitoring systems have been proposed to eradicate the extensive lengths of wires associated with tethered systems [1, 2]. In recent years, some academic and commercial wireless monitoring systems have been proposed [2, 3]. Among them, the academic wireless sensing prototype codeveloped at Stanford University and the University of Michigan has received great attention as it emphasizes the design of a sophisticated computational core that can process measurement data at the wireless sensor level [4–6]. The data acquisition capabilities

of this wireless sensing system have been validated through both laboratory and field experimental studies [7–9].

While wireless monitoring systems offer an economical and feasible technique for data acquisition in SHM, transmitting the lengthy vibration data to the base station can be undesirable due to the limited bandwidth of the wireless communication. Sending a tremendous amount of raw data to a central server consumes excessive battery energy as communication is responsible for more than 80% of energy consumption at full operation mode in ultra-low-power platforms [10]. Overall, wireless data transmission consumes more power than data processing; therefore, one of the efficient strategies for overcoming these difficulties is to embed some data processing and analysis algorithms in the wireless sensor's microprocessor. The embedded algorithms enable wireless sensors to autonomously analyze data, which grants these devices with certain level of intelligence. In addition, the wireless sensors only need to transmit analysis results, which typically have only a fraction of the size of

raw time history data. As a result, the limitations in terms of energy consumption and network bandwidth can be mitigated. This capability is particularly attractive within the context of SHM [1, 2, 5]. So far, a number of data processing and analysis algorithms have been implemented in the academic wireless sensing nodes as discussed by Lynch et al. [4, 5], but their performance still needs to be validated by further tests on different structures.

In this paper, two embedded engineering algorithms implemented in the wireless sensor, including the fast Fourier transform (FFT) and peak-picking (PP) algorithms, are investigated through laboratory experiments on a three-story structural model as well as through field studies on a steel arch bridge under ambient vibration. Focus is placed upon validating the performance of the two embedded algorithms and their effectiveness in reducing energy consumptions. Online data processing and analysis results by the two embedded algorithms are compared to those obtained by offline analysis of the measured raw time-history data. This side-by-side comparison validates the accuracy of the embedded algorithms. Finally, the two embedded algorithms are employed for identifying the modal parameters of the laboratory building model and the steel arch bridge as well as for estimating cable forces in the steel arch bridge based upon the vibration data.

2. Wireless Sensing Units

The overall hardware of the academic wireless sensing prototype codeveloped at Stanford University and the University of Michigan [2, 3] mainly consists of three functional modules: (1) sensing interface, (2) computational core, and (3) wireless communication module, as shown in Figure 1. In the computation core, a low-cost, low-power 8-bit Atmel AVR microcontroller (ATmega 128) is selected to coordinate the hardware components of the wireless unit. The microcontroller, together with ample internal and external memories, provides the capability of onboard data interrogation at the sensor level. Detailed descriptions on the key parameters of ATmega128 and the computational core can be found in Wang [3] and Wang et al. [10]. The wireless sensing unit is particularly designed to balance low power consumption while supporting high-data transfer rate and long communication range typically required for civil structural applications [10].

As shown in Figure 2, the embedded software is structured based upon a multilayer architecture [2, 3, 5]. At the lower layer of the embedded software architecture is the device driver layer which directly manages the wireless sensor hardware. Software, including the FFT and PP schemes, that processes and analyzes sensor data resides on the upper application layer of the software architecture.

3. Implementation of the FFT and PP Algorithms

The fast Fourier transform (FFT) is an efficient algorithm to transform time history data into frequency domain. It

also serves as the foundation for further frequency domain structural identification and damage detection analysis, for example, the peak-picking (PP) algorithm is based upon the results of FFT. In the wireless sensing node, the FFT algorithm is implemented in floating point numbers and is computed based upon the following equation:

$$F_x(k) = \sum_{n=1}^N x(n) \exp\left(-\frac{i2\pi(k-1)(n-1)}{N}\right), \quad 1 \leq k \leq N, \quad (1)$$

where $N = 4096$. The FFT can be executed onboard, as soon as the sensor data is collected. When the interest is focused upon the first few vibration modes of a civil structure, only the FFT results within specific frequency range need to be transmitted from each sensing node to the central server [10]. In addition, the 4096-point complex-valued Fourier spectrum can also be used for further onboard engineering analysis by the wireless nodes, and only the analysis results are transmitted to the server.

The peak-picking (PP) algorithm is a simple approach for estimating the modal properties of a structure. The peak-picking analysis can be based upon output vibration data only, that is, without requiring input measurement, which makes it commonly used in civil engineering. If a structure is lighted and damped with well-separated modes, the natural frequencies and operational mode shapes of the structure can be estimated with the PP approach, using the frequency response functions (FRFs). Assuming a white noise excitation, the FRF can be considered equivalent to the Fourier spectrum of the response data, which is obtained through the fast Fourier transform (FFT). The implementation of the PP algorithm embedded in the wireless sensing nodes is described as follows:

(1) The time history data collected at each sensing node is converted into a FRF by executing the embedded FFT algorithm.

(2) The average value of the FRF over the frequency span is calculated as μ . Then a threshold value, defined as $\beta = n\mu$, is selected, where n is a scaling factor assigned by the user. The threshold value is used to eliminate those small spurious local peaks in the FRF, which exist due to sensor noise and environmental influences. A carefully assigned threshold value assists in eliminating small spurious peaks, while allowing the algorithm to pick up the nonspurious peaks in the frequency spectrum.

(3) Based upon the total number of peaks, p , that are to be identified, each sensing node picks the p peaks by scanning for frequencies at which the absolute values of the corresponding FRF are not only larger than the threshold value β , but also larger than the surrounding points in the FRF spectrum as

$$\begin{aligned} |F_x(k)| &> |F_x(k-1)|, & |F_x(k-2)|, \\ |F_x(k)| &> |F_x(k+1)|, & |F_x(k+2)|, \end{aligned} \quad (2)$$

in which $|F_x(k)|$ is the absolute value of the selected peak in the spectrum. In this approach, it is assumed that the

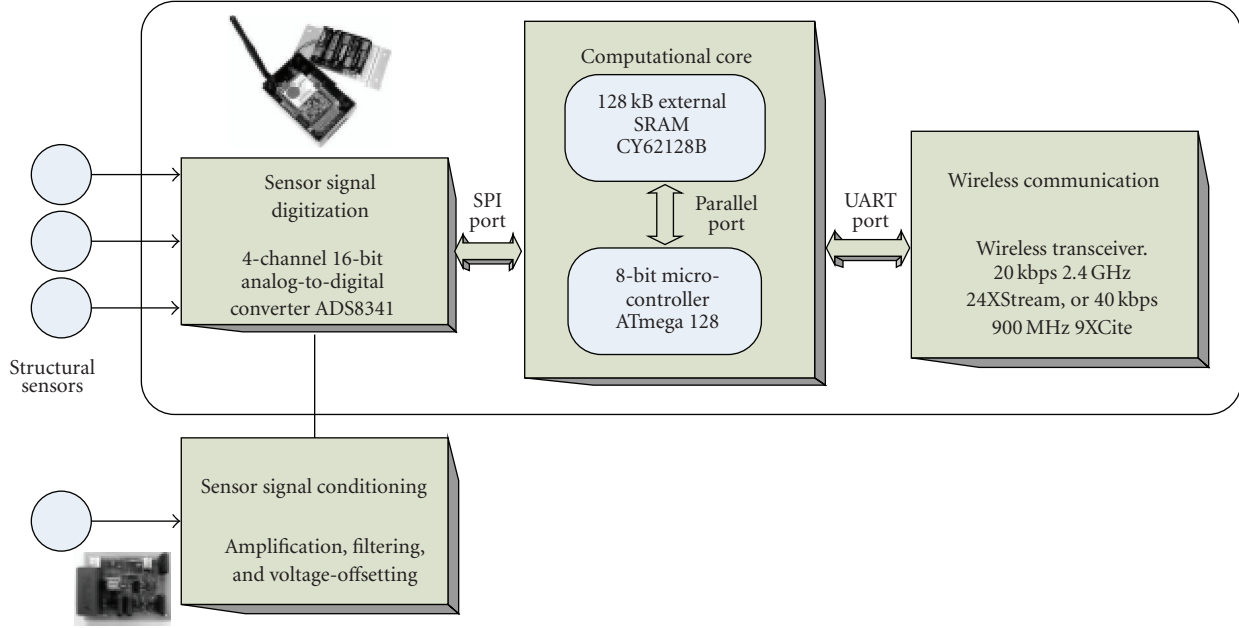


FIGURE 1: Hardware of the academic wireless sensing unit.

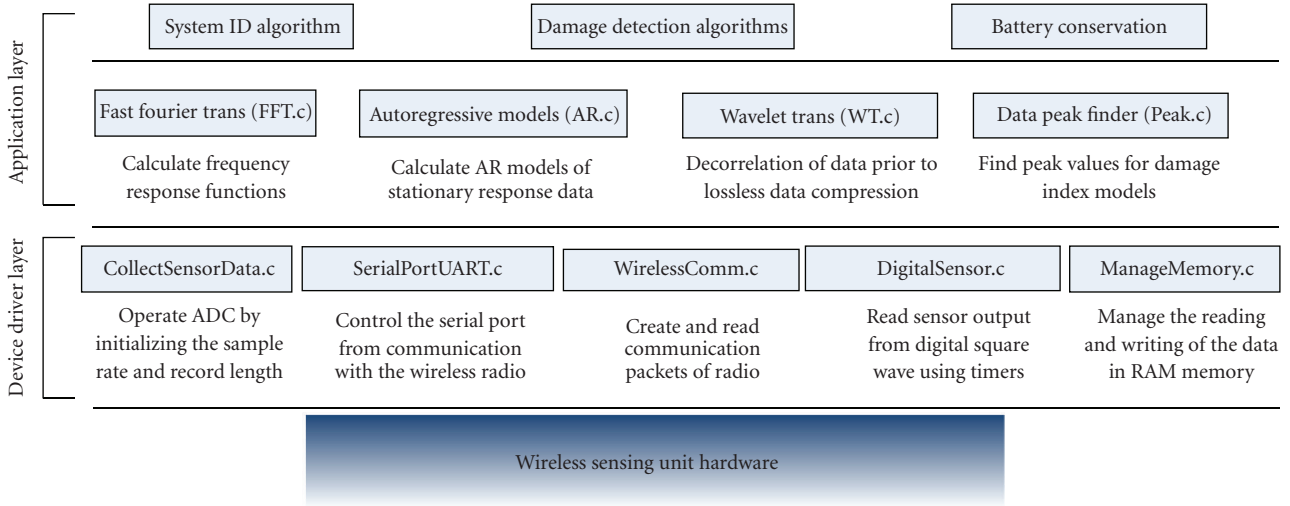


FIGURE 2: Software Architecture of the academic wireless sensing unit.

structure has no closely spaced modes. The frequency values and the imaginary components of the FRF corresponding to the peaks are recorded by each sensing node.

(4) Each sensing node transmits the peak frequencies and the corresponding imaginary components of the FRF to the central server, where the global modal frequencies of the structure are determined. Furthermore, the mode shapes of the structure can be estimated by assembling the imaginary components of the multiple FRFs at the peaks of each sensing node:

$$\{\phi_j\} = \{ \text{Im}[H_1(i\omega_j)], \text{Im}[H_2(i\omega_j)], \dots, \text{Im}[H_n(i\omega_j)] \}^T, \quad (3)$$

where $\{\phi_j\}$ is the j th mode shape, $H_k(i\omega_j)$ is the FRF of the structure at sensor location k , n is the total number of sensing nodes installed on the structure, and $\text{Im}[\cdot]$ denotes the imaginary component of a complex number.

In summary, the PP algorithm is implemented in a wireless sensing network for a quick engineering estimation of modal frequency and mode shapes of a structure. However, PP analysis also has drawbacks compared with other sophisticated methods, for example, PP analysis cannot properly handle closed spaced modes [11]. To investigate the performance of the embedded FFT and PP algorithms in the wireless sensing network, laboratory and field experiments need to be conducted.

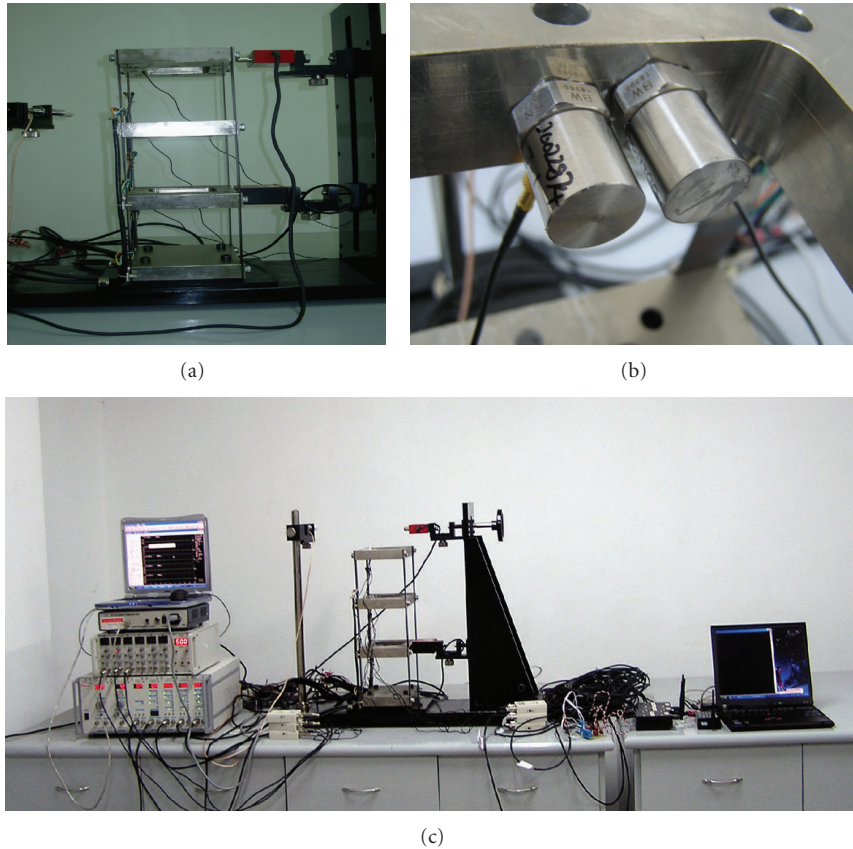


FIGURE 3: Test structure model with wireless sensing system.

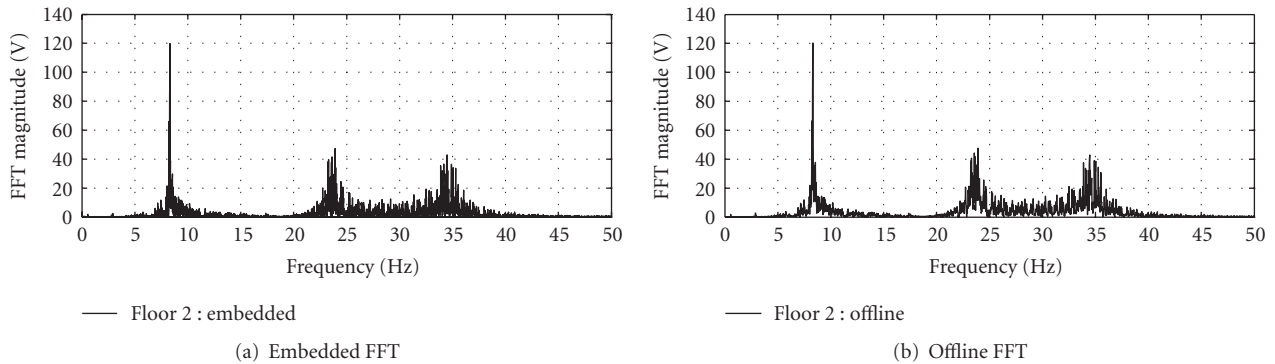


FIGURE 4: Comparison of FFT results. (a) Embedded using the wireless sensing unit. (b) Offline using MATLAB.

4. Laboratory Experimental Studies

The performance of the two algorithms embedded in the wireless sensing network is first studied upon a three-story building structure constructed in the laboratory. The structural model behaves as a lumped-mass shear building because of its rigid floors and flexible columns, as shown in Figure 3. At each floor level, light-weight BW-16200 accelerometers, manufactured by B&W Sensing Tech, are mounted to record the acceleration response of the forced vibration of the building. The wireless sensing network with

embedded algorithms is utilized for both data acquisition and processing.

First, the time-history response data is transformed to the frequency domain via the embedded FFT algorithm. Embedded computing time of the 4096-point FFT by the microcontroller is around 16.5 seconds. Based upon the datasheets of the components in the wireless sensing unit [10, 12], during embedded computing, the microcontroller together with the external memory consumes about only 150 mW. On the other hand, transmission time for the 4096-point raw time-history data is around 12.6 seconds.

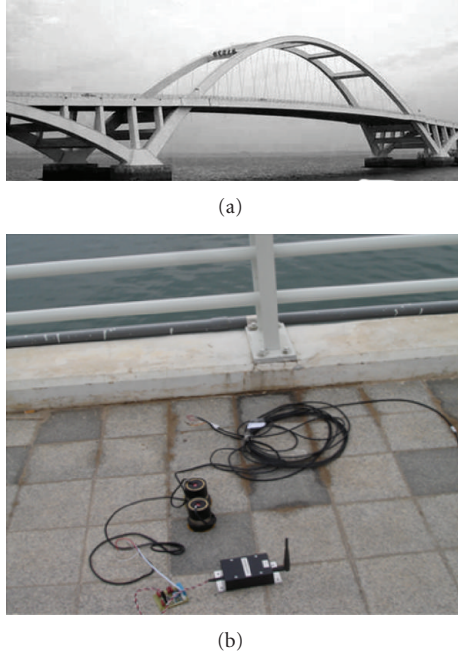


FIGURE 5: (a) Side view of the Wuyuan Bridge; (b) wireless sensing node on the bridge.

The total power consumption for wireless data transmission, including the necessary operations and of the microcontroller, memory units, the transceivers, and so forth, is estimated to be 900 mW, when the 2.4 GHz MaxStream 24XStream transceiver is adopted. Therefore, by employing the embedded FFT algorithm, battery power consumption is reduced by nearly 80%.

To compare the accuracy of the embedded FFT algorithm, the frequency spectrum calculated by the embedded algorithm in the wireless sensing unit at the second floor is compared with that estimated offline by MATLAB using the same raw time-history response transmitted by the wireless sensing unit. As shown in Figure 4, the embedded FFT and offline FFT values are in close agreement.

After the validation of the embedded FFT algorithm, the embedded PP algorithm in each wireless sensing node is employed with the aforementioned procedures. Under forced vibration in the lab tests, relatively high-threshold values can be assigned for executing the embedded PP algorithm. Upon the embedded computing, each wireless sensing unit transmits the identified peak frequencies and corresponding imaginary components of the FRFs to the central data repository. These results are compared with those obtained from an offline PP analysis of the same time-history data transmitted by the three wireless sensing units. As shown in Table 1, the modal frequencies and the imaginary components of the FRFs at those frequencies estimated by embedded and offline PP analysis are identical.

The total execution time of the embedded PP algorithm (including the FFT analysis) by the ATmega128 is around 25 seconds. Then, each sensing node only transmits three peak frequencies and the corresponding imaginary components

in frequency spectrum. A total of 3 (sensing nodes) \times 4 (bytes per floating point number) \times 6 (floating point numbers) = 72 bytes of data are transmitted by the wireless sensing network to the central server, which is much smaller compared with transmitting the 3 (sensing nodes) \times 2 (bytes per ADC sample) \times 4096 (data samples) = 24,576 bytes of raw time-history data recorded by the three sensing nodes. According to the aforementioned power consumption of the microcontroller and the transceiver, energy saving by employing the embedded PP algorithm is again significant.

The embedded FFT and PP algorithms provide a simple approach to estimate the modal frequencies and mode shapes based upon (3). To validate the accuracy of the estimated modal frequencies and mode shapes by the two embedded algorithms, the measured time-history data, which is wirelessly transmitted to the central data repository, is processed by the stochastic subspace identification (SSI) algorithm. The SSI algorithm is an advanced time-domain system identification approach for identifying the modal frequencies and mode shapes of the structure. As shown in Table 2, the modal frequencies and mode shapes identified by embedded FFT and PP algorithms are in close agreement with those from the SSI analysis, except for minor discrepancy in the 3rd mode shape. This minor discrepancy is due to the simplicity and lower accuracy of the PP analysis. Table 2 also illustrates the Modal assurance criteria (MAC) for quantifying the similarity between identified modes.

From the lab testing results, it is shown that the embedded FFT and PP algorithms are executed in a distributed manner by individual wireless sensing nodes, which is well suited for the distributed computing paradigm of the wireless sensing network. Because the lengthy time-history vibration data do not need to be wirelessly transmitted, the decentralized computing architecture is power efficient and can significantly increase the battery life spans of the wireless sensing nodes.

5. Field Experimental Studies on the Wuyuan Bridge

Field experimental studies provide a more realistic way to assess the performance of the embedded FFT and PP algorithms in the wireless sensing network. A wireless sensing network is set up on the Wuyuan steel arch bridge in Xiamen, China. The bridge shown in Figure 5 is a half-through basket-type arch bridge. The main span is 210 m long with the main deck supported by steel hangers from the arched ribs. The bridge is located in Wuyuan bay, as part of the ring road around the Xiamen Island in South East China Sea.

Due to the easy installation of wireless sensors in the field, 45 locations on the bridge deck and arch ribs are mounted with uniaxial or triaxial accelerometers, manufactured by Harbin Institute of Engineering Mechanics, to measure the corresponding vertical and transverse acceleration responses of the bridge under ambient excitation (Figure 6). The uniaxial accelerometer has a sensitivity of 1V/g with a resolution of 10^{-6} g, while the triaxial one has values of

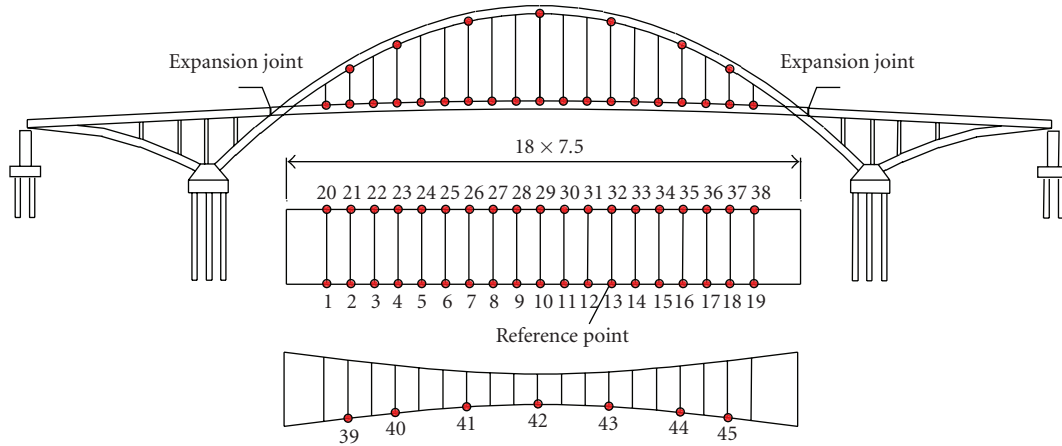
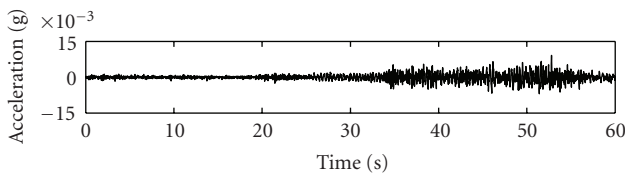


FIGURE 6: Locations of sensing units on the Wuyuan Bridge.

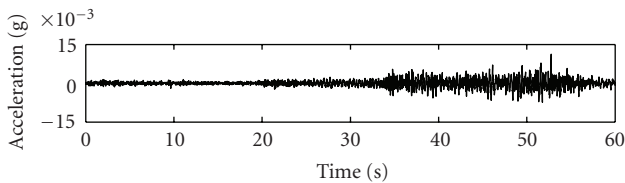
TABLE 1: Comparison of the results by embedded PP and offline PP.

| | 1st Peak | | Embedded PP 2nd Peak | | 3rd Peak | | 1st Peak | | Offline PP 2nd Peak | | 3rd Peak | |
|-----------|----------|--------|-------------------------|--------|----------|-------|----------|--------|------------------------|--------|----------|-------|
| | Freq. | Im(H) | Freq. | Im(H) | Freq. | Im(H) | Freq. | Im(H) | Freq. | Im(H) | Freq. | Im(H) |
| 1st Floor | 8.30 | -68.77 | 23.9 | -96.91 | 34.47 | 27.50 | 8.30 | -68.77 | 23.9 | -96.91 | 34.47 | 27.5 |
| 2nd Floor | 8.30 | -119.8 | 23.9 | -47.26 | 34.47 | -42.8 | 8.30 | -119.8 | 23.9 | -47.26 | 34.47 | -42.8 |
| 3rd Floor | 8.30 | -152.5 | 23.9 | 82.58 | 34.47 | 19.24 | 8.30 | -152.5 | 23.9 | 82.58 | 34.47 | 19.24 |



— Wireless

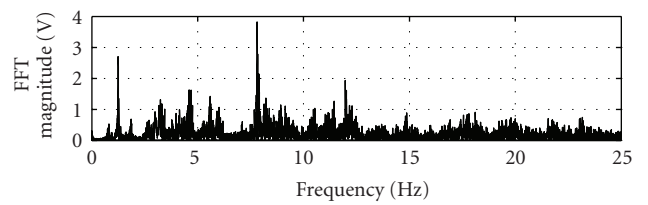
(a)



— Wired

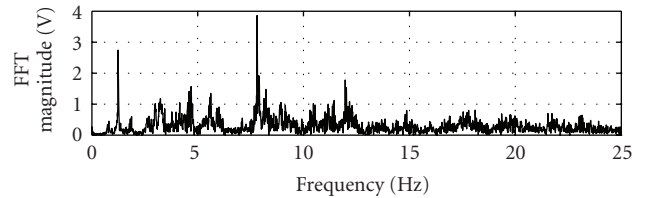
(b)

FIGURE 7: Vertical acceleration time history recorded by sensing node 2.



— Embedded

(a) Embedded FFT



— Offline

(b) Offline FFT

FIGURE 8: Comparison of FFT results at sensing node 5. (a) Embedded using the wireless sensing unit. (b) Offline by MATLAB.

8 V/g and 1.6×10^{-7} g, respectively. For the data acquisition by the wireless sensing network, a sampling frequency of 50 Hz is selected. Figure 7 shows one typical vertical acceleration measurement on the bridge deck. The peak value of the recorded signal is around 0.012 g under normal traffic loading. A signal conditioning circuit proposed by

Lynch et al. [7] and Wang et al. [8] is included in each sensing node to both amplify and band-pass the analog accelerometer signal, which is especially useful for recording weak ambient vibration. Since this paper focuses on studying the performance of the embedded FFT and PP algorithm in the field experiments on the Wuyuan Bridge, more detailed

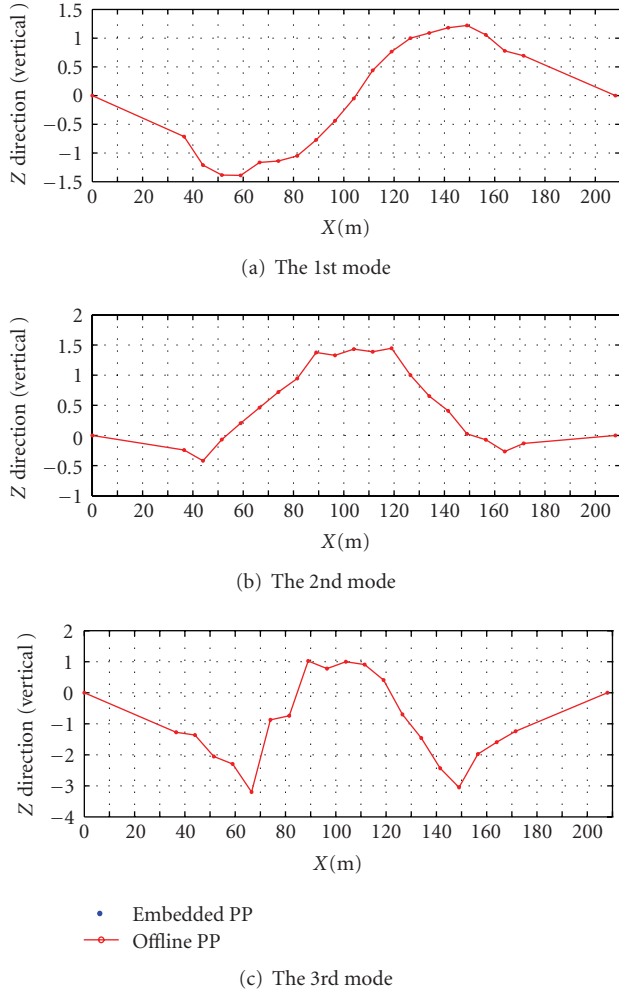


FIGURE 9: Comparison of mode shapes estimated by embedded and offline PP.

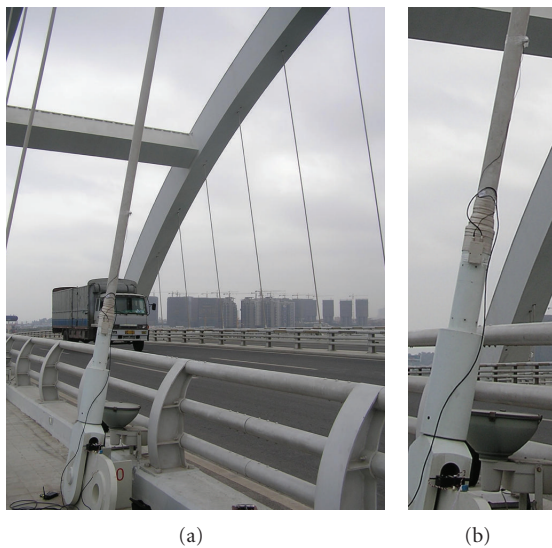


FIGURE 10: Accelerometer with wireless sensor on a hanger.

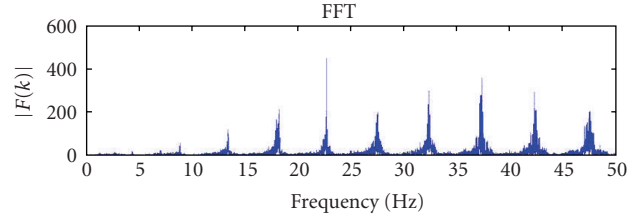


FIGURE 11: Frequency spectrum of the vibration of a hanger.

TABLE 2: Comparison of identified modal frequencies and mode shapes.

| | Mode 1 | | Mode 2 | | Mode 3 | |
|---------------------------|--------|-------|--------|--------|--------|-------|
| | PP | SSI | PP | SSI | PP | SSI |
| Frequency (Hz) | 8.30 | 8.31 | 23.90 | 23.59 | 34.47 | 34.54 |
| 1st Floor Modal Component | 0.451 | 0.450 | -1.174 | -1.177 | 1.429 | 1.839 |
| 2nd Floor Modal Component | 0.786 | 0.786 | -0.572 | -0.545 | -2.224 | -2.24 |
| 3rd Floor Modal Component | 1.000 | 1.000 | 1.000 | 1.000 | 1.000 | 1.000 |
| MAC | 1.000 | | 0.998 | | 0.978 | |

TABLE 3: Identified vibration frequencies of the Wuyuan Bridge in vertical bending by the embedded and offline PP analysis.

| Frequencies | Embedded PP | Offline PP | Mode Shape Description |
|-------------|-------------|------------|------------------------|
| 1 | 0.778 | 0.775 | 1st Vertical Bending |
| 2 | 1.24 | 1.24 | 2nd Vertical Bending |
| 3 | 1.70 | 1.70 | 3rd Vertical Bending |

TABLE 4: Comparisons of the identified frequencies of the cable by embedded PP and offline SSI.

| Frequencies | Embedded PP | Offline SSI |
|-------------|-------------|-------------|
| 1st | / | / |
| 2nd | / | 8.985 |
| 3rd | 13.50 | 13.47 |
| 4th | 18.28 | 18.19 |
| 5th | 22.76 | 22.73 |
| 6th | 27.44 | 27.50 |
| 7th | 32.28 | 32.34 |
| 8th | 37.21 | 37.30 |

information about the field experiments with the wireless sensing network can be found in Lei et al. [9]. First, the time-history response data collected by the sensing nodes is transformed to the frequency domain via the embedded FFT algorithm. As the sampling frequency is 50 Hz and there are 4096 points in the FFT data, the frequency resolution can be estimated as

$$f_r = \frac{f_{Nyquist}}{N/2} = \frac{25}{2048} = 0.012 \text{ Hz.} \quad (4)$$

For validating the accuracy of the embedded FFT algorithm, the raw time history of the acceleration response data collected by the sensing node is also transmitted to the central server and transformed to frequency domain by MATLAB. As shown in Figure 8, the embedded FFT and offline FFT spectra are in close agreement.

Then, the embedded PP algorithm employed to process each vertical acceleration response recorded by the sensing node 1–19 in Figure 6. Under ambient vibration condition in the field, relatively low-threshold values with $\beta = 2\mu$ are assigned in the PP analysis, in order to avoid missing small peaks in the frequency spectra. The total execution time of the embedded PP algorithm (including FFT analysis) by each ATmega 128 microcontroller is still around 25 seconds. Each sensing node transmits the identified peak frequencies and corresponding imaginary components of the FRFs to the central data repository, where global modal frequencies and mode shapes of the bridge in the vertical direction are determined.

To validate the accuracy of the embedded PP algorithm, PP analyses of the same time-history data transmitted by the 19 sensing nodes are also conducted in MATLAB. Table 3 lists the first three vertical bending frequencies of the bridge. The frequencies estimated by the embedded PP algorithm are shown in the second column, and the frequencies estimated by offline PP analysis are shown in the third column. The two sets of results are in close agreement. In addition, Figure 9 shows the corresponding first three vertical bending mode shapes, including the results estimated by both the embedded and offline PP analysis. The two sets of mode shapes are also in close agreement. The errors in the identified mode shapes are due to the fact that PP is a simple and low-accuracy approach for modal analysis.

For identifying the first three vertical modes of the bridge by the embedded FFT and PP algorithms, only 19 (sensing nodes) \times 4 (bytes per floating point number) \times 6 (floating point numbers) = 456 bytes of the analysis results are transmitted by the 19 wireless sensing nodes to the central data repository. However, for offline identification of the modal properties, a total of 19 (sensing nodes) \times 2 (bytes per ADC sample) \times 4096 (data samples) = 155,648 bytes of data need to be wirelessly transmitted. Obviously, employing embedded FFT and PP algorithms can greatly reduce data transmission and energy consumption for a large-scale wireless sensing network deployed in the field.

Bridge cable forces are important parameters for the assessment of bridge safety. Some techniques, including utilizing wireless sensing, have been developed for the measurement of steel bridge cable forces [13–15]. For bridges in service, steel cable forces are usually monitored based upon the vibration frequencies of cables [16]. Through the analysis of the transverse vibration of a steel cable, force T in a steel cable can be approximated by [16]

$$T = 4ml^2 \frac{f_k^2}{k^2} \quad (5)$$

in which l and m are the length and the mass per unit length of the cable, respectively, and f_k is the k th modal frequency of the cable. Therefore, cable forces can be estimated once

the vibration frequencies of a cable are identified. Due to the efficient computing approach offered by the embedded FFT and PP algorithms in the wireless sensing unit, vibration frequencies of a cable can be identified in situ by the wireless unit. An accelerometer is attached to a hanger of the bridge to measure the vibration of the cable and a wireless sensing unit with embedded FFT and PP algorithm is used for data acquisition and processing, as shown in Figure 10.

Only the peak vibration frequencies identified by the embedded PP algorithm are transmitted to the central server. The results are shown in the second column of Table 4. Although a small threshold value is selected in executing the embedded PP algorithm, the amplitudes of the spectrum peaks at the first two frequencies are still too small to be identified, because the accelerometer is attached very close to the end of the hanger. However, since focus is now upon the estimation of the cable forces utilizing (4), which does not require all the peaks in the frequency spectrum, the first and the second vibration frequencies of the cable are not necessary in this study.

To validate the accuracy of the frequencies identified by the embedded PP algorithm, the recorded time-history data by the sensing unit are wirelessly transmitted to the central data repository, where the sophisticated SSI algorithm is applied to process the data. The identified frequencies are shown in the third column of Table 4. From the side-by-side comparison, it is evident that the embedded PP algorithm can pick up the vibration frequencies of the cable accurately. Based upon the identified vibration frequencies, the force in the cable can be estimated using the frequency method as indicated in (4).

6. Conclusions

In this paper, the performance of two engineering algorithms, the fast Fourier transform (FFT) and peak-picking (PP) algorithms, embedded in an academic wireless sensor prototype is investigated through laboratory and field experimental studies. Comparison with the results obtained by corresponding offline FFT and PP analyses of the transmitted time-history data validates the effectiveness of the two embedded algorithms. It is shown that the frequency spectra calculated by the embedded FFT are accurate in both the laboratory and field studies. The embedded PP algorithm provides a simple and efficient approach for estimating the modal frequencies and mode shapes of a structure. The results can also be used to estimate forces in bridge cables. Since self-interrogation of measurement data by the two embedded algorithms greatly reduces the amount of data to be transmitted by the wireless sensor network, intelligent wireless sensing with embedded algorithms offer network solutions that are both scalable and power efficient.

In this paper, emphasis is placed on the implementation and performance of the two engineering algorithms in the wireless sensor system for modal identification through lab and field investigation. The wireless sensor system was installed on the lab structure or on the bridge only for short-term operation, to compare the identification results by the embedded algorithms with those obtained by conventional

offline analyses. Long-term monitoring utilizing the wireless sensor system and performance of the system, including the efficiency of the embedded algorithms in various climatic conditions, were not studied in this work. It will be important to fully investigate the robustness and lifespan of the proposed algorithm and system before they can serve as a substitute for conventional wire-based monitoring system, particularly for long-term monitoring of engineering structures. Such studies will be conducted by the authors in the future.

Acknowledgments

This paper is partially supported by China National High-Tech Research and Development Program through Grant no. 2007AA04Z420. The first author also acknowledges support from the program for New Century Excellent Talents in Universities (NCET) from China National Education Ministry.

References

- [1] B. F. Spencer Jr., M. E. Ruiz-Sandoval, and N. Kurata, "Smart sensing technology: opportunities and challenges," *Structural Control and Health Monitoring*, vol. 11, no. 4, pp. 349–368, 2004.
- [2] J. P. Lynch and K. J. Loh, "A summary review of wireless sensors and sensor networks for structural health monitoring," *Shock and Vibration Digest*, vol. 38, no. 2, pp. 91–128, 2005.
- [3] Y. Wang, *Wireless sensing and decentralized control for civil structures: theory and implementation*, Ph.D. thesis, Department of Civil and Environmental Engineering, Stanford University, Stanford, Calif, USA, 2007.
- [4] J. P. Lynch, A. Sundararajan, K. H. Law, A. S. Kiremidjian, T. Kenny, and E. Carryer, "Embedment of structural monitoring algorithms in a wireless sensing unit," *Structural Engineering and Mechanics*, vol. 15, no. 3, pp. 285–297, 2003.
- [5] J. P. Lynch, "An overview of wireless structural health monitoring for civil structures," *Philosophical Transactions of the Royal Society A*, vol. 365, no. 1851, pp. 345–372, 2007.
- [6] S. D. Glaser, M. Li, M. L. Wang, J. Ou, and J. Lynch, "Sensor technology innovation for the advancement of structural health monitoring: a strategic program of US-China research for the next decade," *Smart Structures and Systems*, vol. 3, no. 2, pp. 221–244, 2007.
- [7] J. P. Lynch, Y. Wang, K. J. Loh, J.-H. Yi, and C.-B. Yun, "Performance monitoring of the Geumdang bridge using a dense network of high-resolution wireless sensors," *Smart Materials and Structures*, vol. 15, no. 6, pp. 1561–1575, 2006.
- [8] Y. Wang, K. Loh, J. P. Lynch, M. Fraser, K. H. Law, and A. Elgamal, "Vibration monitoring of the Voigt bridge using wired and wireless monitoring systems," in *Proceedings of the 4th China-US-Japan Symposium on Structural Control and Monitoring*, Hangzhou, China, October 2006.
- [9] Y. Lei, W. A. Shen, Y. Song, and J. P. Lynch, "Application of wireless monitoring system for the ambient vibration study of the Wuyuan steel arch bridge," in *Proceedings of the 1st World Forum on Smart Materials and Smart Structures Technology (SMSST '07)*, Chongqing & Nanjing, China, 2007.
- [10] Y. Wang, J. P. Lynch, and K. W. Law, "Information driven wireless sensing and control for civil structures," in *Proceedings of the 1st World Forum on Smart Materials and Smart Structures Technology (SMSST '07)*, Chongqing & Nanjing, China, 2007.
- [11] A. T. Zimmerman, M. Shiraishi, R. A. Swartz, and J. P. Lynch, "Automated modal parameter estimation by parallel processing within wireless monitoring systems," *Journal of Infrastructure Systems*, vol. 14, no. 1, pp. 102–113, 2008.
- [12] MaxStream, Inc., "XStream™ OEM RF Module Product Manual v4.2B," Lindon, Utah, USA, 2005.
- [13] G. Feltrin, J. Meyer, R. Bischoff, and M. Motavalli, "Wireless sensor networks for long term monitoring of civil structures," *Journal of Structure & Infrastructure Engineering*, pp. 1–14, 2009.
- [14] G. Feltrin, J. Meyer, and R. Bischoff, "A wireless sensor network for force monitoring of cable stays," in *Proceedings of the 3rd International Conference on Bridge Maintenance, Safety and Management (IABMAS '06)*, Porto, Portugal, 2006.
- [15] S. Cho, C. B. Yun, J. P. Lynch, A. T. Zimmerman, B. F. Spencer Jr., and T. Nagayama, "Smart wireless sensor technology for structural health monitoring of civil structures," *Journal of Steel Structures*, vol. 8, pp. 267–275, 2008.
- [16] J. C. Russell and T. J. Lardner, "Experimental determination of frequencies and tension for elastic cables," *Journal of Engineering Mechanics*, vol. 124, no. 10, pp. 1067–1072, 1998.

Review Article

Structural Health Monitoring Using High-Frequency Electromechanical Impedance Signatures

Wei Yan¹ and W. Q. Chen²

¹ Faculty of Architectural, Civil Engineering and Environment, Ningbo University, Ningbo 315211, China

² Department of Engineering Mechanics, Zhejiang University, Yuquan Campus, Hangzhou 310027, China

Correspondence should be addressed to W. Q. Chen, cwqcmx@yahoo.com.cn

Received 21 August 2009; Accepted 7 December 2009

Academic Editor: Piervincenzo Rizzo

Copyright © 2010 W. Yan and W. Q. Chen. This is an open access article distributed under the Creative Commons Attribution License, which permits unrestricted use, distribution, and reproduction in any medium, provided the original work is properly cited.

An overview of recent advances in electromechanical impedance- (EMI-) based structural health monitoring is presented in this paper. The basic principle of the EMI method is to use high-frequency excitation to sense the local area of a structure. Changes in impedance indicate changes in the structure, which in turn indicate that damages appear. An accurate EMI model based on the method of reverberation-ray matrix is introduced to correlate changes in the signatures to physical parameters of structures for damage detection. Comparison with other numerical results and experimental data validates the present model. A brief remark of the feasibility of implementing the EMI method is considered and the effects of some physical parameters on EMI technique are also discussed.

1. Introduction

Over the last decades, structural health monitoring (SHM) has been recognized as a useful tool for improving the safety and reliability of structures and to thereby reduce their operational cost [1]. Many SHM techniques thus have been developed in the literature [2–4] to quantify and locate the damages in the structures, based on either the global or the local interrogation of the structures [5]. Although these SHM methods have their specific advantages for detecting damages in the structures, the existent drawbacks may limit their applications on some aspects. For example, in global dynamic techniques, it is well known that the structure is subjected to low-frequency excitations and only the first few mode shapes and their corresponding natural frequencies can be accurately extracted. Because localized damages find it hard to alter global parameters such as natural frequency, curvature mode shape, and mode shape data, only large damages can be detected. Meanwhile, signals obtained using these methods are more prone to contamination by ambient vibration noise at low frequencies less than 100 Hz particularly [5]. Other typical local techniques, such as ultrasonic techniques, acoustic emission, and impact echo testing, require expensive and sophisticated

hardware as well as well-trained professional operators [6].

On the other hand, electromechanical impedance (EMI) based structural health monitoring has shown promising successes in monitoring and finding minor changes in structural integrity [5–9]. A key aspect of EMI method is the use of PZT patches as collocated sensors and actuators. To apply PZT as an actuator-sensor simultaneously, a PZT patch bonded to a structure is driven by a fixed alternating electric field. A surface charge is generated in response to an applied mechanical stress (direct effect), and conversely, a mechanical strain is produced in response to an applied electric field (converse effect). The electromechanical impedance defined as the ratio of the applied voltage and the resulting current can then be measured by a commercially available impedance analyzer. Although structural mechanical impedance related to structural properties such as stiffness and damping is difficult to obtain at first hand, the measured electrical impedance is directly related to mechanical impedance of the monitored structure and is also affected by the presence of structural damages. Thus, by observation of the electromechanical impedance of the PZT patch, one can obtain the information about the damage of the monitored structure [10].

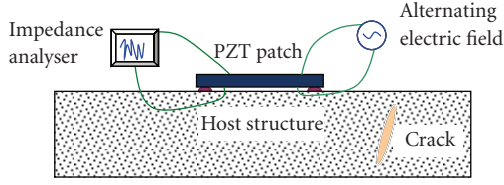


FIGURE 1: The sketch of a PZT patch bonded onto a damaged structure.

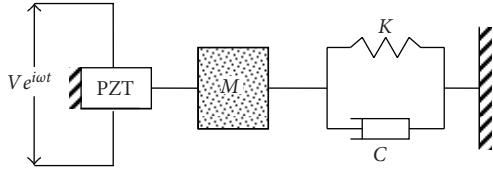


FIGURE 2: 1D model used to represent a PZT-driven dynamic structural system.

In general, the EMI signature is extracted at high frequencies (typically 10–500 kHz) [11]. At such frequencies, the wavelength of the excitation is very small and is therefore sensitive enough to detect minor changes in structural integrity. Many experimental investigations [5, 12–19] have shown the specific advantages of EMI technique over the conventional nondestructive evaluation methods. Sun et al. [12] first used EMI technique to examine a lab-sized truss structure. Ayres et al. [13] presented this qualitative impedance-based health monitoring method in real-time damage evaluation of civil infrastructures such as bridge joints. Soh et al. [14] studied the performance of smart piezoceramic patches in health monitoring of a reinforced concrete bridge at various stages during the loading process. Park et al. [15–17] demonstrated the capability and the effectiveness of this technology to detect damages of composite-reinforced concrete walls, a 1/4-scale bridge element, and a pipe joint, respectively. Bhalla and Soh [5] discussed the feasibility of employing impedance signatures in monitoring the conditions of RC structures subjected to base vibration. Bois et al. [18, 19] detect a single delamination in a laminated composite plate via the EMI signatures of a piezoelectric transducer cemented onto the structure. These experimental researches indicate that the collection and processing of electromechanical impedance signatures are very easy to implement via an Agilent 4294A impedance analyzer and the EMI technique is highly sensitive to detect minor changes in structural integrity using measured data. However, an ideal robust damage detection scheme cannot only identify damages at a very early stage but also provide some estimate of the extent or severity of the damage and even locate the damage within the sensor resolution being used [20]. Thus, appropriate tools of simulation are necessary for monitoring system adapted to monitored structures.

The overview of the impedance method up to 2003 was previously summarized in [21]. The paper aims to give an updated overview of the recent advances in the EMI-based structural health monitoring. The basic principle of the EMI

technique is first reviewed in Section 2. The recent developed approach, which integrates an accurate EMI model, in which both inertia effect of the PZT patch and the bonding property of adhesive are taken into consideration, with a stable high-frequency structural dynamics analysis method, the method of reverberation-ray matrix, is described in Section 3. Based on various sources in literature, Section 4 presents a discussion on the proper selection of parameters associated with the EMI-technique. Some recent applications of the EMI-based SHM method to complex configurations are noticed in Section 5. The paper ends with a brief summary.

2. Conventional EMI Models

Liang et al. [22] addressed that both approaches including a static approach and a dynamic finite element approach have some drawbacks in analyzing the dynamic response of active material systems and the impedance modeling technique is more suitable to reflect the physical essence of an active system. A simple 1-D model is then constructed to describe the interaction between a PZT patch and its host structure as shown in Figure 1. The PZT patch is bonded perfectly to the surface of the structure using a high-strength adhesive to ensure a better mechanical interaction and is assumed as a thin bar undergoing axial vibration in response to applied alternating voltage. A single-degree-of-freedom system is then considered as shown in Figure 2, in which one end of the PZT bar is fixed and the other end is connected to the host structure. According to this model, the constitutive relation of the PZT patch may be expressed as follows [22]:

$$S_1 = \bar{s}_{11}^E T_1 + d_{31} E, D_3 = \bar{\epsilon}_{33}^T E + d_{31} T_1, \quad (1)$$

where S_1 is strain, T_1 the stress, \bar{s}_{11}^E the complex compliance at zero electric field, d_{31} the piezoelectric constant, and D_3 the electric displacement; $\bar{\epsilon}_{33}^T = \epsilon_{33}^T (1 - \delta i)$ is the complex dielectric constant and δ is the dielectric loss factor. By solving the equation for the PZT bar connected to the external mechanical point impedance of the structure, the following expression of electrical admittance (inverse of impedance) in frequency domain can be obtained [23]:

$$Y = i\omega a \left[\bar{\epsilon}_{33}^T (1 - i\delta) - \frac{Z_s}{Z_s + Z_p} d_{31}^2 \bar{E}_p \right], \quad (2)$$

where Y is the electrical admittance, Z_p and Z_s are the mechanical impedances of the PZT and the structure, respectively, \bar{E}_p and a are the complex Young's modulus and the geometric constant of the PZT patch, respectively, and ω is the circular frequency. It should be noted that although (2) is derived from a single-degree-of-freedom system, it is still applicable for 2D or very complex structures [16].

Although a good match between the predicted solutions by 1-D impedance model [22, 23] and the experimental results was achieved, Zhou et al. [24] pointed out that the mechanical impedance coupling in different coordinate directions should be considered for two-dimensional structures and the cross impedance of the host structure has an

impact on the transducer dynamics. With due derivation, the analytical expression of electrical admittance was then obtained based on two-dimensional impedance model [25]:

$$Y = i\omega \frac{w_p l_p}{h_p} \left[\bar{\epsilon}_{33}^T - \frac{2d_{31}^2 E_p}{(1-\nu)} + \frac{d_{31}^2 E_p}{(1-\nu)} \left\{ \frac{\sin \kappa l_p}{l_p} \frac{\sin \kappa w_p}{w_p} \right\} \mathbf{N}^{-1} \begin{bmatrix} 1 \\ 1 \end{bmatrix} \right], \quad (3)$$

where $\kappa = \omega \sqrt{\rho(1-\nu^2)/E_p}$, ν is Poisson's ratio; h_p , w_p and l_p are height, width, and length of the PZT wafer, respectively, and

$$\mathbf{N} = \begin{bmatrix} \mathfrak{A} \left\{ 1 - \nu \frac{w_p}{l_p} \frac{Z_{xy}}{Z_{axx}} + \frac{Z_{xy}}{Z_{axx}} \right\} & \mathfrak{B} \left\{ \frac{l_p}{w_p} \frac{Z_{yx}}{Z_{ayy}} - \nu \frac{Z_{yy}}{Z_{ayy}} \right\} \\ \mathfrak{A} \left\{ \frac{w_p}{l_p} \frac{Z_{xy}}{Z_{axx}} - \nu \frac{Z_{xx}}{Z_{axx}} \right\} & \mathfrak{B} \left\{ 1 - \nu \frac{l_p}{w_p} \frac{Z_{yx}}{Z_{ayy}} + \frac{Z_{yy}}{Z_{ayy}} \right\} \end{bmatrix}, \quad (4)$$

where \mathfrak{A} denotes $\kappa \cos(\kappa l_p)$, \mathfrak{B} denotes $\kappa \cos(\kappa w_p)$, Z_{xx} and Z_{yy} are direct impedance, Z_{xy} and Z_{yx} are cross impedance of the host structure, respectively, and Z_{axx} and Z_{ayy} are mechanical impedance of PZT patch in x and y directions, respectively.

Although the analytical derivations of above equations based on 2-D model are accurate themselves, the experimental difficulties limit their direct application for extraction of the host structure's mechanical impedance [26]. Thus, an effective mechanical impedance model [26, 27] was developed for improving the existing models, in which the mechanical interaction between the PZT patch and the host structure is not restricted at the PZT end points and it extends all over the finite sized PZT patch [26]. The finally obtained expression of electrical impedance is similar to that based on the classical one-dimensional model.

In the classical impedance model, a key problem is to obtain the analytical expression of the mechanical impedance Z_s , which is defined as $Z_s = F/\dot{x}$. (The impedance is determined by calculating the structural dynamic response, \dot{x} , corresponding to an arbitrary force F at the driven point of the transducer [22].) For some simple structures, such as axial rods [28–30], beams [29–31], circular rings [32, 33], thin plates [24, 34, 35], and shells [36], the analytical expression of the electromechanical impedance can be obtained readily based on the impedance modeling approach. However, when damages are induced in structures resulting in possibly inhomogeneity of material properties, analytical formulation is very difficult to be derived. For example, although Zagrai and Giurgiutiu [34] formulated analytical solutions based on EMI spectrum and mechanical response of a circular plate, when a damage is induced into the plate, the assumption for axis-symmetric axial and flexural vibration of circular plates is untenable and the analytical solutions does not hold for damage detection in the plates.

In order to obtain damage information by using changes in electromechanical impedance signature, it is necessary to establish improved correlation between EMI signature

and changes in structural integrity. The finite element method (FEM) seems to be an alternative for the purpose [6, 11, 30, 37–40]. However, FEM is usually subjected to an inherent disadvantage that a large number of finite elements and hence a large number of nodes should be involved for accurately predicting high-frequency response of a structure. As the finite element model becomes finer, the associated mass and stiffness matrices will increase in size and thus requirements on storage and computing time become critical. Other methods such as spectral element method [10] and Ritz method [35] have been applied to quantitatively identify structural damages. But, there are still certain difficulties associated with high-frequency analysis that limit their applications in quantitative analysis of impedance-based health monitoring. The transfer matrix method (TMM) is very powerful to analyze a structure consisting of many members (including damaged members) because the number of resultant simultaneous equations can be greatly reduced. However, significant numerical difficulty at high-frequency limits its application if computation is completely executed on a computer [41].

Moreover, it was assumed in the classical impedance model that the force transmission is just at two ends of PZT patch while the intermediate bonding layer was completely ignored based on pin force model. However, in the experiment of Soh et al. [14] and Giurgiutiu and Zagrai [29], it was found that the bonding between patch and host structure may be damaged. When disbonding occurs, the signature obtained from patch was distorted. Actually, it has been recognized by many researchers [40, 42–45] that the imperfect bonding of PZT patch influences the output EMI signatures significantly and should be investigated carefully.

Due to the complexity of PZT patch-adhesive-host structure coupled structural system and the difficulty of dynamic analysis in the high-frequency range as mentioned above, most existent analytical models of EMI technique fail to correlate changes in the signatures to physical parameters of structures and could not provide further information about the nature of damage. In order to develop a more accurate model to improve sensitivity of impedance signature to damages in structures, two key issues should be dealt with, one is to seek for an appropriate modeling to simulate the behavior of the PZT patch-adhesive-host structure coupled structural system, and the other is to find a powerful high-frequency dynamic analysis technique.

3. Accurate EMI Models Based on MRRM

In some existent EMI model [26, 27, 42], the inertial term of PZT patch was neglected and the mechanical impedance of host structure was assumed to be a constant at all points of the patch attachment. However, because high-frequency electric field with typical propagation wave length comparable to the length of actuator is applied, The inertia effect of actuator should be considered [46, 47]. Furthermore, since the strain/stress transfer between PZT patches and host structures is physically implemented through bonding layers, a more accurate model for improving sensitivity of

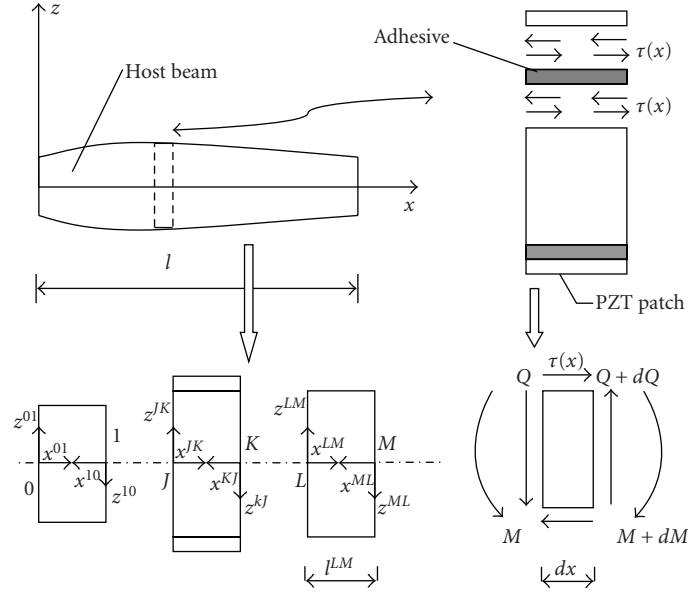


FIGURE 3: Nonhomogeneous beam with adhesively bonded PZT patches and local coordinates.

signature to damages by modulating the property of bonding layers should be developed. A classic shear lag solution was employed by Crawley and Luis [48] and Tong and Luo [49, 50] to analyze piezoelectric actuators as elements of intelligent structures. Bhalla and Soh [42] extended this method to develop an electromechanical impedance model of adhesively bonded piezo-transducers under quasistatic equilibrium and a good match between the predicted solutions and the measured data was observed. Under the consideration of both the inertia effect of actuator and the properties of the adhesive, Yan et al. [51–56], developed an accurate EMI model for detecting damages in classical rods [51], Mindlin-Herrmann rods [52], straight beams [54–56] and framed structures [53]. By taking an Euler-Bernoulli beam adhesively and symmetrically bonded with two PZT patches as an example, we illustrate this EMI model in the following.

As shown in Figure 3, a pair of PZT patches is bonded symmetrically and adhesively onto the top and bottom surfaces of a nonhomogeneous beam and is driven by a fixed alternating electric field out of phase. The equation of motion of the PZT patch, which is assumed to be in a state of 1D axial strain [46, 47], can be written out as

$$E_p \frac{\partial^2 u_p}{\partial x^2} - \frac{\tau}{h_p} = \rho_p \frac{\partial^2 u_p}{\partial t^2}, \quad (5)$$

where u is the axial displacement, ρ and E are the mass density and Young's modulus, and h is the thickness (the subscript p signifies the PZT patch). τ is the interfacial shear stress between the PZT patch (beam) and the adhesive and varies along the bonding length, and t is the time variable. On the other hand, the bond layer is in the state of pure shear based on the shear lag model [48]:

$$\tau = \frac{G}{h_a} (u_p - u_s), \quad u_s = -\frac{h_s}{2} \frac{\partial w}{\partial x}, \quad (6)$$

where G is the shear rigidity of the bonding layer, and u_s and w are the axial displacement and the transverse deflection of beam, respectively. The subscripts s and a correspond to the host beam and bonding layer, respectively.

For an Euler-Bernoulli beam, we then can get the following relations:

$$\begin{aligned} \frac{\partial M}{\partial x} + \tau h_s - Q &= 0, & \frac{\partial Q}{\partial x} &= \rho_s A \frac{\partial^2 w}{\partial t^2}, \\ M &= -E_s I \frac{\partial \psi}{\partial x}, & \psi &= \frac{\partial w}{\partial x}, \end{aligned} \quad (7)$$

where M and Q are the bending moment and shear force, respectively, and I and A are the moment of area and the cross sectional area, respectively. With due derivation, we can obtain the solution of transverse deformation as follows:

$$\bar{w} = a_1 e^{\beta_1 x} + a_2 e^{\beta_2 x} + a_3 e^{\beta_3 x} + d_1 e^{-\beta_1 x} + d_2 e^{-\beta_2 x} + d_3 e^{-\beta_3 x}, \quad (8)$$

in which a_i and d_i ($i = 1, 2, 3$) are undetermined constants, and β_i ($i = 1, 2, 3$) are defined in [55]. For an arbitrary beam segment LM without bonded PZT patches, the well-known solution is expressed as

$$\begin{aligned} \bar{w}^{LM} &= a_1^{LM} e^{ik^{LM} x^{LM}} + a_2^{LM} e^{k^{LM} x^{LM}} \\ &+ d_1^{LM} e^{-ik^{LM} x^{LM}} + d_2^{LM} e^{-k^{LM} x^{LM}}, \end{aligned} \quad (9)$$

where $k^{LM} = [(\rho A)^{LM} \omega^2 / (E_s I)^{LM}]^{1/4}$. Then, the method of reverberation-ray matrix (MRRM), which was originally proposed by Pao et al. [57–59] to study the transient response of a plane truss consisting of elastic members and then developed by Pao and Chen [60, 61] and Chen's research group [62, 63] for high-frequency dynamic analysis, is extended to investigate dynamics of the smart structure

system. In MRRM, the first step is to establish a global scattering relation as follows:

$$\mathbf{d} = \mathbf{S}\mathbf{a} + \mathbf{Q}, \quad (10)$$

where \mathbf{Q} is source vector, $\mathbf{d} = [(\mathbf{d}^0)^T, (\mathbf{d}^1)^T, \dots, (\mathbf{d}^{N-1})^T, (\mathbf{d}^N)^T]^T$ is the global vector associated with departing waves, and $\mathbf{a} = [(\mathbf{a}^0)^T, (\mathbf{a}^1)^T, \dots, (\mathbf{a}^{N-1})^T, (\mathbf{a}^N)^T]^T$ is the global vector associated with arriving waves [57–63]. Then, according to unique physical reality of the smart structures, we can get the total phase relations:

$$\mathbf{a} = \mathbf{P}\bar{\mathbf{d}}, \quad (11)$$

where \mathbf{P} is the total phase shift matrix [57–63] and $\bar{\mathbf{d}}$ and \mathbf{d} contain the same elements but are sequenced in different orders. The two vectors $\bar{\mathbf{d}}$ and \mathbf{d} can be related through a permutation matrix \mathbf{U} as

$$\bar{\mathbf{d}} = \mathbf{U}\mathbf{d}, \quad (12)$$

where \mathbf{U} is a square matrix which contains one unit element in each row as well as one unit element in each column. From (10), (11), and (12), we obtain

$$\mathbf{d} = \mathbf{R}\mathbf{d} + \mathbf{Q}, \quad \mathbf{R} = \mathbf{S}\mathbf{P}\mathbf{U}, \quad (13)$$

where \mathbf{R} is called the reverberation-ray matrix [57–63]. It is then obtained that

$$\mathbf{d} = (\mathbf{I} - \mathbf{R})^{-1} \mathbf{Q}, \quad \mathbf{a} = \mathbf{S}^{-1} (\mathbf{d} - \mathbf{Q}) = \mathbf{S}^{-1} [(\mathbf{I} - \mathbf{R})^{-1} - \mathbf{I}] \mathbf{Q}. \quad (14)$$

Hence, all undetermined constants in (8) and (9) can be solved from (14). Note that the phase matrix \mathbf{P} does not contain exponential functions with large positive indices and hence the numerical instability usually encountered in the conventional transfer matrix method (TMM) can be avoided. This is a crucial point for proper application of MRRM in high-frequency dynamic analysis of structures. Finally, the electric admittance (or electric impedance) of single PZT patch can be obtained as follows:

$$Y = \frac{i\omega w_p l_p (\bar{\epsilon}_{33}^T - d_{31}^2 \bar{E}_p)}{h_p} + i\omega w_p d_{31} \bar{E}_p \left(\sum_{j=1}^3 \frac{c_j}{\beta_j (a_j^{KJ} - a_j^{JK} + d_j^{JK} - d_j^{KJ})} \right). \quad (15)$$

The detailed derivation can be found in [55] and omitted here for brevity.

Numerical results and experimental measurements have validated the effectiveness and precision of the present accurate EMI model. As observed in Figure 4, the two curves obtained by TMM and RMM, respectively, can hardly be distinguished in the low-frequency range less than about 13 kHz. However, in the high frequency range ($f > 13$ kHz), numerical instability appears for TMM, in contrast to the well-performed MRRM.

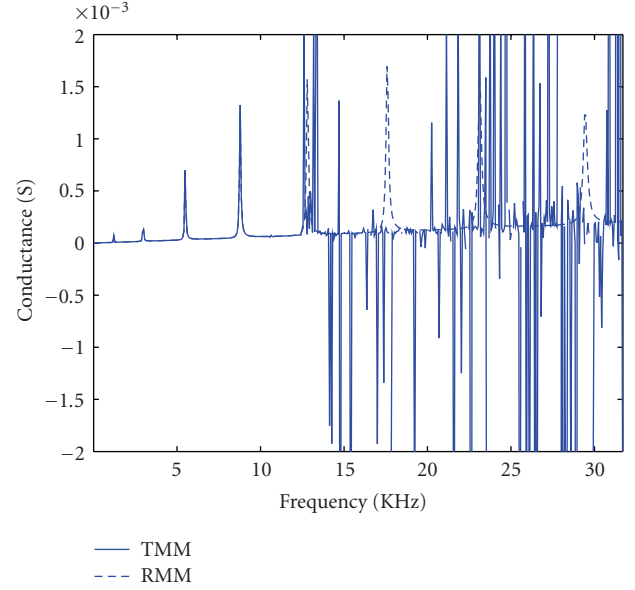


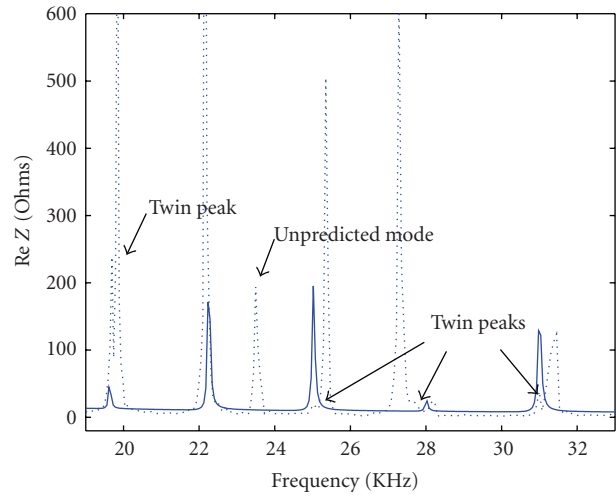
FIGURE 4: Comparison study with TMM.

The experimental results are further compared with analytical prediction of the present model in Figure 5 in the frequency range of 19–33 kHz. It is obvious that most experimentally observed peaks of impedance signatures related to prominent resonance frequencies can be predicted well using the analytical model. Furthermore, the present model can detect the damages in the beams (see Figure 6) and can locate the damages integrated with the curvature mode shape method [64] (see Figure 7). In Figures 6 and 7, D means effective uniform damage magnitude through certain beam segment [65]. The effects of interfacial properties are also investigated as shown in Figure 8 (Γ is the shear lag parameter [48, 55]). Due to imperfect bonding, the impedance signatures change significantly. Furthermore, the accurate EMI model has been extended to Mindlin-Herrmann rods [52], Timoshenko beams [54], cracked continuous beams [56], and framed structures [53], and some significative research results have been obtained for structural health monitoring.

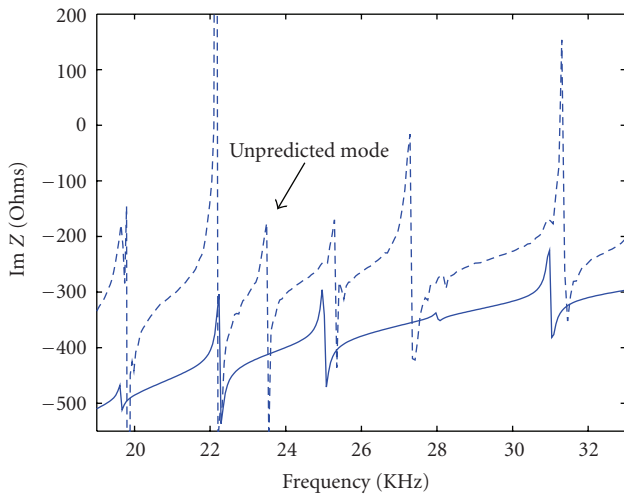
4. Determination of Parameters

In EMI technique, it is very important to select available PZT patches for structural health monitoring. Because one side of the PZT patch is to be bonded onto the monitored structure, the electrode of this side should be wrapped to the other side of the patch [5]. The size of the PZT should make the PZT transducers small enough not to be intrusive; that is, they do not significantly affect the dynamic properties of the host structures [66]. Thus, it is found that PZT patches of size ranging from 5 to 15 mm and thickness from 0.1 to 0.3 mm are best suitable for detecting damages in most structures such as steel and RC structures.

As mentioned in the previous section, the specific advantage of the EMI method over the other SHM techniques



(a)



(b)

FIGURE 5: Experimental and analytical impedance spectra for a steel beam.

is its high sensitivity to incipient damages. Thus, it is necessary for the wavelength of excitation to be smaller than the characteristic length of the damage to be detected [67]. In general, the electrical impedance is measured at high frequencies in the range of 30–400 kHz [20]. Under this high-frequency range, the wavelength of the excitation is small and sensitive enough to detect minor changes in the structural integrity. In EMI method, a frequency range containing 20–30 peaks seems suitable to choose, because a higher density of modes implies that there contains more structural information about the condition of a structure [12]. A frequency range higher than 200 kHz is found to be favorable in localizing the sensing, while frequencies range lower than 70 kHz covers a larger sensing area. Peairs

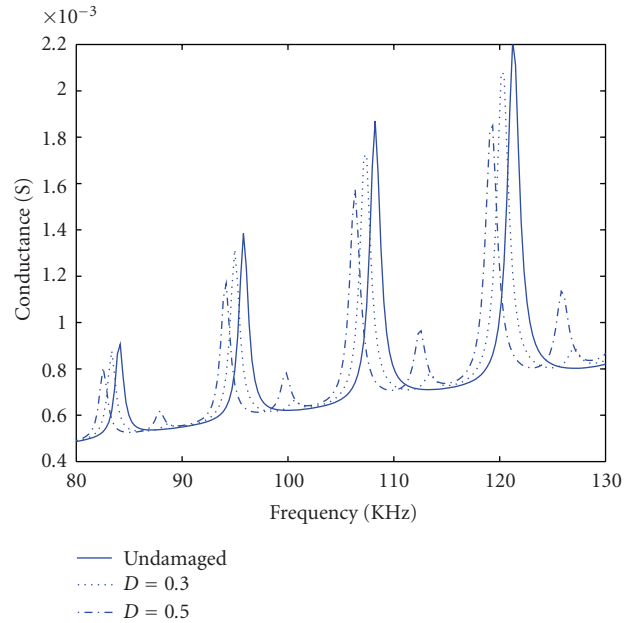


FIGURE 6: EM admittance signatures for various damage growth.

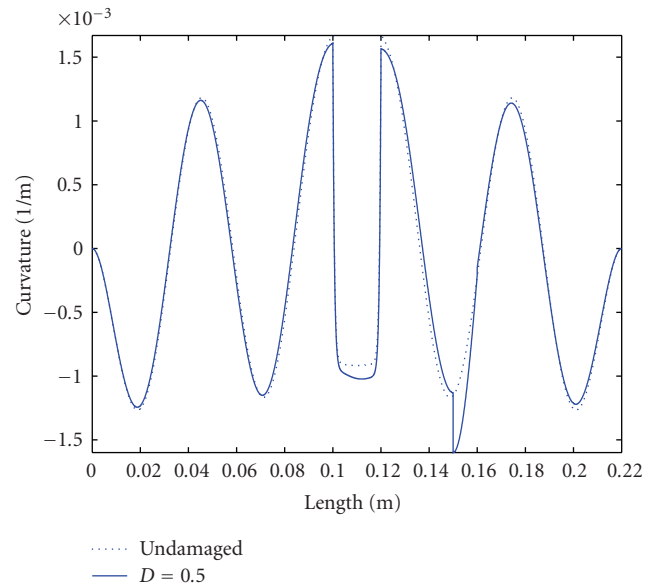


FIGURE 7: Curvature mode shapes along the length of the beam ($D = 0.5$).

et al. [68] remarked that the frequency ranges are usually selected by trial and error, which often involves inducing a removable amount of simulated damage. Their investigation for frequency range selection indicated that the ranges with the sensors/actuators resonances are better for monitoring with the impedance-based method.

Due to the high frequency of excitation used in EMI technique, the monitoring range of effective sensitivity of the PZT transducer is limited to its near vicinity [67]. Based on the knowledge acquired through various case studies, it has been estimated that the sensing area of a single

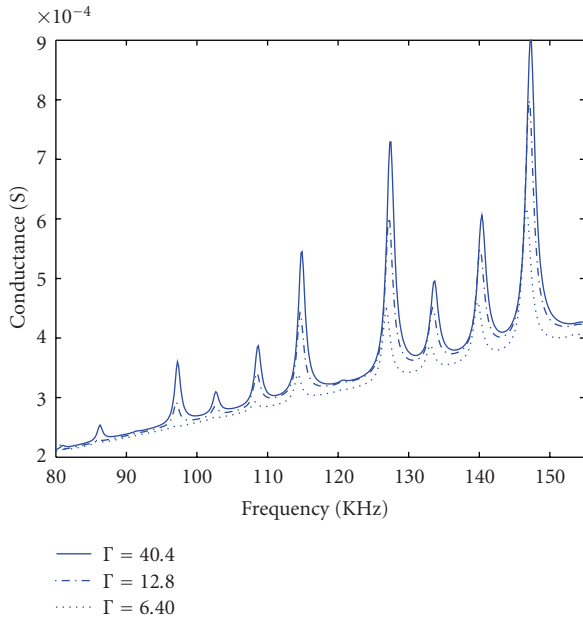


FIGURE 8: EM admittance signatures for various interfacial conditions.

PZT can vary anywhere from 0.4 m (sensing radius) on composite structures to 2 m on simple metal beams [20]. This localized nature of the sensing region provides an advantage in that the impedance sensor is less sensitive to boundary condition changes or any operational vibrations, which usually affect lower-order global modes. On the other hand, this characteristic of limited sensing range usually demands an active sensing network system for real world applications [69–73].

In real life, practical structures are constantly subjected to some form of external action such as external loading and temperature change. The experimental and statistical investigation showed that the EM admittance signature obtained for a constantly loaded structure is different from that obtained when damages are present in the structure and the susceptance signature is a better indicator than the conductance signature for detection damages in the structures [74].

Although regular piezoelectric patches have been found to be unsuitable for damage detection at cryogenic temperatures through a series of experiments and an alternative type of transducer based on smart materials should be sought [75], the EMI technique can still be used to actively monitor the damages in the structures, even with the presence of significant temperature variation in the normal temperature range (25°C to 75°C).

Actually, almost all available transducers are small PZT patches in the EMI method, but some special sensors/actuators such as piezoceramic inertial actuators [76], piezoelectric stack transducers [77], and cement-based piezoelectric ceramic composites [78] are employed to satisfy practical demands or match to the host structures for structural health monitoring. Furthermore, the conventional EMI approach that consists of running wires between the local

sensors and a data acquisition system will no longer be trivial. The cost associated with management and maintenance of such a system can be very high. Thus, an impedance-based wireless sensor node for structural health monitoring was developed by Mascarenas et al. [79] for the first time.

Although EMI method is very sensitive to minor damages in the structures and the EM signature change can be observed visually, it is necessary to employ statistical techniques to quantify it. It is wellknown that many types of nonparametric indices such as root mean square deviation (RMSD), mean absolute percentage deviation (MAPD), covariance (Cov), and correlation coefficient (CC) have been considered to quantify changes in the EMI admittance signatures [80]. Among these nonparametric indices, RMSD seems to be the most suitable damage index to characterize structural damages [80] and has been employed by many researchers for structural health monitoring [72, 74, 81–84]. Furthermore, a hybrid technique integrating neural network features with the impedance method has been proposed for somewhat quantitative damage analysis [85]. In this damage identification scheme, the impedance-based method detects and locates structural damage and provides damage indication in a green/red light form with the use of the modified RMSD firstly, and then the neural networks are used to estimate the severity of structural damage.

5. Recent Applications

Apart from some simple structures, such as axial rods [28–30], beams [29–31, 76, 86, 87], circular rings [32, 33], thin plates [24, 34, 35, 70, 82, 88, 89], shells [36], and framed structures [12, 79, 81, 84], experimental implementation of the EMI-based structural health monitoring technique has been successfully conducted on several complex structures. The detection of cracks, loose connections of pipelines, damages in metallic structures, and debonds and delaminations in composites structures are reported by many researchers.

A masonry wall under step loading was investigated by using EMI method [15]. Five PZT patches are employed on one side of the wall. Four PZT patches are bonded in the corners and an additional PZT in the center. The multiple cracks of the wall appear with the loading increasing. It can be seen that EMI measurements are very sensitive to the presence of damage and from the observations and the damage metric charts the location of the damage can be approximately predicted.

Lim et al. [90] employed a new method for structural identification and damage detection using smart piezoelectric transducers. In this method, the mechanical impedance can be derived using 1-D and 2-D EMI coupling equations. The feasibility of damage detection was well demonstrated through the application on various laboratory-sized engineering structures such as an aluminum beam, an aluminum truss, and a concrete cube.

The experimental investigation for a concrete beam and a concrete slab by Tseng [73] showed that the PZT wafers were able to detect cracks on the surface as well as in depth. When the PZT patches are too far or too close to the damage, the wafers appear not capable of detecting the

damage successfully. In addition, using RMSD index, this technique can give a good indication of the severity and location of the damage even when it is in the early stage. Similarly, Giurgiutiu et al. [91] applied piezoelectric wafer active sensors to aging aircraft structures to monitor the onset and progress of structural damage such as fatigue cracks and corrosion.

Pohl et al. [92] implemented an experimental and theoretical investigation to show the effectiveness of the impedance method in monitoring carbon fiber reinforced polymer (CFRP) composites. Damage, which was introduced by the low-speed impact, was detected by changes in the impedance signatures. The other type damages in CFRPs such as fiber fracture and delamination can also be identified by utilizing electrical impedance tomography [93].

The feasibility of the EMI sensing technique for strength gain monitoring of early-age concrete was also presented by Shin and Oh [94]. The experimental results showed that the EMI signature is sensitive to the strength development of early-age concrete and the RMSD value has also a strong correlation with the amount of the strength development of early-age concrete.

Due to the high-frequency excitation, the EMI-based health monitoring technique is very sensitive to minor defects in a structure and not affected by any far-field changes. The method has been successfully applied to various structures ranging from aerospace [29, 95] to civil structures [1, 7, 14, 15, 94] and is ideal for tracking and online monitoring of damages in various structures

6. Summary

The overview of the development and applications of the electro-mechanical impedance-based structural health monitoring is presented in the paper. Although EMI method is very sensitive to incipient damages in the structures, it has been primarily developed only for qualitative health monitoring and fails to correlate changes in the signatures to physical parameters of structures. In order to develop an ideal robust damage detection scheme by using piezoelectric signatures, an analytical model for simulating the smart structural system is necessary for monitoring system. First, some conventional EMI models and their applications are discussed and an accurate EMI model based on MRRM is further suggested by authors. Comparison with the other numerical results and experimental data validates the present EMI model. The effects of PZT size, excitation frequency range, sensing range of PZT patch; and external action on EMI structural health monitoring technique are then remarked; the most part of discussions may also be found in other references. Finally, the feasibility of implementing the EMI method to detect damages in various lab-sized structures is demonstrated. In the future research, we should pay more attention on the testing of real structures under practical conditions rather than laboratory tests. Moreover, appropriate high-frequency structural theories shall be developed to adapt to the frequency range used in the EMI-technique, which is much higher than that implied in the conventional structural theories.

Acknowledgments

The work was sponsored by the National Natural Science Foundation of China (Grant no. 10725210), the National Basic Research Program of China (no. 2009CB623200), the Zhejiang Provincial Natural Science Foundation of China (no. Y107796), and the Ningbo Natural Science Foundation of China (nos. 2008A610101, 2009A610148).

References

- [1] S. Park, C.-B. Yun, Y. Roh, and J.-J. Lee, "PZT-based active damage detection techniques for steel bridge components," *Smart Materials and Structures*, vol. 15, no. 4, pp. 957–966, 2006.
- [2] R. D. Adams, P. Cawley, C. J. Pye, and B. J. Stone, "A vibration testing for non-destructively assessing the integrity of the structures," *Journal of Mechanical Engineering Science*, vol. 20, no. 2, pp. 93–100, 1978.
- [3] P. Tan and L. Tong, "Identification of delamination in a composite beam using integrated piezoelectric sensor/actuator layer," *Composite Structures*, vol. 66, no. 1–4, pp. 391–398, 2004.
- [4] M. Kisa, "Free vibration analysis of a cantilever composite beam with multiple cracks," *Composites Science and Technology*, vol. 64, no. 9, pp. 1391–1402, 2004.
- [5] S. Bhalla and C. K. Soh, "High frequency piezoelectric signatures for diagnosis of seismic/blast induced structural damages," *NDT and E International*, vol. 37, no. 1, pp. 23–33, 2004.
- [6] S. Bhalla, C. K. Soh, and Z. X. Liu, "Wave propagation approach for NDE using surface bonded piezoceramics," *NDT and E International*, vol. 38, no. 2, pp. 143–150, 2005.
- [7] V. Giurgiutiu, A. Reynolds, and C. A. Rogers, "Experimental investigation of E/M impedance health monitoring for spot-welded structural joints," *Journal of Intelligent Material Systems and Structures*, vol. 10, no. 10, pp. 802–812, 1999.
- [8] G. Park, A. C. Rutherford, H. Sohn, and C. R. Farrar, "An outlier analysis framework for impedance-based structural health monitoring," *Journal of Sound and Vibration*, vol. 286, no. 1–2, pp. 229–250, 2005.
- [9] T. R. Fasel, H. Sohn, G. Park, and C. R. Farrar, "Active sensing using impedance-based ARX models and extreme value statistics for damage detection," *Earthquake Engineering and Structural Dynamics*, vol. 34, no. 7, pp. 763–785, 2005.
- [10] S. Ritdumrongkul, M. Abe, Y. Fujino, and T. Miyashita, "Quantitative health monitoring of bolted joints using a piezoceramic actuator-sensor," *Smart Materials and Structures*, vol. 13, no. 1, pp. 20–29, 2004.
- [11] A. S. K. Naidu and C. K. Soh, "Damage severity and propagation characterization with admittance signatures of piezo transducers," *Smart Materials and Structures*, vol. 13, no. 2, pp. 393–403, 2004.
- [12] F. P. Sun, Z. Chaudhry, C. Liang, and C. A. Rogers, "Truss structure integrity identification using PZT sensor-actuator," *Journal of Intelligent Material Systems and Structures*, vol. 6, no. 1, pp. 134–139, 1995.
- [13] J. W. Ayres, F. Lalande, Z. Chaudhry, and C. A. Rogers, "Qualitative impedance-based health monitoring of civil infrastructures," *Smart Materials and Structures*, vol. 7, no. 5, pp. 599–605, 1998.
- [14] C. K. Soh, K. K.-H. Tseng, S. Bhalla, and A. Gupta, "Performance of smart piezoceramic patches in health monitoring of

- a RC bridge,” *Smart Materials and Structures*, vol. 9, no. 4, pp. 533–542, 2000.
- [15] G. Park, H. H. Cudney, and D. J. Inman, “Impedance-based health monitoring of civil structural components,” *Journal of Infrastructure Systems*, vol. 6, no. 4, pp. 153–160, 2000.
- [16] G. Park, H. H. Cudney, and D. J. Inman, “Feasibility of using impedance-based damage assessment for pipeline structures,” *Earthquake Engineering and Structural Dynamics*, vol. 30, no. 10, pp. 1463–1474, 2001.
- [17] G. Park, D. E. Muntges, and D. J. Inman, “Self-monitoring and self-healing jointed structures,” *Key Engineering Materials*, no. 204–205, pp. 75–84, 2001.
- [18] C. Bois and C. Hochard, “Monitoring of laminated composites delamination based on electro-mechanical impedance measurement,” *Journal of Intelligent Material Systems and Structures*, vol. 15, no. 1, pp. 59–67, 2004.
- [19] C. Bois, P. Herzog, and C. Hochard, “Monitoring a delamination in a laminated composite beam using in-situ measurements and parametric identification,” *Journal of Sound and Vibration*, vol. 299, no. 4–5, pp. 786–805, 2007.
- [20] D. Montalvão, N. M. M. Maia, and A. M. R. Ribeiro, “A review of vibration-based structural health monitoring with special emphasis on composite materials,” *The Shock and Vibration Digest*, vol. 38, no. 4, pp. 295–324, 2006.
- [21] G. Park, H. Sohn, C. R. Farrar, and D. J. Inman, “Overview of piezoelectric impedance-based health monitoring and path forward,” *The Shock and Vibration Digest*, vol. 35, no. 6, pp. 451–463, 2003.
- [22] C. Liang, F. P. Sun, and C. A. Rogers, “Impedance method for dynamic analysis of active material systems,” *Journal of Vibration and Acoustics*, vol. 116, no. 1, pp. 120–128, 1994.
- [23] C. Liang, F. P. Sun, and C. A. Rogers, “Coupled electro-mechanical analysis of adaptive material systems—determination of the actuator power consumption and system energy transfer,” *Journal of Intelligent Material Systems and Structures*, vol. 5, no. 1, pp. 12–20, 1994.
- [24] S.-W. Zhou, C. Liang, and C. A. Rogers, “An impedance-based system modeling approach for induced strain actuator-driven structures,” *Journal of Vibration and Acoustics*, vol. 118, no. 3, pp. 323–331, 1996.
- [25] S.-W. Zhou, C. Liang, and C. A. Rogers, “Integration and design of piezoceramic elements in intelligent structures,” *Journal of Intelligent Material Systems and Structures*, vol. 6, no. 6, pp. 733–743, 1995.
- [26] S. Bhalla and C. K. Soh, “Structural health monitoring by piezo-impedance transducers. I. Modeling,” *Journal of Aerospace Engineering*, vol. 17, no. 4, pp. 154–165, 2004.
- [27] S. Bhalla and C. K. Soh, “Structural health monitoring by piezo-impedance transducers. II. Applications,” *Journal of Aerospace Engineering*, vol. 17, no. 4, pp. 166–175, 2004.
- [28] G. Park, H. H. Cudney, and D. J. Inman, “An integrated health monitoring technique using structural impedance sensors,” *Journal of Intelligent Material Systems and Structures*, vol. 11, no. 6, pp. 448–455, 2000.
- [29] V. Giurgiutiu and A. N. Zagrai, “Embedded self-sensing piezoelectric active sensors for on-line structural identification,” *Journal of Vibration and Acoustics*, vol. 124, no. 1, pp. 116–125, 2002.
- [30] K. K.-H. Tseng and L. Wang, “Impedance-based method for nondestructive damage identification,” *Journal of Engineering Mechanics*, vol. 131, no. 1, pp. 58–64, 2005.
- [31] Y.-D. Kuang, G.-Q. Li, and C.-Y. Chen, “An admittance function of active piezoelectric elements bonded on a cracked beam,” *Journal of Sound and Vibration*, vol. 298, no. 1–2, pp. 393–403, 2006.
- [32] F. Lalande, Z. Chaudhry, and C. A. Rogers, “Impedance-based modelling of induced strain actuators bonded on ring structures,” *Journal of Sound and Vibration*, vol. 201, no. 2, pp. 169–187, 1997.
- [33] Y.-D. Kuang, G.-Q. Li, and C.-Y. Chen, “Dynamic analysis of actuator-driven circular arch or ring using impedance elements,” *Smart Materials and Structures*, vol. 15, no. 3, pp. 869–876, 2006.
- [34] A. N. Zagrai and V. Giurgiutiu, “Electro-mechanical impedance method for crack detection in thin plates,” *Journal of Intelligent Material Systems and Structures*, vol. 12, no. 10, pp. 709–718, 2001.
- [35] J. F. Xu, Y. Yang, and C. K. Soh, “Electromechanical impedance-based structural health monitoring with evolutionary programming,” *Journal of Aerospace Engineering*, vol. 17, no. 4, pp. 182–193, 2004.
- [36] Y. Yang and Y. Hu, “Electromechanical impedance modeling of PZT transducers for health monitoring of cylindrical shell structures,” *Smart Materials and Structures*, vol. 17, no. 1, Article ID 015005, 11 pages, 2008.
- [37] Y. G. Xu and G. R. Liu, “A modified electro-mechanical impedance model of piezoelectric actuator-sensors for debonding detection of composite patches,” *Journal of Intelligent Material Systems and Structures*, vol. 13, no. 6, pp. 389–396, 2002.
- [38] H. A. Winston, F. Sun, and B. S. Annigeri, “Structural health monitoring with piezoelectric active sensors,” *Journal of Engineering for Gas Turbines and Power*, vol. 123, no. 2, pp. 353–358, 2001.
- [39] A. S. K. Naidu and C. K. Soh, “Identifying damage location with admittance signatures of smart piezo-transducers,” *Journal of Intelligent Material Systems and Structures*, vol. 15, no. 8, pp. 627–642, 2004.
- [40] A. V. G. Madhav and C. K. Soh, “An electromechanical impedance model of a piezoceramic transducer-structure in the presence of thick adhesive bonding,” *Smart Materials and Structures*, vol. 16, no. 3, article 14, pp. 673–686, 2007.
- [41] E. C. Pestel and F. A. Leckie, *Matrix Methods in Elasto Mechanics*, McGraw-Hill, New York, NY, USA, 1963.
- [42] S. Bhalla and C. K. Soh, “Electromechanical impedance modeling for adhesively bonded piezo-transducers,” *Journal of Intelligent Material Systems and Structures*, vol. 15, no. 12, pp. 955–972, 2004.
- [43] V. Giurgiutiu, “Tuned lamb wave excitation and detection with piezoelectric wafer active sensors for structural health monitoring,” *Journal of Intelligent Material Systems and Structures*, vol. 16, no. 4, pp. 291–305, 2005.
- [44] X. P. Qing, H.-L. Chan, S. J. Beard, T. K. Ooi, and S. A. Marotta, “Effect of adhesive on the performance of piezoelectric elements used to monitor structural health,” *International Journal of Adhesion and Adhesives*, vol. 26, no. 8, pp. 622–628, 2006.
- [45] W. Yan, J. B. Cai, and W. Q. Chen, “Monitoring interfacial defects in a composite beam using impedance signatures,” *Journal of Sound and Vibration*, vol. 326, no. 1–2, pp. 340–352, 2009.
- [46] X. D. Wang and G. L. Huang, “Wave propagation in electromechanical structures: induced by surface-bonded piezoelectric actuators,” *Journal of Intelligent Material System and Structures*, vol. 12, pp. 105–115, 2001.
- [47] X. D. Wang and G. L. Huang, “The coupled dynamic behavior of piezoelectric sensors bonded to elastic media,” *Journal of*

- Intelligent Material Systems and Structures*, vol. 17, no. 10, pp. 883–894, 2006.
- [48] E. F. Crawley and J. de Luis, “Use of piezoelectric actuators as elements of intelligent structures,” *AIAA Journal*, vol. 25, no. 10, pp. 1373–1385, 1987.
- [49] L. Tong and Q. Luo, “Exact dynamic solutions to piezoelectric smart beams including peel stresses. I. Theory and application,” *International Journal of Solids and Structures*, vol. 40, no. 18, pp. 4789–4812, 2003.
- [50] Q. Luo and L. Tong, “Exact dynamic solutions to piezoelectric smart beams including peel stresses. II. Numerical results, comparison and approximate solution,” *International Journal of Solids and Structures*, vol. 40, no. 18, pp. 4813–4836, 2003.
- [51] W. Yan, W.-Q. Chen, C.-W. Lim, and J.-B. Cai, “Damage detection with high-frequency electric impedance signals,” *Journal of Zhejiang University*, vol. 41, no. 1, pp. 6–11, 2007 (Chinese).
- [52] W. Yan, C. W. Lim, W. Q. Chen, and J. B. Cai, “Modeling of EMI response of damaged Mindlin-Herrmann rod,” *International Journal of Mechanical Sciences*, vol. 49, no. 12, pp. 1355–1365, 2007.
- [53] W. Yan, C. W. Lim, W. Q. Chen, and J. B. Cai, “A coupled approach for damage detection of framed structures using piezoelectric signature,” *Journal of Sound and Vibration*, vol. 307, no. 3–5, pp. 802–817, 2007.
- [54] W. Yan, C. W. Lim, J. B. Cai, and W. Q. Chen, “An electromechanical impedance approach for quantitative damage detection in Timoshenko beams with piezoelectric patches,” *Smart Materials and Structures*, vol. 16, no. 4, pp. 1390–1400, 2007.
- [55] W. Yan, W. Q. Chen, J. B. Cai, and C. W. Lim, “Quantitative structural damage detection using high-frequency piezoelectric signatures via the reverberation matrix method,” *International Journal for Numerical Methods in Engineering*, vol. 71, no. 5, pp. 505–528, 2007.
- [56] W. Yan, W. Q. Chen, C. W. Lim, and J. B. Cai, “Application of EMI technique for crack detection in continuous beams adhesively bonded with multiple piezoelectric patches,” *Mechanics of Advanced Materials and Structures*, vol. 15, no. 1, pp. 1–11, 2008.
- [57] S. M. Howard and Y.-H. Pao, “Analysis and experiments on stress waves in planar trusses,” *Journal of Engineering Mechanics*, vol. 124, no. 8, pp. 884–890, 1998.
- [58] Y.-H. Pao, D.-C. Keh, and S. M. Howard, “Dynamic response and wave propagation in plane trusses and frames,” *AIAA Journal*, vol. 37, no. 5, pp. 594–603, 1999.
- [59] J.-F. Chen and Y.-H. Pao, “Effects of causality and joint conditions on method of reverberation-ray matrix,” *AIAA Journal*, vol. 41, no. 6, pp. 1138–1142, 2003.
- [60] Y.-H. Pao, W.-Q. Chen, and X.-Y. Su, “The reverberation-ray matrix and transfer matrix analyses of unidirectional wave motion,” *Wave Motion*, vol. 44, no. 6, pp. 419–438, 2007.
- [61] Y.-H. Pao and W.-Q. Chen, “Elastodynamic theory of framed structures and reverberation-ray matrix analysis,” *Acta Mechanica*, vol. 204, no. 1–2, pp. 61–79, 2009.
- [62] Y. Q. Guo and W. Q. Chen, “Dynamic analysis of space structures with multiple tuned mass dampers,” *Engineering Structures*, vol. 29, no. 12, pp. 3390–3403, 2007.
- [63] J. Q. Jiang and W. Q. Chen, “Reverberation-ray analysis of moving or distributive loads on a non-uniform elastic bar,” *Journal of Sound and Vibration*, vol. 319, no. 1–2, pp. 320–334, 2009.
- [64] A. K. Pandey, M. Biswas, and M. M. Samman, “Damage detection from changes in curvature mode shapes,” *Journal of Sound and Vibration*, vol. 145, no. 2, pp. 321–332, 1991.
- [65] U. Lee and J. Shin, “A frequency-domain method of structural damage identification formulated from the dynamic stiffness equation of motion,” *Journal of Sound and Vibration*, vol. 257, no. 4, pp. 615–634, 2002.
- [66] G. Park and D. J. Inman, “Structural health monitoring using piezoelectric impedance measurements,” *Philosophical Transactions of the Royal Society A*, vol. 365, no. 1851, pp. 373–392, 2007.
- [67] J. Esteban and C. A. Rogers, “Wave localization due to material damping,” *Computer Methods in Applied Mechanics and Engineering*, vol. 177, no. 1–2, pp. 93–107, 1999.
- [68] D. M. Peairs, P. A. Tarazaga, and D. J. Inman, “Frequency range selection for impedance-based structural health monitoring,” *Journal of Vibration and Acoustics*, vol. 129, no. 6, pp. 701–709, 2007.
- [69] S. Park, C.-B. Yun, and Y. Roh, “Damage diagnostics on a welded zone of a steel truss member using an active sensing network system,” *NDT and E International*, vol. 40, no. 1, pp. 71–76, 2007.
- [70] G. Park, C. R. Farrar, F. L. Di Scalea, and S. Coccia, “Performance assessment and validation of piezoelectric active-sensors in structural health monitoring,” *Smart Materials and Structures*, vol. 15, no. 6, pp. 1673–1683, 2006.
- [71] V. G. M. Annamdas and C. K. Soh, “Three-dimensional electromechanical impedance model for multiple piezoceramic transducers-structure interaction,” *Journal of Aerospace Engineering*, vol. 21, no. 1, pp. 35–44, 2008.
- [72] K. K.-H. Tseng, “Impedance-based non-destructive and non-parametric infrastructural performance evaluation,” *Experimental Mechanics*, vol. 44, no. 1, pp. 109–112, 2004.
- [73] C. C. Cheng and C. C. Lin, “An impedance approach for vibration response synthesis using multiple PZT actuators,” *Sensors and Actuators A*, vol. 118, no. 1, pp. 116–126, 2005.
- [74] V. G. M. Annamdas, Y. Yang, and C. K. Soh, “Influence of loading on the electromechanical admittance of piezoceramic transducers,” *Smart Materials and Structures*, vol. 16, no. 5, pp. 1888–1897, 2007.
- [75] K. K.-H. Tseng, M. L. Tinker, J. O. Lassiter, and D. M. Peairs, “Temperature dependency of impedance-based nondestructive testing,” *Experimental Techniques*, vol. 27, no. 5, pp. 33–36, 2003.
- [76] S. F. Ling and Y. Xie, “Detection mechanical impedance of structures using the sensing capability of a piezoceramic inertial actuator,” *Sensors and Actuators A*, vol. 93, pp. 243–249, 2001.
- [77] D. Mayer, H. Atzrodt, S. Herold, and M. Thomaier, “An approach for the model based monitoring of piezoelectric actuators,” *Computers and Structures*, vol. 86, no. 3–5, pp. 314–321, 2008.
- [78] F. Xing, B. Dong, and Z. Li, “Impedance spectroscopic studies of cement-based piezoelectric ceramic composites,” *Composites Science and Technology*, vol. 68, no. 12, pp. 2456–2460, 2008.
- [79] D. L. Mascarenas, M. D. Todd, G. Park, and C. R. Farrar, “Development of an impedance-based wireless sensor node for structural health monitoring,” *Smart Materials and Structures*, vol. 16, no. 6, pp. 2137–2145, 2007.
- [80] K. K.-H. Tseng and A. S. K. Naidu, “Non-parametric damage detection and characterization using smart piezoceramic

- material,” *Smart Materials and Structures*, vol. 11, no. 3, pp. 317–329, 2002.
- [81] S. Bhalla and C. K. Soh, “Structural impedance based damage diagnosis by piezo-transducers,” *Earthquake Engineering and Structural Dynamics*, vol. 32, no. 12, pp. 1897–1916, 2003.
- [82] V. Giurgiutiu and A. Zagrai, “Damage detection in thin plates and aerospace structures with the electro-mechanical impedance method,” *Structural Health Monitoring*, vol. 4, no. 2, pp. 99–118, 2005.
- [83] M.-H. Kim, “A smart health monitoring system with application to welded structures using piezoceramic and fiber optic transducers,” *Journal of Intelligent Material Systems and Structures*, vol. 17, no. 1, pp. 35–44, 2006.
- [84] A. C. Rutherford, G. Park, and C. R. Farrar, “Non-linear feature identifications based on self-sensing impedance measurements for structural health assessment,” *Mechanical Systems and Signal Processing*, vol. 21, no. 1, pp. 322–333, 2007.
- [85] V. Lopes Jr., G. Park, H. H. Cudney, and D. J. Inman, “Impedance-based structural health monitoring with artificial neural networks,” *Journal of Intelligent Material Systems and Structures*, vol. 11, no. 3, pp. 206–214, 2000.
- [86] Y.-D. Kuang, G.-Q. Li, and C.-Y. Chen, “Admittance function of active piezoelectric elements bonded on a curved cracked beam,” *Journal of Intelligent Material Systems and Structures*, vol. 19, no. 2, pp. 181–191, 2008.
- [87] V. Giurgiutiu and A. N. Zagrai, “Characterization of piezoelectric wafer active sensors,” *Journal of Intelligent Material Systems and Structures*, vol. 11, no. 12, pp. 959–976, 2000.
- [88] Y. Yang, J. Xu, and C. K. Soh, “Generic impedance-based model for structure-piezoceramic interacting system,” *Journal of Aerospace Engineering*, vol. 18, no. 2, pp. 93–101, 2005.
- [89] K. J. Xing and C.-P. Fritzen, “Monitoring of growing fatigue damage using the E/M impedance method,” *Key Engineering Materials*, vol. 347, pp. 153–158, 2007.
- [90] Y. Y. Lim, S. Bhalla, and C. K. Soh, “Structural identification and damage diagnosis using self-sensing piezo-impedance transducers,” *Smart Materials and Structures*, vol. 15, no. 4, pp. 987–995, 2006.
- [91] V. Giurgiutiu, A. Zagrai, and J. J. Bao, “Damage identification in aging aircraft structures with piezoelectric wafer active sensors,” *Journal of Intelligent Material Systems and Structures*, vol. 15, no. 9-10, pp. 673–687, 2004.
- [92] J. Pohl, S. Herold, G. Mook, and F. Michel, “Damage detection in smart CFRP composites using impedance spectroscopy,” *Smart Materials and Structures*, vol. 10, no. 4, pp. 834–842, 2001.
- [93] R. Schueler, S. P. Joshi, and K. Schulte, “Damage detection in CFRP by electrical conductivity mapping,” *Composites Science and Technology*, vol. 61, no. 6, pp. 921–930, 2001.
- [94] S. W. Shin and T. K. Oh, “Application of electro-mechanical impedance sensing technique for online monitoring of strength development in concrete using smart PZT patches,” *Construction and Building Materials*, vol. 23, no. 2, pp. 1185–1188, 2009.
- [95] J. D. R. V. De Moura Jr. and V. Steffen Jr., “Impedance-based health monitoring for aeronautic structures using statistical meta-modeling,” *Journal of Intelligent Material Systems and Structures*, vol. 17, no. 11, pp. 1023–1036, 2006.

Research Article

Laboratory Evaluation of Time-Domain Reflectometry for Bridge Scour Measurement: Comparison with the Ultrasonic Method

Xinbao Yu and Xiong Yu

Department of Civil Engineering, Case Western Reserve University, 10900 Euclid Avenue, Bingham 203C, Cleveland, OH 44106-7201, USA

Correspondence should be addressed to Xiong Yu, xxy21@case.edu

Received 10 December 2009; Revised 28 March 2010; Accepted 6 May 2010

Academic Editor: Piervincenzo Rizzo

Copyright © 2010 X. Yu and X. Yu. This is an open access article distributed under the Creative Commons Attribution License, which permits unrestricted use, distribution, and reproduction in any medium, provided the original work is properly cited.

Bridge scour is a major factor causing instability of bridges crossing waterways. Excessive scour contributes to their high construction and maintenance costs. Design of innovative scour-monitoring instrumentation is essential to ensure the safety of scour-critical bridges. The ability of real-time surveillance is important since the most severe scour typically happens near the peak flood discharge. A new scour-monitoring instrument based on the Time Domain Reflectometry (TDR) principle has been developed to provide real-time monitoring of scour evolution. A framework based on dielectric mixing model has been developed, which can be easily incorporated into an automatic analysis algorithm. This paper introduces a comparative study of TDR method and ultrasonic method for scour measurements. The results indicate that both TDR and ultrasonic methods can accurately estimate scour depth. TDR method, with the developed analysis algorithm, yields information on the river properties such as the electrical conductivity of river water and the density of sediments. TDR methods are also found less influenced by turbulence and air bubbles, both likely to occur during flood events.

1. Introduction

Bridge scour or bridge sediments scour refers to the lowering of the streambed around bridge piers or abutments. Typical types of scour include: (1) long-term degradation of the river bed, (2) general scour including contraction scour, and (3) local scour at the piers or abutments [4]. Among these types of scour, local scour is the most critical (Figure 1). Local scour is caused by the interference of piers and abutments with stream flow. It is characterized by the formation of scour holes surrounding bridge piers or abutments, and as a result, the support provided by the surrounding soils will be reduced.

Bridge scour poses a severe threat to bridge safety. Since 1970 over 1,000 bridges have collapsed with associated deaths due to bridge scour. Bridge scour is also a major factor contributing to the high construction and maintenance cost of bridges. Proper scour prediction is essential for an economical and safe design of bridge piers and abutments. Current scour design relies on the empirical scour prediction equations developed from laboratory data, which generally

do not accurately predict the scour under field conditions [5]. This necessitates collecting scour data from the field to improve current scour prediction theory. Because scour can cause catastrophic failure of bridges without any prior warning such as signs of distress in the superstructure, real-time scour-monitoring systems are critical for providing real-time safety surveillance.

There are a few methods currently available for field scour measurements including yardstick, ultrasonic method, ground penetration radar, and fisher bulb [6]. Each method has shortcomings including: (1) most of the instrumentation is not sufficiently rugged for field applications. (2) most of these methods do not provide real-time monitoring of scour evolution in critical flood events. (3) these instruments are generally not automated requiring an appreciable amount of human involvement for signal interpretation [7].

Instruments based on Time Domain Reflectometry (TDR) overcome these shortcomings and have been used to monitor bridge scour. The potential use of TDR for bridge scour measurement has been explored by a few researchers. Dowding and Pierce [2] developed a TDR

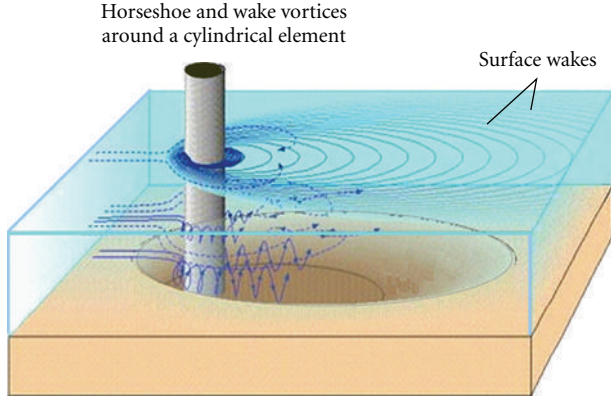


FIGURE 1: Schematic of local scour [1].

scour detection system that utilized small turbines installed along an electrical cable. The turbines would be successively exposed as scour developed. The torque generated by the turbine blades causes the shearing of cable, which can be detected by TDR method, and the scour depth is then estimated (Figure 2(a)). This system is not reusable due to the sacrificial characteristics of the detection cable. Yankielun and Zabilansky [3] also developed a TDR sensor by use of multiple steel pipes. Field evaluation showed that this probe was sufficiently rugged to resist floods and ice loading (Figure 2(b)). The major shortcoming of their design is that the two steel pipes were electrically shorted at the ends, which makes it difficult to develop an automatic signal interpretation algorithm. Efforts were made to improve signal analyses and with limited success [7].

The authors recently developed a new method of TDR signal analysis, which significantly simplifies the procedures of data processing and makes it possible to develop an automatic real-time scour surveillance system [8]. This paper briefly summarizes the principles of this TDR scour measurement system. Ultrasonic method has been chosen for comparison as it is currently the most popular fixed scour-monitoring device according to the survey conducted by Hunt [6]. In this study, the performance of TDR is compared with ultrasonic methods under laboratory simulated scour/sedimentation conditions. The TDR method was found to have accuracy equivalent to the ultrasonic method for scour depth determination. The TDR method has the advantage of being less influenced by factors such as air bubbles and suspended sediments which are likely to form due to turbulent flow conditions during floods.

2. Principles of Time Domain Reflectometry and Ultrasonic Method

2.1. Time Domain Reflectometry. Time Domain Reflectometry (TDR) technology was first utilized by electrical engineers to locate discontinuities in electrical cables. The application was later extended to measure material dielectric properties. The configuration of a typical TDR system is shown in

Figure 3. It generally includes a TDR device (pulse generator and sampler), a connection cable, and a measurement probe. The measurement probe is surrounded by the materials whose properties are to be measured. TDR works by sending a fast rising step pulse or impulse to the measurement probe and measuring the reflections due to the change of system geometry or material dielectric permittivity. A commercial TDR unit TDR100 by Campbell Scientific Inc. was used as the pulse generator and sampler. The device can generate a pulse output with a rising time of less than 300 picoseconds, amplitude of 250 mV, and duration of 14 microseconds. The probe used was the CS605 TDR moisture probe which consists of 3 rods, each 30 cm in length and 0.48 cm in diameter, with spacing between the outer rods of 4.5 cm [9]. The probe was connected to the TDR 100 by a 14 ft long RG58 coaxial cable.

Figure 4 shows a typical measured TDR signal when the probe is installed in a uniform soil. The dielectric constant (which is generally referred to as apparent dielectric constant and is denoted as K_a in this paper) and the electrical conductivity (denoted as EC_b in this paper) can generally be easily obtained from direct analysis of a TDR signal. The dielectric constant is related to the speed of electromagnetic waves in soils. The electrical conductivity is related to the rate of attenuation of the propagating electromagnetic wave. The dielectric constant is calculated by

$$K_a = \left(\frac{L_a}{L_p} \right)^2, \quad (1)$$

where K_a is the measured dielectric constant; L_p is the physical length of probe embedded in soil; L_a is called the apparent length as shown in Figure 4.

TDR measured dielectric constant is strongly related to the water content of soils, and various empirical relationships have been established to describe the correlation. Topp's equation (i.e., (2)) was developed from experiments on various types of cohesionless soils and is generally referred to as a "universal" equation:

$$\theta = 4.3 \times 10^{-6} K_a^3 - 5.5 \times 10^{-4} K_a^2 + 2.92 \times 10^{-2} K_a - 5.3 \times 10^{-2}, \quad (2)$$

where θ is volumetric water content defined as percentage of the total volume that is occupied by water.

The electrical conductivity is calculated by

$$EC_b = \frac{1}{C} \left(\frac{V_s}{V_f} - 1 \right), \quad (3)$$

where V_s is the source voltage. V_f is the long-term voltage level. C is a constant related to probe configuration, which can be obtained by theoretical analysis or by calibration against a reference technology such as an electrical conductivity meter.

The ability of TDR for scour-monitoring lies in the large contrast between the dielectric constant of water (around 81) and that of the air (1) or sediment solids (the dielectric

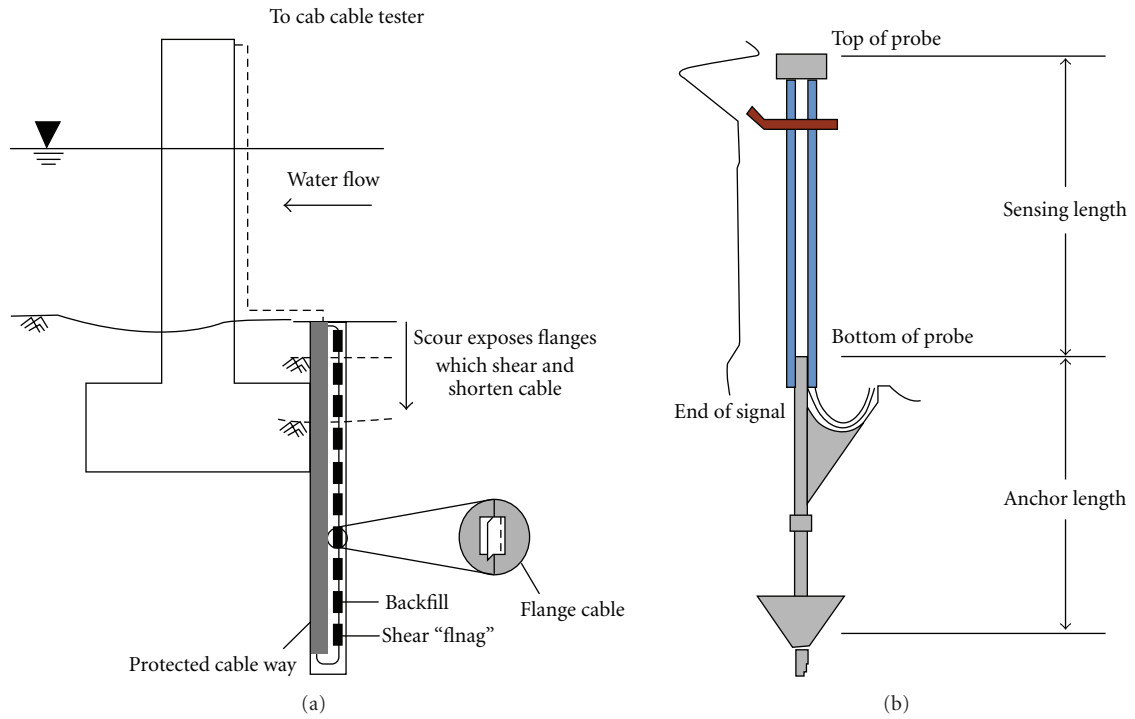


FIGURE 2: (a) TDR scour-monitoring system developed by Dowding and Pierce [2]; (b) schematic of the TDR scour system by Yankielun and Zabilansky [3].

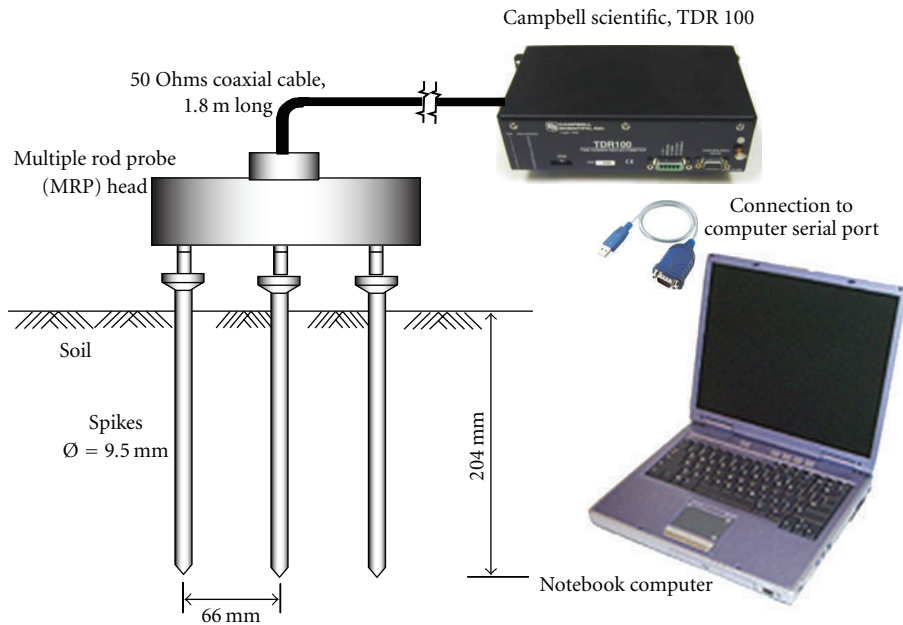


FIGURE 3: Schema of a typical TDR system.

constant for dry solids is between 3 and 7; that of saturated solids varies depending on the degree of saturation). Because of the large contrast in the dielectric properties, reflections will take place at the interfaces between material layers with different dielectric properties (including the air/water interface and the water/sediment interface) (Figure 5).

2.2. *Ultrasonic Method.* The configuration of a typical ultrasonic testing system is shown in Figure 6. The ultrasonic system used in this study includes the following components: a pulse generator by Panametrics-NDT Inc. (model: 5077PR), an ultrasonic transducer of 0.5 MHz (Panametrics-NDT, Waltham, MA, USA), and a PC oscilloscope 3402

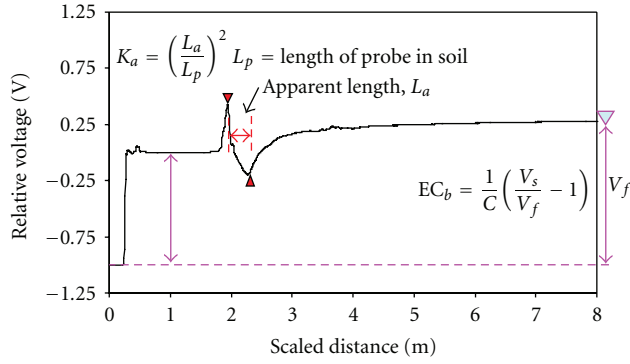


FIGURE 4: A typical TDR output signal.

(Pico Technology Ltd, St. Neots, United Kingdom). The ultrasonic system is set to work in the pulse-echo mode, where a single ultrasonic transducer serves as both transmitter and receiver. In the pulse-echo system, the transmitting transducer introduces a wide-band acoustic signal into the test object. The pulse propagates in the material and is scattered or reflected by the interfaces or inhomogeneities within the object. Because of the large contrast in acoustic impedance, the interface between water and sediment will cause a large amount of acoustic energy to be scattered or reflected. The reflections are picked by the receiving ultrasonic transducer. The returning signal can be displayed as a plot of amplitude versus time (referred to as A-scan). The depth of scour can be determined by determining the transit time required for receiving the echo reflections. A typical signal recorded during application of the ultrasonic method for scour measurement is shown in Figure 7. There are a few recent developments in ultrasonic technology, including a new testing method called direct-sequence, spread-spectrum, ultrasonic evaluation (DSSSUE), which is believed to have higher sensitivity and larger scan area compared with the traditional method. Details about ultrasound methods can be found in the work of Rens et al. [10].

3. Theory and Application Procedures of TDR Scour Detection System

Directly identifying the intermediate reflections at scour interface from a TDR signal can be very challenging. To overcome this difficulty, a new algorithm for TDR scour measurement has been developed by the authors of [8, 11]. It utilizes the information of dielectric constant and electrical conductivity, which can easily be obtained from analyzing a TDR signal. The principles of this system are briefly described in the following context.

3.1. Development and Validation of Mixing Formula for Bulk Dielectric Constant. Applying the semiempirical volumetric mixing model [12] to layered media consisting of water and sediment, the following equation can be obtained:

$$L_1\sqrt{K_{a,w}} + L_2\sqrt{K_{a,bs}} = L\sqrt{K_{a,m}} \quad (4)$$

where $K_{a,w}$ is the dielectric constant of water; $K_{a,bs}$ is the dielectric constant of bulk sand (sand with water mixture); $K_{a,m}$ is the measured bulk dielectric constant; L_1, L_2 , and L are the thickness, of water layer, sand layer and the total thickness respectively (Figure 5).

Let the thickness of sediment L_2 be x , then the thickness of water layer L_1 is $L-x$. Substituting these into (4) and normalizing both sides by $\sqrt{K_{a,w}}$, the following equation can be obtained:

$$\frac{\sqrt{K_{a,m}}}{\sqrt{K_{a,w}}} = \frac{x}{L} \left(\frac{\sqrt{K_{a,bs}}}{\sqrt{K_{a,w}}} - 1 \right) + 1. \quad (5)$$

The equation indicates that square root of the measured bulk dielectric constant by TDR is linearly related to sediment layer thickness. The process of normalization also helps to reduce the potential effects of the measurements system on the results. On the other hand, when the scour depth is determined, the dielectric constant of bulk sediment layer, $K_{a,bs}$ can be determined as follows:

$$K_{a,bs} = \left(\frac{L}{x} \sqrt{K_{a,m}} - \frac{L-x}{x} \sqrt{K_{a,w}} \right)^2. \quad (6)$$

This can then be used to estimate the soil porosity and density using Topp's equation (2).

Figure 8 shows the measured $\sqrt{K_{a,m}}/\sqrt{K_{a,w}}$ ratio versus sediment thickness from experimental data on fine sand in tap water. Also shown in Figure 8 are theoretical predictions, where $\sqrt{K_{a,bs}}$ was estimated from Topp's equation using the density of sand layers from experimental records. The comparison shows that (5), which is based on the dielectric mixing formula, is valid for studying the layered scour/sedimentation process. As an additional comment, the dielectric constant of saturated sediment can also be estimated using a volumetric mixing model [12]:

$$n\sqrt{K_{a,w}} + (1-n)\sqrt{K_{a,s}} = \sqrt{K_{a,bs}}, \quad (7)$$

where $K_{a,bs}$ is the dielectric constant of the saturated sand; $K_{a,w}$ is the dielectric constant of water; n is porosity and $K_{a,s}$ is the dielectric constant of soil solid, typically in the range of 3–5 (an average value of 4 is used for $K_{a,s}$ in this study).

3.2. Development and Validation of Mixing Formula for Electrical Conductivity. Similarly, for a two-layered system made of water and saturated sediment, the mixing formula for electrical conductivity was found to be [8, 11]

$$EC_{b,w}L_1 + EC_{b,bs}L_2 = EC_{b,m}L, \quad (8)$$

where $EC_{b,w}$ is the electrical conductivity of water; $EC_{b,bs}$ is the electrical conductivity of sand layer (sediment); $EC_{b,m}$ is the measured bulk electrical conductivity; L_1 is the thickness of water layer, and L_2 is the thickness of sediment; L is the total thickness.

Equation (8) can be normalized by dividing both sides by $EC_{b,w}$, that is,

$$\frac{EC_{b,m}}{EC_{b,w}} = \left(\frac{EC_{b,bs}}{EC_{b,w}} - 1 \right) \frac{x}{L} + 1. \quad (9)$$

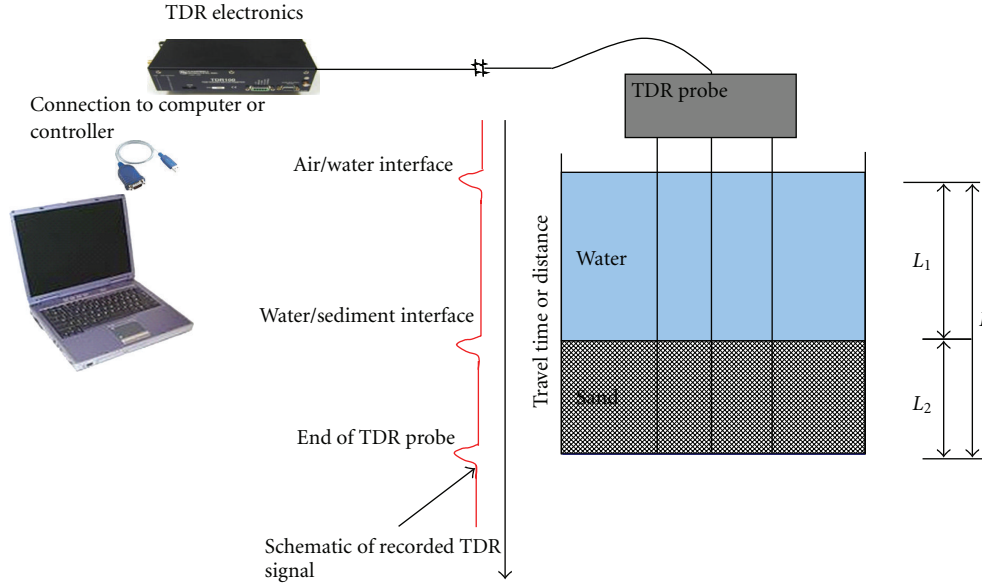


FIGURE 5: Schematic plot of TDR scour measurement principle.

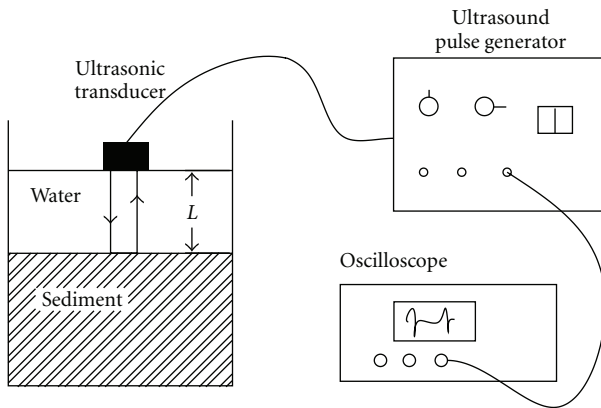


FIGURE 6: Schematic of a typical ultrasonic testing system.

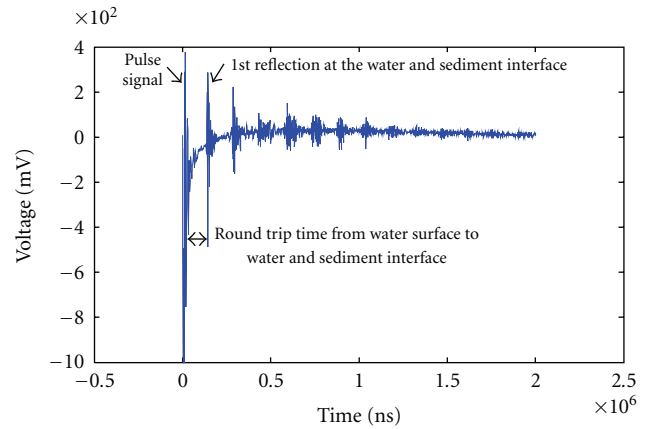


FIGURE 7: A typical ultrasonic signal.

Introducing the concept of formation factor by Archie [13], the following equation can be obtained:

$$\frac{EC_{b,bs}}{EC_{b,w}} = \frac{1}{F} = n^f, \quad (10)$$

where f is form factor, a value of 1.2 for f was recommended for fine sand such as Nevada sand; n is the porosity.

Substituting (10) to (9), we get

$$\frac{EC_{b,m}}{EC_{b,w}} = (n^f - 1) \frac{x}{L} + 1. \quad (11)$$

Equation (11) shows that the measured electric conductivity normalized by the electric conductivity of water is approximately linearly related to the sediment thickness. Figure 9 compares (11) with experimental measurements. The comparison indicates that the mixing formula for the electrical conductivity of sediment system is valid.

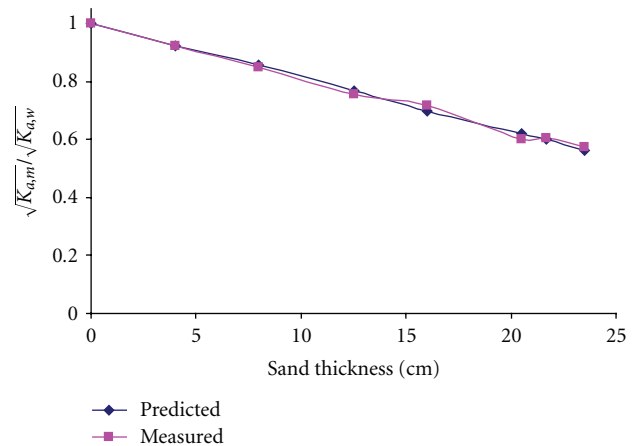


FIGURE 8: Measured and predicted relationship between $\sqrt{K_{a,m}}/\sqrt{K_{a,w}}$ and sediment layer thickness.

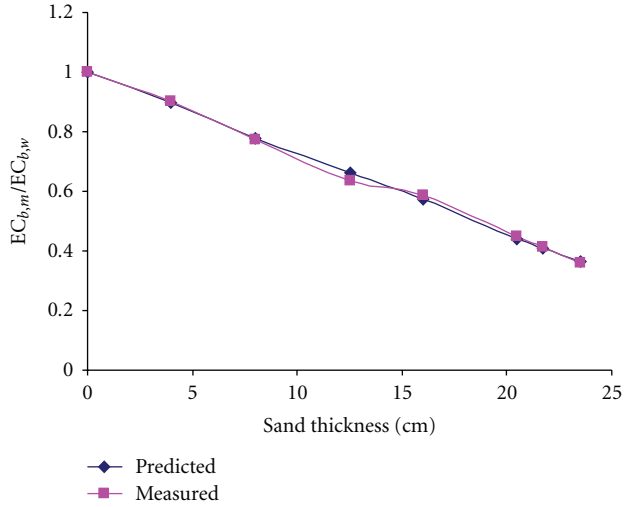


FIGURE 9: Measured and predicted relationship between $BC_{b,m}/BC_{b,w}$ and sediment layer thickness.

3.3. Design Plot and Application Procedures of TDR for Bridge Scour Measurement. Procedures to apply the TDR algorithm were recently developed by the authors of [8, 11]. They are based on two general linear relationships determined from experimental data collected on a few types of sediments (e.g., Figures 10(a) and 10(b)),

$$\frac{\sqrt{K_{a,m}}}{\sqrt{K_{a,w}}} = -0.43x_r + 1 = ax_r + b, \quad (12)$$

$$\frac{EC_{b,m}}{EC_{b,w}} = -0.67x_r + 1 = cx_r + d, \quad (13)$$

where x_r is the ratio of sand layer thickness to the total thickness. a , b , c , and d are coefficients that are dependent upon local geological conditions. The other symbols bear similar meaning as in the previous context.

Considering the dielectric constant of water is not significantly affected by the electrical conductivity under common application conditions [14]. The following procedures can be taken to determine the scour depth and sediment properties.

- (1) Obtaining the calibration constants for (12) from simulated laboratory experiments or from the field data with known scour depth (step 0).
- (2) Determining the bulk dielectric constant, $K_{a,m}$, from measured TDR signal (step 1, Figure 11).
- (3) Determining the ratio of sediment layer to TDR probe length, x (step 2, Figure 11).
- (4) Estimating the scour depth, S_D , from x_r (step 3, Figure 11).

A schematic plot of this procedure is shown in Figure 11.

4. Theory and Application Procedure of the Ultrasonic Method for Scour Detection

Ultrasonic waves are reflected at boundaries where there is a difference in the acoustic impedances of materials on either

side of the boundary. The difference in acoustic impedance is commonly referred to as impedance mismatch. Generally the greater the impedance mismatch, the greater the percentage of energy that will be reflected at the interface or boundary between one medium and another. The reflection coefficient is given as

$$R = \left(\frac{Z_2 - Z_1}{Z_2 + Z_1} \right)^2, \quad (14)$$

where Z_1 and Z_2 are acoustic impedance of materials on either side of a boundary.

The acoustic impedance (Z) of a material is defined as the product of density (ρ) and acoustic velocity (V) of that material.

$$Z = \rho V. \quad (15)$$

The application of ultrasonic method for scour detection is based on determining the time required for receiving the echo signal reflected from the water/sediment interface. The speed of a compression wave in water is 1482 m/s at 20°C, which corresponds to 1450×10^2 g/cm²/s for the acoustic impedance. The acoustic impedance ranges from 2000~4000 $\times 10^2$ g/cm²/s for silty clay to sandy gravel Hamilton [15]. As a result, the difference in acoustic impedance will cause appreciable reflections at the water/sediment interface. The location of the interface, which is a direct measure of scour depth, can be determined by analyzing the recorded ultrasonic signals.

5. Laboratory Test for Comparing TDR Methods and Ultrasonic Methods

5.1. Experiment Design. Figure 12 shows the experimental design for this study. Simulated scour/sedimentation tests were conducted in a cylindrical tank. The TDR probe was installed in the tank to acquire signals as sediments are added. Sediment materials were simulated by fine sand, coarse sand, and a mixture of coarse sand and gravel. The river conditions were simulated by controlling the electrical conductivity of water. The tank was first filled with water with specified salt concentration. Dry sediment material was then gradually poured into the tank. The water level was maintained constant by draining appropriate amount of water through the base of the tank. At each specified sand layer thickness, the amount of sand placed was recorded and used to calculate the density along with a TDR signal.

For comparison of TDR and ultrasonic methods, both the ultrasonic sensor and the TDR sensor were installed and connected to their respective electronics. The simulated sediment material consists of a mixture of coarse sand and gravel at 1 : 1 mass ratio. The tank was first filled with water of 500 ppm Sodium Chloride (NaCl) salt concentration to a level just below the probe head. TDR and ultrasonic signals were obtained for each depth of the sediment deposit. This process proceeded until the mixture completely filled the tank.

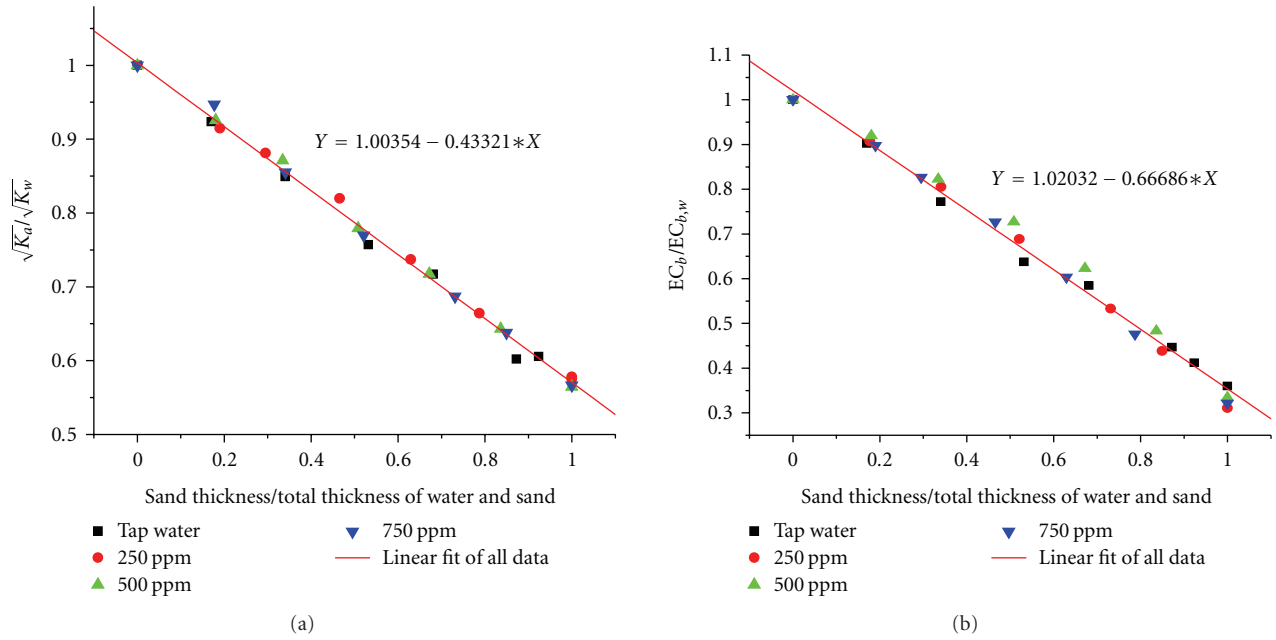


FIGURE 10: (a) Measured $\sqrt{K_a}$ of sediment system normalized by that of water versus the normalized sediment thickness; (b) measured EC_b of sediment system normalized by that of water versus the normalized sediment thickness (sediment: fine sand).

Step 0: Obtaining the calibration constants a and b for (12) from laboratory simulated experiments

Step 1: Determining the bulk dielectric constant $K_{a,m}$ from TDR signal

Step 2: Determining the ratio of sand layer/probe length from design equation

Step 3: Calculating scour depth

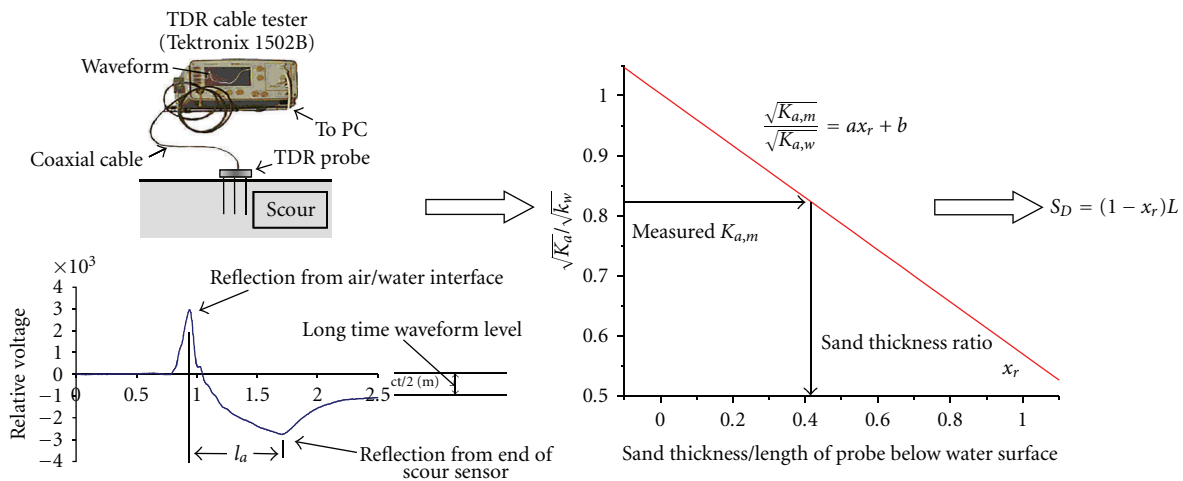


FIGURE 11: Procedures for estimating scour depth and river conditions.

Figure 13 shows variations of the TDR and ultrasonic signals with the thickness of sediment layer. As can be seen, both TDR signals and ultrasonic signals change in a predictable pattern.

5.2. Experiment Results and Analysis. The analysis of TDR signals followed the procedures outlined in the earlier part

of this paper. The scour depths were directly estimated from the measured apparent dielectric constant. This constant was also used to estimate the dielectric constant of the sediment, from which the porosity and density were determined. The electrical conductivity measured from the same TDR signal was used to estimate the electrical conductivity of the water.

The analyses of ultrasonic measurements were based on the determination of the travel time required for the reflected

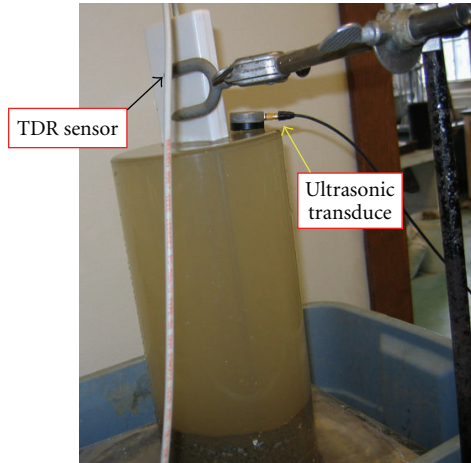


FIGURE 12: TDR probe, ultrasonic transducer, and the experimental tank.

signals. As shown in Figure 13(b), the travel time changes systematically with the distance to the water/sediment interface. The travel time was determined by picking the peaks in the recorded signal, representing the round trip travel time between ultrasonic transducer and surface of sediments. The distance of ultrasonic transducer to the surface of the sediment was then calculated by using the speed of ultrasonic wave in water.

5.3. Validation of the TDR Method. The developed algorithm for the TDR scour measurement system is evaluated by performing simulated scour experiments using a few other different types of sediment materials under different river conditions. The actual depths of scour were manually measured with a precise ruler. The results are summarized in Figure 14. The scour depth predicted by TDR algorithm described in this paper generally falls within ± 1.5 cm of actual measured values. This maps to an accuracy of $\pm 5\%$ if normalized by the length of the TDR scour probe. The accuracy of guided EM wave TDR in determining the interface is not much affected by the length of the probe as long as the signal attenuation is prevented. This can be achieved with the use of a protective coating. It is anticipated that the relative error should reduce at longer TDR probe length.

5.4. Measurement Accuracy of TDR versus Ultrasonic Methods. Figure 15 shows an example where both TDR and ultrasonic methods are applied simultaneously during a simulated test. The results of direct measurement are used as baseline reference. The sediment material is a mixture of gravel and sand.

Two different equations are used for scour depth estimation by the TDR method. The first approach (denoted as TDR method (1) uses (5) which incorporates properties of a specific type of sediment. The second approach (denoted as TDR method (2) uses a general design equation (12) determined from a variety of sediment materials. A detailed

comparison indicates that while results by either method should have sufficient accuracy for practical applications, the result of the TDR method 1 has slightly higher accuracy than that by those of method 2. There are two practical conclusions to be drawn from these observation: (1) A general equation format such as in (12) can be accurately applied for a wide range of sediment materials. (2) properties of local sediment materials can be used to refine (12) and thus further improve the accuracy of TDR scour predictions.

Comparison of the results of the TDR methods and the ultrasonic methods indicate that both methods can accurately estimate the scour depth but the trends of the change in the measurement accuracy are slightly different. Results from the TDR method are more accurate at larger scour depth. The ultrasonic method is more accurate for smaller scour depth. The observed increased accuracy of TDR is attributed to the improved accuracy in determining the reflection points for longer travel times. The observed trend of the change in the accuracy of the ultrasonic method is attributed to the fact that more attenuation and scattering of signal occur for longer distances. Comparatively, the higher measurement accuracy of the TDR methods with increasing scour depth is more desirable from a surveillance point of view since larger scour depths present a higher possibility of induced damage.

5.5. Sediment Density and Electrical Conductivity of Water by TDR. The electrical conductivity of water can be estimated from TDR measurements using (13). The results are shown in Figure 16 where they are compared with the direct measurement results obtained with an electrical conductivity meter. There is a reasonable match between the two.

The dry densities of sediments are estimated from TDR measurement according to step 5 of the application procedures previously described. In making the calculations, the dielectric constant of the soil solids $K_{a,s}$ is assumed to be 4, and the specific gravity of the soil solids is assumed to be 2.65. The results are shown in Figure 17. Also shown in the figure is the dry density calculated from experimental records. The measured density of sediments by the TDR method closely matches that of the actual densities.

5.6. Effects of Turbulence Conditions on TDR and Ultrasonic Methods. The flood process generally brings about turbulent river conditions with a significant amount of air bubbles and suspended sediments. Experiments were completed to investigate the effects of air bubbles and sediments on TDR and ultrasonic methods. Figure 18 shows a photograph of the testing setup where air bubbles were generated at the bottom of the testing tank. The rate of air bubble generation was controlled from low to high levels to investigate its effects. Visual presentations of its effects on TDR and ultrasonic signals are shown in Figure 19. While air bubbles have negligible effects on the TDR signal quality, they show an important influence on the ultrasonic signals. The echo signal of the ultrasonic method is almost totally attenuated at high air bubble content. This is an important factor affecting

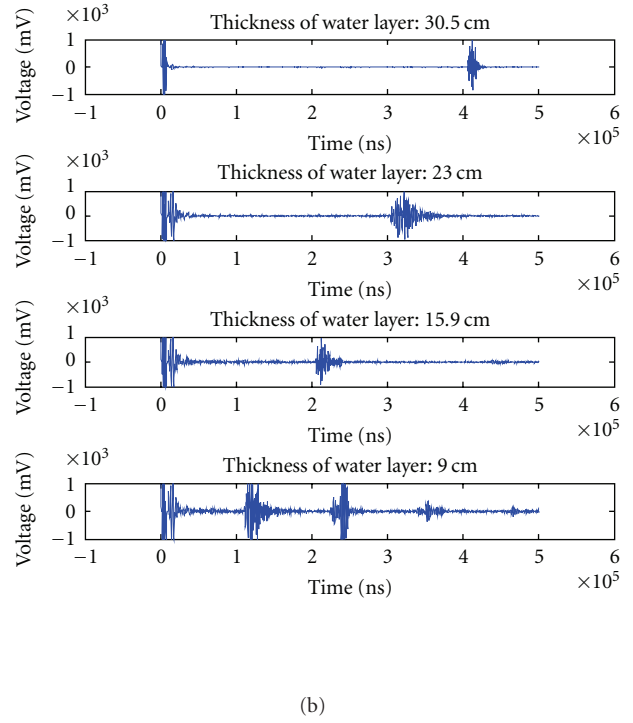
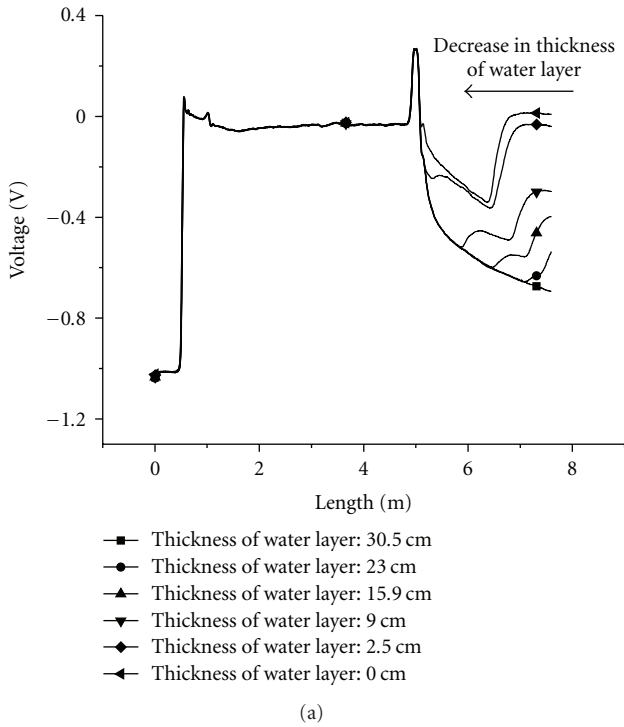


FIGURE 13: (a) Variations of TDR signals with scour depth; (b) variations of ultrasonic signals with scour depth (sediment: coarse sand and gravel mixture).

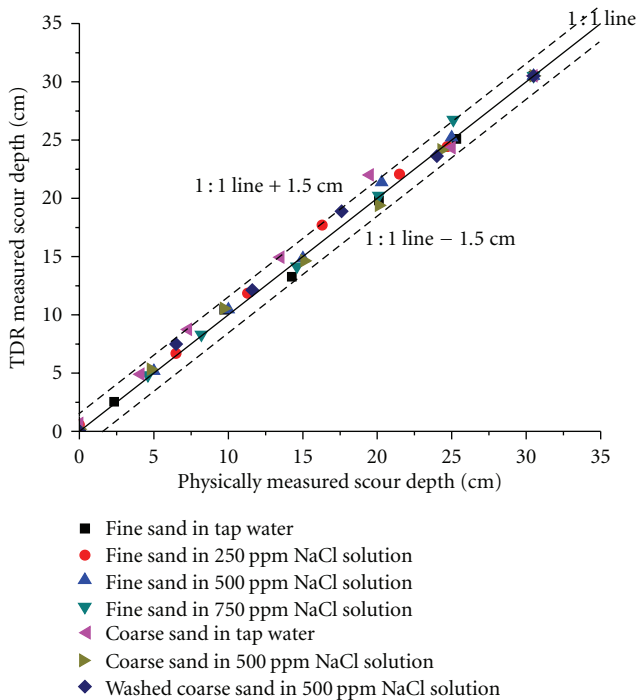


FIGURE 14: TDR measured thickness of sediment layer versus the actual thickness of sediment layer for various types of sediments and water conditions.

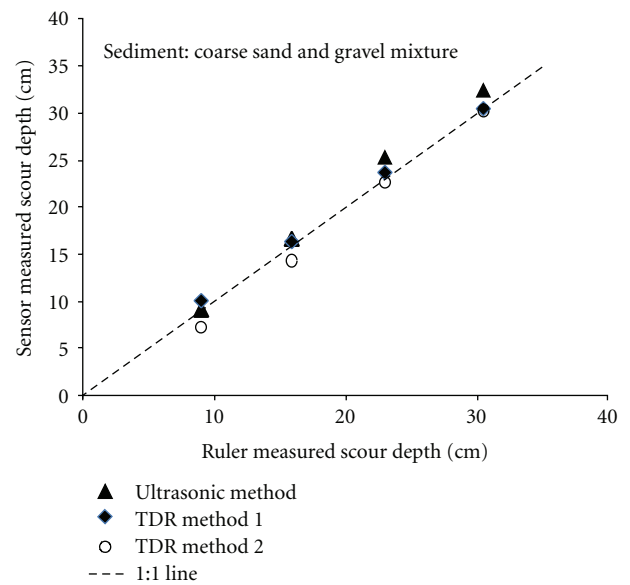


FIGURE 15: Prediction of scour depth using TDR and ultrasonic method (TDR method 1 uses (5); TDR method 2 uses (12)).

the reliability of the ultrasonic method for monitoring the scour during critical flood events. Similar effects were found for suspended solids.

6. Discussion

This study indicates that both the TDR and ultrasonic methods can provide accurate measurements of scour depth. TDR system is advantageous in that it is inexpensive and amenable to automation. These are desirable features for

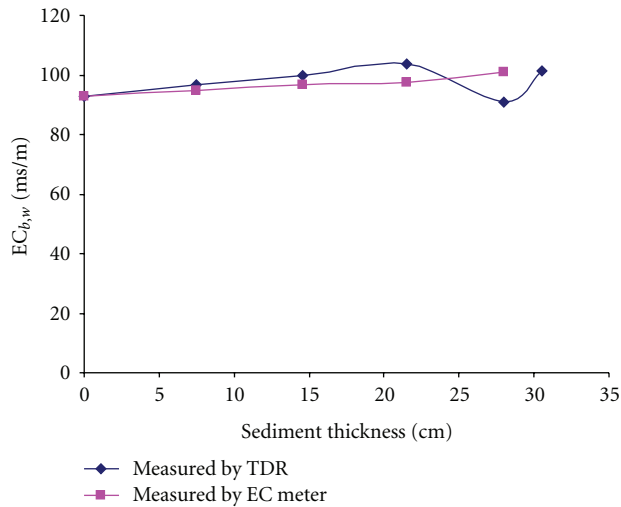


FIGURE 16: Prediction of electrical conductivity of water versus depth (sediment: coarse sand and gravel mixture).

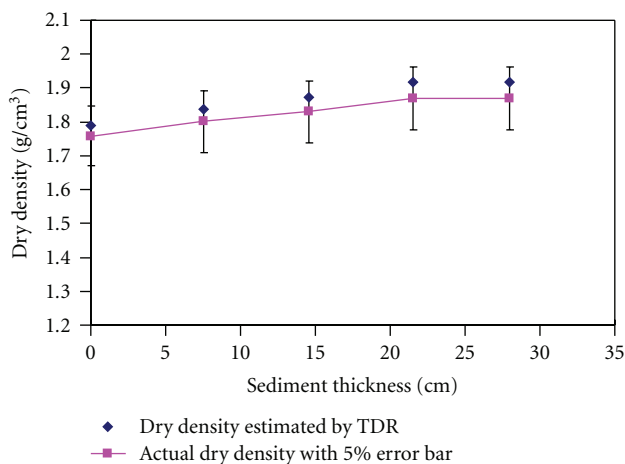


FIGURE 17: Sediment dry densities estimated by TDR at different scour depths (for a mixture of coarse sand and gravel at 1:1 mass ratio).

a real-time scour-monitoring and surveillance system. The ability of real-time surveillance is important since the most severe scour typically happens near the peak flood discharge. As sediments deposit in the scour hole during flood recession, post flood measurements might not truly describe the severity of the historical scour during the flooding process. The procedures introduced in this paper provide easy measurement of scour depth. Information about the sediment status (density) and water conditions (electrical conductivity) are obtained simultaneously. These could be used to enable a mechanistic understanding of scour phenomena. The accuracy of TDR can be affected by the electromagnetic interference and signal attenuation in the cable length. This requires careful planning for deployment of the system in the field. In addition, TDR



FIGURE 18: Generation of air bubble to evaluate its effects on TDR and ultrasonic measurement.

sensors only measure scour at a given point. Multiple TDR probes will be needed to map the shape of the scour hole. A protective coating will be needed to prevent TDR wave signal attenuation for a long TDR scour probe. Potential ways to protect the TDR probe from impacts of debris, include to submerge the probe completely under the water, to place the TDR probe in locations that is less likely to be accessed by debris, and to use a strong supporting element. As mentioned in the introduction section of this paper, the TDR probe developed by Yankielun and Zabilansky [3] has been installed in the field for years and survived flood debris and ice loading. In the authors opinion, the potential impacts of debris can be reduced; however, such impacts might be hard to be completely prevented. The ultrasonic method is valuable for post-event scour measurements. It requires the ultrasonic transducer to be maintained below the water level and provide a local measurement. However, as it is a nonintrusive technology, ultrasonic transducers can be moved to determine the shape of river bed after scour event. The interpretation of ultrasonic signals can be challenging, especially for complex river beds. There could be a significant amount of background noise in the ultrasonic signal caused by air bubbles and suspended solids in the water, that severely affect the identification of the reflected signal.

7. Conclusion

This paper introduces a new scour measurement method based on TDR technology. This method is robust and utilizes simple analysis procedures. Preliminary results show that it provides accurate measurement of scour depth (sediment thickness), density of sediments, and electrical conductivity of river water. A comparative study of TDR and the ultrasonic method for scour measurements is also described. It is found that both TDR and ultrasonic methods can accurately measure the scour depth; however, more information about status of sediments and water can be

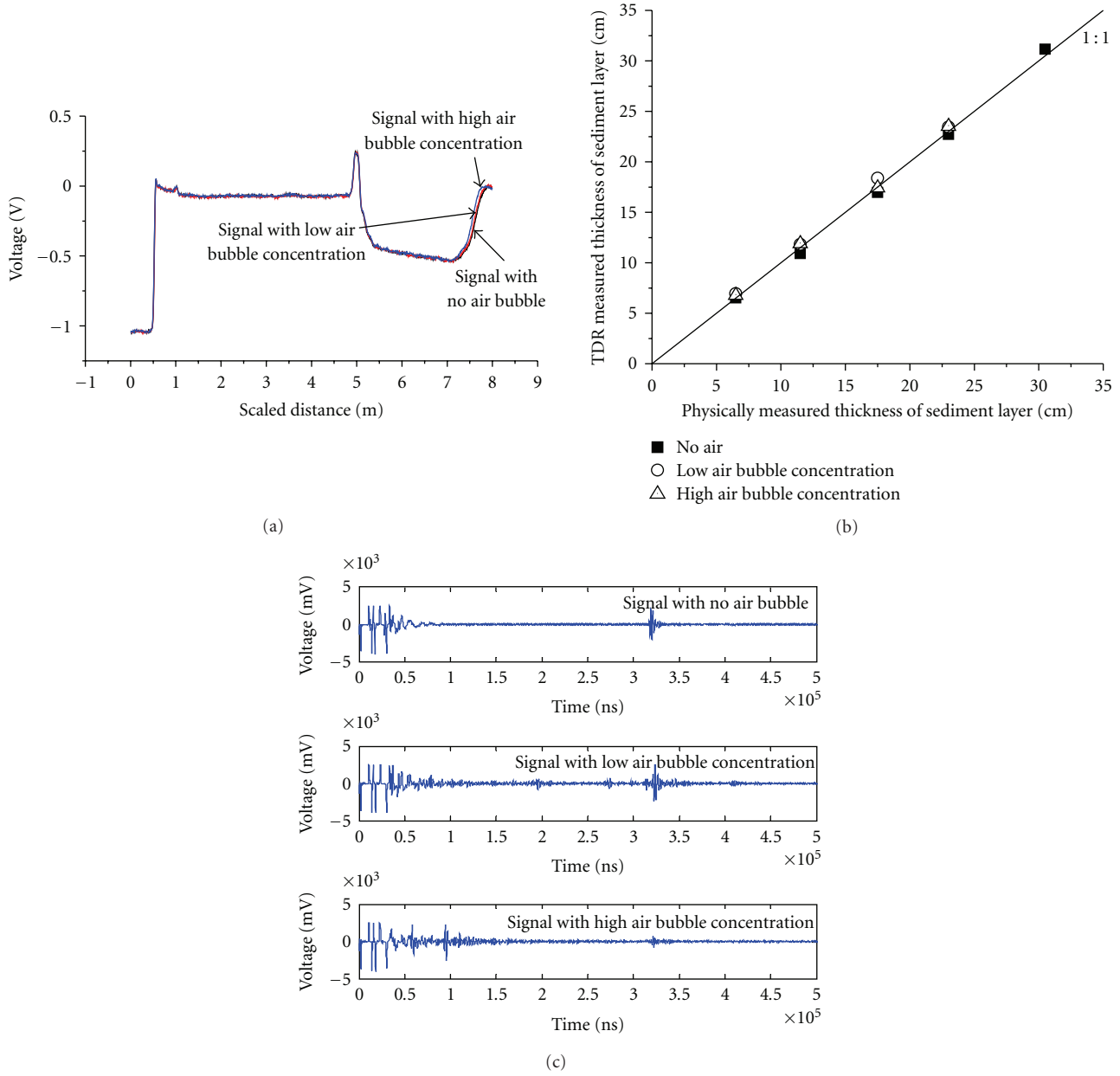


FIGURE 19: Effects of air bubble on (a) TDR signals, (b) TDR scour depth estimation, and (c) Ultrasonic Signals.

obtained from TDR measurements. Experiments indicate that TDR is less influenced by turbulent conditions that result in suspended solids, air bubbles, and fast flowing water, which are typical of flood processes. TDR-monitoring systems are rugged and can provide real-time surveillance. The data they collect on scour evolution during major floods will help examine the various scour mechanisms. Ultrasonic methods, on the other hand, can be a useful tool to rapidly measure the scour contour. On-site monitoring with TDR method in conjunction with postflood survey with ultrasonic methods will enable accurate determination of the status of bridge scour during and post major flood events to help ensure the long-term safety of bridge structures.

List of Notations

- K_a : Measured dielectric constant
- L_p : Physical length of probe in testing materials
- L_a : Apparent length of probe in testing materials
- θ : Volumetric water content
- V_s : Source voltage
- V_f : Long-term voltage level
- C : A constant related to probe configuration
- $K_{a,w}$: Dielectric constant of water
- $K_{a,bs}$: Dielectric constant of bulk sand (sand with water mixture)
- $K_{a,m}$: Measured bulk dielectric constant
- L_1 : Thickness of water layer

L_2 : Thickness of sand layer
 L : Total thickness of sand and water layer
 x : Thickness of sand (sediment) layer
 $EC_{b,w}$: Water conductivity
 $k_{a,s}$: Dielectric constant of soil solid
 $EC_{b,s}$: Electrical conductivity of saturated sand layer
 $EC_{b,m}$: Measured overall electrical conductivity
 F : Formation factor
 f : Form factor
 x_r : Ratio of sand thickness to the total thickness of water and sand
 R : Reflection coefficient
 Z : Acoustic impedance
 ρ : Density
 V : Acoustic velocity.

References

- [1] Modjeski and Masters, August 2006, <http://www.modjeski.com/>.
- [2] C. H. Dowding and C. E. Pierce, "Use of time domain reflectometry to detect bridge scour and monitor pier movement," in *Proceedings of the Symposium and Workshop on Time Domain Reflectometry in Environmental, Infrastructure, and Mining Applications*, pp. 579–587, Northwestern University, Evanston, Ill, USA, 1994.
- [3] N. E. Yankielun and L. Zabilansky, "Laboratory investigation of time-domain reflectometry system for monitoring bridge scour," *Journal of Hydraulic Engineering*, vol. 125, no. 12, pp. 1279–1284, 1999.
- [4] E. V. Richardson and S. R. Davis, *Evaluating Scour at Bridges*, Hydraulic Engineering Circular, no. 18, FHWA NHI 01-001, U.S. Department of Transportation, Washington, DC, USA, 4th edition, 2001.
- [5] P. F. Lagasse, E. V. Richardson, J. D. Schall, and G. R. Price, "Instrumentation for measuring scour at bridge piers and abutments," NCHRP Report 396, 1997.
- [6] B. E. Hunt, "Practices for monitoring scour critical bridges," NCHRP Project, First Draft Report 20-5, Transportation Research Board, National Research Council, National Academy Press, Washington, DC, USA, 2005.
- [7] X. Yu and J. L. Zabilansky, *Time Domain Reflectometry for Automated Bridge Scour Monitoring*, ASCE Geotechnical Special Publications, GeoShanghai, Shanghai, China, 2006.
- [8] X. B. Yu and X. Yu, "Time domain reflectometry automatic bridge scour measurement system: principles and potentials," *Structural Health Monitoring*, vol. 8, no. 6, pp. 463–476, 2009.
- [9] Campbell Scientific, Inc., *TDR100 User Manual*, Campbell Scientific, Inc., Logan, Utah, USA, 2008, <http://www.campbellsci.com/documents/manuals/tdr100.pdf>.
- [10] K. L. Rens, T. J. Wipf, and F. W. Klaiber, "Review of nondestructive evaluation techniques of civil infrastructure," *Journal of Performance of Constructed Facilities*, vol. 11, no. 4, pp. 152–160, 1997.
- [11] X. B. Yu and X. Yu, "Scour measurement by time domain reflectometry," in *Proceedings of the 3rd International Symposium and Workshop on Time Domain Reflectometry for Innovative Soils Applications (TDR '06)*, Purdue University West Lafayette, West Lafayette, Ind, USA, September 2006.
- [12] J. R. Birchak, C. G. Gardner, J. E. Hipp, and J. M. Victor, "High dielectric constant microwave probes for sensing soil moisture," *Proceedings of the IEEE*, vol. 62, no. 1, pp. 93–98, 1974.
- [13] G. E. Archie, "The electrical resistivity log as an aid in determining some reservoir characteristics," *Petroleum Transactions of the AIME*, vol. 146, pp. 54–61, 1942.
- [14] X. Yu and V. P. Drnevich, "Soil water content and dry density by time domain reflectometry," *Journal of Geotechnical and Geoenvironmental Engineering*, vol. 130, no. 9, pp. 922–934, 2004.
- [15] E. L. Hamilton, "Reflection coefficients and bottom glasses at normal incidence computed from Pacific sediment properties," *Geophysics*, vol. 35, pp. 995–1004, 1970.

Research Article

Integration of Networks of Sensors and Electronics for Structural Health Monitoring of Composite Materials

Fabrizia Ghezzi,¹ Anthony F. Starr,² and David R. Smith¹

¹Department of Electrical and Computer Engineering, Duke University, P.O. Box 90291, Durham, NC 27708, USA

²SensorMatrix, 10211 Pacific Mesa Blvd, Suite 408, San Diego, CA 92121, USA

Correspondence should be addressed to Fabrizia Ghezzi, fabrizia.ghezzi@duke.edu

Received 2 September 2009; Revised 24 February 2010; Accepted 29 March 2010

Academic Editor: Piervincenzo Rizzo

Copyright © 2010 Fabrizia Ghezzi et al. This is an open access article distributed under the Creative Commons Attribution License, which permits unrestricted use, distribution, and reproduction in any medium, provided the original work is properly cited.

The low-cost, widespread availability and robust nature of current electronic devices suggest the feasibility of creating a composite structure with integrated networked sensors to monitor in real time the life of civil and aerospace structures while in service conditions. For structures that need to survive to high number of life cycles under varying load-environmental conditions, it is of crucial importance that the strength, stiffness, endurance, and general load-bearing capabilities of the composite not to be severely degraded by the integrated networked components. Therefore, design tools must be developed to achieve optimized, safe, and reliable structures. High values of stress concentrations due to the presence of a rigid device within a highly anisotropic material can trigger the initiation of microcracks in the resin matrix. To quantify these effects, the acoustic emission technique is used to characterize the initiation of microfailures within laminated composites with integrated electronics.

1. Introduction

Health monitoring of composite structures and components for civil and aerospace applications has become of major interest in the past few decades. Advances in the microelectronics industry are clearly showing progressive success at achieving smaller chip and sensors sizes of consuming less power, while increasing the processing and functionality. However, such inclusions may affect the local integrity of fiber reinforced polymers and the limitation of the tolerability of the host material in presence of these devices must be quantified. With respect to structural performance, the effects of the embedded transducers on the host composite may be object of concern. The presence of inclusions causes material and geometrical discontinuities that are responsible of unwanted stress concentrations with consequences on the reduction of the stiffness and the overall material performance. For this reason, effort has been devoted into adding monitoring functionality into composites without compromising the structural integrity. To emphasize the importance of these studies a brief

review of the literature which includes the first historical and significant contributions in this area is needed. These contributions are summarized in Table 1.

By reviewing these experimental studies, and as pointed out in a previous work [16], it appears that in cases where the thickness and the geometry of the implant did not alter significantly the through-the-thickness configuration of the host material, the impact on the surrounding material remains very small and has negligible effects on the material integrity. Where the integrated devices are not of negligible size, the strength reduction of the embedded material as well as the damage mechanisms need to be quantified and further investigated. These observations are of fundamental importance for material design considerations and final application of safe and reliable components.

This paper gives an overview of the failure mechanisms which develop in fiberglass epoxy laminates due to the presence of integrated electronic components which are “*thick*” if compared to the laminated material ply thickness and presents the importance of material design and selection of proper lay-up configurations. These types of autoclaved

TABLE 1: List of some significant experimental contributions on the evaluation of the effects of integrated devices on the structural integrity of composite materials.

| Authors | Devices integrated | Material studied | Main findings and conclusions |
|--|---|---|---|
| Warkentin, and Cawley 1991 [1] | Circuits on silicon chips | Graphite/epoxy composites | No change of in-plane mechanical properties. 15% reduction of the material strength. |
| Kim et al. 1992 [2] | Simulated thermocouples with 0.381 mm wire diameter. Simulated strain gauge Kapton film size: 10.16 mm × 5.08 mm 0.127 mm | Quasi isotropic Fiberite T300/976 or Fiberite APC-2 graphite composites | Negligible effects on the strength in uniaxial compression and 3-point bending. |
| Holl, and Boyd 1993 [3] | Fiber Optic sensors (FO) with 100–200 mm diameter | Unidirectional and quasi isotropic graphite laminates | Failure does not initiate near the fiber-optic sensor. No sensitivity to the embedded sensor is seen in quasi-isotropic cases The transverse strength is reduced. Optical microscopy and Moiré interferometry show no perturbation in the strain state of the material with embedded FO. The material lay-up and its thickness influence the results. |
| Sirkis, and Singh 1994 [4] | Fiber Optic sensors (FO) | Graphite composite laminates | Interlacing results in 42% reduction of the max. interlaminar tensile stress and a 22% reduction of the max. interlaminar shear stress |
| Singh, and Vizzini 1994 [5] | Simulated actuator (glass slice) | AS4/3501-6 graphite/epoxy laminates | The 72% material strength reduction under uniaxial loads improves with interlacing techniques. |
| Shukla, and Vizzini 1996 [6] | Simulated sensors/actuators. Device size: 25.4 mm × 76.2 mm × 1 mm | Unidirectional AS4/3501-6 graphite-epoxy laminates | 4% reduction of strength and Young's modulus. No degradation of the fatigue life. The embedded PZTs maintain a steady output indefinitely if mechanically cycled within their operational strain limits |
| Mall, and Coleman 1998 [7] | Active PZT sensors. Device size: 50 : 8 mm × 25 : 4 mm × 0 : 254 mm | Quasi-isotropic AS4/3501-6 graphite/epoxy laminates | No effects on the strength and the failure modes |
| Paget, and Levin 1999 [8] | Active thin (0.13 mm) PZT sensors | Quasi-isotropic graphite/epoxy laminates | Static tension and tension-tension fatigue of interlaced materials with devices: 33% reduction of strength; endurance is improved; damage initiation delayed with respect to the use of cut-out methods. |
| Hansen, and Vizzini 2000 [9] | Simulated devices (glass slices) size: 76 mm by 25 mm by 1 mm | Unidirectional AS4/3501-6 graphite/epoxy composites | Fatigue of active PZT. Specimens cycled at different max stress levels while exciting the embedded actuator from –10 V to –100 V or 10 V to 100 V. 10 Hz and R = 0.1. Embedded PZT performed better in the out-of-phase than in-phase conditions. |
| Mall, and Hsu 2000 [10] | Zirconate-titanate, PZT actuators integrated with cut-out methods. Device size: 50.8 mm × 25.4 mm × 0.254 mm | AS4/3501-6 graphite/epoxy laminates | Tensile strength and Young's modulus are not affected by the integration of actuator/sensor using the two embedding techniques. No degradation in the fatigue life/strength. The PZT actuator/sensor functions mechanically fatigued or loaded to the maximum stress level equal to its operational design limit. |
| Mall 2002 [11] | Active PZT sensors integrate with or without cut-out method. Device size: 50.8 mm × 25.4 mm × 0.254 mm | Quasi-isotropic AS4/3501-6 graphite/epoxy laminates | The SMART layer does not affect noticeably the strength of the host composite structure, nor promote delamination in 3 point bending tests. |
| Lin., and Chang 2002 [12] | Sensor network: thin flexible dielectric film, SMART layer (printed circuit material with piezoelectric on it). Layer thickness: 0.050 to 0.25 mm | Composites made with RTM methods | The material properties are unaffected by the integration of the fiber-optic sensor. 10% reduction of the tensile strength and 40% decrease of the compressive strength are reported. |
| Shivakumar, and Emmanwori 2004 and 2005 [13, 14] | Samples with 0, 30, 45, 60, 90° FO sensors oriented with respect the fibers direction. | Unidirectional AS4/3501-6 carbon/epoxy laminates | (1) Cutout holes, (2) molded-in holes, and (3) embedding techniques. Manufacturing, durability, dynamic, and structural performance of embedded materials are optimal if materials with devices are made with method (3) |
| Ghasemi-Nejhad et al. 2005 [15] | Active flexible piezoceramic sensors and actuators patches. Patches dimensions: 135 mm × 55 mm × 0.33 mm. | Plain weave carbon/epoxy material | |

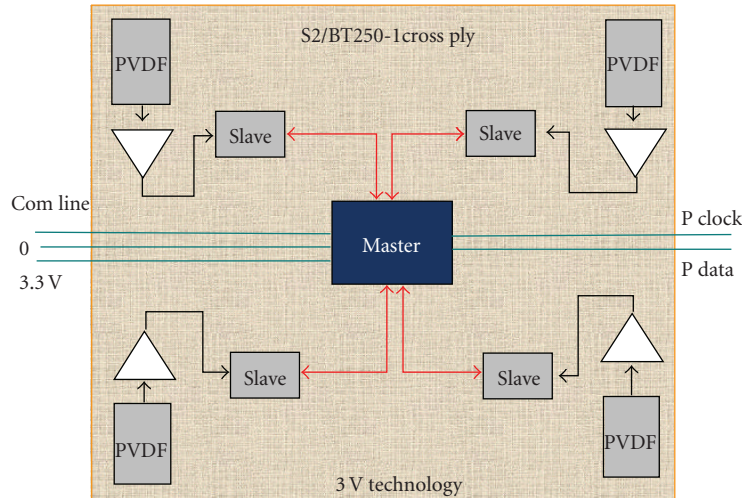


FIGURE 1: Schematic of one module of a 4-tree hierarchical network.

or compression molded materials are of common use in wind energy blades, aircrafts components, military devices, and military vehicles components for shock and blast energy absorption. The design of such structures requires careful experimental analyses on small samples and subsequent proof of research findings on actual components [17]. This last step is necessary since the fabrication and therefore the final quality of these materials combined with the environmental conditions at which the component is subjected during its life can affect the results obtained in the laboratory.

In this paper, laboratory results are mainly considered. Specifically, the quantification of the effects of integrated microelectronic components on the local integrity of the host material was investigated. In previous works [16, 18] the initiation of the damage within the material was assessed by continuously monitoring the samples subjected to tensile load with the acoustic emission technique. It was proved that the presence of notches in unidirectional plies induces microcracks into the resin that can propagate quickly along the fibers direction causing a fast degradation of the material in terms of mechanical properties and structural performance. The results previously obtained for unidirectional 0-degree fiber orientations (where the fiber orientation is considered with respect to the direction of the load applied) are compared with the results of experiments conducted on 45-degree laminates to show the importance of the material lay-up to optimize the resistance of these materials in presence of implanted devices.

2. Materials and Properties

The experimental investigations here presented were conducted in order to overcome some issues encountered for the fabrication, design, and development of an embeddable acoustic sensing network with optimized communication schemes. The targeted network was developed to be integrated into a thin laminated composite in order to enable

the material to sense and locate matrix microcracks. A description of the overall system that was developed is given as an introduction to this section. The discussion will then continue focusing on the specific methodology adopted to overcome some of the issues that were encountered during the development of such system, particularly addressing the problem of stress concentrations due to the integration of external devices into polymeric matrix composites. It is important to point out that the results obtained from the impact that such devices have on the structural integrity of the material in fact—results mainly discussed in this paper—imposed the selection of the small and flexible electronic components that are illustrated and schematically represented in Figure 1. Today, electronic components are getting progressively smaller and more powerful with more memory presenting then the desirable features for our specific application. SiLab 8051 microprocessors ($3 \times 3 \times 1$ mm) were chosen as processing elements (PEs) of a 4-tree hierarchical network [19]. This hierarchical network was selected since it may well represent, even though in its simplicity, neurological networks in living organisms. The integration and spatial allocation of components within the material was studied to maximize the reduction of wires and connections inside the material. The final modular structure created by combining the efforts in material lay-up optimization, proper selection of network and components, is presented in Figure 1.

It can be seen how each node is composed by a flexible and thin Polyvinilidene sensor (PVDF), a signal conditioning circuit (indicated in the figure with the triangle symbol), and a slave microprocessor. Each slave microchip has the function of analyzing the signal acquired by the sensor and amplified through the signal conditioning circuit and communicating the information of interest to the master. The desirable small size of the microprocessors is a limit to the available memory for processing data and basic functions. To overcome the problem due to their limited memory, the damage source identification and the classification of the damage events is

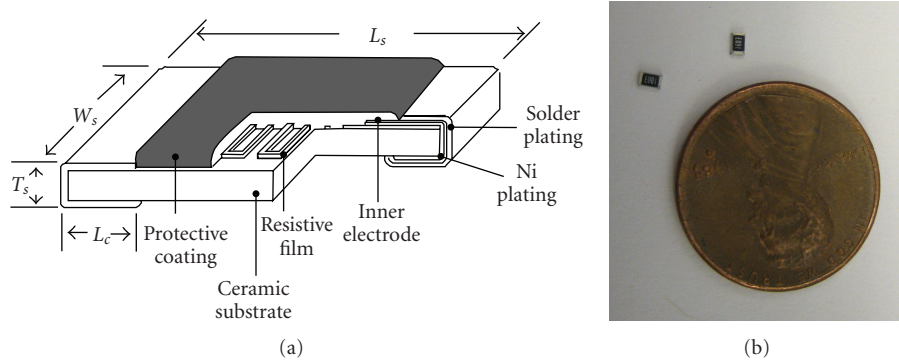


FIGURE 2: Schematic of the chip resistor 805, Koa Speer Electronics Inc.

TABLE 2: S2/BT250E-1LV material properties and lay-ups. * [20].

| Composite materials constituents properties | | | | | | | | |
|---|----------------|----------------|----------------|----------------|---------------------------------|-------------------------------|------------|------------------|
| | | E (GPa) | ν_{12} | G_{12} (GPa) | σ_{tensile} (MPa) | σ_{shear} (MPa) | | |
| S2 fibers | | 86.9 | 0.23 | 35 | 4890 | 35* | | |
| BT250E-1LV resin | | 3.86 | 0.39 | 1.39 | 75 | 35 | | |
| Lamina properties | | | | | | | | |
| E_{11} (GPa) | E_{22} (GPa) | E_{33} (GPa) | G_{12} (GPa) | G_{13} (GPa) | G_{23} (GPa) | ν_{12} | ν_{13} | σ_f (MPa) |
| 47 | 7.6 | 7.6 | 2.77 | 2.77 | — | 0.29 | 0.29 | 1730 |
| Blank samples | | | | $[0]_2$ | $[(\pm 45)_5]_s$ | | | |
| Samples with embedded inclusions | | | | $[0]_6$ | $[(\pm 45)_5]_s$ | | | |

conducted through the analysis of parametric information since they require a very limited use of the processor memory and processing functionalities. In summary, to successfully develop such system, the impact of external devices on the structural integrity of the material was deeply investigated. To do so we observed the effects that a general electronic component can have on the composite resin matrix while the material is subjected to external loads. Since the network was developed to acquire acoustic events in parametric form, the characterization of the material in the laboratory was conducted by monitoring its behavior under stress using the acoustic emission technique and analyzing the acquired parametric data. The main advantage of this method is the fact that the characterization of the acoustic emission behavior of the material in form of parametric information allows the direct implementation of the results into the microprocessors in form of lookup tables which are stored using a very limited amount of memory.

Given such conditions the successful development of this modular system was therefore possible only after the characterization of the acoustic events within the material and the calibration of the system in order to exclude that nonsignificant information (noise and general disturbance) is stored and processed as important event. From this introduction we can derive that the need of finding small electronic components to reduce the impact of such devices on the integrity of the material imposes also the need of searching for methods for efficient and fast data handling and storage. Besides the issues strictly related to the processing functions, the size limitations of these components required

for this application are due to the built-in localized stress concentrations introduced by placing stiff implants into a material whose integrity relies mostly on the health status of its polymeric phase.

The material that has been used for this research is a multilayered composite made of S2 fiber glass BT250E-1LV epoxy resin prepreg by Bryte Composite Technologies Inc.

The samples were fabricated by using a vacuum bag technique with application of external pressure and were classified as follows: blank samples, without embedded implants, and samples with integrated microelectronic elements. To investigate the effects that general implants may have on this material, the microelectronics that were embedded during the hand layup fabrication consist of 0805 chip resistors, by Koa Speer Electronics Inc. These elements are active elements of the signal conditioning circuits for the network previously described. Their cost and availability made them perfectly suitable for these experiments.

These signal conditioning elements were placed at the mid-plane of the material stacking sequence. The 0805 chip resistor dimension is 2.03 mm (L_s) by 1.27 mm (W_s) by 0.55 mm (T_s). The device schematic is shown in Figure 2 with the sole purpose of better understanding the optical microscopy images presented in the following sections.

The samples present the device integrated and centrally located with respect to the two global in-plane axes. The main material and lamina properties are presented in Table 2. Following the standards [21], the fiber volume content, V_f , was found to be 53% for all the fabricated panels. The findings demonstrated that both types of samples, with and

without embedded inclusions, display the same mechanical response (in plane properties and ultimate failure) in quasistatic tensile tests.

As it can be noticed in Table 2, the characterization of the $[0]_n$ laminates that was given in [16, 18] was carried out on six-layer samples in cases with embedded electronic components and two-layer samples in cases of material without inclusions. No changes in the failure mechanisms and acoustic behavior among samples of the same type with different number of plies were observed in these experiments. The failure always starts with matrix micro-crack phenomena induced by stress concentration at the device-composite matrix interface. The microcracks progressively grow and lead the sample to complete failure and loss of stiffness. While the characterization of the material response can be carried out on two ply laminates, four to six layers were necessary to properly integrate a 0.52 mm thick device. The external pressure applied to the vacuum bagged material can damage the fibers and indent them if there is not enough material to fully integrate the device.

The acoustic technique was used in this work to show that early low-medium amplitude events are detected at the rigid implant location in nonzero degree fiber orientations. Micrographic inspections conducted in parallel with the acoustic emission characterization of the material reveal that microcracks initiate at the device-composite matrix interface and grow around the implant causing the debond of the external component from the surrounding resin system. Material inhomogeneities are responsible for the formation of localized residual strains after the material fabrication. This fact is induced by the mismatch of the thermal properties between the resin and fibers [22, 23]. Their negative effects can influence the matrix-fiber interface strength.

It is important to emphasize that the results in terms of amplitude and frequency and other parametric features of the acoustic emissions were not affected by the number of plies that constitute the samples analyzed; however the number of events occurring within the material, if the overall material behavior is considered, may change considerably. For this reason variables such as number of counts and accumulated number of counts were not taken into account for the analyses. The analysis of the characteristic features of the events related to the failure initiation and their classification is here presented. An overview of the overall failure mechanisms and amplitude events distribution is also reported. It can be anticipated that the integrated device did not seem to affect the in-plane material properties (independently from the material lay-up) and had a negligible effect on the material tensile strength in all cases analyzed. However, the failure process can be remarkably different.

3. Experimental Procedure

The samples were subjected to quasistatic tensile load up to failure and performed in ambient laboratory conditions and applying the load at a constant 0.02 mm/sec displacement rate. The tests were monitored continuously by a PCI-2

TABLE 3: Acoustic emission system settings.

| PCI-2 PAC system settings | |
|--------------------------------|---------------|
| Distance between the sensors | 50 mm |
| Number of sensors | 2–4 |
| PDT (peak definition time) | 50 μ sec |
| HDT (hit definition time) | 300 μ sec |
| LDT (lock out definition time) | 800 μ sec |
| Threshold | 30–33 dB |
| Preamplification | 40 dB |
| Sampling rate | 2 MS/s |

acoustic emission system by Physical Acoustic Corporation (PAC).

The acoustic emission technique is extensively used today as a nondestructive method for assessing microchanges and damage in materials and structures. It is generally used for maintenance of metallic as well as composite structures that must be periodically inspected after certain number of life cycles. Many efforts have been already made in the literature to categorize the different sources of damage within composites using this technique, such as matrix cracking, fiber-matrix debonding, fiber pull-out, fiber breakage, and interlaminar delamination through signal amplitude and other classical AE parameters or through frequency and wavelet analysis [24–27]. Since composites are well suited for amplitude distribution analysis, which has been recognized as a useful tool in diagnosing the material status and structural health, the following results are mainly presented as a comparison of the damage events amplitude identified in samples with and without integrated devices. Another reason for choosing to analyze only parametric information of acoustic emission events stands on the fact that the information achievable on the health of the component is possible through a limited number of transducers and limited memory usage. This fact helps in storing limited amount of data, saving processing time, selecting small processing elements and chip components, and consequently limiting the size of the circuits and wires to be integrated into the material.

The acoustic emission (AE) was detected through external R50D sensors with peak frequency at 175 kHz and the data were collected and analyzed using AEWIN software [28]. Hsu-Nielsen tests were considered [29] to determine the speed of the acoustic waves within laminates with different fiber orientations necessary for the location of the acoustic sources. After completing these tests, the settings listed in Table 3 were selected for the use of the Physical Acoustic Corporation (PAC) system in these experiments.

The quasi-static tensile tests were performed using two acoustic transducers mounted on the surface of the sample using vacuum grease as couplant in order to improve the transmission of the signals through the sensor-sample interface. The AE parameters acquired during the experiments include events amplitude, events duration, number of counts per event, signal waveforms, and associated energy. Moreover, the information regarding the very first events



FIGURE 3: Photomicrograph of the resin pocket area around the embedded dummy sensor: side view (along the fiber direction).

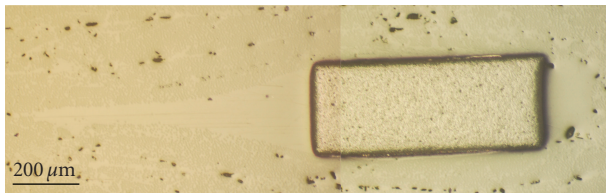


FIGURE 4: Photomicrograph of the resin pocket area around the embedded dummy microprocessor in ± 45 degree laminates.

occurring in the load history was carefully examined. At least three samples were tested until failure and their behavior are compared. Parallel to the acoustic analyses, additional information on the material failure modes was extracted from the observation of the samples microstructure. Four pristine samples of each type (blank and with integrated electronics) were cut and polished and their microstructure was analyzed using standard optical microscopy. Some samples were cut in correspondence of the implant orthogonally to the fibers direction, others along the fibers. Figure 3 presents an amplified view of the sample cross section which shows the device implanted and the resin pocket region in a 0-degree unidirectional fiber composite. As the micrographs show, the integration of relatively thick inclusions as actual commercially available microprocessors and signal conditioning elements forces the plies above and below the implant to deform, leaving large resin-rich regions. These effects were carefully analyzed in past both for fiberglass and for carbon fiber composites materials. The length of the resin-rich area was observed to be around 6 mm. This was noticed to be true for 0- and 90-degree fiber orientations (not shown here). Moreover, two resin-rich areas, symmetrically located with respect to the integrated electronic component, form along the fiber direction. It was demonstrated that orthogonally to the fibers the material around the dummy microprocessor appears uniformly to be distributed through the thickness.

If we compare the microstructure of these samples to nonzero fibers degree orientation samples, nonsymmetrical resin pockets with different shape and length can be observed instead; see Figure 4. Considerably reduced is also the length of this region in $[(\pm 45)]_n$ symmetrical laminates which was estimated to be at least three times shorter than the one in unidirectional laminates. It must be also taken into account that, in general, the shape of this region depends also on the implanted device geometry.

Voids due to the curing of the resin and air eventually trapped within the material during the hand lay-up process

were generally observed to be distributed between two adjacent plies as shown in the previous images. The total area of the sample cross section which is generally occupied by the voids was estimated in previous studies to be around 2% in samples both with and without embedded inclusions through image analysis. Moreover, it was also shown that the resin rich region as shown in Figures 3 and 4 was found to be intact. This was achieved by polishing progressively small coupons with different lay-ups to inspect their microstructure at different distances from the implant. For instance, the first image in Figure 5(a) shows the tip of the resin pocket area at almost 3 mm from the device, Figure 5(b) shows the cross section of the material at approximately 3 mm from the integrated device, while Figure 5(c) shows the surface of the device. In this way, the material microstructure after the fabrication as well as the resin pocket region integrity was explored. The observations were generally repeated on four different coupons.

The same procedure adopted to investigate the microstructure of pristine samples was used also to identify possible sites of micro-crack initiation into the resin matrix in samples that were subjected to predefined stress levels. For samples with integrated devices it was necessary to monitor the acoustic emission activity in order to detect at what stress levels the microdamage located and identified at the implant begins to occur. Given the difficulty associated with the micrographic investigation and the impossibility to predict the size of such cracks and their exact location around the device, the maximum stress level at which the samples were subjected was selected by looking for the acoustic emission results and plots of events location. Once considerable activity was seen at the device location, the test was stopped and the samples were gently removed from the grips by unloading them in a quasistatic mode. The experience gained by testing up to failure a first set of samples while monitoring their acoustic emission activity gave essential information on the stress/strain levels to be achieved in order to keep the cross-section of interest almost undamaged but for the microfailures present around the device. Therefore, after a certain applied stress was reached, the samples were unloaded and removed from the grips to be sectioned, polished, and analyzed. The results and details about these investigations are presented in the following sections.

4. Experimental Results

A recent classification of the acoustic events within glass fiber-reinforced composites is reported in [30]. Additionally, it has been demonstrated that in single-edge-notch laminated composites, the presence of stress concentrators induces a higher number of acoustic events with higher spectrum of frequencies than in unnotched materials [31]. Following these previous works similar results were demonstrated by Ghezzi et al. in [16].

The acoustic results are here presented in terms of the cumulative number of counts, also often referred as cumulative damage, acquired in unidirectional $[0]_n$, and

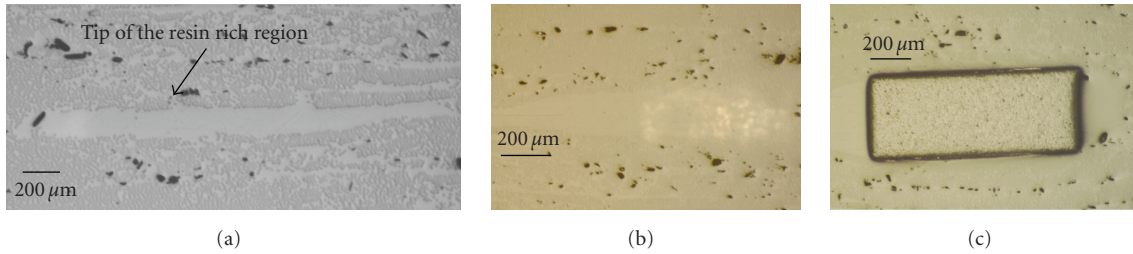


FIGURE 5: Tip of the resin pocket area in a 45-degree fiber orientation sample with integrated resistor at 3 mm from the implant, cross-section (a); at 0.5 mm from the implant, (b) and chip resistor cross-section (c) with magnification 50x.

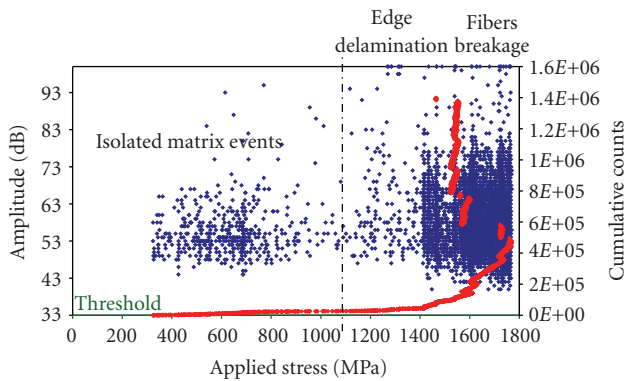


FIGURE 6: Typical acoustic behavior under tensile load of a sample without integrated inclusion.

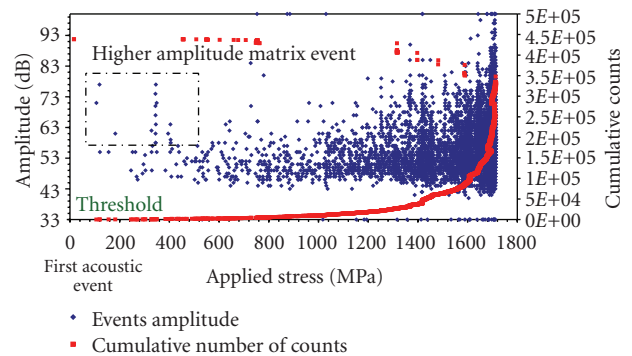


FIGURE 7: Typical acoustic behavior under tensile load of a sample with integrated inclusion.

$[\pm 45]_n$ samples with and without integrated device during the loading history. Besides, the distribution of the events amplitude versus the increasing of the load applied is also shown.

Due to the uniqueness of each test, only some of the results obtained are here reported. However, at least four samples per type were tested and the results were found to be consistent. The results are summarized in Tables 3 and 4 at the end of this work.

4.1. Unidirectional $[0]_n$ Laminates. The results for this case were presented in a previous work [16]. In order to use these findings for comparing the results obtained from the characterization of samples with different fiber orientations we discuss the typical acoustic emission events recorded for these samples as given in Figures 6 and 7 giving some additional insights to this case that are useful for the comparison with nonzero-fiber laminates. The first acoustic emissions detected can be related to specific microfailures that occur inside the material. These two plots show the typical distribution of the events amplitude versus the applied stress in $[0]_n$ blank samples and samples with integrated devices. It can be observed that the acoustic emission events were detected at about 300 MPa that we defined, as from a previous work, $\sigma_{\text{Fac-B}}$ which corresponds to the axial tensile stress at which first acoustic events begin in blank samples.

The amplitude of these initial events was found in a range between 35–60 dB. In samples with embedded inclusions significant but isolated acoustic emissions were acquired at a stress which was named $\sigma_{\text{Fac-E}}$, the tensile stress at which first acoustic events are detected in samples with embedded inclusions. This stress was observed to be from 25% to 33% of $\sigma_{\text{Fac-B}}$, the stress at which first acoustic events are detected in samples without integrated devices for all the tests conducted. The amplitude of these early emissions generally falls into 50–75 dB range. Moreover, the distribution of the events was observed to be quite different in these two cases, and this fact can be attributed to a different failure process, clearly shown in Figures 8 and 9.

In samples with integrated device, the first acoustic emissions were detected and located in the material surrounding the implant. The distribution of the events in the case of samples with integrated device is concentrated at the center of the sample gage length where the device is located. This fact was found to be in agreement with the observed failure initiation and overall material failure. The location of the acoustic sources was determined based on the first threshold crossing time of the signals acquired by the external transducers and was identified at the implant, independently from the material lay-up. In order to correlate these acoustic occurrences with physical events, four $[0]_6$ samples with embedded electronic components were subjected to increasing tensile load until the first emissions were detected. Afterwards, the samples were removed from

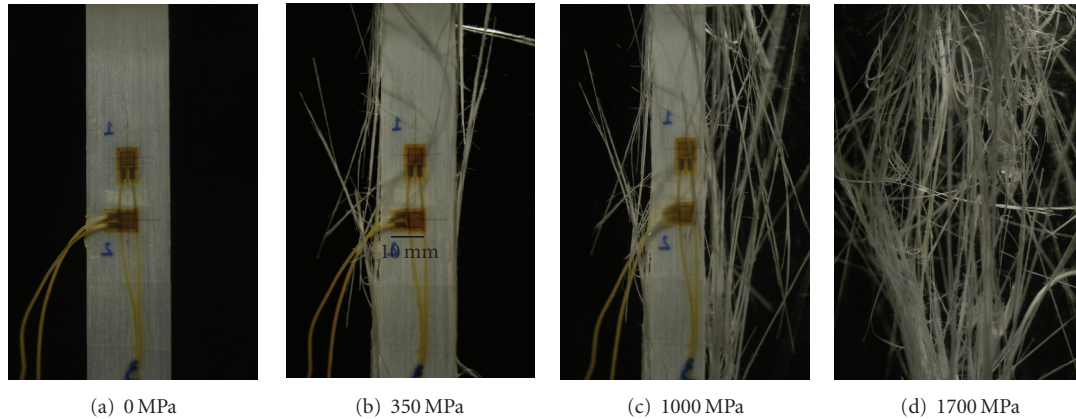


FIGURE 8: Failure by progressive edge delamination in blank samples (a); initiation of the failure (b-c) and slow propagation; final failure (d).

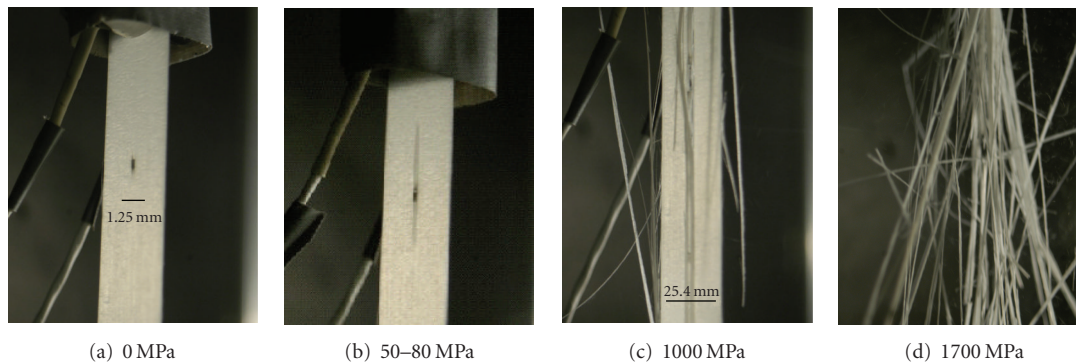


FIGURE 9: (a) through (c) initiation of failure at the implant in $[0]_6$ samples with integrated device; catastrophic failure (d).

the grips, cut orthogonally to the fibers at few millimeters from the implant, and polished. It was observed that even though acoustic events were captured at rather low stress levels, the samples chosen for microstructural investigations were subjected to higher loads in order to render the damage significant and visible; see Figure 10.

Guided by previous works in this field [30–32] and from the optical investigations conducted on tested samples, it appeared that the first acoustic events detected in *blank* glass fiber samples may be attributed to the growth of defects and flaws, fiber pull-out, and matrix microcracking phenomena. It was also observed that these first events are characterized by low amplitude (35–60 dB) and signal peak frequency between 100 and 180 kHz. Moreover, the distribution of the damage seemed to be uniform through the length of the sample.

On the other hand, in samples with integrated devices, localized cracks and debonding are mostly concentrated at the sensor-resin interface. The corresponding events acquired through the AE system are associated with low and medium amplitude signals (50–70 dB) with peak frequency in the range of 150–300 kHz. Even though the number of cumulative counts cannot be compared due to the different number of layers of these samples, the damage curves are qualitatively similar. The much lower cumulative number of

counts acquired in samples with integrated device is however an additional indicator of the fast, catastrophic failure for growth of microcracks that start at the implant-composite interface and then propagate without obstacles within the resin matrix, along the fibers.

4.2. Symmetric $[(\pm 45)_n]_s$ Laminates. Unlike $[0]_n$, $[(\pm 45)_n]_s$ laminates with integrated thick electronic devices presented a different failure mechanism. As shown in Figure 11, the final failure did not occur at the implant location. This fact was observed in all samples tested. Besides, the material response and the overall acoustic events amplitude distribution were found to be the same for both types of samples; see Figures 12 and 13. Even though early microcracks were detected at the implant location, other distributed sources of damage initiation were acquired within the material and the final failure occurred far from the embedded device. The propagation of early microcracks at the sensor-matrix interface therefore seemed to be restrained by the glass fibers. Localized high damage such as resin-sensor interface debonding, cracks opening, and fiber matrix debonding near the dummy microprocessor was identified through a series of micrographic inspections once the early acoustic events were detected.

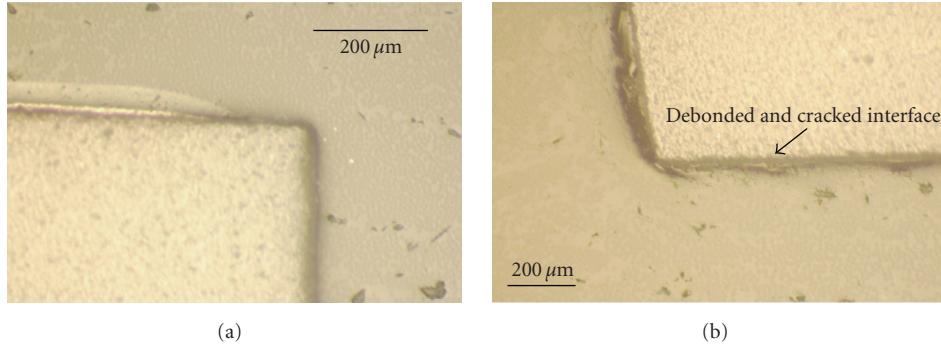


FIGURE 10: Photomicrographs of the cross-section around the dummy sensor of one virgin sample (a) and of one sample tested until 400 MPa (b).

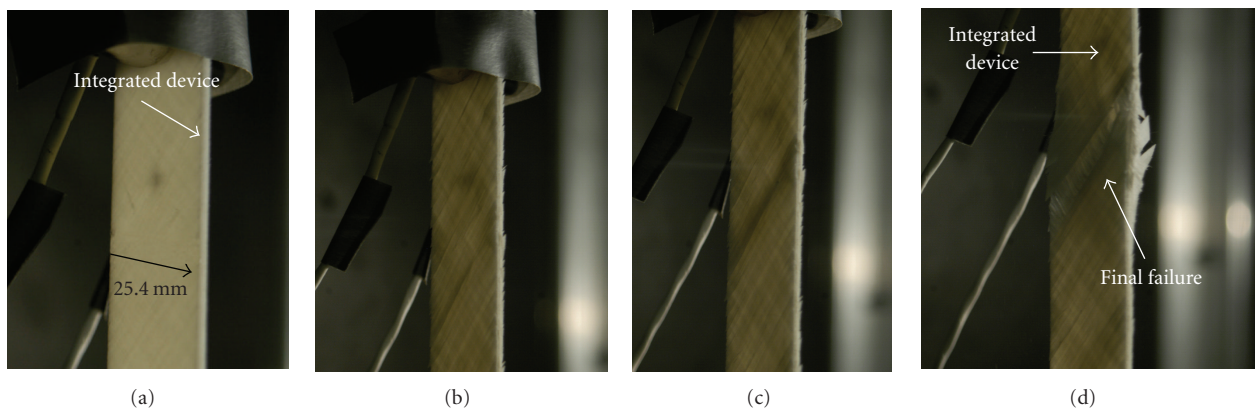


FIGURE 11: Typical failure mode of [(±45)₅]_s samples with integrated dummy microprocessor, sample width 25.4 mm.

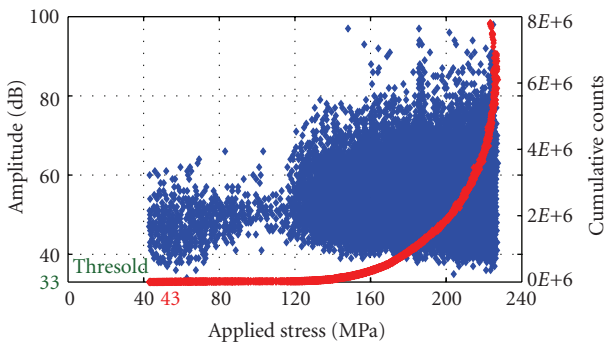


FIGURE 12: Cumulative damage and amplitude distribution of acoustic events in samples without integrated device.

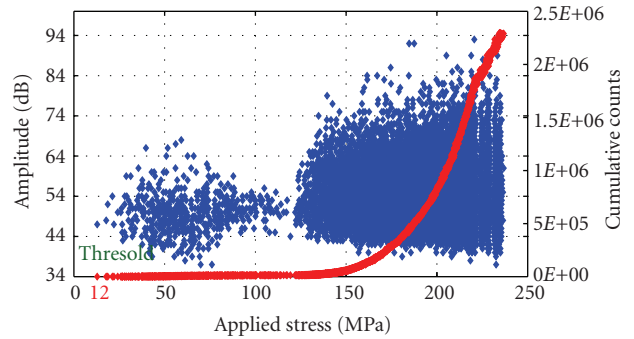


FIGURE 13: Cumulative damage and amplitude distribution of acoustic events in samples with integrated device.

As observed in $[0]_n$ samples, also in $[(\pm 45)_5]_s$ laminates acoustic emission events initiated in samples with integrated inclusion at almost 1/4 of the external stress applied on blank samples which is seen to cause early emissions. The distribution of these events amplitude is characterized by values ranging between 43–65 dB while those observed in blank samples are mainly detected within 40 and 50 dB. Once again, the frequency of these first events is higher than the one of events detected in blank samples. Generally the frequency of these first events was found to be around

180 kHz. Isolated higher-frequency events, up to 350 kHz, were also acquired. In blank samples the frequency range varies between 130 and 170 kHz. As for the previous $[0]_n$ cases, we subjected some samples to a tensile load until the first acoustic events were detected. Afterwards, the samples were removed from the grips and polished in order to inspect their microstructure. The results are presented in Figure 14. Big flaws and voids were observed while the resin rich region was found to be intact. Microcracks were instead observed all around the inclusion.

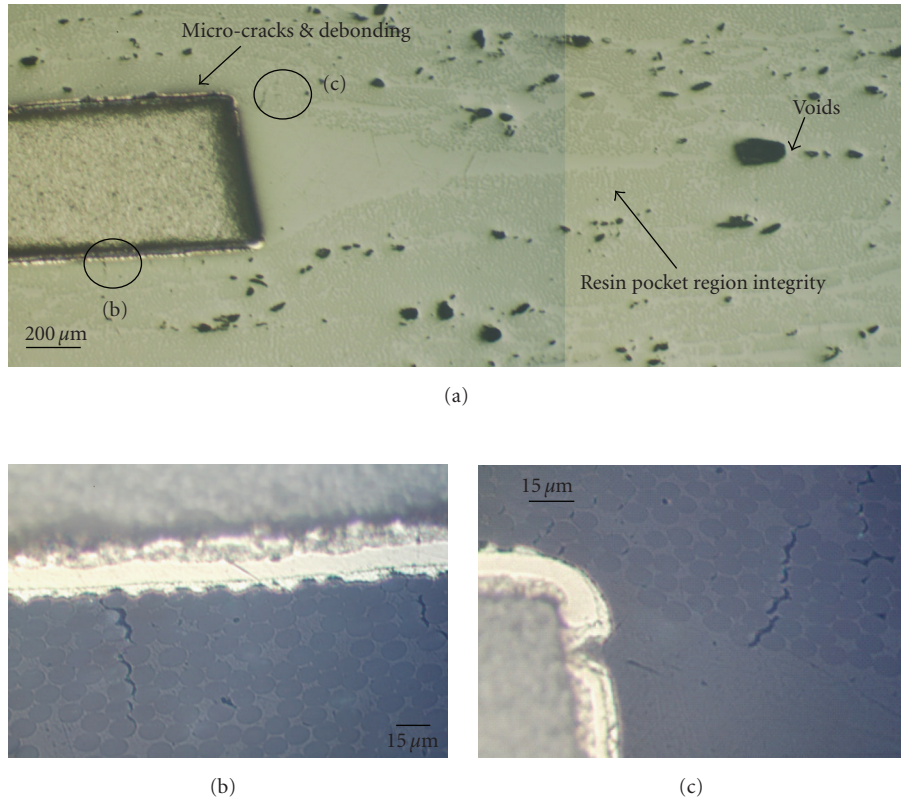


FIGURE 14: Sample cross-section and amplified views of debonding and microcracks around the integrated device after 100 MPa were applied on the sample.

In conclusion, the acoustic emission results obtained on $[0]_n$ and $[(\pm 45)_5]_s$ laminates are summarized in Tables 4 and 5. Further experimental analyses on the initiation of failure within anisotropic media with integrated rigid thick inclusions seem to be still necessary and would greatly improve the understanding of the effects of integrated electronics on the local integrity of layered composites providing essential information for the development of new, thin, and eventually flexible sensors, more compatible with the host composite and therefore with minimal effects on the material.

5. Concluding Remarks

The integrity and mechanical response of fiberglass composites with integrated structural health monitoring sensors and electronic components is presented in this work. Particularly, the damage initiation and identification have been observed by conducting monotonic tensile tests on samples while continuously monitoring their acoustic emissions. A series of micrographic inspections was also conducted. Our major experimental observations can be summarized as follows.

- (i) The mechanical response under quasistatic characterization of $[0]_n$ and $[(\pm 45)_5]_s$ laminates with integrated devices is substantially the same of that characterizing the material without integrated small

signal conditioning components. The tensile strength of $[0]_n$ and $[(\pm 45)_5]_s$ presents a negligible reduction with respect to that of the blank samples.

- (ii) The embedment process causes material and geometrical discontinuities within the composite laminate which creates large interlaminar eye-shaped resin pockets around the implant. Nonuniform fiber spacing is observed around these regions. The length of these resin-rich regions depends on the material lay-up. It is considerably smaller in nonzero degree fiber orientations.
- (iii) Sharp geometrical discontinuities and material inhomogeneities are responsible for localized values of the stress concentrations which affect the initiation of the failure and its development around the inclusion.
- (iv) Early acoustic events are detected at the sensor location at almost one quarter of the stress that is observed to induce acoustic activity in the material without implants. Moreover, the amplitude of the events acquired is usually higher than those noticed in samples without implants.
- (v) The frequency of the early events in $[0]_n$ blank samples is within a 100–180 kHz range and is mainly attributed to the growth of flaws and fiber pull-out, while those detected in samples with integrated

TABLE 4: Material without and with embedded inclusions: tensile strength and acoustic behavior.

| $[0]_n$ | Number of samples | σ_{FAE} Average (MPa) | DS** | CV %** | Strength Average (MPa) | DS | CV % |
|--------------------------------|-------------------|------------------------------|---------|--------|---------------------------------|------|------|
| Blank samples | 5 | 319.6 | 20.07 | 6.15 | 1729.4 | 40 | 2.33 |
| Samples with integrated device | 5 | 89.7 | 22.18 | 24.7 | 1685 | 39.9 | 2.37 |
| $[(\pm 45)_5]_s$ | Results | $^*\sigma_{tE}/\sigma_{tB}$ | 97.42 % | | $\sigma_{FAE-B}/\sigma_{FAE-E}$ | 3.56 | |
| | Number of samples | σ_{FAE} Average (MPa) | DS** | CV %** | Strength Average (MPa) | DS | CV % |
| Blank samples | 3 | 34.46 | 8.05 | 23.37 | 220 | 5.19 | 2.36 |
| Samples with integrated device | 3 | 12.53 | 1.61 | 12.89 | 229 | 5.03 | 2.19 |
| | Results | $^*\sigma_{tE}/\sigma_{tB}$ | 36.37% | | $\sigma_{FAE-B}/\sigma_{FAE-E}$ | 2.9 | |

* σ_{tE} : tensile strength of the material with integrated inclusion; σ_{tB} : tensile strength of blank samples; σ_{FAE-B} : stress at which the acoustic events start in blank samples; σ_{FAE-E} : stress at which the events begin in sample with embedded device.

**DS: Standard Deviation; CV: coefficient of variation; definitions according to ASTM 3039M.

TABLE 5: Material with and without integrated inclusions: stress, amplitude, and frequency range of the first acoustic events, and their classification. The lower and upper limits of each range are the lower and upper values observed among all the experiments conducted. Only the events in a stress window of about 20 MPa have been considered. Results from $[0]_n$ laminates [16] are here reported for comparison.

| Lay-up | Stress range of first AE events (MPa) | First AE Events Amplitude range (dB) | Peak Frequency of first AE events (kHz) | Event type classification based on micrographic inspections |
|-------------------------------------|---------------------------------------|--------------------------------------|---|---|
| Blank Samples $[0]_2$ | 320–400 | 35–60 | 100–180 | Matrix microcracking, fiber pull-out |
| Sample with device $[0]_6$ | 89–106 | 50–75 | 150–300 | Matrix micro-cracking at the sensor interface, debonding events |
| Blank Samples $[(\pm 45)_5]_s$ | 33–43 | 40–50 | 130–170 | Matrix micro-cracking, debonding, |
| Sample with device $[(\pm 45)_5]_s$ | 10–14 | 43–65 | 150–350 | Matrix micro-cracking at the sensor interface, debonding events, friction |

dummy microprocessors fall within a higher range of 150–300 kHz and are classified as matrix cracking and debonding phenomena. A series of micrographic inspections was conducted to support these observations.

- (vi) The frequency of the early events in $[(\pm 45)_5]_s$ samples without inclusions is within a 145–280 kHz range and is again attributed to the growth of flaws and fiber pull-out, and debonding, while that detected in samples with dummy microprocessors falls within a higher range of 150–350 kHz and is classified as matrix cracking and debonding phenomena at the inclusion-matrix interface with friction and debonding phenomena. A series of micrographic inspections was conducted to support these observations.

The experiments show that the failure initiates at the implant-composite resin interface by interface debonding and microcracks around the device due to the high values of interlaminar stress. Large flaws at the implant-composite resin interface that were not generally observed in samples inspected prior to testing indicate that high stresses were likely responsible for the interface failure. Moreover, no sign of damage at the same stress level was observed at the tip of the resin pocket.

6. Discussion

This paper describes the impact of integrated implants on the local integrity of nonzero fiber-laminated composites compared to zero fiber-oriented laminates of standard laboratory size samples. These results add fundamental details on the initiation of the failure at the interface implant-composite resin matrix. The aim of this work has been in fact the identification of the effects of the integration of electronics together with sensors into laminated composites in order to encourage a careful analysis and design optimization while developing smart materials. The embedded implants consist either in signal conditioning devices (chip resistors) or in microprocessors (not shown in this work) which are generally part of circuits to be integrated into the material. Notwithstanding the remarkable improvements achieved in the sensors technology so that miniaturized, thin, highly deformable, resin compatible, and high temperature resistance transducers may be commercially available, electronic devices (microprocessors) still represent rigid thick inclusions to the host material. Therefore, attempting to embed them in order to create material with a fully integrated sensing network still requires some attention. Even though still at laboratory level, this research seems to be not far to its implementation into civil and aerospace materials. Besides,

the analysis and quantification of the stress concentration and the interaction implant-composite can contribute enormously to the development of new electronic devices and sensors stimulating new fabrication techniques and procedures to minimize the impact of the implant on the specific material chosen. To date, there are no in-service components with fully integrated sensing systems hierarchically organized which monitor in real time the damage growth into the material. This fact is partially due to the many aspects and variables involved in the process that leads to the optimization of materials and components performance if in presence of integrated networks. Moreover, in general, the implementation of acoustic sensors seems to be a useful and well-established tool for successful passive and active damage detection with minimum number of sensors, reasonable memory usage, and therefore limited processors functions. In particular, we described the system that was developed taking into account such observations and that consists on a 4-tree hierarchical network of flexible PVDF sensors used for passive acoustic emission detection and connected to small microprocessors with limited memory. The processing functions that consist in location and classification of the damage events were possible using parametric features of the acquired acoustic signals. Minimization of issues due to stress concentration that can be induced by the presence of wires necessary to establish the connections among all sensors and electronics that constitute the network may be avoided by the implementation of systems based on wireless communication. Many of these aspects are currently under investigation.

We can conclude by emphasizing that the development of smart, multifunctional composite materials is possible but can be successful only if a proper sensors design, integration techniques, signal processing, data collection, and investigation of the limits of the material performance for actual components are considered.

Acknowledgments

The authors acknowledge the Center of Excellence for Advanced Materials, Department of Mechanical and Aerospace Engineering at the University of California San Diego, where the tensile tests on the S2/glass fiber samples were conducted, and the National Science Foundation, which supported this work under the Grant no. 0330450.

References

- [1] J. Warkentin and E. F. Cawley, "Embedded electronics for intelligent structures," in *Proceedings of the AIAA/ASME/ASCE/AHS/ASC 32nd Structures, Structural Dynamics and Materials Conference*, pp. 1322–1331, Baltimore, Md, USA, 1991.
- [2] K. S. Kim, M. Breslauer, and G. S. Springer, "Effect of embedded sensors on the strength of composite laminates," *Journal of Reinforced Plastics and Composites*, vol. 11, no. 8, pp. 949–958, 1992.
- [3] M. W. Holl and S. Boyd, "Effect of embedded fiber optics on the mechanical properties of a composite host material," in *Smart Structures and Materials 1993: Smart Materials*, vol. 1916 of *Proceedings of SPIE*, pp. 109–117, 1993.
- [4] J. S. Sirkis and H. Singh, "Moiré analysis of thick composites with embedded optical fibers," *Experimental Mechanics*, vol. 34, no. 4, pp. 300–305, 1994.
- [5] D. A. Singh and A. J. Vizzini, "Structural integrity of composite laminates with interlaced actuators," *Smart Materials and Structures*, vol. 3, no. 1, pp. 71–79, 1994.
- [6] D. R. Shukla and A. J. Vizzini, "Interlacing for improved performance of laminates with embedded devices," *Smart Materials and Structures*, vol. 5, no. 2, pp. 225–229, 1996.
- [7] S. Mall and J. M. Coleman, "Monotonic and fatigue loading behavior of quasi-isotropic graphite/epoxy laminate embedded with piezoelectric sensor," *Smart Materials and Structures*, vol. 7, no. 6, pp. 822–832, 1998.
- [8] C. A. Paget and K. Levin, "Structural integrity of composites with embedded piezoelectric ceramic transducer," in *Proceedings of the Smart Structures and Materials—Smart Structures and Integrated Systems*, Proceedings of SPIE, pp. 306–313, 1999.
- [9] J. P. Hansen and A. J. Vizzini, "Fatigue response of a host structure with interlaced embedded devices," *Journal of Intelligent Material Systems and Structures*, vol. 11, no. 11, pp. 902–909, 2000.
- [10] S. Mall and T. L. Hsu, "Electromechanical fatigue behavior of graphite/epoxy laminate embedded with piezoelectric actuator," *Smart Materials and Structures*, vol. 9, no. 1, pp. 78–84, 2000.
- [11] S. Mall, "Integrity of graphite/epoxy laminate embedded with piezoelectric sensor/actuator under monotonic and fatigue loads," *Smart Materials and Structures*, vol. 11, no. 4, pp. 527–533, 2002.
- [12] M. Lin and F. K. Chang, "The manufacture of composite structures with a built-in network of piezoceramics," *Composites Science and Technology*, vol. 62, no. 7-8, pp. 919–939, 2002.
- [13] K. Shivakumar and L. Emmanwori, "Mechanics of failure of composite laminates with an embedded fiber optic sensor," *Journal of Composite Materials*, vol. 38, no. 8, pp. 669–680, 2004.
- [14] K. Shivakumar and L. Emmanwori, "Failure mechanics of a composite laminate embedded with a fiber optic sensor," *Journal of Composite Materials*, vol. 39, no. 9, pp. 777–798, 2005.
- [15] M. N. Ghasemi-Nejhad, R. Russ, and S. Pourjalali, "Manufacturing and testing of active composite panels with embedded piezoelectric sensors and actuators," *Journal of Intelligent Material Systems and Structures*, vol. 16, no. 4, pp. 319–333, 2005.
- [16] F. Ghezzi, Y. Huang, and S. Nemat-Nasser, "Onset of resin micro-cracks in unidirectional glass fiber laminates with integrated SHM sensors: experimental results," *Structural Health Monitoring*, vol. 8, no. 6, pp. 477–491, 2009.
- [17] A. Dasgupta, Y. Wan, and J. S. Sirkis, "Prediction of resin pocket geometry for stress analysis of optical fibers embedded in laminated composites," *Smart Materials and Structures*, vol. 1, no. 2, pp. 101–107, 1992.
- [18] Y. Huang, F. Ghezzi, and S. Nemat-Nasser, "Onset of resin micro-cracks in unidirectional glass fiber laminates with integrated SHM sensors: numerical analysis," *Structural Health Monitoring*, vol. 8, no. 6, pp. 493–507, 2009.
- [19] F. Ghezzi, P. Rye, Y. Huang, and S. Nemat-Nasser, "Integration of sensing networks into laminated composites," in *Behavior and Mechanics of Multifunctional and Composite Materials*, vol. 6929 of *Proceedings of SPIE*, pp. V.1–V.4, 2008.

- [20] I. M. Daniel and O. Ishai, *Engineering Mechanics of Composite Materials*, Oxford University Press, Oxford, UK, 2006.
- [21] ASTM E976-00, "Standard guide for determining the reproducibility of acoustic emission sensor response".
- [22] S. C. Tan, *Stress Concentration in Laminated Composites*, Technomic, 1994.
- [23] S. G. Lekhnitskii, *Anisotropic Plates*, Gordon and Breach, New York, NY, USA, 1968.
- [24] J. C. Radon and A. A. Pollock, "Acoustic emissions and energy transfer during crack propagation," *Engineering Fracture Mechanics*, vol. 4, no. 2, pp. 295–310, 1972.
- [25] A. A. Pollock, "Acoustic emission-2 acoustic emission amplitudes," *Non-Destructive Testing*, vol. 6, no. 5, pp. 264–269, 1973.
- [26] M. A. Gorman and W. H. Prosser, "AE source orientation by plate wave analysis," *Journal of Acoustic Emission*, vol. 9, no. 4, pp. 283–288, 1991.
- [27] W. H. Prosser, M. A. Gorman, and D. H. Humes, "Acoustic emission signal in thin plates produced by impact damage," *Journal of Acoustic Emission*, vol. 17, no. 1-2, pp. 29–36, 1999.
- [28] PCI-2 Based AE System User's Manual Physical Acoustic Corporation.
- [29] ASTM D 2584-02, "Standard test methods for ignition loss of cured reinforced resins".
- [30] X. Zhuang and X. Yan, "Investigation of damage mechanisms in self-reinforced polyethylene composites by acoustic emission," *Composites Science and Technology*, vol. 66, no. 3-4, pp. 444–449, 2006.
- [31] S. C. Woo and N. S. Choi, "Analysis of fracture process in single-edge-notched laminated composites based on the high amplitude acoustic emission events," *Composites Science and Technology*, vol. 67, no. 7-8, pp. 1451–1458, 2007.
- [32] P. J. De Groot, P. A. M. Wijnen, and R. B. F. Janssen, "Real-time frequency determination of acoustic emission for different fracture mechanisms in carbon/epoxy composites," *Composites Science and Technology*, vol. 55, no. 4, pp. 405–412, 1995.

Research Article

IEEE 802.11-Based Wireless Sensor System for Vibration Measurement

Yutaka Uchimura,¹ Tadashi Nasu,² and Motoichi Takahashi²

¹ Shibaura Institute of Technology, 3-7-5 Toyosu, Koto-ku, Tokyo 135-8548, Japan

² Kajima Corporation, 1-3-1 Motoakasaka, minato-ku, Tokyo 107-0051, Japan

Correspondence should be addressed to Yutaka Uchimura, uchimura@sic.shibaura-it.ac.jp

Received 15 October 2009; Revised 17 December 2009; Accepted 15 January 2010

Academic Editor: Yi Qing Ni

Copyright © 2010 Yutaka Uchimura et al. This is an open access article distributed under the Creative Commons Attribution License, which permits unrestricted use, distribution, and reproduction in any medium, provided the original work is properly cited.

Network-based wireless sensing has become an important area of research and various new applications for remote sensing are expected to emerge. One of the promising applications is structural health monitoring of building or civil engineering structure and it often requires vibration measurement. For the vibration measurement via wireless network, time synchronization is indispensable. In this paper, we introduce a newly developed time synchronized wireless sensor network system. The system employs IEEE 802.11 standard-based TSF-counter and sends the measured data with the counter value. TSF based synchronization enables consistency on common clock among different wireless nodes. We consider the scale effect on synchronization accuracy and evaluated the effect by taking beacon collisions into account. The scalability issue by numerical simulations is also studied. This paper also introduces a newly developed wireless sensing system and the hardware and software specifications are introduced. The experiments were conducted in a reinforced concrete building to evaluate synchronization accuracy. The developed system was also applied for a vibration measurement of a 22-story steel structured high rise building. The experimental results showed that the system performed more than sufficiently.

1. Introduction

Rapid progress of wireless network technology and embedded sensor technology has been integrated into wireless sensor network and various prospective applications are expected to emerge. Among the many sensing network applications, particularly promising one is the structure health monitoring, which monitors the structural health of buildings and civil engineering structures [1]. Since measuring objects such as a bridge and a building are usually huge and installing very long signal cables requires high installation cost. Additionally, long cables leave wires vulnerable to ambient signal noise corruption, thus wireless data transmission is highly beneficial. Structure health monitoring often requires measuring vibration data such as acceleration and velocity. Measured data are analyzed by the modal analysis method to obtain the resonance frequency, damping ratio and spectrum response [2].

For wireless vibration measurements, time synchronization is very important because the vibration measurement for the modal analysis requires simultaneous multipoint sensing data which are often transmitted via multihop relayed wireless devices. Due to the queuing process and stochastic media access method, the data transmissions are randomly delayed. As a result, even if each sensor node acquires data and sends them exactly at the same instant, the arrival time of the data does not match. To avoid it, the received data needs to be adjusted so as to maintain the time consistency on a common time axis. Because when the data are used for modal analysis, a time difference may be misunderstood as a phase shift. To maintain precise time consistency among wireless nodes, time synchronization is indispensable.

In this paper we propose a synchronization method for wireless sensor network system, which utilizes IEEE 802.11-based timing synchronization function (TSF). The function

is a mechanism for synchronizing local timer counter of each wireless device, which is originally used for contention control among wireless node. By embedding the value of TSF counter in a packet with measured data, one can solve the time skew problem on the receiver side.

In the following section, we briefly review the related works. Section 3 describes the adverse effects on vibration sensing caused by a time delay in wireless network and denotes the reason why time synchronization is needed. Section 4 describes a probability of timing synchronization beacon transmission. The section also describes stochastic analysis and simulation studies on the scalability of sensor network. In Section 5, we describe a newly developed wireless sensing system and also describe its hardware and software components. In Section 6, experimental evaluations of time synchronization accuracy and vibration measurement data in a high rise building are presented.

2. Related Works

Time synchronization of network is indispensable to manage transmission timing and to avoid wasteful collisions, therefore several technologies such as GPS, radio ranging have been used to provide global synchronization in networks. GPS-based synchronization offers very precise synchronization, however it is not always available indoor place [3]. In wired network, the Network Time Protocol (NTP) has been developed that has kept the Internet's clocks ticking in phase [4].

RT-Link [5] uses media access control (MAC) based on slotted ALOHA and it employs independent AM carrier-current radio device for indoor time synchronization. However, carrier-current AM is only allowed on the school campus in the United States, so long as the normal FCC Part 15. [6] Berkeley MAC (B-MAC) supports carrier sense multiple access (CSMA) with low power listening where each node periodically wakes up after a sample interval and checks the channel for activity for a short duration. The main concern of these methods is battery life, because time synchronization is one of the most important factors to determine radioactive period, which directly affects battery life. There have been many studies on time synchronization which mainly aimed for conserving battery energy of network nodes.

Meanwhile, IEEE 802.11 [7] standard devices have a timing synchronization function (TSF) by default. We propose to utilize the function for synchronization among nodes to determine the sampling data interval and the time stamping of measured data. IEEE 802.11 is one of the de facto standards of the wireless local area network and so is easily obtained with industrial-level reliability. Furthermore, the modulation employs Direct Sequence Spread Spectrum (DS-SS) and Orthogonal Frequency Division Multiplexing (OFDM) which offer robustness against phasing and noise. Those are advantages against RT-Link and Berkeley Mote which use noise susceptible wireless modulation.

Some studies pointed out the scalability issue on IEEE 802.11 TSF [8] and new protocols such as SATSF [9] and MATSF [10] were proposed to achieve very accurate clock synchronization; however they are still on the research

level and not implemented on market ready products. Even though the current 802.11 TSF is involved with the scalable issue, it depends on the scale and the requirement of accuracy of the application. Our targeted application uses less than 100 nodes and required accuracy is around 1 to 10 milliseconds. Additionally, thanks to the progress of the wireless technology, the synchronization error rates are decreased and consequently accuracy is improved comparing to the results shown in [8].

We made simulation-based analyses and verified that even the original 802.11 TSF is accurate enough for vibration measurement.

3. Time Delay on Wireless Network

The data transmission via a wireless network requires certain amount of time elapsing from the moment when the transmitter sends the data to the moment when the data arrives at the receiver. In the building vibration measurement applications, sensors usually need to be placed at several points on different floors in a building. A measurement station (host computer) is placed at a certain location in the building. In such cases, especially in a high rise building, the wireless radio waves of each sensor node do not directly reach the station. Thus, the multihop network path is required and the packets are transmitted in relays of the wireless sensor nodes.

Therefore, even if all the nodes intend to send packets at exactly the same time, the arrival times may be different. This fact results serious problem when measured data are used for modal analysis, because time delay may cause unexpected fake mode. Therefore we somehow need to maintain consistency of received data on the common time axis.

To resolve this issue, we propose to send the vibration data together with the time stamp at the moment when the data is measured. After the data are received at the host PC, they can be rearranged along the common time axis based on the time stamp. This procedure is valid provided that all clocks of the nodes are matched. However, accuracy of the quartz crystal oscillator is affected by many factors such as temperature and change of current or voltage [11]. Frequency stability of oscillators used for PCs is mostly around 10^{-4} (100 ppm). Imprecision of 100 ppm corresponds to a 1 millisecond (10 msec) error in 10 seconds, or an 18-degree phase error for 100 Hz vibration. Even though the resonant frequency of a building is low (typically less than 10 Hz), a 1 msec difference between the fastest clock and the slowest clock is more than negligible amount. Therefore, periodical time synchronization is indispensable and accuracy of the synchronization is the matter of concern.

4. Synchronization Issue on Scalability

4.1. IEEE 802.11-Based TSF Mechanism and Contention Process. The accuracy of the synchronization is one of the most concerning issues in wireless sensor networks. As described in the previous section, we use IEEE 802.11-based TSF. IEEE 802.11 based TSF synchronizes the clock

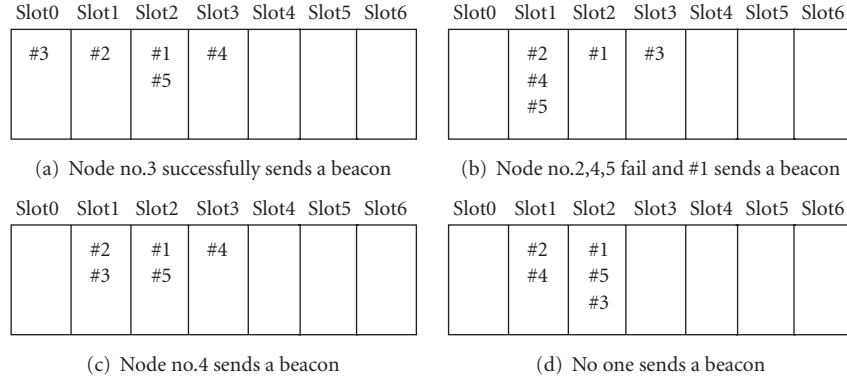


FIGURE 1: Slot allocation and transmission contention.

in stochastic manner, that is, the synchronization contains random factors. As a result, the accuracy can only be evaluated by probability analysis. Before describing the detail of the analysis, we briefly describe the mechanism of TSF.

Suppose there are several nodes within the radio range, which can communicate each other and they form independent basic service set (IBSS). Each node ticks its own TSF counter (64 bit) by 1 nanosecond. The nodes in the IBSS contend a right to send a beacon and one or more nodes becomes eligible to send a beacon. In each beacon transmission period, several slots are prepared and each node is randomly assigned into a certain slot as shown in Figure 1, where no. 1 or no. 2 denotes the number of node. Each slot may hold none or one or more nodes. In the beginning of each beacon transmission period, the nodes in the least slot number send a beacon which contains TSF counter value. If there exist only one node in the slot, the beacon packet is successfully sent (Figure 1(a)) and the other node adjust their TSF counter only if the received value of the TSF counter is larger than the received value. If the received value is smaller, the nodes do not adjust own counter.

On the other hand, if there are two or more nodes in the same slot as shown in Figure 1(b), they start transmitting a beacon packet in the same time, thus the beacon packets collide and transmission results to fail. If it fails, the nodes in the second least slot number transmit a beacon. In Figure 1(b) case, node #1 sends a beacon without collision. These sequences are repeated as long as available slots remain. It may happen that no successful beacon transmission during the beacon period as shown in Figure 1(d), they need to wait for next beacon period (typically 100 milli-seconds later).

In Figure 1 case, we suppose 5 nodes and 7 slot spaces; however one may easily imagine that the chance of successful beacon transmission decreases if the number of nodes increases, while the number of slots is limited. The successful rate depends on the number of nodes and slots. Because the slot allocation is randomly determined, analysis based on probability theory is required.

Huang and Lia [8] pointed out the issue and showed analyses and simulation results on the synchronization error. The paper offered great contribution for the probabilistic analysis; however the specification of the device is obsolete.

For example, the bit-rate in the simulation is fixed to 1 Mbps because it was the maximum speed at that time.

In order to match up to current technology and give a prospective aspect of 802.11-based time synchronization, we made analysis on scalability effect of IEEE 802.11 a/b/g standard based sensor stations. In the followings, we describe the probability theory-based formulas of success rate of the beacon transmission. Then we show results of the numerical analysis in case of various bit rates, modulations and number of wireless stations.

4.2. Probability of Successful Beacon Transmission. In IEEE 802.11 standards, the number of the slots is $2 \cdot \text{aCWmin} + 1$ and each node is scheduled to transmit a beacon at the beginning of one of the slots, where aCWmin is the minimum contention window for the media. The value of aCWmin is 31 in Direct Sequence Spread Spectrum (DSSS) and 15 in Orthogonal Frequency Division Multiplexing (OFDM).

Let us suppose the length of a beacon is L_b (bit), the transmission bit rate is T_r (Mbps) and the time length of a slot time is S_t (μ sec), the integer number of slots occupied by a beacon (N_s) is obtained in (1),

$$\frac{L_b}{T_r S_t} \leq N_s \leq \frac{L_b}{T_r S_t} + 1, \quad (1)$$

where N_s can be also obtained by roundup function of $L_b/T_r S_t$.

Once a beacon transmission starts, other nodes need to be quiet for the time length of N_s slots. If a beacon transmission fails, they resume counting down the back-off timer and contending for the remaining slots. If the collisions occur by m times in series and all available slots are consumed, that is, corresponds the condition in (2) becomes true, the beacon transmission trials fell through

$$2 \cdot \text{CWmin} + 1 - m \cdot N_s \leq 0. \quad (2)$$

As stated above, the beacon transmission is not deterministic, thus we need to analyze it by stochastic manner.

First of all, let us reconfirm the definition of successful beacon transmission. We define that a beacon is transmitted

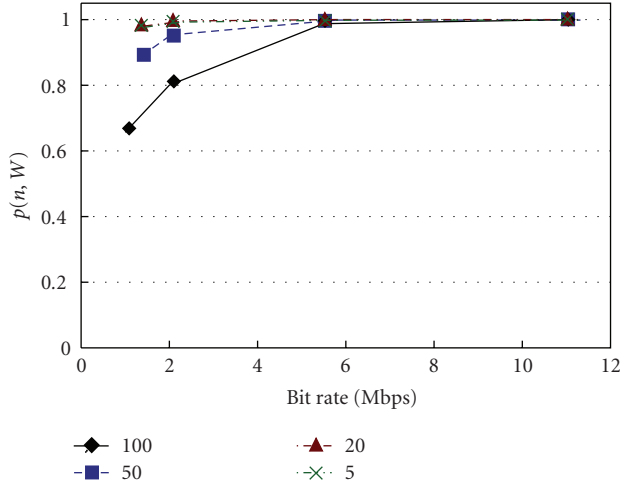


FIGURE 2: Successful beacon transmission rate of 802.11b.

TABLE 1: Specifications of 802.11a/b/g.

| | aCWmin | Bit Rate (Mbps) (min-max) | Slot Time (μ sec) |
|---------|--------|------------------------------|------------------------|
| 802.11a | 15 | 6-54 | 9 |
| 802.11b | 31 | 1-11 | 20 |
| 802.11g | 15 | 6-54 | 9/20 |

successfully if at least one node transmits a beacon successfully during a beacon transmission period. Suppose that the IBSS consists of n nodes and let W be twice the minimum contention window ($W = 2 \cdot \text{aCWmin}$). Let $p(n, W)$ be the probability that at least one of the n nodes succeeds in a beacon transmission, then $p(n, W)$ is given by the recursive formula shown in (3):

$$p(n, W) = \left(\frac{W}{W+1}\right)^n p(n, W-1) + n \left(\frac{1}{W+1}\right) \left(\frac{W}{W+1}\right)^{n-1} + q(n, W). \quad (3)$$

The first term corresponds to the probability of the event that there is no beacon transmission in slot 0, while there is a successful beacon transmission in window $[1, W]$. The second term corresponds that there is a successful beacon transmission in slot 0. The third term $q(n, W)$ is the probability that there is unsuccessful transmission in slot 0, but at least one beacon transmission in window $[1, W]$. The formula for $q(n, W)$ is shown in (4):

$$q(n, W) = \sum_{i=2}^n \sum_j^{n-i} \left\{ C_i^n C_j^{n-i} \left(\frac{W}{W+1}\right)^i \left(\frac{N_s-1}{W+1}\right)^j \left(\frac{W-N_s+1}{W+1}\right)^{n-i-j} p(n-i-j, W-N_s) \right\}, \quad (4)$$

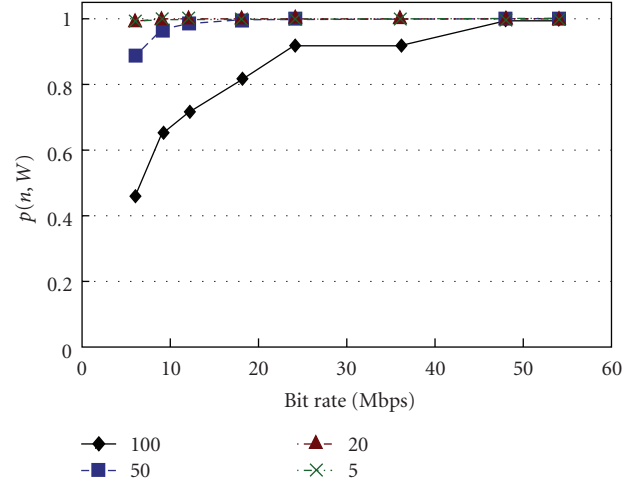


FIGURE 3: Successful beacon transmission rate of 802.11g (20 microsec).

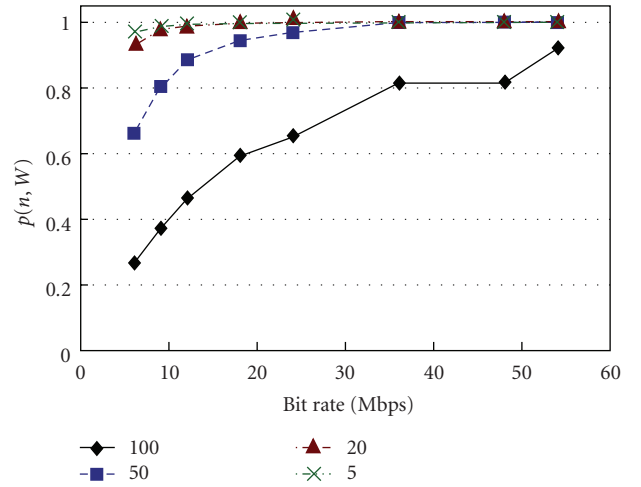


FIGURE 4: Successful beacon transmission rate of 802.11a/ pure g (9 microsec).

where C_k^n is the combination number defined in (5):

$$C_k^n = n(n-1) \cdots \frac{n-k+1}{k!}. \quad (5)$$

4.3. Numerical Analysis on Probability of Beacon Transmissions. Based on the formulas shown in (3) and (4) the probability can be calculated for given n , W , and N_s . Notice that W has a different value depending on the modulation type, which is 63 in DSSS and 30 in OFDM. In IEEE std. based wireless network, 802.11a and 802.11g use OFDM and 802.11b uses DSSS.

N_s defined in (1) is determined based on bit rate T_r (bps), the length of a beacon L_b (bit) and slot time S_t (μ sec). Values of these parameters and their ranges are shown in Table 1.

The slot time for 802.11g is 20 (μ sec) when there is 802.11b node within the radio range, while the slot time of

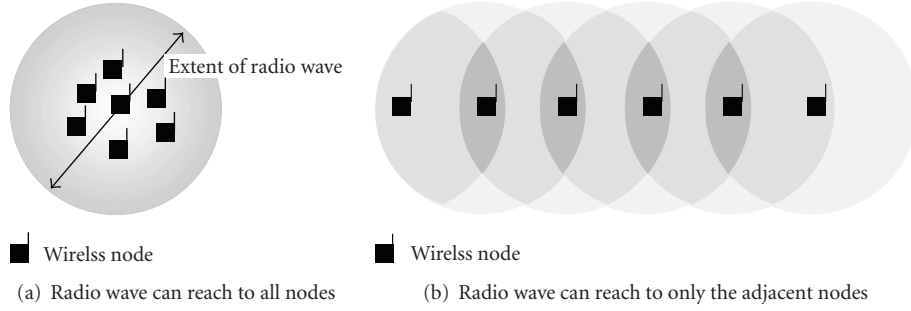
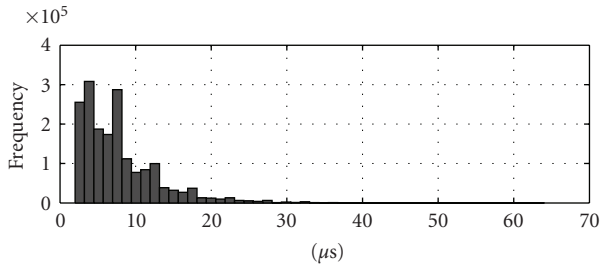
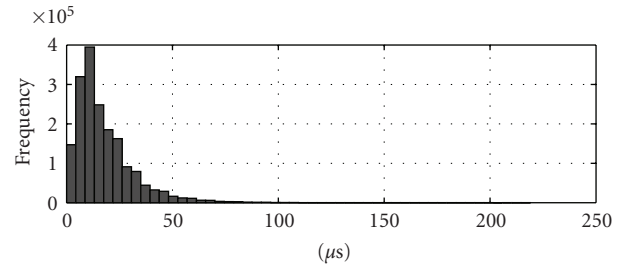


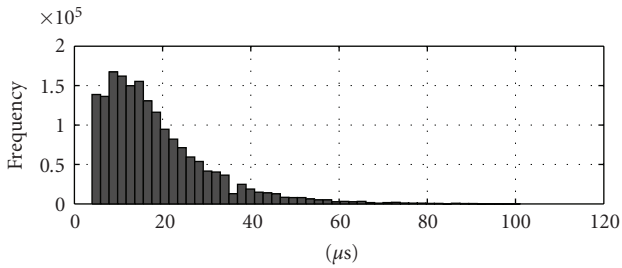
FIGURE 5: Configuration of wireless nodes.



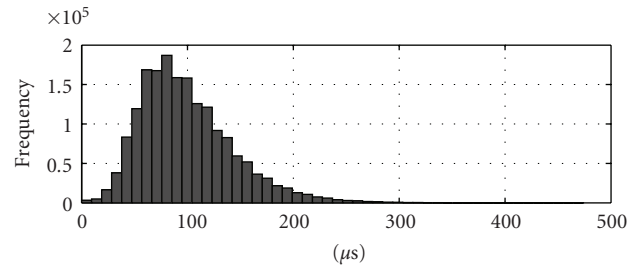
(a) Case 1: Maximum Offset in 5 nodes (microsec)



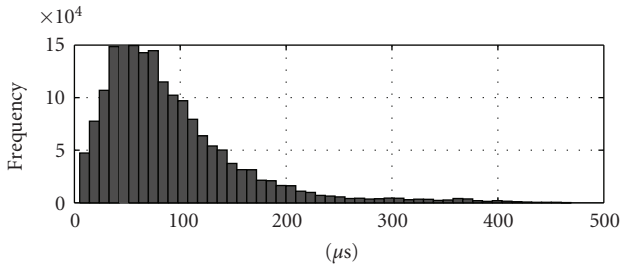
(a) Case 2: Maximum Offset in 5 nodes (microsec)



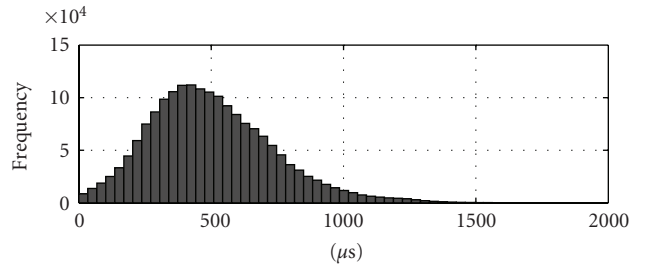
(b) Case 1: Maximum Offset in 20 nodes (microsec)



(b) Case 2: Maximum Offset in 20 nodes (microsec)



(c) Case 1: Maximum Offset in 100 nodes (microsec)



(c) Case 2: Maximum Offset in 100 nodes (microsec)

FIGURE 6: Histogram of the maximum offset value in Case 1.

FIGURE 7: Histogram of the maximum offset value in Case 2.

a pure 802.11g network is 9 (μsec). Length of a beacon depends on the size of contained information. For example, length of the service set ID is between 2 and 34 bytes, the length of supported rates and the extended supported rate are also variable. In the simulation, we assumed the length of a beacon is 110 bytes which is the real beacon size of a prototype system.

Substituting (4) into (3) gives recursive equation of $p(n, W)$. Using the boundary condition $p(0, W) = p(n, 0) = 0$, $p(n, W)$ is calculated for given N_s .

Figures 2, 3, and 4 shows the results of calculation of the probability rate of successful beacon transmission $p(n, W)$. The horizontal axis is bit rates and each plot line shows the case of different number of nodes.

Figure 2 is the result of 802.11b. Figure 3 is the result of 802.11g with 20 μsec slot time and Figure 4 is the result of 802.11 a/g with 9 μsec . As shown in three graphs, the rates increase in larger bit rates. On the other hand, the rate decreases with growth of number of nodes. Another aspect of the results shows that the short slot time deteriorates

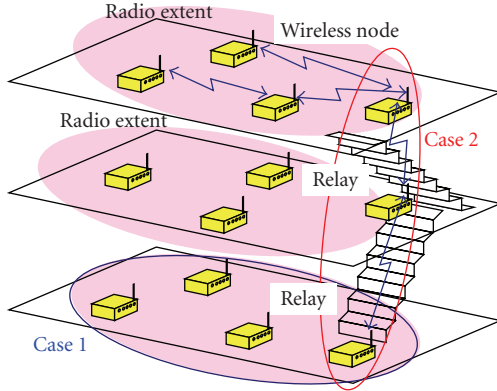


FIGURE 8: Measurement configuration in a building as mixture of Cases 1 and 2.

the beacon successful rate $p(n, W)$, which is observed in comparison of Figures 3 and 5 (802.11g with short slot time). This is because number of occupied slots increases for shorter slot time or low bit rate, and chance of beacon transmission become smaller.

In the case of 802.11a/g with $9 \mu\text{sec}$, $p(n, W)$ drops down to 0.26 for 100 nodes, which is the minimum rates among the results. Considering these results, we made numerical simulations to evaluate the synchronization accuracy.

4.4. Simulations on Synchronization Accuracy. In the TSF-based synchronization, a node which receives a beacon adjusts its TSF counter to the time stamp of the received beacon if the value of the time stamp is later than the node's TSF counter. (It is important to note that clocks only move forward and never backward). Possibility of chance to send a beacon is equal, thus the node whose clock is fastest seldom gain a chance to adjust one's clock to others. As a result, the offset of TSF (the difference of TSF counter between the fastest node and the slowest node) becomes large as the number of nodes in the IBSS grows.

The offset of TSF also strongly depends on the configuration of nodes in the segment. Therefore we classified them into two configuration cases.

Case 1. All nodes exist within the range that radio waves can reach (Figure 5(a)), that is, each node can send a beacon directly to any other nodes.

Case 2. All nodes are arranged so that radio waves can reach two adjacent nodes only (right and left nodes). Figure 5(b) illustrates the allocation of nodes. End-to-end communication is possible only through multihop relays.

Numerical simulations were set up for the two configuration cases. In addition, the probability of beacon transmission which is analyzed in the previous subsection is taken into account in Case 1, while it is not in Case 2. Because a beacon transmission is contended with only adjacent nodes in Case 2, the beacon transmission rate is always almost 100%.

TABLE 2: Hardware specifications of a wireless node.

| | Specification |
|------------------|-------------------------|
| CPU | CPU Geode GX1 300 MHz |
| Chip set | NS Geode 5530A |
| Motherboard | 3.5-inch SBC/NS |
| RAM | SODIMM 256 MB |
| External Storage | Compact Flash |
| Extension Bus | PC104 |
| Wireless LAN | NEC WL54AG |
| Wireless Chip | Atheros 5001X |
| A/D Converter | 16CH, 16 bit Resolution |

We run the simulations assuming that TSF clock frequencies were uniformly distributed in the range of ± 50 ppm ($\pm 5.0 \times 10^{-5}$) and the beacon interval was assumed to be 100 msec. Each simulation trial was conducted for corresponding to 180 seconds elapse of time. In each trial, the TSF clock speed of each node was randomly selected and the total number of trials was 1000 times, which was large enough for data convergence. During the simulation, we recorded the maximum offset which corresponds to the difference between the fastest clock and the slowest clock at each beacon interval. (Notice that the slowest clock does not indicate a clock of specified node.)

Figure 6 shows the results of Case 1 simulation of pure 11g (or 802.11a) with 6 Mbps which is least successful rate of transmission. Figure 6(a) is the case when the total number of nodes is 5 with successful rate 0.969, Figure 6(b) is the case of 20 nodes with successful rate 0.924 and Figure 6(c) is the case of 100 nodes with successful rate 0.262, cf. $p(n, W)$ in Figure 4.

As shown in the figures, the accuracy of time synchronization gets worse as the number of nodes increases. In 5-node case, 99.9% of the data maintained less than $36 \mu\text{sec}$, $87 \mu\text{sec}$ in 20-node, and $428 \mu\text{sec}$ in 100-node case. The median value of 5-node was $6 \mu\text{sec}$, that of 20-node case is $15 \mu\text{sec}$ and $75 \mu\text{sec}$ in 100 case.

Figure 7 shows the results of Case 2. Figure 7(a) is the case of 5 nodes; Figure 7(b) is that of 20 nodes and Figure 7(c) shows 100-node case. The median value in 5-node case was $14 \mu\text{sec}$, $92 \mu\text{sec}$ in 20-node case, and $475 \mu\text{sec}$ in 100-node case. In 5-node case, 99.9% of the data maintained less than $104 \mu\text{sec}$, $303 \mu\text{sec}$ in 20-node, and $1388 \mu\text{sec}$ in 100-node case.

Comparing the results of Cases 1 and 2, daisy chain configuration like Case 2 is inferior in synchronization accuracy even though the beacon successful rate is less than 30%.

In vibration measurement for a building or a civil structure, wireless device allocation is likely to be a mixture of Cases 1 and 2. As illustrated in Figure 8, several wireless nodes are located on the same floor and one of them relays packets to the nodes on a different floor. The relay nodes (Case 2) are located in the staircase area. Because the radio power is much attenuated when passing a reinforced concrete

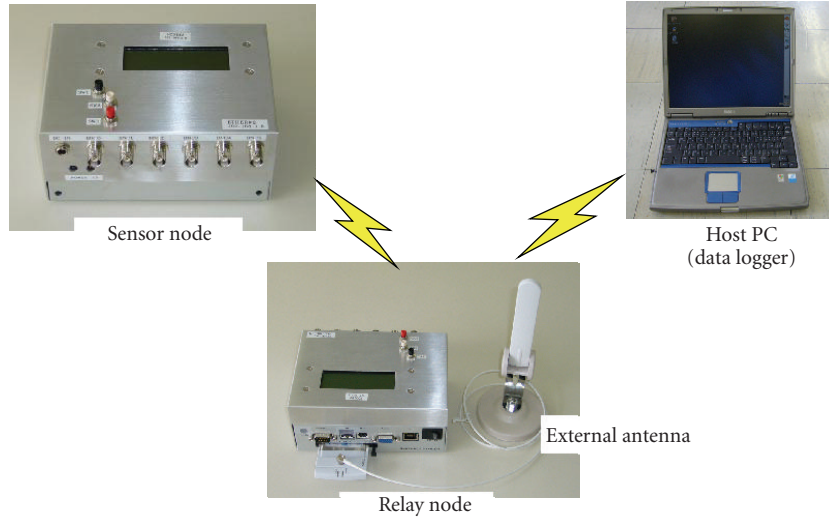


FIGURE 9: Basic components of the developed vibration measurement system.



FIGURE 10: Reinforced concrete building where experiment were conducted.

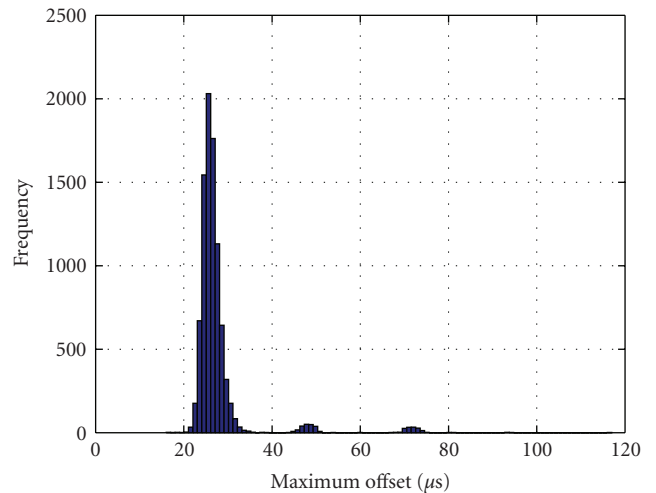


FIGURE 12: Maximum clock offset with three wireless nodes.

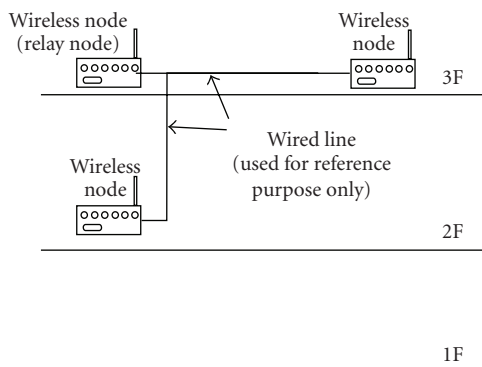


FIGURE 11: Allocation of wireless node.

floor, thus nodes in the different floor can communicate only via Case 2 relay nodes.

The target synchronization accuracy is to maintain within 1 msec. From the simulation results, synchronization accuracy was maintained even when the total number of nodes less than 100 nodes.

5. Development of Wireless Measurement System

We developed a wireless embedded measurement system which can be applicable for vibration measurement. Figure 9 is a photo of basic components of the vibration measurement system which consists of a sensor node, a relay node and a host PC. The sensor node and relay node have identical architecture. Size of a node device is 120×70×50 (mm). Main components and their functions of the wireless node are briefly shown in Table 2. The A/D converter has 16CH single end input and 6CH of them are supplied via the BNC jacks. The sampling rate of A/D depends on the measurement object. In the building measurement case, it is at most 100 Hz. It is for conducting the over sampling with digital filters, even though the resonance frequency of a building is less than 10 Hz. The power consumption of a node is typically 7.5 W.

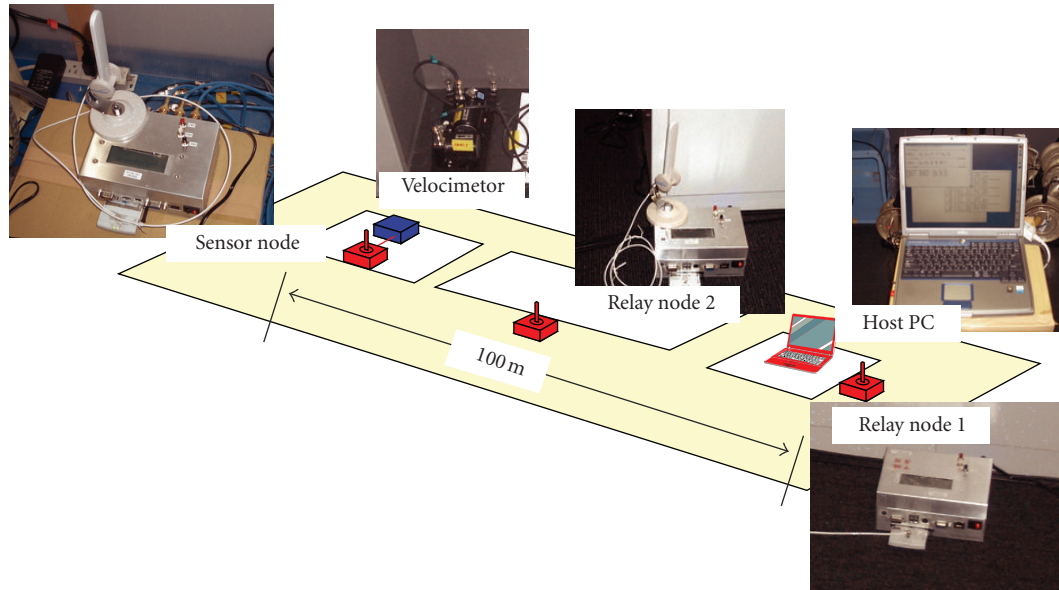


FIGURE 13: Allocation and photos of sensor node, relay node and Host PC.

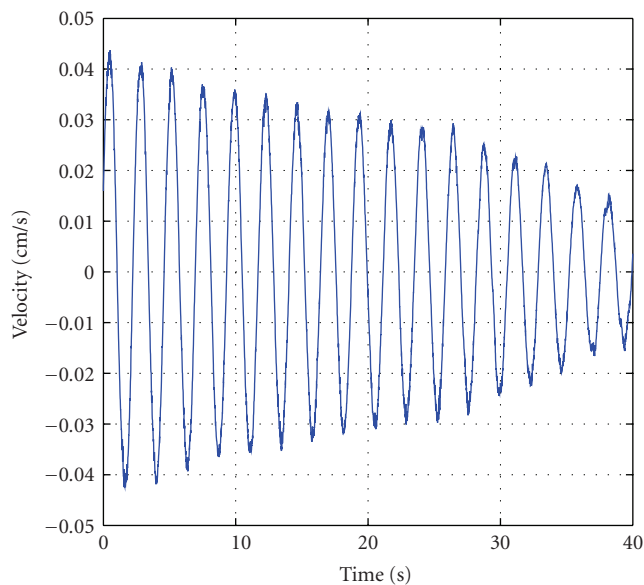


FIGURE 14: Measurement result by the developed wireless system.

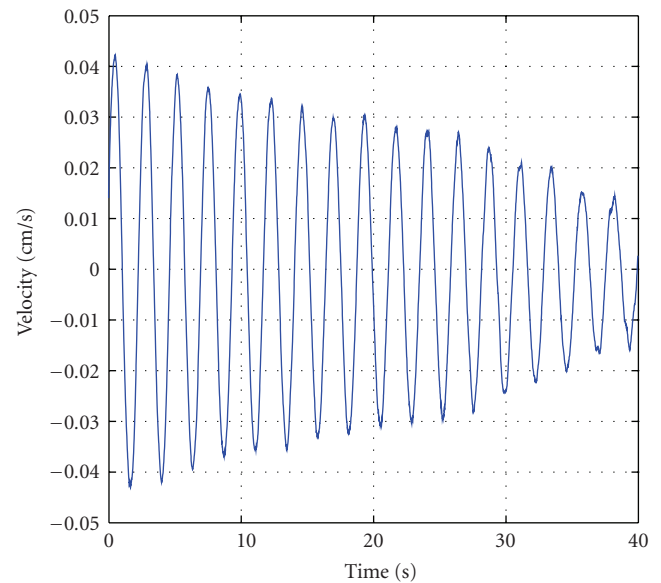


FIGURE 15: Measurement result by the conventional wired data logger.

In this system, sensors are not embedded within it. Because the vibration sensing uses various sensors such as accelerometers or velocity sensors depending on the structure of the buildings, separation of sensor, and wireless node makes it more versatile.

The operating system (OS) for a wireless node is RT-Linux, which is an extension of Linux to a real-time operating system. Software including OS is implemented in a flash memory and the memory can also store measured data. For a wireless device we used IEEE 802.11a/b/g standard wireless network interface card to which an external antenna can be connected.

6. Experimental Evaluation of Synchronization Accuracy

6.1. Experimental Evaluation of Synchronization Accuracy. For the purpose of evaluating TSF-based synchronization, we made experiments in a three-story reinforced concrete building (Figure 10). As well known, the wireless transmission may not go through the reinforced concrete because the mesh of rebar shields the radio waves. Therefore relay nodes are indispensable. The allocation of wireless node is depicted in Figure 11. We used three wireless nodes which were arranged to make two-hop transmission, that is,

the end-to-end communication packets were relayed via the relay node. Wired signal lines were connected to all nodes for the reference purpose and rectangular wave voltage was supplied on the lines to generate hardware interrupt. Every moment when the voltage of square wave rose, an interrupt occurred exactly at the same moment in three wireless nodes. And TSF count was recorded in the hardware interrupt handler routine.

We evaluated the synchronization accuracy by comparing recorded TSF counter of three nodes. The frequency of square wave was set to 10 Hz, that is, the TSF counter value was recorded every 100 msec. One measurement was continued for 15 minutes thus total number of TSF record sets was 9,000. After the measurement, the maximum offset between recorded set was calculated. We made totally 15 times of 15-minute measurements, thus total number of samples were 135,000.

Figure 12 shows the result of the maximum offset of TSF count, which corresponds to synchronization accuracy. As shown the figure, the median value was 27 μ sec. The result is close to the simulation result of Case 2 in 5 nodes. The simulation analysis did not take account for any processing time and bit error rate. Therefore, the experimental results must be more realistic when implementing on a real hardware. Nevertheless, the result shows sufficiently accurate synchronization and it maintained good enough accuracy against targeted 1 msec accuracy.

6.2. Vibration Measurement in a High Rise Building. We also conducted experimental measurements by using the developed wireless system. The vibration measurement was taken placed in a steel structured 22-story building. Figure 13 shows the allocation of the sensor node, relay nodes and host PC in the measurement room. A velocimeter (velocity sensor) on 22th floor is connected to the measurement node by a coaxial signal cable. The distance between the sensor node and the host PC was about 100 m and the path includes areas partitioned by a steel door and some over-the horizon corners. Thus, we allocated two relay nodes for hooking up the ad-hoc network.

The velocity data was also recorded with conventional wired measurement. Figure 14 shows the measured data of the developed wireless system and Figure 15 shows the data of the conventional wired data logger. The data are damped vibration wave obtained during the forced shaking test. When comparing these two results, the response near the peak of sinusoidal wave is a little bit jaggy in Figure 14 while it is smooth in Figure 15. This is because the difference of the cut-off frequency of the low pass-filters. Except that the data plot almost exactly match. The resonant frequency obtained from both data was 0.425 (Hz) and damping ratio was 0.672 (%). These two values obtained by both methods (wired/wireless) were also matched up to three significant figures.

7. Conclusion

For the vibration measurement via wireless network, time synchronization is indispensable. In this paper, we proposed

a new time synchronized wireless sensor network system which employed IEEE 802.11 standard-based TSF counter. It ensured consistency on the common clock among different wireless nodes. The scale effect on the accuracy when the size of nodes increased was evaluated by simulation studies and the result outlined the size which maintains the offset within 1msec. We also described a newly developed wireless sensing system and showed experimental evaluations, which were conducted in a reinforced concrete building. The system was also applied for the vibration measurement of a 22-story steel structured high rise building. The experimental results showed good performance enough for vibration measurement purpose.

References

- [1] J. P. Lynch, et al., "Post-seismic damage assessment of steel structures instrumented with self-interrogating wireless sensors," in *Proceedings of the 8th National Conference on Earthquake Engineering*, pp. 18–22, 2006.
- [2] Y. Wang, et al., "Vibration monitoring of the voigt bridge using wired and wireless monitoring systems," in *Proceedings of the 4th China-Japan-US Symposium on Structural Control and Monitoring*, 2006.
- [3] H. El Natour, et al., "Analysis of the GPS acquisition environment: indoors and outdoors," in *Proceedings of the 2nd International Conference on Information and Communication Technologies*, vol. 1, pp. 127–132, 2006.
- [4] D. L. Mills, "Internet time synchronization: the network time protocol," in *Global States and Time in Distributed Systems*, IEEE Computer Society Press, New York, NY, USA, 1994.
- [5] A. Rowe, R. Mangharam, and R. Rajkumar, "RT-Link: a time-synchronized link protocol for energy-constrained multi-hop wireless networks," in *Proceedings of the 3rd Annual IEEE Communications Society on Sensor and Adhoc Communications and Networks*, vol. 2, pp. 402–411, Reston, Va, USA, September 2006.
- [6] J. Polastre, J. Hill, and D. Culler, "Versatile low power media access for wireless sensor networks," in *Proceedings of the 2nd International Conference on Embedded Networked Sensor Systems (SenSys '04)*, pp. 95–107, 2004.
- [7] ANSI/IEEE Std 802.11, 2007, <http://standards.ieee.org/getieee802/download/802.11-2007.pdf>.
- [8] L. Huang and T.-H. Lai, "On the scalability of IEEE 802.11 ad hoc networks," in *Proceedings of the 3rd International Symposium on Mobile Ad Hoc Networking and Computing (MobiHoc '02)*, pp. 173–182, June 2002.
- [9] D. Zhou and T.-H. Lai, "A compatible and scalable clock synchronization protocol in IEEE 802.11 ad hoc networks," in *Proceedings of the International Conference on Parallel Processing*, pp. 295–302, 2005.
- [10] D. Zhou and T.-H. Lai, "A scalable and adaptive clock synchronization protocol for IEEE 802.11-based multihop ad hoc networks," in *Proceedings of the International Conference on Mobile Adhoc and Sensor Systems Conference*, pp. 8–17, 2005.
- [11] M. D. Lemmon, J. Ganguly, and L. Xia, "Model-based clock synchronization in networks with drifting clocks," in *Proceedings of the Pacific Rim International Symposium on Dependable Computing*, pp. 177–184, 2000.

Research Article

Casing Pipe Damage Detection with Optical Fiber Sensors: A Case Study in Oil Well Constructions

Zhi Zhou,^{1,2} Jianping He,¹ Minghua Huang,¹ Jun He,¹ and Genda Chen²

¹ School of Civil Engineering, Harbin Institute of Technology, Harbin, Heilongjiang 150090, China

² Center for Infrastructure Engineering Studies, Missouri University of Science and Technology, Rolla, MO 65409-0710, USA

Correspondence should be addressed to Zhi Zhou, zhouzhi@mst.edu

Received 14 October 2009; Accepted 2 December 2009

Academic Editor: Jinying Zhu

Copyright © 2010 Zhi Zhou et al. This is an open access article distributed under the Creative Commons Attribution License, which permits unrestricted use, distribution, and reproduction in any medium, provided the original work is properly cited.

Casing pipes in oil well constructions may suddenly buckle inward as their inside and outside hydrostatic pressure difference increases. For the safety of construction workers and the steady development of oil industries, it is critically important to measure the stress state of a casing pipe. This study develops a rugged, real-time monitoring, and warning system that combines the distributed Brillouin Scattering Time Domain Reflectometry (BOTDR) and the discrete fiber Bragg grating (FBG) measurement. The BOTDR optical fiber sensors were embedded with no optical fiber splice joints in a fiber-reinforced polymer (FRP) rebar and the FBG sensors were wrapped in epoxy resins and glass clothes, both installed during the segmental construction of casing pipes. In situ tests indicate that the proposed sensing system and installation technique can survive the downhole driving process of casing pipes, withstand a harsh service environment, and remain intact with the casing pipes for compatible strain measurements. The relative error of the measured strains between the distributed and discrete sensors is less than 12%. The FBG sensors successfully measured the maximum horizontal principal stress with a relative error of 6.7% in comparison with a cross multipole array acoustic instrument.

1. Introduction

Many oil and gas wells in China are drilled with high-pressure water injections and shored with casing pipes bolted or welded together from many sections. Casing damage often occurs as a result of pipe corrosion, joint dislocation, and long-term water injection development. It represents the most important factor for unproductive oil and gas wells. By 2003, a total of 5400 casing pipes had been damaged, accounting for nearly 20% of all oil wells in the Shengli Oilfield in China. By 2005, more than 11,188 oil well casings or 18.54% of all oil wells in the Daqing Oilfield had collapsed. This casing damage resulted in the loss of tens of billions of Chinese Yuan [1, 2]. The problems associated with casing damage continue to grow in Chinese Oilfields. Once damaged, most deeply buried casings are difficult to repair in practice. Therefore, the most effective way to maintain the operation of oil wells is to prevent casing pipes from collapsing, requiring a real-time monitoring and warning system for casing pipes.

Up to date, no cost-effective and reliable sensing technologies and installation techniques exist for long-term monitoring and evaluation of casing pipes. Traditional casing inspection techniques are not suitable for real-time monitoring of casing damage. Other damage detection techniques, such as the fiber downhole video logging tool, combined multifinger imaging and magnetic thickness tool, cross multipole array acoustic technology, and borehole ultrasonic imaging, operate at the detection or inspection level and monitor only the macromechanical deformation or breakage [3–6]. Since the 1990s, optical fiber sensing techniques, both locally high-precision FBG sensors and distributed Brillouin Scattering Time Domain Reflectometry (BOTDR) sensors, have been considered to be most promising for long-term structural health monitoring. They show significant advantages over conventional sensing technologies in terms of accuracy, durability, and sensing distance [7–12]. Oil wells are underground structures whose damages could be substantial, deeply-hidden, and random. Neither FBG nor BOTDR sensing technology alone can meet the requirements

for the effective monitoring of a casing pipe. FBG sensing technology can only give local information, and BOTDR sensing technology offers a low spatial resolution, low test accuracy, low sampling frequency, and high cost system for strain and temperature measurements. A combination of FBG and BOTDR systems, however, is a promising alternative for the real-time monitoring of casing pipes.

This paper proposes a real-time monitoring and early warning system for casing pipes in oil well operations. In this case, the strain/stress state and safety of casing pipes are monitored and evaluated by a combined FBG and BOTDR system. To improve the system robustness, one or two optical fibers (OFs) are embedded into a fiber reinforced polymer (FRP) bar with no optical fiber splice joints, referred to as an FRP-OF bar, to measure the strain distribution of a casing pipe. For casing pipe applications, the FBG and FRP-OF bar installation techniques were also investigated. The effectiveness of the technique was validated by the in situ testing in Daqing oilfield.

2. Optical Fiber Sensing Principle

As two representative types of optical sensing technologies, FBG and BOTDR sensors have been recently applied to many field projects for structural health monitoring. Both the Bragg wavelength and the Brillouin frequency can be related to strain and temperature with calibration coefficients [7, 8, 13, 14]. Without considering the cross-coupling effect of strain and temperature, the Bragg wavelength ($\Delta\lambda_B$) and Brillouin frequency shift ($\Delta\nu_B$) have been shown to be linearly dependant on strain ($\Delta\varepsilon$) and temperature (ΔT) by (1) and (2), respectively,

$$\Delta\lambda_B = \alpha_\varepsilon\Delta\varepsilon + \alpha_T\Delta T, \quad (1)$$

$$\Delta\nu_B = C_\varepsilon\Delta\varepsilon + C_T\Delta T, \quad (2)$$

where α_ε and α_T are the strain and temperature sensitivity coefficients of FBG sensors, respectively; C_ε and C_T are the strain and temperature sensitivity coefficients of BOTDR sensors, respectively. In this study, the FBGs used have $\alpha_\varepsilon = 1.2 \text{ pm}/\mu\varepsilon$ and $\alpha_T = 10.8 \text{ pm}/^\circ\text{C}$. SMF-28 optical fibers were used in BOTDR measurements which have $C_\varepsilon = 0.05 \text{ MHz}/\mu\varepsilon$ and $C_T = 1.0 \text{ MHz}/^\circ\text{C}$.

3. Fabrication of Long FRP-OF Bar

The downhole environment and condition in which the in-service casing pipes of oil and gas wells operate are extremely harsh and complex. Each casing pipe could be kilometers long and must be made in situ by bolting or welding one modular section at a time. Therefore, the surface installation of conventional sensors will either be damaged during installation or have low signal-to-noise ratio due to signal loss over the long distance. In this study, a kilometer-long FRP bar was fabricated by embedding one or two optical fibers into the center of an FRP bar with no optical fiber splice joint. Several glass fibers were pulled from a pulley system, bathed in an epoxy basin, fed together with one or



FIGURE 1: Finished product of FRP-OF bars.

two OFs at the center into the heating furnace, and finally pultruded through a rotating machine to form an FRP bar with embedded OFs as illustrated in Figure 1.

Figure 2 presents the sensing properties of an FRP-OF bar used in this study. The Brillouin frequency shift (BFS) of the sensing bar has a good linear relationship with the applied strain and temperature. The linear fitting in Figures 2(a) and 2(b) has a correlation coefficients of 0.999, and the slope of the linear regressions represents sensitivity coefficients of $0.050 \text{ MHz}/\mu\varepsilon$ and $1.263 \text{ MHz}/^\circ\text{C}$, respectively. In comparison with the sensitivity coefficients of its corresponding bare optical fiber, the temperature sensitivity coefficient is higher by 25%, while the strain sensitivity coefficient keeps constant.

The fabricated FRP-OF bar with two optical fibers is suitable for both BOTDA (Brillouin Scattering Time Domain Analysis) and BOTDR measurements. The function of the sensing fiber is the same, which acts as transmission medium and sensor simultaneously. The difference is that for BOTDA it is a loop configure using two fiber ends; for BOTDR only one end is needed.

4. Installation of Optical Fiber Sensors in Oilfield Applications

4.1. Casing Pipe Damages and Monitoring System. Pump wells in the Daqing Oilfield, China, have been drilled with high-pressure water injection. During the past 20 years, many casing pipes were severely damaged at the oilfield damage. Figure 3 presents the statistics of casing pipe damages in Daqing Oilfield. It indicates that most of the damaged casing pipes took place in the N2, S1, and S2 index beds with nonoil reservoirs. This statistics can be used to guide the design of an optical fiber sensing system. For example, high-precision FBG strain measurements shall be taken in the N2 as well as in the S2-3 index bed according to Figure 3. The remaining beds can be monitored with the BOTDR sensing system for general strain distribution.

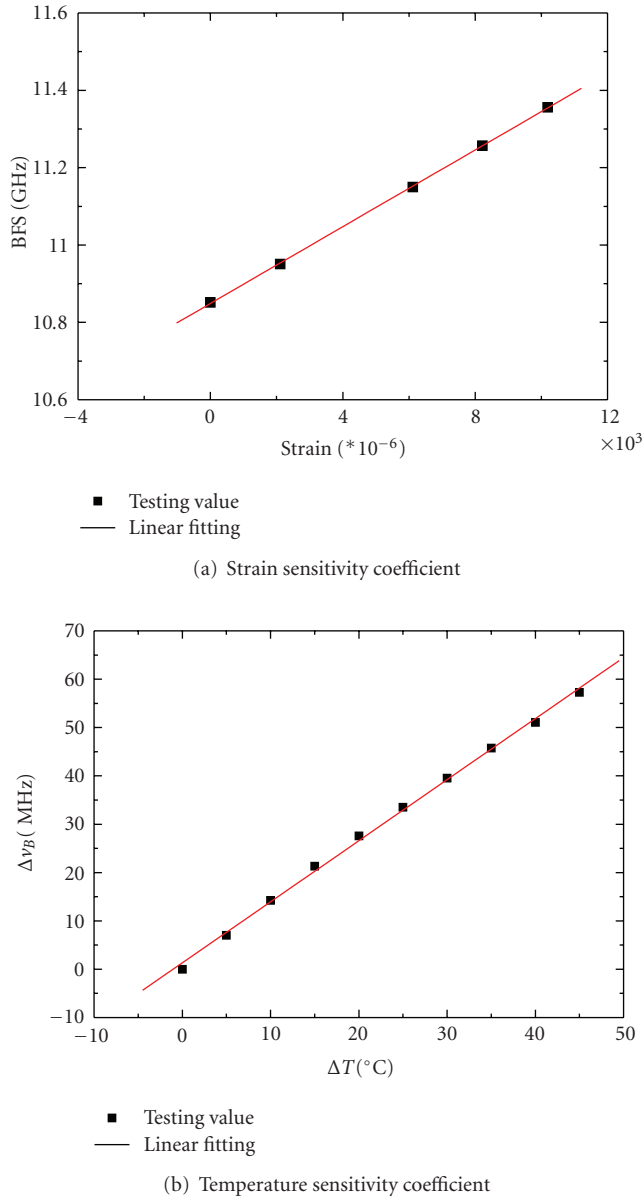


FIGURE 2: Calibration of an FRP-OF bar.

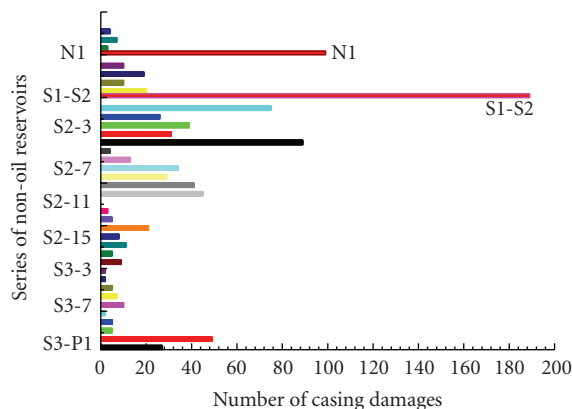


FIGURE 3: Statistics of oilfield well casing damages in various soil conditions.

To alert and prevent casing damages, both FBG and BOTDR sensors were installed on the casing pipe in the Oil Recovery Plant No.5, Daqing Oilfield Corporation Ltd. Figure 4 illustrates a sketch of the casing pipe monitoring system. BOTDR sensors or FRP-OF bars were installed on the surface of the casing pipe above NII or at non-oil reservoirs and FBG sensors were installed on the hot spot of N2 where casing damages often take place.

4.2. FRP-OF Bar Installation Technique. For a successful installation in practical applications, OF sensors must meet three requirements: (a) survive harsh underground environments and in-service conditions, (b) bond perfectly to the casing pipe to be monitored for accurate strain measurements, and (c) make it easy to integrate with other sensors and sensing systems.

An FRP-OF bar based on the Brillouin sensing technology can provide continuous strain/temperature information along the optical fiber. As shown in Figure 5(a), it was thus installed on the surface of the casing pipe over its entire length. To ensure that the FRP-OF bar deforms with the casing pipe, several stainless steel encircling hoops were used to fix the FRP-OF bar on the casing pipe at 2 m intervals. After putting in place in the downhole well, the casing pipe and the FRP-OF sensor were wrapped with cement mortar to enhance their deformation compatibility. Moreover, the two optical fibers were connected in series to form a measurement loop in the case of the BOTDA system. The bottom end of the FRP-OF bar or the position of the optical fiber splice joint must be well protected to prevent damage during the well downhole process. For that purpose, a stainless steel shell was used to cover the optical fiber splice joint, and the gap in the shell was sealed with an epoxy iron mixture, as illustrated in Figure 5(b).

Figure 6 shows the field installation of an FRP-OF bar and a casing pipe in the Daqing Oilfield. It involves three steps: lowering the casing into downhole, filling its outside gap with mud, and placing a mud circle for grouting. The process of oil well cementing involves injection of isolation fluid, cementing, water injection, pressing, decompression, and opposite well.

4.3. FBG Strain Sensor Installation. Four FBG strain sensors were installed at stress concentration areas of the casing pipe. Figure 7 illustrates their locations and field installation on a casing pipe in the Daqing Oilfield. They were distributed around the circumference of the pipe at 90° intervals. For perfect bonding with the casing pipe, the installation surface for each FBG strain sensor must be polished and cleaned. The FBG strain sensors were then covered by a piece of epoxy glass cloth for corrosion protection and durability. For long-term strain/stress measurements, one additional FBG temperature sensor was installed near the FBG strain sensors for temperature compensation. To separate the strain effect, the FBG temperature sensor was inserted into a small steel tube that was filled with silicone fluid to enhance thermal conductivity.

The initial center wavelengths of the five FBG sensors must be at least 3 nm apart for reliable measurements. A

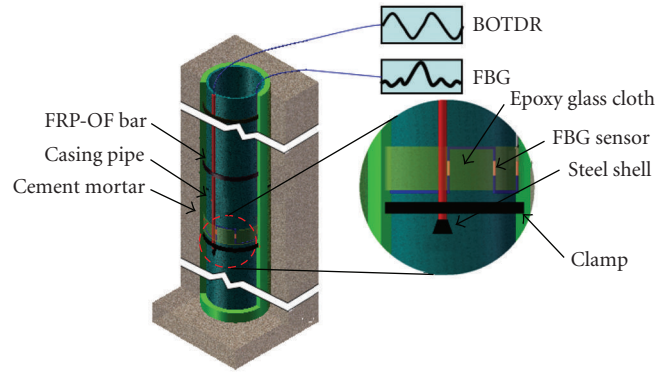


FIGURE 4: Sketch of a structural monitoring system for the casing pipe.

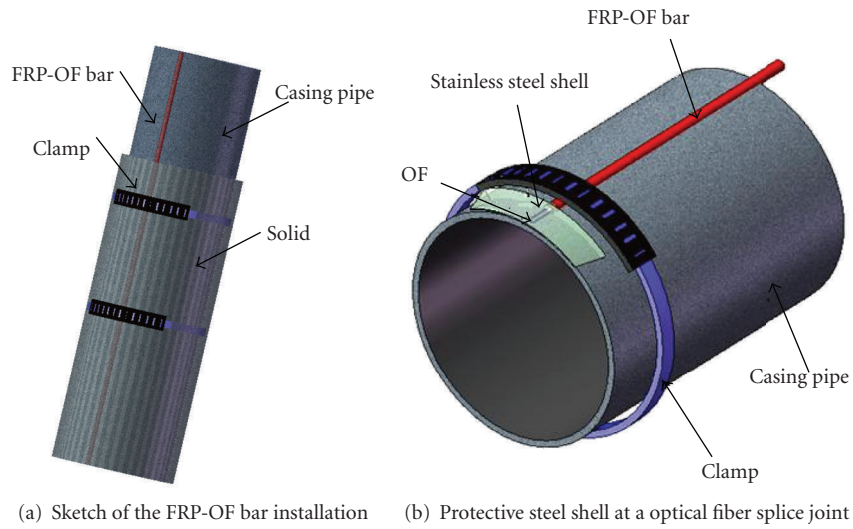


FIGURE 5: FRP-OF bar installation and protection.

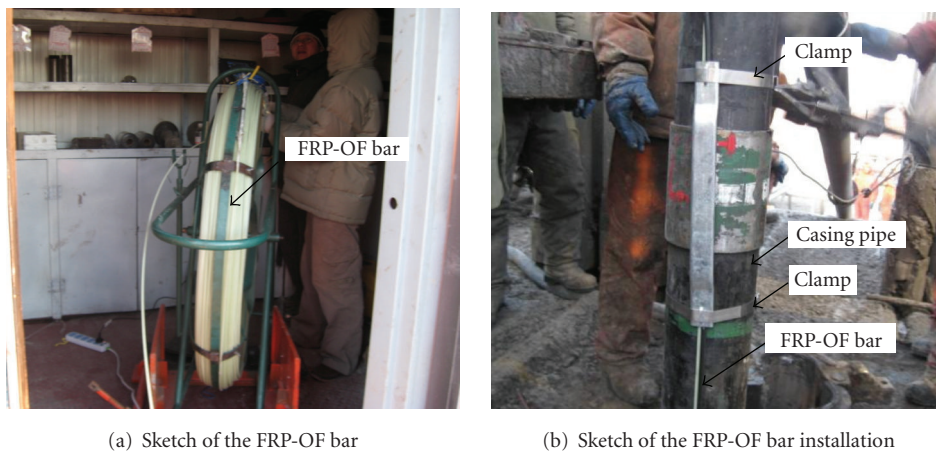
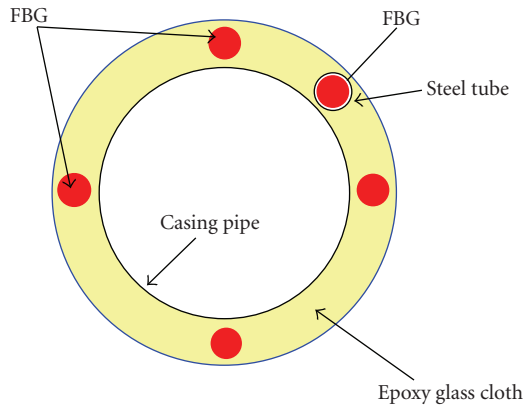
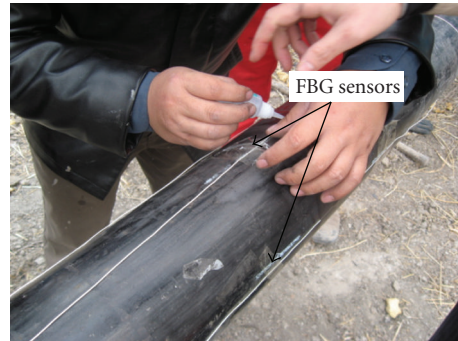


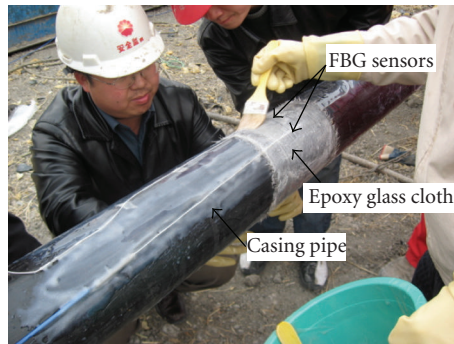
FIGURE 6: Sketch of the FRP-OF bar installation



(a) FBG sensor distribution



(b) FBG sensor locations



(c) Epoxy glass cloth wrapping

FIGURE 7: FBG sensor installation.

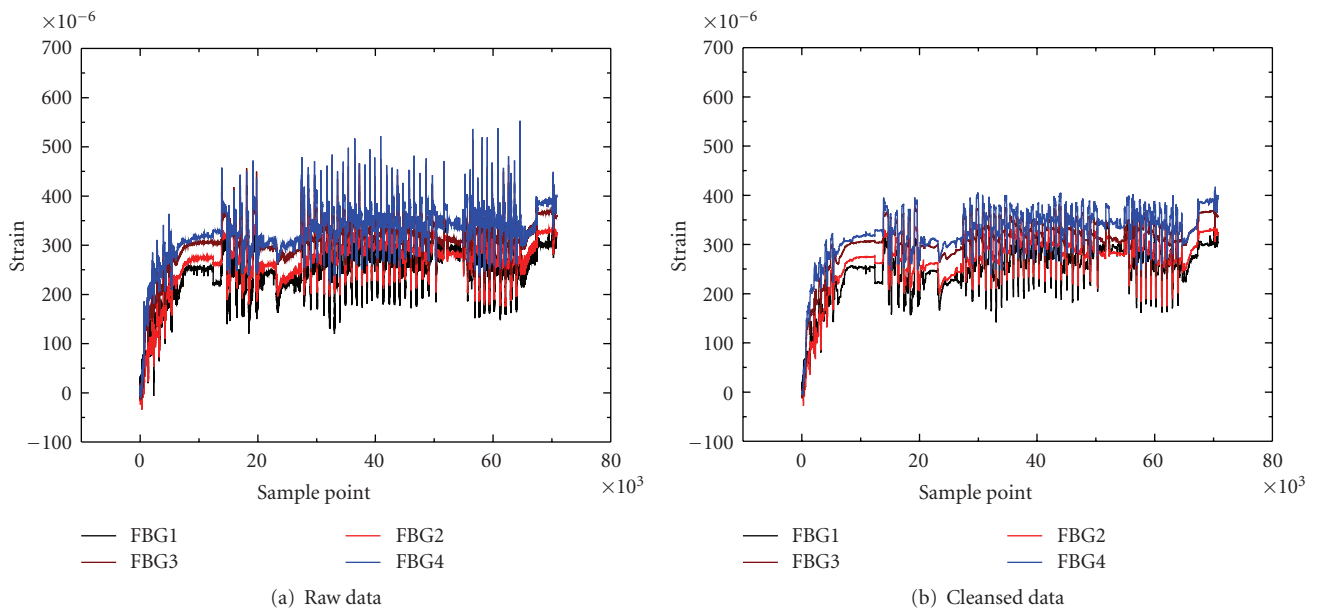


FIGURE 8: Strain measurements during casing of the oil well.

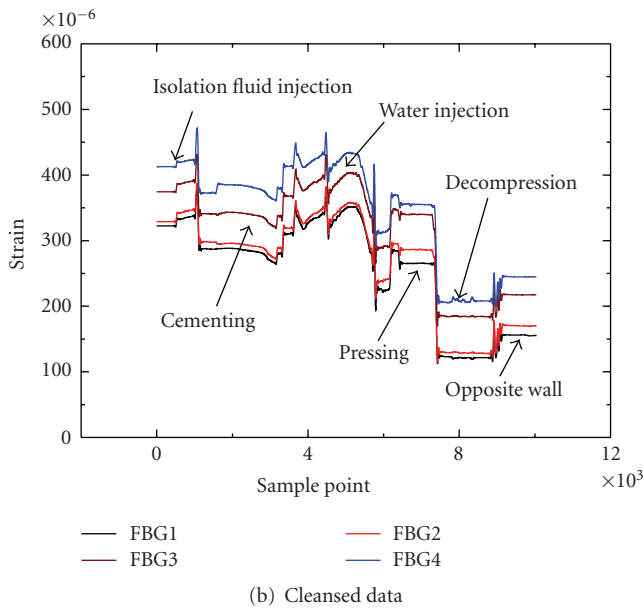
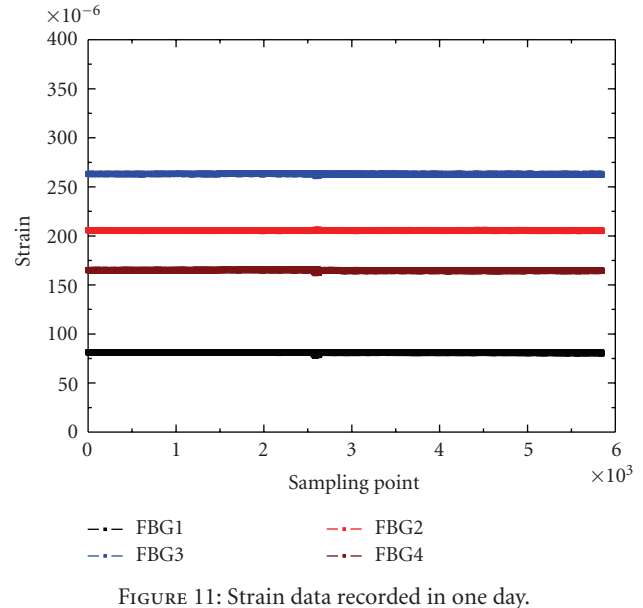
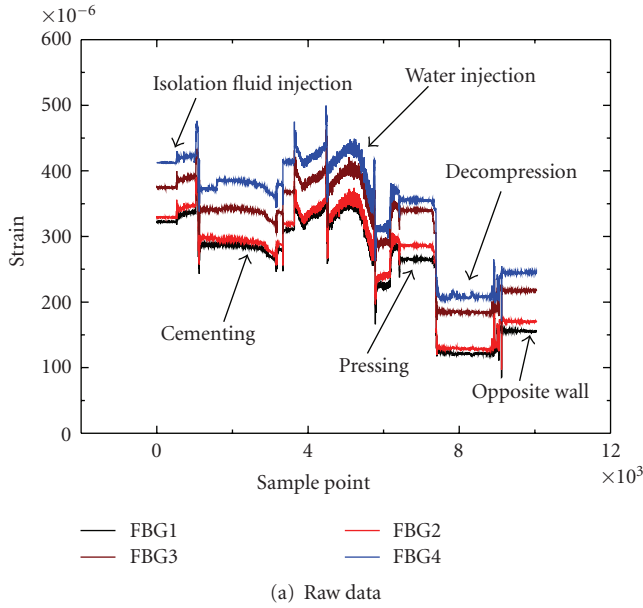
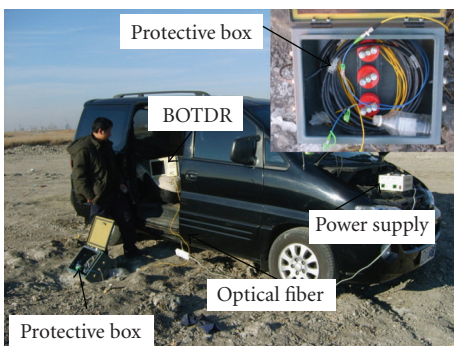


FIGURE 9: Strain measurements during grouting of the oil well.



special fiber optical cable with 8 mm in diameter, protected by a steel strand, transmitted the temperature distribution for compensation to the strain measurements by the FRP-OF bar.

5. Casing Damage Monitoring in the Daqing Oilfield

To validate the installation techniques and measurement effectiveness of both FBG and BOTDR optical fiber sensor, three oil wells in the Daqing Oilfield were selected as test beds, including Xing10-5Bing3112, Xing10-5Bing3022, and Xing13-4-PB335. Each oil well was instrumented with the proposed optical sensors for in situ strain and temperature measurements in its casing pipe.

5.1. Strain Measurements at Xing10-5Bing3112 and Xing10-5Bing 3022. The two FRP-OF bars installed on the casing pipes at two oil wells are 818m in Xing10-5Bing3112 and 838m in Xing10-5Bing3022, respectively. The four FBG strain sensors and the FBG temperature sensor were installed in the area of N2 index bed of Xing10-5Bing3022 for high accuracy measurement.

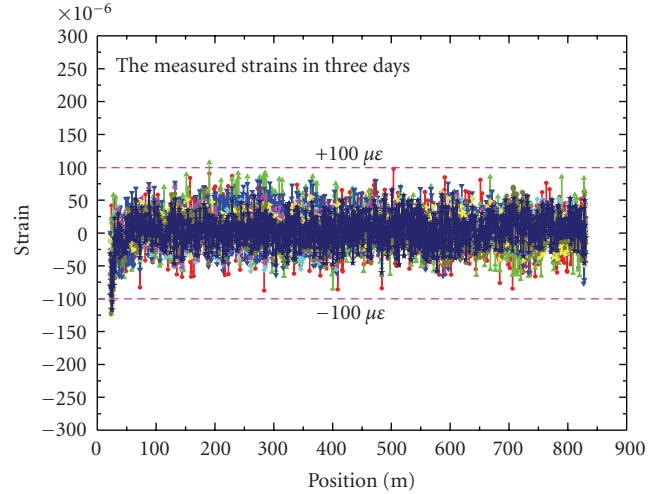
Due to the limitations of the casing downhole technique and the measurement time required by the BOTDR, only the stress concentration areas of the casing pipe were monitored by FBG sensors during the casing downhole and oil well cementing process. The strains measured by the FBG sensors were recorded by an MOI si720 interrogator with a sample frequency of 5 Hz and measurement accuracy of $1 \mu\epsilon$. Figures 8(a) and 9(a) present the raw data of the temperature-compensated strains measured by the FBG sensors during the processes of oil well casing and grouting. The raw data was contaminated by noise and thus cleansed by the db5 wavelet signal processing method [12]. The filtered signals as presented in Figures 8(b) and 9(b) show the significantly

reduced “burr” components. This disappearance may reflect the stress state of the casing pipes during the casing downhole and oil well cementing process, and the maximum strain is about $500 \mu\epsilon$. During both casing and grouting processes, the data points recorded by the four FBG strain sensors follow similar trends, indicating consistent and successful measurements from the case study.

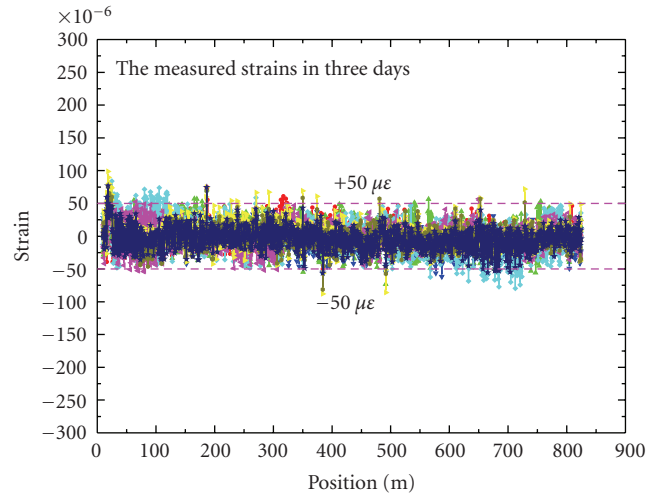
After downhole casing and grouting, the two oil wells were put into operation. The strain data obtained from the FRP-OF bar was recorded by the demodulator BOTDR produced by NTT in Japan, which has a measuring accuracy of $\pm 40 \mu\epsilon$ and minimum spatial resolution of 1 m. Figure 10 shows in situ measurements of the strains of in-service casing pipes. As shown in Figure 11, the strain data points measured by the four FBG sensors all remained stable over a period of one day but varied from one to another sensor.

Figure 12 presents the strain increments measured by FRP-OF sensors on December 15–17, 2007 in addition to the initial strains presented in Figure 11. The measured strain increments remained stable, and all ranged from $-120 \mu\epsilon$ to $+120 \mu\epsilon$. The strains measured over three days by the FRP-OF sensor and its nearby FBG sensor at the stress concentration areas of the Xing10-5Bing3022 oil well are compared in Figure 13. It is observed that the strains measured by the FRP-OF sensor fluctuated around those measured by the FBG sensor, which changed little over the three days. This observation suggests that the FBG sensor is more accurate than the FRP-OF sensor based on the BOTDR technology. Their maximum relative error in strain measurement is approximately 12%. Throughout the monitoring period, the strain state of in-service casing pipes was normal, showing no sign of inward buckling. The casing pipes were safe as confirmed by visual inspections.

5.2. Geostress Measurements and Perforation Experiments for Xing13-4-PB335. Perforation completion and positioning of the geostress orientation are two key factors in oil and gas explorations. To measure the geostress or circumferential stress, a total of 12 FBG strain sensors were installed around the circumference of the casing pipe of Xing13-4-PB335 oil well at 30° intervals, and two FRP-OF bars of 1133 m long were installed along the casing pipe for stress distribution measurement. The orientations of the 12 FBGs were identified by a multiarm caliper logging tool. The orientation of FBG6 corresponding to the mark on the casing pipe as shown in Figure 14 is approximately 311° ; the perforation orientations are 41° and 221° near the FBG9 and FBG3, respectively. As shown in Figures 15 and 16, the orientation of the maximum horizontal stress determined by the cross multipole array acoustic instrument (XMAC) and FBG sensors (before perforation) is approximately 94.67° and 101° , respectively. The relative error between the two measuring techniques is approximately 6.7%. The orientation of the maximum circumferential stress is vertical to that of perforating from the distribution of circumferential stress of the casing pipe before and after perforation completion measured by the FBG sensors as depicted in Figure 16, which agrees well with the actual stress state applied on the casing pipe.



(a) Xing10-5Bing3112



(b) Xing10-5Bing3022

FIGURE 12: Strain distribution of the casing pipe measured by FRP-OF bar at two oil wells.

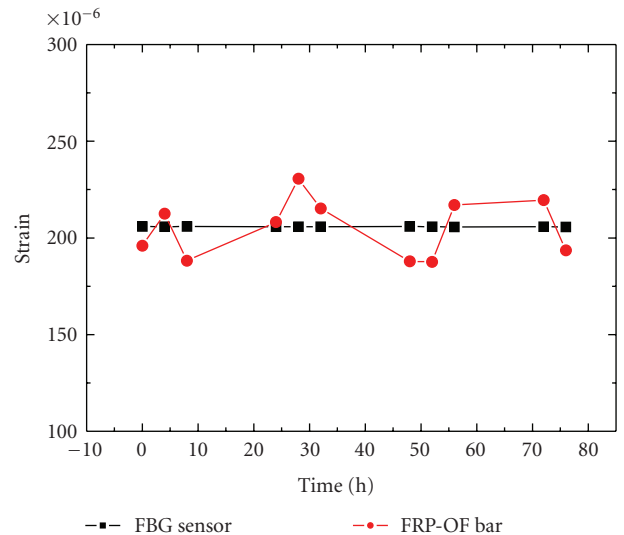


FIGURE 13: Strain comparison from FBG sensor and the FRP-OF bar.



FIGURE 14: Orientation mark of casing pipe.

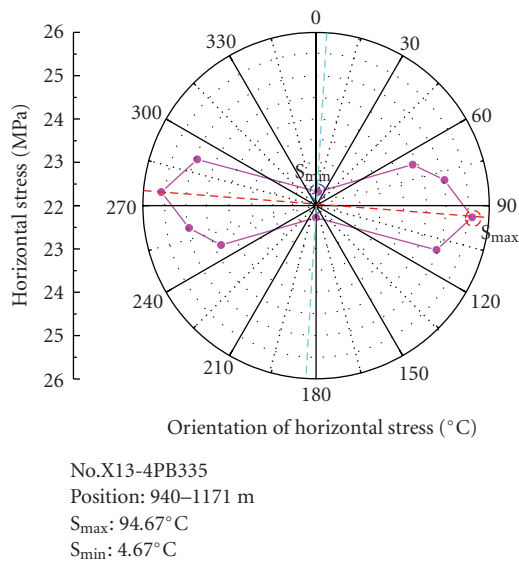


FIGURE 15: The orientation of the maximum horizontal stress by XMAC.

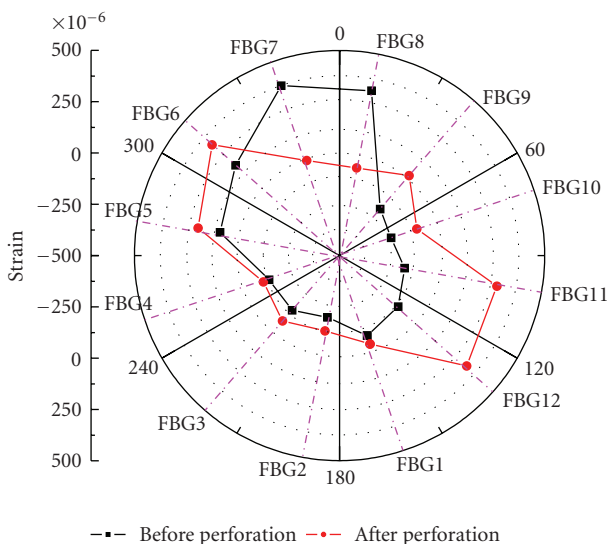
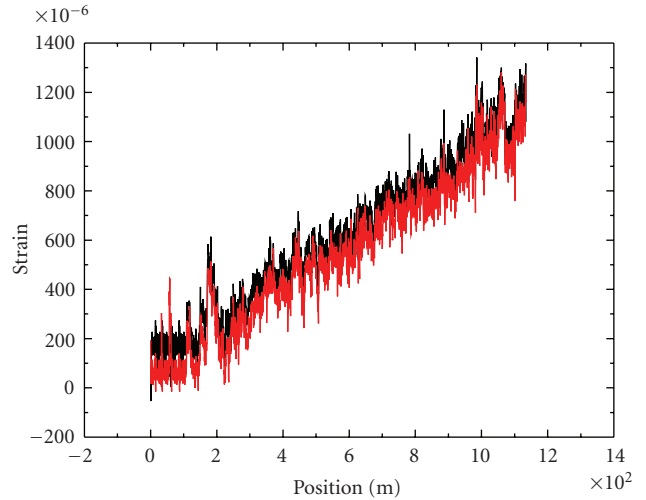
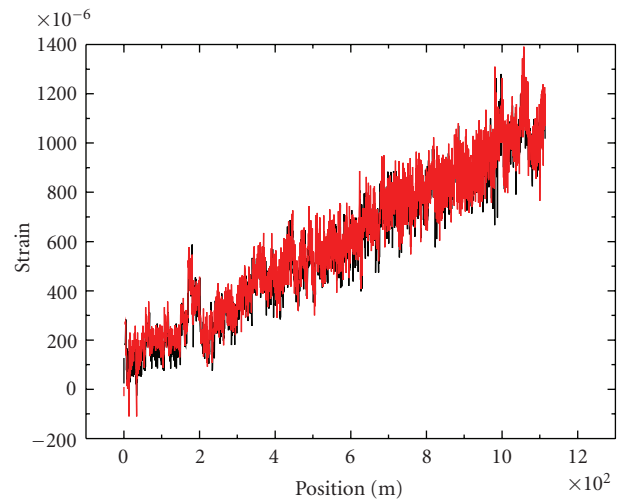


FIGURE 16: The distribution of casing pipe circumferential stress measured by FBG sensors.



— FRP-OF bar1 — FRP-OF bar2
 (a) Before perforation



— FRP-OF bar1 — FRP-OF bar2
 (b) After perforation

FIGURE 17: Strain distribution from the FRP-OF.

Figure 17 shows the strain distribution along the casing pipe before and after perforation completion, which were measured by the two FRP-OF sensors. The readings from the two sensors are consistent. The strain difference at any particular position ranges from $-200 \mu\epsilon$ to $+200 \mu\epsilon$, indicating that the axial strain of the casing pipe remains stable before and after the perforation completion. The average strain appears to be proportional to the distance from the ground surface due to gravity effects.

6. Conclusions

Based on the extensive strain data measured at three oil wells in the Daqing Oilfield and necessary analyses, the following conclusions are drawn.

- (a) This case study represents an innovative application of fiber optical sensors in the condition monitoring of casing pipes in oil well explorations. The experience demonstrated the feasibility of long-term structural health monitoring of oil wells with optical technologies.
- (b) Both the FRP-OF and the FBG sensors wrapped in an epoxy glass cloth were stable and durable. They survived the casing and grouting processes of oil wells in a harsh construction environment and indicated that the installation procedure is effective.
- (c) Both FRP-OF and FBG sensors can effectively monitor the stress/strain state of casing pipes with a relative error of less than 12%. The FBG-measured distribution of circumferential stress in a casing pipe reveals the distribution of geostress. The relative error of the position for orientation of the maximum horizontal stress is approximately 6.7% between the FBG sensors and the XAMC technique.

Acknowledgments

Financial support to complete this study was provided by National Science Foundation of China under Grant nos. 10672048, 50978079, and 50538020 and by the National Scientific Support Project under Grant nos. 2006BAJ03B05 and 2006BAJ13B03.

References

- [1] X. Y. Hu, Q. Y. Niu, and Y. Z. Wang, "Casing damage analysis and control technology," *Environmental Protection of Oil and Gas Fields*, vol. 13, no. 3, pp. 35–37, 2003.
- [2] Q. X. Liu, *The casing condition logging and the study of the method to detect the casing stress*, Doctor dissertation, China University of Geosciences, Beijing, China, 2006.
- [3] L. X. Fu, L. J. Ma, and C. M. Qiao, "Cause and repair & maintenance measures of casing in oil and water well," *Petroleum Drilling Techniques*, vol. 30, no. 4, pp. 53–56, 2002.
- [4] Y. L. Li, Q. Li, and X. R. An, "Application of fiber downhole video logging tool in administering of casing damage well WLT," *Petroleum Instruments*, vol. 19, no. 4, pp. 20–23, 2005.
- [5] F. L. Chen, X. Y. Cai, and Y. Jin, "Inspection and evaluation method of casing damages with multi-arm Caliper log," *Well Logging Technology*, vol. 29, no. 1, pp. 79–81, 2005.
- [6] J. K. Hao, W. L. Liu, and Y. B. Li, "Application of MIT_MTT combination technology for casing detection in changqing oilfield," *Well Logging Technology*, vol. 30, no. 5, pp. 449–453, 2006.
- [7] J. P. Ou, "Some recent advance of intelligent monitoring system for civil infrastructures in Mainland China," in *Proceeding of the 1st International Conference on Structural Health Monitoring and Intelligent Infrastructures*, pp. 131–144, 2003.
- [8] Z. Zhou, *Optical fiber bragg grating sensors and intelligent monitoring system in civil infrastructures*, Doctor dissertation, Harbin Institute of Technology, Harbin, China, 2003.
- [9] D. Inaudi and B. Glisic, "Development of distributed strain and temperature sensing cables," in *Proceedings of the 17th International Conference on Optical Fibre Sensors*, vol. 5855 of *Proceedings of SPIE*, pp. 222–225, May 2005.
- [10] J. P. He and Z. Zhou, "Long-term monitoring of a civil defensive structure based on distributed Brillouin optical fiber sensor," *Pacific Science Review*, vol. 9, pp. 97–102, 2007.
- [11] Z. Zhou, J.-P. He, H.-W. Jia, and J.-P. Ou, "Full scale Brillouin sensing technique based smart parallel wire stay cable," *Journal of Optoelectronics Laser*, vol. 20, no. 6, pp. 766–770, 2009.
- [12] J. P. He, *Full scale BOTDA/R distributed monitoring technology and its application in civil engineering*, Doctor dissertation, Harbin Institute of Technology, Harbin, China, 2009.
- [13] D. Culverhouse, F. Farahi, C. N. Pannell, and D. A. Jackson, "Potential of stimulated Brillouin scattering as sensing mechanism for distributed temperature sensors," *Electronics Letters*, vol. 25, no. 14, pp. 913–915, 1989.
- [14] T. Horiguchi, T. Kurashima, and M. Tateda, "Tensile strain dependence of Brillouin frequency shift in silica optical fibers," *IEEE Photonics Technology Letters*, vol. 1, no. 5, pp. 107–108, 1989.

Research Article

A Neural-Wavelet Technique for Damage Identification in the ASCE Benchmark Structure Using Phase II Experimental Data

Mahmoud M. Reda Taha

Department of Civil Engineering, The University of New Mexico, Albuquerque, NM 87131, USA

Correspondence should be addressed to Mahmoud M. Reda Taha, mrtaha@unm.edu

Received 15 December 2009; Revised 18 March 2010; Accepted 25 May 2010

Academic Editor: Yiqing Qing Ni

Copyright © 2010 Mahmoud M. Reda Taha. This is an open access article distributed under the Creative Commons Attribution License, which permits unrestricted use, distribution, and reproduction in any medium, provided the original work is properly cited.

Damage pattern recognition research represents one of the most challenging tasks in structural health monitoring (SHM). The vagueness in defining damage and the significant overlap between damage states contribute to the challenges associated with proper damage classification. Uncertainties in the damage features and how they propagate during the damage detection process also contribute to uncertainties in SHM. This paper introduces an integrated method for damage feature extraction and damage recognition. We describe a robust damage detection method that is based on using artificial neural network (ANN) to compute the wavelet energy of acceleration signals acquired from the structure. We suggest using the wavelet energy as a damage feature to classify damage states in structures. A case study is presented that shows the ability of the proposed method to detect and pattern damage using the American Society of Civil Engineers (ASCEs) benchmark structure. It is suggested that an optimal ANN architecture can detect damage occurrence with good accuracy and can provide damage quantification with reasonable accuracy to varying levels of damage.

1. Introduction

With the aging of infrastructure worldwide and the increasing availability of cost efficient sensing equipment, the necessity to implement damage identification and classification systems on civil structures has become imperative. Structural health monitoring (SHM) is the nonintrusive collection and analysis of data from structures for damage detection and diagnosis. The intention of SHM is to characterize the structure's performance and to help maintain the structural performance over its years of service. SHM also helps reduce operation costs through early damage detection. Successful SHM techniques have been applied to other engineering disciplines where the mass of the structure is small compared with civil structures. Vibration-based SHM assumes that the structural dynamic response will depart from its normal pattern when damage occurs in the structure. Thus, damage detection is contingent upon successfully extracting sensitive damage feature(s), patterning such feature(s) and realizing changes in these patterns as damage develops.

Over the past two decades numerous research methods with the objective of extracting sensitive damage feature(s) have been suggested and tested on several structures [1–5]. Tools for damage detection using structural dynamics analysis such as modal update, Fourier transform and wavelets have been examined [6]. Some of those pertaining to the ASCE benchmark structure, described in Section 2, are reviewed below in Table 1.

More recently, a few researchers have focused on the use of artificial neural networks (ANN) for damage pattern recognition. ANN consists of a group of interconnected processing units called neurons. Each neuron performs a simple computational process and has a transfer function associated with the layer that operates at the node level. ANN has the capability to learn from example datasets by changing the numerical biases and weights of the network [40]. For feed forward ANN that is considered here, the neurons are organized into layers where the first layer contains one neuron per input and the last layer contains one neuron per output; intermediate layers may contain any number of layers. While Tsou and Shen [41] used differences between

TABLE 1: Summary of damage detection methods for the ASCE benchmark structure.

| Reference | Author(s) | Damage detection method |
|---|--|--|
| Reference document—No data | Johnson et al. [7, 8] | Detailed Description of Phase I—Simulated |
| | Dyke et al. [9] | Detailed Description of Phase II—Experimental |
| Phase I: Simulated data | Dyke et al. [10] | Loss of stiffness of members by optimizing modal parameters |
| | Hera et al. [11] | Spikes in Level 1 details of wavelet decomposed signals |
| | Yang et al. [12] | Spectral analysis to identify stiffness parameters |
| | Hera and Hou [13] | Spikes in Level 1 details of wavelet decomposed signals |
| | Sun and Chang [14] | Covariance of response using wavelet packets |
| | Lam et al. [15] | Loss of stiffness using modal update and identification |
| | Yuen et al. [16] | Loss of stiffness of members using modal parameter extraction and Bayesian modal updating |
| | Lus et al. and Caicedo et al. [17, 18] | State space model, eigensystem realization algorithm and optimization using modal parameters |
| | Bernal and Gunes [19] | Extraction of a matrix proportional to structure flexibility |
| | Lin et al. [20] | Time-frequency features obtained using Hilbert-Huang transform of the intrinsic mode functions |
| | Chase et al. [21] | Recursive least square to identify changes in stiffness matrix |
| | Wu and Li [22] | Eingen-sensitive FE for damage detection in ambient vibration |
| | Yang and Huang [23] | A recursive nonlinear estimation method is used |
| Phase II: Simulated data | Mizuno and Fujino [24] | Haar wavelet decomposition, quantization, and dissimilarity |
| | Zhou et al. [25] | Residual values from subspace-modal identification |
| | Hou and Hera [26] | Spikes in Level 1 details of wavelet decomposed signals using Daubechies and Meyer wavelets |
| | Barroso and Rodriguez [27] | Comparison of healthy to damage curvature in the mode shapes |
| | Casciati [28] | Discrepancy between healthy and damaged states using sum of squared errors |
| Phase II: Simulated and experimental data | Hera and Hou [29] | Modal parameters determined using continuous wavelet transform |
| | Dincal and Raich [30] | Minimization of error term between FRF of experimental & simulated data |
| | Nair et al. [31] | Structural stiffness change based on poles; pattern classification with autoregressive coefficients |
| Phase II: experimental data only | Ching and Beck [32, 33] | Expectation-Maximization algorithm used to find most probable stiffness parameters—Config. 2–9 |
| | Giraldo et al. [34] | Loss of stiffness of members—Config 2–6 |
| | Lynch [35] | Pole location using system identification, Config. 1–5 |
| | Liu et al. [36] | Time-frequency obtained using Hilbert-Huang transform of intrinsic modes—Config. 7 & 8 |
| | McCuskey et al. [37] and McCuskey [38] | Neural-wavelet module—All Configurations |
| | Carden and Brownjohn [39] | Autoregressive moving average (ARMA) to build damage classifiers for different damage configurations |

healthy and damaged eigenvalues as training data for a neural network for damage detection of a spring-mass system, Sexton et al. [42] proved that optimizing neural networks using optimization can lead to better prediction capabilities in operation research modeling.

The application of such stiffness-based techniques to large civil structures has been challenging because of the insignificant effect of the relatively small changes in stiffness due to damage compared with the large mass of these structures. Elkordy et al. [43] trained a neural network

using a finite element model for a large civil structure and compared the results to a physical model. The ability to train a neural network with finite element data is critical for evaluation of structures where sets of data representing healthy performance may not exist.

Several signal processing methods have been promoted for feature extraction such as Fourier transform, Wavelet transform and Wavelet Multi-Resolution Analysis (WMRA) [6, 44, 45]. These methods were combined with means of artificial intelligence (AI) such as ANN [46]. It has been noted by Lam et al. [47] and Yuen and Lam [48] that the influence of ANN architecture has been overlooked by many researchers using ANN for damage pattern recognition. The ANN architecture is crucial to the training of the network as well as getting good performance from the ANN. Lam et al. [47] suggested the use of a Bayesian method (conditional probability) to determine the optimal ANN architecture while using a Ritz vector and modal parameters, respectively, as damage features. A dual function ANN was used for the process of feature extraction and then to establish the needed damage classifier. The use of ANN for establishing nonlinear classifiers has also been suggested by other researchers [49]. A review of a number of combination of AI tools and signal processing techniques, particularly wavelets, for damage feature extraction for SHM, has recently been reported [45]. The use of wavelets and combining ANN and Wavelets for damage detection has also been recommended by investigators Yam et al. [50], Kim and Melhem [51], Diao et al. [52], Jiang and Adeli [53] and Jiang and Mahadevan [54, 55].

Much of the above noted research was focused on damage feature extraction rather than on damage pattern recognition. Sohn et al. [56] suggested classifying damage in structures using statistical pattern recognition methods. Lam et al. [47] discussed the possible use of Bayesian analysis to identify damage classes. Other techniques using fuzzy (nonprobabilistic) damage pattern recognition were reported to enable realizing other types of uncertainty, rather than random uncertainty in damage detection [57].

In this paper, we suggest using available damage observations to identify the optimal ANN structure (i.e., number of hidden layers and number of neurons in each hidden layer). An optimization process is suggested to identify the optimal ANN structure for successful damage pattern classification. Here we used acceleration data collected experimentally from Phase II of the ASCE benchmark structure to develop and test the proposed damage pattern recognition method. Our motivation was to demonstrate the possible use of an optimized neural-wavelet module to detect and quantify damage with reasonable accuracy in the ASCE benchmark structure. The proposed framework is extendable for damage detection and quantification in other structures.

2. The ASCE Benchmark Structure: Background

The American Society of Civil Engineers (ASCE) benchmark study was conducted by the International Association for Structural Control (IASC) ASCE Structural Health Monitoring Task Group as a resource for validating damage detection

techniques. The ASCE Benchmark Group generated structural response data from a 2×2 bay, four story, rectangular steel test structure [9]. A schematic of the structure is shown in Figure 1(a).

Phase I of the ASCE benchmark study was generated by means of a finite element model considering varying levels of damage [7, 8]. Phase II included two parts: Phase II-S where “S” denotes simulation data and Phase II-E where “E” denotes experimental data. The data in Phase II-S was generated using structural dynamics finite element software under MATLAB environment [7]. Phase II-S model included a 120 degrees of freedom (DOF) model and a twelve DOF data model [7, 8]. Phase II-E included experimental data collected from the structural response of the ASCE benchmark rectangular steel structure tested at the University of British Columbia in August 2002 [9]. Table 1 presents a review of all previous research that examined the ASCE benchmark structure to date. It is obvious that the vast amount of this previous research used simulated data, not experimental data. Table 1 also provides a brief description of the damage detection techniques used by each researcher and the type of structural response considered for the cases where experimental data of the benchmark structure was used.

As presented in Table 1, many researchers had success in detecting damage in Phase I and Phase II-S of the benchmark structure, but similar success when using the same techniques to Phase II-E data have not been reported. For example, Nair et al. [31] showed promising results for detecting damage using the Phase II-S data from the benchmark problem with a pattern classification algorithm based on autoregressive analysis of acceleration signals in the time domain. However, Nair et al. [31] reported limited success in using Phase II-E data. Therefore, the research conducted on the experimental benchmark study is not complete or fully inclusive. A major limitation in most of previous work examining the benchmark structure was the focus on damage detection rather than damage quantification. As most researchers tried to validate their metrics for damage detection of the different scenario, no attempts were made to produce an overall damage quantification metric based on the damage feature elected for damage detection. Here, we try to provide a method that provides both damage detection and damage quantification and demonstrate its application to the ASCE benchmark structure.

The ASCE benchmark structure was built at approximately one-third scale and is located at the University of British Columbia [9]. A series of acceleration data was collected from the test structure using nine different levels of damage and three different types of excitation including a shaker using a sine sweep, random excitation and impulse testing [58]. Only the response data from the randomly excited structure was analyzed. Phase II-E data includes acceleration response recorded for Phase I structural configurations. These configurations are described in Table 2. It is important to note that such description in Table 2 does not provide a quantitative value of the level of damage. Therefore, judging a damage detection method becomes quite challenging. This is because of the fact that it is difficult to quantify how removal of one or more

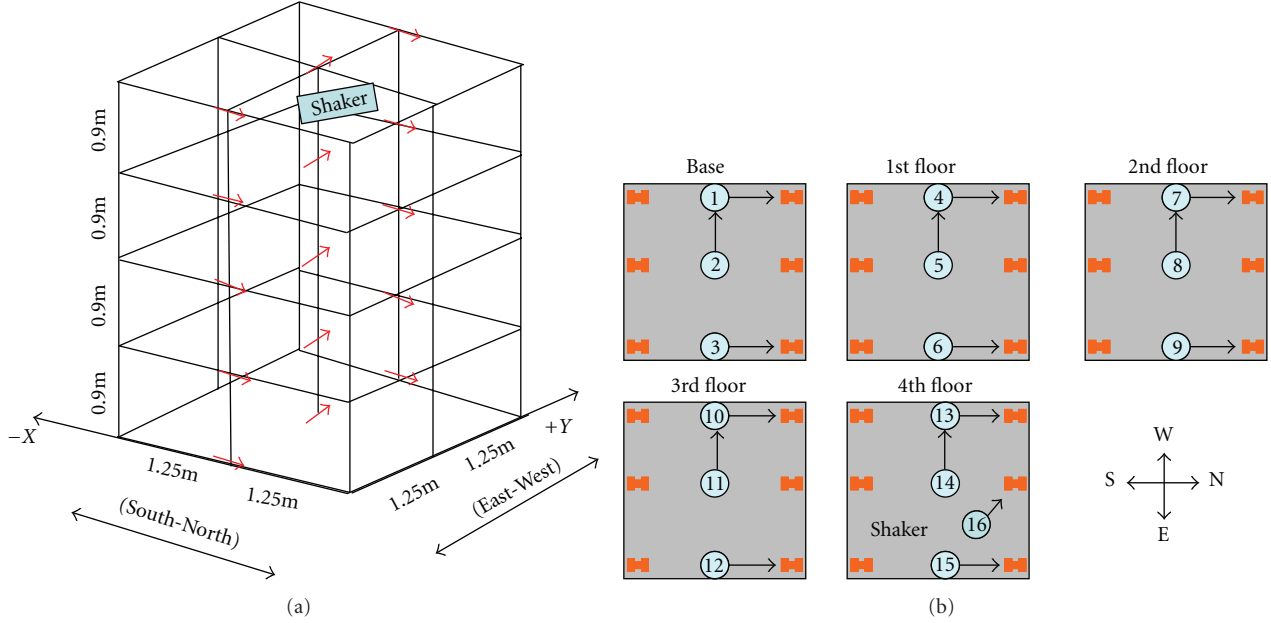


FIGURE 1: (a) 3D schematic of the ASCE benchmark structure. (b) Location of the accelerometers and shaker on the ASCE benchmark structure.

braces will affect structural response. While we propose a simple system to represent the level of damage based on the number of braces removed or joints loosened, we argue that further discussion from the SHM research community is needed to benchmark the levels of damage in the ASCE benchmark structure. Such benchmarking is essential for the experimental data's use by the research community when examining new damage detection methods.

Our proposed damage severity metric, denoted Γ_{ASCE} describes damage in the ASCE benchmark structure, is defined and normalized to a scale between 0 and 100 for the benchmark configurations. The damage severity Γ_{ASCE}^i for the i th damage configuration is computed as

$$\Gamma_{ASCE}^i = \frac{(1.0)n_x^i + (0.5)n_y^i + (0.25)B_x^i + (0.1)B_y^i}{\max((0.1)n_x + (0.5)n_y + (0.25)B_x + (0.1)B_y)}. \quad (1)$$

The symbol n_x is used to denote the number of braces removed in the North-South (strong axis) direction, while n_y corresponds to the number of braces removed in the East-West (weak axis) direction. B_x denotes the number of loosened bolted connections in the North-South (strong axis) direction while B_y is the number of loosened bolts in the East-West (weak axis) direction. Weight factors of 1.0, 0.5, 0.25 and 0.1 are used to describe the significance of each action (e.g., removal of braces) on the level of damage in the structure. For instance, a weight factor of 1.0 is chosen for removal of braces in the strong axis (North-South) direction. The weight factor (0.5) is used to describe the effect of removed bracing braces in the out-of-plane direction (East-West) direction. The weight factor (0.25) is also used to represent the relatively low effect of loosened bolts compared to the effect of removed bracing braces. The factor (0.1) is

used to represent the effect of out-of-plane loosened bolts. The reduction of damage severity in the out-of-plane direction is attributed to the fact that most accelerometers were placed in the North-South direction and the accelerations of interest used in the analysis were in the North-South direction. Figures 1(a) and 1(b) shows a three-dimensional schematic of the ASCE benchmark structure and the location of the accelerometers and shaker on the structure. There are nine testing configurations tested in the experimental investigation of the ASCE benchmark structure [9]. There was an unspecified error in data reported for Configuration 5 according to ASCE Benchmark Group, therefore that dataset for Configuration 5 was not used in this study. The descriptive damage metric Γ_{ASCE} was calculated for the eight damage configurations by means of (1). The damage metric values for these configurations are presented in Table 2. It became obvious that Configuration 1 can be classified as "healthy" ($\Gamma_{ASCE} = 0$), Configurations 2–6 can be classified as "partially damaged" with Γ_{ASCE} ranging between 8.5 and 31.2 and Configurations 7–9 can be classified as "fully damaged" with Γ_{ASCE} ranging between 85.1 and 100. It is important to emphasize that the proposed descriptive damage metric developed for validation of the proposed damage detection method is very specific to the ASCE benchmark structure and the testing configurations examined herein. The weight factors were specifically selected for quantifying the overall damage in the benchmark structure given the structural configurations and the sensor locations.

3. Methods

Here we suggest a computational method for feature extraction and damage recognition based on integrating ANN and WMRA. The proposed method is used for damage feature

TABLE 2: Damage cases and quantified damage metric (Γ_{ASCE}) based on experimental description of damage in ASCE benchmark structure.

| Structure Configuration | Γ_{ASCE} | Damage class |
|---|-----------------|--------------|
| (1) Fully braced | 0 | Healthy |
| (2) All braces removed from East face | 28.4 | PD |
| (3) Braces removed on all floors in SE corner | 21.3 | PD |
| (4) Braces removed 1 & 4 floors, SE corner | 8.5 | PD |
| (5) Removed braces on E & N faces (2nd floor) | 31.2 | PD |
| (6) Braces removed all floors and all faces | 85.1 | FD |
| (7) Config. 7 plus loosened bolts N & E face | 100 | FD |
| (8) Config. 7 plus loosened bolts N & E face (1st & 2nd floors) | 91.1 | FD |

E: East, SE: South-East, N: North, PD: Partially Damaged, FD: Fully Damaged. * Γ_{ASCE} is evaluated using (1).

extraction by realizing the changes in the energy of structural acceleration signals computed in the wavelet domain as a result of damage. The proposed method has been previously validated using simulated and experimental data on bridge structures [59, 60]. Moreover, optimization methods are used to establish a classifier that can provide efficient damage pattern recognition. Design of the classifier is based on minimizing the error of classification by the damage detection method. The classification error is minimized through identifying the optimal architecture of the neural network, including the number of layers and number of neurons in each layer.

The development of the integrated damage pattern recognition method outlined in this paper includes the following steps: (1) data acquisition and signal processing, (2) damage feature extraction, (3) development of a damage classifier, (4) optimization of the neural network architecture using the classifier and (5) evaluation of the integrated damage recognition method (in Section 4).

3.1. Data Acquisition and Signal Processing. The acceleration signals, denoted $x_i(n)$ with subscript i representing the sensor location, were processed using WMRA. WMRA was implemented using the discrete wavelet transform (DWT), specifically the daubechies (db4) mother wavelet [61]. Extensive study has been performed by the authors that showed the daubechies (db4) mother wavelet to be the most suitable wavelet to decompose acceleration signals [61]. Other wavelet functions proposed by other researchers [62, 63] were also examined. The energy of the approximation signal of the damage structures (as will be discussed below) showed more sensitivity to damage when the daubechies (db4) wavelet signal was used to decompose the original signal. Similar observation was reported on analysis of experimental data observed in monitoring of steel bridges [64].

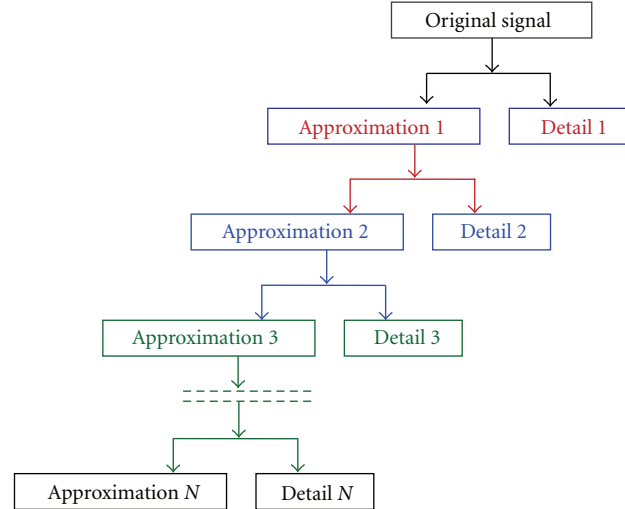


FIGURE 2: Schematic representation of wavelet multi-resolution analysis showing the decomposition of the original signal into N levels of decomposition and details signals.

WMRA enables the decomposition of the acceleration signal in the time domain into component signals at different frequency levels named approximations and details. Scaling a wavelet simply means stretching or compressing it. The smaller the scale, the more the wavelet will be compressed while the larger the scale, the more the wavelet will be stretched. Therefore, low scales allow analyzing rapidly changing details (high frequency components) and high-scales allow analyzing slowly changing features (low-frequency components).

In civil structures, it has been shown that most of the main frequency components are low-frequency components (ranging 5–30 Hz) [6, 31, 64, 65]. Therefore, the low-frequency components of the signal (the approximations) are very important parts of the signal. The “approximations signal” corresponds to the high-scale, low-frequency components of the signal. On the other hand, the high frequency contents carry the details of the signal. The “details signal” corresponds to the low scale high frequency part. WMRA decomposes the signal into various resolution levels as schematically shown in Figure 2. We suggest here using the third approximation signal in lieu of the original signal. This means that all high frequency components of the signal will be neglected. It is important to emphasize that these high frequency components might include useful information about the structure, but the proposed approach is based on the assumption that this information is not necessary for damage detection. The use of high frequency components might provide further insight on damage but will be accompanied with high computational expenses. The threshold at which signal decomposition is limited and the frequency components considered for damage detection shall be based on balancing the computational expenses versus the level of enhancement in damage detection accuracy [66].

Consider the discrete acceleration signal $x(n)$. With the wavelet scaling index (j) and shifting index (k) defined, the

coefficients for the approximation signals ($a_{j,k}$) and detail signals ($d_{j,k}$) can be calculated as

$$\begin{aligned} a_{j,k} &= 2^{(-j/2)} \sum_n x(n) \phi(2^{-j}n - k) \\ d_{j,k} &= \sum_n x(n) \psi_{j,k}(n), \end{aligned} \quad (2)$$

where $\phi(n)$ is the scaling function [61]. The acceleration signals acquired from the ASCE benchmark structure were decomposed to three levels of decomposition. The third approximation signal was used to represent the structure's response.

3.2. Damage Feature Extraction. The proposed framework aims at establishing the complex relationship relating the structural dynamics (here accelerations) between different zones of the healthy structure. This general framework is shown schematically in Figure 3(a). The neural-wavelet module tries to build this relationship at the wavelet decomposed acceleration signals using artificial neural network. When damage occurs in the structure, the relationship between its zones is disturbed. The higher the severity of damage, the further the structure departs from the healthy relationship between its zones. Damage can be thus detected and classified.

We suggest a damage feature denoted λ computed using WMRA and ANN. Acceleration signals recorded at accelerometers 5, 6, 9, 12 and 15 were decomposed using WMRA and the third approximation of the signals were then used as inputs for the ANN. The third approximation of the acceleration signal at accelerometer 13 was used as the desired output as shown in Figure 3(b). Figure 3(b) shows a schematic representation of the computation of the damage feature λ in the ASCE benchmark structure.

The damage feature was obtained by comparing the monitored acceleration signal at sensor 13 and the signal predicted by ANN. The damage feature denoted λ can thus be calculated as:

$$\lambda = \sum_k |a_J(k)|^2, \quad (3)$$

where a is the approximation, J is the level of wavelet decomposition. λ describes the energy of the signal representing the difference between the ANN predicted signal and the third approximation of the monitored acceleration signals and k is the total number of discrete elements used to represent the signal. As ANN is trained to predict healthy performance, the difference between monitored and predicted signal represents the level of departure of the structural response at any time. This different signal is directly related to the level of damage in the structure. The lower the value of λ , the closer ANN's prediction is to the monitored signal, therefore representing a healthy structure. The higher the value of λ , the further ANN's prediction is from the monitored signal. This neural wavelet method has successfully identified damage in other structures, including prestressed concrete [60] and a structural steel model bridge [64].

Here, we only considered the structure's response data from accelerometers 5, 6, 9, 12, 13 and 15 shown on the benchmark structure plans described in Figure 3(b). These accelerometers were excited by an electro-dynamic shaker placed on the top floor of the structure. The choice of this group of accelerometers to form the damage detection module is based on their location in relation to the damaged areas (areas of bracing removal) of the ASCE benchmark structure configurations as described by the ASCE benchmark study report ASCE Benchmark Group [58] and Dyke et al. [9]. The accelerometers chosen as the inputs to the ANN were primarily positioned along the East face of the structure where damage was induced. The output accelerometer was positioned on the West face of the structure where no damage was induced.

ANNs use an iterative process to learn a pattern and generate a nonlinear mapping system between system inputs and output. Here, ANN is used to learn the complex healthy signal of the structure at sensor 13 by observing the signals at sensors 5, 6, 9, 12 and 15. The input layer of ANN in this study has five neurons corresponding to the five acceleration data inputs acquired by accelerometers (5, 6, 9, 12 and 15) and one neuron at the output layer acquired by accelerometer 13. Each neuron has a transfer function associated with the layer that operates at the node level. All layers use the log-sigmoid transfer function, with the exception of the output layer, which has a linear transfer function. The choice of these transfer functions was based on a parametric investigation conducted on the benchmark data [37]. The parametric investigation also showed the need for optimization of the ANN architecture to enable efficient damage classification.

3.3. Developing Damage Classifier. The neural network's ability to accurately mimic the healthy signal is dependent upon the architecture of ANN. In this study we target identifying the optimal architecture of ANN and defining the number of hidden layers and the number of neurons per layer such that damage detection is maximized. Design of ANN usually targets achieving a minimum training error which is considered a modeling tool criterion for acceptance of a neural network. Successful damage detection necessitates that the damage feature (λ) is able to classify the level of damage in the structure. This means high λ values correspond to the "highly damaged" benchmark Configurations 7, 8, and 9. Moreover, low λ values correspond to the "healthy" Configuration 1, and λ values in between these extremes represent the "partially damaged" Configurations 2, 3, 4, and 6.

Successful development shall enable ANN to function as a damage classifier in addition to its role in damage feature extraction. This can be achieved by finding the optimal ANN architecture such that the maximum success rate of the damage classification is achieved. The process of successful classification rate maximization is performed here in the context of system optimization where the objective function that is used for defining the classifier is minimized. The optimization process can be described by defining

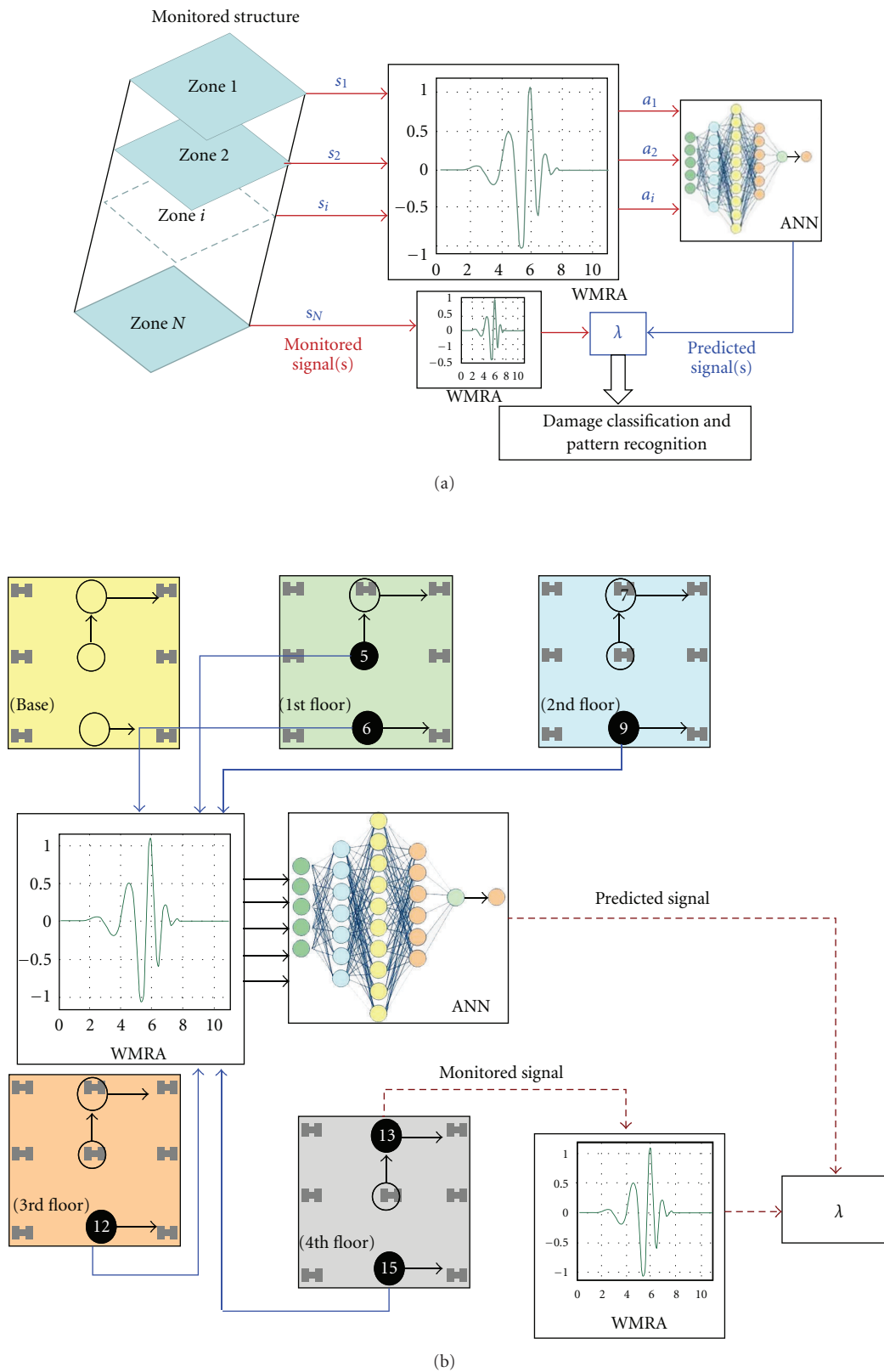


FIGURE 3: Schematic representation of the neural-wavelet damage detection method (a) general application of method to any structure divided to N zones (b) specific method application for damage detection in the ASCE benchmark structure (damage feature λ).

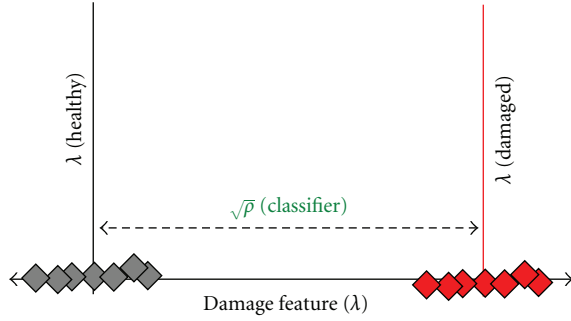


FIGURE 4: $\sqrt{\rho}$ represents the distance between mean value of λ for healthy performance and the mean value of λ for a damaged state.

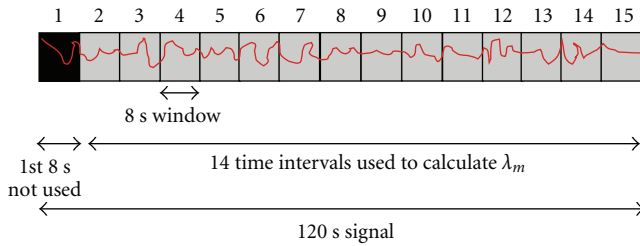


FIGURE 5: Schematic representation of the acceleration signals and the 15 windows in the signals.

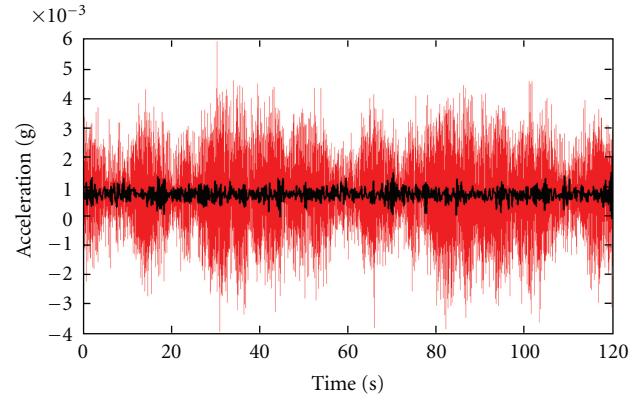
the objective function, the design variables, the design parameters and the optimization constraints.

The *objective function* to be minimized is $-\rho$ with ρ defined as:

$$\rho = \sum_{i=1}^K (\lambda_m^H - \lambda_{m_i}^D)^2 \quad (4)$$

ρ is the damage classifier, $\lambda_{m_i}^H$ is the mean value of the damage feature for a healthy case and $\lambda_{m_i}^D$ is the mean value of the damage feature for the damaged case. Where i is a numerical counter, $i = 1, 2, \dots, K$. K represents the number of structural damage configurations considered when establishing the damage classifier. Defining $-\rho$ as the objective function ensures that the difference between the mean damage feature at the healthy performance and other damage states is maximized and thus the success rate of damage detection is maximized. A schematic representation of the function describing the damage classifier is shown in Figure 4.

The *design variables* describe the number of layers and the number of neurons in each layer of the ANN architecture. The *design parameters* include those parameters that affect the optimization process but are assumed constant during the optimization process. This includes the level of wavelet decomposition, J (here $J = 3$), the mother wavelet function (here db4) and the transfer function per ANN layer (here log-sigmoid). Two optimization *constraints* were considered; the number of neurons per hidden layer constrained between 1 and 15, and the number of hidden layers also constrained between 1 and 3. Both constraints were established to limit computation time. The optimization process was



— Raw acceleration data
— Third approximation

FIGURE 6: Raw acceleration signal (red) observed at sensor 9 in the benchmark structure versus the third approximation of the acceleration signal (black) used for damage detection.

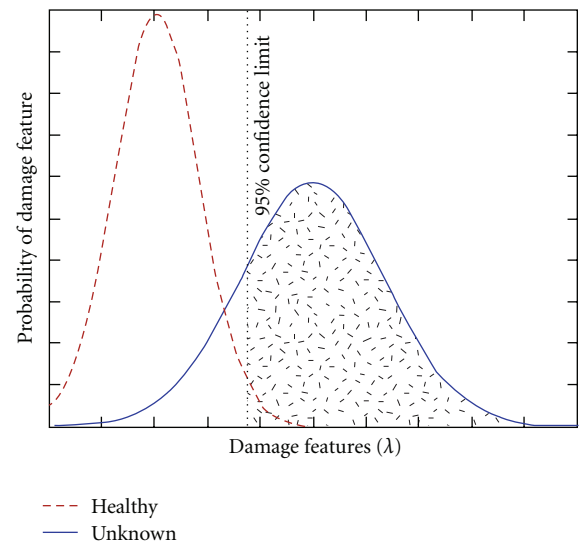


FIGURE 7: Schematic representation of probability of damage. Hatched area represents the cumulative probability of damage representing the neural-wavelet damage metric Γ_{NW} .

performed using derivative-based (Newton gradient-decent) and derivative-free (genetic algorithm (GA)) optimization techniques [67, 68].

Considering the ASCE benchmark Phase II-E data, λ_m^H represents the mean value of the damage feature for the healthy Configuration 1, while $\lambda_{m_i}^D$ represents the mean value of the damage feature of the i th damage configuration in the ASCE benchmark structure. Benchmark Configurations 1, 6, 7 and 8 were used for training of the damage classifier ρ , while Configurations 2, 3, 4 and 9 were reserved for testing the classifier after establishing the optimal ANN architecture. The mean value of the damage feature for the i th damage configuration, $\lambda_{m_i}^D$, was computed as the mean of fourteen values of λ . Each λ represents the energy of an

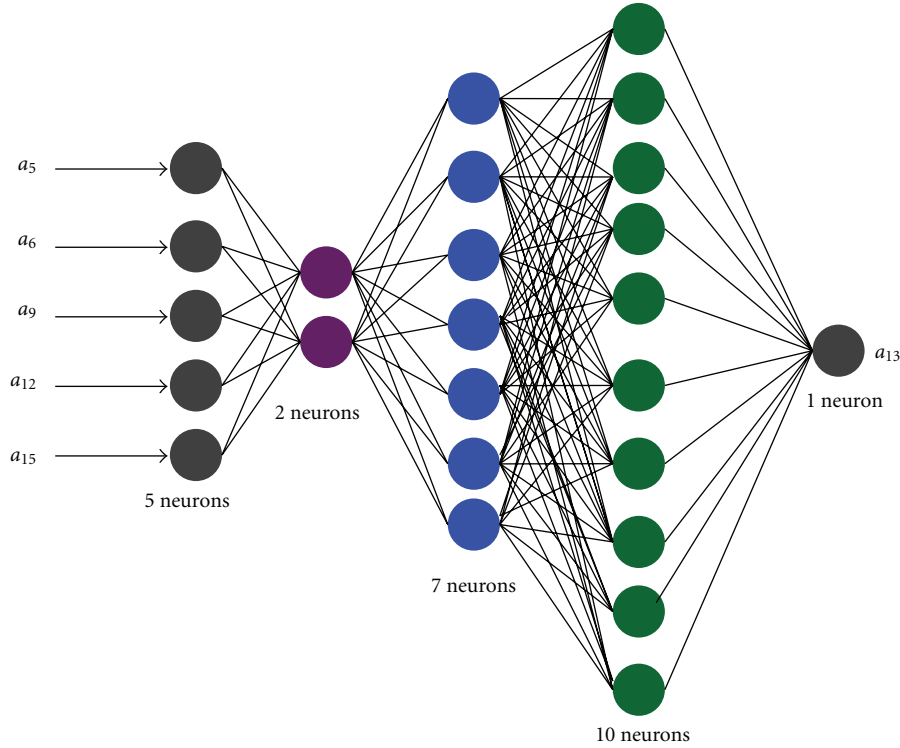


FIGURE 8: Optimal ANN for damage detection using the neural-wavelet method.

eight second window of the signal representing the difference signal between the third approximation of the measured signal and the ANN predicted signal. The energy of the difference signal is computed as

$$\lambda = \frac{1}{T} \sum_{N=1}^T \sum_k |a_d(k)|^2 \quad (5)$$

a_d is the difference signal between the third approximation of the measured signal and the ANN predicted signal, k is the counter for the signal measurements within the 8 second window, N represents the eight second time window and ranges from 1 to T , which is the total number of windows, equals 14. The division of the acceleration signal into windows is presented schematically in Figure 5. The original acceleration signal was 120 seconds long sampled at 500 Hz with 4000 data points in each window. The original signal was decomposed using WMRA. The original signal and the third approximation signal of a typical acceleration signal are shown in Figure 6. The third approximation signal was divided into fifteen windows each 8 seconds long. The first window was neglected for avoiding inaccurate observations at the start of data acquisition. The following 14 windows were used to compute the damage feature λ as represented by (5). The WMRA decomposition was performed on the whole 120 second signal and not at the windows' level to avoid the well known edge effect of the wavelet analysis when short signals are analyzed.

3.4. Testing the Damage Classifier. The optimal ANN architecture and the damage classifier were tested using the testing data including Configurations 2, 3, 4 and 9. These data sets were not used in developing the damage classifier. To consider uncertainty in damage recognition, the probability of damage is used as the damage metric to represent the level of damage in the structure for each testing configuration. The damage metric denoted Γ_{NW}^i (denoting damage quantified using the neural-wavelet (NW) method) at the i th configuration of the benchmark structure can be evaluated using (6), where θ is the confidence limit established by considering a 95% level of confidence from the healthy performance and λ^i is the mean damage feature describing the i th configuration of the benchmark structure

$$\Gamma_{NW}^i = P(\lambda^i \geq \theta), \quad (6)$$

where P represents the probability that the damage feature λ will exceed the damage threshold θ . The probability of damage is schematically represented in Figure 7. The probability distribution function represents the damage feature at any instance. The probability of damage is calculated as the area under the probability density function of the damage state with for values higher than the confidence limit, θ . Therefore, a probability density function for a damage case that does not overlap with the healthy probability density function would have a 100% probability of damage. The suggested method for calculating the probability of damage assumes the damage feature to be monotonically increasing as the level of damage in the structure advances. The damage

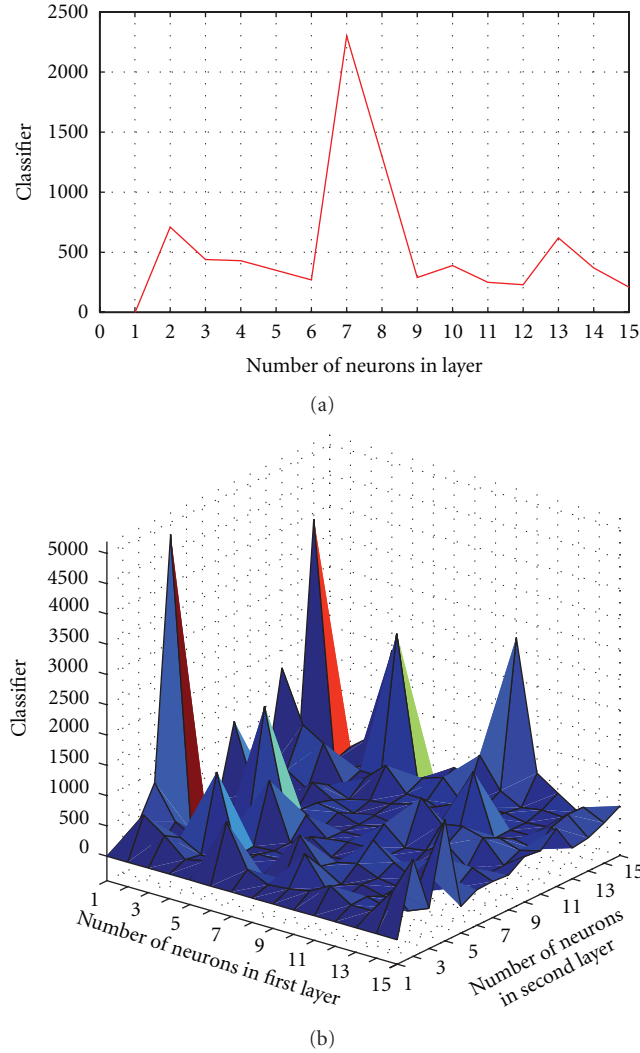


FIGURE 9: Number of neurons versus classifier objective function. (a) One hidden layer for classifier (ρ) showing the peak classifier to occur at $n = 7$ neurons. (b) Two hidden layers for classifier (ρ) showing the peak classifier to occur at $n_1 = 1$ and $n_2 = 5$.

feature is also assumed to follow the normal (Gaussian) probability distribution which was confirmed by analyzing the healthy datasets.

4. Results and Discussion

The optimization process determined that the optimal ANN architecture includes three hidden layers consisting of 2, 7 and 10 neurons on the first, second and third hidden layers respectively. A schematic representation of the optimal network is shown in Figure 8. Figure 9 shows the change in the classifier objective function versus the number of neurons for classifier ρ when the number of hidden layers is one (Figure 9(a)) and for two hidden layers in Figure 9(b). It is interesting to observe the large number of local minima that exist in both domains. The GA optimization technique was

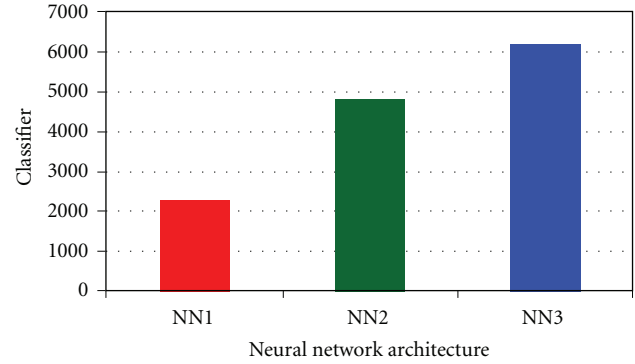


FIGURE 10: Comparison between three optimal neural networks using one hidden layer denoted NN1 ($n_1 = 7$ neurons), two hidden layers denoted NN2 ($n_1 = 1$ and $n_2 = 5$) and three hidden layers denoted NN3 ($n_1 = 2$ and $n_2 = 7$ and $n_3 = 10$) showing the neural network with three hidden layers to have the best performance with the highest classifier ($-\rho$).

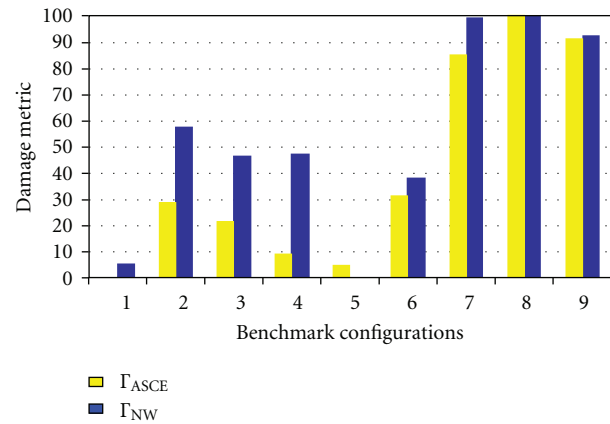


FIGURE 11: Neural-wavelet damage metric (Γ_{NW}) and descriptive damage metric (Γ_{ASCE}) for all ASCE benchmark structure configurations reported in Phase II-E (Configuration 5 is excluded).

more successful than the gradient descent method in realizing the optimal solution. The derivative-based technique was caught in local minima and the optimization process occasionally did not converge.

A comparison between the three optimal neural network architectures with one hidden layer denoted NN1 ($n_1 = 7$ neurons), two hidden layers denoted NN2 ($n_1 = 1$ and $n_2 = 5$) and three hidden layers denoted NN3 ($n_1 = 2$ and $n_2 = 7$ and $n_3 = 10$) showed that the neural network NN3 with three hidden layers to have the highest classifier (ρ). This comparison is shown in Figure 10. The comparison confirms that the optimal ANN architecture have the best ability to classify damage in the benchmark structure. The optimal ANN architecture shown in Figure 8 was used to identify damage in eight testing configurations of the ASCE benchmark structure (excluding Configuration 5) by computing the probability of damage (see (6)) in each configuration. This includes identifying damage in

Configurations 2, 3, 4 and 9 that were not used in training the classifier.

Figure 11 shows the neural-wavelet damage metric Γ_{NW} of eight configurations as identified using the optimal damage classifier. The mean value and the standard deviation for each of the eight configurations was calculated as the mean of 14 time windows, each of them is eight seconds long. Figure 11 also shows the severity of damage metric Γ_{ASCE} based on the damage quantification suggested in this paper (see (1)). Configurations 7, 8, and 9 that were classified as “fully damaged” (Table 2) show probabilities of damage ranging between 90 and 100 percent. The “partially damaged” Configurations 2, 3, 4, and 6 have a damage metric Γ_{NW} ranging between 40 and 60 percent and a descriptive damage metric Γ_{ASCE} between 9 and 31. The “healthy” Configuration 1 showed a damage metric Γ_{NW} that is lower than 5% and a descriptive damage metric Γ_{ASCE} value of zero. It is therefore obvious that a good agreement exists between the descriptive damage metric Γ_{ASCE} and the neural-wavelet damage metric Γ_{NW} .

The above results provide a damage detection method that can detect damage in eight damage configurations of Phase II-E in the ASCE benchmark structure; the proposed damage metric can also be used to classify/quantify damage severity in the benchmark structure with reasonable accuracy. This is attributed to the fact that the damage feature was optimized for classification of damage. The optimization process correctly categorized the “partially damaged” benchmark configurations resulting in probabilities of damage that range from between 40 and 60 percent. The “fully damaged” configurations were also correctly classified for having probabilities of damage ranging between 90 and 100 percent. The optimal neural-wavelet method has proven capable of detecting damage occurrence and showed good sensitivity in quantifying damage severity for low and high damage configurations. However, the model showed less accuracy in quantifying partially damaged cases which might be enhanced if other configurations of partially damage data were used in establishing the classifier.

Finally, the proposed neural-wavelet framework can be applied to damage detection and classification of real world structures. This requires developing a finite element model to simulate the structure dynamic behavior and validate this model using historical data observed from the structure. Damage can then be introduced to the finite element model with different levels of damage severity and at different locations. This simulated data can be used to optimize the ANN and establish the neural-wavelet module. The developed neural-wavelet module can then be used to detect and classify damage in the real structure.

We need to emphasize, however, that the overall damage metric is not unique but provides an indicator to damage severity. It is important to realize that damage is a nonmeasurable quantity and damage metrics cannot be directly compared. This damage quantification inaccuracy is an intrinsic characteristic of damage related to the definition of damage as suggested by many researchers [65, 69–71]. Therefore, the use of absolute numbers for quantifying damage severity and the use of accuracy measures to validate

damage quantification can lead to erroneous conclusions. Validation shall be limited to testing the metric ability to indicate the category of damage such as “low, moderate and high”. The wide range of probabilities describing the damage level in each configuration is attributed to considering uncertainty in quantifying damage. It is obvious that damage quantification is a challenging problem that lends itself to probabilistic, fuzzy or imprecise quantification.

5. Conclusion

We demonstrated that it is possible to establish a damage pattern recognition method by designing a damage classifier that integrates ANN and WMRA. An optimization technique using derivative free optimization (genetic algorithm) was used to identify the optimal ANN architecture. A neural network, including three hidden layers with 2, 7, and 10 neurons in the first, second and third hidden layers respectively, was capable of successfully detecting and quantifying damage in the ASCE benchmark structure with a reasonable sensitivity.

The neural-wavelet method aimed at establishing the underlying relationships between the structural dynamic responses (acceleration signals) at the different locations of the structure during healthy performance then recognized changes in such relationships as damage advanced in the structure. While the use of ANN to learn the underlying relation of structural dynamics proved successful, some drawbacks of ANN are related to their intolerance to uncertainty in training data. It is therefore suggested that other learning methods with higher tolerance to classification uncertainty such as neural-fuzzy inference systems, adaptive fuzzy learning from examples [72] or support vector machines might be examined as an alternative to neural networks in realizing structural dynamic relationships.

Acknowledgments

The author greatly appreciates the financial support by Defense Threat Reduction Agency (DTRA). Special thanks to research assistants: Scott Horton, Molly McCuskey and Erdogan Altunok for their efforts in the SHM research projects with the author.

References

- [1] F. K. Chang, Ed., *Structural Health Monitoring: Current Status and Perspectives, Proceedings of the International Workshop on Structural Health Monitoring*, Stanford, Calif, USA, 1997.
- [2] D. L. Balageas, Ed., *Structural Health Monitoring 2004: Proceedings of the 1st International European Workshop on Structural Health Monitoring*, Paris, France, 2002.
- [3] C. Boller and W. J. Staszewski, Eds., *Structural Health Monitoring 2004: Proceedings of the 2nd International European Workshop on Structural Health Monitoring*, University of Sheffield, Munich, Germany, 2004.
- [4] A. Güemes, Ed., *Structural Health Monitoring 2006: Proceedings of the 2nd International European Workshop on Structural Health Monitoring*, Granada, Spain, 2006.

- [5] F. K. Chang, Ed., *Structural Health Monitoring 2007: Quantification, Validation, and Implementation: Proceedings of the 6th International Workshop on Structural Health Monitoring*, Stanford, Calif, USA, 2007.
- [6] Los Alamos National Laboratory, "A review of structural health monitoring literature: 1996–2001," LA-13976-MS, 2004.
- [7] E. A. Johnson, H. F. Lam, L. S. Katafygiotis, and J. L. Beck, "A benchmark problem for structural health monitoring and damage detection," in *Proceedings of the 14th Engineering Mechanics Conference ASCE*, Austin, Tex, USA, 2000.
- [8] E. A. Johnson, H. F. Lam, L. S. Katafygiotis, and J. L. Beck, "Phase I IASC-ASCE structural health monitoring benchmark problem using simulated data," *Journal of Engineering Mechanics*, vol. 130, no. 1, pp. 3–15, 2004.
- [9] S. J. Dyke, D. Bernal, J. L. Beck, and C. Ventura, "An experimental benchmark problem in structural health monitoring," in *Proceedings of the 3rd International Workshop on Structural Health Monitoring*, Stanford, Calif, USA, 2001.
- [10] S. J. Dyke, J. M. Caicedo, and E. A. Johnson, "Monitoring of a benchmark structure for damage identification," in *Proceedings of the ASCE Engineering Mechanics Conference*, Austin, Tex, USA, 2000.
- [11] A. Hera, Z. Hou, and M. Noori, "Wavelet-based approach for ASCE structural health monitoring benchmark studies," in *Proceedings of 3rd International Workshop on Structural Health Monitoring*, Stanford, Calif, USA, 2001.
- [12] N. Y. Yang, S. Lin, and S. Pan, "Damage detection of a health monitoring benchmark building using Hilbert-Huang spectral analysis," in *Proceedings of International Conference on Advances in Building Technology*, pp. 1017–1024, Hong Kong, December 2002.
- [13] A. Hera and Z. Hou, "Application of wavelet approach for ASCE structural health monitoring benchmark studies," *Journal of Engineering Mechanics*, vol. 130, no. 1, pp. 96–104, 2004.
- [14] Z. Sun and C. C. Chang, "Structural degradation monitoring using covariance-driven wavelet packet signature," *Structural Health Monitoring*, vol. 2, no. 4, pp. 309–325, 2003.
- [15] H. F. Lam, L. S. Katafygiotis, and N. C. Mickleborough, "Application of a statistical model updating approach on phase I of the IASC-ASCE structural health monitoring benchmark study," *Journal of Engineering Mechanics*, vol. 130, no. 1, pp. 34–48, 2004.
- [16] K.-V. Yuen, S. K. Au, and J. L. Beck, "Two-stage structural health monitoring approach for phase I benchmark studies," *Journal of Engineering Mechanics*, vol. 130, no. 1, pp. 16–33, 2004.
- [17] H. Luş, R. Betti, J. Yu, and M. De Angelis, "Investigation of a system identification methodology in the context of the ASCE benchmark problem," *Journal of Engineering Mechanics*, vol. 130, no. 1, pp. 71–84, 2004.
- [18] J. M. Caicedo, S. J. Dyke, and E. A. Johnson, "Natural excitation technique and eigensystem realization algorithm for phase I of the IASC-ASCE benchmark problem: simulated data," *Journal of Engineering Mechanics*, vol. 130, no. 1, pp. 49–60, 2004.
- [19] D. Bernal and B. Gunes, "Flexibility based approach for damage characterization: benchmark application," *Journal of Engineering Mechanics*, vol. 130, no. 1, pp. 61–70, 2004.
- [20] S. Lin, J. N. Yang, and L. Zhou, "Damage identification of a benchmark building for structural health monitoring," *Smart Materials and Structures*, vol. 14, no. 3, pp. S162–S169, 2005.
- [21] J. G. Chase, V. Begoc, and L. R. Barroso, "Efficient structural health monitoring for a benchmark structure using adaptive RLS filters," *Computers & Structures*, vol. 83, no. 8-9, pp. 639–647, 2005.
- [22] J. R. Wu and Q. S. Li, "Structural parameter identification and damage detection for a steel structure using a two-stage finite element model updating method," *Journal of Constructional Steel Research*, vol. 62, no. 3, pp. 231–239, 2006.
- [23] J. N. Yang and H. Huang, "Sequential non-linear least-square estimation for damage identification of structures with unknown inputs and unknown outputs," *International Journal of Non-Linear Mechanics*, vol. 42, no. 5, pp. 789–801, 2007.
- [24] Y. Mizuno and Y. Fujino, "Data archiving and processing method using wavelet decomposition for structural health monitoring," in *Proceedings of the ASCE Conference on Computing in Civil Engineering*, pp. 673–680, Pittsburgh, Pa, USA, 2007.
- [25] W. Zhou, L. Mevel, and H. Li, "Stochastic subspace-based structural identification and damage detection—application to the ASCE benchmark structure," in *Proceedings of the 6th International Workshop on Structural Health Monitoring*, C. Fu-Kuo, Ed., pp. 645–652, Stanford, Calif, USA, 2007.
- [26] Z. Hou and A. Hera, "Progress of phase II study of the ASCE health monitoring benchmark data using wavelet approach," in *Proceedings of the 15th ASCE Engineering Mechanics Conference*, Columbia University, New York, NY, USA, 2002.
- [27] L. R. Barroso and R. Rodriguez, "Application of the damage index method to phase II of the analytical SHM benchmark problem," in *Proceedings for the ASCE Engineering Mechanics Conference*, New York, NY, USA, 2004.
- [28] S. Casciati, "Statistical models comparison for damage detection using the ASCE benchmark," in *Proceedings for the 2nd European Workshop on Structural Health Monitoring*, C. Boller and W. J. Staszewski, Eds., pp. 695–701, University of Sheffield, Munich, Germany, 2004.
- [29] A. Hera and Z. Hou, "Wavelet approach for damage detection using experimental data of ASCE benchmark study," in *Proceedings of the ASCE Engineering Mechanics Conference*, Seattle, Wash, USA, 2003.
- [30] S. Dincal and A. Raich, "Structural damage detection using frequency response function," in *Proceedings of the 5th International Workshop on Structural Health Monitoring*, C. Fu-Kuo, Ed., Stanford, Calif, USA, 2005.
- [31] K. K. Nair, A. S. Kiremidjian, and K. H. Law, "Time series-based damage detection and localization algorithm with application to the ASCE benchmark structure," *Journal of Sound and Vibration*, vol. 291, no. 1-2, pp. 349–368, 2006.
- [32] J. Ching and J. L. Beck, "Two-stage Bayesian structural health monitoring approach for phase II ASCE benchmark studies," in *Proceedings of the IMAC-XXI Conference*, Orlando, Fla, USA, 2003.
- [33] J. Ching and J. L. Beck, "Bayesian analysis of the phase II IASC-ASCE structural health monitoring experimental benchmark data," *Journal of Engineering Mechanics*, vol. 130, no. 10, pp. 1233–1244, 2004.
- [34] D. Giraldo, J. M. Caicedo, and S. J. Dyke, "Experimental phase of the SHM benchmark studies. Damage detection using NeXT and ERA," in *Proceedings of the 16th ASCE Engineering Mechanics Conference*, Seattle, Wash, USA, 2003.
- [35] J. P. Lynch, "Damage characterization of the IASC-ASCE structural health monitoring benchmark structure by transfer function pole Migration," in *Proceedings of the ASCE Structures Congress and the Forensic Engineering Symposium*, pp. 845–854, New York, NY, USA, April 2005.

- [36] J. Liu, X. Wang, S. Yuan, and G. Li, "On Hilbert-Huang transform approach for structural health monitoring," *Journal of Intelligent Material Systems and Structures*, vol. 17, no. 8-9, pp. 721–728, 2006.
- [37] M. M. McCuskey, M. M. Reda Taha, S. R. Horton, and T. J. Baca, "Identifying damage in the ASCE benchmark structure using a neural-wavelet module," in *Proceedings of the 3rd European Workshop on Structural Health Monitoring*, A. Güemes, Ed., pp. 421–429, Granada, Spain, 2006.
- [38] M. C. McCuskey, *Structural damage classification using optimization of a neural-wavelet module and possibility fusion*, M.S. thesis, Department of Civil Engineering, University of New Mexico, Albuquerque, NM, USA, 2007.
- [39] E. P. Carden and J. M. W. Brownjohn, "ARMA modelled time-series classification for structural health monitoring of civil infrastructure," *Mechanical Systems and Signal Processing*, vol. 22, no. 2, pp. 295–314, 2008.
- [40] M. B. Bishop, *Neural Networks for Pattern Recognition*, Oxford University Press, New York, NY, USA, 1996.
- [41] P. Tsou and M. H. H. Shen, "Structural damage detection and identification using neural networks," *AIAA journal*, vol. 32, no. 1, pp. 176–183, 1994.
- [42] R. S. Sexton, R. E. Dorsey, and J. D. Johnson, "Optimization of neural networks: a comparative analysis of the genetic algorithm and simulated annealing," *European Journal of Operational Research*, vol. 114, no. 3, pp. 589–601, 1999.
- [43] M. F. Elkordy, K. C. Chang, and G. C. Lee, "A structural damage neural network monitoring system," *Microcomputers in Civil Engineering*, vol. 9, no. 2, pp. 83–96, 1994.
- [44] E. Douka, S. Loutridis, and A. Trochidis, "Crack identification in beams using wavelet analysis," *International Journal of Solids and Structures*, vol. 40, no. 13-14, pp. 3557–3569, 2003.
- [45] M. M. Reda Taha, A. Noureldin, J. L. Lucero, and T. J. Baca, "Wavelet transform for structural health monitoring: a compendium of uses and features," *Structural Health Monitoring*, vol. 5, no. 3, pp. 267–295, 2006.
- [46] Z. Su and L. Ye, "An intelligent signal processing and pattern recognition technique for defect identification using an active sensor network," *Smart Materials and Structures*, vol. 13, no. 4, pp. 957–969, 2004.
- [47] H.-F. Lam, K.-V. Yuen, and J. L. Beck, "Structural health monitoring via measured ritz vectors utilizing artificial neural networks," *Computer-Aided Civil and Infrastructure Engineering*, vol. 21, no. 4, pp. 232–241, 2006.
- [48] K.-V. Yuen and H.-F. Lam, "On the complexity of artificial neural networks for smart structures monitoring," *Engineering Structures*, vol. 28, no. 7, pp. 977–984, 2006.
- [49] R. O. Duda, P. E. Hart, and D. G. Stork, *Pattern Classification*, Wiley Interscience, New York, NY, USA, 2001.
- [50] L. H. Yam, Y. J. Yan, and J. S. Jiang, "Vibration-based damage detection for composite structures using wavelet transform and neural network identification," *Composite Structures*, vol. 60, no. 4, pp. 403–412, 2003.
- [51] H. Kim and H. Melhem, "Damage detection of structures by wavelet analysis," *Engineering Structures*, vol. 26, no. 3, pp. 347–362, 2004.
- [52] Y.-S. Diao, H.-J. Li, and Y. Wang, "A two-step structural damage detection approach based on wavelet packet analysis and neural network," in *International Conference on Machine Learning and Cybernetics*, pp. 3128–3133, August 2006.
- [53] X. Jiang and H. Adeli, "Pseudospectra, MUSIC, and dynamic wavelet neural network for damage detection of high-rise buildings," *International Journal for Numerical Methods in Engineering*, vol. 71, no. 5, pp. 606–629, 2007.
- [54] X. Jiang and S. Mahadevan, "Bayesian probabilistic inference for nonparametric damage detection of structures," *Journal of Engineering Mechanics*, vol. 134, no. 10, pp. 820–831, 2008.
- [55] X. Jiang, S. Mahadevan, and R. Guratzsch, "Bayesian wavelet methodology for damage detection of thermal protection system panels," *AIAA Journal*, vol. 47, no. 4, pp. 942–952, 2009.
- [56] H. Sohn, D. W. Allen, K. Worden, and C. R. Farrar, "Structural damage classification using extreme value statistics," *Journal of Dynamic Systems, Measurement and Control*, vol. 127, no. 1, pp. 125–132, 2005.
- [57] E. Altunok, M. M. Reda Taha, and T. J. Ross, "Possibilistic approach for damage detection in structural health monitoring," *Journal of Structural Engineering*, vol. 133, no. 9, pp. 1247–1256, 2007.
- [58] ASCE Benchmark Group, <http://wusceel.cive.wustl.edu/asce.shm/benchmarks.htm>.
- [59] E. Altunok, M. M. Reda Taha, D. S. Epp, R. L. Mayes, and T. J. Baca, "Damage pattern recognition for structural health monitoring using fuzzy similarity prescription," *Computer-Aided Civil and Infrastructure Engineering*, vol. 21, no. 8, pp. 549–560, 2006.
- [60] M. M. Reda Taha, A. Noureldin, A. Osman, and N. El-Sheimy, "Introduction to the use of wavelet multiresolution analysis for intelligent structural health monitoring," *Canadian Journal of Civil Engineering*, vol. 31, no. 5, pp. 719–731, 2004.
- [61] S. G. Mallat, *A Wavelet Tour of Signal Processing*, New York Academic, New York, NY, USA, 1999.
- [62] M. Haase and J. Widjajakusuma, "Damage identification based on ridges and maxima lines of the wavelet transform," *International Journal of Engineering Science*, vol. 41, no. 13-14, pp. 1423–1443, 2003.
- [63] A. V. Ovanesoza and L. E. Suárez, "Applications of wavelet transforms to damage detection in frame structures," *Engineering Structures*, vol. 26, no. 1, pp. 39–49, 2004.
- [64] S. Horton, M. M. Reda Taha, and T. J. Baca, "A neural-wavelet damage detection module for structural health monitoring," in *Proceedings of 5th International Workshop on Structural Health Monitoring*, Stanford, Calif, USA, 2005.
- [65] C. R. Farrar and D. A. Jauregui, "Comparative study of damage identification algorithms applied to a bridge: II. Numerical study," *Smart Materials and Structures*, vol. 7, no. 5, pp. 720–731, 1998.
- [66] J. Li, Y. Zhang, and S. Zhu, "A wavelet-based structural damage assessment approach with progressively downloaded sensor data," *Smart Materials and Structures*, vol. 17, no. 1, Article ID 015020, 2008.
- [67] G. Vanderplatts, *Numerical Optimization Techniques for Engineering Design with Applications*, McGraw-Hill, New York, NY, USA, 1984.
- [68] R. L. Haupt and S. E. Haupt, *Practical Genetic Algorithms*, John Wiley & Sons, New York, NY USA, 1998.
- [69] S. Toussi and J. T. P. Yao, "Assessment of structural damage using the theory of evidence," *Structural Safety*, vol. 1, no. 2, pp. 107–121, 1982.
- [70] M. M. Reda Taha and J. Lucero, "Damage identification for structural health monitoring using fuzzy pattern recognition," *Engineering Structures*, vol. 27, no. 12, pp. 1774–1783, 2005.
- [71] M. Chandrashekhar and R. Ganguli, "Uncertainty handling in structural damage detection using fuzzy logic and probabilistic simulation," *Mechanical Systems and Signal Processing*, vol. 23, no. 2, pp. 384–404, 2009.
- [72] T. J. Ross, *Fuzzy Logic with Engineering Applications*, John Wiley & Sons, London, UK, 2004.

Review Article

Smart Sensing Technologies for Structural Health Monitoring of Civil Engineering Structures

M. Sun,¹ W. J. Staszewski,² and R. N. Swamy²

¹Department of Engineering Structures and Mechanics, School of Science, Wuhan University of Technology, Wuhan 430070, China

²Department of Mechanical Engineering, Sheffield University, Sheffield S1 3JD, UK

Correspondence should be addressed to M. Sun, sunmingqing@yahoo.com

Received 31 August 2009; Revised 7 December 2009; Accepted 3 May 2010

Academic Editor: Jinying Zhu

Copyright © 2010 M. Sun et al. This is an open access article distributed under the Creative Commons Attribution License, which permits unrestricted use, distribution, and reproduction in any medium, provided the original work is properly cited.

Structural Health Monitoring (SHM) aims to develop automated systems for the continuous monitoring, inspection, and damage detection of structures with minimum labour involvement. The first step to set up a SHM system is to incorporate a level of structural sensing capability that is reliable and possesses long term stability. Smart sensing technologies including the applications of fibre optic sensors, piezoelectric sensors, magnetostrictive sensors and self-diagnosing fibre reinforced composites, possess very important capabilities of monitoring various physical or chemical parameters related to the health and therefore, durable service life of structures. In particular, piezoelectric sensors and magnetostrictive sensors can serve as both sensors and actuators, which make SHM to be an active monitoring system. Thus, smart sensing technologies are now currently available, and can be utilized to the SHM of civil engineering structures. In this paper, the application of smart materials/sensors for the SHM of civil engineering structures is critically reviewed. The major focus is on the evaluations of laboratory and field studies of smart materials/sensors in civil engineering structures.

1. Introduction

Civil engineering infrastructure is generally the most expensive national investment and asset of any country. In addition, civil engineering structures have long service life compared with other commercial products, and they are costly to maintain and replace once they are erected [1]. Further, there are few prototypes in civil engineering, and each structure leads to be unique in terms of materials, design, and construction. The most important structures include bridges, high-rise buildings, power utilities, nuclear power plants, and dams. All civil structures age and deteriorate with time. The deterioration is mostly the result of aging of materials, continuous use, overloading, aggressive exposure conditions, lack of sufficient maintenance, and difficulties encountered in proper inspection methods. All of these factors contribute to material and structural degradation as internal and external damages emerge and coalesce, and then evolve and progress.

To ensure structural integrity and safety, civil structures have to be equipped with Structural Health Monitoring

(SHM), which aims to develop automated systems for the continuous monitoring, inspection, and damage detection of structures with minimum labour involvement [2]. An effective SHM system can in real time, and online, detect various defects and monitor strain, stress, and temperature so that the optimum maintenance of the structures can be carried out to ensure safety and durable service life. In general, a typical SHM system includes three major components: a sensor system, a data processing system (including data acquisition, transmission, and storage), and a health evaluation system (including diagnostic algorithms and information management). The first step to set up this system is to incorporate a level of stable and reliable structural sensing capability. So, this paper is mainly related to the first component of the SHM system: the sensing system formed by smart materials/sensors. Smart materials/sensors, such as fibre optic sensors (FOS), piezoelectric sensors, magnetostrictive sensors, and self-diagnosing fibre reinforced structural composites, possess very important capabilities of sensing various physical and chemical parameters related to the health of the structures. Since shape memory alloys and

magnetorheological fluids are often used as actuators, they are not introduced in this paper.

FOS, for example, are small and therefore do not affect the performance characteristics of civil engineering structures in which they are embedded. A single fibre can efficiently monitor structural performance at various locations by using multiplexed or distributed sensing technologies. They are unperturbed by electromagnetic interference. Optical waves are suitable for long transmission distances of relatively weak signals. Piezoelectric and magnetostrictive sensors can serve as both sensors and actuators, which make SHM to be an active monitoring system. Furthermore, they can come in a variety of sizes, allowing them to be placed everywhere, even in remote and inaccessible locations, to actively monitor the conditions of various types of structures.

Since the subject matter of SHM has been growing rapidly and significantly over the last few years, the focus of this paper is on a critical state-of-the-art review of various applications of the above smart materials/sensors in SHM of civil engineering structures. It is beyond the scope of the paper to describe all the relevant theories involved, or to report all of practical applications examples. The paper covers the major aspects of fibre optic sensors, piezoelectric sensors, self-diagnosing fibre reinforced composites, and magnetostrictive sensors for applications in civil engineering. Finally, the conclusions of this study are briefly reported.

2. Fibre Optic Sensors (FOSs)

There are several methods to classify FOS. The first method of classifying FOS is based on the light characteristics (intensity, wavelength, phase, or polarization etc.) modulated by the parameters to be sensed. The second method classifies an FOS by whether the light in the sensing segment is modified inside or outside the fiber (intrinsic or extrinsic). FOS can also be classified as local (Fabry-Perot FOS or long-gauge FOS etc.), quasidistributed (fibre Bragg grating) and distributed sensors (Brillouin-scattering-based distributed FOS) depending on the sensing range [3]. This method of classification is adopted here. FOS are generally surface mounted on existing structures, or embedded in newly constructed civil structures, including bridges, buildings, and dams, to yield information about strain (static and dynamic), temperature, defects (delamination, cracks and corrosion), and concentration of chloride ions. The obtained data can be used to evaluate the safety of both new-built structures and repaired structures, and diagnose location and degree of damages. In this section, the application of FOS in monitoring of strain, displacement and defects in civil engineering structures is reviewed. Other relevant details may be found in early reviews of FOS by Merzbacher et al. [4], Ansari [5] and Leung [6].

2.1. Monitoring of Strain and Displacement. Laboratory studies have clarified some basic sensing properties of FOS in applications for civil engineering structures. De Vires et al. [7] reported that Fabry-Perot FOS output signals compared

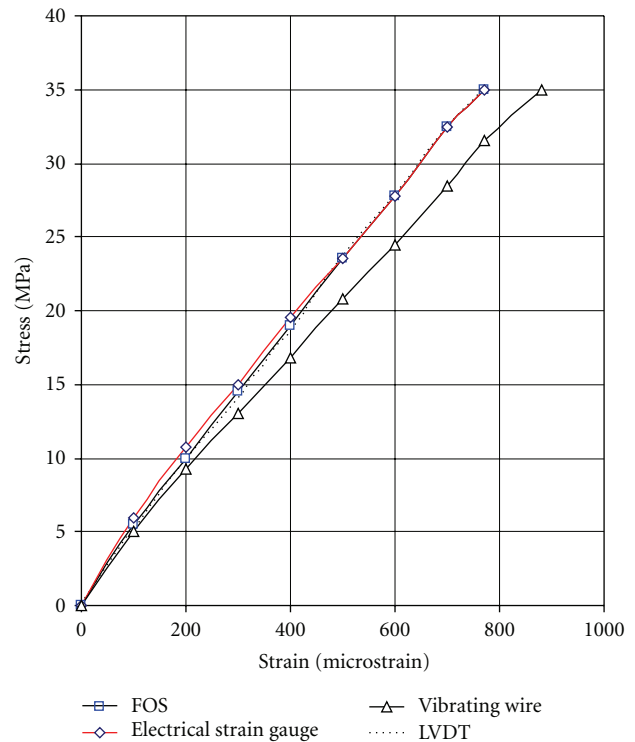


FIGURE 1: Comparison of concrete strains with various sensors [8, 9].

well with the output signals obtained from collocated strain gauge in the test of a concrete cross-beam specimen, and FOS had a much better signal-to-noise ratio than the strain gauge. Quirion and Ballivy [8, 9] have evaluated the performance of the Fabry-Perot FOS when it was embedded in concrete cylinders. Figure 1 shows the measurements obtained with FOS compared to those by vibrating-wire gauges, electrical strain gauges, and LVDT when the level of stress is slightly over 40% of concrete compressive strength. It can be observed that measured strains with the FOS are in good agreement with those measured by the electrical strain gauge and LVDT. Zhang et al [10] conducted a repeated loading test on a concrete slab with embedded FOS. Four million cycles at a frequency of 2 Hz and 3 Hz were applied. The sensors survived the 4 million loading cycles at a strain amplitude of $2000 \mu\epsilon$, and showed good response to dynamic loading. Delepine-lesoille et al. [11] designed a kind of composite-made wave-like sensor body, which could make the stiffness of optical fiber and concrete match to one another. Thus, strain concentrations were reduced, and no theoretical calibration factor had to be taken into account. It also achieved continuous bonding to the concrete and allowed a symmetrical response under tensile and compressive loadings whatever the contact condition was.

Zeng et al. [12] measured the strain distributed along a 1.65-m reinforced concrete beam using one single-mode fibre, called as Brillouin-scattering-based distributed FOS which could measure temperature and strain simultaneously. Strain measurement accuracy reached $\pm 5 \mu\epsilon$ with the resolvable distance of 5 cm. Chen et al. [13] compared two

kinds of distributed sensors: Electric Time Domain Reflectometry cable sensor that was based on the propagation of electromagnetic waves in an electrical cable and Brillouin-scattering-based distributed FOS. They were mounted near the surface of the 80% scale beam-column reinforced concrete assembly. Results showed that the cable sensor could measure a significant change of strain locally while distributed FOS were good candidates for the measurement of slowly-varying strain over a long distance. The cable sensor measured a strain distribution in seconds or shorter and therefore applicable for dynamic signal measurements. However, FOS required several minutes to complete one measurement. Wu et al. [14] installed Brillouin-scattering-based distributed FOS to evaluate the performance of a full-scale prestressed concrete girder. Compared with the measurement results from strain gage, FOS gave good results for tension strain measurement. But, FOS for compression strain measurement included a relatively large error, especially when the compression strain was small.

In aspect of the practical applications of FOS, Beddington Trail Bridge in Calgary, Canada was the first bridge in the world to be monitored by a fibre Bragg grating (FBG) sensing system and the first highway bridge to use carbon fibre reinforced polymer composite (CFRP) prestressing tendons in some of its girders. In this bridge, several tendons were equipped with a total of 18 FBG sensors after prestressing in 1993 [15]; 15 of sensors survived and functioned correctly. The relaxation behaviour of prestressing tendons from the combined effects of distressing, concrete creep and shrinkage, dead loads of the bridge deck and the posttensioning was evaluated. They found that there was a higher net strain relaxation in the steel prestressed concrete girders than that in the CFRP tendon, and continuing stress relaxation existed apparently in all girders eight months after the opening of the bridge to traffic. A dynamic truck test showed that these sensors were still operative six years later, and no structural problems were detected [16]. Above all, the more important significance of their study lies in that this project demonstrated the benefits and advantages of merging optic sensing technology, innovative fibre reinforcement materials and structural engineering. The real-time monitoring of FRP reinforcement components can increase user confidence of their application in concrete structures, since there are no current design standards for structures with FRP reinforcements. On the other hand, the optic sensors can be bonded on the surface of the fibre reinforcement bars so that the bars can provide excellent protection of the sensors and their leads, and yield a very convenient means of instrumenting and monitoring civil engineering structures in the field.

Currently, many bridges around the world have been instrumented with FOS sensing system. Benmokrane et al. [17] applied Fabry-Perot FOS to the rehabilitation project of the Joffre Bridge, Quebec, Canada. They were bonded to the CFRP grids and steel girders to monitor the performance of the FRP reinforced structure, strains of the deck and strains of the girder. The results showed that the temperature was the most important factor influencing the strain variation in the bridge deck under service conditions. The field

measurements were carried out one year after the opening of the bridge to traffic. Using three 25-ton calibrated trucks to evaluate the strain level in the FRP reinforcements, the measured strains in the FRP reinforcements were less than $20 \mu\epsilon$, and strains in the steel girder were less than $120 \mu\epsilon$. Mufti et al. [18] described the procedure of embedding FBG sensors in the Confederation Bridge, Canada, but no data from these sensors have been reported. In Taylor Bridge, a total of 63 FBG sensors and a total of 26 electric strain gauges were bonded to the prestressing CFRP bars to monitor the maximum strain in the reinforcement due to the applied loads. But even though the strain gauges were properly sealed, over 60% of the electric strain gauges malfunctioned due to excessive moisture resulting from steam curing of the concrete girders. Strains recorded by FBG sensors were less than $15 \mu\epsilon$ when a 36-ton truck passed the bridge. Besides these, there are some other demonstration projects in Canada undertaken by ISIS. More details can be found in http://www.isiscanada.com/field/main.htm?field_projects.htm.

Brönnimann et al. [19] reported the application of FBG in two bridges in Switzerland. In the Storchenbrücke in Winterthur, FBG were adhered to CFRP wires to measure the strain of suspension cables. FBG had been working reliably within the strain level around $2000 \mu\epsilon$ for three years by March 1st, 1999. The other was a pedestrian bridge with CFRP as the prestressing cable, where the optical fibre was embedded in CFRP wire during the pultrusion of CFRP. Most of the FBG sensors embedded inside suffered from the high curing temperature of the resin of about $170\text{--}190^\circ\text{C}$ and the high level prestressing strain of $8000 \mu\epsilon$, although two of them failed due to debonding. They have satisfactorily monitored the strain evolution within the cables and the anchor head during the prestressing process and afterwards for over a year.

Inaudi and Vurpillot [20] developed a new method to retrieve the global deformation and curvature of bridges using their long-gauge SOFO sensors. 96 SOFO, with a gauge length of 4 m, were embedded in the first two spans of the Versoix Bridge. Based on the physical model they proposed, global horizontal and vertical deformations of a total length of over 100 m were calculated when the static load was applied on the bridge, and the values matched well with that measured by the dial gauges. In a similar way, the curvature variations of the Lutrive Highway Bridge with truck circulation were monitored. In addition, field displacement monitoring was performed in some phases of construction of the Siggenthal Bridge, such as concreting of different arch, removal of the scaffolding and free standing phase of the arch [21].

Fuhr et al. [22] described the FOS installation process in a 67 m long steel truss bridge spanning the Winooski River in Waterbury, Vermont; 46 FOS were embedded in the deck but only one sensor was broken. They [23] have developed a frequency-domain-based multiplexing sensor to measure pressure and vibration simultaneously. The hydroelectric dam on the Winooski River in Vermont was an example where this kind of FOS was incorporated into. During the initial low-power testing of the generation equipment, an

abnormal frequency was found, which indicated that a main gear in the power train was out-of-round [24].

Ou and Zhou [25] reported their work on FOS applied in bridge monitoring in mainland China, especially in Harbin Institute of Technology. FBG sensors were implemented in over 10 practical bridges to monitor strain, stress and temperature. For example, 40 FBG strain sensors, 10 FBG temperature sensors, and 96 FBG cable sensors have been successfully installed in Yonghe Bridge in Tianjin City, China. The strain of the main beam, the stress of the prestressed reinforcement and the cables were monitored during bridge load test [26]. Liu and Jiang [27] developed a SHM system for the first cable-stayed bridge across the Yangtze River in China. Both the FBG-based overloading vehicle recognition system and remote real-time cable force monitoring system operated successfully.

Habel et al. [28] integrated quasi-distributed FOS into rock anchors to monitor the strain distribution along the fixed anchor length inside the rock. In order to improve the stability of the EDER-dam, Germany, a vertical anchoring of the dam was performed. The quasi-distributed FOS was made by inserting fibre splices at regular intervals along the optical fibre, each segment working as a strain gauge based on time-of-flight measurement. As the anchor was fabricated, an FOS-equipped aramid rod was placed in the centre of the anchor. Data from FOS indicated that only 2 to 2.5 m of the fixed anchor length of 10 m contributed to the bond, and this value varied with the changing water level. The sensing system had survived in such a harsh environment with anchor forces of 4500 kN.

Fiber optic monitoring system has also been introduced into civil structures under extreme exposure conditions. For example, Newhook et al. [29] have designed a FOS health monitoring program for the Hall wharf. It was in both the splash and tidal zones, and subjected to thermal ranges of -35°C in winter and $+35^{\circ}\text{C}$ in summer. Unfortunately the survivability rate of FOS was not high. After the sensors were embedded for one year, 10 of the 17 sensors were not functioning. The main reason for failures of sensors was associated with connector failures. The manufacturing flaw, salt crystals or other dirt caused the failure of the bonding agent holding the connector sheath to the fibre optic cable.

In general civil buildings, Fuhr et al. [30] installed FOS in a five-storey, 65000 square feet concrete structure, named the Stafford Medical Building of Vermont University, to monitor stresses incurred during the construction phase and monitoring of concrete curing as well as internal crack sensing. Kwon et al. [31] used Brillouin-based distributed FOS to measure temperature distribution in a building construction. The optical fibre with a length of 1400 m was installed on the surface of the building. And the temperature of surface changed normally up to 4°C through one day.

Among all smart sensors, only FOS have been used exclusively to monitor so many practical civil structures effectively. These applications show that FOS are more promising for SHM of civil engineering structures than other smart sensors. Of course, the monitoring of the local strain of key components of civil engineering structures and displacement of the whole structure is only one of the

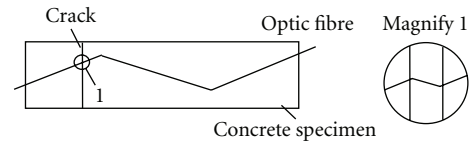


FIGURE 2: The “zig-zag” layout of optic fibre at the bottom of the specimen [33]

important contents of the SHM system. The local strain can be used to detect the working conditions of components. The data obtained are compared to initial design values of the structures under factored gravity and live loads to examine if the structures are in the status expected.

2.2. Detection of Defects. Application of FOS in SHM of civil engineering structures involves detection of defects such as cracks, corrosion, and delamination. Crack detection is dependent on loss of optical transmission, and FOS-based ultrasonic wave methods. Detection of corrosion, pH, and chloride content is mainly dependent on colour modulation.

Rossi and Le Maou [32] used optical fibres to monitor the shape of the crack tip in concrete. The operation of their method was based on the breakage of fibres as a crack propagating in concrete reached the optical fibres. However, its use was limited if one did not know crack location in advance since the polymeric coating of the fibre in the cracking zone had to be removed before embedding it in concrete. Leung et al. [33] developed a method of monitoring flexural cracks in a concrete beam. The optical fibre was laid in a “zig-zag” form at the bottom of the concrete beam (see Figure 2). When a crack opens in the structure, the optical fibre intersecting the crack at an angle other than 90° had to bend. The sudden bending of the fibre at the crack resulted in an optical power loss. For this method to work, the fibre should be free to slide inside the concrete. Preliminary experimental results on concrete specimens showed that the proposed approach could detect the crack opening width as small as 0.1 mm. Recently, their method was used to monitor multiple flexural cracks under static loading, crack monitoring under cyclic loading as well as the detection of shrink crack under restraint in concrete beams [34]. However, this method was not feasible to detect cracks parallel to the surface of the structure. Elvin et al. [35] proposed a FOSs based technique for the monitoring of delamination that was parallel to the surface of the structure. In their method, a moving load was applied on the measured beam with one arm of the Servo-Homoddyne interferometer attached below the surface. The output of the interferometer represented the optical phase shift and was proportional to the integrated strain along the embedded fibre. When the position of loading moved, the curve of the phase change versus load position could be obtained. It was found that the phase change was very sensitive to both the delamination location and size.

Gu et al. [36] employed a quasi-distributed FOS similar to that used by Habel et al. [28] for measurement of crack opening widths along the whole length of reinforced concrete

beams under four-point bending. A linear relationship between the crack opening width and the loss of the optical intensity was concluded. It was found that the embedded FOS could keep a good accounting of the cracks during fatigue loading and monotonic loading.

FOS can also be utilised as ultrasonic/acoustic sensors to detect cracks. Chen and Ansari [37] reported a fibre optic distributed pulse-echo system for monitoring defects in a concrete beam. A PZT transmitter was used for the generation of stress waves. The FOS was adhered to the surface of the beam for sensing the echoed ultrasonic signals. Preliminary laboratory study showed that this system had detected two simulated flaws within the beam based on the resonance method. Chen and Farhad [38] developed an FOS acoustic sensor. It could monitor the acoustic emissions from cracks in a concrete structure. Betz et al. [39] reported that FBG sensors had the ability to sense ultrasonic Lamb waves.

As a whole, major investigations in this field are preliminary laboratory studies. The method proposed by Rossi and Le Maou [32] requires a priori knowledge of crack location; techniques of Leung et al. [33], and Gu et al. [36] can perform distributed or quasi-distributed detection of cracks which is normal to the fibre direction; the approach of Elvin et al. [35] is only for horizontal cracks. Ultrasonic wave methods can work without the limitation of the direction of crack. Previous studies have exhibited the capability of ultrasonic waves to detect delamination, voids, and cracks in concrete structures [40–42].

With respect to corrosion detection, Fuhr and Huston [43] reported their rebar corrosion detection technique using FOS based on colour modulation. When the fibre was in close proximity (<10 mm) to the corroding rebar, the input light from the fibre at its end or at a windowed region was colour modulated. Then the modulated signal travelled back down the fibre and was sensed via standard spectroscopy. By comparing the corroded and uncorroded spectra, peak wavelength shift along with the intensity of the light signal revealed the presence and the level of corrosion. The experimental result coming from this sensor was in agreement with the conventional monitoring methods of steel corrosion. The main limitation of this sensor was its small signal-to-noise ratio. Tennyson et al. [44] examined the loop strain of a concrete column using long-gauge FOS so that steel corrosion in concrete could be monitored as the internal corrosion causes the columns to swell. But, experimental results have not been reported. Wang et al. [45] made use of the microbending characteristic of long-period optical grating (LPPG) to monitor the steel corrosion in concrete structures. As the radial expansion of the steel resulting from the steel corrosion led to the bending of LPPG, the curvature of LPPG could be obtained by analyzing the change of spectrum, and then the steel corrosion depth could be measured. This method was independent of the variety in temperature, strain, and refractive index owing to the inimitable spectrum characteristic of LPPG.

Cosentino et al. [46] developed a fibre optical chloride sensor using Ag_2CrO_4 powder bonded to the end of an optical fibre. This sensor worked when the chloride changed a reddish-brown Ag_2CrO_4 to white AgCl . The colour change

caused the intensity of light propagating through the fibre to increase. They reported that chloride concentration was in proportion to the slope of the light output versus time plots. But the drawback of this sensor was that it was not a reversible sensor, so it was difficult to detect increasing and decreasing chloride concentrations continuously.

Michie et al. [47] reported a distributed moisture and pH detection scheme which used a cable with surface-mounted hydrogel polymer coating and optical fibre. The hydrogel absorbed water and swelled in aqueous media so that the loss of an optical fibre was modulated. The system was tested in a simulated experiment to examine the extent of grout fill in a posttensioned concrete structure tendon duct. In their experiment, voided regions with no water were identified. By selection of the appropriate gel system as the indicator which was responsive to changes in pH, this type of sensor could detect the areas where the pH of the grout dropped. The decrease in pH would expose the tendons to potential corrosion. Grahn et al. [48] developed a FOS system for the measurement of pH in concrete consisting of pH-indicator dyes immobilized in a highly hydrophilic polymer matrix. Change in pH was indicated by a colour change of the dye/polymer system. The sensor system displayed long-term stability even in aggressive media of pH 12–13.

2.3. Concluding Remarks of FOS. FOS have the sensing capability both in the laboratory and in the field as local, quasi-distributed (or multiplexed) and distributed sensors. Various applications of FOS in civil engineering structures, such as monitoring of strain, displacement, vibration, cracks, corrosion, and chloride ion concentration have been developed. Especially, field tests on bridges, hydroelectric projects, and some civil buildings have proved to be effective. FOS can work in the harsh natural environment, and have large sensing scope, joining with low transmission loss and anti-electromagnetic interference, so they are very advantageous to perform SHM of civil engineering structures. However, because the study of FOS in civil engineering structures is relatively recent, and the earliest reports date back only to 1989, their long-term sensing ability under field experimental conditions due to aging has to be investigated further. They are fragile in some configurations, and the damage is difficult to repair when embedded. The optical connection parts, which connect the embedded optical fibre with the outer data recording system, are also weak elements of the FOS system. Field examples using FOS to detect defects and damages have not yet been fully investigated and reported.

3. Piezoelectric Sensors

Based on electrical-mechanical transformation, piezoelectric materials exhibit simultaneous actuator/sensor behaviour. There are various types of piezoelectric materials: piezoelectric ceramics, piezoelectric polymers, and piezoelectric composites. More recently, piezoelectric sensors were introduced into SHM of civil engineering structures as an active sensing technology based on the measurement of electrical impedance and elastic waves.

3.1. Electrical Impedance-Based SHM Method. When a PZT patch attached to a structure is driven by a fixed, alternating electric field, a small deformation is produced in the PZT wafer and the attached structure. Since the frequency of the excitation is very high, the dynamic response of the structure reflects only that of a very local area near the sensor. The response of that local area to mechanical vibration is transferred back to the PZT wafer in the form of an electrical response. When a crack or damage causes change of the mechanical dynamic response, it is manifested in the electrical impedance response of the PZT wafer [49]. Therefore, structural damages can be monitored indirectly through measurement of the electrical impedance of the PZT sensors.

Ayres et al. [50] bonded two PZT patches to a quarter-scale steel truss bridge joint for the acquisition of the electrical impedance when the damage was simulated by loosening bolts in the structure. The real part of admittance (reciprocal of impedance) was extracted as a function of the exciting frequency. Admittance was sensitive to the local damage near the PZT, but was insensitive to damage away from the sensor. Similar tests have been done by Park et al. [51]. However, besides the electrical impedance method, Park et al. have also used Lamb wave method to detect damages in a steel bridge component. Park et al. [52] have monitored the cracking process of a small-scale composite-reinforced masonry concrete wall under uniaxial compression using this method. Besides it, the stability of the impedance-based technique was examined with a civil pipe joint under significant temperature variation in the range of 25–75°C. The impedance changed as temperature varied. However, when damage was introduced, the temperature made little influence on the qualitative detection result. They [53] also developed a compensation technique to minimise the effects of temperature on impedance measurement. The compensation procedure was based on the reconstruction of the damage metric, which minimised the impedance drifts due to temperature. Further, Yang et al. [54] studied the influence of environmental conditions, temperature and thickness of the bonding layer between PZT patches and aluminum plate on the repeatability of electrical admittance signatures. Experimental investigations revealed that under various environmental conditions electrical admittance was stable for a monitoring period of up to one and a half years. The effect of bonding could be neglected even for thickness up to two-thirds of the PZT patch's thickness, provided that the excitation frequency did not exceed 100 kHz. Above this frequency, the adverse effect of thick (larger than one-third of the PZT thickness) bonding was obvious. By comparing the admittance at the high frequency range (200–1000 kHz), a temperature change triggered the shift of the PZT resonance peaks. Some vital experimental observations in [54] have been successfully verified by means of simulation of the PZT–structure interaction using the commercially available software, ANSYS version 8.1 [55].

Soh et al. [56] carried out an impedance-based health monitoring and damage detection using PZT patches on a prototype reinforced concrete (RC) bridge. The bridge was instrumented with 11 PZT patches at key locations. The

patches were scanned for the acquisition of the impedance data at various stages during the loading process. The results showed that the surface mounted PZT patches were very sensitive to the development of cracks in concrete in their local vicinity, but were insensitive to those farther away. Tseng and Wang [57] performed two sets of experimental tests on the concrete beams (100 mm × 100 mm × 500 mm) instrumented with PZT transducers. The root mean-square deviation (RMSD) of the real part of electric admittance increased with the progression of damage on the surface of the specimen or in the depth of the specimen. Lim et al. [58] developed a new method for identifying equivalent structural parameters (stiffness, mass, and damper) from the measured admittance signatures, whereby the identified parameters were used for damage characterization. The method has been applied to detect damages in a truss, a beam and a concrete cube successfully. Comparing with the conventional RMSD, their method gave much better insight into the damage mechanism whereas RMSD gave little clue about the nature of the damage mechanism. While, Wen et al. [59] measured the equivalent circuit parameters of PZT, such as the static compliance, the static resistance, the dynamic inductance, the dynamic resistance, and the dynamic compliance and so forth, to monitor stress and temperature in concrete structures.

The impedance method has used a self-sensing actuator concept: a single PZT acts both as actuator and sensor. The qualitative nature of this technique makes it very accessible for everyone, since it does not require any background knowledge in order to interpret the simple output. Its sensing area is the vicinity of the sensor, which helps to isolate the effect of damage from other far-field changes in loading, stiffness and boundary conditions. But, it is a qualitative method because various types of damage such as cracks, corrosion and delamination will all affect the mechanical impedance similarly, which makes the distinction between each type of damage very difficult. So, once the impedance-based technique detects damage, other quantitative techniques have to be used to determine the exact nature of the damage. Otherwise, the impedance analyzers employed are expensive until now, an efficient and inexpensive methodology for electrical impedance measurement is necessary in the future.

3.2. Elastic Wave-Based SHM Method. Wang et al. [60] and Wu and Chang [61] conducted preliminary studies to detect the debonding between the reinforcing bars and concrete with PZT patches bonded on the steel rebar. A 5-peak burst ultrasonic wave with peak value of 200V was applied on the actuator. Amplitude and time of arrival of the first peak were recorded and analysed. They found that the amplitude of the received signals increased in a linearly proportional manner to the debonding size of the steel bar from the concrete. The arrival time remained constant while the rebar was elastic, but increased as the bar yielded. They [62] also used PZFlex software to simulate the response of the sensor as parameters in RC structures such as crack width, size of debonding and position of the rebar varied. Numerical simulation showed that cracks in RC structures did not affect the sensor output.

When both debonding damage and cracks existed in the structures, debonding damage dominated the output signals. And the depth of the concrete section did not affect the detection of debonding damage.

Kawiecki [63] studied the feasibility of nondestructive damage detection by an array of piezotransducers bonded to the surface of a concrete block. Structural damages were simulated by placing objects with different mass at the surface of the tested specimens. Experimental results indicated that there was a strong correlation between the size and location of a simulated damage and the variation of the magnitude of its transfer function and shift of natural frequency. Anomalies in these signals were repeatable and had distinct characters when they were caused by damages.

Saafi and Sayyah [64] developed an active damage interrogation (ADI) technique to detect delaminations between the repaired concrete and CFRP. As shown in Figure 3, an array of PZT transducers was attached on to the CFRP laminate. The beam has dimensions of $100 \times 150 \times 900$ mm with a notch of $10 \times 25 \times 100$ mm to initiate and accelerate the delamination process. The ADI system actively interrogated the structure through broadband excitation of the transducers. The sensor signals were digitized and the transfer function, cumulative average delta, and damage index of actuator/sensor pairs were computed. Figure 4 shows the relationship between damage index and load. As load increased, the increase of damage index was obvious in Zone 1, while in Zone 2 and Zone 3 damage index started to increase at 160 kN and 200 kN, respectively. So, the process of delamination was detected. The damage was localized with an error of 0.67%.

Sun et al. [65] used PZT patches as sensors or actuators to initiate and receive Rayleigh waves propagating along the surface of concrete beam, and longitudinal waves, shear waves propagating through internal concrete. Results showed that from the velocity of Rayleigh waves and longitudinal waves, both the dynamic modulus of elasticity and dynamic Poisson's ratio of concrete could be calculated. Differences in amplitude of received waves were highly sensitive to the cracking process in concrete due to externally applied loads. Changes in the waveforms could thus reflect the effects of internal microcracking in concrete.

Song et al. [66] have embedded their smart aggregates containing waterproof piezoelectric patches into different types of concrete specimens. The sensor-history damage index matrix and the actuator-sensor damage index matrix were obtained to monitor the time-history and location information of damages in a two-story concrete frame. Their system could also monitor strength of early concrete and impact on the structures. Li et al. [67] reported their research on cement-based 0–3 piezoelectric composites, which had good compatibility with concrete and good piezoelectric properties. Recently, Lu and Li [68] employed sensors made with cement-based 0–3 piezoelectric composites and cement-based 1–3 piezoelectric composites to detect the acoustic waves due to crack propagation in concrete. Both of them provided good results on the accumulated events number of the acoustic emission and crack location. Cracks

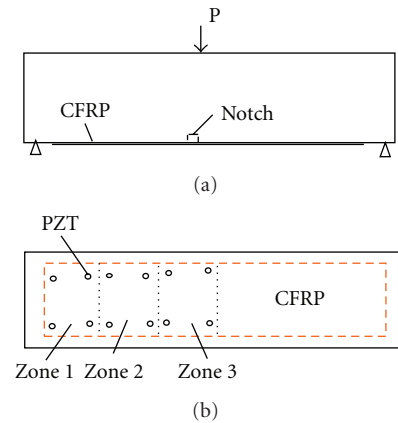


FIGURE 3: Locations of PZT patches on CFRP bonded on concrete beam [64].

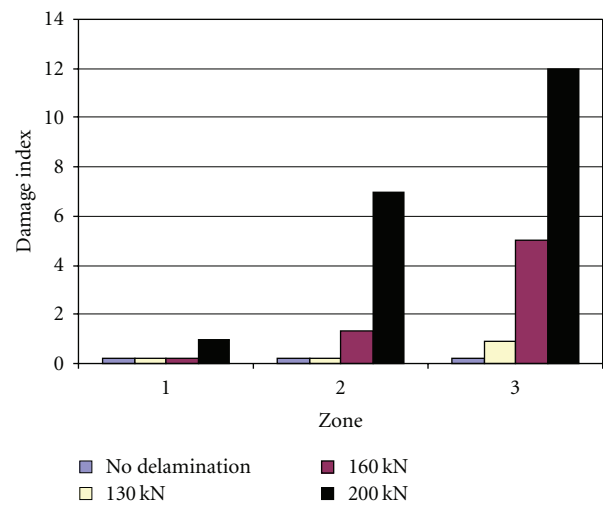


FIGURE 4: The variation of damage index for zone 1, 2 and 3 with applied load increasing [64].

in reinforced concrete beam were monitored by the encapsulated PZT transducers by Zhao et al. [69]. The damage index calculated according to different central frequency elastic wave energy based on continuous wavelet analysis can correctly express the initiation and development of crack in the reinforced concrete beam.

Elastic wave-based approach can detect larger areas than the impedance-based method. Further, the elastic wave-based method can take advantage of more information of the wave propagation to identify damages, such as amplitude and phase of the transfer function, shift in frequencies, amplitude and the arrival time. This method as well as the electrical impedance-based method, is an active sensing method, while most of the SHM techniques are based on passive sensing diagnostics that rely on passive sensor measurements to determine changes in the condition or environment of the structure. However, further studies are needed to verify the feasibility of piezoelectric sensors monitoring methods based on ultrasonic wave propagation to detect various

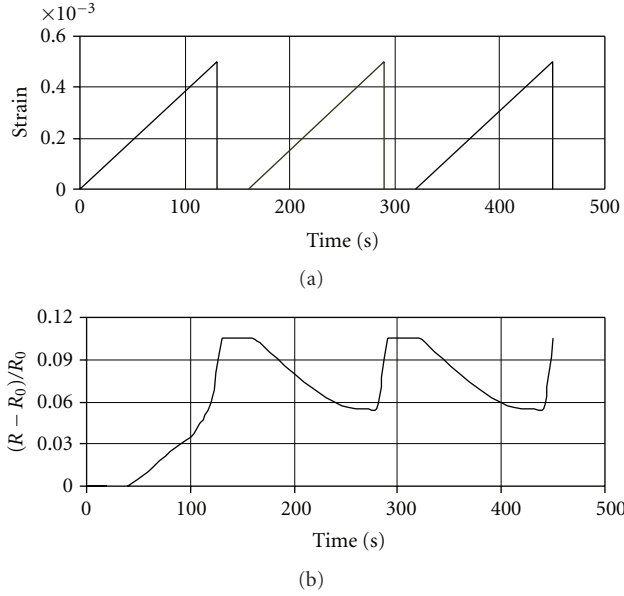


FIGURE 5: $\Delta R/R_0$ and compressive versus time obtained during cyclic loading for CFRC [70].

defects in real concrete elements and reinforced concrete structures by combining other technologies such as wireless communication and algorithms for detection of the positions of damages and the severity of damages.

4. Self-Diagnosing Fibre Reinforced Composites

Self-diagnosing (or self-monitoring) fibre reinforced composites contain an electrical conductive phase such as carbon fibre and conductive powder in the cement or polymer matrix. Table 1 presents the commonly used self-diagnosing fibre reinforced composites and their components. They have the abilities to monitor their own strain, damage, and temperature. Chen and Chung [70, 71] have reported that CFRC can sense strain and damage by its change in electrical resistance. Figure 5 shows the fractional change in resistance along the stress axis as well as the strain during repeated compressive loading within the elastic region. Size of mortar specimens was $5.1 \times 5.1 \times 5.1$ cm, and the content of short carbon fibre was 0.24 vol%. As shown in Figure 5, during the first loading, the irreversibly increasing $\Delta R/R_0$ is due to the weakening of the fibre-matrix interface; during the second and the subsequent loadings, reversibly decreasing $\Delta R/R_0$ during loading is due to fibre push-in, while reversibly increasing $\Delta R/R_0$ during unloading is due to fibre pull-out. At high stress amplitude up to failure, resistance increases greatly. CFRP has similar properties as CFRC [72]. Mao et al. [73] divided the resistance variation of CFRC with strain into three stages: reversible sensing stage, balancing stage (the resistance hardly changes in this phase), and rapidly increasing stage, which corresponded to different phases of crack development in CFRC during loading. Mingqing et al. [74] reported Seebeck effect of CFRC, which was the basis of temperature sensing for CFRC and the cement-based thermoelectric materials.

TABLE 1: Components of self-diagnosing fibre reinforced composites.

| Name of composites | Electrical conductive materials and its volume content in the composites | Matrix materials |
|---|--|---|
| Carbon fibre reinforced concrete (CFRC) | Short carbon fibre (L < 10 mm, <0.5 vol %) | Cement, Mortar, concrete including admixtures (methylcellulose, silica fume et al.) |
| Carbon fiber reinforced Polymer (CFRP) | Short carbon fibre (L < 10 mm, 10 vol %) Continuous carbon fibre (58 vol %) | Resin, curing agent |
| Carbon fiber glass fibre reinforced Polymer (CFGFRP) | Continuous carbon fibre (<0.5 vol %) | Resin, curing agent |
| Carbon powder dispersed in glass-fibre-reinforced plastics (CPGFRP) | Graphite carbon powders (0.15 vol%, average particle diameter = 5 μ m) | Resin, curing agent |
| hybrid carbon fiber reinforced polymer (HCFRP)sensors | high modulus (HM), medium modulus (MM) and high-strength (HS) carbon tows | Resin, curing agent |

L: length

Until now, only some small-scale laboratory studies on smart application of CFRC and CFRP have been conducted. Wen and Chung [75] applied CFRC coatings on the tension and the compression sides of a cement paste beam under flexure. Under cyclic loading and unloading, the resistance of the coating decreased reversibly on the compression face in every cycle, while the resistance increased reversibly on the tension face in every cycle except the first cycle. So, it appears that the CFRC strain-sensing coating was a possible usable form for SHM of concrete structures. Wang et al. [76] found the ultimate load and the stiffness of CFRC-strengthened reinforced concrete (RC) beam are slightly larger than that of the virgin RC beam. Through the measurement of the electrical resistance change, RC beams with the thicker CFRC layer had higher sensitivity to stress and fatigue damage. Wang and Chung [77] also applied CFRP coating containing short carbon fibre on cube specimens of mortar to measure the strain. The sensing limits of this sensor were 0–420 $\mu\epsilon$ in tension and 0–1100 $\mu\epsilon$ in compression respectively. Exceeding these limits was found to cause damages in the coating. It was thus clear that this CFRP coating could not satisfy the requirements for practical applications to monitor the performance of concrete structures in real life.

CFGFRP was designed to be a hybrid of a conductive carbon fibre with a small ultimate elongation value and an insulating glass fibre with a large ultimate elongation value. As shown in Figure 6, during tensile loading, a distinct and significant change in electrical resistance indicated the

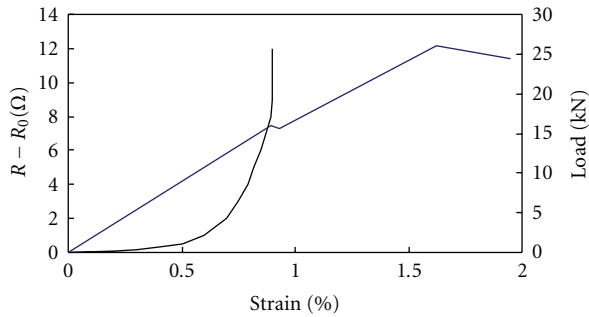


FIGURE 6: Change in electrical resistance with strain increasing [78].

failure of carbon tows. After that, CFGFRP does not fracture suddenly since the load was sustained by the remaining high-elongation glass fibres. So CFGFRP had possibilities of self-diagnosing function without the occurrence of sudden failure. It can be used to give early-warnings of catastrophic failure of structures, and monitor high values of strain through the use of carbon fibres with different ultimate elongation values. A CFGFRP grid has been embedded in the 20th floor slab of the skyscraper known as the Republic Plaza in Singapore, to detect the occurrence of cracks in concrete. CFGFRP has also been used as a security system for security walls with functions of both detecting and preventing burglaries [78, 79].

However, the sensitivity of CFGFRP to strain is very low in the strain range from zero to the point just before carbon fibre fracture. After the breakage of carbon tows, CFGFRP can not continue to sense strain or cracks. Therefore, CFGFRP is generally unsuitable for strain monitoring in the small or medium strain range. However, CPGFRP (carbon powder dispersed in glass-fibre-reinforced plastics) prepared by Muto et al. [80], was superior to CFGFRP with respect to their capability of monitoring in the above-mentioned strain range. But CPGFRP suffered from difficulties of mass production and high cost. While, Yang and Wu [81] employed a new method to improve the sensing capability of CFRP by pulling the impregnated carbon tows repeatedly through a roller with a diameter of 5 cm. Their aim was to preset some microcracks to the carbon tows. Results showed that the pretreatment could enhance the sensitivity of CFRP to strain more than 100 times, especially in a low strain range. Above all, unlike CFGFRP, Yang et al. [82] used three types of carbon tows (high modulus, medium modulus, and high-strength carbon tows, resp.) to design hybrid carbon fiber reinforced polymer (HCFRP) sensors. HCFRP sensors could monitor the whole loading procedure of concrete structures with high sensitivity, including the elastic deformation, the yielding of reinforcing steel bars, and the initiation and propagation of cracks in concrete.

The technique of SHM using self-diagnosing fibre reinforced composites as sensors is a simple technology. One of the most obvious advantages of this type of smart materials is that they work as both structural materials and sensing materials. CFRP and GFRP can be used as reinforcing elements for concrete, as shown in Section 2 of this paper.

CFRC containing small volumes of short fibres possesses higher stiffness, tensile strength and lower drying shrinkage than plain concrete. Thus the incorporation of carbon fibres has not only provided smart abilities, but also improved the mechanical properties of concrete. Laboratory studies have shown that they have the abilities to monitor their own strain, damage and temperature. CPGFRP and HCFRP have better sensitivity than CFGFRP. However, until now, field applications of this kind of smart material in SHM of civil engineering structures have not been developed. Further, the sensing repeatability of self-diagnosing fibre reinforced composites is needed to improve. There are many factors that can affect the repeatability of self-diagnosing fibre reinforced composites, including: (1) distribution state of conductive materials in the matrix; (2) electrical resistance change due to temperature, moisture, and transversal effect; (3) irreversible increase of resistance due to the damages of the sensing materials and interfaces during cyclic loading; and (4) methods of resistance measurement and preparation of materials.

5. Magnetostrictive Sensors

Ferromagnetic materials have the properties that, when placed in a magnetic field, they are mechanically deformed. This phenomenon is called the magnetostrictive effect. The reverse phenomenon, in which the magnetic induction of the material changes when the material is mechanically deformed, is called the inverse magnetostrictive effect. Based on these phenomena, Kwun and Bartels [83] invented a type of magnetostrictive sensor (MsS) which could generate and detect guided waves in the ferromagnetic materials under testing without direct physical contact to the material surface. Khazem et al. [84] utilized MsS to inspect suspender ropes on the George Washington Bridge in New York. They launched a pulse of 10 kHz longitudinal guided wave along the length of the suspender, detected the reflected signals from geometric features and defects in the suspender.

Na and Kundu [85] used MsS for internal inspection of voids and inclusions in concrete-filled steel pipes. It was shown that the MsS system could generate different guided wave modes propagating along the steel pipe; and these waves were sensitive to the defects in the pipe. The received wave amplitudes decreased as the length of voids and inclusions increased. To overcome the major disadvantage of MsS, that is, the relatively low ultrasonic energy transmitted, Na and Kundu [86] developed a hybrid approach combining PZT and MsS. This method was very effective for steel bar-concrete interface inspection. Bouchilloux et al. [87] measured the stress of the steel cable based on the reverse magnetostrictive effect. The accuracy of the MsS was within 3%; but the perturbation of temperature affected the accuracy. The difference between two extremes of temperature, that is, between 10°C and 50°C, was 6%. Rizzo and Di Scalea [88] used the discrete wavelet transform to extract damage-sensitive features from the signals detected by MsS to construct a multidimensional damage index vector. The damage index vector was then fed to an artificial neural

network to provide the automatic classification of the size of the notch and the location of the notch of multiwire strands.

MsS can generate different guided wave modes by simply changing the coil or magnet geometry. They can work without any couplants. Guided waves have strong potentials for monitoring because of the capability for long-distance inspections. However, MsS is only suitable for ferromagnetic materials. Relatively low ultrasonic energy with low signal to noise ratio can be transmitted. And the induced energy is critically dependent on the probe proximity to the object being tested.

6. Concluding Remarks

Smart materials/sensors are a new development with enormous potential for SHM of civil engineering structures. Some of them are currently being applied in the field, while others are being evaluated under laboratory conditions.

FOS are versatile sensors for SHM applications in civil engineering. Various applications of FOS in civil engineering structures, such as monitoring of strain, displacement, vibration, cracks, corrosion, and chloride ion concentration, have been developed. In particular, field tests reported on bridges, hydroelectric projects, and some civil buildings have been found to be effective. FOS can work in a harsh natural environment, and have large sensing scope, joining with low transmission loss, antielectromagnetic interference and distributed sensing, and so they are advantageous to apply for SHM of civil engineering structures. However, the long-term sensing ability of FOS under field experimental conditions due to aging has not been fully established, and needs to be investigated further. They are fragile in some configurations, and the damage is difficult to repair when embedded. The optical connection parts, which connect the embedded optical fibre with the outer data recording system, are also weak elements of the FOS system. Field examples using FOS to detect defects and damages have not yet been fully investigated and reported.

Piezoelectric sensors can be used as an active sensing technology in the SHM of civil engineering structures based on electrical impedance and elastic wave methods. The impedance method depends on the self-sensing actuator concept. It is a qualitative method. Elastic wave-based approaches can detect larger areas of damage than the impedance-based method, and this method can take advantage of additional information arising from the wave propagation to identify damages. However, further studies have to be carried out to verify the feasibility of this method to detect various defects in real concrete structures and reinforced concrete structures.

Self-diagnosing fibre reinforced composites are also available as sensors and offer a very simple technology for the SHM of civil engineering structures. One of the most obvious advantages of this type of smart materials is that they work as both structural materials and sensing materials. Laboratory studies have shown that they have the abilities to monitor their own strain, damage and temperature. CPGFRP and HCFRP have better sensitivity than CFGFRP. However, the

practical applications of this type of smart materials in civil engineering structures are yet to be developed.

MsS can generate different guided wave modes by simply changing the coil or magnet geometry. They can work without any couplants. Guided waves have strong potentials for structural health monitoring because of their long-distance inspection capability. However, it is only suitable for ferromagnetic materials. Relatively low ultrasonic energy with low signal to noise ratio can be transmitted.

SHM system must possess the comprehensive abilities to detect positions and severity of damages. However, until now lots of studies about applications of smart sensors/smart materials in SHM of civil engineering are related to the basic sensing abilities of smart sensors. That is, some damages within structures can be monitored directly using data from sensors, while others can only be detected indirectly through special diagnostic methods. Important civil engineering structures are usually very large. So, many sensors are equipped to make structures sense their health conditions. Wireless transmission and processing the data before transmission will be a useful method to solve the problem of bulk data management in the practical SHM system. And SHM of the practical civil engineering structures will greatly depend on diagnostic algorithms such as inverse problem analysis, artificial neural network, and the expert system. So, real SHM system for civil engineering is the integration of smart sensors/smart materials, data transmission, and advanced diagnostic methods.

Acknowledgments

The authors would like to acknowledge the Chinese Scholarship Council (CSC) for the financial support to the first author during his research study at Sheffield University in UK. The work is also supported by the National Natural Science Foundation of China (no. 50878170) partly.

References

- [1] K. P. Chong, "Health monitoring of civil structures," *Journal of Intelligent Material Systems and Structures*, vol. 9, no. 11, pp. 892–898, 1999.
- [2] F. K. Chang, "Structural health monitoring: a summary report on the first international workshop on structural health monitoring," in *Proceedings of the 2nd International Workshop on Structural Health Monitoring*, F. K. Chang, Ed., pp. 3–11, Technomic Publishing Company, Lancaster, UK, September 1997.
- [3] B. Culshaw and J. Dakin, Eds., *Optical Fiber Sensors. Applications, Analysis, and Future Trends*, vol. 4, Artech House, London, UK, 1996.
- [4] C. I. Merzbacher, A. D. Kersey, and E. J. Friebele, "Fiber optic sensors in concrete structures: a review," *Smart Materials and Structures*, vol. 5, no. 2, pp. 196–208, 1996.
- [5] F. Ansari, "State-of-the-art in the applications of fiber-optic sensors to cementitious composites," *Cement and Concrete Composites*, vol. 19, no. 1, pp. 3–19, 1997.
- [6] C. K. Y. Leung, "Fiber optic sensors in concrete: the future?" *NDT and E International*, vol. 34, no. 2, pp. 85–94, 2001.

- [7] M. De Vries, M. Nasta, V. Bhatia et al., "Performance of embedded short-gage-length optical fiber sensors in a fatigue-loaded reinforced concrete specimen," *Smart Materials and Structures*, vol. 4, no. 1A, pp. 107–113, 1995.
- [8] M. Quirion and G. Ballivy, "Concrete strain monitoring with Fabry-Pérot fiber-optic sensor," *Journal of Materials in Civil Engineering*, vol. 12, no. 3, pp. 254–261, 2000.
- [9] M. Quirion and G. Ballivy, "Laboratory investigation on Fabry-Pérot sensor and conventional extensometers for strain measurement in high performance concrete," *Canadian Journal of Civil Engineering*, vol. 27, no. 5, pp. 1088–1093, 2000.
- [10] B. Zhang, B. Benmokrane, J.-F. Nicole, and R. Masmoudi, "Evaluation of fibre optic sensors for structural condition monitoring," *Materials and Structures*, vol. 35, no. 250, pp. 357–364, 2002.
- [11] S. Delepine-Lesoille, E. Merliot, C. Boulay, L. Quélet, M. Delaveau, and A. Courteville, "Quasi-distributed optical fibre extensometers for continuous embedding into concrete: design and realization," *Smart Materials and Structures*, vol. 15, no. 4, pp. 931–938, 2006.
- [12] X. Zeng, X. Bao, C. Y. Chhoa et al., "Strain measurement in a concrete beam by use of the Brillouin-scattering-based distributed fiber sensor with single-mode fibers embedded in glass fiber reinforced polymer rods and bonded to steel reinforcing bars," *Applied Optics*, vol. 41, no. 24, pp. 5105–5114, 2002.
- [13] G. Chen, B. Xu, R. D. McDaniel, X. Ying, D. J. Pommerenke, and Z. Wu, "Distributed strain measurement of a large-scale reinforced concrete beam-column assembly under cyclic loading," in *Smart Structures and Materials: Sensors and Smart Structures Technologies for Civil, Mechanical, and Aerospace Systems*, vol. 5765, article 55 of *Proceedings of SPIE*, pp. 516–527, San Diego, Calif, USA, March 2005.
- [14] Z. Wu, B. Xu, K. Hayashi, and A. Machida, "Distributed optic fiber sensing for a full-scale PC girder strengthened with prestressed PBO sheets," *Engineering Structures*, vol. 28, no. 7, pp. 1049–1059, 2006.
- [15] R. M. Measures, A. T. Alavie, R. Maaskant, M. Ohn, S. Karr, and S. Huang, "A structurally integrated Bragg grating laser sensing system for a carbon fiber prestressed concrete highway bridge," *Smart Materials and Structures*, vol. 4, no. 1, pp. 20–30, 1995.
- [16] R. C. Tennyson, A. A. Mufti, S. Rizkalla, G. Tadros, and B. Benmokrane, "Structural health monitoring of innovative bridges in Canada with fiber optic sensors," *Smart Materials and Structures*, vol. 10, no. 3, pp. 560–573, 2001.
- [17] B. Benmokrane, H. Rahman, P. Mukhopadhyaya et al., "Use of fibre reinforced polymer reinforcement integrated with fibre optic sensors for concrete bridge deck slab construction," *Canadian Journal of Civil Engineering*, vol. 27, no. 5, pp. 928–940, 2000.
- [18] A. A. Mufti, G. Tadros, and P. R. Jones, "Field assessment of fibre-optic Bragg grating strain sensors in the confederation bridge," *Canadian Journal of Civil Engineering*, vol. 24, no. 6, pp. 963–966, 1997.
- [19] R. Brönnimann, PH. M. Nellen, and U. Sennhauser, "Reliability monitoring of CFRP structural elements in bridges with fiber optic Bragg grating sensors," *Journal of Intelligent Material Systems and Structures*, vol. 10, no. 4, pp. 322–329, 2000.
- [20] D. Inaudi and S. Vurpillot, "Monitoring of concrete bridges with long-gage fiber optic sensors," *Journal of Intelligent Material Systems and Structures*, vol. 10, no. 4, pp. 280–292, 2000.
- [21] D. Inaudi, A. Rufenacht, B. Von Arx, H. P. Noher, S. Vurpillot, and B. Glisic, "Monitoring of a concrete arch bridge during construction," in *Smart Structures and Materials: Smart Systems for Bridges, Structures, and Highways*, vol. 4696 of *Proceedings of SPIE*, pp. 146–153, San Diego, Calif, USA, March 2002.
- [22] P. L. Fuhr, D. R. Huston, M. Nelson et al., "Fiber optic sensing of a bridge in Waterbury, Vermont," *Journal of Intelligent Material Systems and Structures*, vol. 10, no. 4, pp. 293–303, 2000.
- [23] P. L. Fuhr and D. R. Huston, "Multiplexed fiber optic pressure and vibration sensors for hydroelectric dam monitoring," *Smart Materials and Structures*, vol. 2, no. 4, pp. 260–263, 1993.
- [24] D. R. Huston, P. L. Fuhr, T. P. Ambrose, and D. A. Barker, "Intelligent civil structures—activities in Vermont," *Smart Materials and Structures*, vol. 3, no. 2, pp. 129–139, 1994.
- [25] J. Ou and Z. Zhou, "Applications of optical fiber sensors of SHM in infrastructures," in *Smart Sensor Phenomena, Technology, Networks, and Systems*, vol. 6933 of *Proceedings of SPIE*, p. 10, San Diego, Calif, USA, March 2008.
- [26] C. Lan, Z. Zhou, S. Sun, and J. Ou, "FBG based intelligent monitoring system of the Tianjin Yonghe Bridge," in *Smart Sensor Phenomena, Technology, Networks, and Systems 2008*, vol. 6933, article 693312 of *Proceedings of SPIE*, p. 9, San Diego, Calif, USA, March 2008.
- [27] S. Liu and D. Jiang, "The application of structural health monitoring system technology FBG-based to no.2 Wuhan bridge over Yangtze river," in *Photonics and Optoelectronics Meetings: Fiber Optic Communication and Sensors (POEM '08)*, vol. 7278 of *Proceedings of SPIE*, Wuhan, China, November 2008.
- [28] W. R. Habel, I. Feddersen, and C. Fitschen, "Embedded quasi-distributed fiber-optic sensors for the long-term monitoring of the grouting area of rock anchors in a large gravity dam," *Journal of Intelligent Material Systems and Structures*, vol. 10, no. 4, pp. 330–339, 2000.
- [29] J. P. Newhook, B. Bakht, A. Mufti, and G. Tadros, "Monitoring of Hall's harbour wharf," in *Health Monitoring and Management of Civil Infrastructure Systems*, vol. 4337 of *Proceedings of SPIE*, pp. 234–244, March 2001.
- [30] P. L. Fuhr, D. R. Huston, P. J. Kajenski, and T. P. Ambrose, "Performance and health monitoring of the Stafford Medical Building using embedded sensors," *Smart Materials and Structures*, vol. 1, no. 1, pp. 63–68, 1992.
- [31] I. B. Kwon, C. Y. Kim, and M. Y. Choi, "Continuous measurement of temperature distributed on a building construction," in *Smart Structures and Materials: Smart Systems for Bridges, Structures, and Highways*, vol. 4696 of *Proceedings of SPIE*, pp. 273–283, March 2002.
- [32] P. Rossi and F. Le Maou, "New method for detecting cracks in concrete using fibre optics," *Materials and Structures*, vol. 22, no. 6, pp. 437–442, 1989.
- [33] C. K. Y. Leung, N. Elvin, N. Olson, T. F. Morse, and Y.-F. He, "A novel distributed optical crack sensor for concrete structures," *Engineering Fracture Mechanics*, vol. 65, no. 2-3, pp. 133–148, 2000.
- [34] K. T. Wan and C. K. Y. Leung, "Applications of a distributed fiber optic crack sensor for concrete structures," *Sensors and Actuators A*, vol. 135, no. 2, pp. 458–464, 2007.
- [35] N. Elvin, C. K. Y. Leung, V. S. Sudarshanam, and S. Ezekiel, "Novel fiber optic delamination detection scheme: theoretical and experimental feasibility studies," *Journal of Intelligent Material Systems and Structures*, vol. 10, no. 4, pp. 314–321, 2000.

- [36] X. Gu, Z. Chen, and F. Ansari, "Method and theory for a multi-gauge distributed fiber optic crack sensor," *Journal of Intelligent Material Systems and Structures*, vol. 10, no. 4, pp. 266–273, 2000.
- [37] X. Chen and F. Ansari, "Fiber optic stress wave sensor for detection of internal flaws in concrete structures," *Journal of Intelligent Material Systems and Structures*, vol. 10, no. 4, pp. 274–279, 2000.
- [38] Z. Chen and A. Farhad, "Embedded fiber optic sensors for detection of acoustic emissions in structures," *Acta Optica Sinica*, vol. 20, no. 8, pp. 1060–1064, 2000.
- [39] D. C. Betz, G. Thursby, B. Culshaw, and W. J. Staszewski, "Acousto-ultrasonic sensing using fiber Bragg gratings," *Smart Materials and Structures*, vol. 12, no. 1, pp. 122–128, 2003.
- [40] N. R. Swamy and R. M. Wan, "Use of dynamic nondestructive test methods to monitor concrete deterioration due to alkali-silica reaction," *Cement, Concrete and Aggregates*, vol. 15, no. 1, pp. 32–49, 1993.
- [41] M. Sansalone, J.-M. Lin, and W. B. Streett, "Determining the depth of surface-opening cracks using impact-generated stress waves and time-of-flight techniques," *ACI Materials Journal*, vol. 95, no. 2, pp. 168–177, 1998.
- [42] Y.-C. Jung, T. Kundu, and M. R. Ehsani, "A new nondestructive inspection technique for reinforced concrete beams," *ACI Materials Journal*, vol. 99, no. 3, pp. 292–299, 2002.
- [43] P. L. Fuhr and D. R. Huston, "Corrosion detection in reinforced concrete roadways and bridges via embedded fiber optic sensors," *Smart Materials and Structures*, vol. 7, no. 2, pp. 217–228, 1998.
- [44] R. C. Tennyson, T. Coroy, G. Duck et al., "Fibre optic sensors in civil engineering structures," *Canadian Journal of Civil Engineering*, vol. 27, no. 5, pp. 880–889, 2000.
- [45] Y. Wang, D.-K. Liang, and B. Zhou, "Measurement of steel corrosion in concrete structures by analyzing long-period fiber grating spectrum character," *Spectroscopy and Spectral Analysis*, vol. 28, no. 11, pp. 2660–2664, 2008 (Chinese).
- [46] P. Cosentino, B. Grossman, C. Shieh, S. Doi, H. Xi, and P. Erbland, "Fiber-optic chloride sensor development," *Journal of Geotechnical Engineering*, vol. 121, no. 8, pp. 610–617, 1995.
- [47] W. C. Michie, B. Culshaw, M. Konstantaki et al., "Distributed pH and water detection using fiber-optic sensors and hydrogels," *Journal of Lightwave Technology*, vol. 13, no. 7, pp. 1415–1420, 1995.
- [48] W. Grahn, P. Makedonski, J. Wichern, W. Kowalsky, and S. Wiese, "Fiber-optical sensors for in-situ monitoring of moisture and pH-value in reinforced concrete," in *Imaging Spectrometry VII*, vol. 4480 of *Proceedings of SPIE*, pp. 395–403, August 2001.
- [49] C. Liang, F. P. Sun, and C. A. Rogers, "Coupled electro-mechanical analysis of adaptive material systems—determination of the actuator power consumption and system energy transfer," *Journal of Intelligent Material Systems and Structures*, vol. 5, no. 1, pp. 12–20, 1994.
- [50] J. W. Ayres, F. Lalonde, Z. Chaudhry, and C. A. Rogers, "Qualitative impedance-based health monitoring of civil infrastructures," *Smart Materials and Structures*, vol. 7, no. 5, pp. 599–605, 1998.
- [51] S. Park, C.-B. Yun, Y. Roh, and J.-J. Lee, "PZT-based active damage detection techniques for steel bridge components," *Smart Materials and Structures*, vol. 15, no. 4, pp. 957–966, 2006.
- [52] G. Park, H. H. Cudney, and D. J. Inman, "Impedance-based health monitoring of civil structural components," *Journal of Infrastructure Systems*, vol. 6, no. 4, pp. 153–160, 2000.
- [53] G. Park, K. Kabeya, H. H. Cudney, and D. J. Inman, "Impedance-based structural health monitoring for temperature varying applications," *JSME International Journal, Series A*, vol. 42, no. 2, pp. 249–258, 1999.
- [54] Y. Yang, Y. Y. Lim, and C. K. Soh, "Practical issues related to the application of the electromechanical impedance technique in the structural health monitoring of civil structures. I. Experiment," *Smart Materials and Structures*, vol. 17, no. 3, Article ID 035008, p. 14, 2008.
- [55] Y. Yang, Y. Y. Lim, and C. K. Soh, "Practical issues related to the application of the electromechanical impedance technique in the structural health monitoring of civil structures. II. Numerical verification," *Smart Materials and Structures*, vol. 17, no. 3, Article ID 035008, p. 12, 2008.
- [56] C. K. Soh, K. K.-H. Tseng, S. Bhalla, and A. Gupta, "Performance of smart piezoceramic patches in health monitoring of a RC bridge," *Smart Materials and Structures*, vol. 9, no. 4, pp. 533–542, 2000.
- [57] K. K. Tseng and L. Wang, "Smart piezoelectric transducers for in situ health monitoring of concrete," *Smart Materials and Structures*, vol. 13, no. 5, pp. 1017–1024, 2004.
- [58] Y. Y. Lim, S. Bhalla, and C. K. Soh, "Structural identification and damage diagnosis using self-sensing piezo-impedance transducers," *Smart Materials and Structures*, vol. 15, no. 4, pp. 987–995, 2006.
- [59] Y. Wen, Y. Chen, P. Li, D. Jiang, and H. Guo, "Smart concrete with embedded piezoelectric devices: implementation and characterization," *Journal of Intelligent Material Systems and Structures*, vol. 18, no. 3, pp. 265–274, 2007.
- [60] C. S. Wang, F. Wu, and F.-K. Chang, "Structural health monitoring from fiber-reinforced composites to steel-reinforced concrete," *Smart Materials and Structures*, vol. 10, no. 3, pp. 548–552, 2001.
- [61] F. Wu and F.-K. Chang, "A built-in active sensing diagnostic system for civil infrastructure systems," in *Smart Systems for Bridges, Structures, and Highways-Smart Structures and Materials*, vol. 4330 of *Proceedings of SPIE*, pp. 27–35, March 2001.
- [62] F. Wu and F. K. Chang, "Diagnosis of debonding in steel-reinforced concrete with embedded piezoelectric elements," in *Proceedings of the 3rd International Workshop on Structural Health Monitoring: The Demands and Challenges*, F. K. Chang, Ed., pp. 670–679, CRC Press, New York, NY, USA, 2001.
- [63] G. Kawiecki, "Feasibility of applying distributed piezotransducers to structural damage detection," *Journal of Intelligent Material Systems and Structures*, vol. 9, no. 3, pp. 189–197, 1998.
- [64] M. Saafi and T. Sayyah, "Health monitoring of concrete structures strengthened with advanced composite materials using piezoelectric transducers," *Composites Part B*, vol. 32, no. 4, pp. 333–342, 2001.
- [65] M. Q. Sun, W. J. Staszewski, R. N. Swamy, and Z. Q. Li, "Application of low-profile piezoceramic transducers for health monitoring of concrete structures," *NDT and E International*, vol. 41, no. 8, pp. 589–595, 2008.
- [66] G. B. Song, H. C. Gu, and Y.-L. Mo, "Smart aggregates: multi-functional sensors for concrete structures—a tutorial and a review," *Smart Materials and Structures*, vol. 17, no. 3, Article ID 033001, 2008.
- [67] Z. Li, D. Zhang, and K. Wu, "Cement-based 0–3 piezoelectric composites," *Journal of the American Ceramic Society*, vol. 85, no. 2, pp. 305–313, 2002.

- [68] Y. Y. Lu and Z. J. Li, "Cement-based piezoelectric sensor for acoustic emission detection in concrete structures," in *Proceedings of the 11th Aerospace Division International Conference on Engineering, Science, Construction, and Operations in Challenging Environments*, vol. 323, March 2008.
- [69] X. Y. Zhao, H. N. Li, D. Du, and J. L. Wang, "Concrete structure monitoring based on built-in piezoelectric ceramic transducers," in *Sensors and Smart Structures Technologies for Civil, Mechanical, and Aerospace Systems*, vol. 6932 of *Proceedings of SPIE*, p. 8, March 2008.
- [70] P.-W. Chen and D. D. L. Chung, "Carbon fiber reinforced concrete for smart structures capable of non-destructive flaw detection," *Smart Materials and Structures*, vol. 2, no. 1, pp. 22–30, 1993.
- [71] P. Chen and D. D. L. Chung, "Carbon-fiber-reinforced concrete as an intrinsically smart concrete for damage assessment during dynamic loading," *Journal of the American Ceramic Society*, vol. 78, no. 3, pp. 816–818, 1995.
- [72] D. D. L. Chung, "Self-monitoring structural materials," *Materials Science and Engineering*, vol. 22, no. 2, pp. 57–78, 1998.
- [73] Q. Mao, B. Zhao, D. Sheng, and Z. Li, "Resistance change of compression sensible cement specimen under different stresses," *Journal Wuhan University of Technology*, vol. 11, no. 3, pp. 41–45, 1996.
- [74] M. Sun, Z. Li, Q. Mao, and D. Shen, "A study on thermal self-monitoring of carbon fiber reinforced concrete," *Cement and Concrete Research*, vol. 9, no. 5, pp. 769–771, 1999.
- [75] S. Wen and D. D. L. Chung, "Carbon fiber-reinforced cement as a strain-sensing coating," *Cement and Concrete Research*, vol. 31, no. 4, pp. 665–667, 2001.
- [76] W. Wang, H. Dai, and S. Wu, "Mechanical behavior and electrical property of CFRC-strengthened RC beams under fatigue and monotonic loading," *Materials Science and Engineering A*, vol. 479, no. 1-2, pp. 191–196, 2008.
- [77] X. Wang and D. D. L. Chung, "Short carbon fiber reinforced epoxy coating as a piezoresistive strain sensor for cement mortar," *Sensors and Actuators, A*, vol. 71, no. 3, pp. 208–212, 1998.
- [78] N. Muto, H. Yangagida, T. Nakatsuji et al., "Self-diagnosing performance for fracture in CFGRP-reinforced concrete," *Journal of the Ceramic Society of Japan*, vol. 101, no. 1176, pp. 860–866, 1993.
- [79] M. Sugita, H. Yanagida, and N. Muto, "Materials design for self-diagnosis of fracture in CFGFRP composite reinforcement," *Smart Materials and Structures*, vol. 4, no. 1A, pp. 52–57, 1995.
- [80] N. Muto, Y. Arai, S. G. Shin et al., "Hybrid composites with self-diagnosing function for preventing fatal fracture," *Composites Science and Technology*, vol. 61, no. 6, pp. 875–883, 2001.
- [81] C. Q. Yang and Z. S. Wu, "Self-structural health monitoring function of RC structures with HCFRP sensors," *Journal of Intelligent Material Systems and Structures*, vol. 17, no. 10, pp. 895–906, 2006.
- [82] C. Yang, Z. Wu, and Y. Zhang, "Structural health monitoring of an existing PC box girder bridge with distributed HCFRP sensors in a destructive test," *Smart Materials and Structures*, vol. 17, no. 3, Article ID 035032, p. 10, 2008.
- [83] H. Kwun and K. A. Bartels, "Magnetostrictive sensor technology and its applications," *Ultrasonics*, vol. 36, no. 1–5, pp. 171–178, 1998.
- [84] D. A. Khazem, H. Kwun, S. Y. Kim, and C. Dynes, "Long-range inspection of suspender ropes in suspension bridges using the magnetostrictive sensor technology," in *Proceedings of the 3rd International Workshop on Structural Health Monitoring: The Demands and Challenges*, F.-K. Chung, Ed., pp. 384–392, CRC Press, New York, NY, USA, 2001.
- [85] W.-B. Na and T. Kundu, "EMAT-based inspection of concrete-filled steel pipes for internal voids and inclusions," *Journal of Pressure Vessel Technology*, vol. 124, no. 3, pp. 265–272, 2002.
- [86] W.-B. Na and T. Kundu, "A combination of PZT and EMAT transducers for interface inspection," *Journal of the Acoustical Society of America*, vol. 111, no. 5 I, pp. 2128–2139, 2002.
- [87] P. Bouchilloux, N. Lhermet, and F. Claeysen, "Electromagnetic stress sensor for bridge cables and prestressed concrete structures," *Journal of Intelligent Material Systems and Structures*, vol. 10, no. 5, pp. 397–401, 2000.
- [88] P. Rizzo and F. L. Di Scalea, "Wavelet-based feature extraction for automatic defect classification in strands by ultrasonic structural monitoring," *Smart Structures and Systems*, vol. 2, no. 3, pp. 253–274, 2006.

Review Article

Water and Wastewater Pipe Nondestructive Evaluation and Health Monitoring: A Review

Piervincenzo Rizzo

*Laboratory for NDE and SHM Studies, Department of Civil and Environmental Engineering,
University of Pittsburgh, 3700 O'Hara Street, 942 Benedum Hall, Pittsburgh, PA 15261-2294, USA*

Correspondence should be addressed to Piervincenzo Rizzo, pir3@pitt.edu

Received 15 October 2009; Accepted 23 February 2010

Academic Editor: Jinying Zhu

Copyright © 2010 Piervincenzo Rizzo. This is an open access article distributed under the Creative Commons Attribution License, which permits unrestricted use, distribution, and reproduction in any medium, provided the original work is properly cited.

Civil infrastructures such as bridges, buildings, and pipelines ensure society's economic and industrial prosperity. Specifically, pipe networks assure the transportation of primary commodities such as water, oil, and natural gas. The quantitative and early detection of defects in pipes is critical in order to avoid severe consequences. As a result of high-profile accidents and economic downturn, research and development in the area of pipeline inspection has focused mainly on gas and oil pipelines. Due to the low cost of water, the development of nondestructive inspection (NDI) and structural health monitoring (SHM) technologies for fresh water mains and sewers has received the least attention. Moreover, the technical challenges associated with the practical deployment of monitoring system demand synergistic interaction across several disciplines, which may limit the transition from laboratory to real structures. This paper presents an overview of the most used NDI/SHM technologies for freshwater pipes and sewers. The challenges that said infrastructures pose with respect to oil and natural gas pipeline networks will be discussed. Finally, the methodologies that can be translated into SHM approaches are highlighted.

1. Introduction

The soundness of engineering systems such as pipelines, railroads, highways, off-shore platforms, and other structural elements is essential to avoiding (or in order to avoid) catastrophic failures that may be accompanied by severe consequences for the environment, lead to the loss of human life, and produce tonnage of demolition waste. To design structures that are safe for public use, standardized building codes and design methodologies have been created. Unfortunately, structures are often subjected to harsh loading scenarios and severe environmental conditions not anticipated during the design process that will result in long-term structural deterioration [1].

Nondestructive evaluation (NDE) and structural health monitoring (SHM) techniques aim to assess the soundness of existing infrastructure. By preventing failures and detecting damage at an early stage, it may be indirectly inferred that the lifetime of these infrastructures can be expanded. NDE is usually conducted on a time basis by qualified personnel using commercially available technology. Conversely, SHM

systems collect data from sensors, ideally mounted permanently on a given structure. The data are processed according to one of the many damage detection methods that have been proposed in the last two decades, as reported in [2, 3]. In general, SHM can be defined as the process of implementing a damage identification strategy for engineering infrastructure. The damage identification process is generally thought to entail establishing: (i) the existence of damage, (ii) the damage locations, (iii) the types of damage, and (iv) the damage severity [4]. Depending upon the size, location, and operational condition of the engineering system under consideration, a reliable and permanent monitoring system can be very challenging. Therefore time-based approaches are more suitable. This is especially true for water and wastewater pipes that are buried.

In this review paper, we focus on both NDE and SHM methods that have been proposed in the last two decades to inspect or monitor freshwater mains and wastewater pipes. Driven by several high-profile accidents and economic downturn, research and development in the area of pipeline inspection have focused mainly on gas and oil pipelines. Due

to the low cost of water and the technical challenges associated with the monitoring of buried pipes, the NDE/SHM of freshwater systems has received the least attention.

This paper provides a general guideline for those researchers interested in exploring and proposing new solutions to tackle the challenges associated with the inspection/monitoring of freshwater mains or wastewater pipelines.

2. Motivation

The economic and social costs associated with pipeline breaks in modern water supply systems are rapidly rising to unacceptably high levels. Many pipelines were installed in the first part of the 20th century and today are in poor condition and continue to deteriorate. The consequences of a pipeline break include direct costs (cost of repair, cost of water loss, cost of damage to surrounding infrastructure and property, liabilities), indirect costs (cost of supply interruption, cost of potentially increased deterioration rate of surrounding infrastructure and property, cost of decreased fire-fighting capacity), and social costs (cost of water quality degradation due to contaminant intrusion, cost of decrease in public trust and quality of water supply, cost of disruption of traffic and business, cost of disruption of water supply to special facilities) [5, 6].

In a recent document, the United States (U.S.) Environmental Protection Agency (EPA) reported that there are 240,000 water main breaks per year in the U.S. Large utility breaks in the Midwest increased from 250 per year to 2,200 per year during a 19-year period. Deficient water distribution systems cause, according to the U.S. Geological Survey, water loss of 1.7 trillion gallons per year at a national cost of \$2.6 billion dollars per year [7].

In Pittsburgh, Pennsylvania, two recent failures occurred in May 2009. A water main break left a 7.6 m-wide hole in the roadway, prompting the Pittsburgh Water and Sewer Authority (PWSA) to shut down one street. PWSA discovered a 203.2 mm (8-inch) pipe broken which, in turn, caused a sewer to collapse [8]. The break had gone undetected for quite some time, allowing the underground hole to grow large enough to finally cause the roadway above to collapse. A few weeks later, a second break resulted in the closure of Route 88. Rushing water caused the pavement to buckle [9]. On September 2009, a 1.57 m (62-inch) water main broke in the Los Angeles area causing the closure of a road for three days, damaging nearby homes and businesses [10].

3. Pipe Assets

Pipes are one of the principal assets of a water supply system (WSS) and can be divided into transmission mains, distribution mains, and services. A variety of materials and technologies have been used in the production of water supply pipes. The material of a particular pipe depends on the year of installation and the diameter. For large transmission pipelines (with diameters over 300 mm), steel, mild steel cement-lined (MSCL), or prestressed concrete

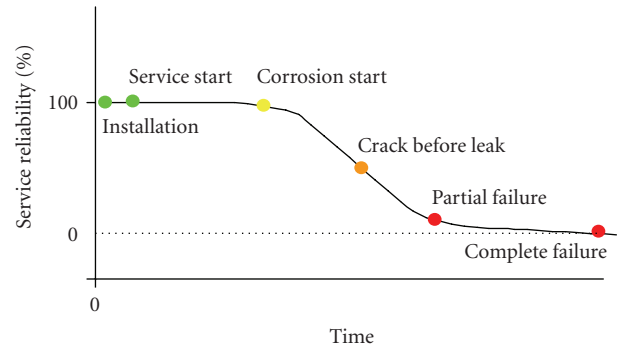


FIGURE 1: Pipe failure development. (Adapted from [6]).

cylindrical pipes (PCCPs) are typically used. Older water-distribution mains are typically made of cast iron or asbestos cement, while mainly ductile iron and poly-vinyl chloride (PVC) are used for newer mains [6].

Pipe failure can be described as a multistep process as shown in Figure 1: installation, initiation of corrosion, crack before leak, partial failure, and complete failure. After the pipe has been in operation for some time, the corrosion processes start on the interior or exterior (or both) surfaces. These processes yield anomalies such as cracks, corrosion pits, and graphitization. In some cases cracks can be initiated by mechanical stress. None of them are severe enough to induce leaks. Developing corrosion pits or cracks reduces the residual strength of the pipe wall below the internal or external stresses, yielding pipe wall breaks and leaks. In some cases, this partial failure is not large enough to be readily detected. Finally, the complete failure of the pipe can be caused by a crack, corrosion pit, preexisting leak/burst, or a third-party interference. Failure is usually followed by water appearing on the ground surface or a considerable change in the hydraulic balance of the system [6].

Kleiner et al. [11] classified the deterioration of pipes into structural deterioration and internal deterioration. The first occurs when the pipe resiliency and the ability to withstand stress decrease. Internal deterioration occurs when the hydraulic capacity or the water quality diminishes, or severe internal corrosion appears. Structural deterioration mechanisms are affected by many factors including the type of pipe, its surrounding environment, and its operational conditions. Pipe breakage, with exception of situations in which it is caused by third-party interference, is likely to occur when the environmental and operational stresses act upon pipes whose structural integrity has been compromised by corrosion, degradation, inadequate installation, or manufacturing defects.

Asbestos cement and concrete pipes are subject to deterioration due to various chemical processes that either leach out the cement material or penetrate the concrete and form products that weaken the cement matrix. Quite often a pipe failure is caused by a combination of some form of damage or manufacturing flaw and applied external forces. PCCP fails when a sufficient number of loops of prestressing wire have broken in the same area. The wires normally break

when corrosion activity has reduced their diameter to the point where the stress applied to them exceeds their yield point. This process may also cause damage to the mortar around the wires (allowing an acceleration of the corrosion process) or to the concrete inside the pipe [12].

Porosity is one of the most common manufacturing defects in cast iron pipes. Inclusions result in a discontinuity of the pipe material and may act as crack-formers. The variation in a pipe's wall thickness may lead to a situation where a part of the pipe's wall might no longer have a sufficient wall thickness for expected maximum pressures.

Pipe breakage types have been classified by O'day [13] into three main categories: circumferential cracking, longitudinal cracking, and bell splitting. In addition, Makar et al. [14] introduced the following failure modes: corrosion pitting and blow-out holes, bell shearing, and spiral cracking. Figure 2 depicts these different types of pipe-breaks.

4. Pipe Inspection

To date, two types of failure management strategies can be applied: proactive asset condition assessment and reactive failure detection and location. The former aims to prevent failure, the latter aims to minimize reaction time and losses associated with failure. However, as infrastructure ages, the price of water rises, the cost of materials increases, and pressure increases on public authorities to shift the management strategy from reactive to proactive.

Due to the different topology and hydraulic characteristics of the transmission (pipelines) and distribution (networks) components of a water supply system, separate failure detection and location techniques were proposed in the past. These techniques can be divided largely according to the physical phenomenon that they exploit: electromagnetic, mechanical, or visual. An extensive description of the principles, advantages, and limitations of each of the above technologies is beyond the scope of this paper. Interested readers may refer to some of the books in the area of NDE and SHM [15–19]. The performance and the feasibility of each technology are associated with their capability to gauge limited or large sections at once, and the need to interrupt service to allow for direct access.

The selection of the inspection method is mainly driven by the pipe's size and material. For instance, eddy currents (EC), electromagnetic testing (EMT), and ultrasonic testing (UT) are used in metal pipes. Acoustic emission (AE), impact-echo (IE), sonar, and visual inspection are used in concrete pipes. Some of these methods are implemented in pipeline inspection gauges (PIGs), which are computerized, self-contained devices inserted into the pipeline and propelled forward by the liquid flowing through the line, recording information as they go. PIGs were originally developed to remove deposits which could obstruct or retard flow through a pipeline [20].

As pointed out by Misiunas [6], in contrast with the oil and gas industries in which pipelines are already well instrumented and large investments in instrumentation are routine, the water distribution mains are usually poorly instrumented and the budget for water utilities does not

allow a large investment for instrumentation. Therefore, most techniques were initially developed or applied to the oil or gas industry.

4.1. Acoustic Emission. AE is formally defined as the “release of transient elastic waves produced by a rapid redistribution of stress in a material” [21]. These waves are then detected by sensors such as piezoelectric transducers, hydrophones, or accelerometers. The actual source of the transient wave is a change within the material which is usually permanent and irreversible, such as the growth of a crack; so the AE method is suitable to detect damage onset and/or propagation, but cannot detect existing or “silent” damage. In PCCP and reinforced concrete pipes, AE is suitable to detect breaks of the steel reinforcement, crack onset, and propagation within the concrete. Other sources of emissions are friction, crack growth, turbulence, leak, and corrosion.

Travers [22] reported on the use of hydrophones to detect the sound caused by the failure and subsequent slippage of the reinforcing wire from PCCP. The work stemmed from the widespread corrosion and failure of the reinforcing wire on over 6 miles of 15-year-old pipes used in the Central Arizona Project in 1990. Initial field testing consisted of a single pair of hydrophones. Successively, there was the continuous monitoring of a 2-mile pipeline by means of an array of 12 hydrophones and a computer system to detect sounds in the pipeline, classify them as either wire-related sounds or extraneous sounds, and, based on the location of the wire-related sounds, map areas of pipe deterioration.

Shehadeh and coauthors [23] proposed a linear array of sensors to locate and reconstitute the time-domain and frequency-domain signatures of AE sources in pipes. Simulated sources on sections of line pipe were used and a range of techniques, including a wavelet-transform technique, a cross-correlation technique, and a filtering and thresholding technique were proposed. The suitability of this approach in the field was not demonstrated.

The available, commercialized systems monitor the pipe using accelerometers, hydrophone arrays, or continuous fiber optic sensors. Following an acoustic event, the recorded signals are analyzed and compared to an existing database to determine the nature of the event. Monitoring PCCP by means of AE may not be very accurate because the method is restricted to detecting ongoing wire breaks, cannot detect already broken wires, and the monitoring period is short compared to the lifespan of the pipe [24].

4.2. Eddy Current. Pipe inspection methods by means of EC use a magnetic coil with alternating current to induce a time-varying magnetic field in the pipe. This magnetic field causes an electric current to be generated in the conducting material. These currents produce small magnetic fields around the material that generally oppose the original field and therefore change the impedance of the magnetic coil. By measuring the change in impedance of the magnetic coil as it traverses the sample, different pipes' characteristics can be identified. The method is restricted to those materials that are electrically conductive. In metal pipes, it has the potential to measure wall thickness and to detect discontinuities that

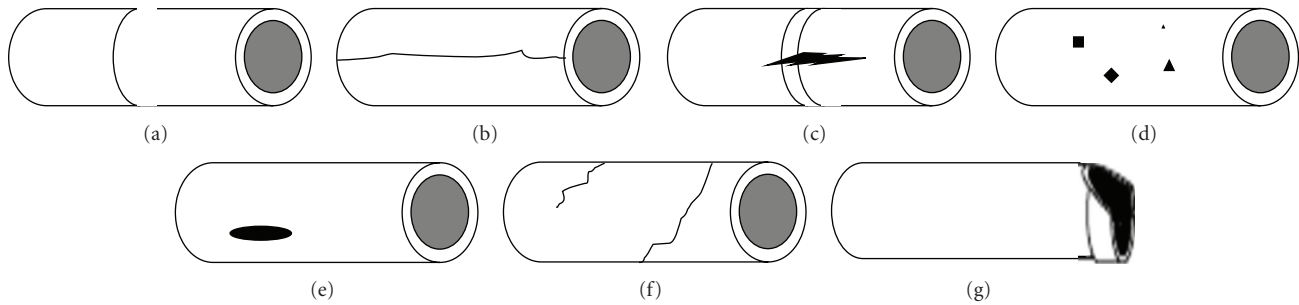


FIGURE 2: Different types of pipe breaks. Adapted from [6]. (a) Circumferential cracking; (b) Longitudinal cracking; (c) Bell splitting; (d) Corrosion pitting; (e) Blow-out hole; (f) Spiral cracking; (g) Bell shearing.

lie in plane transverse to the currents. Wall thickness in pipes as small as 100 mm (94 in.) can be assessed [20]. In reinforced concrete and PCCP, the method is valuable for the qualitative assessment of the steel reinforcement.

The main disadvantage of EC testing is the size of the skin depth, which is the depth of penetration of the alternating current. The skin depth sets the maximum depth to determine defects at a given frequency. To overcome this problem, the remote field eddy current (RFEC) method was proposed [25, 26]. RFEC monopolizes on the existence of a secondary field that completely penetrates the wall thickness, allowing through-thickness inspection [16]. The current can travel along the outside of the pipe and be detected by far field coils, which are separated by approximately two times the pipe diameter from the excitation coils. This method relies on the fact that the remote field signal is larger than the direct eddy current signal measured by the detector coil [20].

The RFEC-based Hydroscope technology [27] consists of a train of sealed modules containing processing and transmission electronics. It is designed to traverse bends and tees, and is usually propelled through the pipe by water flow. Data is transferred by a wire line cable to the service vehicle. In an IRC evaluation [28], this technology was found to be able to locate and size corrosion pits of more than 3,600 mm³ in volume with an accuracy of ± 0.55 m [12]. Hydroscope Technology and Service claims the following practical advantages [20, 27]:

- (i) detection of general wall loss, pitting, graphite corrosion,
- (ii) equally sensitive to internal and external wall loss,
- (iii) tests in either wet or dry pipes,
- (iv) tests through lining and scale; extensive pipe cleaning not necessary,
- (v) ease of access (through hydrant for 6 inches lines),
- (vi) efficiency (up to 3,000 feet per day for typical lines),
- (vii) 100% examination of pipe wall [20].

Another RFEC technology was reported by Jackson and Skabo [29] concerning a Ferroscope system developed by Cyberscope Industries Inc. and used by Russell NDE Systems,

Edmonton (Alberta) [20]. Two probes were pulled through the pipe, one scanning the entire circumference of the pipe for small defects, and the second with three sensors at 120° spacing assessing the size of the damage. This method detected metal loss from 25% to 60% of the original pipe wall thickness. A thorough description of this remote field testing system is presented in [16].

Nestleroth and Davis [30] proposed an alternative approach to the common concentric coil method to induce low-frequency EC for pipes and tubes. Pairs of permanent magnets rotating around the central axis are used to induce high current densities in the material under inspection. Anomalies and wall thickness variations are detected with an array of sensors which measure local changes in the magnetic field produced by the current flowing in the material. A photo of their system is shown in Figure 3.

4.3. Electromagnetic Methods. EC testing is one of the methods based on electromagnetic principles. Other electromagnetic-based methods are ground penetrating radar (GPR) and short-pulse radar, which are the electromagnetic analog of sonic and ultrasonic pulse-echo methods [31]. GPR uses electromagnetic radiation in the microwave band to detect reflected signals from subsurface structures. GPR can be used in a variety of media, including rock, soil, fresh water, pavements, and concrete. Microwaves are sent through materials of different dielectric constants to, for instance, inspect and locate buried objects, or assess rebar in reinforced concrete. Microwave inspection generally consists of measuring various properties of the electromagnetic waves scattered by, or transmitted through, a test article [32]. Transducers or antenna are used as transmitters and receivers.

In pipe applications, pipes can be measured from the ground surface or from the inside by moving the probing system along the pipe length. EM methods provide an accurate estimation of broken wires in some pipe segments. However, some results showed that the number of broken wires in PCCP can be either underestimated or overestimated [24, 33, 34]. Higher accuracy of results requires conducting calibration tests on test pipe sections to better understand the electromagnetic signal and determine the number of broken wires. These methods are not yet able to determine information on the concrete and data analysis and may

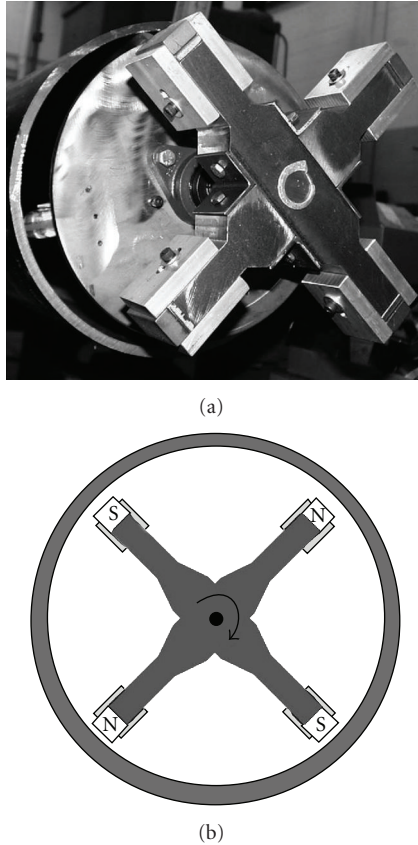


FIGURE 3: Photo of the eddy current system developed by Nestleroth and Davis (2007) [30]. Courtesy of Elsevier.

need to be carried out by experienced personnel. A second level of inspection for ferrous mains would be the use of electromagnetic methods to ascertain the amount of pitting, corrosion, or graphitization that has taken place.

Recently, in the Baltimore area, visual inspection, sounding, and electromagnetic testing were used for a pilot inspection program aimed toward assessing the condition of 17,000 feet of a 54-inch PCCP transmission main. The visual surveys consisted of measuring and checking each pipe for cracks and signs of structural distress. All cracks, circumferential and longitudinal, were noted and photographed. The internal EM probe senses electromagnetic anomalies caused by broken or deteriorated prestressing wires. The results were recorded on a small on-board data acquisition system. The data was subsequently analyzed and used to estimate the location and quantity of wire breaks [34, 35].

Remote Field Eddy Current/Transformer Coupling (RFEC/TC) and Polar wave (P-wave) are two commercially available systems that can provide information on the number of broken wires in PCCP. Both systems use moving platforms to conduct the survey from inside dewatered PCCP with an approximate speed of 1 m/s. The P-wave system consists of an emitter, which generates an electromagnetic field, and a receiver to catch the electromagnetic energy transmitted through the steel wires. The recorded signal shows distortion when a wire is broken, which allows for an

estimation of the number of broken wires in the inspected pipe [24].

4.4. Impact-Echo. IE is a nondestructive method widely used in concrete structures to determine concrete thickness and detect delamination. The method exploits the propagation of stress pulses introduced into a test object by mechanical impact on the surface [36]. The method involves a simple signal processing technique that provides thickness, depth of delamination, and sound velocity inside the concrete, which in turn, is an indicator of the concrete's quality.

IE is feasible for PCCP and reinforced concrete pipes. It allows for the detection of delaminations and cracks in various concrete/mortar/steel interfaces. The method requires dewatering and human access to the pipes' interiors, but it can be done externally if exterior access is available. Although IE was successfully applied to concrete structures, its use to inspect PCCP presented some difficulties [24]:

- (1) the method yields to indications, which are not necessarily related to features that reduce the structural integrity of the pipe [37];
- (2) it is difficult to detect problems in the mortar coating of the pipe [37];
- (3) the method is not yet automated to inspect the entire pipe surface with reasonable speed. Carino [36] stated that the method yields indications, which are not necessarily related to features that reduce the structural integrity of the pipe.

4.5. Hammer Sounding. Similar to impact-echo, hammer sounding inspection is the basic, first, and most used method to inspect PCCP [24]. It is conducted by using a hammer or rod to strike either the outside of an uncovered in-service pipe, or the inside of a pipe which however needs to be taken out of service to allow a crew's entry. The hammer sounding aims to detect a "hollow sound" area, which is often associated with the detachment of the steel cylinder from the concrete core and delamination of the outside mortar coating. External observations include degradation of the mortar coating, longitudinal and/or circumferential cracks in the mortar coating, spalling, broken wires, corroded wires, corroded steel cylinder, rust stains, longitudinal cracks, circumferential cracks, and efflorescence. Internal observations include longitudinal and circumferential cracks in the concrete core, stains, construction, and previous repair errors and joint problems.

4.6. Leak Detectors and Transient Analysis. Acoustic leak detectors (ALD) and transient analysis are passive approaches to detect leaks in pipelines. ALD systems consist of listening devices attached to the pipes or appurtenances to detect leak-induced sound. Traditional techniques have relied on the detection of leakage from above ground using accelerometers or hydrophones attached at strategic locations [38]. Ground microphones can also be used to listen and pinpoint leaks by listening on the pavement surface or soil directly above the pipe [39]. The water

service department of the city of Bristol, UK, studied the performance of acoustic noise loggers for leak location in water networks. The study found that acoustic loggers underperformed when compared to a professional leakage inspector [40]. Recently noise loggers were integrated with amplifiers and noise filters to enhance the signal-to-noise ratio. The effectiveness of ALD methods has been successfully demonstrated for metallic pipes [41, 42] and plastic pipes [43]. A detailed review of ALD methods is presented in [44].

In ALD systems, the most common technique of leak location is the cross-correlation. Measured vibrations or acoustic signals from two receivers are transmitted to the leak noise correlator, which computes a cross-correlation function of the two signals. If a leak is present between the sensors, the cross-correlation function will have a distinct peak. A corresponding time delay indicates the difference in arrival times of the leak noise signals at each sensor and is related to the location of the sensors. By knowing the acoustic speed in water, the leak location can be pinpointed [6, 39]. Cross-correlation testing results are presented in [43, 45].

Sahara (Figure 4) is a pigging technology based on ALD principles. A sensor mounted on an umbilical cable is introduced into the pipe and a small parachute uses the flow of water to draw the sensor through the pipeline. As the sensor passes any leak it detects the sound generated and gives an indication to the operator. The umbilical cable allows its position along the pipe to be controlled [46, 47].

Methods based on transient analysis measure water pressure, hydraulic characteristics, and use back calculation (inverse analysis) to detect and locate leaks. The methods rely upon the fact that a sudden pipe break creates a negative pressure wave that travels in both directions away from the breaking point and is reflected at the pipeline boundaries. Using the pressure data measured at one location along the pipeline, the timing of the initial and reflected transient waves induced by the break determines the location of the break. The magnitude of the transient wave provides an estimate of the break size. The method can be enhanced by using advanced pattern recognition systems and/or signal processing techniques such as genetic algorithms [48, 49].

Misiunas and coauthors [5] proposed a continuous monitoring approach for detecting and locating breaks in pipelines. The continuous monitoring technique was verified by using results from both laboratory and field experiments, and showed potential for detecting and locating sudden breaks in real pipelines.

Karney et al. [39] reported on the use of inverse transient analysis on an initial simulation phase of a study which aimed to assess the applicability and effectiveness of inverse transient analysis to the detection of leaks in real water distribution systems. Simulation was conducted on various scenarios of transient severity and leak sizes. As summarized by Misiunas [6], limited experiences from laboratory and field tests [50, 51] include single pipe cases in which a controlled transient is introduced to detect and locate a leak. The challenge for field application is the need to possess an accurate modeling of the transients and boundary conditions

of the pipe system. Colombo and coauthors [52] offer a selective literature review of transient-based leak detection methods. While not exhaustive, numerous publications are cited in an attempt to provide a reasonable cross-section of research activity and the various methodologies. The review shows that field work and verification of these techniques are still generally lacking.

4.7. Magnetic Flux Leakage. MFL consists of magnetizing a test part, generally a ferromagnetic material, and scanning its surface with some form of a flux-sensitive sensor [19]. The magnetic lines of force (or flux) flow through the material and complete a magnetic path between the pole pieces. When the flux is contained within the test piece, its detection in the air space surrounding the object is very difficult. However, if a structural anomaly disrupts the surface of the magnetized structure, the permeability is changed and leakage flux will emanate from the discontinuity [53]. Defects are therefore detected by measuring changes in the pipe's magnetic permeability.

In pipe inspection, MFL is assembled into pigs carrying permanent magnets or electro-magnets that generate magnetic flux in the pipe so that the field travels in the same direction as the pipe axis. This method is feasible for buried or surface cast iron and steel pipes to detect metal loss associated with corrosion and to detect circumferential and longitudinal cracks. In areas where there is corrosion or metal loss, the pipe wall thickness is reduced, which leads to the decrease in the amount of magnetic flux compared with that carried in a full thickness wall. That means that magnetic flux leaks when defects occur on the pipe's surface. The leakage of magnetic flux can be measured by sensors located inside the pipe [12, 20, 54–56]. The leakage depends on the physical size of the pipe, the magnetic characteristics of the pipe and nearby materials, the stresses in pipelines, and the shapes and dimensions of the defects. MFL may have limited performance to detect cracks, including axial stress corrosion cracks and seam weld cracks, because they are extremely shallow, long, or narrow [57]. Lijan et al. [58] claimed that aMFL tool can move through the pipes at a speed of 0.7 to 4 m/s with test runs of at least 100 km. The level of magnetization is a key factor in providing reliable and accurate inspection results [20].

Since 1965, when Tuboscope introduced the first MFL in-line inspection tool for pipelines, MFL has been increasingly employed in the pipeline industry. MFL inspection in water pipes requires close contact between the pig and the pipe wall. Makar and Chagnon [12] stated that the use of MFL tools in the water industry is limited to cleaned, unlined pipes. Generally, four types of MFL tools are available to be chosen from according to different testing levels of sensitivity. They are Standard or Low-Resolution tools, High Resolution (High-Res) tools, Extra High-Resolution (XHR) tools, or The XHR “newest generation” systems. The four MFL tools mainly differ in the resolution or the accuracy of the data collection by changing the size and spacing (number) of sensors [59].

As for many other NDE/SHM techniques, the use of advanced signal processing is pivotal to improve the

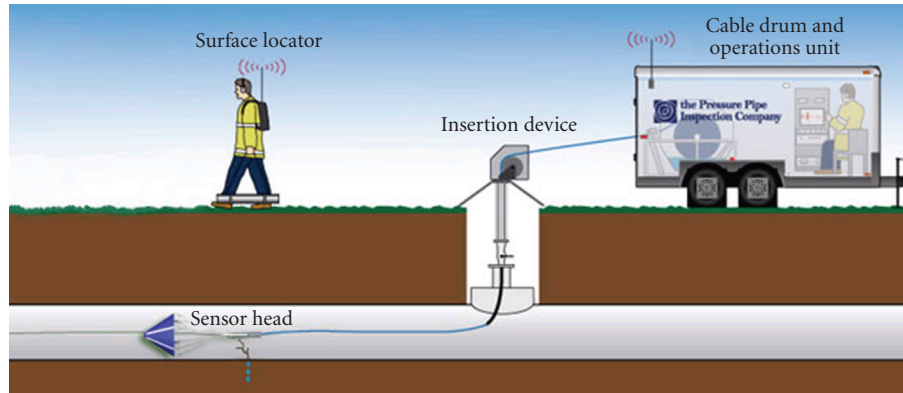


FIGURE 4: The Sahara system 46. Image Courtesy of the Pressure Pipe Inspection Company.

performance of MFL systems as well. Mukhopadhyay and Srivastava [55] suggested the use of a discrete wavelet transform for denoising MFL signals and for the classification of defects. Joshi et al. [60] proposed a method on adaptive wavelets and radial basis function neural network (RBFNN). They used a new approach of iterative inversion using a multiresolution wavelet transform to predict 3D defect geometry from MFL measurements obtained from a gas transmission pipeline inspection.

4.8. Sonar. Sonar measures the time it takes for a burst of sound to travel from a source to a target and back again. By knowing the velocity of sound through the appropriate medium, the distance from the source to the target can be determined. Sonar is mainly used in wastewater management to provide pictorial evidence of sewers beneath the flow line. Sonar can generate a 360-degree outline of the interior of a fill pipe, or the outline of the wetted area only, and is suitable to “see” the surface profile. Sonar can be operated in air or water but it cannot be operated in both air and water simultaneously. Consequently, only the part of the pipe above the water line, or conversely the part of the pipe below the waterline, can be assessed [20, 38, 61]. In Section 4.9, systems that combine Sonar-based technologies and closed-circuit television (CCTV) will be discussed.

4.9. Ultrasonic Testing. Methods based on the propagation of ultrasonic stress waves use one or more probes to send broadband or narrowband mechanical waves through a medium. Conventional UT, such as local thickness gauging, use bulk waves to test a limited region within the ultrasonic probe. Such approaches may be time consuming when applied to large structures. A commercial system based on ultrasonic B-scan and C-scan is the UltraScan CD inspection tool [62]. The CD tool directs ultrasonic waves circumferentially into the pipe wall at an angle that generates 45° shear-waves within the metal. The transducers are mounted on a flexible carriage at the rear of the tool. With large numbers of transducers generating pulses and receiving their reflections, as many as ten simultaneous readings can be taken from each flaw or pipeline feature.

Whenever an ultrasound propagates into a bounded media, a guided ultrasonic wave (GUW) is generated. The wave is termed “guided” because it travels along the medium guided by the medium’s geometric boundaries. GUWs propagate along, rather than across, the waveguide. In pipe applications, GUWs may propagate along the pipe’s longitudinal direction and excite the entire cross-section [19, 63, 64], and therefore GUWs are effective when large inspection coverage is required. The advantage of GUW inspection is its ability to probe long lengths of the pipe, locating cracks and notches from few monitoring points, while providing full coverage of the pipe’s cross-section [63–66]. In addition, by combining the methodology with opportune signal processing, the method is feasible for the permanent monitoring of the pipe’s health.

The ability of guided waves to locate cracks and notches in pipes has been demonstrated in several laboratory works [63, 66–69]. One of the advantages of GUWs in pipelines is that the theoretical foundation of wave propagation is well formulated (see, e.g., [19]). In addition, numerical methods, such as the DISPERSE package developed by the Imperial College in the U.K. [70], have been developed for extracting modal solutions from a variety of waveguides, including empty and filled pipes. Another numerical method is the 2D Finite Element Method, or Semi-analytical Finite Element (SAFE) Method, which can model waveguides of arbitrary cross-sections by simply discretizing a bidimensional domain [71–73].

Gauthier et al. [74] reported on an ultrasonic wave inspection technique using horizontally polarized shear waves. These waves can follow curvature and thus enable inspection along bends and other irregular geometric shapes. They tested steel pipe samples and found that shallow cracks larger than 10% of the wall thickness could be detected. Demma and coauthors [75] studied experimentally and numerically the reflection of the torsional $T(0,1)$ guided mode from defects in pipes in the frequency range 10–300 kHz. Both crack-like defects with zero axial extent and notches with varying axial extents were considered. The results showed that the reflection coefficient from axisymmetric cracks increases monotonically with depth at all frequencies, and increases with frequency at any given depth.

With nonaxisymmetric cracks, the reflection coefficient is a roughly linear function of the circumferential extent of the defect at relatively high frequencies, the reflection coefficient at low circumferential extents falling below the linear prediction at lower frequencies. With nonaxisymmetric defects, mode conversion to the flexural $F(1,2)$ mode was seen, and at lower frequencies the flexural $F(1,3)$ mode was also produced.

Field applications of GUWs were recently reported. Ledesma et al. [76] presented a case study of the guided wave testing of a nonpiggable gas transmission pipeline of an approximate length of 1 km. The pipeline was partially above ground and partially underwater or buried in soil. They used equipment developed by Guided Ultrasonics, Ltd [77]. Vinogradov [78] verified the capability of magnetostrictive transducers to generate GUWs to screen an empty buried pipe mockup. The study did not include in-service water pipes. Sun et al. [79] and coauthors used the propagation of longitudinal wave $L(0, 2)$ to screen a 40-meter-long heating pipe in the residential area of the Bohai Oil Company in Tianjin city, China. Factors, such as the number of transducers and transducer ring spacing, were discussed.

Ultrasonic methods for PCCP inspection make use of an ultrasonic pulser in the pipe wall and analyze recorded time and frequency pulses' characteristics (using an array of sensors placed near the source) to determine the possibility of wire breakage. The test can be conducted either from the inside dewatered pipe or from the outside in-service pipe. Velocity and frequency of pipe resonance are measured to determine the concrete quality and detect delamination and/or cracks. Even though the Sonic/Ultrasonic method provides information on concrete, its accuracy in detecting broken wires is not yet clear. The method appears to be good for testing selected uncovered PCCP sections from the outside [24]. As concrete is more attenuative than metals, the area inspected by conventional UT or GUWs is smaller compared to metal pipes. In addition, the ultrasonic frequencies used must be lower.

4.10. Visual Inspection. Visual methods are related to the use of *closed-circuit television* (CCTV). This is the standard technology for the NDE of the internal condition of sewers and storm water pipes [47]. The CCTV technique involves the use of a robot-mounted forward-looking pan/tilt and zoom camera and lighting system mounted on a wheeled carriage that travels between two manholes. CCTV equipment is operated by certified operators who are trained to control the camera and interpret video streams. CCTV can identify defects such as longitudinal/circumferential cracks, fractures, deformation, collapse, breaks, open or displaced joints, surface abrasion or corrosion, tree root penetration, encrustation, and lateral connections. Each sewer is rated based on the number and severity of defects. The defect codes are then assigned scores based on their severity. These scores are then used to calculate the total, peak, and mean scores. Based on these scores, a condition grade is calculated on a 1–5 scale [80]. New advances in digitizing the video stream have made this tool more users-friendly. CCTV still



FIGURE 5: The PANORAMO system. (Source: <http://www.werf.org/AM/CustomSource/Downloads/uGetExecutiveSummary.cfm?FILE=ES-01-CTS-7.pdf&ContentFileID=1960>. Courtesy of WERF.

requires an operator's subjective interpretation of observed defects and is limited to the pipe surface located above the flow surface. Moreover, CCTV is mainly qualitative in nature. Recently, software in support of the operator has been developed like AQUA-selekt, AQUA-WertMin [81], or other image processing techniques. CCTV systems are capable of (1) detecting anomalies along the interior wall surface, (2) storing large amount of images, and (3) providing a pictorial view of the structure. CCTV has come a long way since then and is now the dominant force in state-of-the-art inspections receiving widespread use within the industry [20].

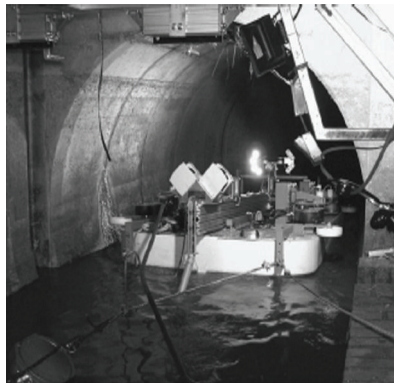
Systems like the Panoramo 3D shown in Figure 5 mount *optical scanners* which provide the same information as digital CCTV, with the added benefit of being able to unwrap the pipe size. The cost for this level of inspection is nearly the same as CCTV, but it does have the benefit of providing a measurable analysis.

Sarshar and coauthors [80] described the development of a software system to semiautomatically extract historical condition data information from archived sewer inspection CCTV files. The software was used to access, analyze, and evaluate sewer condition data from CCTV video files and particularly to automate the detection of other types of defects, for example, excessive debris, penetrating roots, and displaced joints. Images from the City of Regina in Canada were analyzed. The use of image-processing techniques for automated identification of cracks in sewer pipes has been studied [82, 83].

Systems combining CCTV and sonar, mounted one above the other, were recently proposed to survey pipes above the waterline (by means of CCTV) and below the waterline (by means of sonar). An example of such a system is the cable-guided swimming system (SEK) which was developed in Germany to inspect wastewater mains and is shown in Figure 6. SEK allows sewer operators to inspect free-gradient sewers with large diameters which, because of their filling levels, are normally inaccessible (e.g., before treatment plants) [84]. The strategy includes a three-stage approach. In



(a)



(b)

FIGURE 6: (a) SEK prototype; (b) SVM. Photos from [84]. Courtesy of IWA Publishing.

the first stage, SEK is employed in the sewer for inspection. It inspects and measures the entire sewer line and conducts camera inspections, recording major abnormalities such as erosion, deposits, obstacles, and leaks in the gas space. At the same time, it checks whether the cleaning and inspection systems detailed below can be deployed. An SEK is able to center itself even in curved pipes in the sewer covering a length of 600 m. In the second stage, the wheel-driven cleaning device eliminates deposits detected by the SEK in the bed area and cleans the sewer wall before the inspection system is deployed. In the third stage, aSVM (damage survey device) system surveys the sewer completely, measuring joint widths, pipe offsets, and cracks with greater accuracy than the SEK. An SEK is equipped with several flashlights for illumination. In contrast to the SEK, the SVM achieves greater accuracy. It is carried by (1) floating systems for large sewer diameters and (2) wheeled chassis for smaller sewer diameters. The floating systems are limited by the required water level. Wheel-guided car systems are used when the filling level is low or when the nominal diameters are smaller. Sensors for determining the position in the sewer (laser ranging sensors and inclination sensors) and sensors for damage surveys (laser scanners, ultrasound scanners, camera system, ultrasound crack sensor) are installed on the SVM. Ultrasound scanners, laser scanners, and camera systems are mounted on a linear axis and can precisely measure the pipe profile over a length of approximately 1.5 meters.

The Sewer Scanner and Evaluation Technology (SSET) developed by TOA Grout, CORE Corp., and the Tokyo Metropolitan Government's Sewer Service (TGS) Company utilizes optical scanner and gyroscope technology, in addition to standard CCTV technology [85, 86]. Survey speed for the SSET is reported as 60 m/hour. The SSET system has been evaluated through the Civil Engineering Innovative Technology Evaluation Centre, an innovation center within the American Society of Civil Engineers (ASCE), Civil Engineering Research Foundation (CERF). The evaluation included field demonstrations performed at thirteen municipal public works agencies throughout North America. The evaluation assessed the functional performance, constructability/practicality, maintainability, safety, and environmental characteristics [20]. Advantages of SSET include its ability to produce a digital record of the pipe, to identify vertical deflection in pipes, and to deliver easily comprehensible and manageable results. The main disadvantages of the SSET include its inability to see into laterals or to operate in dark-colored pipes. A full evaluation report was released in 2001 [87].

4.11. *Other.* As for the SEK-SVM and SSET systems described in the previous section, there are few other systems that carry multiple technologies to assess wastewater pipes: the Sewer Assessment by Multi-Sensors (SAM) funded by the German Research Foundation and the Pipe Inspection Real-time Assessment Technique (PIRAT) developed by Melbourne Water and CSIRO and funded by the Australia's research agency are multisensor systems. The SAM platform includes [88]

- (i) a commercial CCTV system in addition to optical triangulation which permits optical 3D measurement of the pipe shape (diameter and deviations from ovality),
- (ii) a microwave, rotatable sensor to inspect the soil state behind sewerage pipes,
- (iii) a geoelectrical sensor for the identification of leak points,
- (iv) hydrochemical sensors for the detection of groundwater infiltration,
- (v) radioactive sensors to detect sewer leaks, holes behind sewer pipes, and small orifices in water mains,
- (vi) acoustic systems suitable for detecting cracks and determining the state of connections and pipe bending.

PIRAT [89, 90] was developed to detect, classify, and rate defects using artificial intelligence by building a cylindrical-polar geometric model of the interior of the sewer using a scanner (laser or sonar) carried by a robotic in-pipe vehicle. The vehicle carries the scanner along the centerline of the sewer and has a forward-facing color video camera, lighting, and other sensors.

5. Discussion and Conclusions

This paper provides an agile and general review of the most used NDE techniques for the inspection and monitoring of water mains and wastewater networks. The attention has mainly focused on electromagnetic methods such as eddy current, ground penetrating radar, and magnetic flux leakage, mechanical methods such as acoustic emission, ultrasonic testing, impact-echo, acoustic leak detection, and sonar, and visual inspection methods based on the use of closed-circuit cameras. For each method the main advantages and principles and its mode of employment in freshwater and wastewater pipes were discussed. A few representative works conducted in academia and in the private sector have been reviewed. The latter focused on inspection tools deployed and tested in the field. A distinction in terms of needs and challenges between metal and concrete pipes has been made. Finally, a few case studies are reported. Interested readers may refer to [91] for a review on fourteen case studies conducted at different water municipalities worldwide.

All systems discussed here present many advantages but also carry some limitations as well. The inspection of wastewater pipes by means of CCTV, laser scanning, or sonar can be improved by enhancing the image resolution of CCTV but still the methods are limited to the detection of surface anomalies. The development of automatic image processing will make the analysis of long and tedious images less prone to the subjective evaluation of the inspectors.

The periodic inspection or the permanent monitoring of freshwater mains or distribution pipes may be greatly benefited by a trenchless untethered system that can probe the structures from the inside without service interruption. Such a system would definitely bring a technological leap in the area of water pipe inspection. None of the methods discussed in this review paper seems to satisfy such ideal technologies. Electromagnetic methods or stress waves-based methods either require the structure temporarily out of service to inspect from the inside or require excavation in order to conduct the inspection from the outside. Acoustic leak detectors are promising if the technology can become untethered. However, these detectors are not suitable to detect anomalies that have not yet deteriorated into leaks. Finally, as for any structural health monitoring strategy, pipe health monitoring includes other importance issues, such as modeling of damages, establishing criteria, or setting up indices for damage evaluation. These aspects were not discussed here as beyond the scope of the present paper.

References

- [1] J. P. Lynch and K. J. Loh, "A summary review of wireless sensors and sensor networks for structural health monitoring," *The Shock and Vibration Digest*, vol. 38, no. 2, pp. 91–128, 2006.
- [2] S. W. Doebling, C. R. Farrar, and M. B. Prime, "A summary review of vibration-based damage identification methods," *Shock and Vibration Digest*, vol. 30, no. 2, pp. 91–105, 1998.
- [3] H. Sohn, C. R. Farrar, F. M. Hemez, et al., "A review of structural health monitoring literature: 1996–2001," Tech. Rep. LA-13976-MS, Los Alamos National Laboratory, Los Alamos, NM, USA, 2004.
- [4] K. Worden, C. R. Farrar, G. Manson, and G. Park, "The fundamental axioms of structural health monitoring," *Proceedings of the Royal Society A*, vol. 463, no. 2082, pp. 1639–1664, 2007.
- [5] D. Misiunas, J. Vítkovský, G. Olsson, A. Simpson, and M. Lambert, "Pipeline break detection using pressure transient monitoring," *Journal of Water Resources Planning and Management*, vol. 131, no. 4, pp. 316–325, 2005.
- [6] D. Misiunas, *Failure monitoring and asset condition assessment in water supply systems*, Ph.D. dissertation, Lund University, Lund, Sweden, 2005.
- [7] US Environmental Protection Agency, "Addressing the challenge through innovation," 2007, <http://www.epa.gov/nrmrl/pubs/600f07015/600f07015.pdf>.
- [8] "Sewer collapse closes chateau street on north side," May 2009, <http://www.post-gazette.com/pg/09134/970143-100.stm>.
- [9] "Water main break closes Route 88," May 2009, <http://www.post-gazette.com/pg/09146/972733-100.stm>.
- [10] <http://latimesblogs.latimes.com/lanow/2009/09/coldwater-canyon-could-be-closed-for-3-days-due-to-destructive-water-main-break.html>.
- [11] Y. Kleiner, B. J. Adams, and J. S. Rogers, "Water distribution network renewal planning," *Journal of Computing in Civil Engineering*, vol. 15, no. 1, pp. 15–26, 2001.
- [12] J. Makar and N. Chagnon, "Inspecting systems for leaks, pits, and corrosion," *Journal of American Water Works Association*, vol. 91, no. 7, pp. 36–46, 1999.
- [13] D. O'day, "Organizing and analyzing leak and break data for making main replacement decisions," *Journal of American Water Works Association*, vol. 74, no. 11, pp. 588–594, 1982.
- [14] J. Makar, R. Desnoyers, and S. McDonald, "Failure modes and mechanisms in gray cast iron pipe," in *Underground Infrastructure Research: Municipal, Industrial and Environmental Applications*, M. Knight and N. Thomson, Eds., pp. 303–310, Swets & Zeitlinger, Lisse, The Netherlands, 2001.
- [15] D. E. Adams, *Health Monitoring of Structural Materials and Components*, John Wiley & Sons, London, UK, 2007.
- [16] P. J. Shull, *Nondestructive Evaluation: Theory, Techniques, and Applications*, Marcel Dekker, New York, NY, USA, 2002.
- [17] J. L. Rose, *Ultrasonic Waves in Solid Media*, Cambridge University Press, Cambridge, UK, 1999.
- [18] J. D. Achenbach, *Wave Propagation in Elastic Solids*, North-Holland, New York, NY, USA, 1984.
- [19] D. E. Bray and R. K. Stanley, *Nondestructive Evaluation. A Tool in Design, Manufacturing, and Service*, CRC Press, Boca Raton, Fla, USA, 1997.
- [20] Trenchless Technology Network, *Underground Mapping, Pipeline Location Technology and Condition Assessment*, Infrastructure Engineering and Management Research Centre, The University of Birmingham, 2002.
- [21] W. Prosser, "Acoustic emission," in *Nondestructive Evaluation: Theory, Techniques, and Applications*, P. J. Shull, Ed., Marcel Dekker, New York, NY, USA, 2002.
- [22] F. A. Travers, "Acoustic monitoring of prestressed concrete pipe," *Construction and Building Materials*, vol. 11, no. 3, pp. 175–187, 1997.
- [23] M. Shehadeh, J. A. Steel, and R. L. Reuben, "Acoustic emission source location for steel pipe and pipeline applications: the role of arrival time estimation," *Journal of Process Mechanical Engineering*, vol. 220, no. 2, pp. 121–133, 2006.

- [24] R. Al Wardany, "Condition assessment of prestressed concrete cylindrical water pipes," in *Proceedings of the 60th Annual WCWWA Conference and Trade Show*, Regina, Canada, September 2008, NRCC-50562, Protecting Our Water.
- [25] E. R. MacClean, US patent 2,573,799, November 1951.
- [26] T. R. Schmidt, D. L. Atherton, and S. Sullivan, "Use of one-dimensional skin-effect equations for predicting remote-field characteristics, including wall-thickness versus frequency requirements," *Materials Evaluation*, vol. 47, no. 1, pp. 76–79, 1989.
- [27] <http://www.picacorp.com/>.
- [28] J. Makar and S. McDonald, "Assessment of the hydroscope 201TM condition index evaluation of gray cast iron pipe from gatineau," Tech. Rep. QUEBEC NRC REPORT A-7015.3, National Research Council, Ottawa, Canada, 1996.
- [29] R. Z. Jackson and R. Skabo, "Nondestructive testing of water mains for physical integrity," American Water Works Association (AWWA) Research Foundation, 1992, <http://www.waterresearchfoundation.org/research/TopicsAndProjects/projectSnapshot.aspx?pn=507>.
- [30] J. B. Nestleroth and R. J. Davis, "Application of eddy currents induced by permanent magnets for pipeline inspection," *NDT & E International*, vol. 40, no. 1, pp. 77–84, 2007.
- [31] G. C. Clemena, *Short-Pulse Radar Methods in Handbook of Nondestructive Testing of Concrete*, V. H. Malhotra and N. J. Carino Ed., CRC Press, Boca Raton, Fla, USA, 2004.
- [32] A. J. Bahr, R. Zoughi, and N. Qaddoumi, "Microwave," in *Nondestructive Evaluation: Theory, Techniques, and Applications*, P. J. Shull, Ed., Marcel Dekker, New York, NY, USA, 2002.
- [33] B. Mergelas and X. Kong, *Electromagnetic Inspection of Prestressed Concrete Pressure Pipe*, AWWA Research Foundation, Denver, Colo, USA, 2001.
- [34] F. H. Donaldson, T. J. Dilego, M. S. Higgins, E. A. Padewski, and J. S. Peluso, "Assessing and managing PCCP water transmission mains—Baltimore County, Maryland—a case study," in *Proceedings of the Pipeline Division Specialty Conference*, p. 9, Chicago, Ill, USA, July-August 2006.
- [35] F. H. Donaldson, R. S. Morrison, O. Singh, D. Lieu, J. Peluso, and B. Wright, "Baltimore's pilot water main inspection program becomes emergency rehab/replacement project," in *Proceedings of the Pipelines: Advances and Experiences with Trenchless Pipeline Projects*, p. 69, 2007.
- [36] N. J. Carino, *Stress Wave Propagation Methods in Handbook of Nondestructive Testing of Concrete*, V. H. Malhotra and N. J. Carino Ed., CRC Press, Boca Raton, Fla, USA, 2004.
- [37] M. Dingus, J. Haven, and R. Austin, *Nondestructive, Noninvasive Assessment of Underground Pipelines*, AWWA Research Foundation, Denver, Colo, USA, 2002.
- [38] M. Eiswirth, C. Heske, L. S. Burn, and D. DeSilva, "New methods for water pipeline assessment," in *Proceedings of the 2nd World Water Congress of the International Water Association*, Berlin, Germany, October 2001.
- [39] B. Karney, D. Khani, M. R. Halfawy, and O. Hunaidi, "A simulation study on using inverse transient analysis for leak detection in water distribution networks," Tech. Rep. NRCC-50452, 2009.
- [40] F. C. van der Kleij and M. J. Stephenson, "Acoustic logging—the bristol water experience," in *Proceedings of The IWA Specialised Conference: Leakage Management—A Practical Approach*, International Water Association, Lemesos, Cyprus, November 2002.
- [41] M. Fantozzi, G. Di Chirico, and F. Tonolini, "Leak inspection on water pipelines by acoustic emission with cross-correlation method," in *Proceedings of the AWWA Annual Conference and Exposition*, San Antonio, Tex, USA, June 1993.
- [42] H. V. Fuchs and R. Riehle, "Ten years of experience with leak detection by acoustic signal analysis," *Applied Acoustics*, vol. 33, no. 1, pp. 1–19, 1991.
- [43] O. Hunaidi, W. Chu, A. Wang, and W. Guan, "Detecting leaks in plastic pipes," *Journal of American Water Works Association*, vol. 92, no. 2, pp. 82–94, 2000.
- [44] O. Hunaidi, A. Wang, M. Bracken, T. Gambino, and C. Fricke, "Acoustic methods for locating leaks in municipal water pipe networks," in *Proceedings of the International Conference on Water Demand Management*, Dead Sea, Jordan, May-June 2004, <http://irc.nrc-cnrc.gc.ca/pubs/fulltext/nrcc47062/nrcc47062.pdf>.
- [45] Y. Gao, M. J. Brennan, P. F. Joseph, J. M. Muggleton, and O. Hunaidi, "A model of the correlation function of leak noise in buried plastic pipes," *Journal of Sound and Vibration*, vol. 277, no. 1-2, pp. 133–148, 2004.
- [46] <http://www.pic.com/services/sahara.shtml>.
- [47] Water Environment Research Foundation, October 2009, <http://www.werf.org/AM/CustomSource/Downloads/uGet-ExecutiveSummary.cfm?FILE=ES-01-CTS-7.pdf&Content-FileID=1960>.
- [48] J. P. Vitkovský, A. R. Simpson, and M. F. Lambert, "Leak detection and calibration using transients and genetic algorithms," *Journal of Water Resources Planning and Management*, vol. 126, no. 4, pp. 262–265, 2000.
- [49] J. G. Saldarriaga, D. A. A. Fuentes, and L. F. C. Galvis, "Implementation of the hydraulic transient and steady oscillatory flow with genetic algorithms for leakage detection in real water distribution networks," in *Proceedings of the 8th Annual Water Distribution Systems Analysis Symposium*, p. 52, Cincinnati, Ohio, USA, August 2006.
- [50] M. Stephens, M. Lambert, A. Simpson, J. Vitkovsky, and J. Nixon, "Field tests for leakage, air pocket, and discrete blockage detection using inverse transient analysis in water distribution pipes," in *Proceedings of the World Water and Environmental Resources Congress: Critical Transitions in Water and Environmental Resources Management*, G. Sehlke, D. F. Hayes, and D. K. Stevens, Eds., vol. 138–147, pp. 4779–4788, ASCE, 2004.
- [51] D. Covas, H. Ramos, A. Young, I. Graham, and C. Maksimovic, "Uncertainties of leak detection by means of hydraulic transients from the lab to the field," in *Proceedings of the International Conference on Water Management for the 21st Century (CCWI '05)*, vol. 2, pp. 143–148, Exeter, UK, September 2005.
- [52] A. F. Colombo, P. Lee, and B. W. Karney, "A selective literature review of transient-based leak detection methods," *Journal of Hydro-Environment Research*, vol. 2, no. 4, pp. 212–227, 2009.
- [53] P. Mix, *Introduction to Nondestructive Testing, A Training Guide*, John Wiley & Sons, Hoboken, NJ, USA, 2nd edition, 2005.
- [54] J. B. Nestleroth and T. A. Bubenik, "Magnetic flux leakage (MFL) technology for natural gas pipeline inspection," Tech. Rep., The Gas Research Institute, February 1999, <http://www.battelle.org/pipetechnology/mfl/mfl98main.html>.
- [55] S. Mukhopadhyay and G. P. Srivastava, "Characterization of metal loss defects from magnetic flux leakage signals with discrete wavelet transform," *NDT & E International*, vol. 33, no. 1, pp. 57–65, 2000.

- [56] M. Afzal and S. Udpa, "Advanced signal processing of magnetic flux leakage data obtained from seamless gas pipeline," *NDT & E International*, vol. 35, no. 7, pp. 449–457, 2002.
- [57] P. C. Porter, "Use of magnetic flux leakage (MFL) for the inspection of pipelines and storage tanks," in *Nondestructive Evaluation of Aging Utilities*, vol. 2454 of *Proceedings of SPIE*, pp. 172–184, Oakland, Calif, USA, May 1995.
- [58] Y. Lijan, F. Haiying, and W. Yumei, "Research on intelligent pipeline magnetic flux leakage detector," in *Proceedings of the 10th APCNDT Conference, Technology and Beyond*, Brisbane, Australia, September 2001.
- [59] R. Bickerstaff, M. Vaughn, and G. Stoker, "Review of Sensor Technologies for In-line Inspection of Natural Gas Pipelines," http://www.netl.doe.gov/technologies/oil-gas/publications/Status_Assessments/71702.pdf.
- [60] A. V. Joshi, L. Udpa, S. Udpa, and A. Tamburrino, "Adaptive wavelets for characterizing magnetic flux leakage signals from pipeline inspection," *IEEE Transactions on Magnetics*, vol. 40, no. 10, pp. 3168–3172, 2006.
- [61] I. G. Vickridge and D. Leontidis, "Sewer surveys," in *Sewers—Rehabilitation and Construction*, G. F. Read and I. G. Vickridge, Eds., vol. 1 of *Repair and Renovation*, pp. 84–102, Arnold London, London, UK, 1997.
- [62] http://www.ge-energy.com/prod_serv/serv/pipeline/en/insp-srvcs/crack_detection/ultrascan_cd/index.htm.
- [63] J. L. Rose, J. J. Ditri, A. Pilarski, K. Rajana, and F. Carr, "A guided wave inspection technique for nuclear steam generator tubing," *NDT & E International*, vol. 27, no. 6, pp. 307–310, 1994.
- [64] J. L. Rose, D. Jiao, and J. Spanner Jr., "Ultrasonic guided wave NDE for piping," *Materials Evaluation*, vol. 54, no. 11, pp. 1310–1313, 1996.
- [65] M. J. S. Lowe, D. N. Alleyne, and P. Cawley, "The mode conversion of a guided wave by a part-circumferential notch in a pipe," *Journal of Applied Mechanics, Transactions*, vol. 65, no. 3, pp. 649–656, 1998.
- [66] D. N. Alleyne, B. Pavlakovic, M. J. S. Lowe, and P. Cawley, "Rapid long-range inspection of chemical plant pipework using guided waves," *Insight*, vol. 43, no. 2, pp. 93–96, 2001.
- [67] R. Thompson, G. Alers, and M. Tennison, "Application of direct electromagnetic Lamb wave generation to gas pipeline inspection," in *Proceedings of the IEEE Ultrasonic Symposium*, pp. 91–94, New York, NY, USA, 1971.
- [68] W. Mohr and P. Hoeller, "On inspection of thin-walled tubes for transverse and longitudinal flaws by guided ultrasonic waves," *IEEE Transactions on Sonics and Ultrasonics*, vol. 23, no. 5, pp. 369–374, 1976.
- [69] D. N. Alleyne, M. J. S. Lowe, and P. Cawley, "The reflection of guided waves from circumferential notches in pipes," *Journal of Applied Mechanics, Transactions ASME*, vol. 65, no. 3, pp. 635–641, 1998.
- [70] B. Pavlakovic, M. J. S. Lowe, D. Alleyne, and P. Cawley, "DISPERSE: a general purpose program for creating dispersion curves," in *Reviews of Progress in Quantitative Nondestructive Evaluation*, D. Thompson and D. Chimenti, Eds., vol. 16, pp. 185–192, Plenum, New York, NY, USA, 1997.
- [71] A. Marzani, E. Viola, I. Bartoli, F. Lanza di Scalea, and P. Rizzo, "A semi-analytical finite element formulation for modeling stress wave propagation in axisymmetric damped waveguides," *Journal of Sound and Vibration*, vol. 318, no. 3, pp. 488–505, 2008.
- [72] T. Hayashi, W. J. Song, and J. L. Rose, "Guided wave dispersion curves for a bar with an arbitrary cross-section, a rod and rail example," *Ultrasonics*, vol. 41, no. 3, pp. 175–183, 2003.
- [73] J. N. Barshinger and J. L. Rose, "Guided wave propagation in an elastic hollow cylinder coated with a viscoelastic material," *IEEE Transactions on Ultrasonics, Ferroelectrics, and Frequency Control*, vol. 51, no. 11, pp. 1547–1556, 2004.
- [74] J. Gauthier, V. Mustafa, A. Chabbaz, and D. R. Hay, "EMAT generation of horizontally polarized guided shear waves for ultrasonic pipe inspection," in *Proceedings of the 1st Pan American Conference for Nondestructive Testing (PACNDT '98)*, vol. 4, 1998.
- [75] A. Demma, P. Cawley, M. Lowe, and A. G. Roosenbrand, "The reflection of the fundamental torsional mode from cracks and notches in pipes," *Journal of the Acoustical Society of America*, vol. 114, no. 2, pp. 611–625, 2003.
- [76] V. M. N. Ledesma, E. P. Baruch, A. Demma, and M. J. S. Lowe, "Guided wave testing of an immersed gas pipeline," *Materials Evaluation*, vol. 67, no. 2, pp. 102–115, 2009.
- [77] <http://www.guided-ultrasonics.com/>.
- [78] S. A. Vinogradov, "Magnetostrictive transducer for torsional guided waves in pipes and plates," *Materials Evaluation*, vol. 67, no. 3, pp. 333–341, 2009.
- [79] L.-Y. Sun, X.-D. Yang, and Y.-B. Li, "Research on transducer and frequency of ultrasonic guided waves in urban pipe inspection," in *Proceedings of the 4th IEEE Conference on Industrial Electronics and Applications (ICIEA '09)*, pp. 2708–2711, 2009.
- [80] N. Sarshar, M. R. Halfawy, and J. Hengmeechai, "Video processing techniques for assisted CCTV inspection and condition rating of sewers," in *Proceedings of the Stormwater and Urban Water Systems Modeling Conference, Conceptual Modeling of Urban Water Systems*, Monograph no. 17, pp. 129–149, Toronto, Canada, 2008.
- [81] "Sewer Rehabilitation," February 2010, <http://www.sewer-rehabilitation.com/>.
- [82] S. K. Sinha and M. A. Knight, "Intelligent system for condition monitoring of underground pipelines," *Computer-Aided Civil and Infrastructure Engineering*, vol. 19, no. 1, pp. 42–53, 2004.
- [83] S. Iyer and S. K. Sinha, "Segmentation of pipe images for crack detection in buried sewers," *Computer-Aided Civil and Infrastructure Engineering*, vol. 21, no. 6, pp. 395–410, 2006.
- [84] B. Teichgräber, J. Stemplewski, H. Althoff, and N. Elkmann, "Remote controlled inspection device for large sewers," *Water Practice & Technology*, vol. 1, no. 4, 2006.
- [85] T. Iseley, D. M. Abraham, and S. Gokhale, "Condition assessment of sewer systems," in *Proceedings of the ASCE Conference on Trenchless Pipeline Projects*, pp. 43–51, Boston, Mass, USA, June 1997.
- [86] R. Wirahadikusumah, D. M. Abraham, T. Iseley, and R. K. Prasanth, "Assessment technologies for sewer system rehabilitation," *Automation in Construction*, vol. 7, no. 4, pp. 259–270, 1998.
- [87] CEITEC, "Evaluation of SSET: the sewer scanner and evaluation technology," Tech. Rep. CERF Report 40551, ASCE, New York, NY, USA, 2001.
- [88] M. Eiswirth, C. Frey, et al., "Sewer Assessment by multi-sensor system," in *Proceedings of the 2nd World Water Congress of the International Water Association*, Berlin, Germany, 2001.
- [89] G. Campbell, K. Rogers, and J. Gilbert, "PIRAT—a system for quantitative sewer pipe assessment," in *Proceedings of the International Conference on Trenchless Construction (No-Dig '95)*, Dresden, Germany, September 1995.

- [90] R. Kirkham, P. D. Kearney, K. J. Rogers, and J. Mashford, "PIRAT—a system for quantitative sewer pipe assessment," *International Journal of Robotics Research*, vol. 19, no. 11, pp. 1033–1053, 2000.
- [91] D. Marlow, S. Heart, S. Burn, et al., "Condition assessment strategies and protocols for water and wastewater utility assets," Tech. Rep. 03-CTS-20CO, Water Environment Research Foundation, 2007.

Research Article

Decision Fusion for Structural Damage Detection: Numerical and Experimental Studies

Yong Chen,¹ Senyuan Tian,¹ and Bingnan Sun^{1,2}

¹Department of Civil Engineering, Zhejiang University, Hangzhou, Zhejiang 310058, China

²Ningbo Institute of Technology, Zhejiang University, Ningbo, Zhejiang 315100, China

Correspondence should be addressed to Yong Chen, cecheny@zju.edu.cn

Received 31 August 2009; Revised 28 December 2009; Accepted 23 March 2010

Academic Editor: Yi Qing Ni

Copyright © 2010 Yong Chen et al. This is an open access article distributed under the Creative Commons Attribution License, which permits unrestricted use, distribution, and reproduction in any medium, provided the original work is properly cited.

This paper describes a decision fusion strategy that can integrate multiple individual damage detection measures to form a new measure, and the new measure has higher probability of correct detection than any individual measure. The method to compute the probability of correct selection is presented to measure the system performance of the fusion system that includes the presented fusion strategy. And parametric sensitive studies on system performance are also conducted. The superiority of the fusion strategy herein is that it can be extended to deal with the multiresolution subdecision or blind adaptive detection, and corresponding methodologies are also provided. Finally, an experimental setup was fabricated, whereby the vibration properties of damaged and undamaged structures were measured. The experimental results with the undamaged structural model provide information for producing an improved theoretical and numerical model via model updating techniques. Three existing vibration-based damage detection methods with varied resolutions were utilized to identify the damage that occurred in the structure, based on the experimental results. Then the decision fusion strategy was implemented to join the subdecisions from these three methods. The fused results are shown to be superior to those from single method.

1. Introduction

In the structural health monitoring (SHM) for civil engineering, the monitoring system that consists of numerous sensors is usually employed to achieve more accurate damage detection results, and a number of detection methods have been developed to identify the damages in accordance with structural vibration information (see, e.g., [1–5]). However, there is no perfect damage detection method that is capable of dealing with all kinds of structures, sensors or damages. Focusing on achieving a perfect single damage detection method to solve all damage detection problems does not sound feasible especially for civil engineering structures. Consequently, combining many detection methods together and fusing the sub-results to obtain more accurate detection results would be reasonable. Damage detection-oriented decision fusion that has this ability attracted increasing attentions of researchers studying SHM-based damage detection.

Actually, the initial data fusion researches were predominantly in the defense systems (see, e.g., [6]). It can

be traced back to Tenney and Sandell's achievements [7], and it has been developed quickly in recent years. In early research, Chair and Varshney concentrated on binary decision fusion [8]. Demirbas provided a decision rule, based on maximizing the posteriori probability using binary detection results [9]. The work of Baek and Bommareddy brought the decision fusion research into a new field in which multiple hypotheses are for decision making [10]. Subsequently, blind adaptive decision fusion was developed to deal with the unknown system (see, e.g., [11–13]). Sinha et al. classified the modern decision fusion methods into five categories including linear opinion pool, log linear opinion pool, voting/ranking method, classifier fusion, and artificial neural net (ANN) fusion (see [6] for more details).

Similar as in fault diagnosis, image analysis, safety assessment, and others (see, e.g., [14–16]), many beneficial and novel studies on applying decision fusion method were conducted in structural damage detection. It is found that decision fusion can significantly improve the reliability and robustness of monitoring system through fusing multiple

damage detection results. Dempster-Shafer (D-S) evidential theory has been proved to be a powerful information fusion strategy, many studies on its application to structural damage detection have been conducted. Guo and Zhang applied a weighted balance evidence theory to identifying the damages of a two dimensional truss structure [17]. Zhou et al. utilized D-S evidential theory to merge the multiresolution decision results [18]. Li et al. combined the ANN detection methods and Dempster-Shafer evidential theory together to identify the damages in civil structures, and ANN was used to obtain sub-decision results [19]. In respect of statistical inference, the effort is also seen. Tshöpe and wolff developed a self-learning method which applies classifier in order to identify objects or assess their states, and this method was experimentally verified in damage identification of an aluminum plate and a carbon fiber reinforced plastic plate [20]. Based on Bayesian probability principles, Tian et al. provided a statistical decision fusion methodology, defined as maximum joint probability (MJP) decision rule for damage detection [21]. With regard to comparison of decision fusion strategies, Wang et al. applied four decision fusion strategies, including voting scheme, Bayesian inference, D-S evidential theory, and fuzzy inference, to a damage detection case of a plate structure, and the corresponding experimental studies were also conducted [22].

In this paper, we introduced extended utilizations of MJP decision rule to deal with the multiresolution decision fusion and adaptive decision fusion. With this method, a fusion scheme was proposed for experimental damage detection. Firstly, a cantilever beam was experimentally set up in laboratory and numerically modeled by finite element method (FEM), and the FEM model was updated by the use of experimentally obtained vibration information of undamaged beam. By the use of updated numerical model, damages were simulated numerically, and corresponding natural frequencies were calculated. Noises were added to the natural frequencies for simulating the experimental error. Then, using these numerical results, the probabilities of correct selection of three damage detection methods were obtained. Subsequently, the experimentally acquired vibration information of the damaged physical beam was treated as input of three damage detection methods. Thus, the detection results and priori probabilities obtained in advance were integrated by decision fusion rules to attain a final detection results. The probabilities of correct selection of this fusion system were also obtained, and superiority was found while comparing with that of single damage detection system.

2. Damage Detection Oriented Decision Fusion

Multiple damage cases and multiresolution damage detection requirements are the predominant factors in applying the decision fusion rules to damage detection. This section provides extended forms of MJP decision fusion strategy to deal with those difficulties. For convenience of theoretical expression, it is noted that the concepts of hypothesis, sub-decision system, and decisions those expressions in statistical theory have the same meaning as damage case,

damage detection method (detector or damage detector), and damage detection results, respectively.

2.1. MJP Fusion Rule. MJP fusion rule (see [21] for more details) is trying to make a decision that is capable of minimizing the Bayesian risk function based on Bayesian probability theory. It is assumed that there exist $M + 1$ hypotheses, which can be represented by variable $\mathbf{H} = \{H_0, H_1, H_2, \dots, H_M\}$, and $P(H_j)$ refers to the priori probability of the j th hypothesis. It is also assumed that there exist N damage detectors. The sub-decision made by each detector can be designated as $u_i (i = 1, \dots, N)$, and all of sub-decisions would form a decision state vector $\mathbf{u} = \{u_1, u_2, \dots, u_N\}$. For the i th detector, the description of its performance can be represented by a conditional probability matrix \mathbf{h}^i , in which each element is actually a conditional probability and has a form of

$$h_{jk}^i = P(u_i = h_j | H_k), \quad (1)$$

$$i = 1, \dots, N, \quad j = 0, 1, \dots, M, \quad k = 0, 1, \dots, M,$$

where h_{jk}^i is the probability of the case that the j th hypothesis is selected by the i th detector while the k th hypothesis occurs, and h_j is the j th hypothesis selected by detector.

By the use of the Bayesian risk function (see [23] for more details) and the definition of the final decision $f(\mathbf{u}) = h_B$ in which $B \in \{0, 1, \dots, M\}$, we have Bayesian risk as

$$R_P(f | \mathbf{u}) = E_{H|\mathbf{u}}L(H, f) = \sum_{k=0}^M L(H_k, f)P(H_k | \mathbf{u}), \quad (2)$$

in which the decision rule $f(\mathbf{u})$ yields a final decision $f(\mathbf{u}) = h_B$ that leads to a minimum Bayesian risk. $L(H_k, f(\mathbf{u}))$ is the Loss Function defined as

$$L(H_k, f(\mathbf{u}) = h_j) = \begin{cases} 0, & \text{if } k = j, \\ 1, & \text{otherwise.} \end{cases} \quad (3)$$

Substituting (3) into (2) yields

$$\begin{aligned} R_P(f = h_B | \mathbf{u}) &= \min R_P(f | \mathbf{u}) \\ &= \min_{j \in \{0, 1, \dots, M\}} \left[\sum_{k=0}^M L(H_k, u = h_j)P(H_k | \mathbf{u}) \right] \\ &= \sum_{k=0}^M P(H_k | \mathbf{u}) - \max_{k \in \{0, 1, \dots, M\}} [P(H_k | \mathbf{u})] \\ &= 1 - \max_{k \in \{0, 1, \dots, M\}} [P(H_k | \mathbf{u})]. \end{aligned} \quad (4)$$

Accordingly, if a $P(H_B | \mathbf{u})$ is the largest value among all $P(H_k | \mathbf{u})$, thus the final decision $f(\mathbf{u}) = h_B$ is the selection that minimizes the Bayesian cost function. This decision process could be denoted as

$$f(\mathbf{u}) \triangleq \max_{k \in \{0, 1, \dots, M\}}^{-1} [P(H_k | \mathbf{u})]. \quad (5)$$

It is also assumed that the detectors work independently. Thus, the joint probability of combined decision state can be obtained by

$$P(\mathbf{u} | H_k) = \prod_{i=1}^N P(u_i | H_k). \quad (6)$$

With consideration that $P(\mathbf{u})$ is a constant, using Bayesian rule, (6) leads to a new form of the decision rule, that is,

$$\begin{aligned} f(\mathbf{u}) &\triangleq \max_{k \in \{0, 1, \dots, M\}}^{-1} \left[P(H_k) \prod_{i=1}^N P(u_i | H_k) \right] \\ &= \max_{k \in \{0, 1, \dots, M\}}^{-1} I_k, \end{aligned} \quad (7)$$

in which $I_k = P(H_k) \prod_{i=1}^N P(u_i | H_k)$ is defined as the picking index of hypothesis H_k under determined \mathbf{u} . Equation (7) also means that the decision rule derived herein is to select a hypothesis that maximizes the joint probability of all detectors' decisions,

According to (7), the final decision $f(\mathbf{u}) = h_B$ satisfies

$$\frac{P(H_B) \prod_{i=1}^N P(u_i | H_B)}{P(H_l) \prod_{i=1}^N P(u_i | H_l)} \geq 1, \quad l \in \{0, 1, \dots, M\}, l \neq B, \quad (8)$$

that is,

$$\ln \frac{P(H_B)}{P(H_l)} + \sum_{i=1}^N \ln \frac{P(u_i | H_B)}{P(u_i | H_l)} \geq 0, \quad l \in \{0, 1, \dots, M\}, l \neq B. \quad (9)$$

The picking coefficient v_j^i for i th detector whose decision is h_g can be represented as

$$v_j^i = \begin{cases} 1 & \text{if } j = g, \\ 0 & \text{otherwise.} \end{cases} \quad j = 0, 1, \dots, M. \quad (10)$$

Using the weight factors denoted as

$$\begin{aligned} w_{k,l} &= \ln \frac{P(H_k)}{P(H_l)}, \\ w_{i,j,k,l} &= \ln \frac{P(u_i = h_j | H_k)}{P(u_i = h_j | H_l)} \end{aligned} \quad (11)$$

and the picking coefficients also leads to a new form of the decision rule, that is, the final decision $f(\mathbf{u}) = h_B$ is the hypothesis that satisfies

$$\sum_{\substack{l=1 \\ l \neq B}}^M \text{sign}(y_{B,l}) = M, \quad (12)$$

where

$$y_{k,l} = w_{k,l} + \sum_{i=1}^N \sum_{j=0}^M v_j^i w_{i,j,k,l}, \quad (13)$$

and the definition of $\text{sign}(\cdot)$ is

$$\text{sign}(x) = \begin{cases} 1 & \text{if } x \geq 0, \\ 0 & \text{otherwise.} \end{cases} \quad (14)$$

As well as (7), (12) is also another form of decision rule, and it is easy to be utilized while considering an adaptive fusion problem. Summarily, the decision rule derived herein is to achieve the maximum joint probability of the sub-decisions state $\{u_1, u_2, \dots, u_n\}$ while an actual unknown damage case occurs. Accordingly, it was defined as maximum joint probability (MJP) decision rule (see [21]).

2.2. Probability of Correct Selection. It is necessary to be aware of the probability of correct selection (PCS) of the whole fusion system. According to the definition of the Loss Function in (4), the Bayesian risk function presented by (3) is actually the probability of system making a wrong decision. Therefore, the probability of failure (PF) for a decision made according to MJP decision rule (see [21]) is

$$W(f(\mathbf{u}) = u_B | \mathbf{u}) = 1 - P(H_B) \frac{\prod_{i=1}^N P(u_i | H_B)}{P(\mathbf{u})}, \quad (15)$$

where

$$P(\mathbf{u}) = \sum_{k=1}^M P(\mathbf{u}H_k)P(H_k) = \sum_{k=1}^M P(H_k) \prod_{i=1}^N P(u_i | H_k) \quad (16)$$

and the PCS is

$$Q(f(\mathbf{u}) = u_B | \mathbf{u}) = 1 - W(f(\mathbf{u}) = u_B | \mathbf{u}). \quad (17)$$

For the entire decision system in association with decision rule f , the PF and PCS of the whole system, denoted as $W(f)$ and $Q(f)$, respectively, are formed (see [21]) as

$$W(f) = \sum_{\mathbf{u}} W(f(\mathbf{u}) = u_B | \mathbf{u})P(\mathbf{u}), \quad (18)$$

$$Q(f) = 1 - W(f). \quad (19)$$

2.3. Multiresolution. Damage detection results can be conventionally classified into three levels: damage acknowledgment, damage localization and damage quantification (see [5]). Variable l is used to represent these three levels of resolution. The damage detection method on the first level ($l = 1$) is able to determine whether the damage occurred or not. If a damage detection method is on the second level ($l = 2$), it means that this method can alarm not only the occurrence of damage but also the location of damage. The third level ($l = 3$) is the highest level, and on this level the damage detection method can provide both localization and quantification of a damage.

Figure 1 illustrates an application of the definition of resolution. The bridge in Figure 1 consists of three segments, and there are two grades of damage quantity to be identified. Thus, in case of the lowest level, the hypotheses for decision fusion are Damaged and No Damage. For the second level, the hypotheses for decision fusion would be No Damage and

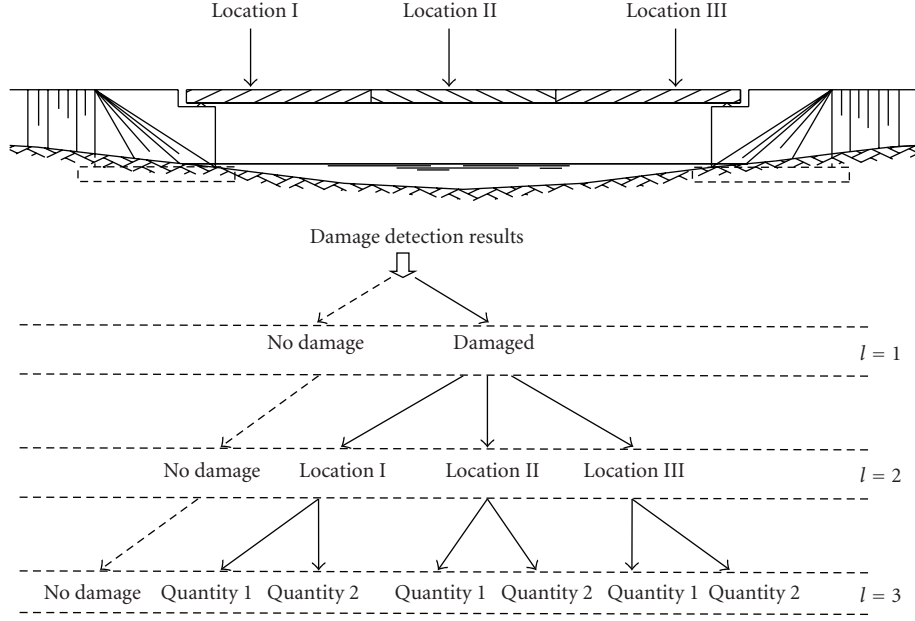


FIGURE 1: Three damage resolutions of damage detection methods.

Damaged-Location I, Damaged-Location II, and Damaged-Location III. With respect to the highest level, a total of seven hypotheses would be No Damage, Damaged-Location I-Quantity 1, Damaged-Location I-Quantity 2, Damaged-Location II-Quantity 1, Damaged-Location II-Quantity 2, Damaged-Location III-Quantity 1, and Damaged-Location III-Quantity 2. For example, we assume that the damage occurred in the second segment with a damage degree that is Quantity 2. We also assume that three damage detection methods are on different resolution levels, and they are sorted by resolution from the lowest to highest. If the detectors detected the damage correctly, the results from these three damage detection methods would sequentially be Damaged, Damaged-Location II, and Damaged-Location II-Quantity 2. For convenience, the hypotheses are conventionally numbered sequentially from zero, and a correlation table is prepared to describe the relationship between the number and hypothesis. Thus, the detection results in this example should be 1, 2 and 4 sequentially.

In terms of multiresolution, the hypotheses or damage cases are determined by the damage detection method that is on the highest resolution level among all detectors. With a consideration of a detector being on the highest level ($l = 3$), the damage case vector $\{h_0^{l=3}, h_1^{l=3}, \dots, h_M^{l=3}\}$ has a size of $M = s \times r$, in which s and r represent the number of damage locations and grades, respectively. For example, if considering the problem in Figure 1, then s is 3 and r is 2. Hence, on the reduced level ($l = 2$) of resolution for the same detection method, the damage cases for identifying should be No Damage and the damage localizations, that is, $\{h_0^{l=2}, h_1^{l=2}, \dots, h_s^{l=2}\}$. Also, they would be No Damage and Damaged, that is, $\{h_0^{l=1}, h_1^{l=1}\}$, while the resolution is reduced again to the first level ($l = 1$). The resolution level, that is, $l = 1, 2$ or 3 , is marked as a superscript of the sub-decision,

as well as the detectors and the hypotheses. For instance, $u_2^{l=2}$ means that the second detection method is on level 2.

A damage detection method with the highest level ($l = 3$) resolution can be reduced to a method on the level of $l = 2$. The corresponding conditional probability $P(u_i^{l=2} = h_q^{l=2} | H_k)$ of the latter can be computed through $P(u_i^{l=3} = h_j^{l=3} | H_k)$ of the former, that is,

$$h_{qk}^i = P(u_i^{l=2} = h_q^{l=2} | H_k) = \begin{cases} \sum_{j=(q-1)r+1}^{qr} P(u_i^{l=3} = h_j^{l=3} | H_k) & \text{if } q = 1, \dots, s, \\ P(u_i^{l=3} = h_0^{l=3} | H_k) & \text{if } q = 0. \end{cases} \quad (20)$$

Similarly, if a method's resolution is reduced from level 2 to level 1, the new conditional probabilities $P(u_i^{l=1} = h_0^{l=1} | H_k)$ and $P(u_i^{l=1} = h_1^{l=1} | H_k)$ for the lowest resolution level would be

$$h_{1k}^i = P(u_i^{l=1} = h_1^{l=1} | H_k) = \sum_{q=1}^s P(u_i^{l=2} = h_q^{l=2} | H_k),$$

$$h_{0k}^i = P(u_i^{l=1} = h_0^{l=1} | H_k) = P(u_i^{l=2} = h_0^{l=2} | H_k). \quad (21)$$

According to the maximum joint probability decision rule, for a multiresolution case, optimal final decision is also the one that achieves a maximum joint probability of sub-decisions made by detection methods with different resolutions. For example, three sub-decisions are made but on different resolution levels. If the sub-decisions for k th

hypothesis are $u_1^{l=1} = h_1^{l=1}$, $u_2^{l=2} = h_2^{l=2}$, and $u_3^{l=3} = h_2^{l=3}$, thus the picking index in (7) is

$$\begin{aligned}
 I_k &= P(H_k) \prod_{i=1}^N P(u_i | H_k) \\
 &= P(u_1^{l=1} = h_1^{l=1} | H_k) P(u_2^{l=2} = h_2^{l=2} | H_k) \\
 &\quad \times P(u_3^{l=3} = h_2^{l=3} | H_k) P(H_k) \\
 &= h_{1k}^1 h_{2k}^2 h_{2k}^3 P(H_k)
 \end{aligned} \tag{22}$$

Then we can vary the hypothesis and make a comparison, and the hypothesis corresponding to the maximum one is the final decision.

Multiresolution decision fusion strategy can be carried out on the reduced level, by taking advantage of (20) and (21) and modifying the value range of k in (7) by

$$k \in \begin{cases} \{0, 1, \dots, M\} & \text{if } l = 3, \\ \{0, 1, \dots, s\} & \text{if } l = 2, \\ \{0, 1\} & \text{if } l = 1. \end{cases} \tag{23}$$

3. Parametric Study in Same Resolution Case

In the parametric study for system performance, it is assumed that all of the detectors have the same resolution. Also, the priori probability of each damage case is known as

$$P(H_k) = \frac{1}{(M + 1)} \quad k = 0, 1, \dots, M, \tag{24}$$

where M represents number of damage cases. The probability of correct selection by damage detection method numbered i is

$$Q_i = \sum_{j=0}^M P(u_i = h_j | H_j) P(H_j) \tag{25}$$

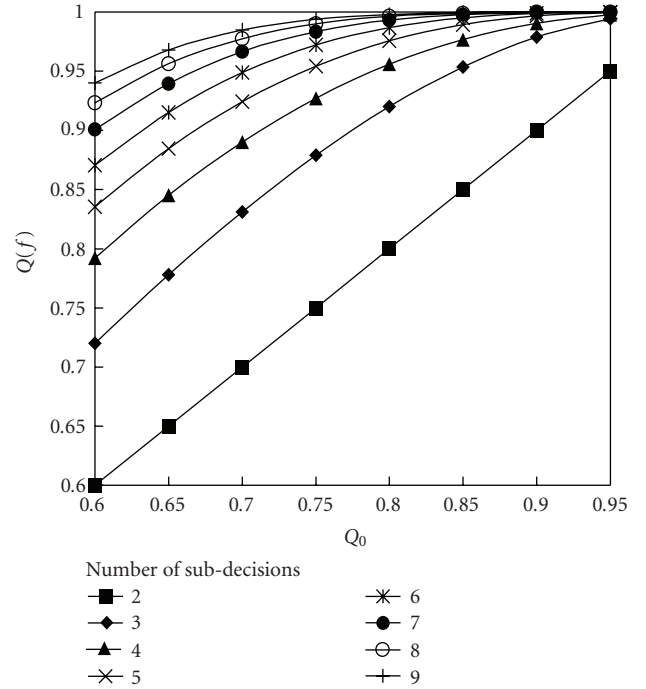
It is also assumed that each damage detection method has the same performance which means that they have the same PCS, that is, all $P(u_i = h_j | H_j)$ of the detectors are equal to Q_0 . And all $P(u_i = h_j | H_k)$ in which $j \neq k$ are equal for each damage detection methods. Summarily, the conditional probability matrixes of the detectors are the same, and the elements in the matrixes are

$$h_{jk}^i = P(u_i = h_j | H_k) = \begin{cases} Q_0 & \text{if } j = k \\ \frac{(1 - Q_0)}{M} & \text{otherwise} \end{cases} \tag{26}$$

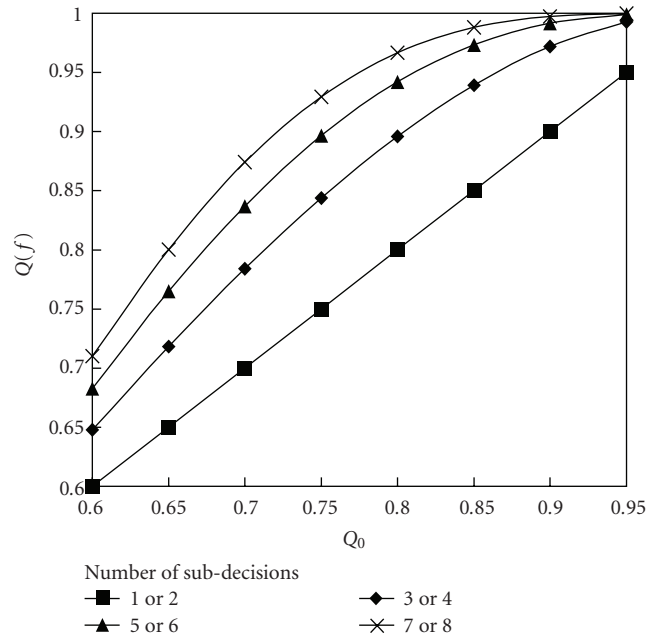
$$i = 1, \dots, N; \quad j = 0, 1, \dots, M; \quad k = 0, 1, \dots, M.$$

Following Figures 2, 3, and 4 are based on these assumptions represented by (24) and (26), and the PCS of fusion system can be computed through (19).

Figure 2 illustrates the curves of the PCS of fusion system versus that of sub-decision system. In case of using five damage cases as shown in Figure 2(a), it is found that the



(a) Use five damage cases



(b) Use two damage cases

FIGURE 2: PCS of fusion system versus that of sub-decision system.

PCS of the fusion system is improved while we increase the number of sub-decision methods and the PCS of the sub-decision systems. Also, the increment descends while adding supplemental sub-decision methods. In case of using two damage cases as shown in Figure 2(b), the similar phenomenon is observed. It is also found that using either $2k - 1$ or $2k$ sub-decisions will achieve the same PCS of the fusion system, and $k = 0, 1, \dots$

The PCS of the sub-decisions in Figure 3 is fixed at 0.8. It is found that if the number of the sub-decision systems exceeds three, the PCS of the fusion system is significantly improved, and it increases with the increasing of the number of the damage cases. If we fix the number of sub-decisions at four, Figure 4 also indicates that increasing the number of the damage cases is beneficial to improve the PCS of the fusion system.

4. Adaptive Decision Fusion

4.1. Algorithm. For an unknown system, the knowledge of performance of the sub-decision systems, that is, conditional probabilities, is not available, as well as the priori probabilities of the hypotheses. That means the weight factors, which are necessary for the decision fusion rule formed as (7) or (13), are not available. Adaptive decision fusion strategy has capability of dealing with that. A simple counting rule-based (see, e.g., [11, 12]) adaptive strategy for MJP are introduced herein to make a final decision by self learning and sensing the system continually.

In accordance with the simple counting rule, relative frequency (see, e.g., [11, 12]), which is the ratio of the numbers of two events, is utilized to evaluate the weight factors. Since the true hypothesis is unknown for fusion system, we use a *reliable hypothesis* to replace the true hypothesis. This reliable hypothesis during the whole adaptive fusion procedure can be the final decision that is made by the decision fusion system, and we put a notation “ \wedge ” above H to distinguish the reliable hypothesis from the true hypothesis. Accordingly, notation “ \wedge ” marked weight factors are used to indicate that they are based on the reliable hypothesis. Let a_k be the number of \hat{H}_k , a_l be the number of \hat{H}_l , $a_{i,j,k}$ be the number of decisions that is the j th hypothesis which is made by the i th detector while \hat{H}_k occurs, and $a_{i,j,l}$ be the number of decisions that is the j th hypothesis which is made by the i th detector while \hat{H}_l occurs, thus the weight factors in (13) can be approximately estimated by

$$\begin{aligned}\hat{w}_{k,l} &= \ln \frac{P(\hat{H}_k)}{P(\hat{H}_l)} \approx \ln \frac{a_k}{a_l}, \\ \hat{w}_{i,j,k,l} &= \ln \frac{P(u_i = h_j, \hat{H}_k)}{P(u_i = h_j, \hat{H}_l)} - \ln \frac{P(\hat{H}_k)}{P(\hat{H}_l)} \approx \ln \frac{a_{i,j,k}}{a_{i,j,l}} - \hat{w}_{k,l},\end{aligned}\quad (27)$$

whereby, we have

$$\begin{aligned}a_l &\approx \frac{a_k}{\exp(\hat{w}_{k,l})}, \\ a_{i,j,l} &\approx \frac{a_{i,j,k}}{\exp(\hat{w}_{i,j,k,l} + \hat{w}_{k,l})}.\end{aligned}\quad (28)$$

Then, the partial derivatives of the weight factors are

$$\begin{aligned}\frac{\partial \hat{w}_{k,l}}{\partial a_k} &\approx \frac{1}{a_k}, \\ \frac{\partial \hat{w}_{k,l}}{\partial a_l} &\approx -\frac{1}{a_l} \approx -\frac{1}{a_k} \exp(\hat{w}_{k,l}), \\ \frac{\partial \hat{w}_{i,j,k,l}}{\partial a_k} &\approx -\frac{1}{a_k}, \\ \frac{\partial \hat{w}_{i,j,k,l}}{\partial a_l} &\approx \frac{1}{a_l} \approx \frac{1}{a_k} \exp(\hat{w}_{k,l}), \\ \frac{\partial \hat{w}_{i,j,k,l}}{\partial a_{i,j,k}} &\approx \frac{1}{a_{i,j,k}}, \\ \frac{\partial \hat{w}_{i,j,k,l}}{\partial a_{i,j,l}} &\approx -\frac{1}{a_{i,j,l}} \approx -\frac{1}{a_{i,j,k}} \exp(\hat{w}_{i,j,k,l} + \hat{w}_{k,l}).\end{aligned}\quad (29)$$

By substitution of (29) into the increment form of (27), the updating rule for weight factors can be

$$\begin{aligned}\hat{w}_{k,l}^+ &= \hat{w}_{k,l}^- + \Delta \hat{w}_{k,l} \\ \hat{w}_{i,j,k,l}^+ &= \hat{w}_{i,j,k,l}^- + \Delta \hat{w}_{i,j,k,l},\end{aligned}\quad (30)$$

where

$$\begin{aligned}\Delta \hat{w}_{k,l} &= \begin{cases} \frac{1}{a_k} & \hat{H} = \hat{H}_k, \\ -\frac{1}{a_k} \exp(\hat{w}_{k,l}^-) & \hat{H} = \hat{H}_l, \\ 0 & \hat{H} \neq \hat{H}_k, \hat{H} \neq \hat{H}_l, \end{cases} \\ \Delta \hat{w}_{i,j,k,l} &= \begin{cases} -\frac{1}{a_k} + \frac{1}{a_{i,j,k}} & \hat{H} = \hat{H}_k, u_i = h_j, \\ -\frac{1}{a_k} & \hat{H} = \hat{H}_k, u_i \neq h_j, \\ \frac{1}{a_k} \exp(\hat{w}_{k,l}^-) & \\ -\frac{1}{a_{i,j,k}} \exp(\hat{w}_{i,j,k,l}^- + \hat{w}_{k,l}^-) & \hat{H} = \hat{H}_l, u_i = h_j, \\ \frac{1}{a_k} \exp(\hat{w}_{k,l}^-) & \hat{H} = \hat{H}_l, u_i \neq h_j, \\ 0 & \hat{H} \neq \hat{H}_k, \hat{H} \neq \hat{H}_l, \end{cases}\end{aligned}\quad (31)$$

in which the superscript “+” means the current step, and “-” the previous step.

4.2. Numerical Simulation Study. To justify the efficiency of the proposed adaptive fusion methodology, a three hypothesis problem was numerically studied. It is assumed that the true priori probabilities of hypotheses are listed as

$$P(H_0) = 0.4, \quad P(H_1) = 0.2, \quad P(H_2) = 0.4. \quad (32)$$

It is also assumed that there are four independently working detectors. The true conditional probability matrices of these four sub-decision systems are assumed to be

$$\mathbf{h}^1 = \begin{bmatrix} 0.90 & 0.04 & 0.06 \\ 0.05 & 0.90 & 0.04 \\ 0.05 & 0.06 & 0.90 \end{bmatrix}, \quad \mathbf{h}^2 = \begin{bmatrix} 0.82 & 0.07 & 0.08 \\ 0.09 & 0.85 & 0.09 \\ 0.09 & 0.08 & 0.83 \end{bmatrix},$$

$$\mathbf{h}^3 = \begin{bmatrix} 0.91 & 0.04 & 0.05 \\ 0.05 & 0.91 & 0.05 \\ 0.04 & 0.05 & 0.90 \end{bmatrix}, \quad \mathbf{h}^4 = \begin{bmatrix} 0.85 & 0.07 & 0.08 \\ 0.08 & 0.86 & 0.08 \\ 0.07 & 0.07 & 0.84 \end{bmatrix}. \quad (33)$$

For adaptive fusion system, the true conditional probability matrices and priori probabilities of hypotheses are unknown. Equations (32), (33) are merely utilized to generate the events and corresponding sub-decisions, as input data of adaptive fusion system. A total of 10000 random events were generated according to (32). Based on these events, a total of 10000 sets of sub-decisions are also individually simulated according to (33). Each set of them consists of four pseudo sub-decisions on the corresponding event. Thus, by using the fusion strategy and (30), the adaptation of the weight factors can be figured out.

Figures 5 and 6 illustrate the adaptations of selected two weight factors, and compare them with true values. In the figures, the true values computed by (27) are horizontal straight lines and the true values are pointed out by variables without “^”. As shown in Figures 5 and 6, the convergence of these curves justifies the effectiveness of the adaptive strategy we proposed. However, a very slow speed of convergence is observed, which is not suitable for civil structural damage detection. It is necessary to improve the speed of convergence in the future study.

5. Experimental Study

In this section, the framework of using decision fusion is introduced. We used two models for the same test structure, one is physical model for test and the other one is numerical model for performance study of detectors. The fusion scheme can be described as follows.

Step 1. Obtain the priori probabilities of hypotheses and conditional probability matrices of detectors;

Step 2. Detectors make sub-decisions based on the test results of actual structure.

Step 3. By the use of decision fusion, provide a final decision to determine the damage which occurred in actual structure.

The work in Step 1 should be completed in advance before starting damage detection, and it requires a lot of computational time and data preparation for civil engineering structures. The priori probabilities of hypotheses can be approximately obtained by taking advantage of expert experience or lots of statistical inspections of the existing

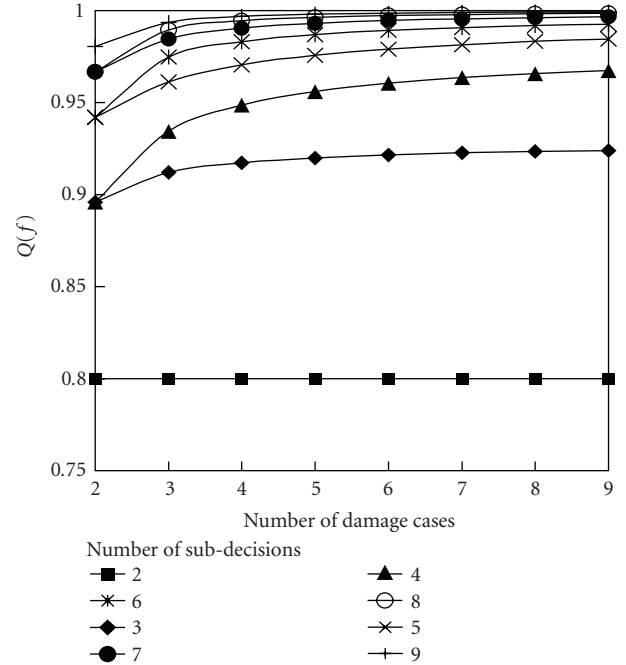


FIGURE 3: PCS of system versus number of damage cases in case of $Q_0 = 0.8$.

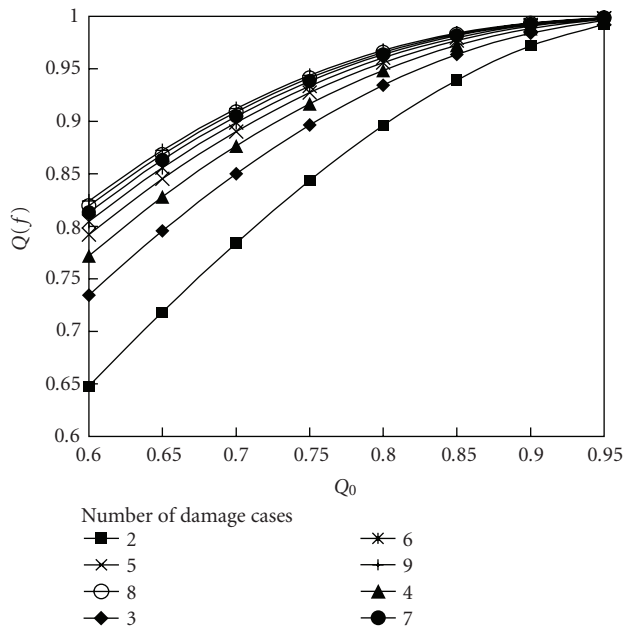
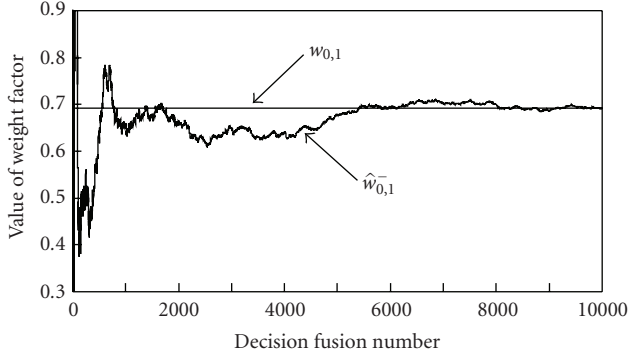
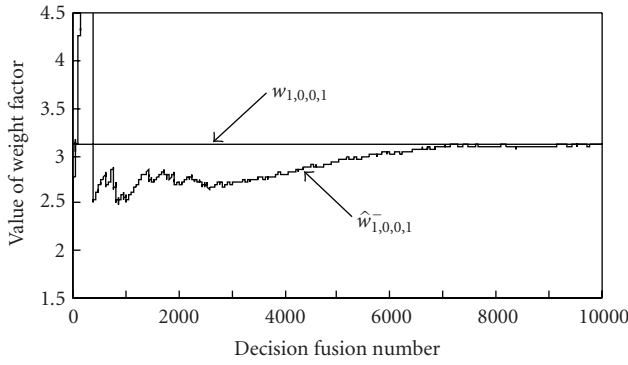


FIGURE 4: PCS of system versus that of sub-decision system, number of sub-decisions is four.

structures that considered congeneric with the test structure. The conditional probability matrixes of the detectors can be acquired according to the experience from applications, or by supplier.

We also introduce a countermeasure to obtain the conditional probability matrixes based on numerical damages that are simulated by using finite element analysis (FEA) method.

FIGURE 5: Adaptation of $\hat{w}_{0,1}^{-}$.FIGURE 6: Adaptation of $\hat{w}_{1,0,0,1}^{-}$.

At first, numerical damage cases were simulated by the use of FEA method, and corresponding natural frequencies of undamaged and damaged structures were calculated. It is well known that the failure in detecting is due to the test noise. Therefore, we added a numerical white noise on the natural frequencies that are calculated by FEA. The noise level is the same as that of the actual measuring system, and the actual noise can be obtained by repeated tests on the actual structure. Thus, numerous noised samples were obtained. Whereby, all of the detectors are examined to detect the numerical simulated damage. For each detector, by taking statistical analysis on the detection results on all events, it is easy to approximately achieve conditional probability matrixes.

Damage detections in Step 2 are a kind of blind damage detection, since the structural damage is unknown. The detection results made by the detectors may agree or disagree with each other, and each detection result is provided with a probability of correct selection. If we stop at this step, the only reasonable selection is the one provided by the detector that has the highest PCS. If we go on, and fuse these detection results by decision fusion rule with the priori probabilities and the conditional probability matrixes in Step 1, then a final decision that has a higher PCS will be obtained.

Regarding the experimental application presented in this section, Figure 7 illustrates the corresponding strategy for damage detection, which is based on decision fusion. The strategy utilized three vibration-based (actually natural

TABLE 1: Natural frequencies of cantilever beam (Hz).

| Order | 1 | 2 | 3 | 4 | 5 |
|----------------------|------|-------|-------|-------|-------|
| Experimental results | 7.39 | 45.46 | 128.6 | 256.5 | 415.8 |
| Numerical results | 7.66 | 47.44 | 134.0 | 263.5 | 433.9 |
| After model updating | 7.39 | 45.46 | 128.5 | 253.0 | 414.6 |

frequency-based) damage detection methods as sub-decision systems. Since the detection methods employed herein are different in resolution, we use a multiresolution fusion rule to carry out the decision fusion.

5.1. Test Structure. The specimen for the experimental study is a steel cantilever beam with 1 m in length as shown in Figure 8. Three accelerometers SA1, SA2 and SA3, were installed at different positions of the structure to measure the accelerations of the beam. The location of excitation is EP in Figure 8, where force hammer was used to give an impulse excitation.

The vibrations under impulse excitation were measured to identify the natural frequencies of undamaged structure. The identified natural frequencies are also compared with FEA results, as shown in Table 1. Though a small error between numerical and experimental results is found, it would not be good enough for damage detection. This is because the damage detection methods used herein merely rely on the variation of natural frequency of structure, and it is well known that the frequency variation of structural vibration is not sensitive to the change of stiffness which could be caused by structural damage. Furthermore, this FEA numerical model will be employed to simulate the numerical damages. Thus, the more accurate the FEA model is, the closer it would be between the numerical results and experimental results. Also, the conditional probability matrix evaluated through numerical simulation will be closer to that through experiments. Therefore, model updating techniques should be utilized to achieve a relative accurate FEA model. Due to implementing blind damage detection in Step 2, the model updating is merely applied to undamaged structure, that is, taken to obtain a numerical undamaged FEA model.

The model updating technique used herein is a kind of parametric method, which updates the model by minimizing the objective function that includes system parameters. Whereby, we construct an objective function $J(\mathbf{v})$ as

$$J(\mathbf{v}) = \sum_{i=1}^N \beta_i \left[f_i^T - f_i^C(\mathbf{v}) \right]^2 \quad (34)$$

in which f_i^T and f_i^C represent the natural frequencies obtained by vibration test and FEA respectively, N is the number of frequencies and is assigned a value of five, β_i is the weight factor for i th natural frequency, and \mathbf{v} is a vector consisting of elastic module, dimensions of cantilever, and mass of accelerometers.

To minimize the objective function, stochastic research method was implemented to solve this optimization problem. Whereby, we achieved an updated model, and the

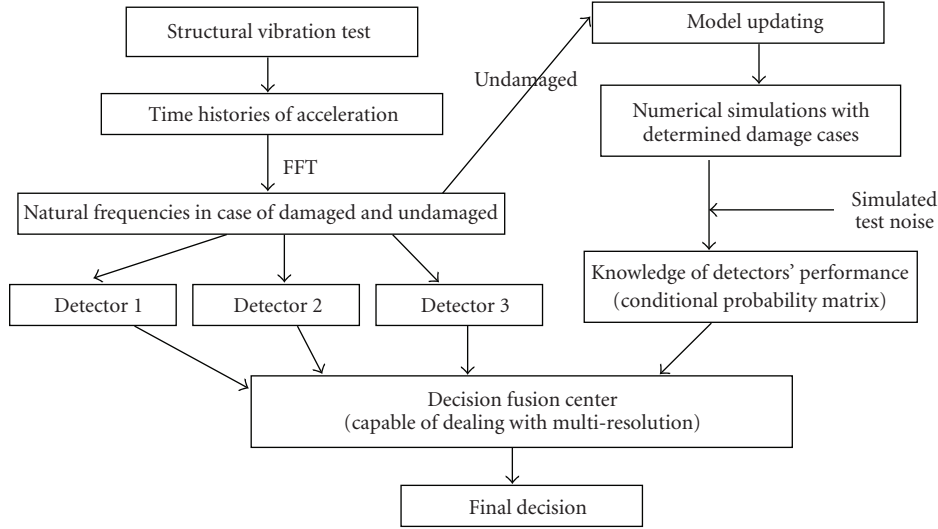


FIGURE 7: Decision fusion-based damage detection.

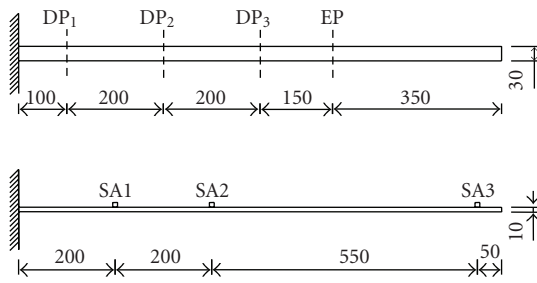


FIGURE 8: Dimensions of cantilever beam.

natural frequencies obtained through FEA are very close to those through vibration tests, as shown in Table 1.

5.2. Detection Methods. A total of three damage detection methods are employed to identify the damage in the structure. These vibration-based methods employ a linear motion system governed by

$$\mathbf{M}\mathbf{x}'' + \mathbf{C}\mathbf{x}' + \mathbf{K}\mathbf{x} = \mathbf{f}(t), \quad (35)$$

where \mathbf{M} , \mathbf{C} and \mathbf{K} are mass, damp and stiffness matrix, respectively, and \mathbf{x} is displacement vector, and $\mathbf{f}(t)$ is external excitation.

5.2.1. Damage Detection Method 1. Damage will cause the changes of both mass and stiffness matrices, and lead to a change of natural frequency ω and mode φ . According to the work by Hearn and Testa [2], if mass change and second order items can be ignored, we have the square of the i th natural frequency increment, $\Delta\omega_i^2$, formed as

$$\Delta\omega_i^2 = \frac{\varphi_i^T \Delta\mathbf{K} \varphi_i}{\varphi_i^T \mathbf{M} \varphi_i}. \quad (36)$$

It is assumed that the change of stiffness matrix caused by damage can be represented by the original stiffness matrix

multiplied by a scalar α_i . Thus, we divide the structure into n elements and consider the l th element, and (36) can be

$$\Delta\omega_i^2 = \frac{\alpha_i \varepsilon_i^T(\varphi_i) \mathbf{k}_i \varepsilon_i(\varphi_i)}{\varphi_i^T \mathbf{M} \varphi_i}, \quad (37)$$

where $\varepsilon_i(\varphi)$ is the element's deformation that can be calculated by changed mode due to damage. Thus

$$\frac{\Delta\omega_i^2}{\Delta\omega_j^2} = \frac{\varepsilon_i^T(\varphi_i) \mathbf{k}_i \varepsilon_i(\varphi_i)}{\varepsilon_j^T(\varphi_j) \mathbf{k}_j \varepsilon_j(\varphi_j)} \cdot \frac{\varphi_j^T \mathbf{M} \varphi_j}{\varphi_i^T \mathbf{M} \varphi_i}. \quad (38)$$

Equation (38) indicates that the ratio of any two $\Delta\omega^2$ would be a function of damage location, but independent of damage quantity. Hence, this method is on the second resolution level, and the detection result $u_1 = h_j$ obtained is merely capable of localizing the damage or indicating no damage.

5.2.2. Damage Detection Method 2. According to Stubbs and Osegueda's work [1], for the i th natural frequency, we use a variation rate b_i to describe the ratio of $\Delta\omega_i^2$ to ω_i^2 for the i th natural frequency, that is,

$$b_i = \frac{\Delta\omega_i^2}{\omega_i^2} = \frac{\alpha_i \varepsilon_i^T(\varphi_i) \mathbf{k}_i \varepsilon_i(\varphi_i)}{\varphi_i^T \mathbf{K} \varphi_i} \quad (39)$$

It was considered that n damaged elements were involved and p modes were measured, therefore (39) can be rewritten as

$$\mathbf{A}_{p \times n} \mathbf{X}_{n \times 1} = \mathbf{B}_{p \times 1}, \quad (40)$$

where vector $\mathbf{B} = [b_1, b_2, \dots, b_p]^T$ consists of p variation rates, vector $\mathbf{X} = [\alpha_1, \alpha_2, \dots, \alpha_n]^T$ is damage vector whose each element is the same as α_l in (37), and matrix \mathbf{A} represents the relationship matrix of damage and changing

rate. According to (39), the elements in \mathbf{A} can be computed by

$$\begin{aligned} A_{ij} &= \frac{\varepsilon_j^T(\varphi_i) \mathbf{k}_j \varepsilon_j(\varphi_i)}{\varphi_i^T \mathbf{K} \varphi_i} \\ &= \frac{b_i}{a_j} \quad (i = 1, 2, \dots, p, j = 1, 2, \dots, n) \end{aligned} \quad (41)$$

The matrix \mathbf{A} should be obtained in advance before starting damage detection, thus, numerical damage simulation is conventionally employed to obtain it. Firstly, we attain the natural frequencies of the numerical model with a damage of α_i by FEA. Then, the variation rate vector \mathbf{B} can be achieved by (39). Finally, the elements of \mathbf{A} can be computed by (41).

With knowledge of that $n < p$ may occur frequently during actual damage detection, thus (40) would lead to an undetermined system. The countermeasure suggested herein to solve (40) is to minimize an objective function J_s as

$$J_s = \frac{1}{2} \|\mathbf{A}\mathbf{X} - \mathbf{B}\|_2^2 - 1 \leq \alpha_j \leq 0, \quad j = 1, \dots, n. \quad (42)$$

Obviously, the second method is on the highest resolution level, which means that it can both localize and quantify the damage which occurred in the structure.

5.2.3. Damage Detection Method 3. The third selected method is a kind of ANN method, which utilizes neural network to identify damage. According to the achievements of Ko et al. [4], we used a three-layer BP neural network, with seven outputs representing seven damage cases, three inputs representing the first three natural frequency variation rates, and a hidden layer of eight nodes. After simulating the numerical damage, corresponding variation rates and damage cases were put into the neural network for training. Then, the trained neural network is ready for damage detection.

5.3. Damage Cases and Tests. Three damage locations are considered as shown in Figure 8, and they are named as DP_1 , DP_2 and DP_3 . The damage cases for each location would be no damage, damaged with a gap in depth ≤ 3 mm, and damaged with a gap in depth > 3 mm. Then we achieved a total of seven damage cases or a seven hypothesis problem, as shown in Table 2.

In dynamic test, we used three test specimens to physically simulate the damages of three locations. Table 1 just lists the results of one of the specimens. For each specimen, we measured the vibrations of the undamaged beam, that is, whose gap is zero deep, and the damaged beam. The damage beam is a beam that has a gap, and the gap is sequentially cut in depth of 1, 2, 3, 4, 5, and 6 mm on the side at the same location. Five repeated vibration tests were conducted for the gap in each depth, whereby, we conducted a total of 35 tests for one specimen and 105 tests for total three specimens. Then, these tests were classified according to Table 2. Whereby, 105 samples are prepared for damage identification, and the corresponding results would include the manufacturing errors and measuring errors.

5.4. Final Decision

5.4.1. Priori Perception. The priori perception for damage detection is the information that should be achieved before starting damage detection. As described in Step 1, the priori perception herein includes the priori probabilities of hypotheses and the conditional probability matrixes of all detectors.

For this experimental study, it is assumed that the hypotheses are equally probable, that is, the damage case obeys discrete uniform distribution. Thus, all of the priori probabilities of hypotheses are equal and each one is equal to $1/7$.

The conditional probability matrixes of three detectors were numerically studied. By using the updated FEA model, we also constructed the FEA models for the damage beams. The damage kind of gap is simulated through eliminating the finite elements where damage occurs. A total of 35 damage cases are simulated, and the corresponding natural frequencies are obtained through FEA. Thus by adding the pseudo experimental errors, which were numerical simulated according to the statistics of dynamic test results, to those natural frequencies, we generated lots of numerical samples. With these, three detectors were then examined, and the sub-decisions obtained were counted to approximately estimate the conditional probability matrixes. These matrixes are listed as

$$\begin{aligned} \mathbf{h}^1 &= \begin{bmatrix} 84.1 & 40.2 & 0.8 & 50.3 & 0.2 & 51.6 & 0.1 \\ 3.8 & 36.6 & 78.8 & 10.3 & 5.2 & 5.3 & 0 \\ 5.2 & 16.2 & 18.9 & 38.5 & 94.5 & 4.5 & 0.1 \\ 6.9 & 7.0 & 1.5 & 0.9 & 0.1 & 38.6 & 99.8 \end{bmatrix} \%, \\ \mathbf{h}^2 &= \begin{bmatrix} 34.5 & 7.6 & 0 & 3.2 & 0 & 7.5 & 0 \\ 8.4 & 78.3 & 0.6 & 4.3 & 0 & 4.5 & 0 \\ 0 & 2 & 99.4 & 0 & 0 & 0 & 0 \\ 22.7 & 0.1 & 0 & 83.2 & 0.8 & 26.7 & 0 \\ 0.1 & 0 & 0 & 3 & 99.2 & 0 & 0 \\ 34.2 & 12 & 0 & 6.3 & 0 & 61.3 & 1.8 \\ 0.1 & 0 & 0 & 0 & 0 & 0 & 98.2 \end{bmatrix} \%, \\ \mathbf{h}^3 &= \begin{bmatrix} 56 & 20 & 0 & 6.9 & 0 & 10.5 & 0 \\ 3.1 & 73.3 & 13.3 & 2.3 & 0 & 18.2 & 0 \\ 0.2 & 0 & 86.7 & 0 & 0 & 0 & 0 \\ 25.2 & 0 & 0 & 81.3 & 4.9 & 28.7 & 0 \\ 0.3 & 0 & 0 & 0.3 & 95.1 & 0 & 0 \\ 15.1 & 6.7 & 0 & 9.2 & 0 & 42.6 & 2.8 \\ 0.1 & 0 & 0 & 0 & 0 & 0 & 97.2 \end{bmatrix} \%. \end{aligned} \quad (43)$$

However, by taking advantage of actual test results, the statistics of the sub-decisions by the detectors also provides the conditional probability matrixes of the detectors. We use an overbar to distinguish these experimental results from

the numerical results given in (43), and these experimentally obtained matrixes are

$$\begin{aligned} \bar{\mathbf{h}}^1 &= \begin{bmatrix} 86.7 & 33.3 & 0 & 53.3 & 0 & 66.7 & 0 \\ 0 & 40 & 80 & 6.7 & 6.7 & 0 & 0 \\ 6.7 & 20 & 20 & 40 & 93.3 & 0 & 0 \\ 6.7 & 6.7 & 0 & 0 & 0 & 33.3 & 100 \end{bmatrix} \%, \\ \bar{\mathbf{h}}^2 &= \begin{bmatrix} 33.3 & 6.7 & 0 & 6.7 & 0 & 0 & 0 \\ 6.7 & 80.0 & 0 & 6.7 & 0 & 0 & 0 \\ 0 & 0 & 100 & 0 & 0 & 0 & 0 \\ 26.7 & 0 & 0 & 80.0 & 0 & 26.7 & 0 \\ 0 & 0 & 0 & 0 & 100 & 0 & 0 \\ 33.3 & 13.3 & 0 & 6.7 & 0 & 73.3 & 0 \\ 0 & 0 & 0 & 0 & 0 & 0 & 100 \end{bmatrix} \%, \\ \bar{\mathbf{h}}^3 &= \begin{bmatrix} 60 & 20 & 0 & 6.7 & 0 & 6.7 & 0 \\ 0 & 73.3 & 13.3 & 0 & 0 & 20 & 0 \\ 0 & 0 & 86.7 & 0 & 0 & 0 & 0 \\ 26.7 & 0 & 0 & 86.7 & 0 & 26.7 & 0 \\ 0 & 0 & 0 & 0 & 100 & 0 & 0 \\ 13.3 & 6.7 & 0 & 6.7 & 0 & 46.7 & 0 \\ 0 & 0 & 0 & 0 & 0 & 0 & 100 \end{bmatrix} \%. \quad (44) \end{aligned}$$

Comparing the conditional probability matrixes from numerical simulations with those from tests, only a small difference could be observed. Accordingly, it is reasonable to use the conditional probability matrixes from the numerical analysis results. Usually, the performance of the detector is not available, experience from applications is absent, and dynamic tests for damaged structure could not be realized, in civil engineering. Therefore, this numerical simulation-based method is useful to achieve those conditional probability matrixes.

5.4.2. Damage Detections by Detectors and Fusion. With the priori probability of hypotheses as introduced in the Section 5.4.1, and the detectors' performance matrix as listed in (43), the priori perception for this experimental study of decision fusion are prepared now. Whereby, (7) is capable of achieving a final decision while the sub-decisions are made. It is noted that the sub-decisions made by the detectors for a damage case should be based on the actual test results, because we are dealing with blind damage detection.

Firstly, for each one of 105 tests in Section 5.3, all of three damage detection methods should make a decision to determine the damage case, according to the experimental results from that test. Then, by the use of priori perception and (7), the sub-decisions were fused to achieve a final decision about damage case. It is noted, because the detectors employed herein are in different resolutions, the fusion strategy for multiresolution should be implemented.

The Selected 6 samples with corresponding three damage detection results u_i ($i = 1, 2, 3$) and final decision u are listed in Table 3, in which the value is the damage case number. The actual damage cases represented by H are also presented in Table 3, for comparison.

It is shown that a decision fusion system can make a more reliable decision, compared with using single damage detection method. It often happens that the final decision conforms well to the actual damage case but conflicts occur

TABLE 2: Damage cases denoted according to damage location and degree.

| Damage case no. | H_0 | H_1 | H_2 | H_3 | H_4 | H_5 | H_6 |
|-----------------|-------|-------------|----------|-------------|----------|-------------|----------|
| Damage location | None | DP1 | DP1 | DP2 | DP2 | DP3 | DP3 |
| Damage degree | | ≤ 3 mm | > 3 mm | ≤ 3 mm | > 3 mm | ≤ 3 mm | > 3 mm |

TABLE 3: Selected samples and fusion result.

| Samples no. | H | u_1 | u_2 | u_3 | u | Correct or Wrong |
|-------------|-----|-------|-------|-------|-----|------------------|
| 1 | 0 | 0 | 0 | 0 | 0 | ✓ |
| 2 | 0 | 0 | 3 | 0 | 0 | ✓ |
| 3 | 0 | 2 | 0 | 5 | 0 | ✓ |
| 4 | 1 | 0 | 1 | 0 | 1 | ✓ |
| 5 | 1 | 3 | 5 | 4 | 0 | × |
| 6 | 1 | 2 | 1 | 1 | 1 | ✓ |

among three damage detectors. After applying the decision fusion to the results of 105 vibration tests, we also achieved a conditional probability matrix, as shown in (45), which shows superiority to that of any one of the detectors.

$$\bar{\mathbf{h}}^u = \begin{bmatrix} 80 & 13.3 & 0 & 20 & 0 & 26.7 & 0 \\ 6.7 & 66.7 & 0 & 0 & 0 & 0 & 0 \\ 0 & 20 & 100 & 0 & 0 & 0 & 0 \\ 0 & 0 & 0 & 80 & 0 & 0 & 0 \\ 0 & 0 & 0 & 0 & 100 & 0 & 0 \\ 13.3 & 0 & 0 & 0 & 0 & 73.3 & 0 \\ 0 & 0 & 0 & 0 & 0 & 0 & 100 \end{bmatrix} \%. \quad (45)$$

6. Conclusion

Decision fusion method can integrate individual damage detection measures to obtain a single measure, and achieve a higher probability of correct selection than any individual one. This paper introduced the implementation of decision fusion in structural damage detection. The MJP decision fusion rule was employed to deal with multiple hypotheses detection, fusing sub-decisions in multiple resolutions, and blind adaptive detection. An implementation using experimental structure was conducted. The whole detection and fusion process were illustrated.

MJP method relies on the priori perception of system, including priori probability of damage cases and conditional probability matrixes of detectors. Therefore, we introduced a method to obtain the conditional probability matrix of detectors by FEA method. This method was approved by comparing the matrixes from numerical simulation with those from test results. A cantilever beam structure was set up for experimental study, and 105 vibration test samples were obtained for damage detection. Then, three vibration-based detectors were employed to make sub-decisions based on test results. In terms of priori perceptions and these sub-decisions, a final decision can be obtained by using the MJP decision fusion rule. Thus, 105 final decisions were achieved,

and it was found that the final decisions were superior to those from a single damage detection method.

References

- [1] N. Stubbs and R. Osegueda, "Global non-destructive damage evaluation in solids—experimental verification," *The International Journal of Analytical and Experimental Modal Analysis*, vol. 5, pp. 81–97, 1990.
- [2] G. Hearn and R. B. Testa, "Modal analysis for damage detection in structures," *Journal of Structural Engineering*, vol. 117, pp. 3042–3063, 1991.
- [3] Y. Zou, L. Tong, and G. P. Steven, "Vibration-based model-dependent damage (delamination) identification and health monitoring for composite structures—a review," *Journal of Sound and Vibration*, vol. 230, no. 2, pp. 357–378, 2000.
- [4] J. M. Ko, Y. Q. Ni, X. T. Zhou, and J. Y. Wang, "Structural damage alarming in Ting Kau Bridge using auto-associative neural networks," in *Advances in Structural Dynamics*, J. M. Ko and Y. L. Xu, Eds., vol. 2, pp. 1021–1028, Elsevier Science, Oxford, UK, 2000.
- [5] Z. Sun and C. C. Chang, "Structural damage assessment based on wavelet packet transform," *Journal of Structural Engineering*, vol. 128, no. 10, pp. 1354–1361, 2002.
- [6] A. Sinha, H. Chen, D. G. Danu, T. Kirubarajan, and M. Farooq, "Estimation and decision fusion: a survey," *Neurocomputing*, vol. 71, no. 13–15, pp. 2650–2656, 2008.
- [7] R. R. Tenney and N. R. Sandell Jr., "Detection with distributed sensors," *IEEE Transactions on Aerospace and Electronic Systems*, vol. 17, no. 4, pp. 501–510, 1981.
- [8] Z. Chair and P. K. Varshney, "Optimum data fusion in multiple sensor detection systems," *IEEE Transactions on Aerospace and Electronic Systems*, vol. 22, no. 1, pp. 98–101, 1986.
- [9] K. Demirbas, "Maximum a Posteriori approach to object recognition with distributed sensors," *IEEE Transactions on Aerospace and Electronic Systems*, vol. 24, no. 3, pp. 309–313, 1988.
- [10] W. Baek and S. Bommareddy, "Optimal m-ary data fusion with distributed sensors," *IEEE Transactions on Aerospace and Electronic Systems*, vol. 31, no. 3, pp. 1150–1152, 1995.
- [11] N. Ansari, J.-G. Chen, and Y.-Z. Zhang, "Adaptive decision fusion for unequidistributed sources," *IEEE Proceedings on Radar, Sonar and Navigation*, vol. 144, no. 3, pp. 105–110, 1997.
- [12] N. Mansouri and M. Fathi, "Simple counting rule for optimal data fusion," in *Proceedings of the IEEE Conference on Control Applications*, vol. 2, pp. 1186–1191, 2003.
- [13] B. Liu, A. Jeremic, and K. M. Wong, "Blind adaptive algorithm for M-ary distributed detection," in *Proceedings of the IEEE International Conference on Acoustics, Speech and Signal Processing (ICASSP '07)*, vol. 2, pp. 1025–1028, 2007.
- [14] M. N. Liu and X. Yang, "Image quality assessment by decision fusion," *IEICE Electronics Express*, vol. 5, no. 15, pp. 537–542, 2008.
- [15] H. Seraji and N. Serrano, "A multisensor decision fusion system for terrain safety assessment," *IEEE Transactions on Robotics*, vol. 25, no. 1, pp. 99–108, 2009.
- [16] A. Kyriazis and K. Mathioudakis, "Gas turbine fault diagnosis using fuzzy-based decision fusion," *Journal of Propulsion and Power*, vol. 25, no. 2, pp. 335–343, 2009.
- [17] H. Guo and L. Zhang, "A weighted balance evidence theory for structural multiple damage localization," *Computer Methods in Applied Mechanics and Engineering*, vol. 195, no. 44–47, pp. 6225–6238, 2006.
- [18] C. Zhou, Y. Chen, and B. Sun, "Result-merging algorithm of structure damage identifications with multi-resolution based on D-S evidential theory," *Journal of Vibration and Shock*, vol. 25, no. 6, pp. 5–8, 2006 (Chinese).
- [19] H. Li, Y. Bao, and J. Ou, "Structural damage identification based on integration of information fusion and Shannon entropy," *Mechanical Systems and Signal Processing*, vol. 22, no. 6, pp. 1427–1440, 2008.
- [20] C. Tshöpe and M. Wolff, "Statistical classifiers for structural health monitoring," *IEEE Sensors Journal*, vol. 9, no. 11, pp. 1567–1576, 2009.
- [21] S.-Y. Tian, Y. Chen, and B.-N. Sun, "Maximum joint probability fusion rule for multi-resolution decision of structure damage detection," *Journal of Zhejiang University (Engineering Science)*, vol. 41, no. 1, pp. 126–133, 2007 (Chinese).
- [22] X. Wang, G. Foliente, Z. Su, and L. Ye, "Multilevel decision fusion in a distributed active sensor network for structural damage detection," *Structural Health Monitoring*, vol. 5, no. 1, pp. 45–58, 2006.
- [23] J. K. Ghosh, M. Delampady, and T. Samanta, *An Introduction to Bayesian Analysis: Theory and Methods*, Springer, New York, NY, USA, 2006.

Research Article

Truly Distributed Optical Fiber Sensors for Structural Health Monitoring: From the Telecommunication Optical Fiber Drawing Tower to Water Leakage Detection in Dikes and Concrete Structure Strain Monitoring

Jean-Marie Henault,¹ Gautier Moreau,¹ Sylvain Blairon,¹ Jean Salin,¹
Jean-Robert Courivaud,² Frédéric Taillade,³ Erick Merliot,³ Jean-Philippe Dubois,⁴
Johan Bertrand,⁴ Stéphane Buschaert,⁴ Stefan Mayer,⁴ and Sylvie Delepine-Lesoille^{3,4}

¹ EDF R&D, 6 quai Watier, 78401 Chatou, France

² EDF CIH, Savoie Technolac, 73370 Le Bourget du Lac, France

³ LCPC, 58 bld Lefebvre, 75015 Paris, France

⁴ Andra, 1-7 rue Jean Monnet, 92298 Chatenay-Malabry, France

Correspondence should be addressed to Sylvie Delepine-Lesoille, sylvie.lesoille@andra.fr

Received 1 September 2009; Revised 18 January 2010; Accepted 11 February 2010

Academic Editor: Jinying Zhu

Copyright © 2010 Jean-Marie Henault et al. This is an open access article distributed under the Creative Commons Attribution License, which permits unrestricted use, distribution, and reproduction in any medium, provided the original work is properly cited.

Although optical fiber sensors have been developed for 30 years, there is a gap between lab experiments and field applications. This article focuses on specific methods developed to evaluate the whole sensing chain, with an emphasis on (i) commercially-available optoelectronic instruments and (ii) sensing cable. A number of additional considerations for a successful pairing of these two must be taken into account for successful field applications. These considerations are further developed within this article and illustrated with practical applications of water leakage detection in dikes and concrete structures monitoring, making use of distributed temperature and strain sensing based on Rayleigh, Raman, and Brillouin scattering in optical fibers. They include an adequate choice of working wavelengths, dedicated localization processes, choices of connector type, and further include a useful selection of traditional reference sensors to be installed nearby the optical fiber sensors, as well as temperature compensation in case of strain sensing.

1. Introduction

Specifications for large-sized engineering structures such as the Rion-Antirion bridge (Greece) or the Millau viaduct (France) now commonly include instrumentation in order to address monitoring requirements, not only during the construction period, but also to allow lifetime structural health monitoring.

EDF's (French Electricity Company) potential applications include dams, dike and power plant reactors monitoring. Andra's (French National Radioactive Waste Management Agency) potential applications include surface and deep geological radioactive waste disposal structure

monitoring, for instance, within the future geological repository that would contain highly instrumented disposal cells. LCPC is in charge of the surveillance of various French bridges developing structural pathologies due to aging.

Controlling the state of a structure's health, more commonly designated by the acronym SHM (Structural Health Monitoring), requires a large number of sensors. For this application, optical fiber sensors [1] (OFS) are found to be exceptional tools, especially as they enable distributed measurements [2] thus providing data over the entire structure instead of being limited to point data at sensor locations. Monitoring with a single fiber can thus provide information of the overall structure behavior, and

thus overcome limitations of traditional sensors, whose information is restricted to local effects. Some 20 years of developments have been necessary to overcome the initial disappointments and fully utilize the specificities of these sensors [3], whose application has since become state of the art.

This article focuses on temperature and strain distributed sensing with optical fibers for structural health monitoring. After an initial summary description of fiber optic sensing technologies, the focus will be put on distributed temperature and strain sensors. These will be illustrated by an in-depth description of two field applications: Water leakage detection in dikes using temperature distributed sensing and concrete structure monitoring by strain and temperature monitoring. Although commercially-available sensors and interrogation unit are numerous, the global measuring chain may provide disappointing monitoring results to the end-users, unless a number of specific considerations are taken into account. These are further developed within this article, with an emphasis on practical recommendations that seem essential for a successful transition from laboratory to field applications.

2. Overview of Optical Fiber Sensor Technologies

An optical fiber is a waveguide with a diameter in the order of 0.1 mm that enables conveying light upon kilometer range distances. A wide array of optical fibers, called single-mode or multimode, have been developed in either glass or plastic, with solid or hollow cores, packaged in very diverse shapes to convey signals that may be visible or invisible. As described with great details in [1], OFS offers many advantages when compared to traditional electronic sensors: they are light, small (expected to be non invasive) and insensitive to electromagnetic fields, not subject to metallic corrosion (unless a metallic cladding is chosen), and resist to high temperatures. They also make it possible to take measurements over great distances (in the kilometer range) taking advantage of very low attenuation coefficient and multiple sensors can be multiplexed in one fiber. Applications range from material sensing to oil exploration and production monitoring.

A large variety of OFS have been successfully commercialized in the past three decades essentially based on Bragg-gratings and Fabry-Perot cavities (FP), providing one or several, localized measurements [1]. These technologies require a specific, localized treatment of the fiber, for example localized surface grating, to create a localized, sensitive element susceptible to produce a measurable signal. These OFS technologies remain limited in their applications by the predefined and “point-like” nature of data they can provide. For civil engineering, a large number of such “point-like” OFS need to be multiplexed to instrument real decametric structures [4]. A wide variety of multiplexing schemes have been developed to enable simultaneous measurement of several tens of sensors. However, even if a thousand of sensors are available, the choice of their

locations may be highly sensitive, and is an intensive research topic.

In comparison, distributed sensing provides a more versatile and powerful monitoring tool as it requires much less *a priori* knowledge of the structure behavior. The term *distributed sensor* designates the case in which the optical fiber itself becomes a sensor. It is thus no longer necessary to implement anticipated sensor positions since measurements are being performed all along the optical fiber connected to the reading device (as well as within the extension cables). The remainder of this article is focused on OFS technologies allowing for such distributed sensing.

2.1. Truly Distributed Sensors: Localization Processes. Various techniques may be utilized to develop a continuously distributed measurement system within an optical fiber. The most common would be OTDR (for Optical Time Domain Reflectometry), which could eventually be combined with a study of light-matter interactions such as the Raman effect (temperature-dependent) and the Brillouin effect (temperature and deformation-dependent) as depicted afterwards.

Initially created to analyze losses inside optical telecommunication lines [5], OTDR is categorized as an optical pulse-echo technique. The technique consists in injecting a laser pulse within an optical fiber and then measuring the backscattered intensity versus time: a period Δt corresponds to a pulse round-trip between the lead and a given point on the fiber located at $c/(2n \cdot \Delta t)$ from the lead. The temporal width of the pulse necessitates an OTDR spatial resolution; a 10-ns width corresponds to a resolution of 1 m. OTDR serves to carry out intensity variation measurements over distances in the tens of kilometers, with a spatial resolution at the meter scale.

Other localization techniques are available whose performances are quite complementary; some for example are based on frequency modulations, hence the acronym OFDR (Optical Frequency Domain Reflectometry). Detailed principle can be found in [5–7]. OFDR spatial resolution can reach $10 \mu\text{m}$, although the corresponding measurement range (possible fiber length) diminishes considerably to around 100 meters.

Whatever the technique, a major issue of distributed sensing is the uncertainty on the measurement locations along the fiber as will be illustrated in the field application descriptions provided in the following.

2.2. Scattering at the Origin of Truly Distributed Sensors. As shown in Figure 1, the light backscattered by an optical fiber segment without any defects or abnormal characteristics is spectrally decomposed into three distinct peaks corresponding to three outstanding phenomena.

The first relates to Rayleigh scattering, originated from interaction between the electromagnetic wave propagating in the fiber core and silica impurities. Intensity variations in the backscattered signal at the same wavelength as the injected wave are related with local optical fiber modifications: an abrupt return peak is interpreted as a mirror reflection (connector or damage on the fiber), and a sudden drop in intensity corresponds for example to shear loss. Beyond detection,

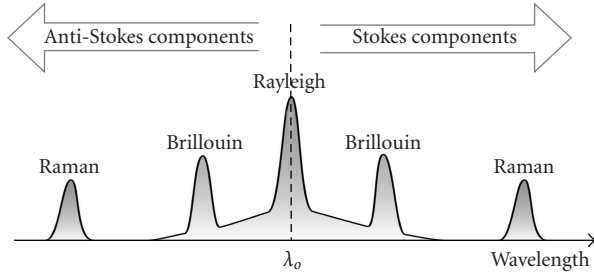


FIGURE 1: Backscattering spectrum of a monochromatic wave within an optical fiber.

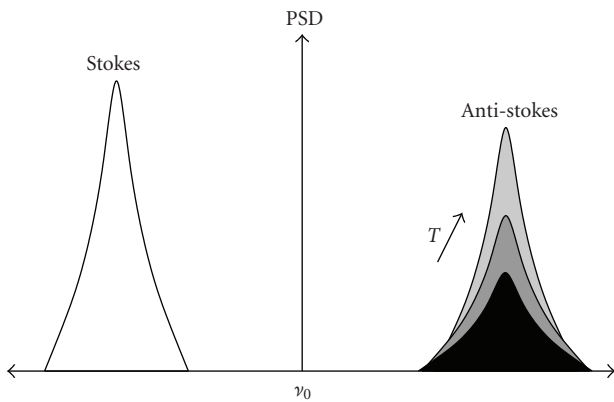


FIGURE 2: Raman scattering sensitivity to temperature (“PSD” stands for power spectral density).

to conduct temperature or strain measurements, the value of the Rayleigh backscattering signal in optical fibers must be associated with another technique, the simplest being an association with punctual sensors, such as microbend sensors or another configuration that incorporates precalibrated losses [8]. In this case, the continuously-distributed aspect of the measurement would be lost. In single-mode fibers, polarization measurements may be added [9], parameter quite interesting when application requires pressure or magnetic field sensing.

Another possibility is to perform correlation between various Rayleigh measurements as proposed by the optical backscattered reflectometry (OBR) instrument described in Section 2.2.3. An alternative is to use the two other scattering lines, Raman and Brillouin, described in Sections 2.2.1 and 2.2.2, respectively.

2.2.1. Distributed Temperature Sensing Based on Raman Scattering. To perform distributed temperature measurement, Raman scattering [1, 10] is the most advanced technology.

Raman scattering originates from laser light photon interaction with thermal vibration of silica molecules (thermal phonons). More precisely, as sketched in Figure 2, the anti-Stokes absorption mainly depends on temperature. As a consequence, Raman distributed sensing systems may use OTDR pulsed technique to perform distributed intensity

measurement of the anti-Stokes backscattered light. However, the anti-Stokes intensity evolution must be augmented with a reference measurement since optical fiber losses vary with time (increase with fiber aging, connector dirt, or optical fiber curvatures, etc.). A number of commercially available distributed temperature sensing devices automatically compensate for this loss by analysing the ratio between the Anti-Stokes and Stokes absorption line intensities.

Paired with multimode fibers and OTDR localisation techniques, repeatability of Raman distributed temperature devices are on the order of 0.1°C for distance ranges of several kilometres and spatial resolution of 1 m. It degrades with increasing distance but can be maintained by increasing the device acquisition time. Maximal distance range is 30 km. Applications include leakage detection along oil and gas pipelines, monitoring of underground storage and boreholes, fire detection [10], monitoring of waste disposal sites and seepage detection in dams and dikes [11]. Few instruments offer the possibility to perform Raman scattering measurement into single-mode fiber. A preliminary test is reported in Section 5.2.2.

2.2.2. Distributed Temperature or Strain Sensing Based on Brillouin Scattering. As sketched in Figure 1, another inelastic phenomenon occurs when an optical pulse is launched into an optical fiber, called Brillouin scattering. This Brillouin frequency shift ν_B is linked to the acoustic mode phase velocity [12]. As a consequence, the Brillouin shift variations are known to be proportional to temperature (ΔT) and strain (ϵ) variations [13] as in:

$$\Delta\nu_B = C_T\Delta T + C_\epsilon\epsilon. \quad (1)$$

C_T and C_ϵ are characteristics of the optical fiber type. At the operating wavelength (1550 nm), for standard G652 single-mode fiber, C_T and C_ϵ are in the order of 1 MHz/ $^{\circ}\text{C}$ and 0.05 MHz/ $\mu\epsilon$ [13].

Instruments based on Brillouin scattering would thus perform either temperature or strain measurements. In 2002, the first commercial B-OTDR system was implemented. In 2007, the market had expanded to include at least five suppliers of Brillouin interrogation systems. The performance derived is on the order of 1°C or $20\mu\epsilon$ and 1 m of spatial resolution, over spans extending several tens of kilometers. The most widespread application is currently pipeline leak detection, based on temperature measurements [14]. Compared with Raman sensing, sensitivity is reduced by a factor 10. However, Brillouin sensing enables measurement along longer distance ranges, up to 80 km. Both differences are mainly related to the optical fiber type, respectively, multimode and single-mode for Raman and Brillouin sensing.

2.2.3. Distributed Temperature or Strain Sensing Based on Relative Rayleigh Measurements: The OBR Instrument. Another approach to perform strain or temperature distributed measurement consists in carrying out relative Rayleigh measurements, as offered by an instrument called “Optical

Backscatter reflectometry" (OBR) commercialized by the American company Luna Technologies.

It relies on two OFDR (see Section 2.1) measurements, the ongoing measurement and a reference state, processed with an advanced correlation method that analyses the spectral lags of the Rayleigh backscattering peak. As detailed in [7], the frequency shift $\Delta\nu$ of the Rayleigh backscatter pattern is proportional to temperature or strain changes along the fiber axis. For standard single-mode fiber G652 type, at 1550 nm typical values are -0.1499 (GHz/ ϵ) and -1.248 GHz/ $^{\circ}\text{C}$.

OBR has been commercially available since spring 2006. It enables measuring approximately optical fiber deformations (at homogeneous temperature) over 100 m with a centimeter-sized spatial resolution and a level of precision equal to a few microstrains (resp., 0.1°C at homogeneous strain).

2.3. Influence of the Optical Fiber outside Coating. Up to this point, optoelectronic devices have been described. A distributed sensing system pairs such an instrument with a sensitive part including an optical fiber. A major difficulty encountered during the transition from the laboratory to the field is that the optical fiber cannot be used wrapped in its standard coatings. Either external coatings are far too fragile for outdoor test, or the coatings developed by the telecommunication industry isolate the fiber from its environment in order to protect it. The related question is how to transform an optical fiber into a transducer, as will be illustrated for the two applications described further.

3. A Simple Qualification Methodology

Despite many advantages described in Section 2.1, truly distributed optical fiber sensors have not invaded SHM applications yet, due to a lack of standardization in claimed performances and dedicated qualification processes.

The described overall process is inspired from [15]. The global chain evaluation must be adapted to the application. For OFS, it was chosen to study both sensing cables and optoelectronic instruments separately, before pairing such elements and focusing on data processing. Global test sequence includes the following.

- (1) The SHM system is selected regarding commercially-available technologies versus needs and requirements. If they do not match, internal developments are engaged, as illustrated for strain sensing cables (see Section 5.1).
- (2) Special test benches are developed in laboratory to qualify metrological behaviour of the whole sensing chain under controlled conditions. For instruments, basic test can be performed in laboratory as illustrated for Raman distributed temperature device tests in Section 4.1. For embedded sensors, spatial resolution drives test structure size, which may lead to mock-up realisation as detailed in Section 4.2 for temperature sensing and Section 5.1 for strain sensing. Controlled conditions are necessary to develop

quantitatively fitted data processing algorithms, as shown in Figure 7.

- (3) The on field-implementation-specific requirements are finally analysed, addressed in Sections 4.3 and 5.2.3.

This qualification methodology is put in practice for two main applications: dike monitoring with Raman temperature sensing and strain distributed measurements for concrete structure monitoring. As many technical aspects were already reported elsewhere, the article rapidly mentions references dealing with the first two global test sequences, to focus on caveats for field implementation.

4. Raman Scattering into Optical Fibers Applied to Water Leakage Detection in Dikes

Internal erosion is a major cause of failures of embankment dams and dikes. This pathology, characterized by water leakage in the structure, remains nowadays detected by conventional method based on visual inspection. In order to improve the safety of the installation, new monitoring methods are developed.

Temperature is a good tracer of seepage [16]. Two main techniques are proposed. The passive technique is based on seasonal temperature variations in the water channel and in the ground. The active method is based on heating-up the soil.

To perform temperature measurement, optical fiber distributed sensors is a good candidate as it provides continuous monitoring in space and time. Since the beginning of the 2000s [17], EDF has launched several research programs on optical fiber instrumentation and data processing so as to get an automated Structural Health Monitoring technique able to detect seepage flows in dikes with minimized false alarm rate. The developed system relies on optical fiber technology. Although it takes advantage of commercially available elements, many difficulties had to be solved before EDF recently decided to spread the technique to various exploited structures. The following paragraphs detail difficulties to transform a laboratory instrument into a monitoring system suited to field use.

4.1. Laboratory Evaluation of Commercially Available Systems.

As summarized in Section 2.2.1, several commercially-available optoelectronic devices perform distributed temperature measurements using the Raman effect. As seepage detection threshold depends on the uncertainties of the measuring system, it is of major importance to determine the metrological behavior of the optoelectronic device. As direct comparison of specification sheets of the different products is not obvious, EDF decided to perform a common testing program for different commercially-available devices.

Fiber bending radius is known to influence measurement quality. Moreover, unlike standard sensors (small electronic devices), Raman measurement is averaged over 1 meter scale, because instruments rely on OTDR technique. As a result, it is mandatory to ensure a very stable temperature over

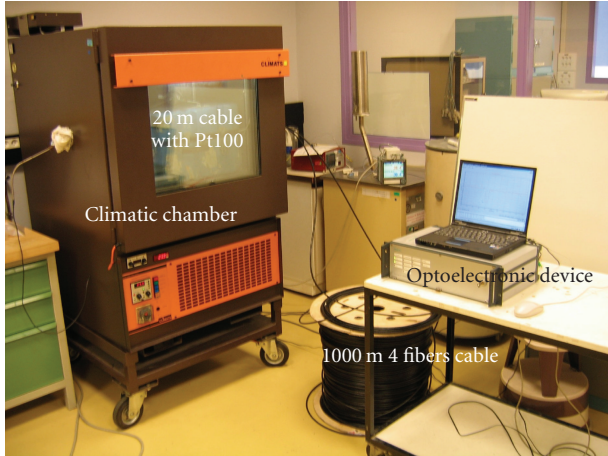


FIGURE 3: Different optoelectronic devices comparison thanks to a specific bench composed by a climatic chamber including a water bath equipped with fiber cables.

few meters with as less enrollment as possible. Finally, performances are expected to be closely related to average time and distance range.

A specific bench was developed, suited to water leakage application. Described in great detail in [18], it enables measuring stable temperature over 20 m, every 1 km, up to 4 km. As shown in Figure 3, a commercially available cable that includes 4 multimode fibers is partially installed in a bath placed into a climatic chamber. Doing so, the cable has a minimum curvature radius of 35 cm. Temperature is controlled with a platinum probe (Pt100 type) whose measurements show a 0.01°C stability over several hours. As derived from [19], repeatability is defined by the dispersion of successive measurements in the same conditions; error is derived from the difference between the device measurements and the Pt100 measurements.

Between 2005 and 2008, the same test program was applied to 7 multimode devices from different suppliers. It includes range of temperature of the bath between 0°C to 50°C and acquisition time between 30 s to one hour. It resulted [20] that for each device (i) the error revealed to be quite independent from the selected parameters (bath temperature, acquisition time and distance to the device) over the spans explored during the tests; (ii) the repeatability did not depend on temperature (between 0°C and 50°C) but, as shown in Figure 4, was strongly affected by acquisition time and distance to the device.

As these laboratory tests were performed using a common procedure, the results could be compared giving a common grid evaluation that could be used to guide device choice. For instance, for an acquisition time of 5-minutes at a distance of 4000 m and at a temperature of 20°C, repeatability and error of the 7 devices tests with the described procedure are given in Table 1.

If the need is to get a device which demonstrates a repeatability of 0.1°C and an error of ±1°C, over 4 km with 5 minutes acquisition time, the common comparison grid reveals that only one device is acceptable.

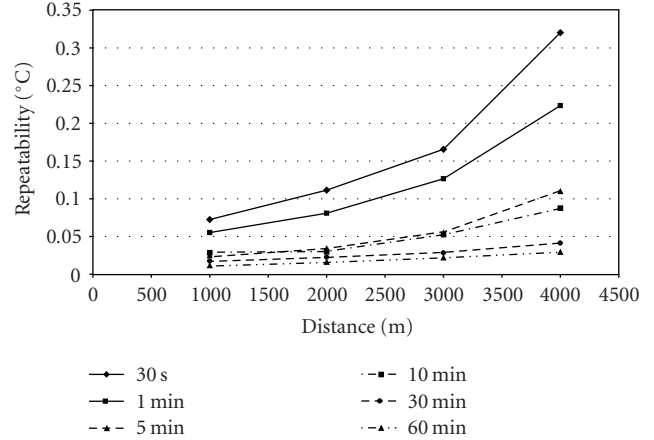


FIGURE 4: Example of repeatability results for one device tested showing the influence of acquisition time and distance from the device.

TABLE 1: Example of compared performances obtained with the described procedure for 7 devices, for an acquisition time of 5 minutes, at a distance of 4 km and at a temperature of 20°C.

| Raman device no. | Repeatability °C | Error °C |
|------------------|------------------|----------|
| A | 0.06 | <0.1 |
| B | 0.11 | -0.2 |
| C | 0.11 | -0.2 |
| D | 0.29 | 4.6 |
| E | 0.43 | -0.4 |
| F | 0.57 | -0.2 |
| G | 0.58 | 0.6 |

Meanwhile tests were being performed, Raman technology improved significantly. The comparison grid must be regularly up-dated.

4.2. *Mock-up Evaluation of the SHM Technique.* In order to evaluate the whole SHM system, that is to say an optoelectronic device paired with a sensing cable and a data processing method, a mock-up evaluation proved to be necessary. More precisely external parameters (air temperature, solar influx...) may compromise detection.

A full-scale mock-up was designed: a basin was built in 2006 at the Cemagref facilities, in the South of France, during the Eureka HYDRODETECT project. As described in [21] and sketched in Figure 5, the basin is composed of controlled soil materials. It enables realising artificial leaks with controlled flow rate. The optical fibers are included inside the mock-up and connected to an optoelectronic Raman device installed in a specific cabinet near the basin. Pt100 sensors, used as reference sensors, complete the instrumentation.

Raman raw measurements give a poor sensitivity to leaks (Figure 6).

As illustrated in Figure 7, specific data algorithms proved to be essential for efficient leakage detection.

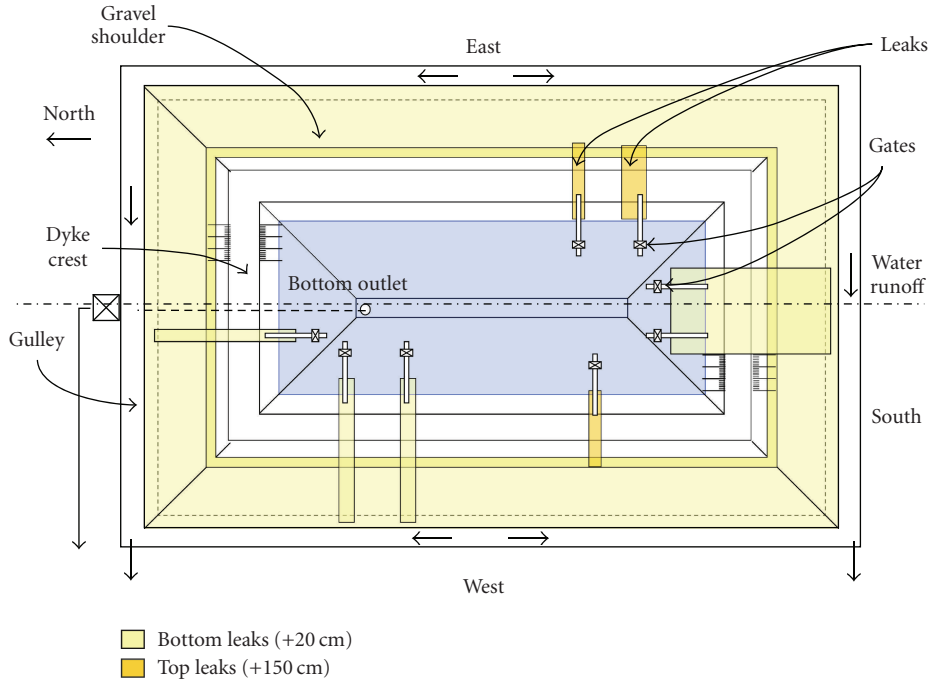


FIGURE 5: Full-scale basin equipped with 3 levels of optical fibers and artificial leaks.

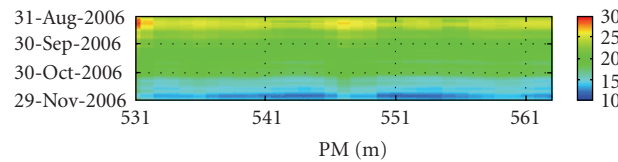


FIGURE 6: Raman temperature measurements obtained along one fiber when 3 leaks are created on the west side of the basin.

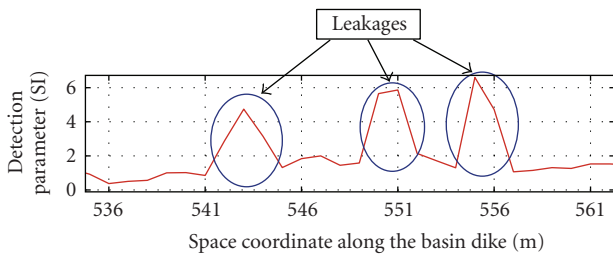


FIGURE 7: Detection of 3 leakages imposed in the West side of the basin based on raw Raman measurements given in Figure 6 processed with a specific algorithm.

At this stage, the data obtained with this mock-up enabled determining the sensitivity of the whole sensing system for leakage detection: it enables detection with a flow-rate as low as 1 L/m/min [22]. In the future, beyond detection, the data will then be used to provide quantitative information. To do so, it is planned to develop a more complex algorithm to assess leakage flow rate based on dike modelisation. The mock-up will be essential for algorithm validation as leakage flow rate cannot be accurately measured on field with traditional instrumentation as flowmeters.

4.3. On-Field Implementation. To complete laboratory and mock-up evaluations, two field installations were realized. The first dike installation is located in the South-East of France and was equipped in 2002 with a 2.3 km hybrid cable including 4 multimode optical fibers and 6 copper wires. Electrical wires ensure heating mandatory to test active method [16]. Figure 8 is a picture of the dike and related cable. The second dike installation is located in the North-East of France and was equipped in 2006 with 2 similar cables of 1 km. The cables are embedded at the toe of the dikes at about 1 m deep.

4.3.1. Material Recommendations. These installations enabled testing and validating several aspects of an on-field implementation. First, the cable has to be robust in order to endure real civil engineering works conditions: handling, soil compaction, and so forth. Moreover, it must resist to chemical aggressive environment (water and salinity). Inside dikes, rodents happened to destroy a cable, which can be solved by metallic protections. As a consequence, it is recommended to choose hybrid telecommunication cables meant for soil embedment. Moreover, its rigidity limits bending radius to approximately 0.5 m. For instance, Leoni supplies the cable described above.

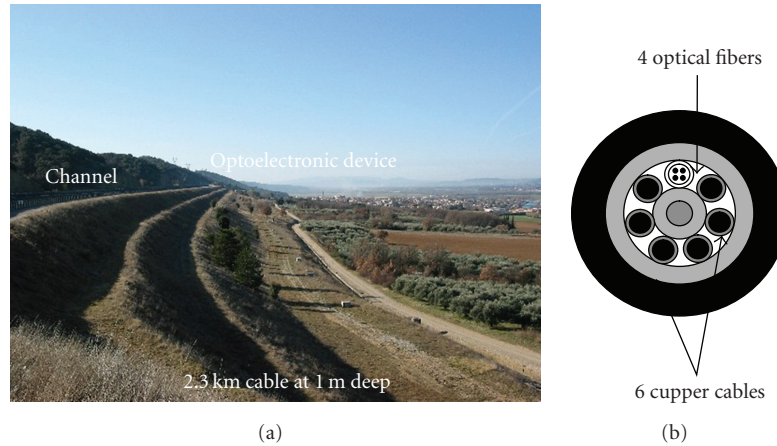


FIGURE 8: On-field installation in the South East of France.

Second, attention must be paid to selection of complementary materials. For both cases, the Raman devices were located within hydraulic power plants. The electromagnetic interferences generated by transformers and ambient temperature variations ruined measurements: approximately 50% time for the first two years of acquisition. Optoelectronic devices had to be included inside shielded and temperature regulated cabinets, with Uninterruptible Power Supply. Apart from the interrogation unit, E2000/APC connectors were chosen for eye safety reasons. At the other extremity, at the end of the cable, the fiber was placed inside a closure within a cable connection pit for ulterior extension of the installation.

While dealing with distributed data, a major difficulty is accurate event localization. Indeed, optoelectronic devices provide measurements in curvilinear abscissa along the sensing cable, which is far from the Euclidian distance at the surface of the dike. In practice, the sensing cable crosses a cable connection pit every 1 km. Such access points enable creating artificial events by cooling or heating the cable, thus producing a clearly recognizable signal to which a known position on the structure can be attributed.

Similarly with longitudinal localization difficulty, transversal positioning is required. When an event is detected by this SHM technique, the soil needs to be dug to verify whether it is due to a leakage. To facilitate detection of cable position, in order to minimize digging works, commercially-available RFID devices were buried with the cable. This significantly enhances practical use of the technique.

Third, as instrumented structures are distant from end-users, remote controlled solutions were implemented to provide rapidity in data processing and related warnings.

Last, but not least, to perform valuable measurements, Raman systems require reference measurements, as clearly learnt from experience. To do so, Pt100 are included in the cabinet to enable easy and periodic device calibration. What is more, the 4 fibers are spliced by pair at the far extremity of the cable in order to create an optical loop. As a result, the Pt100 is artificially compared to Raman measurements at

two locations, one extremely closed and the second very far from the device. It also avoids maintaining reference sensors on-field.

4.3.2. Data Processing. Raman temperature measurements have been successfully acquired continuously for several years on both sites.

Various analysis methods were developed [22, 23] and compared. For one site, one year measurement postprocessing identified suspected areas. These results are in accordance with visual inspection reports from the owner.

4.4. Dike Monitoring Conclusions: A Success. Distributed temperature sensing thanks to Raman scattering into optical fibers was studied by EDF since the beginning of 2000s to detect leakages in dikes. The qualification methodology based on (i) laboratory (ii) mock-up evaluation under controlled conditions, and (iii) on complementary on-field tests was positively conducted. The metrological behavior of optoelectronic Raman devices of the market was evaluated. The sensitivity of the SHM technique was determined thanks to a Full-scale basin. Two industrial installations were realized in real conditions.

On the basis of the positive results obtained during the last years, EDF concludes to the qualification of this SHM technique and decides to improve the surveillance of 2 industrial sites per year by this monitoring technique. Overall results demonstrated efficiency of this whole leakage detection system based on Raman optical fiber sensing. Ongoing developments focus on quantification of leakages.

Another perspective is to take advantage of similar systems with embedded optical fibers into dikes to perform underground hole detection, as recently reported [24, 25]. As a matter of fact, internal erosion has two main consequences: water leakage and soil deformation. For this perspective, strain distributed measurements are needed.

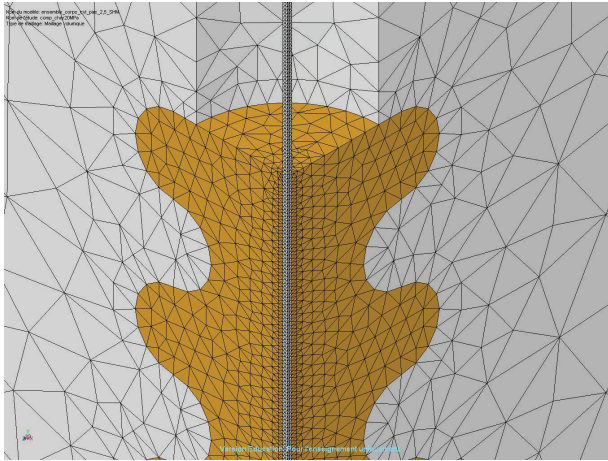


FIGURE 9: Sensor coating design with finite element calculations.

5. Structural Health Monitoring of Concrete Structures Based on Strain Distributed Optical Fiber Sensors

Optical fiber distributed strain sensing systems were evaluated in view of concrete structure monitoring. Instrumentation of this structure material is of major importance for Andra, as underground repository galleries and intermediate level radioactive long-lived waste disposal cells within future geological repository are likely to have an instrumented concrete lining. Similarly, LCPC and EDF are in charge of many concrete structures where safety is to be justified to authorities. Thus, monitoring is implemented in power plants, concrete dams, and a few bridges having particular features.

5.1. Sensing Cable Design and Experimental Validation. As mentioned in Section 2.3, special attention is to be paid to the way the optical fibers are linked with the structure, in order to perform accurate distributed temperature and strain measurements.

LCPC started developing a sensing cable dedicated to concrete instrumentation in 2002 within the EOLBUS French national project. At that time, distributed strain Brillouin sensing units were becoming commercially available, but very few related sensors were offered. More precisely, in order to perform continuous measurement of concrete strain over very long distances, the challenge is to ensure a continuous link between the host material and the optical fiber with an optimized transfer of strain and temperature fields.

As described in great detail in [26], a composite-made wave-like sensor coating was designed so as to enable continuous bonding between optical fiber and concrete. As illustrated in Figure 9, finite element analysis showed that the stiffness of the optical fiber can be adapted to the concrete's, reducing strain concentrations and the need for a theoretical calibration factor. Moreover, unlike the body of traditional I-shaped sensors (for instance vibrating wire sensor), wave-like

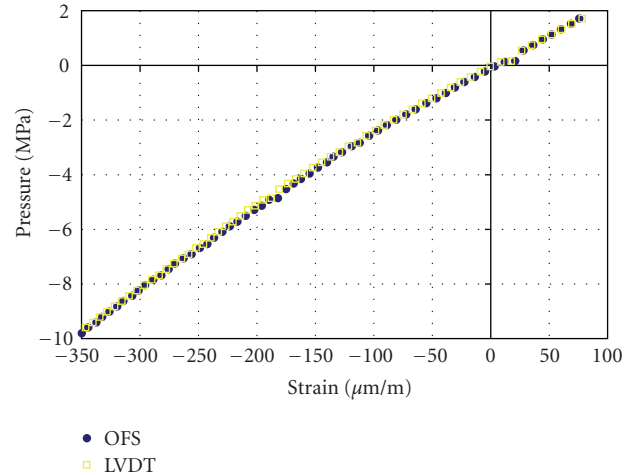


FIGURE 10: Experimental laboratory validation of interferometric wave-like sensors placed into small-concrete samples.

sensor body should enable symmetrical response in tensile and compressive loadings whatever the contact conditions may be.

First, experimental validations were performed with low-coherence interferometry measurements instead of truly distributed measurements. Indeed, the 1 m spatial resolution of Brillouin-OTDR instruments prevents from direct comparison with reference sensors whose lengths are around 10 cm. Partial mirrors were inserted inside the optical fiber core so as to realise short optical fiber gauges that can be interrogated by a low-coherence interferometer [26]. Experiments with 10 cm sensors embedded into concrete cylinders placed under press (see Figure 10) as well as field trials with 70 cm sensors [27] showed a very good agreement between the wrapped optical fiber extensometers and the reference extensometers placed nearby. Strain measurement threshold as low as $\pm 1 \mu\text{m}$ per meter of extensometer basis was reached. Despite its wave-shape, the proposed sensor body does not introduce any losses or strain that would result from fiber microbendings.

Then, the experimental validations were performed with truly distributed measurements [28]. One major difficulty encountered at this stage was the realization of representative-scale test structures, compatible with the 1 m spatial resolution of commercially-available Brillouin-OTDR (at the time, Brillouin instruments with centimetric spatial resolution were restricted to laboratory experiments). A 3 m long concrete beam ($300 \times 50 \times 25 \text{ cm}^3$) was equipped with electronic temperature sensors and mechanical strain gauges near 2.8 m optical fiber sensing cables. These sensors were composed of standard single-mode optical fiber (G652 type and others) wrapped into the wave-like composite coating and paired with a commercially available Brillouin-OTDR. Temperature measurements during concrete beam casting agreed with reference measurements, and showed the significant sensor coating influence. A month later, strain measurements performed during a four-point bending experiment showed promising results: linearity and



FIGURE 11: Picture of concrete slab pouring when concrete embeds reference sensors.

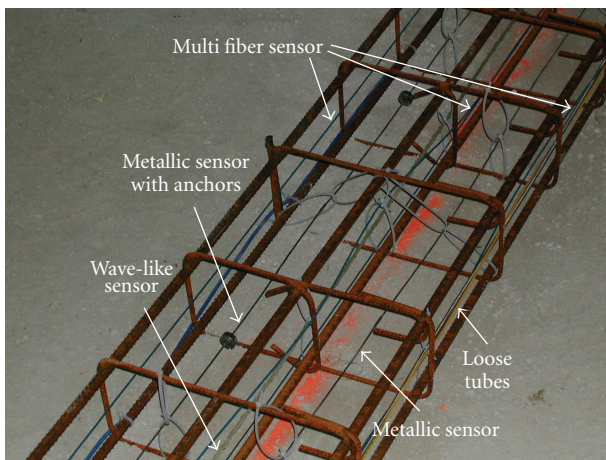


FIGURE 12: Optical fiber sensing cables fixed on reinforcing bar frame embedded into a concrete slab.

reliability of measurements were demonstrated, under tensile as well as compressive loadings.

These developments lasted from 2002 to 2006. They highlighted that Brillouin sensing practical implementation is restrained by three major limitations: (i) the 1 m spatial resolution, (ii) the poor repeatability in the order of magnitude of 1°C and $20\ \mu\text{m}/\text{m}$, and (iii) the separation of temperature and strain influences.

Spatial resolution has recently been improved with centimeter spatial resolution claimed by two industrial suppliers of Brillouin instrument and extensively demonstrated in laboratories [6, 29–32]. Moreover, although not based on Brillouin scattering, the OBR instrument claims distributed strain sensing with the centimeter spatial resolution (see Section 2.2.3). Separation of temperature from strain influence has also been extensively studied for the last 3 years. Both improvements have been tested in an outdoor test described in Section 5.2.3.

5.2. Outdoor Test. As illustrated in Figure 11, Andra's Technological Exhibition Facility construction was an opportunity to compare the laboratory performances of optical fiber measuring chains (sensors and optoelectronics) with field conditions. It is a $4700\ \text{m}^2$ industrial building hosting exhibits of various prototype equipments such as containers, large machines for radioactive waste handling (for instance, a waste disposal container pushing robot), with the purpose of communicating with the general public and enhancing their understanding of geological repositories for radioactive wastes.

As illustrated in Figure 12, several optical fiber sensing cables were installed at the core of the building concrete slab during summer 2008 construction. Five commercially-available sensors meant for distributed strain sensing had been selected after prior mechanical and thermal laboratory tests. Only two appeared promising for strain distributed sensing, among which the wave-like sensor depicted in Section 5.1.

5.2.1. Material Recommendations. Sensor connections are of major importance. They necessitate extreme care during any handling which slower the instrumentation process. The optical fiber line was 250 m long interrupted by 18 FC/APC connectors and two splices. Unexpectedly, few fiber splices were degraded, whereas connectors appeared well suited even in terms of power budget. For civil engineering application, standard telecommunication splices revealed too stiff. Yet connectors are likely to degrade because dust size is similar with optical fiber core one.

Uncertainty on the measurement location remains a challenge. Following prescription proposed in [33], as the fiber line was composed of different sensor types, all assigned to a specific Brillouin frequency shift, localisation was already ensured every 10 m. Moreover, inspired by dike instrumentation know-how, the instrumentation map was drawn with a heating device enabling various controls prior to concrete pouring.

5.2.2. Data Processing: Temperature Influence Compensation. To filter out temperature influence on strain measurements performed by Brillouin scattering instruments, various methods were developed based on the signal analysis [34] or the choice of the optical fiber type [35–37]. These solutions remain at a research and laboratory stage. As industrial solutions, loose tubes (where the optical fiber is supposed to be mechanically isolated) are often implemented, sometime inserted inside the same sensing cable [14]. An alternative is to pair a single-mode Raman device (single-mode is mandatory for strain sensing) with a distributed strain sensing instrument into a single optical fiber. These two industrial solutions were implemented during concrete pouring of Andra Technological Space slab: loose tube and combination of Raman and Brillouin scattering were implemented for temperature compensation.

The results reported in [38] and illustrated in Figure 13 highlighted the need for careful means while associating Raman and Brillouin technologies. Raman temperature

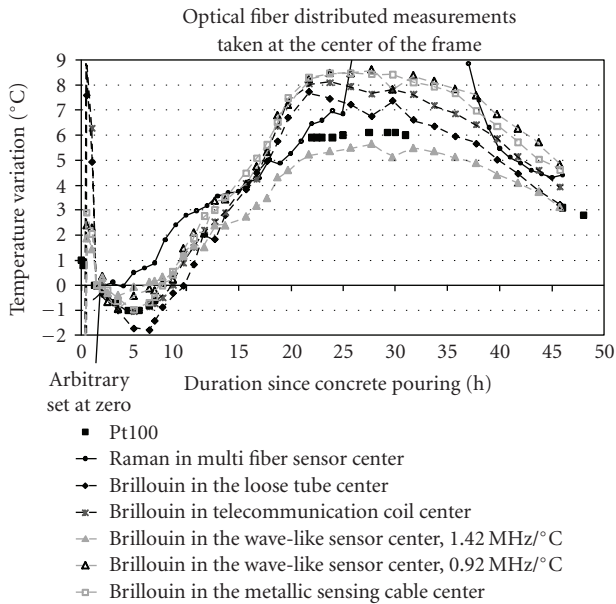


FIGURE 13: Distributed temperature measurement during concrete hardening: Reference sensors versus Raman and Brillouin distributed optical fiber sensors taken at the center of the frame.

measurements turned out to be more accurate than B-OTDR ones. The confidence acquired for dike instrumentation presented in Section 4 is, however, restricted to multimode Raman distributed temperature sensing, which was also previously tested in the laboratory. When single-mode fibers were used, sensitivity to curvature was enhanced and skewed measurements obtained during our field application (see Figure 13 after 25-hour measurements). Therefore, as no Brillouin device is available to provide measurements on multimode fibers, the necessary use of single-mode fibers prevents a combination with Raman measurements on the same fiber. While choosing a Raman single-mode device, special attention must be paid to the optoelectronic instrument working wavelength related to the sensing cable fiber. Raman Stokes intensity is a few times larger than anti-Stokes intensity and its bandwidth is usually much larger than the pump spectrum which degrades accuracy. Moreover, some of the phenomena at the origin of optical fiber losses (bending losses especially in single-mode fibers, hydrogen darkening...) are wavelength-dependent, which may ruin the method mentioned in Section 2.2.1, based on the ratio of the intensity of the two Stokes and Anti-Stokes lines: the wavelength separation between these two lines reaches 80 nm at 1.55 μm (typical single-mode device working wavelength) versus 10 nm at 514.5 nm. Recent developments implemented in most recent instruments combine various laser wavelengths [39]. To conclude, single-mode Raman device advantages and drawbacks are to be evaluated as proposed in Section 4.1.

The test of the alternative solution, the association of Brillouin instrument with sensing cable isolated form mechanical solicitation, is also detailed in [38]. It has been observed that loose tubes suffered from frictions were locally



FIGURE 14: Picture of containers movements on the instrumented concrete slab.

sensitive to strain and therefore cannot be yet considered as temperature sensors while paired with B-OTDR.

5.2.3. *Strain Sensing Outdoor Test with OBR (Correlated Rayleigh Measurements)*. The instrumented part of the concrete slab is now hosting heavy concrete containers, up to 15 tons that can be handled thanks to an overhead travelling crane. Distributed strain measurements can thus be performed.

Among the five sensing cables (2 loose tubes, 2 metallic sensors, 1 wave-like sensor), one broke during the first months after concrete pouring. It could be withdrawn of the sensing chain thanks to a connection pit inspired by dike instrumentation know-how, as detailed in Section 4.3. Without such care, the entire distributed measurement system would have been compromised.

Brillouin-OTDR measurements were performed few months after pouring. Seasonal thermal variations are the main detected phenomenon. Few measurement points do not follow the global sensing chain behavior, but the 1 m spatial resolution and the 20 $\mu\text{m}/\text{m}$ repeatability limit accurate interpretation. New optoelectronic Brillouin units with improved spatial resolution have not been tested yet. The distributed strain sensing experiment described in this subsection deals with relative Rayleigh measurements performed by the OBR instrument.

Inside the same sensing line, measurements were performed in June 2009 with the OBR instrument described in Section 2.2.3. As relative measurements are needed to derive strain, concrete containers were (i) lifted as illustrated in Figure 14 and then (ii) piled up one on the other.

Although total weight could reach 19 T (6.6 T and 12.4 T for first and second containers, resp.), induced strain in the slab did not exceed a few microstrains. With such small events, temperature variations, although smaller than 0.8°C, induced misinterpretations. Once corrected, the two types

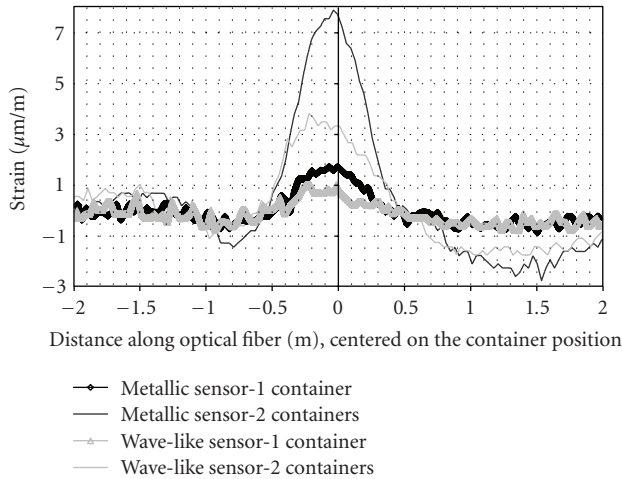


FIGURE 15: Distributed strain measurement performed by relative Rayleigh-OFDR measurements along two different strain sensing optical fiber cables.

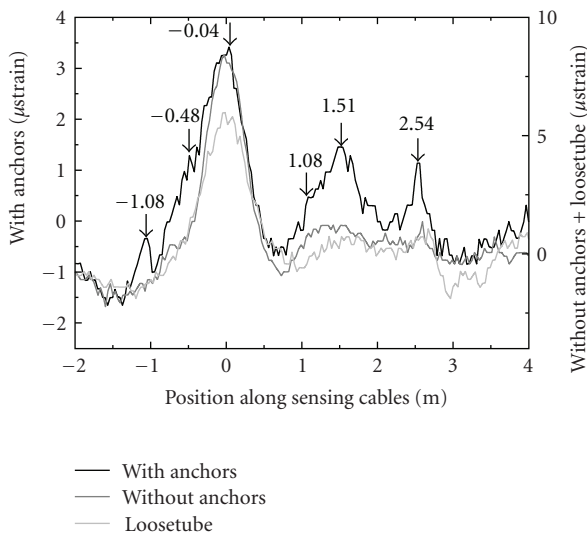


FIGURE 16: Distributed strain measurement performed by relative Rayleigh-OFDR measurements along the “loose tube” and the two metallic sensors, highlighting the influence of the anchors.

of optical fiber sensor coating, namely, wave-like composite coating and metallic coating, detect charges as showed in Figure 15. Differences between the two sensors can be correlated with (i) cable transfer functions and (ii) slightly different locations. As stated in Section 2.3, this experimental test highlights the influence of the sensor coating.

Another example of sensor coating influence is shown in Figure 16, which plots the measured strain along the loose tube and the two metallic sensing cables. As a reminder (cf. Figure 12), these metallic sensing cables differ by the addition of anchors every 50 cm on one of them, with the intention to enhance sensor adhesion to concrete. Localized strain peaks are observed every 50 cm. They reflect artificial measurements induced by the presence of these anchors. The anchors’ addition thus revealed unnecessary (it did not

improve sensor adhesion to concrete) and degraded the strain field transfer function.

Figure 16 also showed that the specific loose tubes dedicated to temperature measurement and theoretically insensitive to strain were as sensitive to strain as the strain sensing cables. At this stage, it would however seem premature to generalize this result to all commercially available loose tubes.

Moreover, false events occurred along all sensing cables (not shown), in locations corresponding to outside coating variations, such as entrance into protective tubes to reach extracting cable room. Importance of an accurate instrumentation map is enhanced. As will be described elsewhere, measurements are also in great accordance with theoretical response and with the VWS placed nearby. This test confirmed that distributed sensing gives access to the complete data curve describing structure response to a solicitation, and thus allows for example to locate and measure the strain field maxima. Results obtained using only localized sensors are highly sensitive to the initial choice of location and may “miss” the location and magnitude of maximum strain. This outdoor test, despite the difficulties and lessons learnt in relation to adequate choice and implementation of material, as well as to adequate temperature compensation, could nevertheless demonstrate the usefulness of distributed measurements for structural health monitoring. It therefore highlights the key advantages of distributed optical fiber sensors over localized, optical fiber of other traditional sensors, in providing for a more comprehensive monitoring of a civil engineering structure.

5.3. Conclusions on Strain Sensing in Concrete Structures.

As a conclusion, strain distributed sensing systems are still limited by temperature influence. Neither loose tube nor association with Raman instrument proved to be efficient within the described field applications. For concrete structure monitoring, sensing systems based on Brillouin-OTDR are limited by poor accuracy (1 m spatial resolution combined with 20 μm/m resolution). However, using the same fibers and pairing them with a high-spatial resolution and high-strain-sensitive optoelectronic instrument (OBR), two types of strain sensing cable showed very promising results to monitor concrete slab evolutions.

6. Overall Conclusion

Civil engineering instrumentation is in rapid evolution, in particular because optical fiber sensors are moving from the laboratories to the field applications after almost 30 years of developments.

Various types of optoelectronic instruments are commercially available and may be paired with many different sensing cables to provide either temperature or strain distributed measurements. As a result, it may be difficult to select the combination of technologies (sensing cable and optoelectronic interrogation method) best suited for a given application.

Two civil engineering applications were described: water leakage detection in dikes and concrete structures monitoring. Laboratory validation process revealed mandatory before any outdoor experiment. Specific methods are proposed to evaluate (i) commercially-available optoelectronic instruments namely, Raman distributed temperature instruments and (ii) sensing cable including optical fibers for strain sensing. Pairing these different sensing chain components needs advised end-user as successful outdoor tests require careful consideration of all elements influencing the measurement chain, as well as considerations related to an adequate choice of reference sensors and related to temperature compensation. A number of recommendations and lessons learnt were described in this article.

In particular, signal location along the distributed measurements over the fiber, and the correlation with actual structure position proved to be a major issue. Descriptions of various localization processes were proposed. The importance of optical fiber ends (connectors, splice, cable connection pits) was underlined. The influence on the sensing cable outside coating has also been highlighted. For water leakage detection in dikes, advanced data processing revealed mandatory. In the future, it should enable improving the ability of the optical fiber system from detection to quantification of water leakage. For concrete structures monitoring, a remaining limitation is temperature compensation on strain measurements.

Taking into account these considerations, distributed temperature and strain sensing now proves to be an efficient and unmatched tool for structural health monitoring.

References

- [1] J. M. Lopez-Higuera, *Handbook of Optical Fiber Sensing Technology*, John Wiley & Sons, New York, NY, USA, 2002.
- [2] A. Rogers, "Distributed optical-fiber sensing," *Measurement Science Technology*, vol. 10, no. 8, pp. 75–99, 1999.
- [3] S. Delépine-Lesoille, E. Merliot, and Y. Gautier, "Optical fiber strain sensors for use in civil engineering: state-of-the-art, industrial applications and outlook," BLPC no. 272, October–November 2008.
- [4] J. M. Ko and Y. Q. Ni, "Technology developments in structural health monitoring of large-scale bridges," *Engineering Structures*, vol. 27, no. 12, pp. 1715–1725, 2005.
- [5] J. Beller, "OTDRs and backscatter measurements," in *Fiber Optic Test and Measurement*, D. Derickson, Ed., chapter 11, Prentice-Hall, Upper Saddle River, NJ, USA, 1998.
- [6] D. Garus, K. Krebber, F. Schliep, and T. Gogolla, "Distributed sensing technique based on Brillouin optical-fiber frequency-domain analysis," *Optics Letters*, vol. 21, no. 17, pp. 1402–1404, 1996.
- [7] M. Froggatt and J. Moore, "High-spatial-resolution distributed strain measurement in optical fiber with Rayleigh scatter," *Applied Optics*, vol. 37, no. 10, 1998.
- [8] K. T. Wan and C. K. Y. Leung, "Fiber optic sensor for the monitoring of mixed mode cracks in structures," *Sensors and Actuators A*, vol. 135, no. 2, pp. 370–380, 2007.
- [9] A. J. Rogers, "Polarization optical time domain reflectometry: a new technique for the measurement of field distribution," *Applied Optics*, vol. 20, no. 6, pp. 1060–1074, 1981.
- [10] Z. Liu and A. K. Kim, "Review of recent developments in fire detection technologies," *Journal of Fire Protection Engineering*, vol. 13, no. 2, pp. 129–151, 2003.
- [11] S. Großwig, A. Graupner, E. Hurtig, K. Kühn, and A. Trostel, "Distributed fiber optical temperature sensing technique—available tool for monitoring task," in *Proceedings of the 8th International Symposium on Temperature and Thermal Measurements in Industry and Science*, June 2001.
- [12] G. P. Agrawal, *Nonlinear Fiber Optics*, Academic, New York, NY, USA, 3rd edition, 2001.
- [13] M. Nikles, L. Thevenaz, and P. A. Robert, "Simple distributed fiber sensor based on Brillouin gain spectrum analysis," *Optics Letters*, vol. 21, no. 10, pp. 758–760, 1996.
- [14] D. Inaudi and B. Glisic, "Distributed fiber-optic sensing for long-range monitoring of pipelines," in *Proceedings of the 3rd International Conference on Structural Health Monitoring of Intelligent Infrastructure*, Vancouver, Canada, 2007.
- [15] Qualification guide FD CEN/TR 14748, "Non-destructive testing—methodology for qualification of non-destructive tests," 2005.
- [16] O. Kappelmeyer, "The use of near surface temperature measurements for discovering anomalies due to causes at depths," *Geophysical Prospecting*, vol. 5, no. 3, pp. 239–258, 1957.
- [17] J.-J. Fry, "Détection de fuite sur les digues par acquisition de profils de température le long d'une fiber optique," in *Sécurité des Digués Fluviales et de Navigation, Congrès Français des Grands Barrages*, Orléans, France, November 2004.
- [18] J.-M. Henault and S. Blairon, "Exemple d'application de capteurs à fibre optique—détection de fuites dans les digues en terre par thermométrie à fibre optique," in *Colloque Contrôle et Mesures Optiques pour L'Industrie (CMOI '06)*, Arcachon, France, 2006.
- [19] ISO/IEC Guide 99, "International vocabulary of metrology—basic and general concepts and associated terms (VIM)," 2007.
- [20] S. Blairon and J.-M. Henault, "Evaluation d'interrogateurs à fibre optique pour la mesure de température," in *Proceedings of the 14th International Congress of Metrology*, Paris, France, 2009.
- [21] C. Guidoux, Y.-H. Faure, O. Artières, et al., "Measurement results on full scale field experiment using optical fibre detection methods," *Wasser Wirtschaft*, vol. 97, no. 10, pp. 66–68, 2007.
- [22] P. Cunat, Y.-L. Beck, J.-J. Fry, J.-R. Courivaud, and J.-P. Fabre, "Leakage detection based on temperature measurement with fiber optic: methods and results," in *Colloque HYDRO*, Lyon, France, 2009.
- [23] A. A. Khan, V. Vrabie, J. I. Mars, A. Girard, and G. D'Urso, "A source separation technique for processing of thermometric data from fiber-optic DTS measurements for water leakage identification in dikes," *IEEE Sensors Journal*, vol. 8, no. 7, pp. 1118–1129, 2008.
- [24] V. Lanticq, E. Bourgeois, P. Magnien, et al., "Soil-embedded optical fiber sensing cable interrogated by Brillouin optical time-domain reflectometry (B-OTDR) and optical frequency-domain reflectometry (OFDR) for embedded cavity detection and sinkhole warning system," *Measurement Science and Technology*, vol. 20, no. 3, 2009.
- [25] M. Kihara, K. Hiramatsu, M. Shima, and S. Ikeda, "Distributed optical fiber strain sensor for detecting river embankment collapse," *IEICE Transactions on Electronics*, vol. E85-C, no. 4, pp. 952–960, 2002.
- [26] S. Delépine-Lesoille, E. Merliot, C. Boulay, L. Quénel, M. Delaveau, and A. Courteville, "Quasi-distributed optical fibre extensometers for continuous embedding into concrete:

- design and realization,” *Smart Materials and Structures*, vol. 15, no. 4, pp. 931–938, 2006.
- [27] S. Delépine-Lesoille, E. Merliot, Y. Gautier, L. Quétel, M. Delaveau, and A. Courteville, “Multiplexed long-base flexible optical fiber extensometers and temperature bragg sensors interrogated by low-coherence interferometry,” *IEEE Sensors Journal*, vol. 8, no. 7, pp. 1145–1151, 2008.
- [28] V. Lanticq, M. Quiertant, E. Merliot, and S. Delépine-Lesoille, “Brillouin sensing cable: design and experimental validation,” *IEEE Sensors Journal*, vol. 8, no. 7, pp. 1194–1201, 2008.
- [29] L. Zou, X. Bao, Y. Wan, and L. Chen, “Coherent probe-pump-based Brillouin sensor for centimeter-crack detection,” *Optics Letters*, vol. 30, no. 4, pp. 370–372, 2005.
- [30] K. Hotate and T. Hasegawa, “Measurement of Brillouin gain spectrum distribution along an optical fiber using a correlation-based technique-proposal, experiment and simulation,” *IEICE Transactions on Electronics*, vol. E83-C, no. 3, pp. 405–411, 2000.
- [31] A. W. Brown, B. G. Colpitts, and K. Brown, “Dark-pulse Brillouin optical time-domain sensor with 20-mm spatial resolution,” *Journal of Lightwave Technology*, vol. 25, no. 1, pp. 381–386, 2007.
- [32] L. Thévenaz and S. Foa Leng Mafang, “Distributed fiber sensing using Brillouin echoes,” in *19th International Conference on Optical Fibre Sensors*, vol. 7004 of *Proceedings of SPIE*, Perth, Western Australia, April 2008, 70043N.
- [33] N. Honda, M. Inoue, N. Araki, and Y. Azuma, “New optical fiber line testing system function for highly accurate facility location using Brillouin frequency shift assigned optical fiber,” in *Proceedings of the Optical Fiber Communication Conference*, Optical Society of America, 2009, paper no. OWU3.
- [34] P. C. Wait and T. P. Newson, “Landau Placzek ratio applied to distributed fibre sensing,” *Optics Communications*, vol. 122, no. 4–6, pp. 141–146, 1996.
- [35] C. C. Lee, P. W. Chiang, and S. Chi, “Utilization of a dispersion-shifted fiber for simultaneous measurement of distributed strain and temperature through Brillouin frequency shift,” *IEEE Photonics Technology Letters*, vol. 13, no. 10, pp. 1094–1096, 2001.
- [36] L. Zou, X. Bao, V. Afshar, and L. Chen, “Dependence of the Brillouin frequency shift on strain and temperature in a photonic crystal fiber,” *Optics Letters*, vol. 29, no. 13, pp. 1485–1487, 2004.
- [37] M. Froggatt, D. Gifford, S. Kreger, M. Wolfe, and B. Soller, “Distributed strain and temperature discrimination in unaltered polarization maintaining fiber,” in *Proceedings of the 18th Optical Fiber Sensors Conference*, Optical Society of America, Cancun, Mexico, 2006, paper no. ThC5.
- [38] J.-P. Dubois, S. Delépine-Lesoille, V.-H. Tran, et al., “Raman versus Brillouin optical fiber distributed temperature sensing: an outdoor comparison,” in *Proceedings of the 4th International Conference on Structural Health Monitoring on Intelligent Infrastructure (SHMII '09)*, Zurich, Switzerland, 2009.
- [39] C. Lee, K. Suh, and T. Landry, “The implementation of self calibration techniques in Raman backscatter based fiber optic distributed temperature system (DTS) technology,” in *Proceedings of the Transmission and Distribution Conference and Exposition*, pp. 1–6, 2008.